DETONATION AND THE HYDRODYNAMICS OF REACTIVE SHOCK WAVES

Roger A. Strehlow

Department of Aeronautical and Astronautical Engineering
University of Illinois, Urbana, Illinois

INTRODUCTION

The contents of this review may be conveniently separated into two rather distinct parts. On the one hand this review covers our current understanding of detonation as a unique natural phenomena, while on the other hand the review discusses the limitations that hydrodynamics places on the utility of the shock tube as a tool for studying high temperature reaction kinetics. Specific reaction kinetic studies are not covered because they are so extensive that it is difficult to do them justice in a short review. The reader is referred to recent more extensive reviews for this purpose[1-5].

DETONATION

I. Theories Relating to Structure and Stability

The Zel'dovich[6], von Neumann[7], Doring[8] (ZND) model of a one-dimensional steady detonation wave as a shock discontinuity followed by a zone of homogeneous chemical reaction is probably the most useful concept to evolve prior to the mid 1950's. Even though this model must now be modified to accommodate non-steady and three-dimensional effects, its implication that an element of the flow may be treated as containing an exothermic chemical reaction triggered by a strong shock, which may in itself be handled as a discontinuity in the flow, represents a useful tool for understanding the structure and non-steady behavior of detonation waves.

The Chapman[9]-Jouguet[10], (CJ), concept that a minimum steady one-dimensional mass flow exists for any specific exothermic system undergoing reactive shock transition is at present useful only insofar as it allows a rather exact calculation of the velocity and pressure in a detonation wave. Unfortunately, at the present time, this success must be considered to be either fortuitous or at least empirical because recent work has shown that a one-dimensional detonation traveling at the CJ velocity is dynamically unstable.

The first attempt to look at time-dependent stability in a detonation wave was made by Shchelkin[11] in 1958. He used a square wave detonation as his model. In this model the chemical reaction is concentrated at the CJ plane and this plane is separated from the shock wave by an induction zone. In his model, he perturbed the position of the CJ plane with time and discussed the consequences of this perturbation. He found that the detonation will be unstable to this type of perturbation if the induction zone reactions have a sufficiently large activation energy. This model is unrealistic because one cannot truly cause the CJ plane to suffer a perturbation, since it is a steady concept. However, Shchelkin was the first to discuss the effect of a time-dependent perturbation on stability.

Since 1963, there have been a number of papers[12-19] which discuss the stability of the square wave detonation. However, recent work on detonation stability, using models which allow for an extended heat release

zone, show quite definitely that all the interesting amplification mechanisms which lead to instability occur in the region of heat release. Therefore, the square wave model appears to be unsuitable for discussing stability.

Two approaches have been used to investigate the stability of a ZND detonation wave with an extended reaction zone. Erpenbeck[20-21] has examined stability by following the response of the shock discontinuity to a purely transverse harmonic perturbation in the flow downstream of the shock wave (i.e., in the reaction zone). His analysis is applicable to disturbances of arbitrary wave length but requires a model for the heat release reactions throughout the entire reaction zone. He has not formally examined the CJ detonation case, but has always worked with detonations that have some arbitrary overdrive. His analysis, which is performed in Laplace transform space, is very complex and he finds that stability in the general case can be discussed only by resorting to numerical techniques. His results indicate that the occurrence of instability is dependent on the frequency of the disturbance, the activation energy of the first order heat release reaction that he has used in his model and the amount of the overdrive present in the detonation. In a following paper, Erpenbeck[22] has extended his analysis to transverse waves of high frequency. In this case, he finds that there are three types of stability regimes which may be present in the reaction zone of the detonation. The type of regime that is present is dependent on the local value of the quantity $d(a^2-u^2)/dx$ where x is measured from the shock and a and u are the sound velocity and flow velocity at a point in the steady flow behind the shock. He observed that this quantity either increases, goes through a maximum, or decreases, in that order, as one passes from the shock wave to the plane where heat addition is terminated. If the quantity simply decreases in the reaction zone he finds that the detonation will be stable to a high frequency transverse wave. If this quantity goes through a maximum or if it increases, he finds that the detonation behaves unstably to a high frequency transverse perturbation. In the limit behavior which he investigated, the ultimate stability is found to be dependent on the activation energy of the first order chemical reaction which was assumed in the analysis. Specifically, systems with a sufficiently low activation energy were found to be stable.

In the other approach to the stability problem, Strehlow and Fernandes[23] and Barthel and Strehlow[24] have used a ray tracing technique to discuss the behavior of a high frequency coherent transverse acoustic wave in the reaction zone of a ZND detonation. They also find that the quantity $d(a^2-u^2)/dx$ is important to the behavior of these coherent transverse waves. For a transverse wave propagating in a flowing gas, the direction of propagation of the energy trapped in the acoustic front (i.e., the ray direction) is the direction which is of interest. They find that, in the region where the quantity $d(a^2-u^2)/dx$ is decreasing, an acoustic wave front of any orientation (except for one very specific orientation) subsequently passes through the reaction zone of the detonation at most only twice (due to reflection from the shock front). However a wave front of the proper orientation was found to asymptotically approach the plane where $d(a^2-u^2)/dx$ has a maximum value. Furthermore, this ray was found to subsequently propagate parallel to the shock front for an infinitely long time. Thus, if the detonation did not have a plane where $d(a^2-u^2)/dx$ was maximum, their theory also predicted that the detonation would be dynamically stable to a transverse wave perturbation. They also noted that since the ray propagating at the plane $d(a^2-u^2)/dx$ = maximum is propagating in a region where a temperature and

density sensitive exothermic chemical reaction is occurring, its rate of amplitude growth is dependent on the details of the chemical reaction. Briefly, they came to the conclusion that any exothermic reaction that has been observed in nature would produce transverse wave amplification under these conditions.

In the region where the quantity $d(a^2-u^2)/dx$ is increasing they found another interesting behavior. In this region, wave fronts which have a particular range of initial orientations convolute with time in such a manner that an element of the wave front propagates some distance away from the shock front, then turns around and returns to the front to reflect and repeat the process. Since this behavior is occurring in a region which contains a temperature-sensitive exothermic reaction, it is also expected that the amplitude of this wave front will grow with time. Interestingly enough they found that this wave front eventually produces multiple shock contacts which asymptotically approach a regular spacing and that this spacing is dependent on the extent and the detailed structure of the reaction zone of the detonation.

Relative to the problem of longitudinal instability in detonation waves, Erpenbeck[21] has performed an analysis for transverse waves with arbitrarily long wave lengths (which effectively become a longitudinal disturbance in the flow). He once again found values of overdrive above which instability occurs. In a recent paper, Fickett and Wood[25] have performed a one-dimensional non-steady method of characteristic analysis on a propagating overdriven detonation produced by a piston motion. They carried their analysis out to very long times and observed a continued large oscillation in the shock velocity for the case that Erpenbeck predicted would be unstable. They also observed no sustained oscillations for one of Erpenbeck's stable cases. In a following paper, Erpenbeck[26] has been able to predict the magnitude of these large scale oscillations by extending his analysis to include nonlinear terms.

From the above we see that one should expect hydrodynamic instabilities in many of the flow situations in which a shock wave is closely followed by exothermic chemical reaction. Specifically, these results show that the CJ plane is not important to the occurrence of flow instabilities and therefore that the self sustenance of detonation is not a requirement for instability. In other words, the instabilities observed on self-sustaining detonations are quite certainly a restricted example of a general class of hydrodynamic instabilities which occur in flows containing a heat release zone following a shock transition.

II. Structure

A number of investigators have observed that essentially all detonations propagate with a complex non-steady frontal structure. Early work in this area was performed primarily by Russian investigators and has been summarized in a number of recent Russian texts.[27,28,29,30] The primary findings of these and subsequent investigators is that the main shock front consists of many sections which are locally convex towards the upstream flow and the intersection of these sections are traveling across the front as waves (see for example the early photographs obtained by White[31]). Both the occurrence and structure of these transverse waves are intimately connected to the chemistry of the reactions occurring in the detonation. In the following sections our current understanding of the nature of this transverse structure and its interaction with the chemistry will be discussed.

a. The Nature of Transverse Waves

The transverse waves that propagate across the front of a detonation have been found to occur at the front as Mach stems or triple shock intersections of finite amplitude[27,32,33]. The single spin detonation that occurs in a round tube is unique because it was the first non-one-dimensional structure to be observed and because it is the only example of a transverse wave structure which is steady in the proper coordinate system. (In this case, the coordinate system which renders the wave motion steady is one which rotates at the spin frequency with its axis of rotation along the tube axis.) Spinning detonation contains a very complex double Mach stem pattern which has been described by Voitsekhovskii, Mitrofanov and Topchian[27] and verified by the careful work of Duff[32] and Schott[33]. In all other observed transverse structures, there are always opposing transverse waves propagating across the front simultaneously and the structure at the front is necessarily two or three-dimensional non-steady.

At the present time, all the details of this complex structure are not understood. However, as mentioned above, it is known that these transverse waves consist of Mach stem interactions at the front. These have been observed experimentally, both on propagating detonations[34,35,36] and as an artifically produced reactive Mach stem on the "laminar" detonation which White and Cary[37] first produced by expanding an overdriven detonation through a cylindrical nozzle. A spark interferogram of such an artifically produced Mach stem and an analysis of its triple point structure is shown in Figure 1. This structure was observed by White and Cary[37] and analyzed by Strehlow.[38] Strehlow found that even though the shock triggered a highly exothermic reaction a few microseconds after it passes an element of the gas, the triple point structure is still controlled by an unreactive-unreactive slipstream balance. The observations on propagating detonations have not been analyzed as extensively at the present time. There are still serious questions concerning the disposition of the reflected shock and the manner in which it interacts with the reaction zone.

The triple points propagating on the shock front of the detonation have been found to have the property that they will "write" a line on a smoked surface. This behavior was first observed by Antolik[39] in 1875 and was used by E. Mach in conjunction with his studies of spark discharges and the interaction of shock waves produced by bullets fired in the laboratory. The technique lay dormant for over 80 years until in 1958, Denisov and Troshin[40] started to use it to study detonation structure. Oppenheim and Utriew[41] have recently verified that the triple point is writing the pattern by direct laser schlieren photography looking through the smoked film.

This property has been very helpful in the study of transverse wave phenomena in detonations. To perform an experiment, one simply smokes a surface with either wood, acetylene, kerosine, or any other appropriate smoke and exposes it to the detonation. After exposure the film is "fixed" with a clear lacquer spray. The quality is almost as good as that of a photographic negative. A few examples of smoke track records obtained with detonations propagating in a rectangular tube are shown in Figure 2.

In Figure 3, the results of studying a symmetric interaction using the smoke track technique are summarized[42]. In this case, a number of sand grains were placed on the smoke plate before the detonation

passed over the plate and each grain wrote a wake pattern whose axis is normal to the local orientation of the leading shock wave of the detonation. The intersection geometry is therefore completely determined and one may calculate all shock and flow properties in the neighborhood of the intersection. From this calculation one concludes that the normal shock velocity is discontinuously increased by about 30 to 40% at the center line of the intersection and therefore that all portions of the leading shock are attenuating very rapidly in the detonation. This is very disturbing, because even though the shock is locally propagating at a velocity which varies from 10 to 20% below CJ to 10 to 20% above CJ, the detonation as a whole is still observed to propagate at very close to the CJ velocity. The mechanism which makes this possible is not understood at the present time.

b. Acoustic Coupling and Limits

The transverse waves on the detonation front exhibit a degree of regularity which is dependent on the geometry of the detonation tube and on the chemical system which is supporting the detonation. The effect of detonation tube geometry is primarily caused by the fact that the high pressure regions propagating across the front (immediately behind the Mach stem) produce transverse pressure waves in the gas column following the front and that these transverse waves have a tendency to couple with resonant transverse modes of the gas column downstream of the front. Manson[43] and Fay[44] predicted this behavior for near limit detonations approximately 15 to 20 years ago. It now appears, however, that this coupling is incidental to the occurrence of transverse waves on the front. For example, Duff and Finger[45] have observed transverse structure on a spherical detonation. However, the occurrence of transverse waves on the front is not incidental to the self-sustenance of the detonation wave. It has been noted repeatedly in the literature that as the initial pressure is lowered or as the detonable mixture is diluted with an inert gas, the characteristic spacing of the structure gets larger. It also has been observed that the last transverse frontal structure that occurs in any specific tube corresponds to the lowest transverse acoustic mode of the hot gas column following the front in that tube. In the case of round tubes, this mode is the single spin mode. It is also now quite certain, that detonations propagating just inside these limits propagate at an average velocity lower than the CJ velocity. This is evidently caused because a significant fraction of the chemical energy released in the reaction zone resides in transverse wave energy for an appreciable length of time in these limit detonations.

In certain chemical systems, the tube geometry has a very marked effect on the regularity of the writing pattern. Figure 4 illustrates that extremely regular patterns can be observed in rectangular and planar (very narrow rectangular) geometries. Incidentally, the planar mode occurs when the preferred transverse spacing of the detonation is at least five times the width of a narrow channel. It is the simplest self-sustaining detonation mode which may be studied, since it is two-dimensional non-steady. In other chemical systems however, it has been observed that the regularity of the transverse structure is poor in all tube geometries. Typical smoke track records are shown in Figure 2 and results for a number of fuel-oxidizer mixtures are summarized in Table 1. The reason for this behavior has not been discovered at the present time. It is, however, quite obviously related to the chemistry of the system which is detonating.

c. Spacing of Transverse Waves and Chemistry

In systems which show a reasonably regular writing pattern in rectangular tubes, it has been observed that the characteristic size of the pattern is dictated by the initial pressure level and the dilution[42]. The transverse wave spacing of regular smoke track patterns is usually defined as the average distance between two successive waves propagating in the same direction measured along a line parallel to the average orientation of the leading shock wave, i.e., along the diameter of the tube.

The most extensive data on spacing has been taken in the hydrogen-oxygen system containing argon as an inert diluent. This data is summarized and compared with the acoustic predictions for the spacing and with average induction zone and recombination zone lengths in Figure 5. Here the recombination zone length has been approximated by normalizing the reciprocal of the maximum rate of recombination and using the flow velocity at the start of recombination. We notice from this figure that the spacing is always larger than the sum of the induction plus recombination zone lengths in this system and therefore that each element of the detonatable mixture is never traversed by more than one transverse wave of the same family before it completes its reaction. We also note from Figure 5 that the spacing predicted from the acoustic theory is considerably less than any of the reaction lengths or than the spacing of the transverse wave at the front of the detonation. Thus it appears that the acoustic theory cannot be used to predict the spacing of the finite amplitude transverse waves that are observed on propagating detonations. This is not surprising, however, since the interaction of opposing waves appears to be the regulating mechanism in a propagating detonation[42]. However, it is interesting that the spacings which are measured and the spacings which are calculated using the acoustic theory are roughly proportional to each other.

d. Spontaneous Growth of Transverse Waves

The acoustic theory of Strehlow and Fernandes[23] predicts that coherent transverse waves should grow in amplitude as they propagate through the reaction zone of the detonation and the Barthel and Strehlow[24] theory predicts that a single acoustic front should convolute to produce a number of evenly spaced shock contacts after some time. This contention has been verified experimentally for at least one case, during the homogeneous initiation of detonation behind a reflected shock wave in a hydrogen-oxygen-argon mixture. Figure 6 contains an (x,t) initiation photograph and a smoke track record obtained simultaneously on a side wall of the tube. It is interesting to note that during this nicely one-dimensional initiation experiment, very weak transverse waves appear on the front and then grow in amplitude (as indicated by an increase in the refraction of opposing waves at their intersection). In a recent paper, Strehlow, Liaugminas, Watson and Eyman[42] have shown that the appearance location on the smoke track records may be used to predict a reasonably constant exponential coefficient for the linear theory of acoustic growth. From these experimental results we may deduce that there is little doubt but that the acoustic theory of amplitude growth offers a viable mechanism for the appearance of the finite amplitude transverse waves that occur on propagating detonations.

III. Initiation and Failure

a. Flame to Detonation Initiation

This subject has been studied extensively in tubes of varying geometry and in many chemical systems. By far the most quantitative study of the subject has been performed by Oppenheim, Urtiew and co-workers[46-52] at Berkeley. The phenomena is complex and the process of flame acceleration (eventually leading to detonation) is very dependent on the condition of the tube walls and the presence of obstacles in the flow.

In general the process develops in the following manner. A flame, generated at the closed end of tube produces a compression wave in the gas which steepens into a shock wave some distance from the end of the tube. This flow develops a boundary layer which becomes turbulent and causes the flame to accelerate. The acceleration of the flame then subsequently reinforces the original shock wave. Eventually, the shock preheats the gas sufficiently to cause the onset of detonation. However, the actual occurrence of detonation is sometimes obscured by the proximity of a very turbulent flame in the neighborhood of the initiation point and in general the process is not one-dimensional. The acceleration process depends very strongly on the ratio of the burning velocity to the sound velocity in the combustible mixture. High values of this ratio cause more rapid acceleration in the system and therefore cause a shorter detonation "induction" distance. If the tube has a finite length and is closed at both ends, shock reflection from the far end may occur before ignition. The reflection process will always preferentially trigger detonation and it has the added disadvantage that it produces very high pressures before the detonation occurs. This type of initiation is extremely important to the prediction of possible hazardous detonations in large industrial installations. It appears, from the information now available that one may make quite realistic estimates of the possibility of detonation for any specific apparatus and combustible mixture.

b. Homogeneous Initiation

Homogeneous one-dimensional initiation has been observed behind a reflected shock wave in a conventional shock tube[54,55,56]. Figure 6 shows an x,t schlieren inferogram of such an initiation process. The gas dynamics of this process have been modeled by Gilbert and Strehlow[56] using an (x,t) method of characteristics analysis. They assumed that each element of the gas reacts with kinetics which are dependent only on the previous time-temperature pressure history and that the gas dynamics may be modeled in a conventional manner. The results of their analysis agreed with experimental observations of high temperature reflected initiation in every detail and showed that this type of initiation process is directly caused by the interaction of reaction kinetics and inviscid gas dynamics. In short, they found that because shock heating is a wave process it generates a reaction wave which interacts with and accelerates the shock wave in a manner which is completely predictable if the kinetics are well understood. Furthermore they found that for this process thermal conduction and diffusion are unimportant to the wave development process.

In a following work, Strehlow, Crooker, and Cusey[57] have experimentally and theoretically studied the process of detonation initiation when a step shock wave passes into a slowly converging channel. Once again they observed that the first point of initiation, in real time, in the converging channel could be predicted by simple application of non-steady gas dynamics and the proper reaction kinetics.

c. Hot Spot Initiation

The most extensive studies of initiation have been performed in the hydrogen-oxygen system[56,58,59]. At high temperature and low pressure this system exhibits a strictly homogeneous initiation behavior in simple flow geometries. However at low temperature (900°-1100°K) and high pressure (i.e., at high reactant concentrations) the system shows a very unusual type of initiation which is difficult to categorize. At its first appearance, the initiation occurs as a series of "hot spots" and these propagate in a number of spherically growing flames until the coalescence of these flames leads to the initiation of detonation. An example is shown in Figure 7. This behavior appears to occur in the pressure and temperature region which is roughly above and to the left of a line on a (P,T) explosion limit diagram obtained by extrapolating the second limit line into the "explosion" region. It appears that this behavior occurs under conditions where appreciable quantities of the species HO_2 are able to accumulate in the mixture[59]. More quantitative work on this type of initiation is needed.

d. Detonation Failure

In this reviewer's estimation the problem of detonation failure has not adequately been studied at the present time. It is quite apparent that each frontal element of a self-sustaining detonation is failing at a rate which is quite rapid when compared to the rate of heat release in the reaction zone. It is also true that if the detonation is allowed to propagate into an enlargement of the tube, sections of the detonation are observed to "fail" because opposing transverse waves are not reflected from the wall and momentarily fail to intersect[60]. However there has never been a truly quantitative study of this process. To date there has been only one theoretical study of this problem and this study is relatively incomplete. Strehlow and Hartung[61] constructed a "steady" one-dimesional overdriven detonation and then allowed it to interact with a strong rarefaction fan approaching it from the rear. The kinetics were assumed to be zero order with a constant activation energy. Rapid failure of the detonation was found to occur for activation energies of 18 and 50 kcal. For a third case, when the activation energy was assumed to be zero, the results were inconclusive because the detonation did not decay to below the CJ velocity. As mentioned above, more work is needed on failure of detonation waves.

IV. The Use of Detonations in Reaction Kinetic Studies

There have been two major techniques developed to study reaction kinetics in actual detonations. White and Cary[37] have produced "laminar" detonations by passing an ordinary detonation through a convergent-divergent nozzle. While this flow is non-steady it is still useful for rates studies. They have applied it to the study of vibrational relaxation in exothermic systems and to the study of the effect of vibrational relaxation processes on induction zone kinetics. This technique has also been used to study induction zone kinetics by Mullaney and co-workers[62,63]

In another technique, a one-dimensional detonation has been stabilized in a wind tunnel and the reaction profile studied by observing the pressure profile downstream of the normal shock[64]. This technique has interesting engineering implications because it measures overall rates of heat release directly in a nicely controlled one-dimensional geometry.

Unfortunately, it appears that all attempts to resolve the reaction zone in ordinary self-sustaining detonations are doomed to failure, because of the presence of transverse waves. Soloukhin in his discussion of what are, in his terminology, "multi-fronted detonations"[60], has pointed out that either averaging across the transverse structure with optical techniques or using pressure transducers at the wall will always yield results which are incorrect in terms of a one-dimensional theory. Thus the utility of ordinary propagating detonations for kinetic studies is at best marginal.

SHOCK TUBE HYDRODYNAMICS

Since the inception of its use in the early 1950's the chemical shock tube has greatly expanded the temperature range available for quantitative experimental studies of the physico-chemical properties of gases. The success of its application as a research tool may be gauged by the fact that throughout the world the extant chemical shock tube literature consists of over a thousand references[65,1] and is presently being increased at the rate of approximately 150 references per year.

In the field of reaction kinetics studies, there are two fundamental reasons for this success. In the first place the step shock wave produced during the operation of an ideal shock tube yields an extremely precise and reproducible heating cycle with excellent initial conditions. In the second place the shock tube is particularly suited for studies in systems that are highly diluted with an inert gas and studies in such dilute systems have consistently yielded the best quantitative kinetic data. Therefore, one might say that gas dynamics is the servant which allows one to make relatively precise rate measurements at high temperatures in a chemical shock tube. However, it is also the master of the situation in that, (1) the geometry of the chemical shock tube is dictated primarily by gas dynamics considerations, (2) specific gas dynamics non-idealities limit the utility of the apparatus and (3) the coupling of the chemical reaction and the gas dynamics is always important to the study of reaction kinetics; particularly in exothermic systems.

At the present time sufficient information has been compiled concerning the behavior of shock tubes, so that the design of a shock tube for precise chemical rate studies is possible. This portion of the paper will present a critical discussion of the relative merite of various experimental techniques and in addition will review recent work on non-ideal shock tube behavior and recently acquired knowledge concerning the occurrence of those flow idealities caused by the presence of exothermic reactions.

I. Studies Behind "Steady" Incident Shock Waves

The most precise measurement of a chemical reaction rate constant may be obtained by observing the reaction immediately behind the incident shock wave produced in a conventional shock tube. For the

highest precision it is imperative that these measurements be made at high dilution in a monatomic gas and that both the rate measurement and the shock velocity measurement be extrapolated to the instant the shock uncovered the observation station. In all other cases flow non-idealities will cause difficulties in the interpretation of the data. This type of extrapolation is possible in only certain specific cases, for example, in the study of the initial dissociation rate of a diatomic or more complex molecule. Typical examples of investigations which have yielded results of high precision using this technique are the measurements of the dissociation rate of triatomic molecules by Olschewski, Troe and Wagner[66,67,68,69], the measurement of hydrogen dissociation by Myerson, Thompson and Joseph[70] and the measurement of oxygen atom recombination by Kiefer and Lutz[71].

In cases where the reaction process must be followed for a long time after shock passage the measurement of a correct rate is not really very straightforward. The raw data after being reduced with the help of ideal shock tube theory must still be corrected for the non-ideal flow behavior in the particular tube that is being used in the experiment. Since combustion drivers, heated gas drivers, double diaphragm tubes, detonation drivers, etc., produce notoriously non-ideal flow situations in the test gas, we will discuss correction procedures which must be used for only the simplest driving process: a cold gas driver operating with a simple pressure burst in a conventional constant area shock tube. Even in this case there are three overlapping but relatively independent corrections which must concern the investigator if he is to obtain reasonable rate constants. The first of this concerns the diaphragm material used in the study. Diaphragm opening time is a function of both the inertia and the tearing properties of the diaphragm material[72,73]. Probably the best material in this respect is cellulose acetate because it disintegrates so thoroughly on bursting. Mylar is quite slow and irregular and has been shown to produce irreproducible late pressure pulses[74] (probably due to flapping or late tearing) which could lead to scatter in the rate measurements. Metal diaphragms in general appear to open rather slowly but reasonably reproducible, if scored uniformly.

It has been observed that even when reproducible, the rate of the diaphragm opening process is extremely important in determining the early behavior of the shock tube flow. White[72] and Alpher and White[73] have shown that for a slow diaphragm opening process, the shock velocity increases for a considerable distance and only then exhibits the decay that one would expect from boundary layer growth. It has been shown theoretically that this slow acceleration may easily yield velocities which are slightly above the theoretical velocity for that bursting pressure ratio. Since this is the formative period for the shock wave, it is best to make kinetic measurements outside of this region. This region extends for a distance from the diaphragm clamp which is a function of the diaphragm material, the bursting pressure ratio and the tube diameter. White[72] reports an accelerating shock 40' from the clamp with a metal diaphragm in a 3 1/4" square tube at M = 15 in argon. However at a shock Mach number of 8 he found that the maximum velocity occurred only 12 feet from the diaphragm. If one remains clear of this accelerating region the major problem which may arise from the diaphragm bursting process is the problem of late spurious pressure signals from materials such as mylar.

Other flow non-idealities that occur in a shock tube during the late flow are all connected to the development of the boundary layer behind the incident shock. These effects have been reviewed by Spence and Woods[75] and by Holbeche and Spence[76]. In addition, Mirels[77,78,79,80,81], in a number of papers has discussed the seriousness of this problem. If one assumes an ideal diaphragm burst it has been found that the flow essentially divides itself into two regimes. The first of these is a period when the shock is decaying due to the boundary layer growth. During this period, the length of the hot column of test gas is growing at a reasonably constant rate that is somewhat below the theoretical rate predicted by ideal theory. After this initial period the boundary layer has grown to such an extent that it is accumulating test gas from the main sample at the same rate as the incident shock is accumulating new test gas. In this situation, the rate of decay in the incident shock velocity becomes less than before and the length of the test gas column becomes relatively constant. This effect was first reported by Duff[82]. Recently Fox, McLaren and Hobson[83] have shown that Mirel's theory quite adequately predicts the observed behavior.

There are two distinctly different types of corrections necessary because of these flow non-idealities. In this paper the effects of non-ideal flow will be discussed for only the state property temperature because reaction rates are primarily temperature sensitive. In the first place the shock wave is continually decelerating -- at first rapidly and later slowly -- and this introduces a temperature gradient in the gas sample which can be large. This temperature gradient may be calculated if one assumes that the shock attenuates at a specific rate and that there are two possible limit behaviors for the pressure decay behind the front. These are: 1. Each fluid element retains its shock transition pressure. In this case the gas contains a relatively step pressure gradient due to attenuation and 2. Each element of gas after shock compression, is isentropically expanded to the instantaneous shock transition pressure. The real behavior behind the decaying shock lies somewhere between these two limit behaviors. These two assumptions yield the following equations for the temperature gradient in the gas following the shock wave.

1. With a residual pressure gradient (no pressure change after shock transition)

$$\frac{dT_2}{T_1} = \frac{4(\gamma-1)}{(\gamma+1)^2}\left(\frac{\gamma M_1^4+1}{M_1^2}\right)\frac{dM_1}{M_1}$$

2. With isentropic expansion

$$\frac{dT_2}{T_1} = \frac{4(\gamma-1)}{(\gamma+1)^2}\,\frac{(M_1^2-1)^2}{M_1^2}\,\frac{dM_1}{M}$$

Figure 8 is a plot of T_2/millisecond in the flow behind a shock wave in argon with an attenuation rate of 1% per meter. As this figure shows, the gradients are sizable and very dependent on the testing temperature T_2.

The second correction has been estimated by Mirels[81] on the basis of a boundary layer development theory. In his theory for the late flow he assumes a constant velocity shock wave propagating down the tube and he calculates the changes in flow properties along the tube axis due to

the boundary layer growth. His results are plotted as a function of the dimensionless distance from the shock wave l/l_m where l_m is the equilibrium length of the hot gas column. In general he finds that all state properties increase in value as one travels away from the shock. Specifically for a gamma = 5/3 gas at M = 3 he finds that the temperature rises to about 1.07 T_2 at a distance $l = 0.2\ l_m$ and then remains relatively constant for the remainder of the transit time. However he finds that an even more serious correction than this is the correction to the testing time that must be included for strong shocks. Specifically, the real testing time for a strong shock increases rapidly over the ideal testing time and at a position $l = 0.2\ l_m$ the real testing time is 3/2 of the ideal testing time. This has been verified quantitatively by Fox, McLaren and Hobson[83].

The non-ideal temperature drifts caused by the effects of shock velocity attenuation and boundary layer growth are in the same direction (each yielding a temperature increase as one travels away from the shock) and they may be added to a good first approximation. The testing time correction augments both of these temperature gradients and can in itself cause large errors if ideal flow is assumed. It appears as though some of the extant reaction kinetic data obtained in shock tubes should be re-evaluated in the light of these developments. It should be pointed out that these corrections can change the apparent activation energy of the reaction as well as the absolute rate because in all cases the correction becomes more severe as the run temperature increases.

In the previous discussion it was implied that dilution with an inert monatomic gas is desirable for accurate kinetic rate measurements. Modica and La Graff[84] have recently studied the decomposition of N_2F_4 using both argon and nitrogen as a diluent and their comparative results reinforce the contention that monatomic gas dilution is necessary to reduce the ambiguity of results. In another interesting experiment along these same lines Seery and Britton[85] have shown that xenon is apparently not a completely inert diluent during the dissociation of fluroine.

II. Reflected-Shock Time-Resolved Techniques

Rate measurements made behind the reflected shock offer certain advantages over measurements made using the incident technique. In particular, sampling with a time-of-flight or quadrapole mass spectrometer is possible and laboratory time is real time because the gas is relatively quiescent in the neighborhood of the end-wall. Also, for the same initial conditions the reflected technique produces considerably high temperatures than an incident technique.

In this section we will discuss some difficulties exhibited by only the simplest time-resolved reflected techniques, those in which a sample is drawn from the end wall for mass spectrometer analysis or in which an emission or absorption spectroscopic technique is used to observe a gas sample trapped near the back wall. In these cases the initial temperature behind a reflected shock may be calculated quite accurately from the incident shock velocity measured at the moment of impact, assuming that the gas is entirely inert. The shock velocity at impact must be determined by extrapolating upstream measurements and the calculation is only valid for the case where the reactant is highly diluted with a monatomic carrier gas. As in the case of incident measurements, if it is not possible to extrapolate

the rate to the shock, corrections for the flow non-idealities must be included to accurately determine the rates.

Boundary layer corrections are still important in this case. If one operates near the back wall (within approximately 5mm of the back wall) the testing time correction ceases to be important and if one operates with a monatomic carrier gas, bifurcation problems are not serious[86]. However the pressure rise in the gas traveling behind the incident shock does cause a serious perturbation to the pressure-time and temperature-time history of the gas sample trapped near the back wall. As the reflected shock propagates away from the back wall, it encounters this pressure increase and transmits signals to the gas at the back wall. Fortunately the sample near the back wall is compressed isentropically during this process and for a monatomic gas the temperature increase may be estimated rather accurately using the equation:

$$\frac{\Delta T}{T_2} = \frac{\gamma - 1}{\gamma} \frac{\Delta p}{p_2} \simeq 0.4 \frac{\Delta p}{p_2}$$

Thus a pressure gauge may be used to monitor the rate of pressure change at the back wall and this rate of change may be used to estimate the equivalent temperature drift near the back wall. Alternately, Mirels' theory may be used in conjunction with Rudinger's simplified method of characteristics analysis[87] to calculate a pressure and temperature change at the back wall for the particular shock tube and initial conditions of the experiment.

In the case of mass spectrometer analyses sampling techniques are important and the correction for heat transfer to the wall should be considered in any calculation[88]. These corrections are reasonably straightforward, however, since in this time scale convection does not occur. Therefore, only a conduction equation need be solved to determine the necessary correction. Heat transfer can also be important in spectroscopic techniques because absorption in the cold boundary layer gases at the wall can completely dominate the measurement in certain cases[89]. Allen, Textoris and Wilson[99] have developed an ingenious apparatus to circumvent this difficulty.

In addition to the above, reflected-shock, time-resolved techniques suffer from two unique difficulties related to the chemistry. In the first place, the occurrence of chemical reaction behind the incident shock cannot always be dismissed in an a priori manner but should be examined for each experimental system. This problem is particularly serious for a first order reaction with a relatively low activation energy and could also be serious for a second order reaction with a very low activation. In the second place, the occurrence of a reaction behind the reflected shock leads to a non-steady reflected shock behavior. There are two reasons for this; either the molecular weight or the enthalpy of the gas may change due to the occurrence of the chemical reaction. By far the most important of these two changes under ordinary conditions is the enthalpy change associated with the reaction process. If an endothermic reaction occurs behind the reflected shock, the shock wave will decelerate and this will cause a pressure decrease and an attendant isentropic temperature decrease at the back wall. Johnson and Britton[90] have discussed the main features of this flow and a detailed method of characteristic calculation of the interaction for the vibrational relaxation of oxygen has been reported by Nafzinger[92]. He found that the shock relaxation process

took approximately 7 τ_v where τ_v is the characteristic relaxation time behind the reflected shock at the back wall. He also observed that this non-steady process led to a substantial residual entropy gradient along the tube axis in the neighborhood of the back wall. The effect of exothermic reactions will be discussed in Section IVb.

III. Single Pulse Techniques

Single pulse techniques[93] suffer from a number of relatively distinct problems. In this reviewer's opinion, the sum total of these deficiencies are serious enough to make the technique very difficult for quantitative kinetic studies. It is, however, still a useful technique for qualitative and comparative studies for new or complex systems.

Let us first consider those difficulties that are inherent in a single pulse experiment performed with an ideal shock tube. Even in this case, there are five major problems which limit the technique's utility. These are: 1. Analyses are performed after the experiment is completed. Thus only stable products may be identified and, at best, only the systems overall behavior may be studied. Therefore the deduction of responsible individual reactions with a concordant determination of their rates is very difficult. 2. The heating cycle is not the same for the entire gas sample. Therefore, an average processing time must be estimated for the run. 3. Contact surface tailoring is necessary to obtain long test times and thereby reduce the errors caused by the averaging process mentioned in Part 2 above. However off-design tailoring will cause substantial temperature changes during the last (and usually major) part of the testing time and this is serious if the reaction has a high temperature sensitivity. 4. Cooling must necessarily be produced by a rarefaction fan and this introduces yet another uncertainty into the calculated testing time. 5. If the reaction is not thermally neutral, effects of self-heating must be included. These last two problems have been discussed by Palmer, Knox and McHale[94].

The non-ideality of a real shock tube flow compounds these problems. By far the most serious non-ideality is the growth of the boundary layer behind the incident shock. This leads to three distinct difficulties which cause problems. In the first place the temperature cannot be held constant for the desired testing time because the upward drift is always appreciable on a time scale of 1 to 4 milliseconds. Secondly, tailoring cannot be exact because of the shift in properties caused by the boundary layer growth. Thirdly, the growing boundary layer can entrain a sizable quantity of the test gas. Therefore the entire reactive sample is not treated by the test pulse. This last difficulty is particularly serious if the entire contents of the tube are being analyzed after the run and may be alleviated to some extent by analyzing only that portion of the test gas that was in the neighborhood of the back wall during the pulse cycle.

The majority of the difficulties mentioned above cause errors in both the activation energy and the actual magnitude of the rate measured with a single pulse tube. This is because the severity of most of these corrections increase as the temperature of the test run increases.

There have been many variations of the single pulse technique introduced in the past few years. Tsang,[95,96,97,98,99,100] for example, has applied the technique to the study of hydrocarbon decomposition and rearrangement reactions using a mixture that contains a small quantity of "propyl chloride" as a trace reactant. This specie is used to independently

obtain information on the temperature-time pulse so as to increase the accuracy of the experimental decomposition measurement. This type of "trace reaction" technique has utility only if it can be proved in an unambiguous manner that the trace reaction is occurring independently of the unknown reaction. It should have the highest accuracy when the activation energies of the two reactions are approximately equal.

Tschuchikow-Roux[101,102,103] has proposed a ball valve technique which may be used to isolate a sample either between the ball valve and the end plate of the tube or just in the bore of the ball valve. However, his heating cycle analysis is based on ideal shock tube flow theory and since he proposes to calculate heating time by subtracting two large times which are themselves calculated by using ideal theory, the accuracy of his calculation will be low. However, there is the possibility of improving the accuracy by including the necessary boundary layer growth corrections.

Lifshitz, Bauer and Resler[104] have introduced and used a tube with a side dump tank on the test section leg. In conjunction with this they operate the tube without a tailored interface. Instead they "tune" the length of the driver section by inserting plugs at the end wall so that the strong rarefaction fan in the driver gas, after reflecting from the end of the driver section, will overtake the contact surface at the instant that it is met by the reflected shock wave. Thus, testing time in the sample theoretically ranges from zero to approximately 2 t_{ave}. The technique suffers, however, from the fact that non-ideal boundary layer growth will always cause the contact surface to intersect the reflected shock earlier than the theoretical time. If this effect is not included in the "tuning" operation the test gas sample will suffer a complex time-temperature heating cycle and the interpretation of the data will be difficult. The presence of a side dump tank modifies the downstream flow in the test section but a reasonable constant shock velocity is still attained near the end plate. The side dump tank is used primarily to prevent multiple high pressure reflections in the gas sample. It is probably adequate for this purpose.

IV. Exothermic System Instabilities

In addition to all the difficulties mentioned above, in exothermic systems the application of the shock tube to reaction kinetic studies is limited by the occurrence of non-steady flow processes which may be triggered by the presence of the exothermic reaction. Specifically, two distinct types of flow instabilities may occur and it has been found that two independent criteria may be used to predict the occurrence of these instabilities on the basis of known flow properties of the particular system which is under investigation. The two criteria will be called the Chapman-Jouguet criterion and the tube diameter criterion.

a. The Chapman-Jouguet Criterion

Consider a gas mixture capable of sustaining a reaction which drives the system toward a state of full chemical equilibrium. With this restriction we define the mixture to be "exothermic" if, in the (P,V) plane, the Rayleigh line through the point (P_1,V_1) which just tangents the equilibrium Hugoniot represents a shock transition whose Mach number, M_{CJ}, is greater than unity. We call the value of this minimum Mach number for steady shock propagation the Chapman-Jouguet criterion for instability. It

may, of course, be calculated quite accurately if thermodynamic properties are available for the system in question.

An example of the application of this criterion may be discussed with the help of Figure 9. The system considered in this figure is a stoichiometric hydrogen-oxygen mixture diluted with various amounts of argon at the initial conditions $T_1 = 300^oK$ and $P_1 = 100$ torr. The unreactive shock temperature for a shock of Mach number $M = M_{CJ}$ is plotted versus the mixture composition in this figure. The vertical lines approximate regions in which studies have been reported, admittedly for different stoichiometrics and pressure levels (the numbers on the lines are reference numbers). The approximation is reasonably good because, however, pressure shifts the curve in Figure 9 only slightly and stoichiometry changes are effectively dilution changes on the basis of a CJ calculation. Region I, above and to the left of the stability line $M = M_{CJ}$, corresponds to the experimental conditions under which steady incident shock waves may be produced and studied in this system, while region II, below and to the right of the stability curve represents initial shock conditions for which a steady shock wave with chemical reaction cannot exist. Note that Belles and Lauver[107] worked with incident shocks just at the edge of region I and that all other extant incident shock studies were performed well inside region I. It is interesting that Belles and Lauver report instability difficulties at low temperatures.

In region II of Figure 1, kinetic studies must necessarily be performed in conjunction with a flow which is longitudinally non-steady. For this reason well controlled and reproducible initial conditions are important to the design of these experiments. For example, the simple fact that the initial flow produced by the diaphragm bursting process is neither one-dimensional nor reproducible obviates the use of a conventional incident shock technique for region II studies. There are, however, four shock tube techniques which either have been used or have a potential use for performing kinetic studies under region II conditions. These will be discussed individually.

The first of these techniques uses the reflected shock region. Reflected shock studies, when performed in a gas mixture with a high heat capacity ratio, yield a reasonably one-dimensional heating cycle with well defined initial conditions[54]. Even though the flow following reflection remains non-steady for an extended period of time (and indeed may yield a detonation wave propagating away from the end wall) the gas near the end wall may be used for kinetic studies since it is quiescent, it suffers no additional shock transitions after reflected shock pasage and its pressure-time history during the reaction process may be predicted reasonably well[55]. This technique has been used successfully by numerous investigators[54,105,106] in situations where the steady incident technique would not be applicable in terms of the CJ criterion.

The second technique consists of passing a weak, but well established, step shock wave produced in a conventional constant area shock tube into and through a section of tubing whose cross sectional area is slowly decreasing with distance. If the rate of decrease of area is sufficiently slow (a maximum wall angle to the center line of approximately 1^o for example) the flow will become a quasi one-dimensional non-steady flow in which the leading shock wave is

continually accelerating. In this situation a non-steady flow calculation is required to sort the reaction kinetics from the gas dynamics effects. This experiment has been performed and such a calculation has been made for a tube in which $d(\ln A)/dx = -k$ during convergence[57]. Figure 10 contains iso-temperature and iso-pressure plots in an (x,t) coordinate system for a typical theoretical run assuming that the flow is entirely inert. The region which is mapped is bounded by the leading shock wave, the reflected shock wave and the "explosion line". The locus of the "explosion line" in this figure was determined by assuming that the fraction of the delay time to explosion which has been used at each instant along each separate particle path may be calculated using the relation.

$$d\phi = \frac{dt}{\tau(T,P)}$$

where

$$\tau = \frac{A}{[O_2]} \exp(-E/RT)$$

With this model the points at which

$$\int_0^t \frac{dt}{\tau(T,P)} = 1$$

on each particle path describe the locus of the explosion line. This approach assumes that the reaction is thermally neutral during the induction period and therefore that the reaction does not interact with the flow. Furthermore, as presently constructed, the model only allows one to predict the location of the minimum time in the explosion line locus on an (x,t) plot since the effect of heat release during the explosion is not included in the model. Reference 57 contains a more complete discussion of this technique.

To this author's knowledge the third possible non-steady technique has not yet been applied to the study of reaction kinetics in exothermic systems. It is an incident technique which involves the use of a ball valve whose internal bore is exactly equal to the diameter of the shock tube. This type of ball valve shock tube has been used in the study of endothermic systems[101] and to prevent premature explosions in reflected shock studies[54]. If the initial pressure were adjusted externally before opening the valve and if the shock tube were operated vertically, density separation of an inert gas near the diaphragm and the explosion mixture downstream could be maintained until a well formed incident shock wave passes the location of the ball valve. Observation at a number of window stations downstream of the valve would then allow reaction kinetic studies to be studied even though the flow was non-steady. This technique has two advantages relative to the converging channel technique in that both the construction of the apparatus and the calculation of the flow would be simpler. A simpler calculation of the flow may be made because one may assume the flow in the reactive mixture to be pseudo steady until an

appreciable amount of chemical reaction has occurred. This technique also has an advantage over the reflected shock technique for those cases where the system to be studied cannot be diluted to repress bifurcation. This is because, in the ball valve technique only simple boundary layer growth can occur to perturb the incident flow.

The fourth possible technique involves direct expansion of an incident shock wave through a suitably instrumented two-dimensional nozzle. This technique has been described by White and Cary[37] and has been discussed in Section IVa.

b. The Tube Diameter Criterion

Even in circumstances where incident shock wave studies are allowable on the basis of the CJ criterion, transverse instabilities may appear during an experiment. This type of behavior has been reported by Schott[110], Schott and Bird[111] and Hawthorne[112] and is important to the kineticist because it can produce state variable fluctuations across the tube which may be misinterpreted if the usual one-dimensional assumptions are used in reducing the data.

Schott[110] has shown that in acetylene-oxygen mixtures diluted with 97.5 percent argon, this type of instability behavior produces soot track writings which are equivalent to those obtained when a self-sustaining detonation propagates over a smoked foil. This experimental evidence implies that the transverse instabilities observed in reaction kinetic studies in the shock tube are of the same type as those observed[42] on propagating detonations. This is really not very surprising since the theoretical results discussed in Section a show that detonation per se is not necessary for the appearance of transverse instabilities.

It is also known that all self-sustaining detonations exhibit a transverse wave spacing which is roughly proportional to the "thickness" of the detonations reaction zone. Thus, theoretical predictions and experimental observations both lead to the conclusion that the transverse structure associated with an exothermic reaction zone triggered by shock passage should exhibit a characteristic spacing which is roughly proportional to the reaction zone thickness.

One more experimental observation must be mentioned before we may present a criterion for the occurrence of transverse wave instability in a reactive shock wave propagating in a specific channel. Both Manson[43] and Fay[44] have shown that transverse structure fails to couple with transverse acoustic modes of the tube when the preferred transverse spacing at the front becomes somewhat larger than the major transverse dimension of the tube. Thus it appears that this type of resonance must be possible before transverse instabilities will appear.

Unfortunately, at the present time, the relation between the reaction zone thickness and the characteristic cell size of the structure is not known except for a few systems and then only in an empirical manner. Therefore, at the present time, the "tube diameter" criterion for the occurrence of transverse instabilities in a steady incident shock wave experiment must be stated as follows: Transverse instability may occur in a steady shock wave followed by exothermic reaction only if the bulk of the exothermic process occurs as close to the shock wave as the major transverse dimension of the tube.

This criterion correctly predicts the occurrence of the currently observed transverse instabilities during incident shock reaction kinetic studies in a shock tube. More quantitative information on this subject is available in Schott's report in this symposium volume.[113]

SUMMARY

Detonations in premixed gases contain a very complex internal wave structure which is related to the exothermic chemical reactions occurring behind the leading waves. This structure negates many of the classical one-dimensional arguments concerning detonation and the full reasons for its existence and form are not understood at the present time. The mechanism of self-sustenance of a propagating detonation is also open to question at the present time. The situation is not hopeless, however, because it appears that the application of the principles of non-steady reactive gas dynamics (in which all shocks are considered to be infinitely thin non-reactive discontinuities in the flow) will eventually allow a complete description of the structure from first principles.

The discussion of shock tube hydrodynamics indicates that while the shock tube is an extremely useful apparatus for high temperature gas phase reaction kinetic studies, it has its limitations. These are primarily caused by gas dynamic non-idealities due to boundary layer growth and to the interaction of the chemistry and the flow. The implication of this section is that a good kinetic rate measurement may be obtained from a shock tube experiment only if the full contribution of these non-idealities are considered.

REFERENCES

1. Bradley, J. N., Shock Waves in Chemistry and Physics, Wiley, New York (1962b).
2. Gaydon, A. G. and Hurle, I. R., The Shock Tube in High-Temperature Chemical Physics, Reinhold, New York (1963).
3. Greene, E. F. and Toennies, J. P., Chemical Reactions in Shock Waves, Academic Press, New York (1964).
4. Bauer, S. H., "Shock Waves", in Annual Review of Physical Chemistry, Vol. 16, Annual Reviews Inc., Palo Alto, Calif. (1965).
5. Strehlow, R. A., Shock Tube Chemistry, a chapter in Vol. II of High Temperature Physics, Chemistry and Technology, Pergamon Press (1967) (In Press).
6. Zel'dovich, Y. B., J. Exptl. Theo. Phys. (USSR) 10, 542, (1940): English Translation NACA TM 1261, (1950).
7. von Neumann, J., "Theory of Detonation Waves", Prog. Rept. No. 238, (April 1942) OSRD Report No. 549, (1942).
8. Doring, W., Ann. Physik, 43, 421 (1943).
9. Chapman, D. L., Phil. Mag. 213, Series A, 47, 90, (1899).
10. Jouguet, M., J. Math. Pure and Appl., 70, Series 6, 1, 347, (1905); 71, Series 6, 2, 1, (1906).
11. Shchelkin, K. I., Soviet Physics, JETP 9 (36), 416, (1959).
12. Erpenbeck, J. J., Ninth Symposium (International) on Combustion, (Academic Press, New York, N. Y.) p. 442, (1963b).
13. Zaidel, R. M. and Zel'dovich, Ya. B., Zh. Prikl. Mekh. i Tekh. Fiz., No. 6, 59, (1963).
14. Pukhnachov, V. V., Zh. Prikl. Mekh. i Tekh. Fiz., No. 4, 79, (1965).
15. Shchelkin, K. I., Dokl. Akad. Nauk, SSSR, 160, 1144, (1965b).
16. Ilkaeva, L. A. and Popov, N. A., Fiz. Gor. i Vzr., No. 3, 20, (1965).
17. Aslanov, S. K., Dokl. Akad. Nauk, SSSR, 163, 667-671, (1965).

18. Aslanov, S. K., Dokl. Akad. Nauk, SSSR, 169, 136-9, (1966a).
19. Kuznetsov, N. M., Dokl. Akad. Nauk, SSSR, 164, 1097, (1965).
20. Erpenbeck, J. J., Phys. Fluids, 7, 684, (1964a).
21. Erpenbeck, J. J., Phys. Fluids, 8, 1192, (1965).
22. Erpenbeck, J. J., Phys. Fluids, 9, 1293, (1966).
23. Strehlow, R. A. and Fernandes, F. D., Comb. and Flame, 9, 109, (1965).
24. Barthel, H. O. and Strehlow, R. A., Phys. Fluids, 9, 1896, (1966).
25. Fickett, W. and Wood, W. W., Phys. Fluids, 9, 903, (1966).
26. Erpenbeck, J. J., Phys. Fluids, 10, 274, (1967).
27. Voitsekhovskii, B. V., Mitrofanov, V. V. and Topchian, M. E., Structure of a Detonation Front in Gases, Izd-vo Sibirsk, Otdel. Akad. Nauk, SSSR, Novosibirsk, (1963): English Translation, Wright-Patterson Air Force Base, Report FTD-MT-64-527, (AD 633-821) February 1966.
28. Soloukhin, R. I., Shock Waves and Detonations in Gases, Mono Book Corp., Baltimore, Maryland, (1966c).
29. Shchelkin, K. I. and Troshin, Ya. K., Gasdynamics of Combustion, Mono Book Corp., Baltimore, Maryland, (1965).
30. Shchetinkov, E. S., Fizika Gorenia Gazov (Physics of Gaseous Combustion) Izadtel'stvo "Nauk" Glavnnaa Redaktsia Fiziko-Matematiches-koi Literatury, Moscow, (1965).
31. White, D. R., Phys. Fluids, 4, 465, (1961).
32. Duff, R. E., Phys. Fluids, 4, 1427, (1961).
33. Schott, G. L., Phys. Fluids, 8, 850, (1965).
34. Edwards, D. H., Parry, D. J., and Jones, A. T., J. Fluid Mech., 26, 321, (1966a).
35. Edwards, D. H., Parry, D. J. and Jones, A. T., Brit. J. App. Phys., 17, 1507, (1966b).
36. Oppenheim, A. K., Astron. Acta., 11, 391, (1965).
37. White, D. R. and Cary, K. H., Phys. Fluids, 6, 749, (1963).
38. Strehlow, R. A., Phys. Fluids, 7, 908, (1964b).
39. Antolik, K., Paggendorp Ann. Phys. und Chemie, 230, sec 2, 154, 14, (1875).
40. Denison, Yu. H. and Troshin, Ya. K., Doklady Akad. Nauk, SSSR, 125, 110, (1959): Translation, Phys. Chem. Sect. 125, 217, (1960).
41. Oppenheim, A. K. and Urtiew, P. A. (Private Communication, Summer 1966).
42. Strehlow, R. A., Liaugminas, R., Watson, R. H. and Eyman, J. R., Eleventh Symposium (International) on Combustion, Mono Book Corp., Baltimore, Maryland, p. 177, (1967).
43. Manson, N., Compt. Rend., 222, 46 (1946).
44. Fay, J. A., J. Chem. Phys., 20, 942, (1952).
45. Duff, R. E. and Finger, M., Phys. Fluids, 8, 764, (1965).
46. Oppenheim, A. K., Arch. Mekh. Stosowanej, 216, 405, (1964).
47. Oppenheim, A. K., Urtiew, P. A. and Weinberg, F. J., Proc. Roy. Soc. London, A291, 279, (1966).
48. Urtiew, P. A., Experimental Study of Wave Phenomena Associated with the Onset of Detonation, Report AS-65-1, Univ. of Calif., Berkeley, February 1965, (AD 621-214) (1965).
49. Urtiew, P. A., Laderman, A. J. and Oppenheim, A. K., Tenth Symposium (International) on Combustion, (The Combustion Institute, Pittsburgh, Pa.) 797, (1965).
50. Urtiew, P. A. and Oppenheim, A. K., Comb. and Flame, 9, 405, (1965).
51. Urtiew, P. A. and Oppenheim, A. K., Proc. Roy. Soc., 295, 13, (1966).
52. Urtiew, P. A. and Oppenheim, A. K., Eleventh Symposium (International) on Combustion, Mono Book Corp., Baltimore, Maryland, (1967).
53. Bollinger, L. E., Fong, M. C., Laughrey, J. A. and Edse, R., Experimental and Theoretical Studies on the Formation of Detonation Waves in Variable Geometry Tubes, NASA TN D-1983, June 1963.

54. Strehlow, R. A. and Cohen, A., Phys. Fluids, 5, 97, (1962).
55. Gilbert, R. B. and Strehlow, R. A., AIAA Journal, 4, 1777, (1966).
56. Soloukhin, R. I., Zh. Prikl. Mekh. i Tekh. Fiz., #4, 42, (1964).
57. Strehlow, R. A., Crooker, A. J. and Cusey, R. E., Comb. and Flame, 11, (1967) (In Press).
58. Schott, G. L. and Kinsey, J. L., J. Chem. Phys., 29, 1177, (1958).
59. White, D. R., "A Study of Shock Wave Induced Reactions," ARL Report 66-D177, Office of Aerospace Research, USAF Wright-Patterson AFB, Ohio, (September 1966) (AD 646-559).
60. Soloukhin, R. I., Comb. and Flame, 10, 51, (1966a).
61. Strehlow, R. A. and Hartung, W., Comb. and Flame, 9, 423, (1965).
62. Mullaney, G. J. and Arave, R., "Determination of Induction Times in One-Dimensional Detonations," Boeing Scientific Laboratory Research Report, D1-82-0324, Boeing Aircraft Corp., Seattle, Washington, (December 1963).
63. Mullaney, G. J., Ku, P. S. and Botch, W. B., AIAA Journal, 3, 873, (1965).
64. Rubins, P. M. and Panesci, J. H., "Experimental Standing Wave Shock-Induced Combustion for Determining Reaction Kinetic Histories," AIAA Paper 65-607, (June 1965).
65. Nesterichin, Y. E. and Soloukhin, R. I., "Rapid Instrumentation Methods for Gasdynamics and Plasma Physics," Novosibirsk Hydrodynamic Institute, Novosibirsk, (1965); English Translation: JPRS 39,657 TT 67-30306, CFSTI, Washington, D. C., (January 1967).
66. Olschewski, H. A., Troe, J. and Wagner, H. Gg., Z. Physik. Chem., (Frankfurt) 47, 383, (1965c).
67. Olschewski, H. A., Troe, J. and Wagner, H. Gg., Z. Physik Chem., (Frankfurt) 45, 329, (1965b).
68. Olschewski, H. A., Troe, J. and Wagner, H. Gg., Ber. Bunsen Ges. Physik. Chem., 70, 450, (1966b).
69. Olschewski, H. A., Troe, J. and Wagner, H. Gg., Eleventh Symposium (International) on Combustion, Mono Book Corp., Baltimore, Maryland, (1967).
70. Myerson, A. L., Thompson, H. M. and Joseph, P. S., J. Chem. Phys., 42, 3331, (1965).
71. Kiefer, J. H., Lutz, R. W., J. Chem. Phys., 42, 1709, (1965b).
72. White, D. R., J. Fluid Mech., 4, 585, (1958).
73. Alpher, R. A. and White, D. R., J. Fluid Mech., 3, 457, (1958).
74. Dyner, H. B., Phys. Fluids, 9, 879, (1966).
75. Holbeche, T. A. and Spence, D. A., Proc. Roy. Soc., A279, 111, (1964).
76. Spence, D. A. and Woods, B. A., J. Fluid Mech., 19, 161, (1964).
77. Mirels, H., Phys. Fluids, 6, 1201, (1963).
78. Mirels, H. and Mullen, J. F., Phys. Fluids, 7, 1208, (1964).
79. Mirels, H., AIAA Journal, 2, 84, (1964).
80. Mirels, H., Phys. Fluids, 9, 1265, (1966a).
81. Mirels, H., Phys. Fluids, 9, 1907, (1966b).
82. Duff, R. E., Phys. Fluids, 2, 207, (1959).
83. Fox, J. N., McLaren, T. I. and Hobson, R. M., Phys. Fluids, 9, 2345, (1966).
84. Modica, A. P. and LaGraff, J. E., J. Chem. Phys., 45, 4729, (1966b).
85. Seery, D. J. and Britton, D., J. Phys. Chem., 70, 4074, (1966).
86. Strehlow, R. A. and Cohen, A., J. Chem. Phys., 30, 257, (1959).
87. Rudinger, G., Phys. Fluids, 4, 1463, (1961).
88. Modica, A. P., J. Phys. Chem., 69, 2111, (1965).
89. Charatis, G. and Wilkerson, T. D., Phys. Fluids, 2, 578, (1959).
90. Allen, R. A., Textoris, A. and Wilson, J., J. Quant. Spectr. Radiative Transfer, r, 95, (1965).
91. Johnson, C. D. and Britton, D., J. Chem. Phys., 38, 1455, (1963).

92. Nafzinger, L. E., "Non-Steady Relaxation Phenomena Behind a Reflected Shock Wave," M.S. Thesis, University of Illinois, (August 1966).
93. Glick, H. S., Squire, W. and Hertzberg, A., Fifth Symposium (International) on Combustion, Reinhold, New York, 393, (1955).
94. Palmer, H. B., Knox, B. E. and McHale, E. T., AIAA Journal, 1, 1195, (1963).
95. Tsang, W., J. Chem. Phys., 40, 1171, (1964a).
96. Tsang, W., J. Chem. Phys., 40, 1498, (1964b).
97. Tsang, W., J. Chem. Phys., 41, 2487, (1964c).
98. Tsang, W., J. Chem. Phys., 42, 1805, (1965a).
99. Tsang, W., J. Chem. Phys., 43, 352, (1965b).
100. Tsang, W., J. Chem. Phys., 44, 4283, (1966).
101. Tschuikow-Roux, E. and Marte, J. E., J. Chem. Phys., 42, 2049, (1965); Erratum: 43, 1438.
102. Tschuikow-Roux, E., Phys. Fluids, 8, 821, (1965a).
103. Tschuikow-Roux, E., J. Chem. Phys., 42, 3639, (1965b).
104. Lifshitz, A., Bauer, S. H. and Resler, E. L., J. Chem. Phys., 38, 2056, (1963).
105. Voevodskii, V. V. and Soloukhin, R. I., Tenth Symposium (International) on Combustion, The Combustion Institute, Pittsburgh, Pennsylvania, 279, (1965).
106. Miyama, H. and Takeyama, T., J. Chem. Phys., 41, 2287, (1964).
107. Belles, F. E. and Lauver, M. R., J. Chem. Phys., 40, 415, (1964).
108. Skinner, G. B. and Ringrose, G. H., J. Chem. Phys., 42, 2190, (1965).
109. Schott, G. L., J. Chem. Phys., 32, 710, (1960).
110. Schott, G. L., Los Alamos Scientific Lab., Los Alamos, New Mexico, Private communication, (1963).
111. Schott, G. L. and Bird, P. F., J. Chem. Phys., 41, 2869, (1964).
112. Hawthorne, R. D. and Nixon, A. D., "Shock Tube Ignition Delay Studies of Endothermic Fuels," AIAA Paper, #65-594. Presented at AIAA Joint Propulsion Specialists Meeting, Colorado Springs, Colorado, (June 1965) also Hawthorne, R. D., Shell Development Co., Emeryville, Calif., Private communication, (1965).
113. Schott, G. L., "Detonation Spin in Driven Shock Waves in a Dilute Exothermic Mixture," Division of Fuel Chemistry Preprints for Symposium on Detonations and Reactions in Shock Waves, ACS National Meeting, Chicago, Illinois, (September 1967).

Table I Structure Regularities of Transverse Waves in Detonations

MIXTURE		DILUENT	% DILUTION	REGULARITY
H_2 — O_2	1	—	—	POOR
	1	N_2	50	POOR
	1	CO_2	40	POOR
	1	He	70	EXCELLENT
	1	Ar	60 85	EXCELLENT
	1	Ar & N_2	60 & 16	EXCELLENT
	1.5	—	—	POOR
	.5	Ar	60	GOOD
	1.5	Ar	40	POOR
	.75 2.06	Ar	40	GOOD
C_2H_2 — O_2		—	—	POOR
	1	Ar	75 85	EXCELLENT
C_2H_4 — O_2	1	—	—	POOR
	1	Ar	50	GOOD
	1	Ar	75	EXCELLENT
CH_4 — O_2	1	Ar	0 80	IRREGULAR
	1 2.0	Ar	50	IRREGULAR
C_2H_6 — O_2	1	Ar	50 80	POOR
C_3H_8 — O_2	1.25	—	—	POOR
	1.25	Ar	80	POOR
CO — O_2	1	Ar	50	GOOD
NH_3 — O_2	1	—	—	IRREGULAR
	1	Ar	40	IRREGULAR

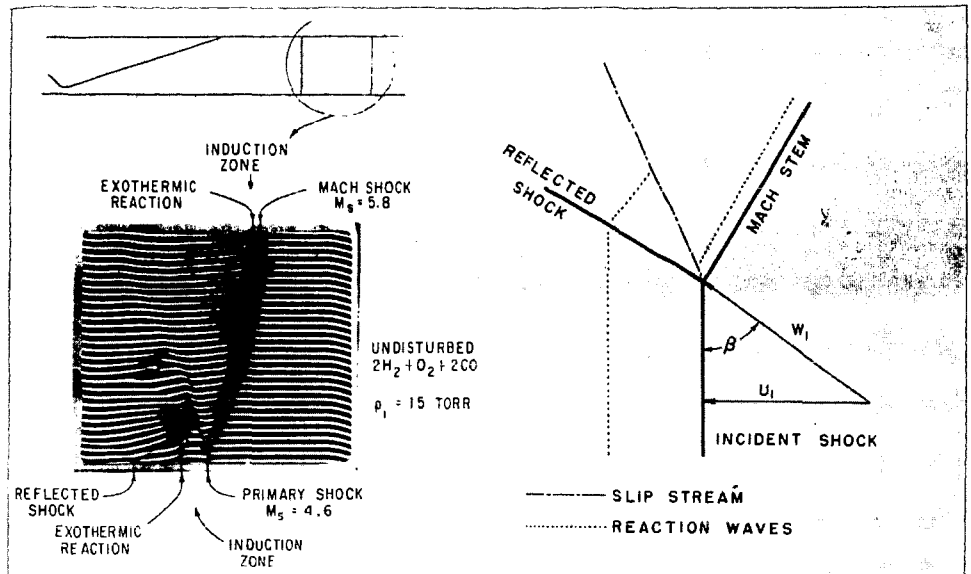

FIGURE 1. ARTIFICIALLY PRODUCED REACTIVE MACH STEM. (COURTESY REF. 37)

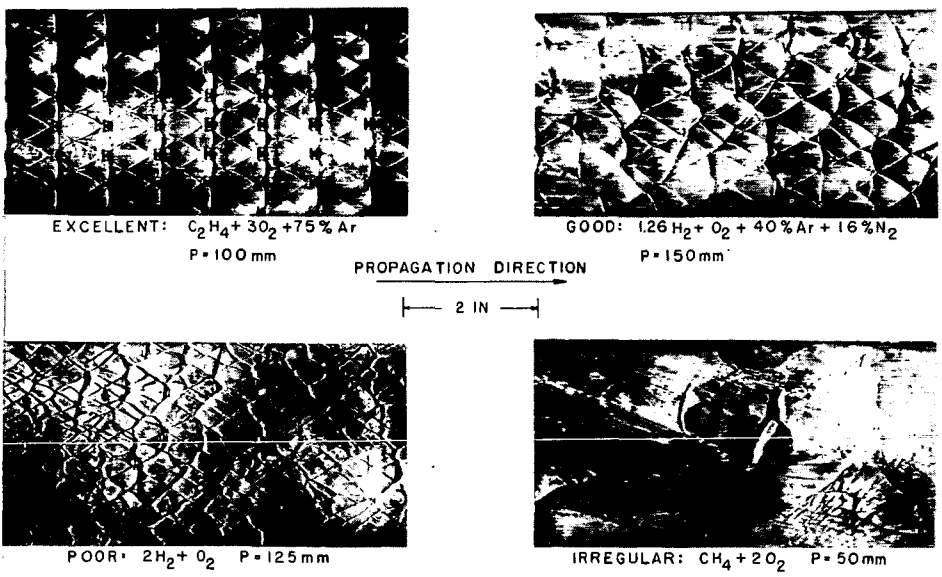

FIGURE 2. A FEW EXAMPLES OF SMOKE TRACK RECORDS. $3\frac{1}{4} \times 1\frac{1}{2}$ DETONATION TUBE.

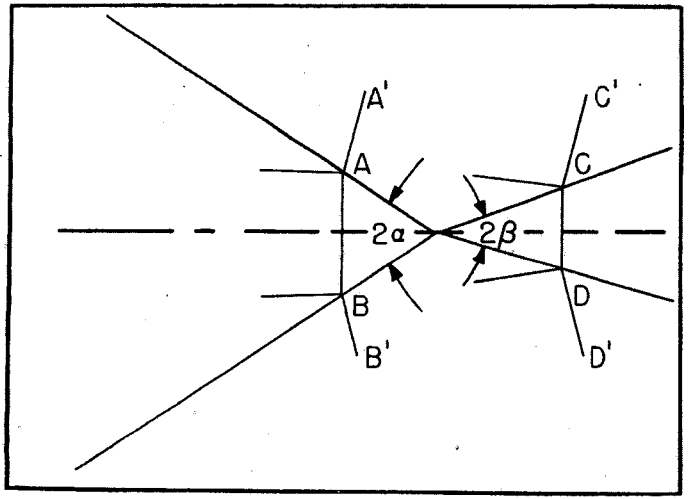

FIGURE 3 – ANALYSIS OF A SYMMETERIC INTERACTION

SIDE ⟵ 2 IN. ⟶

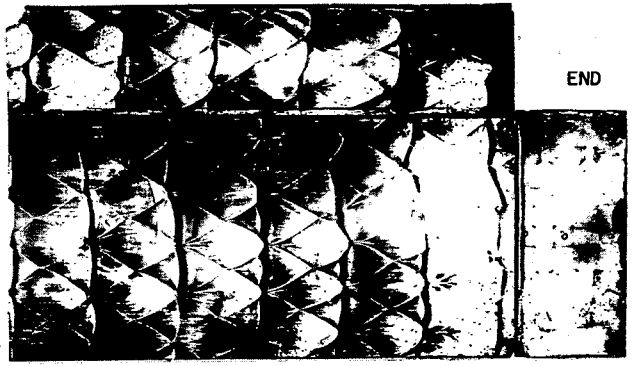

BOTTOM

RECTANGULAR MODE $2H_2 + O_2 + 70\%Ar$ 105 TORR

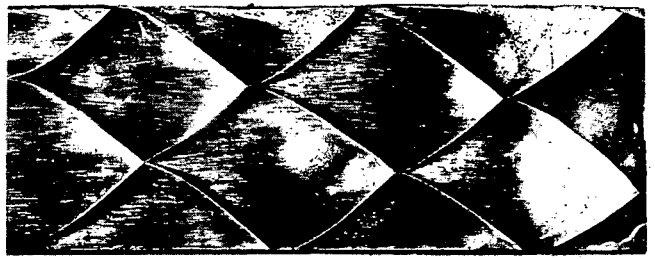

PLANAR MODE $2H_2 + O_2 + 70\%Ar$ 70 TORR

FIGURE 4 – SMOKE TRACK RECORDS SHOWING REGULARITY

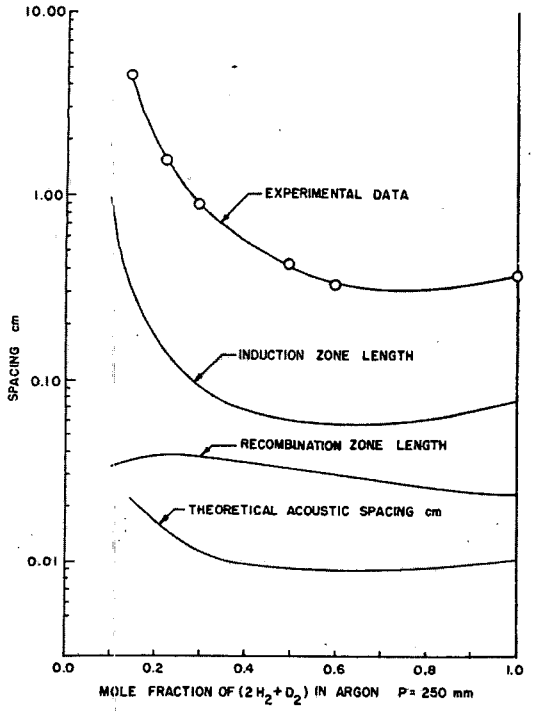

FIGURE 5 – TRANSVERSE WAVE SPACINGS IN THE $2H_2 + O_2$ SYSTEM

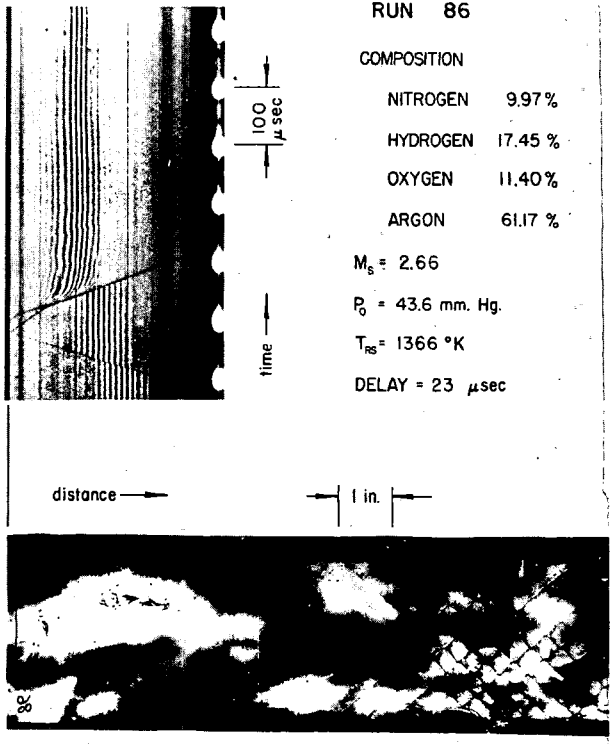

FIGURE 6 – THE APPEARANCE OF TRANSVERSE WAVES DURING INITIATION BEHIND A REFLECTED SHOCK

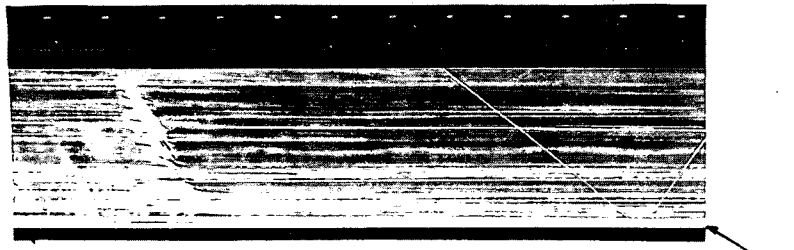

a) P_o = 18 TORR T_{rs} = 972° K

END PLATE

TIME

100 μSEC

END PLATE

b) P_o = 24.9 TORR T_{rs} = 1020° K

FIGURE 7 – HOT SPOT INITIATION IN $0.08H_2 + 0.02O_2 + 0.90Ar$ MIXTURES BEHIND REFLECTED SHOCK
COURTESY A. COHEN, BALLISTIC RESEARCH LABORATORIES.

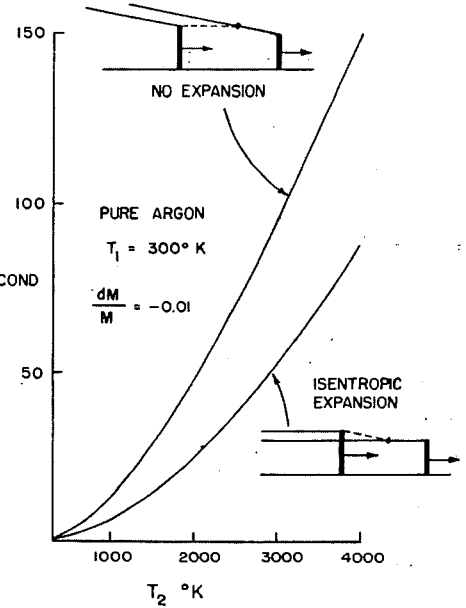

FIGURE 8 – TEMPERATURE CORRECTION FOR SHOCK ATTENUATION

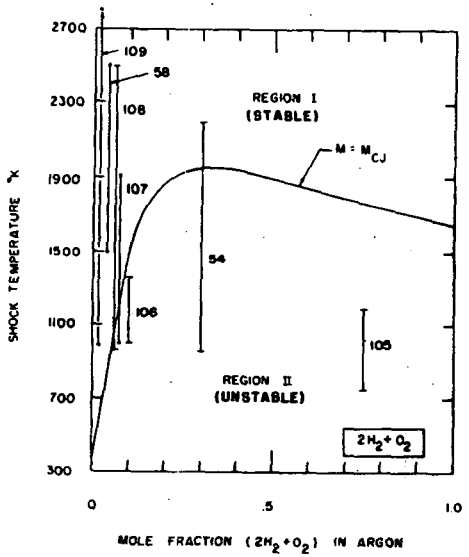

FIGURE 9 - STABILITY REGIONS DEFINED BY THE CJ CRITERION

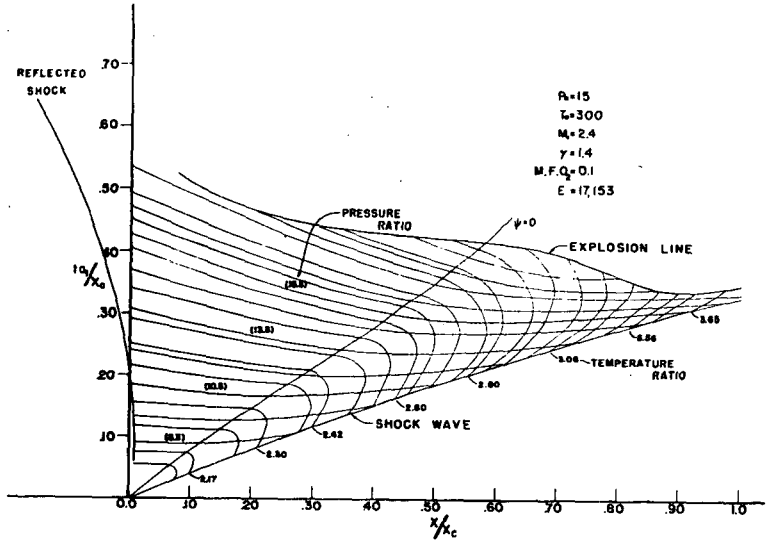

FIGURE 10 - NONSTEADY FLOW BEHIND A STEP SHOCK PROPAGATING INTO A CONVERGING CHANNEL. REF. 57

Detonation Spin in Driven Shock Waves in a Dilute Exothermic Mixture

Garry L. Schott

University of California, Los Alamos Scientific Laboratory,
Los Alamos, New Mexico 87544

There have been many uses of shock waves in diluted mixtures of exothermic reactants for studies of chemical reaction rates. It was once commonly thought, for lack of evidence to the contrary, that one could operate in a regime free of complications from spontaneous "detonation" phenomena arising from the deposition of the reaction energy in the flowing gas by generating shock waves faster and stronger than the Chapman-Jouguet wave for the dilute mixture. Such shock waves are in reality overdriven detonation waves, and the only basis for distinguishing them from strong detonation waves in more concentrated mixtures is the fact that the dilute mixtures, if not supported, may fail to sustain a slower, Chapman-Jouguet velocity wave. This distinction is one of degree rather than of kind, and recent experience with unsupported detonations and overdriven detonations in detonable gas mixtures indicates that three-dimensional structure which characterizes the Chapman-Jouguet velocity waves remains present, on a progressively finer scale, in overdriven waves.[1,2]

The occurrence of transverse waves or other instabilities in driven shock waves in dilute, only mildly exothermic mixtures has been less completely characterized. Indeed, many successful investigations of kinetics of exothermic reactions have been carried out in shock waves in dilute mixtures without major or even noticeable interference. On the other hand, there have been isolated reports of "instabilities", in the reaction zones in particular, under circumstances where the system was diluted well beyond the limit of detonability and the shock wave was clearly stronger than a Chapman-Jouguet wave. Examples of these occurrences may be found in studies of the hydrogen - bromine reaction,[3] ozone decomposition,[4] and hydrogen-oxygen combustion.[5] The present paper reports the occurrence of such instabilities in shock waves in a mixture of 1% C_2H_2, 1.5% O_2, 97.5% Ar and the identification of conditions where the phenomena exhibit the recognizable and quasi-reproducible form of single-headed spin.[6,7]

Experimental

The experiments reported here were carried out in the 10 cm i.d. circular brass shock tube used for several previously reported chemical investigations.[5] Several different test section configurations were utilized for the various kinds of diagnostic experiments. Either brass shim stock or Mylar sheet diaphragms were used, and the driver gas was hydrogen. The several batches of 1.0% C_2H_2, 1.5% O_2, 97.5% Ar test gas mixture were prepared manometrically from tank argon and a single, homogeneous stock mixture of 40% C_2H_2, 60% O_2 prepared initially from tank supplies. The composition of one batch was checked by mass spectral analysis, and 0.03% N_2 was the only detected departure from the intended composition. Experiments were carried out at initial shock tube pressures, p_0, of 20, 50, and 120 Torr.

Shock wave speeds were monitored by raster oscilloscope recording of the progress of the shock front past five piezoelectric pressure transducers spaced at 30 cm or longer intervals along a 140 cm or longer segment of the tube beginning 200 cm or 350 cm from the diaphragm.

In other experiments, where the departure of the shock front from planarity was under examination, four of the piezoelectric gauges were arranged at 90° intervals around the tube perimeter in a plane perpendicular to the axis, and their responses were displayed on four synchronized oscilloscope traces.

The presence of OH radicals in the combustion zone was monitored in many of the experiments by oscilloscope recording of the absorption of a beam of ultraviolet

OH molecular line radiation[9] which passed diametrically across the tube through quartz windows.

Mylar foils coated with wood smoke soot[2] were placed against the interior surface of the shock tube end flange in many of the experiments to record the presence of irregularities in the shock front reaching the tube end. Smoked foils lining the side walls along a 14 cm length of the test section were also used in sone experiments. The loci at the tube wall of the abrupt intersections of segments of creased shock waves are recorded as inscriptions in the soot coating.

Finally, open shutter photography in a 60 cm long glass extension of the test section was used to record the luminous trajectory of the spinning reaction zone - shock front complex in shock waves exhibiting the single-headed spin phenomenon.

Results

The initial results which suggested that spin-like irregularities might be present in promptly reactive shock waves in the 97.5% Ar mixture consisted of the occurrence of quasi-periodic undulations in spectrophotometric records of OH radical concentration in the reaction zone, which persisted for several hundred microseconds after passage of the shock wave. These records did not identify the instability definitively, nor have they proven to be even reliable indicators of the presence of instability in all instances. Accordingly, the investigation of the instability phenomena turned to the inclusion of other diagnostic techniques with which we have experience from the study of gaseous detonations.[2,6]

Positive confirmation of the occurrence of single-headed spin was made with a smoked foil along the inside wall of the tube. After passage of a spinning wave, the smoke layer bears a helical, ribbon-like inscription. The forward edge of the ribbon is the path of the backward pointing crease in the otherwise convex shock front. The trailing edge is the path of the rear terminus of the transverse detonation wave which propagates in the compressed, unreacted gas accumulated behind the weaker region of the primary shock front. This promptly reactive transverse compressional wave couples the revolving crease in the primary shock front to the predominantly circumferential acoustic oscillation of the pressure of the column of burned gas flowing behind the combustion wave system. The phase of the helix in the tube and also the pitch angle, θ, whose tangent is the ratio of the axial to the circumferential velocity component, is recorded by the side wall smoked foil. Good specimens of these single spin records were obtained at initial pressures of 20 and 50 Torr. These differ from the records of single spin in unsupported detonations, however, in that the fine structure found within the transverse wave band in the latter records[2,6] is absent. Foils placed only on the end wall are more durable and are generally easier to work with. These record the location of radially or circumferentially propagating creases in the shock front anywhere in the tube cross section upon arrival of the wave at the end. Single spinning waves are recognized by the presence of a single, more or less radially oriented mark extending inward from the rim.[2]

Another prominent characteristic of single spinning waves is severe departure of the shock front from planarity.[2,6,7] This leads to scatter in the apparent shock wave velocity deduced from the time intervals between arrival of the shock at gauges spaced arbitrarily along the tube. This scatter in apparent velocity was observed to be as great as $\pm 10\%$ over 30 cm intervals in waves where the end foils revealed the presence of single spin. That this scatter is in fact attributable to the revolving, nonplanar shock front which moves at much more nearly constant average axial velocity is confirmed by the differences in arrival times measured by the four pressure gauges placed in a ring around the tube. These differences were as great as 11 μsec, corresponding to a 15 mm differential in axial position, in shock waves where the smoked foil confirmed the presence of single-headed spin.

Finally, the occurrence of single-headed spin is demonstrated very graphically in the open shutter photograph reproduced in Fig. 1.

Quantitative examination of the conditions under which spin and related instability phenomena occur is hampered by the uncertainty in the measurement of the axial velocity with the present interval method. Nevertheless, determination of the approximate ranges of conditions under which spin is observed has been pursued. The Chapman-Jouguet velocity of the 1% C_2H_2, 1.5% O_2, 97.5% Ar mixture initially at room temperature and ca. 0.1 atm pressure is about 0.9 km/sec, and the velocities of the shock waves studied were between 1.0 and 2.0 km/sec. At each of the three initial pressures studied, there is a range of shock velocities above 1.0 km/sec in which neither single-headed spin nor any other discernible perturbation at the shock wave front was observed. At p_0 = 20 and 50 Torr, the occurrence of chemical reaction behind the shock front was indicated at shock velocities above ca. 1.1 km/sec by the growth and subsequent leveling off of absorption of the ultraviolet line radiation of OH. But evidence of spin was not present in smoked foil or open shutter photographic records except at velocities above ca. 1.2 km/sec for p_0 = 50 Torr and above ca. 1.33 km/sec for p_0 = 20 Torr. At 120 Torr, single-headed spin occurred at velocities as low as ca. 1.10 km/sec, but not at still lower velocities. At these lower velocities, where for normal shock waves the temperature before reaction lies below about 1300°K, OH radical absorption did not provide a good means of detecting the occurrence of reaction, even though other work[9] has shown that the induction zone, scaled for density of reactants, lies well within the time and space regimes of the present experiments. Evidently, little OH is formed unless the combustion takes place at higher temperatures than this.

When the shock velocity was raised above the threshold range for single spin, spin modes of higher multiplicity were obtained. For example, at p_0 = 50 Torr, single-headed spin was obtained fairly reproducibly near 1.3 km/sec, but shock fronts with 2, 3, or 4 visible creases extending to the perimeter of the end plate smoked foils were common near 1.4 km/sec. The ability of smoked and plate foils to record the impingement of highly segmented fronts in the interior of the shock tube, as has been done so successfully in unsupported detonations,[2,10] was disappointing. At shock velocities above ca. 1.5 km/sec at p_0 = 50 Torr, only small, isolated segments of wave intersection tracks were recorded. Thus while the presence of persistent spin-like perturbations is indicated, it was not possible to observe any orderly structure or study variation of structure with shock velocity.

OH absorption oscillograms showed pronounced undulations not only in experiments where single spin was indicated, but also in experiments with coarse multiheaded spin. In still faster shock waves, though, the structure was evidently of sufficiently fine scale and/or low intensity that properties averaged over the tube diameter, as by a photon beam absorption experiment, may become usable for determination of combustion stoichiometry and the course of slow chemical changes that follow behind the induction zone.

Another regime of interesting phenomena was found in reactive shocks at velocities just below those at which single-headed spin was observed. OH absorption oscillograms were not reproducible, sometimes indicating abrupt formation of large quantities of OH and on other occasions, under closely similar conditions, showing scarcely detectable appearance of OH. Raster oscilloscope records of the shock wave progress down the tube showed scatter which was appreciable, with differences in apparent velocity as large as 3% between successive 30 cm intervals. Tests revealed corresponding departures of the shock fronts from planarity, which were only about one-third as large as those found when spin was identifiable. Smoked foil records showed no creases extending to the perimeter of the tube. Instead, end plate foils showed patches of indistinct disturbance in the interior of the tube.

On the basis of this somewhat incomplete characterization of these subspinning instabilities, it is hypothesized that they represent irregularities in the reaction zone which are not of sufficient, localized exothermicity to extend their influence in large amplitude form to the shock front or are not of proper wavelength to couple to acoustic oscillations of the burned gas. Attention is here drawn to interferograms of reactive shock waves in dilute exothermic systems,

including an NH_3 - O_2 system[11] and one of the H_2 - O_2 - Ar mixtures[12] previously used for kinetics studies in our Laboratory[5] in which at initial pressures between 100 and 200 Torr there had been pronounced undulations in OH absorption oscillograms. These interferograms showed that the shock front is quite flat, though slightly tilted in the tube, but the reaction zone is much more significantly disturbed. It also seems appropriate to report that attempts to record smoked foil inscriptions in the H_2 - O_2 - Ar mixture under these same conditions gave negative results.

To relate the present work in acetylene - oxygen mixtures to other work in the same system, we note that most of the kinetics studies,[13] some of which have used more concentrated mixtures than the present one, have been done in an initial pressure regime an order of magnitude lower. In addition, many of the studies have been done using reflected shock waves and in ways which are not so subject to interference by transverse waves either at the shock front or in the reaction zone.

The occurrence of spin in an environment divorced from marginally propagating detonation would appear to offer a heretofore unrealized opportunity to study the limiting conditions for the occurrence of spin with additional variables at one's command in the hope of elucidating detonation limit phenomena. The lack of sharpness of the limits observed in the present system detracts somewhat from the attractiveness of this approach, but further work may be appropriate.

A brief attempt is made here to relate some parameters of the single spinning waves observed in these driven shock waves to known properties of the chemical mixture. From the admittedly approximate values of the threshold velocities for spin, $D_{threshold}$, at the three experimental initial pressures, the induction times t_i and axial induction zone lengths x_i for the temperature and density behind the axially normal portions of the convex spinning shock fronts have been evaluated from independent induction period data.[9] These values are recorded in Table I, where it can be seen that the induction zone lengths for these spinning waves are not constant, but become smaller at lower density, and are all smaller than the 100 mm tube diameter.

The mean pitch angle, θ, from smoked side foils and the mean axial velocity, D, were obtained from separate experiments, done for p_0 = 20 and 50 Torr, each at constant tube loading conditions. These data were combined to determine the circumferential velocity component of the single spin under these two conditions. In Table II these are recorded and compared with the perimetral velocity for pure fundamental circumferential oscillation in the reacted gas estimated for a plane shock wave at the axial velocity D with reaction to chemical equilibrium (1.84 times the sound velocity, c).[14] Also tabulated are the Chapman-Jouguet detonation velocities D'_{CJ} for the unsupported detonation of the hot, compressed, unreacted gas behind the primary shock front having velocity D. The circumferential velocity of the transverse spin wave at the tube perimeter is seen to lie between these two characteristic velocities of the system, which are sufficiently different from each other under the present experimental circumstances that the spinning wave cannot be in close resonance with both, as it has been found to be in certain unsupported spinning detonations.[14,15]

In simplest terms, the experiments described here show that the occurrence of single-headed spin, which may be universally associated with unsupported detonations at the limits of their ability to propagate, is not exclusively a property of unsupported waves or of Chapman-Jouguet flow.

The initial experiments in which the occurrence of spin in this acetylene - oxygen - argon mixture was first identified were carried out in July 1963 by E. P. Eastman and P. F. Bird, and in collaboration with Prof. R. A. Strehlow. J. L. Young and J. G. Williamson carried out most of the subsequent experimental work.

Table I. Normal Shock Induction Zones at Spin Threshold for 1% C_2H_2, 1.5% O_2, 97.5% Ar in 10 cm diameter tube.

P_0	$D_{threshold}$	T	t_i	x_i
Torr	km/sec	°K	μsec	mm
20	1.33	1820	52	20
50	1.20	1518	83	29
120	1.10	1317	122	41

Table II. Circumferential Velocity Considerations for Single-Headed Spins in Driven Shock Waves.

P_0	D	θ	1.84 c	D cotθ	D'_{CJ}
Torr	km/sec		km/sec	km/sec	km/sec
20	1.38	46°	1.59	1.33	1.25
50	1.31	43°	1.53	1.40	1.24

References

1. D. R. White, Phys. Fluids 4, 465 (1961).
2. R. E. Duff, Phys. Fluids 4, 1427 (1961).
3. D. Britton and R. M. Cole, J. Phys. Chem. 65, 1302 (1961); also D. Britton and N. Davidson, J. Chem. Phys. 23, 2461 (1955).
4. W. M. Jones and N. Davidson, J. Am. Chem. Soc. 84, 2868 (1962).
5. G. L. Schott and P. F. Bird, J. Chem. Phys. 41, 2869 (1964).
6. G. L. Schott, Phys. Fluids 8, 850 (1965).
7. B. V. Voitsekhovskii, V. V. Mitrofanov, and M. E. Topchian, "The Structure of a Detonation Front in Gases," USSR Academy of Sciences, Siberian Division, Novosibirsk, 1963; (English transl. FTD-MT-64-527, AD 633821, issued by U.S. Air Force, Wright-Patterson AFB, Ohio, 1966.)
8. S. H. Bauer, G. L. Schott, and R. E. Duff, J. Chem. Phys. 28, 1089 (1958).
9. R. I. Soloukhin, Combust. Flame 9, 51 (1965).
10. R. A. Strehlow, R. Liaugminas, R. Watson, and J. R. Eyman, Symp. Combust. 11th, Univ. Calif., Berkeley, Calif., 1966 (1967).
11. R. I. Soloukhin, "Some Shock Tube Methods in Chemical Physics," USSR Academy of Sciences, Siberian Division, Novosibirsk, 1966, Fig. 19, page 38. (Text in Russian and English.)
12. D. R. White, General Electric Research Laboratory, Private Communication, July, 1964.
13. W. C. Gardiner, Jr., W. G. Mallard, K. Morinaga, D. L. Ripley, and B. F. Walker, Symp. Combust. 11th, Univ. Calif., Berkeley, Calif., 1966 (1967); and refs. cited therein.
14. J. A. Fay, J. Chem. Phys. 20, 942 (1952).
15. B. V. Voitsekhovskii, Dokl. Akad. Nauk SSSR 114, 717 (1957). (English transl. Proc. Acad. Sci. USSR, Appl. Phys. Sect. 114, 193 (1957).)

Figure 1.

Still photograph of luminosity of driven shock, D = 1.3 mm/μsec, in 1.0% C_2H_2, 1.5% O_2, 97.5% Ar at 50 torr. in 10 cm diameter glass tube. Shock motion left to right.

Transition from Branching Chain Kinetics to Partial Equilibrium in the Shock-Induced Combustion of Lean Hydrogen-Oxygen Mixtures

W. C. Gardiner, Jr., K. Morinaga, D. L. Ripley
and T. Takeyama

Department of Chemistry, The University of Texas, Austin, Texas

The chemical kinetics of the high-temperature reaction between hydrogen and oxygen has been the subject of numerous experimental studies. For the case of combustion in shock waves through hydrogen-oxygen mixtures highly diluted with argon, the kinetics may be divided into three regimes: in the initiation regime, small concentrations of atoms and/or radicals are generated by slow, unknown reactions; in the induction regime, bimolecular branching chain reactions lead to exponential increase in the concentrations of H,O and OH; in the recombination regime, termolecular reactions cause evaluation of heat and establishment of chemical equilibrium. The induction regime kinetics are thought to be explicable in terms of the mechanism

$$H + O_2 = OH + O \quad (1)$$

$$O + H_2 = OH + H \quad (2)$$

$$OH + H_2 = H_2O + H \quad (3)$$

When the OH radical concentration is high, the fast reaction

$$OH + OH = H_2O + O \quad (4)$$

also contributes to interconversion of species. Neglecting the step

$$H + O_2 + M = HO_2 + M \quad (5)$$

which is important for $p \gtrsim 1$ atm, $T \lesssim 1200°K$, defines the limits of validity of this mechanism. Rate constant expressions for all of these steps, based on a variety of experiments, have been proposed[1]. The agreement among the various investigators is good.

The separation between induction and recombination regimes lies essentially in the fact that the termolecular reactions of the latter are far slower than the bimolecular reactions of the former. Steps (1-4) have, as a consequence, almost equal forward and reverse rates during the recombination regime, leading to a condition of partial equilibrium[2]. It was shown recently by Hamilton and Schott[3] that in mixtures with $[H_2]/[O_2] \equiv R$ either $\gg 1$ or $\ll 1$ the transition between induction regime kinetics, governed by the rates of (1-3) and the partial equilibrium condition, governed by the equilibrium constants of (1-3) could involve transient effects capable of yielding worthwhile information on the rate constants of (1-4). They investigated the situation with $R \gg 1$. They predicted large O-atom spikes, and from the experimental absence of OH spikes, they were able to deduce an upper limit for k_1/k_3. We have investigated the situation for $R \ll 1$. The OH spikes absent in $R \gg 1$ mixtures are found to be quite pronounced for $R < .1$. Quantitative investigation of incident shocks in $H_2/O_2/Ar = 1/10/89$ mixtures, $p_o = 10$ torr, $1400 < T < 2500°K$ is reported here. The experimental technique combined OH concentration measurement by the Bi(3067) method[4] with conventional shock tube methods.

The OH absorption signal for a run at 1680°K is shown in Fig. 1.

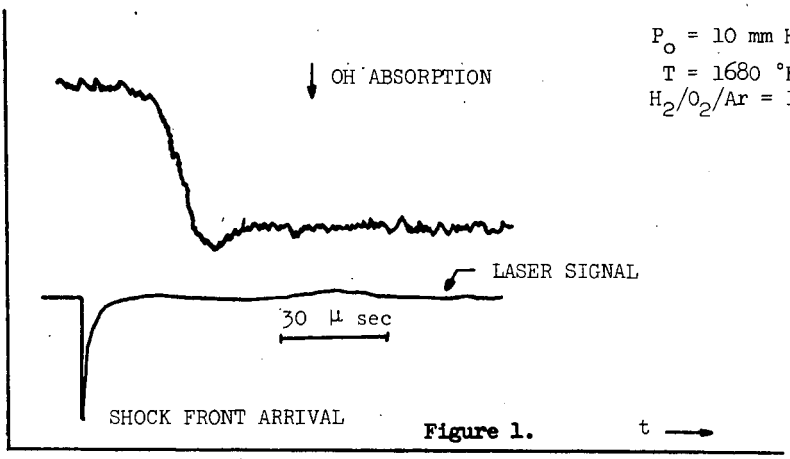

Figure 1.

In order to convert the data to graphical form, some approximations are needed. First, the extinction coefficient for the Bi(3067) method fluctuates considerably from run to run. For these experiments each run was used as its own calibration point, and Beer's Law was taken to calculate the ratio [OH](spike)/[OH](partial equilibrium), with the level portion of the trace assigned to the partial equilibrium condition, for which [OH] can be readily computed from the shock speed. To assign error limits to this ratio, the appropriate extreme points were read from the records and likewise substituted into Beer's Law to get the upper and lower limits for the [OH](spike)/[OH](partial equilibrium) ratio. Since the full width of the spikes is difficult to determine both on the experimental records and on the computed profiles, we use the apparent full width at half height for the quantitative shape parameter. By apparent half width is meant the width which would be obtained on the accurate computer plotout of the profile by extrapolating the slightly sloped post-spike [OH] (a small amount of recombination does occur on the time scale of these experiments via Reaction (5)) back to the center of the spike, and then measuring the full width of the spike half way between the back extrapolation and the top. On the records themselves, this means reapplication of Beer's Law to get the correct half height. The results are presented in Figs. 2 and 3.

The first approach to interpret these data is to search for a set of rate constants for the mechanism (1-4) which will predict the correct spike heights and spike durations. This is greatly assisted by the availability of much good data, and a suggestion by Schott that lean mixture maxima would be favored by large values of the ratio k_2/k_3. We started with the rate constant expression for k_1 given by Baldwin and Melvin[1b], the k_2 expression given by Clyne and Thrush[1c], and the k_3 and k_4 expressions given by Kaufman and DelGreco[1a]. A recent experiment by Gutman and Schott[1f] provides a new value for k_1 which can also be used as input. For the critical k_2, there are three studies which supercede the consensus of Clyne and Thrush, all giving higher values of k_2; these were done by Wong and Potter[1g] Westenberg and de Haas[1e], and Gutman and Schott[1f] again. A higher value of k_4 has been reported by Dixon-Lewis, Wilson and Westenberg[1h]. The hint regarding the k_2/k_3 ratio may be understood in the following way. In order to produce a spike in the OH profile, the induction period reactions must behave in such a way that OH production temporarily exceeds OH destruction as the H_2 concentration suddenly drops from its induction period value to its partial equilibrium value. Reaction (4) unambiguously destroys OH rapidly at this time; Reaction (1) provides reactants for both (2) and (3) at equal rates; this leaves (2) and (3) as the primary generators of the OH profile. Both of them have the same dependence on H_2, so both will have rates which drop suddenly as the last H_2 is consumed. Overproduction of OH by (2) can then lead to more OH than can be consumed by (3) when H_2 comes into

short supply, and an overshoot occurs. This analysis is rather oversimplified, as our subsequent analysis will show; however, the direction of seeking high values of k_2 is clear. Whether or not it will be fruitful to seek low values of k_3 will depend on the value of k_4.

First consider the peak heights and half widths which are predicted by numerical integration using the k_1 and k_2 values of Gutman and Schott. (Figs. 2 and 3.) The half widths are approximately correct, but the heights are far lower than the data indicate. Immediately we can conclude that it is unnecessary to investigate further with the k_2 value of Clyne and Thrush, for it is lower than Gutman and Schott's at 1500°K by factor 2. Next, increase the value of k_2 and see what happens. Just as expected, the heights increase; the half widths decrease. By trial and error, a k_2 value 5 times that of Clyne and Thrush, or 2-1/2 times that of Gutman and Schott, is found to give the right height and half width at 1500 °K. In subsequent calculation it is found that the right temperature dependence is found also, although the high temperature values are perhaps somewhat high. The influence of k_1 in place of the Gutman and Schott value. It is seen that the difference is minor. Varying k_3 has little effect. When the rates of the reactions are checked, it is found that the lack of effect of k_3 is simply due to the fact that OH is mostly consumed by (4) rather than (3) at the spike time. Therefore, in order to try to reproduce the spike by lowering the OH consumption rate at the time of the spike, k_4 must be reduced. It is indeed possible to increase the heights somewhat by this procedure; however, the predicted half widths are seen to become far too large, and we conclude that it is useless to try to predict the spikes by lowering the OH destruction rate from that predicted by the consensus rate constants.

To summarize this approach to predicting the spikes by numerical integration of the conventional mechanism, we find that reasonably satisfactory agreement is obtained if k_2 is taken as about 2-3 times the value predicted by the expressions of Gutman and Schott, Wong and Potter, or Westenberg and de Haas. Furthermore, this is the only way to predict spikes with this mechanism. The shortcomings of this approach are the disagreement with other values for k_2 and the impossibility of reconciling high values for k_2 with the observed dependence of ignition delays upon R.[4]

There are several other ways in which OH-spikes might be produced. The possibility that the observed oscilloscope traces are due to an inadequacy in the Bi(3067) method arising from its sensitivity to OH(v=0) may be rejected as a quantitative explanation by noting that at 1500°K only 7% of the OH molecules are in excited vibrational states. The maximum thermal effects of vibrational relaxation are only 3-4% for these mixtures. Trace amounts of impurities could only affect the results by bimolecular catalysis of the recombination reactions or by intervention in the already fast branching mechanism. We see no way to accomplish either of these, although they cannot be rejected on our evidence. Finally, it must be allowed that some combination of causes could be the source of the observed spikes.

We conclude that the observed OH profiles in shock-induced combustion of lean H_2-O_2-Ar mixtures can be explained on the basis of the conventional mechanism if the rate for $O + H_2 = OH + H$ is assumed to be about twice the current best value from other experiments. Since such an assumption leads to substantial discrepancies in the interpretation of other experiments, we consider this explanation to be suggestive only, and subject to refinement as further experimentation is done on the high-temperature chemistry of the H_2-O_2 reaction.

Acknowledgement

We are indebted to B. F. Walker and C. B. Wakefield for assistance with the computational aspects of this research. Our work was supported by the U. S. Army Research Office - Durham, The Robert A. Welch Foundation and The University of Texas Research Institute.

References

1. (a) F. Kaufman and F. P. DelGreco, Symp. Combust. 9th, Cornell University, Ithaca, New York, 1962, 659 (1963); (b) R. R. B ldwin and A. Melvin, J. Chem. Soc. 1964, 1785; (c) M. A. A. Clyne and B. A. Thrush, Nature 189, 135, 1961; (d) R. W. Getzinger and G. L. Schott, J. Chem. Phys. 43, 3237 (1965); (e) A. A. Westenberg and N. de Haas, J. Chem. Phys. 46, 490 (1967); (f) D. Gutman and G. L. Schott, J. Chem. Phys., to be published, 1967; (g) D. L. Ripley and W. C. Gardiner, Jr., J. Chem. Phys. 44, 2285 (1966); (h) G. Dixon-Lewis, W. E. Wilson and A. A. Westenberg, J. Chem. Phys. 44, 2877 (1966); (i) W. S. Watt and A. L. Myerson, 6th International Shock Tube Symposium, Freiburg, 1967; (j) E. L. Wong and A. E. Potter, J. Chem. Phys. 43, 3371 (1965).

2. G. L. Schott, J. Chem. Phys. 32, 710 (1960).

3. C. W. Hamilton and G. L. Schott, Symp. Combust. 11th, University of California, Berkeley, 1966.

4. D. L. Ripley, dissertation, The University of Texas, January 1967.

Note for Figs. 2 and 3. The solid error bars denote runs made using the Bi(3067) method; the dashed error bars denote runs made using the water lamp method.

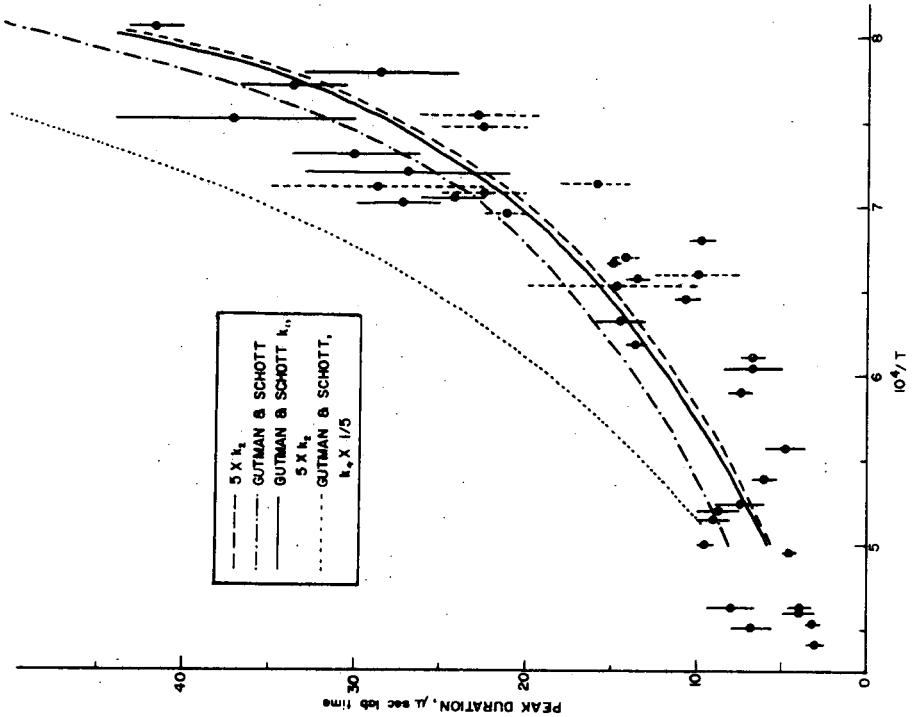

Figure 3.

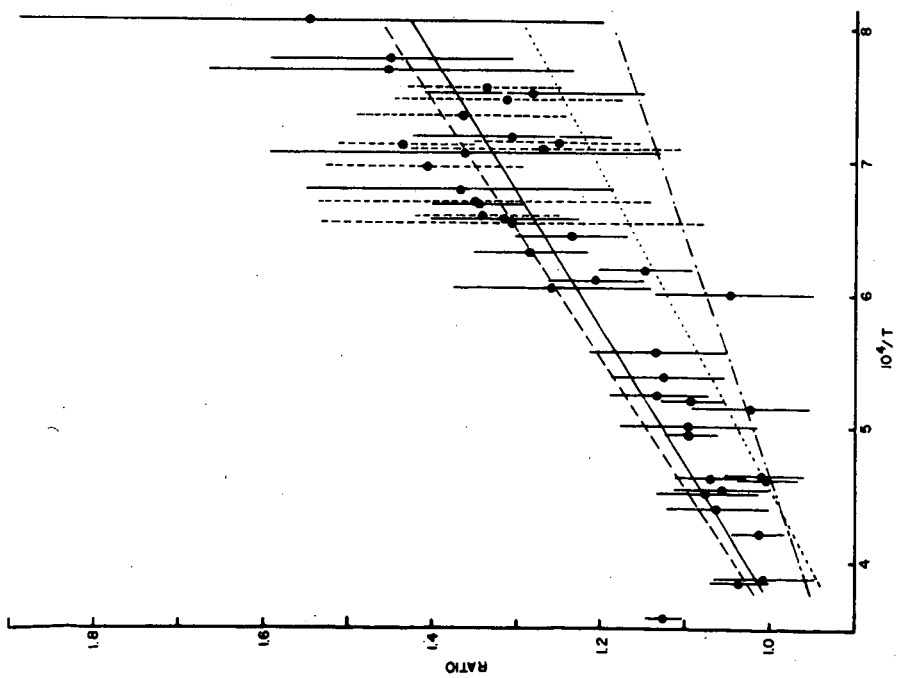

Figure 2.

INITIATION OF DETONATION BY INCIDENT SHOCK WAVES IN HYDROGEN-OXYGEN-ARGON MIXTURES

G.B. Skinner
Wright State Campus, Dayton, Ohio

G. Mueller, U. Grimm and K. Scheller
Aerospace Research Laboratories, Wright-Patterson Air Force Base, Ohio

INTRODUCTION

The steps involved in the initiation of detonation by incident shock waves have been outlined by Strehlow and Cohen (1). In their words, "An exothermic reaction occurring in a small region of a flowing gas causes an increase in the local pressure .... Since this region is subsonic the pressure increase will propagate to the front and increase the velocity of the front, thereby increasing the temperature of the next element of gas heated by shock compression. This process is self-accelerating and in general a steady-state wave will not be obtained until the wave is traveling at or above the Chapman-Jouguet velocity for the mixture."

For dilute hydrogen-oxygen-argon mixtures, ignition induction times ranging from microseconds to milliseconds can be obtained over a range of temperatures (2,3). In a shock tube equipped with several velocity-measuring stations, we have shock-heated such mixtures to temperatures at which induction times are a few milliseconds long, and observed in considerable detail the process by which the reaction wave, initiated several meters behind the shock wave, overtakes and couples with the shock wave.

Earlier measurements (4,5,6) have indicated the increase in shock velocity due to coupling of the reaction to the shock wave, but have not shown many of the details of the process. Strehlow and co-workers (1,7,8) have made extensive studies of initiation of exothermic reactions behind reflected shock waves. Oppenheim, Laderman, and Urtiew (9,10) have reported extensive studies on the initiation of detonations in gaseous mixtures where the ignition source was a spark, a flame, or a hot wire.

EXPERIMENTAL

A square shock tube 7.62 cm. on a side was used. This had a driver gas section 1.83 meters long and a sample gas section 6.10 meters long. Diaphragms were of 1.22 mm. thick aluminum, scribed diagonally so that, when they burst, four triangular sections would fold back, one along each side of the tube. Air was used as driver gas.

When a run was made, the air was added to the driver section at the desired pressure (below the bursting pressure of the diaphragm), then the diaphragm was ruptured by a plunger. This permitted close control (about 0.5%) over the driver gas pressure.

The sample gas section was instrumented with thin-film platinum heat transfer gauges for velocity and heat transfer measurements, and with SLM Model 603 piezoelectric gauges (Kistler Instrument Corporation, Clarence, New York) for pressure measurements. The positions of these gauges with respect to the diaphragm are listed in Table I.

Table I

Positions of Gauges with Respect to Shock-Tube Diaphragm

Gauge	Distance Downstream from Diaphragm, Meters
Heat transfer No. 1	3.2004
Heat transfer No. 2	3.8100
Heat transfer No. 3	4.4196
Heat transfer No. 4	4.6482
SLM No. 1	4.6991
Heat transfer No.13	4.6991
Heat transfer No. 5	4.8006
Heat transfer No. 6	4.9022
SLM No. 2	4.9530
Heat transfer No. 7	5.0038
Heat transfer No. 8	5.1054
Heat transfer No. 9	5.2070
Heat transfer No.10	5.3086
Heat transfer No.11	5.3594
Heat transfer No.12	5.9690

Heat transfer gauges 1, 2, and 3, and SLM gauge 1 were mounted on the side of the tube; the others were on the top. Heat transfer gauge 13 was used to measure the rate of heat transfer from the gas to the wall. The time base for all velocity measurements was a Tektronix Model 180A time-mark generator. Outputs from the piezoelectric gauges were fed into charge amplifiers, then recorded using a

Tektronix Model 555 oscilloscope. The piezoeletric gauges were calibrated statically against a precision laboratory pressure gauge.

RESULTS

In the temperature range under study, the induction time for ignition of a hydrogen-oxygen-argon mixture varies rapidly with temperature. Accordingly, a good many experiments were necessary to determine the conditions needed to bring about coupling of the reaction and shock waves in the right part of the tube. This point is illustrated by the data of Figure 1, which apply to a gas mixture containing approximately 4% H_2 and 2% O_2 by volume in argon.

With sample pressures above about 0.086 atm., the variation of shock speed with sample pressure is as one would expect when no chemical reaction is occurring. In the sample pressure range of 0.082 to 0.086 atm., the shock speed reaches a high value as the reaction wave catches up to the incident wave. For lower sample pressures, the reaction has coupled to the shock wave before the wave reached the measuring station. The effects of small differences in initial pressure, and of other minor variables such as the speed of diaphragm rupture, are shown by the three different shock speeds measured for presumably identical runs at 0.084 atm. Complete data for these three runs show that in one case the peak shock speed occurred before heat transfer gauge 8, in one case between gauges 8 and 9, and in the other case after gauge 9.

A complete set of data for the run that gave the highest velocity in Figure 1 is shown in Figures 2 and 3. The data of Figure 3 have been redrawn from the original oscilloscope records in order to have the same time scale for all the records, and the same pressure scale for the pressure records.

Similar sets of data were obtained for gas mixtures containing approximately 6% H_2 and 3% O_2, and 8% H_2, and 4% O_2. For these mixtures, of course, the energy release by chemical reaction was greater than for the first mixture studied, and the pressure and velocity effects correspondingly more pronounced. Data for a run with the more concentrated mixture are shown in Figures 4 and 5.

DISCUSSION

The data presented in Figures 2 to 5 can best be related by drawing wave diagrams for each experiment. Sufficient data are available to draw reasonably complete wave diagrams, which are given in Figures 6 and 7.

The procedure for drawing Figure 6 was as follows: From Figures 1 and 2 it can be seen that the first velocity measurement of Figure 2 corresponds to a shock wave unaffected by chemical reaction.

Therefore, the shock velocity from the diaphragm to heat transfer gauge 2 will be constant (neglecting diaphragm opening effects and attenuation) at a velocity of approximately 870 meters/sec. (The shock speed that is calculated from the pressures of sample and driver gas, by means of Markstein's graphical method (11), is 880 meters/sec., in close agreement.) If the diaphragm opening time is taken as 0, the incident shock wave will reach heat transfer gauge 2 in 4.38 milliseconds (point A of Figure 6). From this point on, the times to reach various points on the tube are given directly by the data.

It is evident from the slow rise in shock speed between 3.5 and 4.9 meters (Figure 2) that the chemical reaction first produces a gentle pressure wave that travels through the shock-heated gas with velocity u + a, where u is the flow velocity behind the shock wave (551 meters/sec) and a is the speed of sound in the heated gas (557 meters/sec). Accordingly, a characteristic line with u + a, of 1108 meters/sec. can be drawn back from Point A, to represent the path of this first pressure wave that communicates energy from the reaction to the shock wave.

The origin of this wave is undoubtedly near the driver-sample interface, at which is located the part of the gas sample that was heated first (point B of Figure 6). It is apparent that the ignition induction time was about 2 milliseconds, or a little less if it is considered that some of the sample next to the diaphragm will be cooled by driver gas and not react. The calculated temperature behind the incident shock wave is 880°K., and the pressure 0.68 atm.

From Point B the reaction front first appears as a line parallel to the incident shock wave. That is, once the gas has been heated for 2 milliseconds, it starts to react. However, as pressure waves from the reaction increase the incident shock speed, they also increase u and a behind the shock wave. This means, first, that the ignition induction times of successive elements of the gas become shorter, so that the velocity of the reaction wave exceeds that of the shock wave, and second, that pressure waves can catch up with waves sent out previously, thereby generating a shock wave. The formation of this second shock wave is shown in Figure 3. It was just beginning to form as it passed SLM gauge 1, and was better formed as it passed SLM gauge 2. The average velocity in the interval, 1340 meters/sec., is just a little greater than u + a, as one would expect for a weak shock wave. Once the two waves coalesce, the temperature behind the wave is close to 2000°K., at which temperature the induction time is about 20 microseconds (2,3). By this time, then, the reaction wave is close behind the shock wave, as shown in Figure 6.

The wave diagram for the more concentrated gas mixture, Figure 7, is similar in many ways to Figure 6. One notable difference is that the first evidence of chemical reaction to reach the incident shock wave was a well-developed second shock wave, of velocity

2080 meters/sec., which had overtaken and assimilated weak pressure waves sent out earlier when reaction started. The fact that the shock wave had the same shape at the two pressure measuring stations suggests that this is a detonation wave in the gas which had been preheated to 830°K., compressed to 0.79 atm., and accelerated to 555 meters/sec. by the incident shock wave. A calculation of the detonation properties made by standard methods (12) gave the following data, which are compared to the experimental measurements.

Property	Observed	Calculated
Detonation velocity relative to unreacted gas	1,525 meters/sec.	1,465 meters/sec.
Detonation pressure	4.6 atmospheres	5.7 atmospheres
Temperature after reaction	-	2,700°K

The agreement, while not highly accurate, is sufficiently close to confirm the identity of the wave.

The data for this run do not indicate where the detonation wave started, nor where it caught up with the first pressure wave from the reaction zone. Two extreme cases can be considered.

1. The detonation wave formed as soon as reaction started, so a line drawn back from the intersection of the detonation wave with the incident shock wave (Point C of Figure 7) with a slope corresponding to 2080 meters/sec intersects the driver-sample inter-face at the point of initial reaction, at a time of 4.9 milliseconds.

2. The detonation wave overtook the first pressure wave from the reaction just before the latter reached SLM gauge 1, so that a characteristic drawn back from the detonation wave at this point, with a slope corresponding to a u + a of 1110 meters/sec., intersects the driver-sample interface at the point of initial reaction, at a time of 3.2 milliseconds. The wave diagram has actually been drawn half-way between these two extremes, on the assumption that the induction time was 4.0 milliseconds.

The fact that the speed of the incident shock wave goes through a maximum value as the reaction wave couples to it, than later decreases somewhat, is to be expected from the mechanism of the process. Since no reaction occurs during the first few milliseconds, the rate of energy release by chemical reaction reaches a transient maximum value significantly above the normal rate as the reaction wave catches up with the shock wave.

More quantitatively, the velocity of a shock wave with heat release can be calculated, and the calculation gives a value lower than the maximum velocity of Figure 2. We have used Markstein's graphical method (11) in these calculations also. With reference to the experimental conditions of Figure 2, if the induction time was zero an ordinary-looking shock wave would be obtained, with a velocity of 1110 meters/sec., a pressure of 0.75 atm., and a temperature of 1460°K (compared to calculate values of 880 meters/sec., 0.71 atm and 890°K when no reaction occurs). The shock velocity of 1110 meters/sec. would be reached eventually in our experiment with an induction time, if the tube were long enough and attenuation could be neglected. Once this steady situation was reached the pressure would be uniform from the shock front to the driver gas expansion region.

When the same type of calculation is made for the gas mixture containing more hydrogen and oxygen, corresponding to Figures 4 and 5, it is found that the air driver is not capable of maintaining sufficient flow velocity to keep the pressure constant behind the incident shock wave when reaction occurs. The final steady state wave would,therefore, have an appearance between a shock and an ordinary detonation wave, with some drop in pressure, temperature and flow velocity behind the shock front.

ACKNOWLEDGEMENT

One of the authors (G.B.S.) wishes to acknowledge that several preliminary experiments were carried out at Monsanto Research Corporation, Dayton, Ohio, while he was employed there. Mr. Donald L. Zanders assisted materially in these preliminary experiments. He also wishes to acknowledge financial assistance from the Aerospace Research Laboratories under Contract AF33(615)-1915 with The Ohio State University Foundation.

REFERENCES

1. R.A. Strehlow and A. Cohen Phys. Fluids 5, 97 (1962).
2. G.L. Schott and J.L. Kinsey. J.Chem. Phys. 29, 1177 (1958).
3. G.B. Skinner and G.H. Ringrose. J.Chem. Phys. 42, 2190 (1965).
4. J.A. Fay, Fourth Symposium (International) on Combustion, 1952, p. 501.
5. M. Steinberg and W.E. Kaskan. Fifth Symposium (International) on Combustion, 1954, p. 664.
6. F.E. Belles and J.G. Ehlers. Am. Rocket Soc. J. 32, 215 (1962).
7. R.A. Strehlow and H.B. Dyner, AIAA Journal 1, 591 (1963).
8. R.B. Gilbert and R.A. Strehlow, AIAA Journal 4, 1777 (1966).
9. A.J. Laderman and A.K. Oppenheim, Proc. Roy. Soc. A268, 153(1962).
10. P.A. Urtiew and A.K. Oppenheim, Proc. Roy. Soc. A295, 13(1966).
11. G.H. Markstein. Am. Rocket Soc. J. 29, 588 (1959).
12. B. Lewis and G. von Elbe. Combustion, Flames, and Explosions of Gases, Second Edition, New York, Academic Press, Inc., 1961, p. 524.

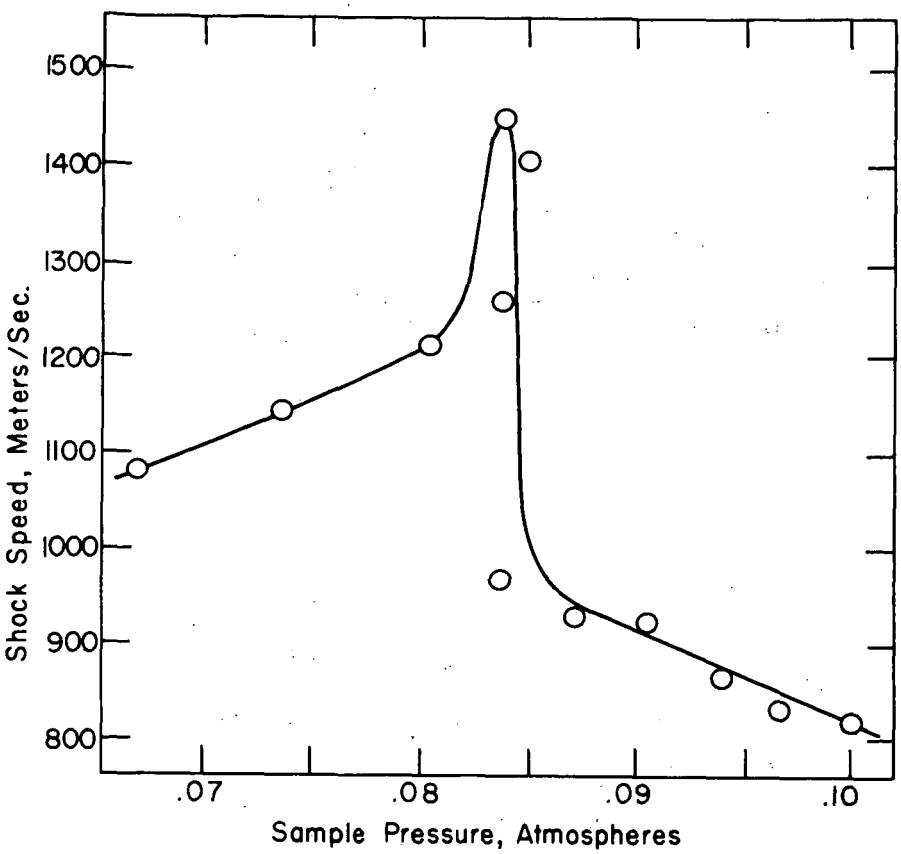

Figure 1. Incident shock speeds measured between heat transfer gauges 8 and 9 for a gas mixture containing 4.33% H_2 and 1.88% O_2 by volume in argon. Driver gas 17.0 atm. of air.

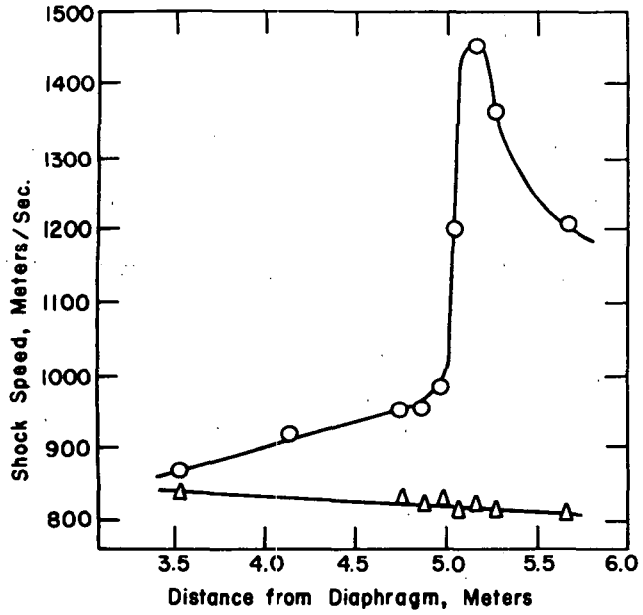

Figure 2. Incident shock speeds measured at different positions along the tube for a gas mixture containing 4.33% H_2 and 1.88% O_2 by volume in argon. Driver gas 17.0 atm. of air. O Sample pressure 0.084 atm.; Δ Sample pressure 0.100 atm., for comparison

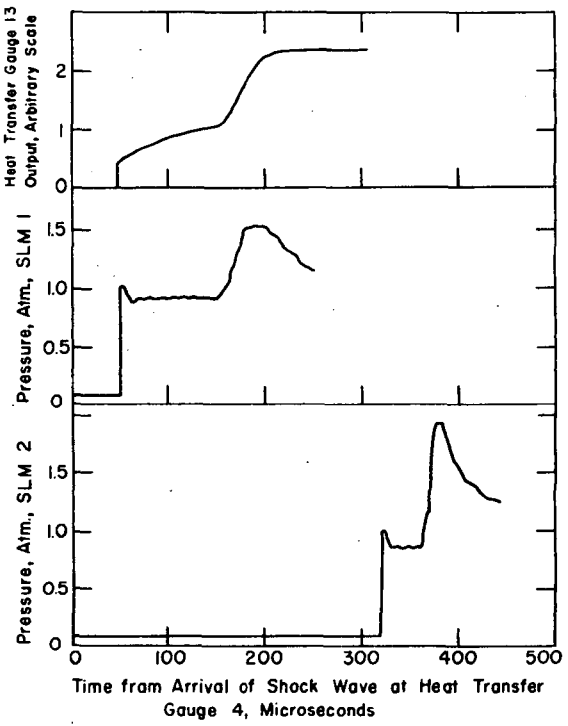

Figure 3. Pressure and heat transfer records for the same experiment as Figure 2(sample pressure 0.084 atm.).

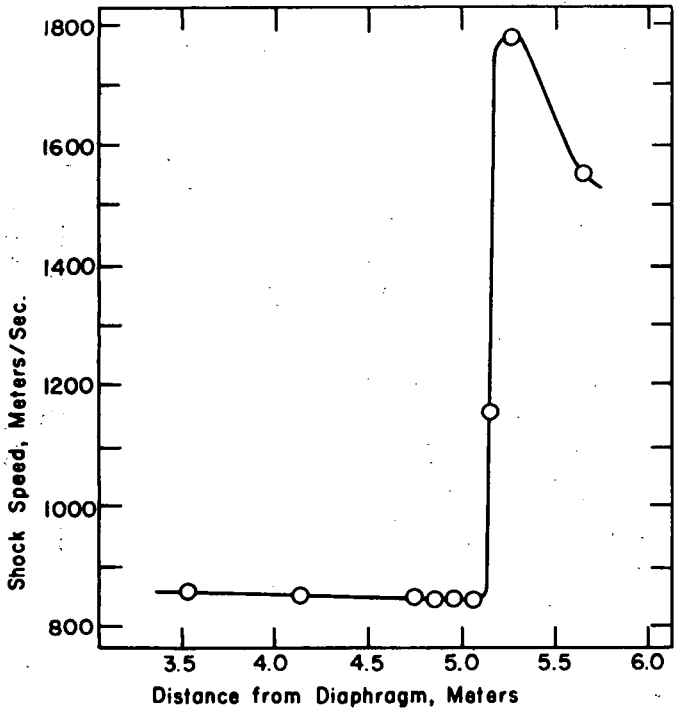

Figure 4. Incident shock speeds measured at different positions along the tube for a gas mixture containing 7.82% H_2 and 4.46% O_2 by volume in argon. Sample pressure 0.100 atm., driver gas 17.0 atm. of air.

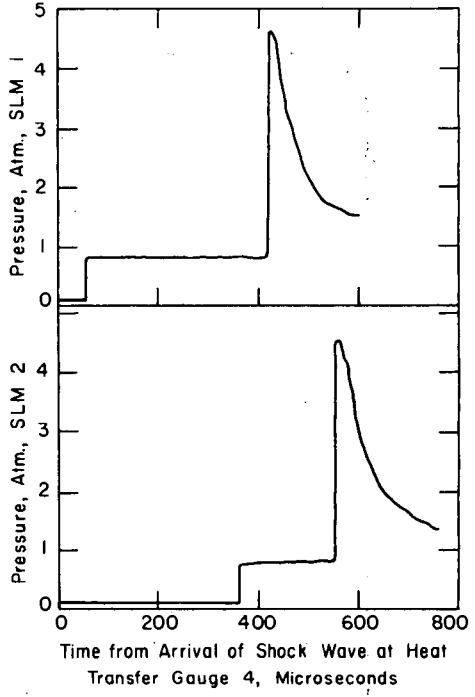

Figure 5. Pressure gauge records for the same experiment as Figure 4.

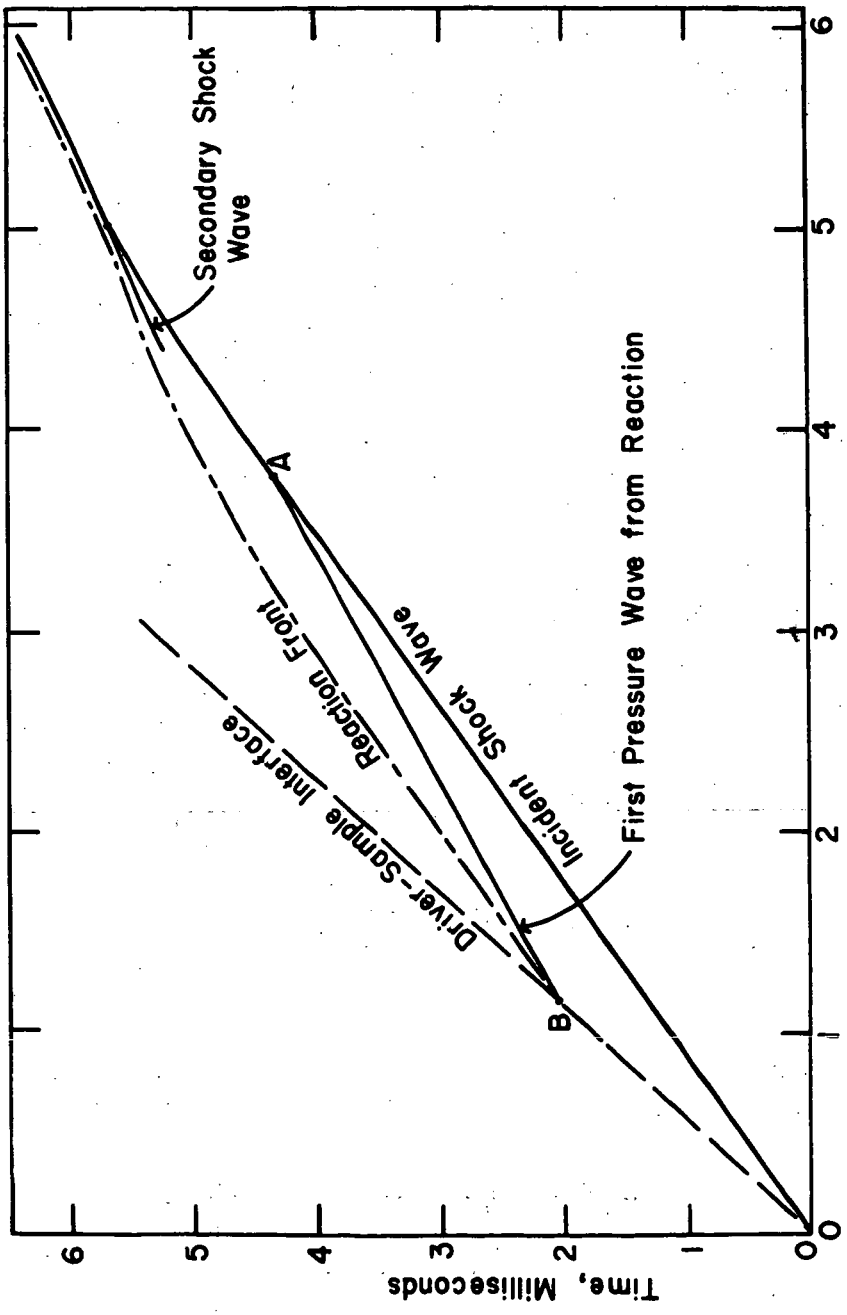

Figure 6. Wave diagram drawn from data of Figures 2 and 3.

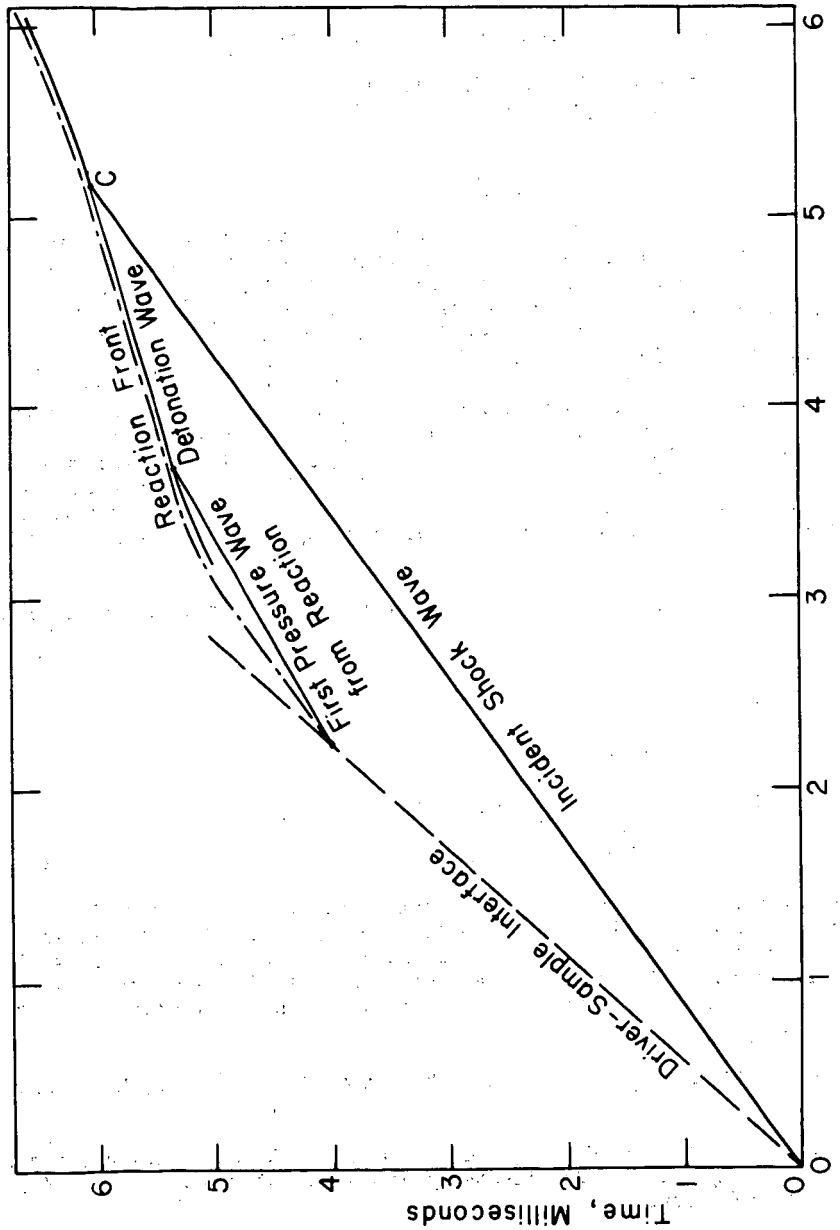

Figure 7. Wave diagram drawn from data of Figures 4 and 5.

SHOCK TUBE STUDY OF THE $H+O_2+Ar \rightarrow HO_2+Ar$ REACTION USING A NEW END-ON TECHNIQUE

David Gutman and Edward A. Hardwidge

Department of Chemistry, Illinois Institute of Technology, Chicago, Illinois 60616

INTRODUCTION

The reaction $H + O_2 + M \rightarrow HO_2 + M$ is an important radical recombination step in many gaseous oxidation reactions and plays a particularly vital role as a chain-terminating process at the second limit of the H_2-O_2 reaction. In this study we have determined the rate constant of this reaction for M=Ar (k_4^{Ar}) in the temperature range 1125-1370°K. The purpose of this study was twofold: first, to obtain accurate values of this constant for use in the analysis of future shock tube studies of combustion reactions (which are most often studied in a high argon dilution) and, second, to assess the potential of the "end-on" shock tube technique for studying recombination reactions. Our experiments consisted of shock-heating H_2-O_2-CO-Ar mixtures and subsequently monitoring the exponential growth of the O-atom concentration during the induction period of this reaction. Values for k_4^{Ar} were obtained from the chain-branching equation using the measured exponential growth constants and known rate constants.

The significant reactions during the induction period of the H_2-O_2 reaction are:[1]

$$H_2 + O_2 \xrightarrow{R_0} O, H, OH \qquad (0)$$

$$H + O_2 \xrightarrow{k_1} OH + O \qquad (1)$$

$$O + H_2 \xrightarrow{k_2} OH + H \qquad (2)$$

$$OH + H_2 \xrightarrow{k_3} H_2O + H \qquad (3)$$

$$H + O_2 + M \xrightarrow{k_4} HO_2 + M \qquad (4)$$

When mixtures of H_2 and O_2 are suddenly heated, a short induction period is observed during which there is a negligible depletion of reactants and an exponential rise in the concentration of the chain carriers [e.g. $[O] = [O]_o e^{\alpha t}$] at essentially constant temperature and pressure. Kondratiev[1] and others have shown that this exponential growth constant α is the positive root of the equation

$$\alpha^3 + (K_1+K_2+K_3+K_4[M])\alpha^2 + (K_2K_3 + K_2K_4[M] + K_3K_4[M])\alpha + (K_2K_3K_4[M]-2K_1K_2K_3) = 0 \qquad (I)$$

where $K_1 = k_1[O_2]$, $K_2 = k_2[H_2]$, $K_3 = k_3[H_2]$ and $K_4 = k_4[O_2]$. Using literature values[2] for k_1-k_3 and the experimentally determined values for α and [M], Equation (I) was solved for k_4.

EXPERIMENTAL

In order to measure the exponential growth of the O-atom concentration during the induction period, H_2-O_2-CO-Ar mixtures were shock-heated and the chemiluminescent emission from the $O + CO \rightarrow CO_2 + h\nu$ was monitored. Since the emission intensity is proportional to [CO][O] and since the concentration of CO is constant during the induction period, the emission will exhibit the same exponential growth as the O-atoms. To obtain sufficient emission intensity for our induction period measurements, we used a special end-on technique, in which we studied the reaction behind the reflected shock wave by monitoring the total light emitted axially through a 7.6 cm diameter window mounted in the end flange of the shock tube. Under suitable conditions, the exponential growth constant of the integrated emission observed by this technique is identical to that for the free radical growth during the induction period.

The apparatus and experimental techniques were basically the same as those described earlier and therefore will only be summarized here.[2] The 10 cm diameter stainless steel shock tube used in this study has a 3.96 meter long test section and a 1.82 meter long driver section. Five thin film heat guages used to measure the shock velocity are mounted 25.4 cm apart along the tube, the last one located 15.0 cm from the end of the shock tube. The end flange of the shock tube was fitted with a 10 cm diameter and 1.25 cm thick Pyrex glass disk, masked on the outside to provide a 7.6 cm diameter axial window. A plano-convex lens (focal length 57.1 cm, diam. 8.6 cm) located 3 cm behind the window focused the light, which is emitted parallel to the axis of the shock tube, onto a telecentric aperture 1.9 cm in diameter located at the focal point. The light intensity was recorded by am Amperex 150 AVP photomultiplier tube (S-11 response) located behind the aperture. The output of the cathode follower was directed to a Tektronix 545 oscilloscope (CA preamplifier) fitted with a Polaroid camera. A thin film heat gauge deposited on the window provided the signal that triggered a single sweep of the oscilloscope upon arrival of the shock wave at the end of the tube.

All experiments were performed in gas mixtures containing 0.50% H_2 - 0.50% O_2 - 3.0% CO - 96% Ar with the exception of three runs made with the same H_2-O_2 amounts but with 0.50% CO and 98.5% Ar. The gases were taken from commerical cylinders and were purified by passing them through a Drierite-filled trap cooled to dry-ice temperature. Two sets of experiments were performed - a high density set with densities in the range of $4.2 - 5.8 \times 10^{-2}$ moles/liter and a low density set having densities between $1.1 - 2.5 \times 10^{-2}$ moles/liter.

DATA REDUCTION

The shock velocity at the end of the tube was obtained from extrapolation of the data from the five thin film gauges mounted near the end of the shock tube. Hugoniot calculations for conditions of no chemical reaction behind both incident and reflected shock waves were used to determine the temperature and concentration conditions in each experiment. In all experiments, the vertical deflection was read from the oscillogram and plotted as a function of time on semi-log paper. A straight line was hand drawn through the data points and an experimental time constant $\alpha(sec^{-1})$ was calculated for each. The results are listed in Table I.

Solving Equation I for k_4, we obtain

$$k_4 = \frac{-8\alpha'^3 - 4(k_1 + k_2 n + k_3 n)\alpha'^2 - 2k_2 k_3 n^2 \alpha' + 2k_1 k_2 k_3 n^2}{4[M]\alpha'^2 + 2(k_2 n[M] + k_3 n[M])\alpha' + k_2 k_3 n^2 [M]} \qquad \text{(II)}$$

where $\alpha' = \alpha/2[O_2]$ and $n = [H_2]/[O_2]$.

By using Equation II and the experimentally determined growth constants α, we obtained a value for k_4 for each high density experiment. These values are given in the last column of Table I and are plotted in Figure II.

The calculated values for k_4 depend strongly on the value assumed for k_1 and only to a minor extent on the values used for k_2 and k_3. This is because Reaction 1 is the slow step in the branching mechanism under our experimental conditions and is almost rate limiting. To obtain accurate and self-consistent values for k_1 for our calculations, we solved Equation I for α and varied k_1 until the experimental α values at high temperature and low density (where Reaction 4 is unimportant) corresponded to the calculated value. The best fit was with an expression $k_1 = 1.25 \times 10^{11} \exp(-14.97 \text{ kcal/RT})$ which yields values 30% higher than the expression reported by Gutman and Schott.[2] The Arrhenius expressions for k_2 and k_3 used for both the α and k_4 calculations were $k_2 = 3.25 \times 10^{10} \exp(-10.0 \text{ kcal/RT})$ liter/mole-sec[3] and $k_3 = 6.15 \times 10^{10} \exp(-5.90 \text{ kcal/RT})$ liter/mole-sec.[4] The lines drawn through the experimental points in Figure I are solutions to Equation I using: (1) the above values for k_1, k_2, and k_3; (2) a smoothed density function $[M] = M(T)$ obtained from the experimenatl densities (one for each line); and (3) the expression $k_4^{Ar} = 6.83 \times 10^{11}/T^{0.74}$ (liter^2/mole^2-sec) which is explained below. [Hereafter units of liter^2/mole^2-sec are implied for k_4.]

To obtain a temperature dependent function of k_4 for use in the above calculations and also for use in comparing our results with others at different temperatures, we evaluated the parameters in the expression $k_4^{Ar} = A/T^n$ by joining the point $k_4^{Ar} = 3.75 \times 10^9$ at 1087°K at the low temperature end of our study with a value of $k_4^{Ar} = 12.5 \times 10^9$ at 225°K reported by Clyne and Thrush.[5] The resulting expression is $k_4^{Ar} = 6.83 \times 10^{11}/T^{0.74}$.

The error limits for our k_4 values vary from ±30% at the low temperature end of our study to ±100% at the high temperature end. This change in accuracy is a result of the decreasing effect of Reaction 4 in the branching kinetics as the temperature increases and the density decreases. These limits were obtained from assigning a ±20% overall uncertainty to α' and are shown as error bars in Figure II.

Because of the rapidly increasing limits of error toward our higher temperature results, we have chosen the mean value $k_4^{Ar} = 3.75 \times 10^9$ liter^2/mole^2-sec at 1087° as our best value and assign it an accuracy of ±30%.

DISCUSSION

The effects of adding CO to the H_2-O_2 system were discussed previously.[2] However, in this study an additional consideration is important due to the high densities used here. The reaction $O + CO + M \xrightarrow{k_6} CO_2 + M$, although slow,

was taken into account. It was added to the kinetic mechanism and a new cubic equation was obtained for α, which in turn was solved for k_4^{Ar}. Using a value of 1×10^8 liter^2/mole^2-sec,[6], there was a negligible change in the calculated k_4. We performed four experiments with 0.5% CO and obtained from these experiments calculated k_4 values in agreement with the others performed with mixtures containing 3% CO.

Our results are virtually in complete agreement with the value for k_4^{Ar} recently reported by Getzinger and Blair.[7] They report a value of $k_4^{Ar} = 2.5 \times 10^9$ in the temperature range 1500-1700°K. Extrapolating our value to their temperature range, we calculate values 10-20% higher than theirs. Other values for k_4, especially for k_4^{H2}, have been reported near 800°K based on explosion-limit studies. These studies are in fair agreement with one another and report values for k_4^{H2} near 8×10^9 liter^2/mole-sec.[8] Converting these to a value for k_4^{Ar} gives 1.4×10^9 (assuming the presently accepted ratio $k_4^{H2}/k_4^{Ar} \cong 5$). At 800°K our k_4^{Ar} expression gives the value 6×10^9. No explanation is offered at this time to account for this large discrepancy. A value for $k_4^{H2O} = 100 \times 10^9$ has been reported by Fenimore and Jones from flame studies near 1350°K.[9] If this value is adjusted to give a value for k_4^{Ar} using $k_4^{H2O}/k_4^{Ar} = 20$, it yields a value somewhat higher but in good agreement with our k_4^{Ar} curve. The agreement might well be fortuitous, since their error limits are rather large and the correction for the relative efficiency of water is somewhat uncertain.

CONCLUSIONS

The end-on technique provides a means of making measurements during the induction period of chain-branching reactions. Since during this period radical concentrations are low, only those reactions which have a single radical reactant have an appreciable rate. Hence, this technique allows one to study combustion processes unperturbed by radical-radical reactions. In the case of $H_2 + O_2$ reaction, use of the end-on technique has resulted in values for k_1, k_2, and k_4. In other systems where the mechanism is not clearly understood, measurements of the chain-branching coefficient under a variety of initial conditions could help to identify the important reactions.

ACKNOWLEDGEMENTS

We wish to thank Frank Dougherty, Robert W. Lutz, and Jacqueline Mutel for their help in performing the experiments and evaluating the data. This research was supported by the National Science Foundation and the Petroleum Research Foundation.

BIBLIOGRAPHY

1. V. N. Kondratiev, Chemical Kinetics of Gas Reactions, Pergamon Press, Inc., New York, 1964, Sec. 39.

2. D. Gutman and G. L. Schott, J. Chem. Phys., 46, in press.

3. The expression for k_2 is from Reference 2 and agrees closely with that recently reported by A. A. Westenberg and N. de Haas, J. Chem. Phys., 46, 490 (1967). Their expression $k_2 = 4.0 \times 10^{10} \exp(-10.2 \text{ kcal/RT})$ liter/mole-sec is derived from measurements made from 300-1000°K.

4. F. Kaufman and F. P. DelGreco, Symp. Combust. 9th, Cornell Univ., Ithaca, New York, 1962, 659 (1963).

5. M. A. A. Clyne and B. A. Thrush, Proc. Roy. Soc. (London), A275, 559 (1963).

6. This value for k_6 is taken from a line joining the room temperature results of V. N. Kondratiev and I. I. Prichkin (Kinetika i Kalatiz, 2, 292 (1961)) and those of T. A. Brabbs and F. E. Belles, (NASA TM X-52197) at 3000°K. The latter results were presented at the Eleventh Symp. Combust., Berkeley, California, 1966.

7. R. W. Getzinger and L. S. Blair, Paper presented at the Sixth International Shock-Tube Symposium, Freiburg, Germany, April, 1967. R. W. Getzinger and G. L. Schott, J. Chem. Phys., 43, 3237 (1965) reported a value for $k_4^{Ar} = 1.42 \times 10^9$ liter^2/mole^2-sec at 1500°K using almost the same experimental procedure as in the above paper.

8. For a review of these studies see B. A. Thrush in Progress in Reaction Kinetics, Vol III, Pergamon Press, New York, 1965, p. 63.

9. C. P. Fenimore and G. W. Jones, Symp. Combust. 10th, Cambridge, England, 1964, 489 (1965).

Table I

Experimental Results of induction period emission experiments
$X_{H_2} = 0.0050$; $X_{O_2} = 0.0050$; $X_{CO} = 0.030$; $X_{Ar} = 0.960$

Low Density Experiments

$\alpha \times 10^{-5}$ (sec^{-1})	$[M] \times 10^2$ (mole/liter)	$\alpha' \times 10^8$ (liter/mole-sec)	θ_T (°K)	$K_4^{Ar} \times 10^{-10}$ (liter^2/mole^2-sec)
1.44	1.096	13.300	2040	
1.48	1.096	13.500	2040	
1.40	1.152	12.130	2000	
1.38	1.206	11.140	1943	
1.15	1.298	8.860	1793	
9.8	1.274	7.700	1750	
1.01	1.382	7.310	1705	
0.728	1.238	5.890	1655	
0.836	1.528	5.490	1613	
0.920	1.466	5.280	1608	
0.921	1.584	5.820	1600	
0.808	1.510	5.350	1577	
0.783	1.510	5.180	1576	
0.813	1.498	5.430	1555	
0.705	1.650	4.270	1515	
0.702	1.740	4.040	1465	
0.562	1.614	3.480	1455	
0.602	1.840	3.300	1440	
0.511	1.608	3.180	1437	
0.527	1.744	3.020	1395	
0.434	1.856	2.220	1355	
0.418	2.024	2.060	1325	
0.391	1.880	2.080	1296	

Low Density Experiments

$\alpha \times 10^{-5}$ (sec^{-1})	$[M] \times 10^{2}$ (mole/liter)	$\alpha' \times 10^{8}$ (liter/mole-sec)	T (^{o}K)	$K_7^{Ar} \times 10^{-10}$ ($liter^2/mole^2$-sec)
0.339	2.040	1.660	1296	
0.359	2.020	1.780	1280	
0.333	2.080	1.600	1270	
0.250	2.138	1.170	1220	
0.240	2.080	1.150	1192	
0.206	2.070	1.000	1182	
0.218	2.200	0.990	1173	
0.202	2.000	1.010	1160	
0.159	2.260	0.702	1130	
0.160	2.040	0.783	1110	
0.150	2.420	0.620	1105	
0.160	2.410	0.673	1100	
0.142	2.120	0.670	1100	
0.150	2.536	0.592	1060	

High Density Experiments

1.035	4.75	2.180	1370	0.419
1.065	4.59	2.320	1370	0.337
0.885	4.75	1.865	1295	0.173
0.561	5.30	1.060	1260	0.458
0.522	5.44	0.960	1220	0.334
0.338	5.52	0.610	1200	0.453
0.404	5.56	0.727	1180	0.307
0.268	5.80	0.462	1175	0.511
0.383	5.54	0.690	1175	0.309
0.279	5.59	0.529	1160	0.404
0.198	5.77	0.343	1155	0.423
0.163	5.83	0.279	1125	0.362
0.113	5.92	0.191	1130	0.422
*0.832	5.22	1.590	1285	0.270
*0.381	5.42	0.700	1185	0.346
*0.284	5.67	0.501	1166	0.380
*0.186	5.81	0.320	1135	0.371

* Experiments performed with:
$X_{H_2} = 0.0050$; $X_{O_2} = 0.0050$; $X_{CO} = 0.005$; $X_{Ar} = 0.985$

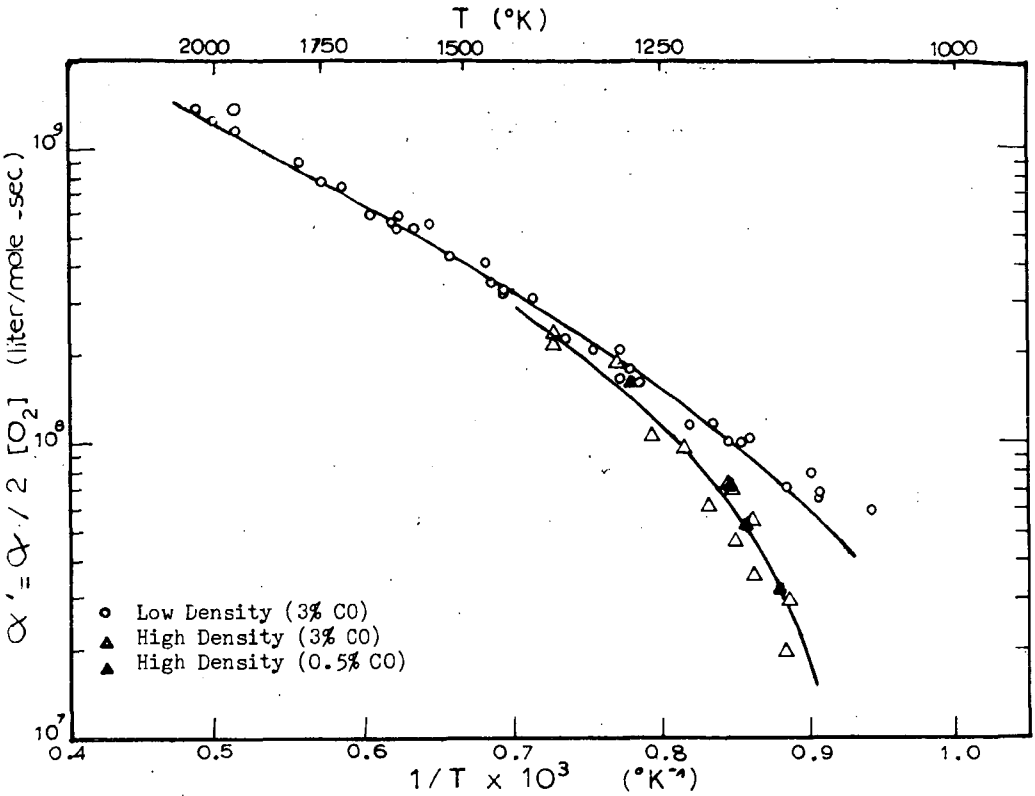

Figure I. Plot of $\alpha / 2\ O_2$ vs. 1/T.

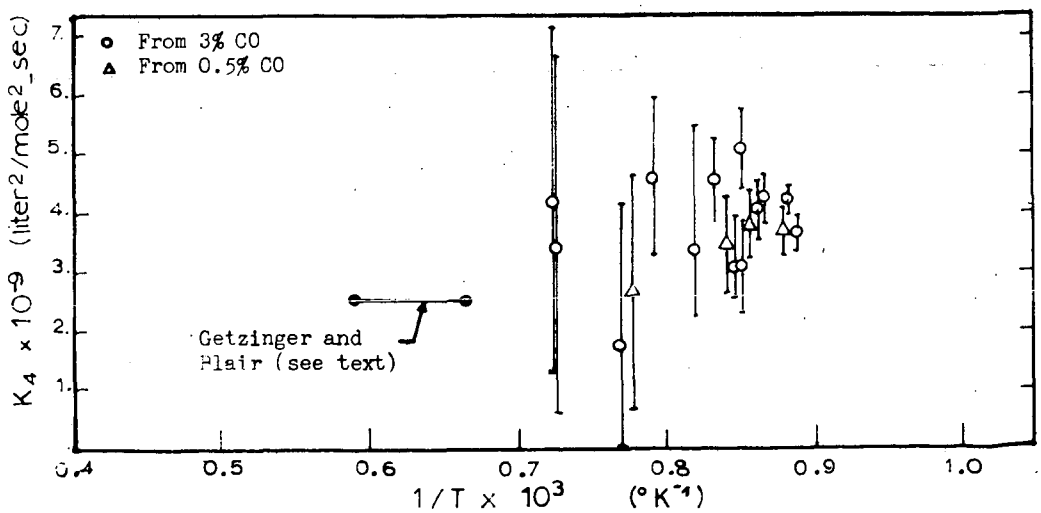

Figure II. Calculated values for k_4^{Ar} from corresponding points on high density curve in Figure I.

SHOCK FRONT STRUCTURE - A CHEMICAL KINETICS VIEW

S. H. Bauer

Department of Chemistry, Cornell University, Ithaca, New York 14850

INTRODUCTION

In the analysis of shock front structures in real gases, intermolecular processes which fall within the province of chemical kineticists play a dominant role. The determination of shock front profiles in density, temperature and in the concentrations of chemical species, provide kineticists with powerful techniques for exploring mechanisms for reactions which cannot be studied otherwise. This has been recognized for over a decade. Advances made in the state of the art through 1963 can be measured by the content of an 850-page treatise on shock tubes by H. Oertel[1], which covers theory, practice and applications in a detailed and thorough manner. More recent assessments may be obtained from the 94 abstracts of papers which were submitted for presentation at the 6th International Shock Tube Symposium ;[2] and the 37 reports given at the AGARD Colloquium on "Recent Advances in Aerothermochemistry." [3]

In this summary attention is called to several developments which have advanced the "state of the art" during the past year. A brief overall assessment shows that there is continued emphasis on the improvement of experimental techniques. These center around cleanliness of operation (good vacuum technique, insistence on low leak rates, etc.), the use of polished inner walls to reduce boundary layer perturbations, improved control of species concentrations, increased precision in shock speed measurements, refinement in sensitivity and reduction of response times for diagnostic devices used in recording the profiles of shock fronts, etc. In addition there is greater sophistication in the design of experiments. The improvements may be categorized into three groups: (1) use is being made of newly available devices, such as lasers; (2) it is now general practice to record in many channels concurrently, such as the mass spectra of several species, the concurrent recording of emission and absorption spectra at different wavelengths as a function of time; (3) combining shock tube techniques with other techniques for the preparation of samples to be studied; for example, preliminary flash photolysis or imposition of a glow discharge through the sample prior to its being exposed to the shock wave. Along with increased sophistication in the performance of experiments, extended computer programs are used routinely, both for equilibrium compositions and for obtaining kinetic profiles; also, to facilitate data reduction.

These trends will continue because they have already proved their worth, but they occur at the expense of increased complexity in equipment, leading inevitably to the need for collaboration among several persons in operating a facility. What remains for the lone experimenter? It appears to me that for some time to come the single-pulse shock tube technique will remain one of a few individualistic activities. The investigator will have to be ingenious in designing kinetic experiments in which knowledge of the concentrations of species after a specified reaction time permits an identification of a mechanism. Single-pulse shock tubes allow the exploration of complex systems in a qualitative manner, and provide the basis for selecting reactions which are critical steps in a complex reaction scheme for detailed study by other techniques.

TECHNIQUES AND DIAGNOSTIC DEVICES

A representative selection of interesting developments in technique is presented in Table 1. The use of narrow electron beams for exciting molecular spectra in a flowing medium merits an additional comment. The characteristic spectra excited permit identification of the species present, and an estimation of their densities (if proper calibrations are made). Vibrational and rotational temperatures can be obtained from band contours. In the hands of a careful experimentalist, this technique may give translational speeds as well (Doppler widths of spectral lines). For example, in a supersonic jet of nitrogen expanding from room temperature in an axi-symmetric nozzle,[8] the rotational temperature was observed to follow the isentropic curve initially, but at the lower temperatures the rotational population "froze" to a fixed distribution leading to a substantial degree of non-equilibrium.

Perhaps one of the most sensitive devices for measuring gradients at a shock front with high resolution is the laser-schlierien method described by Kieffer and Lutz.[11] Gradients as low as 10^{-5} gm/liter mm can be detected in argon, and characteristic times (lab scale) as short as 0.2μ sec. have been measured. Vibrational relaxation times for hydrogen and deuterium have thus been quantitatively determined for the first time. This technique has been effectively used to scan the heat release profile during the high temperature oxidation of acetylene.[12]

The best illustration of concurrent multichannel recording to provide a large amount of information for a single shock, and thus to correlate a variety of parameters, is the use of a rapid-scan mass spectrometer. A time-of-flight spectrometer coupled to a shock tube via a minute leak has been described by Kistiakowsky,[13] Dove,[14] Diesen[15] and Modica.[16] The successful application of a quadruple mass filter for the analysis of products extracted from a back-reflected shock has been recently reported by Gutman.[17] As described this relatively low cost instrument could be set to record only one mass at a time; however, current developments in Gutman's laboratory indicate that it may be possible to set four mass filters for concurrent recording. The fidelity of sampling of back-reflected shocked gases through 0.002 inch apertures remains to be demonstrated. To avoid confusion of the desired sample with end-wall cooled gases and boundary layer perturbations, Marsters[18] extracts the sample from a rapidly quenched incident shock and by a sequence of large aperture nozzles converts the jet to a molecular beam for analysis by a time-of-flight spectrometer.

There is an intriguing possibility of using a small mass spectrometer to detect the onset of ionization (in particular, the onset of production of a particular species) and correlating this profile with spectroscopic data (chemiluminescence, or the appearance of a characteristic absorption). In this connection one should mention the successful application of a Nier-type mass spectrometer by Sturtevant[19] who demonstrated that the first ions to appear in shock-heated argon, at a threshold approximately four volts below the ionization potential of argon, were H^+ and O^+, presumably from a very low level water impurity.

The technique of preparing equilibrium samples at elevated temperatures (as with reflected shocks) and quenching them so rapidly that one may study kinetic processes which occur during the cooling path has not attracted many devotees, although expansion through a small aperture in the end wall of a shock tube for sampling purposes is being used by mass spectrometrists. To avoid boundary layer problems and to achieve very rapid cooling, Wilson[20] inserted a pair of divergent airfoils in a shock tube, so that the incident shock passed through a double Prandtl-Meyer

expansion. This setup was used effectively for measuring the recombination rate of oxygen atoms at elevated temperatures, and is currently being developed in our laboratory for investigating condensation processes in metal vapors produced under supersaturated conditions by shock-heating metal carbonyls. The expansion generated by the interaction of the contact surface with the reflected shock was used for a kinetics study of the association of CN radicals prepared by shock-heating C_2N_2/Ar mixtures to about 2000°, [21] the CN concentration was followed spectrophotometrically. It was found that the rate of CN disappearance was first order in CN and first order in C_2N_2 (or C_mN_m polymers), and that the average polymer number under these conditions, $m \approx 10$. Finally, a rapid-quench sampling probe for non-equilibrium air flows has been described by Stoddard and Watt[22] in which a small sample scooped from the free stream region in a shock tunnel is rapidly cooled by contact with the walls of an explosively sealed probe.

An example of interesting results obtained from use of combined techniques is the glow tube described by Hartunian, et al[23] in which a steady-state concentration of reactive species is prepared in a glow-discharge flow system, and fully characterized (at room temperature). The plasma is then subjected to a shock, initiated by rupture of a diaphragm upstream from the rf source. Typically, the shock strength is less than that which causes further dissociation; the shock compresses, heats and accelerates those species which are already present in the glow tube. Thus, a means is provided for studying the temperature dependence of the gas phase recombination processes and of chemiluminescent reactions. This combination provides a considerable extension of atom fluxes for study of kinetic processes. In contrast to heating with shock waves, Petrella et al[24] describe a combination flash photolysis-flash pyrolysis system in which heating is accomplished by the comparatively slower process of allowing the gaseous sample to contact a flash-heated solid grid.

References to several current analyses on the non-ideal behavior of shock tube operation are listed in Table II, while Table III is a summary of papers in which the measurement of ionization cross-sections and of optical oscillator strengths are discussed.

MEASUREMENT AND CONTROL OF VIBRATIONAL STATE POPULATIONS

During the past two years much effort has been devoted to the study of the excitation of vibrational modes due to intra- and inter-molecular energy transfer processes. For many decades it has been accepted by kineticists that the measured reaction rate constants depend on the facility for energy transfer between the various parts of reacting molecules when in the transition state. The mere difficulty of properly estimating the density and symmetry character of the highly excited states even in simple systems, led to an attitude of futility, as expressed by the observation that there seems to be little relation between the states of interest to chemical kineticists and the transition probabilities measured for low-lying vibrational states. However, several examples are now known for which the measured rate constants may be calculated from measured vibrational relaxation times. The basis for the current activity is in part due to the recognition of the presence of strong coupling between vibrational modes and dissociation, and in part to the current explosive development in laser technology.

It has been known for several years that vibrational relaxation times for small molecules containing hydrogen atmos are much shorter than those predicted on the basis of the Slawsky-Schwartz-Herzfeld theory, and the observed relaxation times did not fit the correlation diagram proposed by Millikan and White. For example, the

vibrational relaxation times for HCℓ, DCℓ and HI measured by the spectrophone method[43] (at room temperature) are consistent with the high temperature data (infrared emission from shocked gases at 2000°)[44] in that the relaxation times were several orders of magnitude shorter than those predicted by the SSH theory. They are in better agreement with Cottrell's vibration-rotation theory[45]. That rotational motion plays a role in exciting vibrational states was demonstrated by Millikan[46] who measured the relative rates of collisional deactivation of vibrationally excited CO by ortho and para hydrogen. Another example of the inadequacy of the SSH theory are the vibrational relaxation times for H_2-Ar, H_2-H_2, D_2-Ar, D_2-D_2 reported by Kiefer and Lutz[11]. These data are better accounted for by Parker's semi-classical theory[47] with an angle-dependent potential used for calculating both rotational and vibrational relaxation times. Even though there is agreement for collision numbers with argon and krypton as collision partners, there remains an order of magnitude disagreement for self collisions of H_2 and D_2. A good summary of relaxation processes involving rotational-vibrational interactions and resonance collisions was given by R. C. Millikan;[48] a simple two-parameter model was developed by C. B. Moore.[49]

The relaxation of NO $X^2\Pi$ (v = 1) in D_2S, H_2O, H_2S, D_2O and CH_4 was investigated by microwave-flash pulse-flash spectroscopy.[50] Deactivation by all the hydrides was very fast compared with the rate of self deactivation. The rate coefficient showed a systematic variation with the minimum energy which had to be converted to translation. The authors propose that the uniformly fast relaxation by the triatomic hydrides may arise from the formation of an intermediate complex between NO and the H_2S or H_2O. However, this does not account for the effect of isotopic substitution. For comparison, helium is $\approx$0.1 as effective as NO, which in turn is $\approx$0.01 as effective as H_2S.

The vibrational relaxation of oxygen in the presence of small amounts of methane (0.5% to 1.6%) was measured at room temperature by ultrasonic techniques.[51] The relaxation frequency did not vary linearly with the methane concentration. It appears that translation-vibration excitation occurs only for methane, but that oxygen molecules become excited only by vibration-vibration transfer from the methane. A similar mechanism for energy transfer was reported by Millikan in the quenching of carbon monoxide fluorescence by methane.[48] In contrast, for nitrogen-hydrogen mixtures ($\approx$2% H_2) White[52] found that the vibrational relaxation time fitted their systematical correlation diagram.

The density profile at the shock front due to vibration relaxation in oxygen was explored with the laser-schlieren technique, in pure oxygen and in oxygen-ozone mixtures.[53,54] Kiefer and Lutz report:

$$p\tau_{(O_2\text{-}O_2)} = (2.92 \pm 0.20) \times 10^{-10} \exp\left[(126.0 \pm 0.9)/T^{1/3}\right], \text{ atm. sec.}$$

$$p\tau_{(O_2\text{-}O)} = (4.35 \pm 0.19) \times 10^{-8} - (7.75 \pm 0.81) \times 10^{-12} T, \text{ atm. sec.}$$

The latter is the deduced value for oxygen molecules dilute in an atmosphere of atoms. These clearly differing temperature dependencies indicate a strong chemical effect, possibly similar to those previously suggested for the CO_2-H_2O system and CO-$C\ell_2$ systems, but more likely due to atom exchange:[55]

$$O_2 + O' \rightarrow O + OO'.$$

Measurement of the vibrational relaxation times in nitrogen presents an interesting case history. Sodium-spectrum line-reversal measurements for N_2 in

normal shocks gave vibrational relaxation times which checked well with interferometer-shock tube investigations. (Extrapolation to temperatures below 1500°K gives values which are orders of magnitude higher than sound dispersion and impact tube results.) However, when the line reversal technique was used to scan the vibrational non-equilibrium produced in supersonic expansions of undissociated nitrogen from reservoir temperatures 2800-4600°K (15° axi-symmetric nozzle, coupled to the end of a shock tube), the probability for de-excitation appeared to be $\approx$50 times greater.[56] This short relaxation time has now been confirmed by following the CO vibrational relaxation (introduced as a tracer in the expanding nitrogen stream), and by the electron beam technique in a low density non-steady expansion. For a while it was believed that the rapid relaxation was due to impurities present in the reservoir gas, but this was proven untenable.[57] A plausible explanation has now been proposed by Treanor and coworkers.[58] They point out that inadequate consideration has been given to effects of anharmonicity on vibrational relaxation for vibration-vibration exchange dominated regimes. When the translation temperature is quite low and the vibrational energy content is high (as in a rapidly expanding nozzle flow) vibration-vibration exchange introduces a slight but definite non-Boltzmannian vibrational population distribution. In such a case the population of the lowest vibrational level may be considerably lower than what it would be if the system were to relax through a sequence of Boltzmann distributions, thus indicating an apparent rapid relaxation time. Current experiments at CAL on the vibration relaxation in expanding nozzle flows for CO parallel the above observations reported for nitrogen. It is interesting to note that for the ascending path, i.e., the vibrational excitation of nitrogen, as followed by monitoring the v"=9 level (U.V. absorption at 1176Å), the recorded times[59] are consistent with the Shuler-Rubin-Montroll theory that the populations of vibrational levels relax via a continuous sequence of Boltzmann distributions (3000°-5500°K). For temperatures in excess of 5500°K, the local value for the characteristic relaxation time (τ_v) becomes increasingly dependent on the degree of vibrational excitation.

A large amount of attention is currently being devoted to studies of the vibrational relaxation processes that occur in carbon dioxide. One must consider not only intermolecular energy exchange (V-T) and (V-V) with various colliders for CO_2 molecules in its different vibrational states, but also vibrational energy redistribution in CO_2 molecules due to collisions with ambient gases. To date ultrasonic dispersion studies have uncovered only three gases which show two dispersion frequencies: SO_2, $CH_2C\ell_2$, and C_2H_6. Many shock tube investigations have shown that the vibration-translation relaxation in CO_2 follows a single relaxation time. On the basis of careful measurements of the variation of density behind incident shock waves in carbon dioxide, up to temperatures 2500°K, Simpson, et al[60] report that only a single relaxation time is discernable even though the density behind the shock front does not change strictly exponentially with distance; the departure is due to changes in the translational temperature which must accompany the relaxation process. A similar conclusion was reached by Weaner, et al[61] who made simultaneous measurements of the flow density with a Mach-Zehnder interferometer at the shock front and of the infrared emission at 4.3μ. While the emission intensity monitored the population of the ν_3 level, the density provided a measure of the energy flow into all the vibrational modes. The single relaxation time was thus interpreted as evidence that equilibrium among all the vibrational modes was attained within the rise time of their detector (1.5 μsec). However, the situation gets more complicated when one considers (V-V) energy transfer.

Moore and coworkers[62] measured decay curves of laser-excited vibrational fluorescence from the (00°1) level of CO_2 (asym. stretch), as dependent on the admixed gases. He

deduced (V-V) transfer rates at room temperature which ranged from 15.5 atm-μsec for He as a collision partner, to 3.76 (self), to 0.34 (H_2) to 0.055 (H_2O). Ultrasonic data give relaxation times for the (01'0) level (V-T). Corresponding values, for self collision, CO_2 6.8 ± .3 atm-μsec; with He (0.39), H_2 (0.015) and H_2O (0.0030). They also deduced the energy transfer probability for the reaction.

$$CO_2\ (00^o1) + N_2(0) \rightarrow CO_2\ (00^o0) + N_2(1)$$

to be (2.0 ± .4) x 10^{-3}. The significant catalytic role of water for CO_2 laser operation is now evident. At elevated temperatures over the range 800 to 3000°K shock tube measurements[63] with very short response time detectors show comparable differences between the several relaxation processes. Taylor and Bitterman[64] have prepared an exhaustive survey of vibrational relaxation data for processes important in the CO_2-N_2 laser system. A brief review on (V-V) transfer efficiencies as deduced from ultrasonic measurements has been published by Lambert.[65]

UNSOLVED PROBLEMS IN THE DISSOCIATION OF SMALL MOLECULES

One of the basic problems in chemical kinetics is the detailed analysis of the processes which occur when in diatomic molecules are dissociated thermally but homogeneously. Although a qualitative description has been given decades ago, it was not possible to perform the experiments nor to test details of the theory until the advent of shock tube techniques. One of the essential features required is the possibility to separate in time the vibrational excitation processes from the dissociation steps. It is now evident that conventional kinetic descriptions are not adequate. For example: The dissociation rate of very pure hydrogen at low concentrations in argon (0.01%-1.0%) has been measured by Watt and Myerson[66] using atomic absorption spectrophotometry (Lyman α line). An Arrhenius plot for the bimolecular rate constant gives an activation energy of 94.5 kcal over the temperature range 2200°K. These rates are approximately a factor of five lower than rates reported by previous investigators, presumably because their samples were contaminated with slight amounts of oxygen which accelerated the dissociation rate through the reaction $H + O_2 \rightarrow OH + O$, followed by $O + H_2 \rightarrow OH + H$. For contrast Hurle reported about a year ago[67] his studies of dissociation rates in hydrogen-argon mixtures (20% to 60% H_2) covering the temperature range 2500° to 7000°K, based on the Na-spectrum line-reversal technique for temperature measurement. He then deduced degrees of dissociation as a function of time (or distance behind the shock front), and was able to assign relative efficiencies to Ar, H_2, and H atoms as colliders. When his results were converted to recombination rate constants it appears that H_2 is several times more efficient than argon as a chaperon for the $2H \rightarrow H_2$ recombination but both show an approximate T^{-1} dependence. However, the efficiency of H atoms as chaperons appears to be equal to that of H_2 for temperatures above 5500°K but as the temperature is lowered the efficiency rises sharply and at 3000° is about 30 times greater than that for H_2. Furthermore, there are indications that for temperatures below 2500°K the efficiency drops again and the room temperature H atoms may be only three times as effective as H_2.

The following observations are typical of most of the homoatomic diatom dissociation processes.[68] In all cases the self atom is much more efficient for the dissociation-association steps as a chaperon than is the molecule or an inert gas. That is not surprising since there are strong indications that the vibrational excitation efficiency of the self atom as a collider is greater than of any other molecular species.[54,55] However, it is difficult to explain the observed temperature dependence of the atom-chaperon rate constants; they do not fit into the scheme proposed by Keck under the "variational theory of reaction

rates."[69] I believe it is essential for the experimentalists to provide boundary conditions for the theories which will be developed; in this instance, data on deuterium are needed to check the effect of mass (possible tunnelling).

Recent publications describing dissociation rate studies of various diatoms are listed in Table IV. Inspection of such data shows that for the homatomic diatoms, simple Arrhenius plots gives lines with a slope for effective activation energies which are 7 to 10 kcal lower than the spectroscopic values. This is believed to be due to a statistical factor, i.e., the depletion of the upper vibrational states due to the slowness of the recombination reaction (3 body) such that their populations fall below the Boltzmann value calculated for the ambient translational temperature. This explanation is clearly not adequate to account for the much larger departures between the effective activation energies deduced from Arrhenius plots and the spectroscopic D_o's for the hydrides HF, HCℓ, and DCℓ. The dissociation rate of HF in shock waves has been studied in two laboratories. When the data published by Jacobs et al[76] were replotted and fitted by least squares, the bimolecular rate constant was well represented by $k_d = 10^{14.14}\exp(-108{,}600/RT)$, $cm^3 mole^{-1} sec^{-1}$. Independently Spinnler[77] found $k_d = 10^{14.16}\exp(-113{,}700/RT)$. The close agreement is striking, since Jacobs followed the rate of reaction by recording the IR emission intensity behind incident shocks while Spinnler looked at absorption behind reflected shocks. A larger discrepancy has been reported for HCℓ and DCℓ by Jacobs and coworkers[78] and confirmed by Fishburne.[79] The observed apparent activation energy is 70 kcal for both gases while the spectroscopic values are 102 for HCℓ and 103 for DCℓ. It does not make sense to try to force these data to a rate expression with a T^{-1} or T^{-2} pre-exponential factor, when the resulting coefficient has a magnitude of over 10^{21} in units of cm^3 $mole^{-1}$ sec^{-1}.

In summary, considerable progress has been made in formulating an appropriate statistical mechanics for a dissociation reaction in a thermal bath, in which cognizance is taken of the departure from Boltzmann distribution in the upper vibrational levels.[80] Virtually no progress has been made in calculating transition probabilities for molecular encounters which produce dissociation. No explorations have been undertaken of the sensitivity of such probabilities to the shape of the interaction potentials but it is established experimentally that diatoms are specially sensitive to the self atoms as colliders.

THE HOMOGENEOUS PYROLYSIS OF POLYATOMIC MOLECULES

While the theoretical underpinnings of current collision theories for diatom dissociations are of dubious dependability, there are even more questions regarding the interpretation of rate data for triatomic fragmentations. The minimum activation energy anticipated for the first step is the thermochemical value minus some correction for the depletion effect due to depopulation of the upper vibrational levels. Shock tube data for one case (N_2O) gave an E_A value which was greater than the corresponding ΔE_T^o, in full agreement with results obtained by conventional kinetics; there are several systems in which E_A was slightly less than ΔE_T^o, as expected, but there are a disturbing number of studies which led to $E_A < \Delta E_T^o$ by 25-50 kcal/mole.

The molecule which has been subjected to the most intensive investigation has been nitrous oxide. The homogeneous unimolecular decomposition (high dilution in argon) was studied in both the low and high pressure regimes. Shock temperatures were 1300° to 2500°K, and pressures between 0.8 and 300 atm (concentration range 5×10^{-6}-2×10^{-3} moles per liter).[81] This pyrolysis was also studied in an adiabatic compression device,[82] and the overall results may be summarized in the following equations:

$$N_2O + Ar \xrightarrow{k_1} N_2 + O + Ar; \qquad k_1 = 10^{14.7}\exp(-58,000/RT), cm^3 mole^{-1} sec^{-1}$$

[High pressure limit: $10^{11.1}\exp(-59,500/RT)$, sec^{-1}]

$$N_2O + O \xrightarrow{k_2} 2\ NO \qquad k_3/k_2 \approx 3 \pm 1$$

$$N_2O + O \xrightarrow{k_3} N_2 + O_2 \qquad (k_2 + k_3) \approx (2.4 \pm 0.8) \times 10^{11}, cm^3 mole^{-1} sec^{-1} \text{ at } 1800^oK.$$

The pyrolysis of the N_2O was also studied with a shock tube leaking into a quadruple mass filter.[17]

At the AGARD Colloquium, Troe and Wagner[83] proposed a general treatment for the dissociation of small molecules, as a semi-quantum mechanical extension of unimolecular reaction rate theory. They considered both tri- and tetra-atomics and divided the former into two groups, those which follow spin-allowed dissociations and those which require a net change in spin. The latter include N_2O, CS_2, and CO_2. This analysis was amplified by Olschewski, Troe and Wagner.[84] The first step in the decomposition of 0.001% CS_2 in argon was observed, completely isolated from the consecutive reaction $S + CS_2 \rightarrow CS + S_2$, using a UV absorption technique. They also studied the rate of dissociation of SO_2 at concentrations below 0.3% in Ar, and of very dilute mixtures of water. The spin-forbidden dissociations approach their high pressure unimolecular limits at a few hundred atmospheres, but this condition cannot be reached for melecules which dissociate to the ground state atom species, as does H_2O. It is interesting to note that when one observes the rate of disappearance of water, say from its emission intensity in the infrared, at concentrations 0.02% to 0.2%, the rate constant is given by $k^o_{uni} = (Ar)\ 10^{14.2}\exp(-105000/RT)$, $cm^3 mole^{-1} sec^{-1}$. Here, as in the case of SO_2, over the temperature range 2700° to 4000°, the measured rate is twice the magnitude for the first step, because the initial dissociation of the water is followed by the very rapid reaction, $H + H_2O \rightarrow OH + H_2$. Above 4500°K only the first step is recorded, since all the subsequent steps are very rapid and the first step essentially controls the overall OH production. However, if the course of the reaction is followed by recording the amount of OH produced, (OH absorption at 3063A°)[85] the energy activation is about 50 kcal/mole. This was confirmed by the Göttingen investigators. Clearly, at the lower temperatures and higher concentrations the initial dissociation step is followed by a host of radical chains which involve OH; these are so rapid that they control the overall rate of its appearance.

One of the triatomic molecules which produces a product in an electronically excited state is CO_2. Davies[86] reported that his shock tube study covered the temperature range 6000°-11000°K (1% in Ar). Dissociation was monitored by the infrared emission intensity at 2.7 and 4.3μ. His results were essentially confirmed by E. S. Fishburne and coworkers[87] (3000-5000°K; 1% to 10% in Ar or N_2). Their results are:

$$k_{Ar} = 7.11 \times 10^{11} T^{\frac{1}{2}} \exp(-84500/RT); \quad k_{N_2} = 5.33 \times 10^{11} T^{\frac{1}{2}} \exp(-79000/RT), \ cm^3 mole^{-1} sec^{-1}$$

The thermochemical dissociation energy is 125.3 kcal/mole. The Göttingen investigators also studied CO_2 but at low concentrations and very high pressures in Ar.

They report a preliminary rate constant, $k_u^{\infty} \approx 2 \times 10^{11} \exp(-111{,}000/RT)$, sec^{-1}, which they found to be practically independent of the argon concentration at levels of 5×10^{-9} moles/cm^3. Thus, in this case also, the use of reagent concentrations of 1% or higher and modest Ar pressures permits steps subsequent to the first to confuse the dissociation process. Olschewski and coworkers[88] also found the bimolecular rate constant for CS_2 to be: k_b = (Ar) $10^{15.56} \exp(-80{,}300/RT)$, $cm^3 mole^{-1} sec^{-1}$.

Other tri- and tetra-atomic species have been studied but not with the care devoted to the few molecules listed above. All of these show apparent activation energies considerably lower than the corresponding
These include HCN,[89] NH_3[90] NF_2,[91] C_2N_2[92] and others.

The following is a brief discussion of pyrolysis investigations of more complex species. Mass spectrometer and spectrophotometric detection (λ2536Å) of the decomposition of fluoroform on shock heating to 1600°-2200°K was reported by Modica and LaGraff.[93] As anticipated, the first step appears to be splitting of the molecules to HF and CF_2, for which the limiting high pressure rate constant is $k_u^{\infty} = 7.03 \times 10^{11} \exp(-58{,}400/RT)$, sec^{-1}. At pressures 0.29 atm they assumed that the reaction had attained the second order limit. The dissociation of C_2F_4 into difluorocarbenes has been previously studied using Ar as the diluent; Modica and LaGraff[94] repeated this work with N_2, in reflected shocks (1200°-1600°K). There is a difference in that during the course of the reaction the nitrogen was vibrationally unrelaxed. In turn, the CF_2 radicals generated facilitated vibrational relaxation such that in a 1% tetrafluorethylene-nitrogen mixture the relaxation time was a factor (10-50) less than in pure nitrogen. Finally, on shocking mixtures of C_2F_4 and NO, Modica[95] concluded from mass spectra and UV absorptions that over the temperature interval 1600°-2500°K, there were the reversible reactions: $C_2F_4 \rightleftharpoons 2\ CF_2$; $CF_2 + NO \rightleftharpoons CF_2NO$. Above 2500°K, $2\ CF_2NO \rightarrow 2\ CF_2O + N_2$. He does believe that the latter reaction occurs as a bimolecular event.

An extensive investigation of the interconversion of fluorocarbons in shock tubes has been reported by Bauer and coworkers.[96] Mixtures ranging from 0.5% to 3% in argon of perfluorinated ethylene, cyclopropane, cyclobutane, cyclohexane, propene and butadiene were investigated in a single-pulse shock tube. The reaction mixtures were maintained for about 1 millisecond at specified temperatures and rapidly quenched. Plots of product distribution as a function of reflected shock temperatures were prepared. For example, a product distribution plot for perfluoroethylene shows the initial production of cyclobutane, its rapid decline at 1000°K with a concurrent rise in the amount of propene and cyclopropane, followed by a slow rise in the production of butene-2. These products pass through a maximum between 1800 and 1900°K, and then decline. Above 2100°K, decomposition of perfluoroethylene leads to products which are not preserved in the gas phase. All the products observed may be accounted for by simple sets of fragmentation steps in which CF_2 is the dominant radical. The kinetic simplicity of the C/F system is in striking contrast with the still unresolved complexities of the kinetics of the C/H system; the crucial differences are (a) the relative ease of migration of hydrogen atoms and (b) the high stability of the CF_2 radical. Thus, C/F compounds pyrolyze by breaking C-C bonds, but there is little rearrangement in the free radicals due to F atom migration.

The pyrolysis of ethylene highly diluted in neon was investigated by Gay and coworkers.[97] The temperature range covered 1710°-2170°K in reflected shock with pressures of 225 to 1600 torr. Products of pyrolysis were analyzed by leaking into a mass spectrometer. The reported rate law shows unit order dependence on ethylene and half order dependence on neon.

$$-\frac{d[C_2H_4]}{dt} = k_{3/2}[C_2H_4][Ne]^{\frac{1}{2}};\quad \log_{10} k_{3/2} = 0.01 - 50{,}500/2.303RT;\ \text{concs. in molecules cm}^{-3}$$

These results may be fitted equally well by a unimolecular process and by a free radical chain mechanism. However, the low activation energy is difficult to explain since it is only slightly larger than the difference between the enthalpies of acetylene plus hydrogen and of ethylene at the reaction temperatures.

Wing Tsang is continuing with his single-pulse shock tube studies of the thermal decomposition of low molecular weight alkanes and alkenes.[98,99] Many of the difficulties inherent in single-pulse shock tube techniques are minimized in this work, since he measures comparative rates, using the unimolecular decyclization of cyclohexene as an internal standard.

$$k_u\ (C_6H_{10} \rightarrow C_2H_4 + 1,3\text{-}C_4H_6) = 10^{15.02} \exp(-66{,}700/RT),\ \text{sec}^{-1}.$$

His results are summarized in Table V (taken from Table II, ref. 99). The possibility of extending the comparative rate method to other types of reactions is intriguing, but it appears to be difficult to apply to other than unimolecular decompositions. It is essential that the reference reaction remain unaffected, and not participate in the reaction being studied. When free radicals abound, the possibility of maintaining parallel but independent paths for concurrent reactions is small indeed.

BRIEFLY ON HOMOGENEOUS ATOM EXCHANGE PROCESSES

There are very few clearly established gas phase reactions of the type $AB + X_2 \rightarrow AX + BX$; those which are known do not follow the simple rate expression

$$\frac{d[AX]}{dt} = \frac{d[BX]}{dt} = k\,[AB]\,[X_2].$$

It should be noted that to force this reaction to follow a molecular mechanism (4-center transition state) it must be carried out under strictly homogeneous conditions (no hot walls), at the lowest possible temperatures, to minimize contributions from $X_2 \xrightarrow{\text{wall}} 2X$; $X + AB \rightarrow AX + B$; $AB + X \rightarrow A + BX$. The results of a shock tube study of the homogeneous four-center reaction $H_2 + D_2$ have been reported over a year ago, as was the exchange reaction between CH_4 and D_2.[100,101] Heuristic rate expressions for these systems are summarized in Table VI. These results, although unexpected, can be rationalized by assuming that exchange occurs with high probability only during the encounters between pairs of diatoms, one of which is vibrationally excited to a state approximately 0.4 of the way to dissociation. It appears that the probability for metathesis is low when molecules in low-lying vibrational states collide, even when the relative kinetic energy along the line of centers (plus vibrations) exceeds the activation energy. Support for this mechanism is provided by approximate calculations of the pre-exponential term for the exchange rate constant from vibrational relaxation data.

These simple reactions present a challenge to the theorist. The only calculation[106] which has been made of the transition probability for exchange as a function of vibrational excitation ($H_2 + H_2$) does show that the probability increases rapidly with vibrational excitation. However, it does not do so rapidly enough to overcome the lower population of the vibrationally excited states as controlled by the Boltzmann term. In this calculation, the representative point for the collision event moves in a classical trajectory, but the potential surface was obtained by a semi-empirical quantum mechanical procedure. We can only reach the conclusion that

apparently classical collision theory is not adequate. This is supported by the observation that in the vibrational excitation of homoatomic diatomic molecules the self atoms have a very high efficiency for vibrational excitation and for dissociation, but these effects have not yet been deduced theoretically.

SHOCK TUBE STUDIES OF COMBUSTION REACTIONS

Shock tube investigation of ignition delays is continuing at a modest level. The emission of visible light was used as a criterion for ignition in estimating delays as the function of temperature and composition for propane and methylcyclohexane.[107] Inhibition of the hydrogen-oxygen reaction by small amounts of methane, ethylene, trifluoromethylbromide, and 1,2-$C_2F_4Br_2$ was measured over the temperatures 970°-1300°K.[108] Ignition was detected photoelectrically from the light emitted at the 3090-3100Å band pass for OH, while the induction time was defined as that between the arrival of the reflected shock at the window and the time at which emission reached a maximum. The compounds listed inhibit ignition by reacting with the hydrogen atoms and other radicals which propagate the chain, but it is not essential that the additives first decompose. As for the initiation step of the branching chain for the H_2/O_2 reaction, Ripley and Gardiner[109] showed, by comparing experimental ignition delays with those calculated utilizing a full set of reactions, that initiation by a path other than diatom dissociation must occur. They proposed the exchange reaction $H_2 + O_2 \rightarrow 2\ OH$ as one which would account for the data.

Gardiner and coworkers[12] have effectively used the laser-schlierien technique for measuring density gradients and correlating the time profile for chemiluminescence with that for heat release in the oxidation of acetylene. They found that the OH absorption appeared at the end of the combustion, and that the OH profile was not directly related to the induction period chemistry. Apparently the OH profiles were related to the approach to partial equilibrium, including the reaction $OH + CO \rightleftarrows CO_2 + H$. The formation of C-O bonds at partial equilibrium conditions indicates that the heat of reaction is liberated without recombination steps, in contrast to the thermal sequence which is followed in the $H_2 + O_2$ reaction. The C_2H_2/O_2 reaction has also been investigated by Homer and Kistiakowsky[110,111] who recorded emissions by CO and CO_2 in the infrared, and compared them with the UV emission at the band head 433Å ($A^2\Delta - X^2\pi$) transition for CH. They concluded on the basis of the observation that the time constants for CO and CO_2 were identical; that the reaction CO + OH CO_2 + H does not apply to the initial stages of oxidation. They demonstrated that the time constant for CO emission was twice that for CH*, which supports those mechanisms wherein CH* is produced by second order processes in the chain, such as $C_2 + OH \rightarrow CO + CH^*$. These results are not in disagreement with the mechanism for C_2H_2 combustion proposed by Glass et al.[112]

A large amount of shock tube data has been assembled on the oxidation of ethylene.[113] Chemiluminescence by CH* revealed induction periods, followed by exponential rise of the signals. Measurements of time-dependent species composition with a TOF mass spectrometer can be represented by a rather complex reaction scheme, based on branching chain oxidation steps. The most abundant chemi-ions were $C_3H_3^+$ and H_3O^+. The mechanism proposed for C_2H_4/O_2 is tentative. A similar technique was followed in the study of the pyrolysis and oxidation of formaldehyde in shock waves.[114] The pyrolysis shows first order dependence on the formaldehyde and on the inert gas. There is a temperature-dependent induction period. Experiments with formaldehyde-d_2 show that the pyrolysis proceeds by a radical chain mechanism. The formation of the radical H_3CO has been detected. The observed activation energy (28 kcal/mole) is surprisingly low but is consistent with many other low values observed for initial stages of pyrolytic reactions as measured in shock tubes. The

first stage in the oxidation consists mainly of the decomposition of CH_2O into CO and H_2, followed by a branching chain oxidation of the hydrogen as well as of the remaining formaldehyde.

The oxidation of ammonia under homogeneous conditions has been studied by Takeyama and Miyama.[115] When mixtures of NH_3, O_2 and Ar were shock-heated to temperatures 1550°-2300°K, there was a delay in the appearance of OH, and as in the case of the H_2/O_2 reaction, log $(O_2)\tau$ varied linearly with the reciprocal of the temperature. Following the induction period, the early stages of the reaction were monitored by recording the UV absorption by NH_3 at 2245Å. They found

$$-d[NH_3]/dt = k_o [NH_3]^{1.5} [O_2]^{0.5} [Ar]^{0.5}$$

The apparent activation energy is 38.8 ± 2.6 kcal/mole.

The oxidation of hydrogen sulfide in shock waves[116] was observed by measuring the concentration of OH (in absorption) and of the generated SO_2 at 2909Å and 2812Å. The studies covered the temperature range 1350° to 2450°K. Two regimes were recognized; below 1560°K, OH and SO_2 appear concurrently after an induction period. Above 1700°K, SO_2 appears before OH. The authors proposed a branching chain mechanism, which at the higher temperatures includes the reaction $O + H_2S \rightarrow SO + H_2$. This provides an additional route for the formation of SO_2 and leads to a reduction in its induction period. They also found that the addition of hydrogen did not alter the basic features of the hydrogen sulfide oxidation. Additional hydrogen did reduce the induction period for the appearance of SO_2 and OH. The oxidation of H_2S is accelerated by hydrogen but the oxidation of hydrogen appears to be inhibited by H_2S.

A single-pulse shock tube study of the oxidation of perfluoroethylene was referred to above.[96] The mechanism of oxidation of fluorocarbons is characterized by comparative simplicity, in contrast to the many unresolved problems which remain in the area of hydrocarbon oxidations. The key feature is the rapid production of CF_2, which reacts with the oxygen according to the following scheme:

								ΔH^o_{300} (JANAF) kcal/mole
(a)		C_2F_4		$\rightleftharpoons$	$2\ CF_2$			+ 76.1
(b)	CF_2	+ O_2		$\rightarrow$	CF_2O	+	O	- 52.4
(c)	O	+ C_2F_4		$\rightarrow$	CF_2O	+	CF_2	- 95.5
(d)	CF_2	+ CF_2O		$\rightarrow$	CF_3	+	CFO	+ 38.4
(e)	CF_2	+ CFO		$\rightarrow$	CF_3	+	CO	- 58.5
(f)		$2\ CF_3$		$\rightleftharpoons$	C_2F_6			- 92.8
(g)	CF_2	+ C_2F_4		$\rightleftharpoons$	C_3F_6 (propene)			- 63.8
(h)	C_3F_6	+ O		$\rightarrow$	CF_2O	+	C_2F_4	-107.8
(i)	CF_2	+ C_2F_6		$\rightarrow$	CF_4	+	C_2F_4	- 17.0
(j)	CF_3	+ CFO		$\rightarrow$	CF_4	+	CO	- 91.

(b') $CF_2 + O_2 \not\rightarrow CF_2O_2$

(c') $O + CF_2 \rightarrow CF_2O$ $\approx$-171.

This sequence accounts for the observed product distributions as functions of the temperature, for several compositions of ethylene and oxygen. The detailed confirmation of the individual steps and their reaction rate constants will have to be obtained from mass spectrometric diagnostics.

CONCLUSION

It is amusing to attempt to pinpoint the salient features of shock tube chemical kinetics. Among the many attractive ones, the most worthwhile in my opinion is the specificity in identification of transient species (and of states) on a time-resolved basis; the most troublesome is the lack of sufficiently precise temperature measurement; the most intriguing is the need to exploit sophisticated computer programs in order to unravel the coupling of reactions in a complex system.

ACKNOWLEDGMENT

This work was supported by the AFOSR under Grant No. AF49(638)-1448, to whom sincere thanks are due.

TABLE I. Instrumentation and Techniques

Description	Function	Author	Ref.
Heated shock tube; driven gas; pure Cs vapor (1 torr)	Plasma generation (16,000°K); Study of magneto-fluid dynamics	H. G. Ahlstrom and P. A. Pincosy	STS #1
Heated shock tube (300°C) driven gas: Hg vapor	Plasma dynamics and spectroscopic studies	Y. W. Kim and O. Laport	STS #F10
Vaporization of aerosol in shock tube; metal wire exploded in controlled atm. prior to shock heating	0.05μ particles $A\ell$ produced; spectra of vaporized ablation products	W. H. Wurster	STS #B3
Particles dispersed in test gas prior to shock heating (3-5μ teflon)-record emission and absorption spectra	Study of burn-up rates of small particles	R. Watson, et al	STS #F4
Alkali halide smoke in Ar - record absorption spectra	Study dissociation of MX into ions-time resolved spectra	M. Coplan, et al	STS #E8
Electric shock tube	Improvement in linear driver	R. G. Fowler	(4)
Spectraradiometric pyrometer; resolving time: 10μ sec	Measure temperatures of shock heated gases, and of self sustaining detonations	G. J. Penzias, et al	(5)
Relative emission intensities at two wavelengths in a molecular band system	Estimate temperature of shock heated gases	R. Watson	(6)
Induction flow meter (transverse Field)	Measure gas velocities in shock tubes-ionizing conditions	P. A. Croce	(7)
Electron beam probe: fluorescence stimulated by 17.5 KV electrons	Measure density in free jets and shock fronts; estimate rotational and vibrational temperatures	P. V. Marone	(8)
	Diffusive separation of He, Ar in jets	D. E. Rothe	(9)
Laser light source	For schlierien and interferometer systems - measure densities and gradients	A. K. Oppenheim, et al	(10)
Single-pulse shock tube - double diaphragm design (exploding wire diaphragm opener)	General pyrolysis studies	S. Wittig	STS #48

TABLE II. On Non-Ideal Behavior of Shock Tubes

Topic	Coverage	Author	Ref.
Temperature variation behind attenuating shocks	2000°-2700°K in O_2, N_2 Used Na line reversal	T.A. Holbeche and D.A. Spence	(25)
Flow non-uniformity when shock front and contact surface have reached maximum separation	All fluid properties increase in value; non-uniformity greatest when γ is large and M is low; applies to turbulent and laminar boundary layers.	H. Mirels	(26)
Attenuation of shock due to non-equilibrium ionization and radiation	Attenuation calculated using linearized theory, with $\alpha \ll 1$.	J. Rosciszwewski	(27)
Radiative cooling and self absorption--- effect on flow field and on heat transfer behind reflected shock waves in air	Numerical calculations for radiating reflected shock heated plasmas (air)	R.M. Nerem and R.A. Golobic	(28)
Brightness temperature of shock waves in xenon and air	Effect of self-absorption of radiation emitted by shock front on estimation of brightness temperature; theoretical analysis	A.E. Voitenko, et al	(29)

TABLE III. Ionization Cross-Sections and Oscillator Strengths

Substances	Measurement of --	Results	Author	Ref.
Kr and Xe	Identify ions in shock heated mixtures via mass spectra	Impurity ions present; no diatomic ions appeared	R. Creswell, et al	(30)
Ar, Kr and Xe (5000°-9000°K)	Ionization relaxation times from microwave attentuation; high purity system	Quadratic dependence on density; rate controlling step is excitation to lowest group of excited states	A.J. Kelly	(31)
Ar (monitor continuum emission at 4900°A)	Effect of impurities on time required to reach half of maximum intensity	Pronounced effects due to H containing impurities	P.B. Coates	(32)
Ar	Ionization relaxation times (microwaves)	Impurities blamed for very short times	S. Naki, et al	(33)
Air	Ionization rates behind strong shocks from IR emission at 6μ (free-free bremsstrahlung).	$N + O \rightarrow NO^+ + e^-$ is predominant mechanism for shock speeds less than 9.5 mm/μsec	J. Wilson	(34)
$Cr(CO)_6$ in Ar	Ionization mechanism for Cr, from time resolved Cr(I) and Cr(II) emission spectra	Initial rate controlled by excitation to 3.1 ev lengths for Cr(I); rapid excitation to higher levels; ionization from excited states	W.L. Shackelford et al	(35)
$Cr(CO)_6$ in Ar--reflected shocks	gf - values for Cr(II) from emission intensities at 8000°K	21 lines in region 3118-4559Å; these values are $\approx$0.1 of values obtained from arc spectra	W.L. Shackelford	(36)
Ar-CO (1/1)	C_2 emission; matrix element for $^3\Pi_g - ^3\Pi_u$ (Swan) bands	Calculated equi. C_2 concentration; Report $f = -.022 \pm .008$	A.G. Sviridov, et al	(37)
Ar-CO (1/1)	C_2 absorption - Swan band system	Calculated equi. C_2; estimated $\lvert R_e \rvert^2 = 0.44 \pm 0.08$ a.u.	A.G. Sviridov, et al	(38)
C_2H_2, C_2N_2, CO	Incident shocks - Swan band emission	$f_{Swan} = -0.033 \pm 0.012$	A.R. Fairbairn	(39)
$C_2C\ell F_3$, CF_4, C_2F_4	Emission intensities for C_2 ($A\ ^3\Pi - X\ ^3\Pi$), and CF ($A\ ^2\Sigma - X\ ^2\Pi$)	$f_{Swan} = -0.028 \pm .009$ $f_{CF} = 0.0051 \pm .0015$	J.A. Harrington et al	(40a, b)
Air	Various band systems for N_2, O_2 NO, H_2O	Oscillator strengths for intense bands; (ff) and (fb) continua	xxx	(41)
SO_2-Ar	Spectroscopically resolved emission intensities	Broad band due to three excited states (C, $^1B_2$, $^3B_1$)	B.P. Levitt and D.B. Shien	(42)

TABLE IV: Dissociation Rate Studies

Molecule	Medium	Experiment or Theory	Results	Author	Ref.
O_2	Ar	Analysis of ladder climbing process	$k_d \propto [1 - \exp(-h_\omega/kT)]x \exp(-D/RT)$	N. V. Kondratiev and E. E. Nikitin	70
$2O \rightarrow O_2 + h\nu$		Radiative recombination data; 2500° to 3800°K	Intensity $\propto (O)^2$ apparent $E_A = 28.9 \pm 2.2$	B. F. Myers and E. R. Bartle	STS #29
O	O_2	Gladstone-Dale constant measured for O_2 and O	O_2: G.D. = 1.93 cm^3/gm O: G.D. = 2.04 cm^3/gm	J. H. B. Anderson	STS #E4
N_2	Ar	Dissociation rates; incident shocks (6000° - 9000°K)	Relative efficiencies N>N_2>Ar by 15:1:$\frac{1}{2}$	S. Byron	71
N_2	Kr	Dissociation rates; incident shocks (5000°-9000°K) 5%-10%-25%-50%	Analysis incomplete (results agree with 71)	E. Wachsler	72
F_2	Ne, Ar	TOF mass spec (1650°-2700°K)	$E_A \approx 27$ kcal/mole; general agreement with previous work	R. W. Diesen	73
F_2	Kr, Xe	Light absorption; dependence on F_2 concentration	For Ar, $E_A = 27.3 \pm 2.5$ kcal/mole Kr essentially like Ar; Xe-F_2 complex indicated (under shock conditions)	D. J. Seery and D. Britton	74
$C\ell_2$	Ar	Radiative recombination rates for 1:5 $C\ell_2$-Ar mixtures; 1735°-2582°K.	$k_d = 10^{13.94} \exp(-48,300/RT)$ $cm^3 mole^{-1} sec^{-1}$	R. A. Carabetta and H. B. Palmer	75
Br_2	Ar	Radiative recombination rates	Details not given- cite agreement with previous investigations	T. R. Lawrence and G. Burns	STS #B5

TABLE V. Rate Parameters for the Fission of Simple Hydrocarbons

(from ref. 99)

	$\dot{C}H_3$		$CH_3\dot{C}HCH_3$		$CH_3\overset{CH_3}{\overset{\vert}{\dot{C}}}-CH_3$		$CH_2=CH-\dot{C}H_2$	
Reaction Product	$\log_{10}A$	E_A	$\log_{10}A$	E_A	$\log_{10}A$	E_A	$\log_{10}A$	E_A
$\dot{C}H_3$	15.0	82.8	16.0	80.2	16.1	78.2	15.0	70.3
$CH_3\dot{C}HCH_3$			16.1	76.0	16.2	73.0	15.7	67.9
$CH_3\overset{CH_3}{\overset{\vert}{\dot{C}}}-CH_3$					16.3	68.5	15.8	65.5
$CH_2=CH-\dot{C}H_2$							14.2	59.3

TABLE VI. Summary of Molecular Exchange Reactions, in Shock Tubes

$$d[AX]/dt = k[AB]^{\alpha}\,[X_2]^{\beta}\,[Ar]^{\gamma}$$

AB	X_2	α	β	γ	E_A(kcal/mole	$A(T^{\frac{1}{2}})$ [moles/liter]	Ref.
H_2	D_2	0.38	0.66	0.98	42.26 ± 2.1	$10^{9.84}\,T^{\frac{1}{2}}$	100
HSH	D_2	0.47	0.98	0.61	52.3 ± 2	$10^{10.43}T^{\frac{1}{2}}$	103
HNH_2	D_2	≈0	≈1	≈1	39 ± 3	$10^{8}\,T^{\frac{1}{2}}$	102
HCH_3	D_2	0.3	1.1	0.6	52.00 ± 2.2	$10^{9.04}\,T^{\frac{1}{2}}$	101
$N_2(28)$	$N_2(30)$	0.5	0.5	1.0	116 ± 3	$10^{10.82}$	104
$O_2(32)$	$O_2(36)$	0.5	0.5	≈1.0	37 ± 4	10^{9}	105

REFERENCES

1. H. Oertel, STOSSROHRE, Springer-Verlag, Wien, 1966, 1030 pages; bibliography (p. 858-981), author and subject indices (p. 986-1030); 621 figures, 152tables. Mss. completed in October 1963 but some publications which appeared in 1964 are included in the bibliography.
2. Abstracts, 6th International Shock Tube Symposium, Freiburg, Germany, April 12-14 (1967).
   [References to these abstracts will be designated by STS # xx]
3. AGARD Colloquium (28th Propulsion and Energetics Panel Meeting) Oslo, Norway, May 16-20 (1966).
4. R. G. Fowler, Rev. Sci. Inst., 37, 545 (1966).
5. G. J. Penzias, S. A. Dolin and H. A. Kruegle, Applied Optics, 5, 225 (1966).
6. R. Watson, Applied Optics, 5, 215 (1966).
7. P. A. Croce, Rev. Sci. Inst., 36, 1561 (1965).
8. P. V. Marrone, Phys. of Fluids, 10, 521 (1967).
9. D. E. Rothe, Phys. of Fluids, 9, 1643 (1966).
10. A. K. Oppenheim, P. A. Urtiew and F. J. Weinberg, Proc, Roy. Soc. (London), 291, 279 (1966).
11. J. H. Kiefer and R. W. Lutz, J. Chem. Phys., 44, 658, 668 (1966); 45, 3889 (1966).
12. W. C. Gardiner, et al, J. Chem. Phys., 44, 4653 (1966).
13. G. B. Kistiakowsky and P. H. Kydd, J. Am. Chem. Soc., 79, 4825 (1957).
14. J. E. Dove and D. McL. Moulton, Proc. Roy. Soc., A283, 216 (1965).
15. R. W. Diesen and W. J. Felmlee, J. Chem. Phys., 39, 2115 (1963).
16. A. P. Modica, J. Phys. Chem., 69, 2111 (1965).
17. D. Gutman, A. J. Hay and R. L. Bedford, J. Phys. Chem., 70, 1786 (1966).
18. G. F. Marsters, S. H. Bauer and E. L. Resler, Jr., Proc. 5th International Shock Tube Symposium, U. S. Naval Ord. Lab., May 1966, Ed. W. S, Filler (p. 155). See also: T. A. Milne and F. T. Greene, Summary Tech, Report to Power Branch, ONR, 8 May 1967 [Contract, Nonr-3599(00); Project No. 092-513].
19. B. Sturtevant, J. Fluid Mech., 25, 641 (1966).
    See also: Dissertation submitted by C. P. Wang, May 1967 to Cal. Inst. Tech., Graduate Aeronautical Labs.
20. J. Wilson, J. Fluid Mech., 15, 497 (1963).
    Also, see M. W. Slack, et al, STS #A4.
21. S. H. Bauer and W. S. Watt, J. Chem. Phys., 44, 1327 (1966).
22. F. J. Stoddard and W. S. Watt, Report to Arnold Engineering Development Center, distributed May, 1967 by Cornell Aero Lab, [AEDC-TR-67-65].
23. R. A. Hartunian, W. P. Thompson and E. W. Hewitt, J. Chem. Phys., 44, 1766 (1966). See also: R. W. F. Gross, STS #F1.
24. R. V. Petrella, T. L. Spink and L. T. Finlayson, Rev. Sci. Inst., 37, 1500 (1966).
25. T. A. Holbeche and D. A. Spence, Proc. Roy. Soc. (London), A279, 111 (1964).
26. H. Mirels, Physics of Fluids, 9, 1907 (1966).
27. J. Rosciszewski, Physics of Fluids, 10, 269 (1967).

28. R. M. Nerem and R. A. Golobic, STS #30.

29. A. E. Voitenko, I. Sh. Model' and I. S. Samodelov, Soviet Physics (Doklady) 11, 596 (1967).

30. R. Creswell, M. A. DiValentin and J. E. Dove, Physics of Fluids, 9, 2285 (1966).

31a. A. J. Kelly, J. Chem. Phys., 45, 1723 (1966).

31b. A. J. Kelly, J. Chem. Phys., 45, 1733 (1966).

32. P. B. Coates, Nature, 211, 300 (1966).

33. S. Nakai, K. Kasuya and C. Yamanaka, J. Phys. Soc. Japan, 21, 805 (1965).

34. J. Wilson, Physics of Fluids, 9, 1913 (1966).

35. W. L. Shackleford and S. S. Penner, J. Chem. Phys., 45, 1816 (1966).

36. W. L. Shackleford, J. Quant. Spectrosc. Radiat. Transfer, 5, 303 (1965).

37. A. G. Sviridov, N. N. Sobolev and V. M. Sitovski, J. Quant. Spectrosc. Radiat. Transfer, 5, 525 (1965).

38. S. G. Sviridov, N. N. Sobolev and M. Z. Novgorodov, J. Quant. Spectrosc. Radiat. Transfer, 6, 337 (1966).

39. A. R. Fairbairn, J. Quant. Spectrosc. Radiat. Transfer, 6, 325 (1966).

40a. J. A. Harrington, A. P. Modica and D. R. Libby , J. Chem. Phys., 44, 3380 (1966).

40b. However, note also, T. Wentink, Jr. and L. Isaacson, J. Chem. Phys., 46, 603 (1967).

41a. D. R. Churchill and R. E. Meyerott, J. Quant. Spectrosc. Radiat. Transfer, 5, 69 (1965). [For remaining parts of ref. 41, see end of list.]

42. B. P. Levitt and D. B. Sheen, Trans. Farad. Soc., 63, 540 (1967).

43. M. G. Ferguson and A. W. Read, Trans. Farad. Soc., 63, 61 (1967).

44. P. Borrell, Chem. Soc. Spec. Publication 20, (Academic Press, 1966) p. 263.

45. T. L. Cottrell, Int. Inst. Chem., 12th Conference, 1962 (Interscience N. Y. 1964).

46. R. C. Millikan, E. Switkes and L. A. Osburg, Bull. Amer. Phys. Soc., 11, 201 (1966).

47a. J. G. Parker, Phys. Fluids, 2, 449 (1959).

47b. J. G. Parker, J. Chem. Phys., 45, 3641 (1966).

48. R. C. Millikan, Molecular Relaxation Processes, Chemical Society Special Publication No. 20, pp. 219-233 (Burlington House, London, 1966).

49. C. B. Moore, J. Chem. Phys., 43, 2979 (1965).

50. A. B. Callear and G. J. Williams, Trans. Farad. Soc., 62, 2030 (1966),

51. J. G. Parker and R. H. Swope, J. Chem. Phys., 43, 4427 (1965).

52. D. R. White, J. Chem. Phys., 46, 2016 (1967).

53. R. W. Lutz and J. H. Kiefer, Phys. of Fluids., 9, 1638 (1966).

54. J. H. Kiefer and R. W. Lutz, private communication.

55. S. H. Bauer and S. C. Tsang, Phys. Fluids, 6, 182 (1963).

56. I. R. Hurle, A. L. Russo and J. G. Hall, J. Chem. Phys., 40, 2076 (1964).

57. A. L. Russo, J. Chem. Phys., 44, 1305 (1966).

58. C. E. Treanor, J. W. Rich, and R. G. Rehm, report to Mechanics Division of the AFOSR under Contract No AF49(638)-1488.

59. J. P. Appleton, STS #B7; see also, J. P. Appleton and M. Steinberg, J. Chem. Phys., 46, 1521 (1967).

60. C. J. S. M. Simpson, K. B. Bridgman and T. R. D. Chandler, STS #B9.

61. D. Weaner, J. F. Roach and W. R. Smith, Bull. Am. Phys. Soc., 12, 836 (1967).

62. C. B. Moore, R. E. Wood, B-L. Hu, and J. T. Yardley - pre-publication manuscript.

63. R. L. Taylor, M. Camac and R. M. Feinberg, AVCO Everett Research report #250, May 1966; To appear: Proceedings 11th Combustion Symposium.

64. R. L. Taylor and S. Bitterman, Pre-publication report.

65. J. D. Lambert, Quart. Reviews, 21, 67 (1967.
J. D. Lambert, D. G. Parks-Smith and J. L. Stretton, Proc. Roy. Soc., A, 282, 380 (1964).

66. W. S. Watt and A. L. Myerson, STS #E3.

67. I. R. Hurle, 11th Symposium (International) on Combustion, Berkely, California, August 1966.

68. S. H. Bauer, AGARD Colloquium, May 1966.

69. J. C. Keck, Discussion Farad. Soc., 33, 173 (1962).

70. V. N. Kondratiev and E. E. Nikitin, J. Chem. Phys., 45, 1078 (1966).

71a. S. Byron, J. Chem. Phys., 44, 1378 (1966).

71b. K. L. Wray and S. Byron, Phys. Fluids, 9, 1046 (1966); and B. Cary, Phys. Fluids, 9, 1047 (1966).

72. E. Wachsler, Dissertation, Cornell University, 1967.

73. R. W. Diesen, J. Chem. Phys., 44, 3662 (1966).

74. D. J. Seery and D. Britton, J. Phys. Chem. 70, 4074 (1966).

75. R. A. Carabetta and H. B. Palmer, J. Chem. Phys., 46, 1325, 1333, 1538 (1967).

76. T. A. Jacobs, R. R. Giedt and N. Cohen, J. Chem. Phys., 43, 3688 (1965).

77. J. F. Spinnler, Report No. S-127, Rohm and Haas Redstone Arsenal Research Labs., April 1967.

78. T. A. Jacobs, N. Cohen and R. R. Giedt, J. Chem. Phys., 46, 1958 (1967).

79. E. S. Fishburne, J. Chem. Phys., 45, 4053 (1966).

80a. H. J. Kolker, J. Chem. Phys., 44, 582 (1966).

80b. C. A. Brau, J. C. Keck and G. F. Carrier, Phys. Fluids., 9, 1885 (1966).

80c. C. A. Brau, Avco Everett Research Laboratory, Report 261, December 1966.

80d. N. S. Snider, J. Chem. Phys., 45, 3299 (1966).

81 H. A. Olschewski, J. Troe and H. Gg. Wagner, Ber. Bunsengesellschaft. physik chem., 70, 450 (1966).

82. A. Martinengo, J. Troe, and H. Gg. Wagner, Zeit. Phys. Chem. 51, 104 (1966).

83. J. Troe and H. Gg. Wagner, AGARD Colloquium, Oslo, May 1966.

84. H. A. Olschewski, J. Troe and H. Gg. Wagner, 11th Symposium (International) on Combustion, Berkeley, August 1966.

85. S. H. Bauer, G. L. Schott, and R. E. Duff, J. Chem. Phys., 28, 1089 (1958).

86. W. O. Davies, J. Chem. Phys., 43, 2809 (1965).

87. E. S. Fishburne, K. R. Bilwakesh and R. Edse, J. Chem. Phys., 45, 160 (1966).

88. H. A. Olschewski, J. Troe and H. Gg. Wagner, Zeit. Physik. Chem., 45, 329 (1965).

89. D. Marshall and S. H. Bauer, unpublished data, Cornell University report to NASA, January 1966.

90. H. J. Henrici, Dissertation, Göttingen, 1966.

K. W. Michel and H. Gg. Wagner, 10th Symposium (International) on Combustion, The Combustion Inst., Pittsburgh, (1965), p. 353.

91. A. P. Modica and D. F. Hornig, J. Chem. Phys., 43, 2739 (1965).

92. W. Tsang, S. H. Bauer, and M. Cowperthwaite, J. Chem. Phys., 36, 1768 (1962); See also: D. Schofield, W. Tsang and S. H. Bauer, J. Chem. Phys., 42, 2132 (1965).

93. A. P. Modica and J. E. LaGraff, J. Chem. Phys., 44, 3375 (1966).

94. A. P. Modica and J. E. LaGraff, J. Chem. Phys., 45, 4729 (1966).

95. A. P. Modica, J. Chem. Phys. 46, 3663 (1967).

96. S. H. Bauer, K. C. Hou, and E. L. Resler, Jr., STS #E7.

97. I. D. Gay, R. D. Kern, G. B. Kistiakowsky, and H. Niki, J. Chem. Phys., 45, 2371 (1966).

98. W. Tsang, J. Chem. Phys., 44, 4283 (1966).

99. W. Tsang, J. Chem. Phys., 46, 2817 (1967).

100. S. H. Bauer and E. Ossa, J. Chem. Phys., 45, 434 (1966).

101. W. S. Watt, P. Borrell, D. Lewis, and S. H. Bauer, J. Chem. Phys., 45, 444 (1966).

102. A. Lifshitz, C. Lifshitz, and S. H. Bauer, J. Am. Chem. Soc., 87, 143 (1965).

103. D. Lewis, et al, Prepublication report

104. A. Bar-Nun and A. Lifshitz [Prepublication report].

105. H. Carroll, and S. H. Bauer, Prepublication report.

106. K. Morokuma, L. Pedersen and M. Karplus, In press.

107. R. D. Hawthorn and A. C. Nixon, AIAA Journal, 4, 513 (1966).

108. G. B. Skinner and G. H. Ringrose, J. Chem. Phys., 43, 4129 (1965).

109. D. L. Ripley and W. C. Gardiner, Jr., J. Chem. Phys., 44, 2285 (1966).

110. J. B. Homer and G. B. Kistiakowsky, J. Chem. Phys., 45, 1359 (1966).

111. J. B. Homer and G. B. Kistiakowsky, Submitted to Journal of Chemical Physics.

112. G. P. Glass, et al. J. Chem. Phys., 42, 608 (1965).

113. I. D. Gay, G. P. Glass, R. D. Kern and G. B. Kistiakowsky, Submitted to The Journal of Chemical Physics.

114. I. D. Gay, G. P. Glass, G. B. Kistiakowsky and H. Niki, J. Chem. Phys., 43, 4017 (1965).

115. T. Takeyama and H. Miyama, Bull. Chem. Soc., Japan, 39, 2352 (1966); Bull. Chem. Soc., Japan, 38, 1670 (1965).

116. J. N. Bradley and D. C. Dobson, J. Chem. Phys., 46, 2865, (1967); J. Chem. Phys., 46, 2872 (1967).

NOTE

The complete set of references that comprise (41) are:

41a. D. R. Churchill and R. E. Meyerott, J. Quant. Spectrosc. Radiat. Transfer, 5, 69 (1965).

41b. K. L. Wray and T. J. Connolly, J. Quant. Spectrosc. Radiat. Transfer, 5, 111 (1965).

41c. R. A. Allen, A. Textoris and J. Wilson, J. Quant. Spectrosc. Radiat. Transfer, 5, 95 (1965).

41d. M. Jeunehomme, J. Chem. Phys., 44, 4253 (1966).

41e. R. W. Patch, J. Quant. Spectrosc. Radiat. Transfer, 5, 137 (1965).

A SHOCK TUBE STUDY OF METHANE OXIDATION

Daniel J. Seery and Craig T. Bowman

United Aircraft Research Laboratories
East Hartford, Connecticut 06108

Although the oxidation of methane has been studied extensively there are still many unsolved problems related to the kinetics and mechanism of the reaction. The objective of the present investigation is to provide information on the reaction mechanism and chemiluminescence for the high temperature oxidation of methane. To this end an experimental study of methane oxidation behind reflected shock waves has been carried out. In this study pressure, OH, CH, CO, C_2 and H_2O emission and OH absorption were monitored during the reaction. In conjunction with the experimental work, an analytical study of methane oxidation was carried out. Using a proposed fifteen-step reaction mechanism, temperature, pressure and concentration profiles were calculated for the conditions of the experiment.

EXPERIMENTAL

The experimental study was carried out in a stainless steel cylindrical shock tube (shown in Fig. 1) having an internal diameter of 3.8 cm. The driver gas used in all experiments was room-temperature helium. To assure uniform diaphragm bursting pressures, a double diaphragm technique was employed (Ref. 1). Shock velocities were measured using four platinum heat transfer gauges mounted along the wall of the tube. The signals from these heat transfer gauges were displayed on a raster-sweep oscilloscope. The observation station was located 5.70 m from the diaphragm, and consisted of four observation ports. These ports were used to make various spectroscopic and pressure measurements. The reaction was studied behind reflected shock waves at a location 1 cm from the reflecting surface. This configuration gave a maximum test time of approximately 2 msec.

Pressure measurements were made using a piezoelectric pressure transducer (Kistler Model 605) with a 0.375 cm diameter pressure-sensitive diaphragm and a rise time of 3 μsec. Two optical paths were available to monitor the emission and/or absorption of characteristic radiation during the reaction. The principal spectroscopic instrument was a 0.5 m Seya-Namioka vacuum monochromator equipped with an EMI/US 6255B photomultiplier. The entrance and exit slit widths were set to give a bandwidth of approximately 25 Å. The monochromator was used for both emission and absorption experiments. For the absorption experiments a Hg-Xe arc lamp (Hanovia 528B-1) was employed. Additional emission data were obtained from the other optical station using an EMI/US 9558BQ or a Philips 56CVP photomultiplier with various narrow-band pass interference filters. Sapphire windows were used for all optical stations. The output signals from the pressure transducers and photomultipliers were displayed on two dual-beam oscilloscopes which were triggered by one of the heat transfer gauges. The rise time of the photomultiplier/oscilloscope system was 2-3 μsec.

The methane, oxygen and argon used in the experiments were Matheson Ultrapure Grade (> 99.9%), and the nitrogen was Linde High Purity Dry (99.9%).

Gas mixtures were prepared manometrically and stored in stainless steel or glass vessels. These vessels were evacuated to a pressure of less than 1 μ Hg before preparing the mixture. Mixture total pressures varied from 300-3000 mm Hg. Composition of the gas mixtures was confirmed using a mass spectrograph. The mixtures were allowed to stand for at least 48 hours before use in an experiment.

Before a run, the experimental section of the shock tube was evacuated to less than 1 μ Hg. The leak and outgassing rate was less than 2 μ Hg/min. Initial pressures of the gas in the experimental section varied between 15-150 mm Hg.

In all the experiments the temperature behind the reflected wave was obtained from the ideal shock equations and the measured incident shock velocity at the reflecting surface with a suitable correction for "non-ideal" shock reflection (Refs. 2 and 3). In the present investigation a temperature correction of -35 deg K with an uncertainty of 35 deg K was employed. This correction was based on the results of a study of reflected shock temperature in argon. In this study reflected shock temperatures were obtained from measurements of incident and reflected shock velocities using an approach suggested by Skinner (Ref. 3). This approach could not be used with the fuel/oxidizer mixtures due to gas dynamic acceleration of the reflected shock wave in the vicinity of the reflecting plate. Hence a direct determination of a temperature correction was not possible for the fuel/oxidizer mixtures.

Due to boundary layer effects, the pressure behind the reflected shock wave decreased in time. It was assumed that pressure and temperature behind the reflected wave were related through the isentropic equations. This assumption is not strictly correct due to heat transfer and chemical reaction effects. It is felt, however, that the error introduced by this assumption is small.

The temperature for a given run was assumed to be a linear average of the temperature directly behind the reflected shock wave (corrected for "non-ideal" reflection) and the temperature directly before the increase in pressure accompanying the chemical reaction. A similar averaging technique was employed for the pressure. Since variations in temperature and pressure behind the reflected wave were small, a linear averaging is acceptable.

EXPERIMENTAL RESULTS

The oxidation reaction was studied using pressure measurements and spectroscopic observations. The spectroscopic measurements involved the emission and absorption of the OH radical (3067 Å) and the emission of CH (4315 Å), CO (2200 Å), C_2 (5165 Å) and H_2O (9300 Å). Typical oscilloscope traces are shown in Figures 2, 3 and 4. The bottom trace in Figures 2 and 3 is the output of the pressure transducer. The arrival of the incident and reflected shock waves at the observation station and the increase in pressure due to chemical reaction are indicated in the figures. The top trace in Fig. 2 is the photomultiplier output showing OH emission. From the pressure and OH emission traces of Fig. 2 it is seen that the reaction appears to pass through two phases - a first (induction) phase in which the pressure and OH emission increase slowly followed by a second phase in which the pressure and OH emission increase rapidly. As will be discussed later, these observations are consistent with the results of the analytical study. The top trace in Fig. 3 is the photomultiplier output showing CH emission. From this figure it is seen that excited $CH(^2\Delta)$ is probably short-lived, undergoing a maximum in concentration just prior to the onset of fast reaction. In Fig. 4 the top trace is the photomultiplier output showing OH emission and the bottom trace shows OH absorption. It is apparent that the onset of emission and absorption occur simultaneously, indicating that the concentration of excited state ($^2\Sigma$) and ground state ($^2\Pi$) OH increase approximately at the same time.

For the purpose of comparing the experimental and analytical results it is convenient to characterize the oxidation of methane by an induction time. There is no generally accepted definition of induction time. In the present study the induction time was defined to be the time between the heating of the gas by the reflected shock wave and the rapid increase in pressure or characteristic emission or absorption. This definition permits a simple comparison between experimental and analytical results and is not dependent on the threshold of the instrumentation.

Induction time data for methane oxidation are presented in Figs. 5 through 8. In these figures the mole percent of methane, oxygen and argon or nitrogen in the mixture is given together with the fraction stoichiometric, Φ , where

$$\Phi = \frac{(X_{CH_4}/X_{O_2})}{(X_{CH_4}/X_{O_2})_{\text{stoichiometric}}}$$

and X is the mole fraction. The solid lines through the data points are a least-squares fit of the experimental data to an equation of the form

$$\tau = A \exp (E/RT)$$

where τ = induction time, T = temperature, and A and E = constants. The parameters A and E and the standard deviation in E are obtained from the least-squares reduction of the data, and are tabulated in Table 1.

Table 1. Least-Squares Parameters: Methane-Oxygen-Diluent

Φ	Diluent	P(atm)	A(sec)	$E\left(\frac{kcal}{mole}\right)$	σE
0.5	N_2	1.7	1.6×10^{-10}	44.7	3.7
0.5	Ar	1.7	2.3×10^{-10}	44.3	1.4
0.5	Ar	3.7	4.5×10^{-11}	46.6	4.3
0.5	Ar	6.0	2.1×10^{-12}	53.2	6.0
1.0	Ar	2.0	5.8×10^{-11}	49.0	2.1
2.0	Ar	1.7	2.1×10^{-10}	45.4	4.8

The induction time for oxidizer-rich (Φ = 0.5) methane/oxygen/argon and methane/oxygen/nitrogen mixtures for an average pressure of 1.7 $\pm$ 0.3 atm is presented as a function of temperature in Fig. 5. In this figure the induction time is based on the rapid increase in pressure. It is noted that in the present study there was no observed difference between induction times based on rapid increase in pressure or those based on rapid increase in characteristic emission or absorption. The solid line is the least-squares fit of the methane/oxygen/argon data. From Fig. 5 and Table 1 it is seen that within the experimental uncertainty and for a given temperature the induction time is the same for the methane/oxygen/argon and the methane/oxygen/nitrogen mixtures. Hence for the conditions of the present investigation replacing nitrogen by argon in the oxidizer does not have a significant effect on the induction time.

The induction time for a stoichiometric methane/oxygen/argon mixture at an average pressure of 2.0 $\pm$ 0.3 atm is presented as a function of temperature in Fig. 6. From this figure it is seen that there is no significant difference between induction times based on OH emission or OH absorption.

The dependence of the induction time on the fraction stoichiometric (Φ = 0.5, 1.0, 2.0) is presented in Fig. 7. The difference between the least-squares lines shown in this figure are within the experimental uncertainty presented in Table 1. Therefore there is no significant variation of the induction time with fraction stoichiometric in the range of Φ = 0.5 to 2.0 (for induction times between 50 μsec and 1 msec).

A comparison of the induction times for an oxidizer-rich methane/oxygen/argon mixture (Φ = 0.5) at average pressures of 1.7 $\pm$ 0.3 atm, 3.7 $\pm$ 0.4 atm and 6.0 $\pm$ 0.3 atm is presented in Fig. 8. It is apparent that for a given temperature as the pressure increases from 1.7 atm to 3.7 atm the induction time decreases. As the pressure increases to 6.0 atm no further decrease in induction time is observed. Also shown on Fig. 8 is a least squares fit of the ignition delay data of Snyder, et al (Ref. 4) for CH_4-air, P = 4 atm and Φ = 0.5. It is seen that there is good agreement between the two sets of data.

ANALYTICAL INVESTIGATION

In order to gain insight into the reaction mechanism for methane oxidation and to aid in understanding the experimental results a model calculation was performed using a fifteen-step reaction mechanism. The calculations were made using a computer program which numerically integrates the system of reaction kinetic and state equations to give the time rate of change of compositions and thermodynamic properties. In the present study the calculations were made assuming an adiabatic, constant volume reaction. Hence the model calculation closely approximates conditions behind a reflected shock wave.

The mechanism for methane oxidation at high temperature is probably different from the low-temperature, low-pressure mechanism of Enikolopyan (Ref. 5) which is used by many investigators. It is more probable that the same reactions that are important for methane flame propagation also are important in the high temperature oxidation of methane. The reaction mechanism and rate constants used for the calculations are presented in Table 2.

Table 2. Reaction Mechanism

Reaction	Rate Constant = A exp (-B/T) A*	B	Ref.
1. $CH_4 \rightarrow CH_3 + H$	3.8×10^{14}	51,900	6
2. $CH_4 + H \rightarrow CH_3 + H_2$	2.0×10^{14}	5,800	7
3. $CH_4 + OH \rightarrow CH_3 + H_2O$	2.85×10^{13}	2,500	8
4. $CH_4 + O \rightarrow CH_3 + OH$	1.0×10^{13}	4,030	7
5. $CH_3 + O_2 \rightarrow CH_2O + OH$	1.0×10^{11}	-o-	9
6. $CH_3 + O \rightarrow CH_2O + H$	1.9×10^{13}	-o-	7
7. $CH_2O + OH \rightarrow HCO + H_2O$	3.5×10^{14}	503	9
8. $HCO + OH \rightarrow CO + H_2O$	$5.4 \times 10^{12}\ T^{0.5}$	252	9
9. $CO + OH \rightarrow CO_2 + H$	3.1×1011	300	8

Table 2. Reaction Mechanism (Continued)

Reaction	Rate Constant = A exp (-B/T) A*	B	Ref.
10. $H + O_2 \rightarrow OH + O$	2.2×10^{14}	8,310	9
11. $O + H_2 \rightarrow OH + H$	1.1×10^{13}	4,730	9
12. $O + H_2O \rightarrow 2OH$	4.2×10^{13}	9,120	9
13. $H + H_2O \rightarrow H_2 + OH$	5.0×10^{13}	10,100	9
14. $H + H + M \rightarrow H_2 + M$	$5.0 \times 10^{18}\ T^{-1}$	-0-	9
15. $H + OH + M \rightarrow H_2O + M$	$4.5 \times 10^{21}\ T^{-1}$	-0-	9

* A is in $cm^3\ mole^{-1}\ sec^{-1}$ except for (1) where the units are sec^{-1}

This mechanism is derived primarily from the flame studies of Fristrom and Westenberg (Ref. 7) and Fenimore and Jones (Ref. 9) plus the methane dissociation reaction to assist the initiation.

DISCUSSION

Before proceeding to a discussion of the experimental data it is of interest to consider some of the results of the analytical study (Figs. 9 and 10). Figure 9 shows the calculated temperature and pressure profiles for an initial temperature of 2000 deg K, an initial pressure of 3.4 atm and 0.5 fraction stoichiometric. The temperature and pressure increase slowly during the induction period and then increase rapidly. Calculated concentration profiles for several important species for the above conditions are presented in Fig. 10. The concentrations of the intermediates increase very rapidly during the early stages of the reaction and then maintain a nearly constant value through most of the induction period. The product species have different concentration profiles. CO and H_2O show a rapid increase early in the induction period and then increase almost linearly to their equilibrium concentrations. CO_2, on the other hand, increases almost linearly from the start and only at the very end of the induction period does it increase rapidly.

Calculations similar to those discussed above also have been made for initial temperatures of 1900 deg K and 1800 deg K (stoichiometry and initial pressure were identical with the 2000 deg K calculation). Qualitatively the temperature, pressure and concentration profiles are the same as for the 2000 deg K calculation except on a longer time scale. Since the calculated and observed pressure profiles are qualitatively the same, it is possible to compare calculated and observed induction times (based on rapid increase in pressure). The calculated induction times, presented in Fig. 8, exceed the experimental values by a factor of ten at 1800 deg K and by a factor of five at 2000 deg K. Considering the uncertainty in some of the

specific rate constants used in the reaction mechanism the difference between experiment and analysis is not unexpected. As an example, if the rate constant for reaction 10 is varied by a factor of ten there is a 30-40 percent variation in the calculated induction time at 2000 deg K. At lower temperatures variations in the rate constants of chain-branching reactions could have an even greater effect on the calculated induction times. In addition the neglect of certain chemical species in the analysis (e.g. HO_2 and H_2O_2) may contribute to the discrepancy especially at the lower temperatures.

At the present time the calculated concentration profiles only can be compared qualitatively with the experimental data. In particular it is noted that after the first few microseconds the calculated OH concentration increases approximately exponentially in time. Experimental results indicate that OH absorption (which is a measure of ground state OH concentration) also increases approximately exponentially in time.

It is of interest to compare the time variation of CH and OH emission and OH absorption in methane oxidation with similar observations in acetylene oxidation. Stubbeman and Gardiner (Ref. 10) have studied the oxidation of acetylene in a shock tube and observed OH emission and absorption (3067 Å) and visible chemiluminescence (4320 Å). It is probable that the 4320 Å emission is due to the $^2\Delta$-$^2\Pi$ transition in CH. During the reaction a peaking of the 4320 Å emission (similar to that shown in Fig. 3) was observed. Coincident with the 4320 Å peak a pulse of OH emission at 3067 Å was observed. Following the tail-off of emission an increase in OH absorption was observed. In methane oxidation a peaking of CH emission is observed (Fig. 3); however OH emission and OH absorption are found to increase simultaneously during the reaction. If the lag between CH emission and OH absorption in acetylene oxidation is real then there must be different mechanisms for chemiluminescence in methane and acetylene oxidation. Indeed, Deckers (Ref. 11) has suggested that in acetylene oxidation there are two possible reactions for producing CH ($^2\Delta$) but that only one of the reactions is important in methane oxidation.

ACKNOWLEDGEMENTS

The authors thank T. F. Zupnik, Pratt & Whitney Aircraft, for providing the computer program used for the reaction kinetic calculations. This work was sponsored, in part, by the Air Force Aero Propulsion Laboratory (Wright-Patterson) under Contract No. AF 33(615)-3179.

References

1. Wurster, W. H., J. Chem. Phys., 36, 2112 (1962).

2. Strehlow, R. A. and C. T. Case, J. Chem. Phys., 35, 1506 (1961)
Johnson, C. D. and D. Britton, J. Chem. Phys., 38, 1455 (1963).

3. Skinner, G. B., J. Chem. Phys., 31, 268 (1959).

4. Snyder, A. D., J. Robertson, D. L. Zanders and G. B. Skinner, Shock Tube Studies of Fuel-Air Ignition Characteristics, Monsanto Research Corporation Report AFAPL-TR-65-93. August 1965.

5. Enikolopyan, N. S., Seventh Symposium (International) on Combustion, London, Butterworths (1959), p. 157.

6. Palmer, H. B. and T. J. Hirt, J. Phys. Chem., 67, 709 (1963).

7. Fenimore, C. P. and G. W. Jones, J. Phys. Chem., 65, 1532 (1961), ibid., p. 2200.

8. Wilson, W. E., paper presented at 1967 Spring Meeting, Western States Section The Combustion Institute, LaJolla, Calif., April 24-25, 1967.

9. Fristrom, R. M. and A. A. Westenberg, Flame Structure, New York, McGraw-Hill, 1965. See also Fristrom, R. M., Ninth Symposium (International) on Combustion, New York, Academic Press (1963), p. 560.

10. Stubbeman, R. F. and W. C. Gardiner, Jr., J. Phys. Chem. 68, 3169 (1964).

11. Deckers, J. M., Energy Distribution in Flames and Electric Discharges, Final Report Grant AF-AFOSR 375-65, Lash Miller Chemical Laboratories, University of Toronto, August 1966.

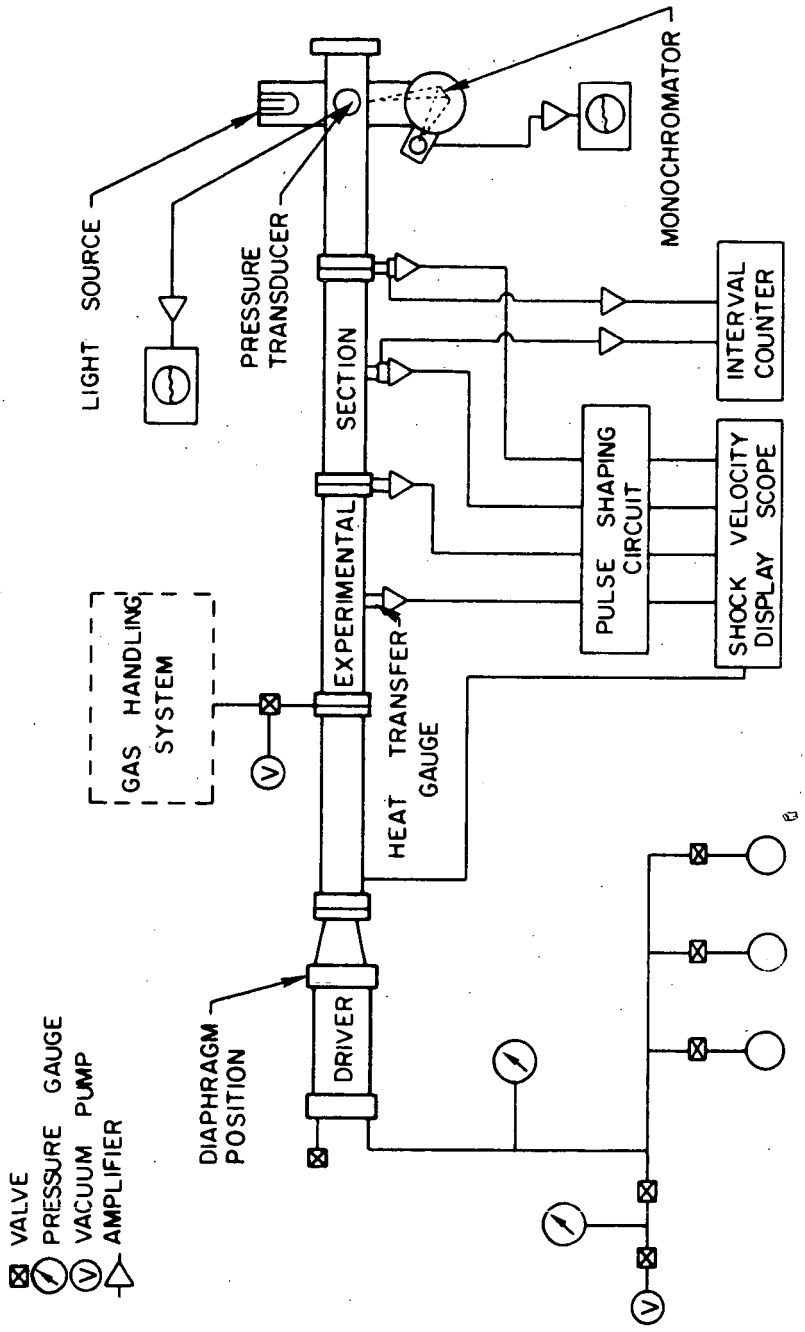

FIGURE I. SCHEMATIC DIAGRAM OF EXPERIMENTAL APPARATUS

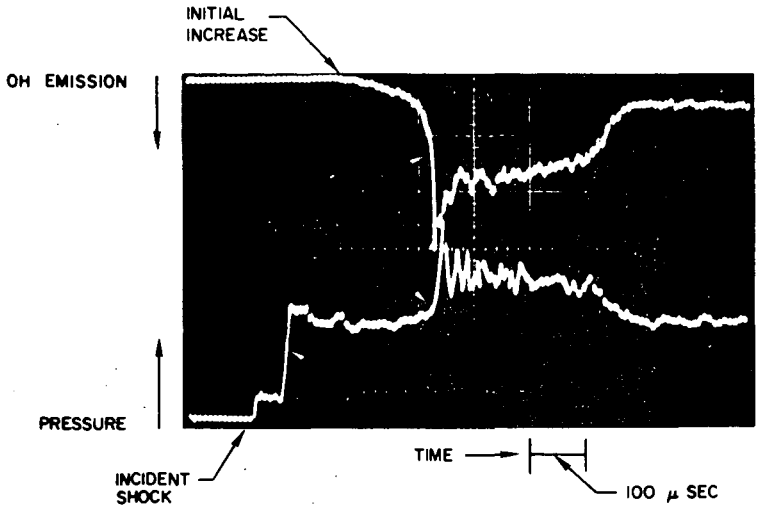

FIGURE 2. PRESSURE CHANGE AND OH EMISSION DURING INDUCTION PERIOD FOR METHANE IGNITION

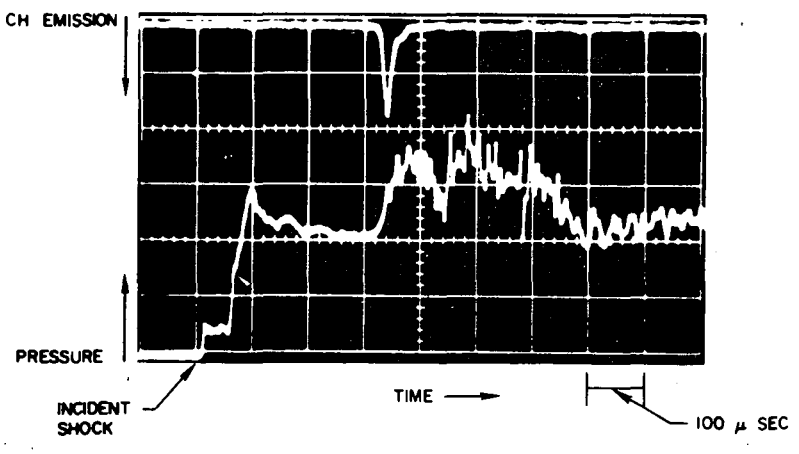

FIGURE 3. PRESSURE CHANGE AND CH EMISSION DURING INDUCTION PERIOD FOR METHANE IGNITION

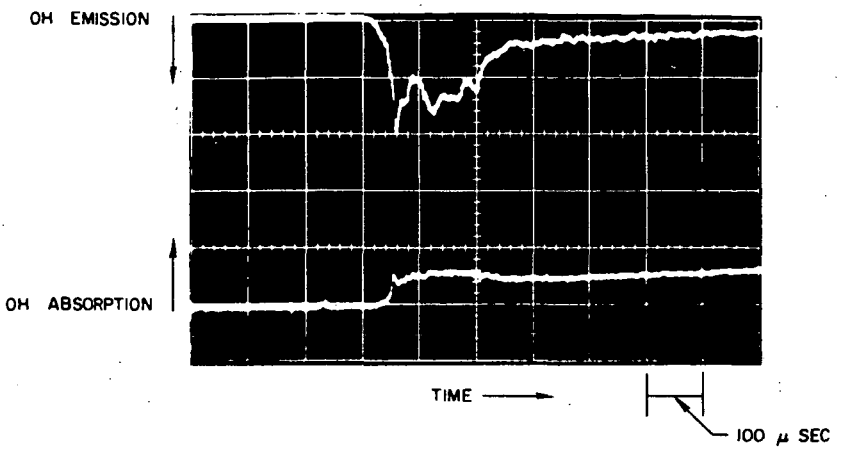

FIGURE 4. OH EMISSION AND ABSORPTION DURING INDUCTION PERIOD FOR METHANE IGNITION

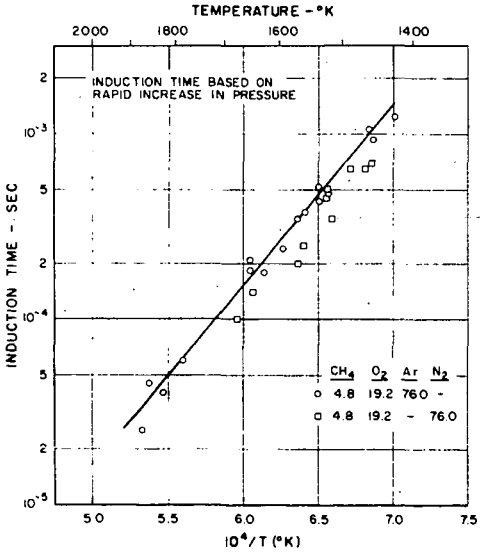

FIGURE 5. TEMPERATURE DEPENDENCE OF INDUCTION TIME FOR P=1.7 ATM AND $\Phi = 0.5$

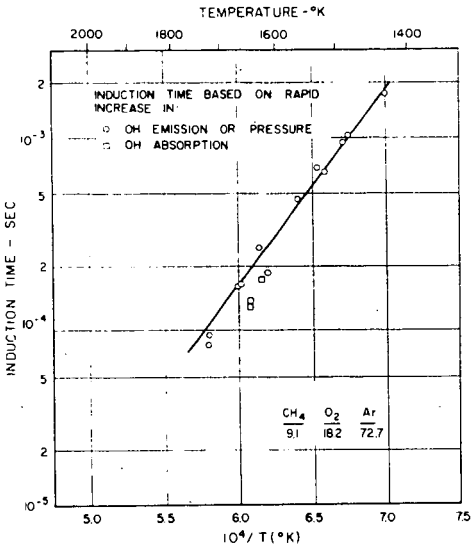

FIGURE 6. TEMPERATURE DEPENDENCE OF INDUCTION TIME FOR P = 2.0 ATM AND Φ = 1.0

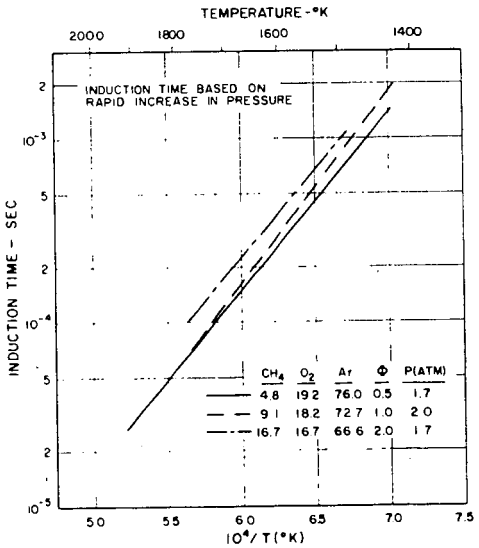

FIGURE 7. TEMPERATURE DEPENDENCE OF INDUCTION TIME FOR SEVERAL Φ

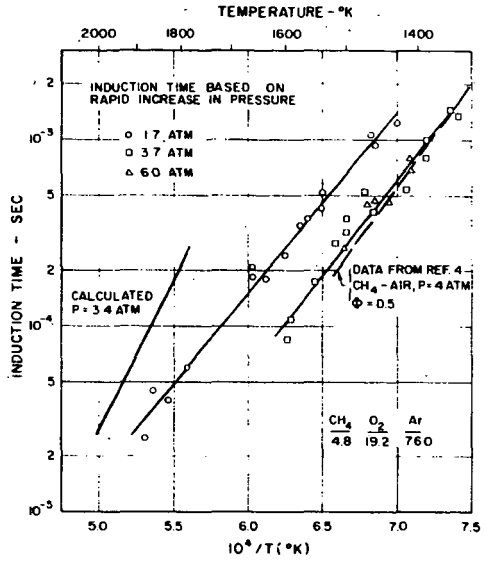

FIGURE 8. TEMPERATURE DEPENDENCE OF INDUCTION TIME FOR SEVERAL PRESSURES

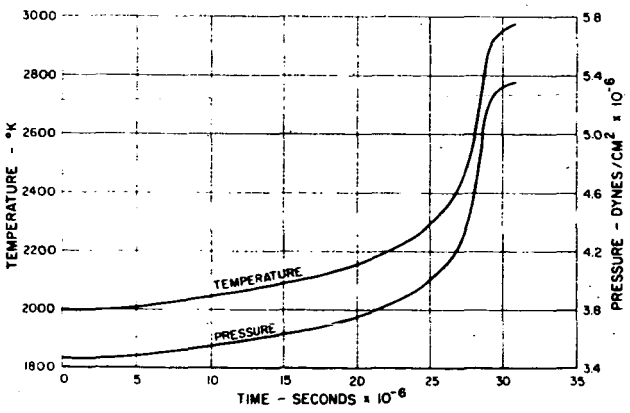

FIGURE 9. CALCULATED TEMPERATURE AND PRESSURE PROFILES FOR T=2000°K, P=3.4 ATM AND Φ=0.5

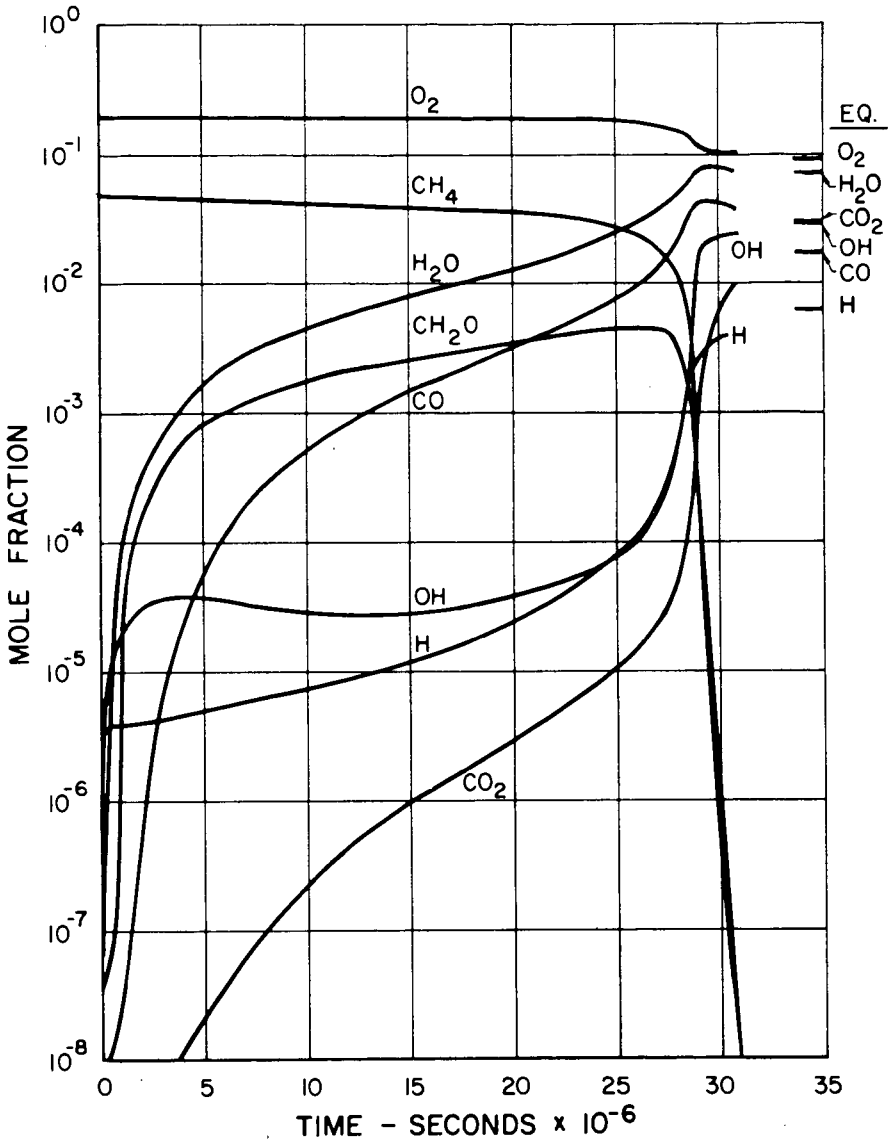

FIGURE 10. CALCULATED CONCENTRATION PROFILES FOR T = 2000°K, P = 3.4 ATM AND Φ = 0.5

KINETICS OF THE NITROUS OXIDE - HYDROGEN REACTION

Hans Henrici, Margaret Hunt, and S. H Bauer

Department of Chemistry, Cornell University

Ithaca, New York 14850

The reaction between nitrous oxide and hydrogen was investigated over the temperature range 1700°-3000°K in shock heated mixtures, diluted 1%-3% (for each reagent) in argon. Incident shock densities were (1-7) 10^{-6} moles cm^{-3}. Most of the rate data were obtained by recording the absorption of characteristic OH radiation at 3094Å; additional spectrophotometric measurements were made at 2259Å (for NO) and at 2300 Å (for N_2O). The first objective was to determine whether the literature values for the rate constants of the elementary steps adequately account for the observed OH profiles, and the second, to deduce more reliable values for those constants the magnitudes of which are in doubt. Preliminary analysis of the data indicated that the OH concentration exceeded its equilibrium level particularly at the lower temperatures; this was also the case for NO. Detailed analyses using a shock kinetics program for 14 reactions (and their inverses) show that the "best" values generally accepted for the various rate constants lead to much faster rise times but lower maximum concentrations of OH than were observed. In view of the consensus currently being reached regarding the constants for the O/H reactions, our data place lower limits on the magnitudes for the (N_2O + O) steps and an upper limit for the (N_2O + H) step.

STATEMENT OF THE PROBLEM

The reaction between nitrous oxide and hydrogen at high temperatures is very rapid. While the main outlines of the mechanism may be formulated with reasonable certainty, the magnitudes of the kinetics parameters are not well established. In particular, several of the critical rate constants have been measured at lower temperatures only, and information which permits extrapolation to the higher temperature regime (up to 3000°K) is not available. The entire sequence of steps may be divided into three groups.

I. The following involve oxygen and nitrogen only;

the initiation reaction

1. $N_2O + M \rightarrow N_2 + O + M$

the depletion reactions

2. $N_2O + O \rightarrow N_2 + O_2$

3. $N_2O + O \rightleftarrows 2\,NO$

scrambling and recombination steps

7. $O + NO \rightleftarrows O_2 + N$

8. $O + N_2 \rightleftarrows NO + N$

14. $O + O + M \rightleftarrows O_2 + M$

II. This group involves oxygen and hydrogen only; all but the termolecular reactions are very rapid.

the primary step

4. $O + H_2 \rightleftarrows OH + H$

secondary steps

9. $O + OH \rightleftarrows O_2 + H$

10. $OH + H_2 \rightleftarrows H_2O + H$

11. $OH + OH \rightleftarrows H_2O + O$

13. $OH + OH \rightleftarrows H_2 + O_2$

6. $H + H + M \rightleftarrows H_2 + M$

12. $H + OH + M \rightleftarrows H_2O + M$

III Reactions which couple the N/O to the H/O system;

the primary step

5. $H + N_2O \rightarrow N_2 + OH$

secondary steps (of little consequence under shock conditions)

16. $NO + H_2 \rightleftarrows HNO + H$

17. $NO + H_2O \rightleftarrows HNO + OH$

15. $HNO + M \rightleftarrows H + NO + M$

18. $N_2O + OH \rightleftarrows HNO + NO$

The reactions for which the rate constants are best established are the initiation step and some of the reactions in group (II). The rate constant for reaction (1) has been measured[1] over four powers of ten between 1500° and 2500°K. These experiments were conducted at a total density starting at 5×10^{-6} moles/cm^3 and into the high pressure saturation region. The rate of N_2O decomposition was found to be proportional to the density up to 6×10^{-5} moles/cm^3, a level which is much higher than the highest densities in our experiments. In group (II), the best known rate constants are those for reaction (9), which was determined to within 10% over the temperature range 1300° to 1700°K, and for reaction (4) which was determined in the same study combined with literature values available at lower temperatures. Reaction (5), the primary coupling step between groups (I) and (II) is the least well established of the controlling steps in the overall process. The thermochemical parameters for the above reactions are known with considerable precision, except possibly those involving HNO. The relevant data used in the following calculations were taken from the JANAF Tables.

The reaction rates between nitrous oxide and hydrogen were measured in shock heated mixtures (incident regime) over the temperature range 1700°-3000°K. The first objective was to determine whether the literature values for the rate constants of the elementary steps do adequately account for such data; the second, to deduce more reliable values for those constants the magnitudes of which are in doubt. The (N_2O + H_2) reaction is typical of complex oxidation systems and is particularly well suited for a shock tube study. Several spectroscopic probes are available as "handles" on the course of the reaction. Most of the data collected during this investigation were obtained by recording the absorption of characteristic OH radiation; additional spectrophotometric measurements were made in absorption for NO and for N_2O. When both of these gases were present, the net absorption at 2259Å was corrected for that due to N_2O. Other probes which are available for following this reaction are the intensities of emission in the infrared due to OH, H_2O and NO; these were not used in the present study. The mixtures of N_2O/H_2 used were, 1/1, 1/2, 1/3, 3/1, 3/3% in argon, with total densities from (1-7) 10^{-6} moles cm^{-3}. The levels of OH generated ranged 1.2×10^{-8} to 2.3×10^{-9} moles cm^{-3}.

EXPERIMENTAL PROGRAM

All our data were obtained in the incident shock regime, using a 6" I.D. stainless steel shock tube. It has an 8' driver section and a 30' test section. The observation windows are 26' downstream from the diaphragm. Prior to filling, the experimental section was pumped down to 10^{-4} torr; the apparent leak rate was 2.5×10^{-6} torr/min. Mylar diaphragms of 0.008" thickness were cross-cut to 0.005" and pressure broken. The speed of the incident shock wave was measured with a raster system, upon which calibrated markers were superposed at 10μsec. intervals. The raster was triggered by a piezoelectric pressure transducer. Further downstream were three platinum heat gauges with known separation. The error in the shock speed was estimated to be about 0.1%. The peizoelectric gauge also triggered the other electronic devices, including the discharge through the H_2O vapor lamp. We estimated the time constant of the recording system to be about 5μsec.

The N_2O used in these studies was doubly distilled in vacuum, mixed with hydrogen and argon in large glass vessels or in glass lined metal tanks and kept at least 10 hours before using, to insure complete mixing. Mass spectrometric checks revealed no oxygen impurity above the background level of the spectrometer.

The source of characteristic OH radiation was described previously[15]. The lamp emission was made parallel before entering the shock tube, and the exit light was focused onto the entrance slit of a Jarrell-Ash 500 mm focal length monochromator (JACO 8200), which has a 16A/mm dispersion. In order to discriminate against the emission from the shock heated gas, the focusing lens was placed 70 cm from the exit window of the shock tube. Forty micron entrance and exit slits permitted selection of a portion ($\Delta\lambda$ = 0.64Å) of the Q branch head (3094Å) of the $^2\Sigma^+ - {}^2\Pi_i$ transition. The time rate of change in the concentration of N_2O and the final concentration of NO were measured using a deuterium arc*, as a source of continuum radiation.

For the NO absorption measurements, a wavelength region around 2259Å (±2.7Å) was selected, this belongs to the γ band (0, 0 of $^2\Sigma^+ - {}^2\Pi_{3/2,\ 1/2}$) transition. The average of 8 runs with 1% NO in argon, the absorption coefficient between 1800° and 2100°K was determined to be 8.55 (± 0.3) $\times 10^{+4}$ cm^2/mole. For these measurements the NO was obtained from a commercial cylinder, and doubly distilled to remove N_2

* WHS 200 lamp, Dr. Kern, Göttingen.

and the higher oxides of nitrogen. Since N_2O absorbs only at shock temperatures, a reliable determination of the NO concentration in the reacting mixture was possible only after the N_2O had decomposed. The absorption of the generated NO remained constant for at least 1 msec, laboratory time, when the gas consisted initially of a mixture of pure N_2O in Ar, and also when hydrogen was added. The absorption coefficient of N_2O at 2300Å as a function of temperature, has been determined by Troe[16]. The few preliminary measurements made in our laboratory do not disagree with that determination.

Test times ranged up to 500 μsec; however, most of the runs were taken up to 350 μsec only. Particle times were therefore of the order of 1500 μsec.

TYPICAL RESULTS AND PRELIMINARY ANALYSIS

Within the limits of the time constants of these measurements the OH concentration rises linearly with a finite slope for a period of 50 to 100 μsec, then slowly bends over and appears to approach a level value. In some cases there were clear indications that this passed through a maximum. The preliminary assumption that the maximum level of OH corresponded to the equilibrium concentration proved misleading. An equilibrium shock program not only gave values for the final reaction temperature (which ranged from 100-250° above shock temperatures calculated for no reaction) but also gave the equilibrium concentration of all the species. Comparison of the calculated with the observed values, based on the approximate absorption coefficient (for OH) of 2.2×10^6 cm^2/mole is shown in Table I. It is clear that the overshoot is higher at the lower temperature. The cause for the overshoot is the same as in the H/O system, in that three body processes which reduce the atom and free radical concentrations are slow compared to the steps which produce OH, or bring it into local equilibrium with the other radicals. These preliminary studies also showed that the simplifying assumption regarding the OH production [i.e. that it is primarily controlled by reactions (1), (2), (3), and (4)] does not account for the data. Under the steady-state assumption for the oxygen atoms,

$$\frac{d(OH)}{dt} = k_1 [N_2O][M]\left[1 + \frac{k_3 + k_4}{k_2}\frac{[N_2O]}{[H_2]}\right]^{-1} \quad ; \text{ see Fig. 1.}$$

A test of this equation can be made by assuming literature values for k_2[1A], k_3[2], and k_4[3]. This reduction is not acceptable in view of the fact that runs with different concentrations of N_2O and H_2 do not lie on the same line, nor does the dissociation rate constant for N_2O agree with the currently accepted value[1]. However, the various curves are close to one another and fall below the previous data on the N_2O decomposition[1A].

Not only does the OH concentration overshoot but the NO appears to behave likewise; this has been observed previously in studies of the N_2O decomposition[1A]. The proof requires measurement of the limiting value of the NO concentration, referred to the initial concentration of N_2O, which disappears completely by the time the test period is over. The ratio (in the absence of H_2),

$$\beta \equiv \frac{(NO)^{\infty}}{(N_2O)^{i}} = \frac{1}{1 + (a + b)} \approx 0.47; \; (a + b) \approx 1.1$$

where a measures the fraction of oxygen atoms used in reaction (2), and b is the fraction of oxygen atom which follow reaction (14), compared with reaction (3) as a reference. Table II is a summary of magnitudes of β for several typical runs. The sum $(a + b) = 1.1$ indicates approximately comparable depletion of oxygen atoms by reactions (2), (3), and (4). In contrast, when hydrogen is present the observed value for β is

considerably less, also shown in Table II. The values for β in absence of hydrogen check with those obtained by Gutman[1A], who reported $\beta = 0.56$ at 2515°K, with no detectable temperature dependence. Thus, in the presence of hydrogen a considerable fraction of the oxygen atoms are removed by the primary reaction (4), and the secondary step (9). The partition of oxygen atoms among the various reactions, in the presence of hydrogen, cannot be directly estimated from the measured β, but this does provide an additional boundary condition on the correct assignment of reaction rate constants. One may now list the available experimental parameters:

(a) the initial slope of the OH curve (absence of an induction period)
(b) the time required for the OH concentration to reach 63% of its final value
(c) the magnitude of the OH at the maximum
(d) the value of β
(e) the time required for the disappearance of N_2O to 1/2 of its initial value.

The matching of the OH concentration-time profile, and the parameters listed above were used to test combinations of rate constants, as described in the next section.

EXTENDED CALCULATIONS AND CURRENT STATUS OF THE PROBLEM

Because of the coupling of a large number of reactions and their approximately comparable contributions, no simplifying assumptions permit an analytic solution of the coupled set of differential equations. Therefore a general kinetics program was introduced to obtain calculated values for the concentration profiles of all species. The program which was obtained from Cornell Aeronautical Laboratory[18], permits the insertion of the enthalpy and free energy for each specie as a function of temperature. The thermodynamic functions are expressed as polynomials in the temperature. For the rate constants specific values must be inserted for the pre-exponential factor, the pre-exponential temperature dependence and the activation energy. This incident shock program computes the equilibrium constant for each reaction, obtains the rate constant for its reverse and gives the net rate of formation (Q_{ij}) for each species (j) from every reaction (i). It also gives the concentration of each species as a function of time and computes the temperature profile behind the shock. The printout of the Q_{ij}'s as a function of time is probably the most useful part of the output. It provides a measure of how dependent the net concentration profile for any species is on the contribution from each reaction. It helps to gauge how effectively coupled the system is, and whether some reactions which were introduced can be discarded because of their minor contributions. For example, this was found to be the case for OH derived from reactions (15, 16, 17 and 18).

In the tests which will be described below no change was made in the value for the dissociation rate constant for step (1). The study from which we took the rate constant[1] covered a wide range of total pressures and of temperatures for low concentrations of N_2O in Ar. The reported values show very little scatter from an Arrhenius line. In addition the same results were obtained behind incident and reflected shock waves, and they were crosschecked by experiments with an adiabatic piston[19]. Nevertheless, in our system, there still may be some uncertainty about the rate constant for this reaction due to the unknown collision efficiencies for activation by the species produced in the N_2O/H_2 reaction. These may be much larger than that for argon. The other rate constants were obtained from a survey of the literature and from discussions with several workers in the field; they are listed in Table III.

In a first group of tests the rate constants for reactions (2) and (3) were accepted, and only those of the H_2/O_2 system and that of reaction (5) were varied in an attempt to obtain a fit to the experimental OH profile at 2000°K. These tests showed that the computed rate of OH-formation, which was much faster than the observed, could be fitted only by

reducing the rate constants of reactions (5) and (10) by a factor of 30 to 40. In order to achieve a better fit for experiments at different concentrations, it was also necessary to reduce the rate constants for (9) by a factor of 10, and for (4) by 1/2. This is clearly an unacceptable combination. Figure 2a shows the contributions of the five critical reactions to the OH concentration profile (Q_{ij}) for a typical run with 1% of N_2O and 1% H_2 in Argon; Fig. 2b shows the net OH profiles, calculated and observed as well as the calculated adiabatic temperature.

In view of the consensus now being reached as to the magnitudes of the rate constants for group II, the second exploration involved the rate constants for the depletion reaction (2) and (3), and the primary coupling reaction (5). At this stage it was demonstrated that reactions (15) to (18) have no discernable effect on the OH profile. Table IV is a summary of the various combinations tested, and Figures 3a and 3b show the Q_{ij} and the net OH profile for one of the more successful combinations found to date.

As in the first series of tests for specified k_2 and k_3, the OH profile depends most sensitively on the rates of reactions (5) and (10). A difficulty in all these attempts to fit the experimental data was that the computed OH profiles yielded maximum values for the OH concentrations which were at most half as large as those observed. Whether this is due to an uncertainty in the absorption coefficient of OH or to an incorrect combination of the rate constants will be tested in calibration measurements designed to determine the absolute OH concentrations under these conditions.

If the present set of rate constants is a reasonable approximation, the effect of the different reactions on each other and on the OH profile can be described as follows. The reaction is initiated by (1) which is rapidly followed by either (2) and (3) or by (4). If NO plays no further role, the only way in which reactions (2) and (3) contribute toward the building up of OH is through (9), the reaction of the O_2 generated in reaction (2) with hydrogen atoms. Between 1100°K and 1700°K[3] k_9 is by now known to within ± 10%. If the extrapolation to 2000°K is correct, reaction (9) makes only a minor contribution to the OH generation, at least when there is no large excess of N_2O over H_2.

Apart from the current experiments there is other evidence for the stability of NO under conditions similar to those of the shock tube investigation. The decomposition of NO is a slow process as is also its rate of reaction with molecular hydrogen, reaction (16). The rate of production of HNO would have to be at least a 100 times faster than that determined by Bulewicz and Sugden[13], in order to contribute measurably. Further, the decay of pure N_2O in argon is at least 100 times faster than the loss of N_2O through[22]:

$$N_2O + NO \rightarrow NO_2 + N_2 \qquad (19)$$

The absorption by NO_2 at its band maximum (4200 Å) was not detectable in the Göttingen studies on the N_2O decomposition.

It follows that, apart from the contribution of reaction (9), oxygen atoms which react with N_2O via reactions (2) and (3) are lost for the production of OH. The net rate of OH production is therefore sensitive to the ratio: $k_4/(k_2 + k_3)$. The above preliminary experiments of the magnitude for β indicate that an increase in the rates of k_2 and k_3 is required to account for the observed ratio of $[NO]^{\infty}/[N_2O]^{1}$. Once the ratio $k_4/(k_2 + k_3)$ is fixed, the concentration profile of OH depends strongly on the coupled reactions (5) and (10). At the beginning, when little water is present, reaction (10) is faster than reaction (5), resulting in a net consumption of OH. As reaction (10) approaches local equilibrium, reaction (5) takes over until the N_2O is consumed. By

then, the buildup of OH is completed, and OH decays slowly via three body processes.

This relatively simple picture is complicated by the fact that reactions (9) and (11) also contribute to the OH profile but by an amount which is smaller than the contributions from reactions (4), (5), and (10). However, the significance of (9), (11) can be established only after the rate constants for (2), (3), and (5) have been measured. In order to achieve this, the experiments to determine β as a function of the H_2 concentration, and the profile for N_2O disappearance will be continued.

ACKNOWLEDGEMENTS

This work is being supported by the AFOSR, Contract AF49(638)-1448. We are particularly grateful to the Aerodynamics Research Group at the Cornell Aeronautical Laboratory for making available to us both the equilibrium and non-equilibrium shock programs used in this investigation. We wish to thank Dr. G. L. Schott for informative discussions of the "best" values for the rate constants for the hydrogen-oxygen reaction, and Professor J. E. Dove for sending us mass spectrometer data on the N_2O-H_2 reaction.

REFERENCES

1. H. A. Olschewski, J. Troe, and H. Gg. Wagner, Ber. Bunsenges. physik. Chem. 70, 450 (1966).

1A. D. Gutman, R. L. Belford, A. J. Hay, and R. Pancirow, J. Phys. Chem., 70, 1793 (1966).

2. C. P. Fenimore, and G. W. Jones, 8th (International) Symposium on Combustion, Williams and Wilkins, Baltimore 1962, p. 127.

3. D. Gutman, and G. L. Schott, in print.

4. C. P. Fenimore, "Chemistry in Premixed Flames", International Encyclopedia of Physical Chemistry and Chemical Physics, Topic 19, Vol. 5, MacMillan, New York, 1964.

5. A. L. Myerson, W. S. Watt, and P. J. Joseph, in print.

6. K. L. Wray, and J. D. Teare, J. Chem. Phys., 36, 2582 (1962).

7. H. G. Glick, J. J. Klein, and W. Squire, J. Chem. Phys., 27, 850 (1957).

8. D. L. Ripley and W. C. Gardiner, Jr., J. Chem. Phys., 44, 2285 (1966).

9. W. E. Kaskan and W. G. Browne, "Kinetics of the $H_2/CO/CO_2$ System", General Electric Reentry Systems Dept., Document 635D848 (1964).

10. H. A. Olschewski, J. Troe, and H. Gg. Wagner, Z. physik. Chem., NF, 47, 353 (1965).

11. G. L. Schott, private communication.

12. K. L. Wray, 10th (International) Symposium on Combustion, The Combustion Institute, Pittsburgh, Pa., 1965, p. 523.

13. E. M. Bulewicz and T. M. Sugden, Proc. Roy. Soc. (London), A277, 143 (1964).

14. K. A. Wilde, Report No. S-121, Rohm and Haas Company, Redstone Research Laboratories, Huntsville, Alabama 35807.

15. S. H. Bauer, G. L. Schott and R. E. Duff, J. Chem. Phys., 28, 1089 (1958).

16. J. Troe, Dissertation, Gottingen, 1965.

17. C.A.L. Equilibrium Normal Shock Program, Cornell Aeronautical Laboratory, Inc., Buffalo, New York 14221, September 1966.

18. L. J. Garr, P. V. Marrone, W. W. Joss, and M. Williams, Inviscid Non-equilibrium Flow Behind Bow and Normal Shock Waves, Cornell Aeronautical Laboratory, Inc., Buffalo, New York 14221,
CAL - Report No. QM - 1626 - A - 12 (I), May 1963
QM - 1626 - A - 12 (II), May 1963
and revised QM - 1626 - A - 12 (III), October 1966.

19. A. Martinengo, J. Troe, and H. Gg. Wagner, Z. physik. Chem., NF, 51, 104 (1966).

20. E. Freedman and J. W. Daibler, J. Chem. Phys., 34, 1271 (1961).

21. K. L. Wray and J. D. Teare, J. Chem. Phys., 36, 2582 (1962).

22. F. Kaufman, and J. R. Kelso, J. Chem. Phys., 23, 602 (1955).

TABLE I

Run No.	p_o(total) torr.	$p_o \times 10^{-4}$ dynes/cm^2	U_{shock} mm/μs	T_2 °K equilibrium	obs. (OH) $\times 10^9$ plateau	calc. (OH) $\times 10^8$ equil.	(OH) obs. / (OH) eq.
N_2O:H_2:Ar/3:3:94							
82	43.2	5.7595	1.332	2078	9.965	0.194	5.12
83	37.7	5.0262	1.403	2235	12.224	0.398	3.08
79	16.5	2.2000	1.478	2386	10.292	0.438	2.35
85	13.2	1.7599	1.568	2551	9.179	0.695	1.32
N_2O:H_2:Ar/3:1:96							
64	27.0	3.5997	1.397	2110	8.424	0.244	3.45
54	21.0	2.7998	1.445	2222	9.900	0.317	3.12
92	12.5	1.6665	1.521	2394	7.642	0.384	1.99
93	10.3	1.3732	1.610	2586	7.620	0.540	1.41
N_2O:H_2:Ar/1:1:98							
31	27.0	3.3331	1.385	2064	5.558	0.0674	8.25
73	21.2	2.8261	1.446	2209	5.167	0.126	4.09
17	14.7	1.9598	1.515	2372	6.036	0.1939	3.12
16	13.3	1.7732	1.568	2494	5.905	0.249	2.37
N_2O:H_2:Ar/1:3:96							
48	13.0	1.733	1.548	2405	2.848	.0744	3.83
47	13.1	1.747	1.610	2554	2.310	.158	1.29

TABLE II

Determination of $\beta \equiv \frac{[NO]^{\infty}}{[N_2O]^{i}}$ in mixtures of N_2O: Ar = 2:98, and N_2O:H_2:Ar = 2:1:98

Total density: $(0.8 - 1.1 \times 10^{-5}$ moles/cm^3

No.	T (^{o}K)	β	
1	2009	0.42	
3	2085	0.48	
4	2100	0.50	N_2O:Ar = 2:98
5	2212	0.48	
17	1910	0.064	
18	1590	0.083	
19	1965	0.063	N_2O:H_2:Ar = 2:1:97
20	1995	0.072	

TABLE IV

Factors by which rate constants of Table III were varied in the second group of tests.

No.	Reaction	Test 1	Test 2	Test 3	Test 4	Test 5	Test 6	Test 7
2	$O + N_2O \rightleftarrows H_2 + O_2$	10	10	10	10	10	30	30
3	$O + N_2O \rightleftarrows 2\,NO$	10	10	10	10	10	30	30
4	$O + H_2 \rightleftarrows OH + H$	1	1	1	1	1/2	1	1
5	$H + N_2O \rightleftarrows N_2 + OH$	1	1/3	1/3	1/10	1/10	1/3	1/10
10	$OH + H_2 \rightleftarrows H_2O + H$	1	1	2	1	1	1	1

TABLE III: "Best" literature values for k_i

No.	Reaction	ΔH°_{2000} kcal/mole	ΔS°_{2000} cal/mole deg.	K_{p2000} (atm)	$k_f \left[\frac{\text{moles}}{\text{cm}^3 - \text{sec}}\right]$	Ref.
1	$N_2O + M \rightleftharpoons N_2 + O + M$	39.87	32.59	5.85×10^{2}	$10^{14.7}\, e^{-58/RT}$	1
2	$O + N_2O \rightleftharpoons N_2 + O_2$	-82.18	0.65	1.32×10^{9}	$10^{13.93}\, e^{-28.0/RT}$	1A
3	$O + N_2O \rightleftharpoons 2\,NO$	-38.92	6.73	5.29×10^{5}	$10^{14}\, e^{-28.0/RT}$	2
4	$O + H_2 \rightleftharpoons OH + H$	2.09	1.66	1.36×10^{0}	$10^{13.51}\, e^{-10.0/RT}$	3
5	$H + N_2O \rightleftharpoons N_2 + OH$	-66.50	5.56	3.02×10^{8}	$10^{14.48}\, e^{-16/RT}$	4
6	$H_2 + M \rightleftharpoons 2\,H + M$	108.46	28.69	2.63×10^{-6}	$1.18 \times 10^{12}\, T^{\frac{1}{2}}\, e^{-94.5/RT}$	5
7	$O + NO \rightleftharpoons O_2 + N$	32.07	-3.05	6.77×10^{-5}	$10^{9.5}\, T\, e^{-39.1/RT}$	6
8	$N + NO \rightleftharpoons N_2 + O$	-75.32	-3.03	3.69×10^{7}	$10^{13.18}$	7
9	$H + O_2 \rightleftharpoons OH + O$	15.67	4.91	2.28×10^{-1}	$10^{13.89}\, e^{-14.45/RT}$	3
10	$OH + H_2 \rightleftharpoons H_2O + H$	-14.80	-2.81	1.01×10^{1}	$10^{13.6}\, e^{-5.7/RT}$	8
11	$2\,OH \rightleftharpoons H_2O + O$	-16.89	-4.47	7.38×10^{0}	$10^{12.88}\, e^{-1/RT}$	9
12	$H_2O + M \rightleftharpoons H + OH + M$	126.26	31.51	2.61×10^{-7}	$10^{15.3}\, e^{-109/RT}$	10
13	$H_2 + O_2 \rightleftharpoons 2\,OH$	17.76	6.57	3.16×10^{-1}	$10^{12.4}\, e^{-39/RT}$	11
14	$O_2 + M \rightleftharpoons 2\,O + M$	122.04	31.94	4.40×10^{-7}	$10^{16.41}\, T^{\frac{1}{2}}\, e^{-118/RT}$	12
15	$H + NO + M \rightleftharpoons HNO + M$	-52.71	-29.11	3.99×10^{0}	$10^{18.99}\, T^{-1}$ (b)	13
16	$H_2 + NO \rightleftharpoons HNO + H$	55.75	-0.41	6.60×10^{-7}	$10^{14.48}\, e^{-57.9/RT}$	13 (a)
17	$OH + HNO \rightleftharpoons H_2O + NO$	-70.55	-2.40	1.53×10^{7}	$10^{13.95}$	13
18	$NO + HNO \rightleftharpoons N_2O + OH$	-14.73	-4.65	3.92×10^{0}	$10^{12.79}\, e^{-34.1/RT}$	14

a. Calculated from reverse rate constants through $K_{eq.}$

b. Units are $\text{mole}^{-2}\,\text{cm}^{6}\,\text{sec}^{-1}$.

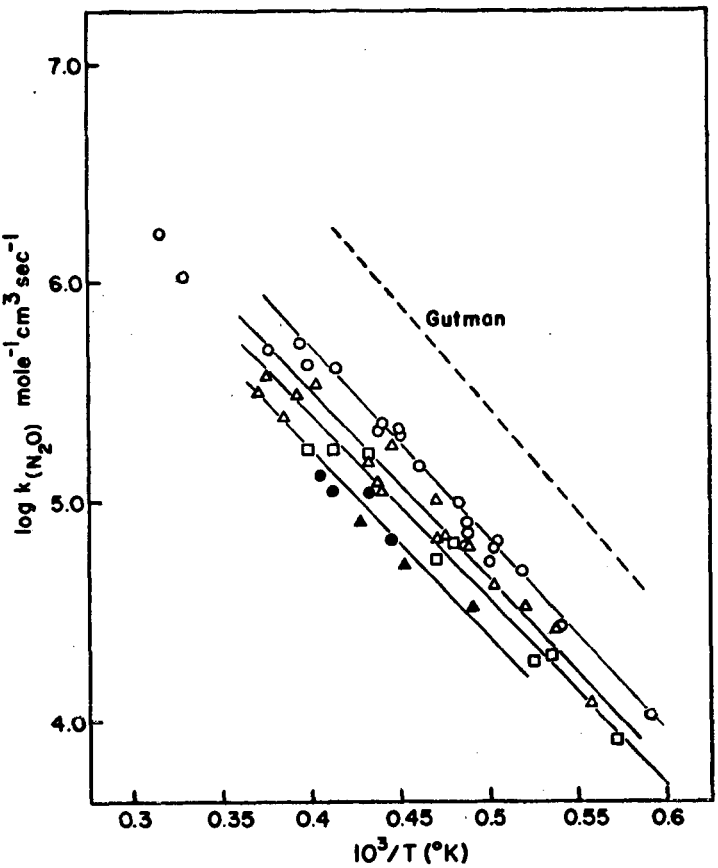

Figure 1. Bimolecular dissociation rate constant for N_2O, deduced from preliminary reduction of initial [OH] slopes.
$[N_2O]_o/[H_2]_o$ = 1:1 ○; 3:1 △; 3:3 □; 1:3 ● and 2:4 ■

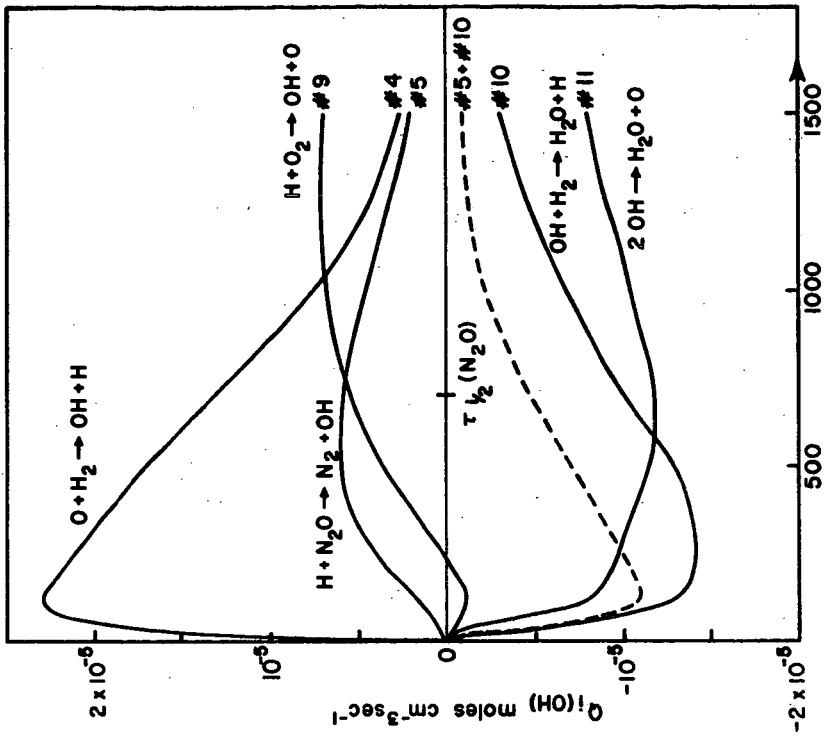

Figure 2a. Typical profiles for OH production rates from various reactions; 1st test on $N_2O/H_2 = 1:1$.

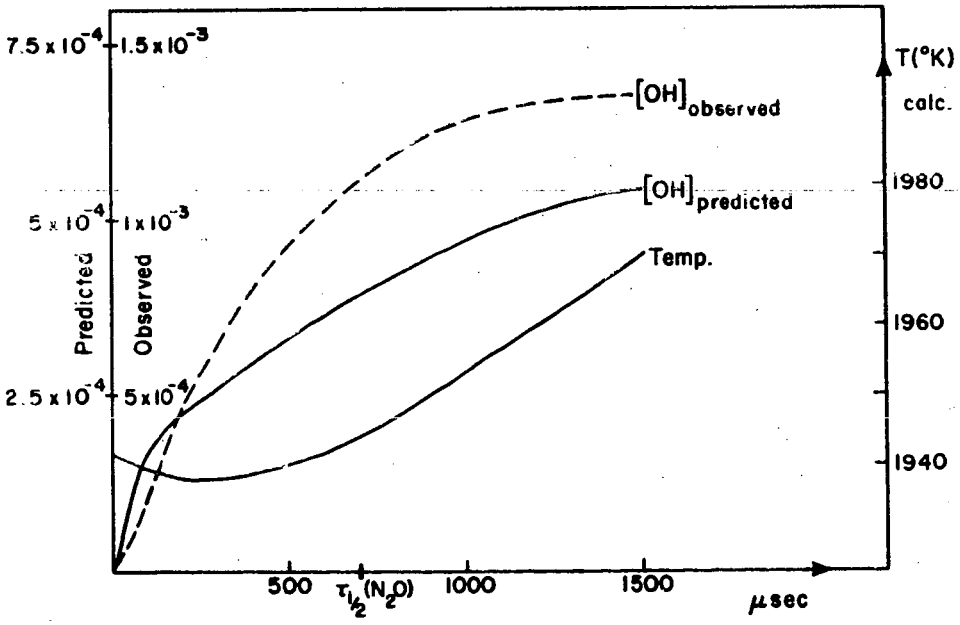

Figure 2b. Net [OH] produced, as a function of time.

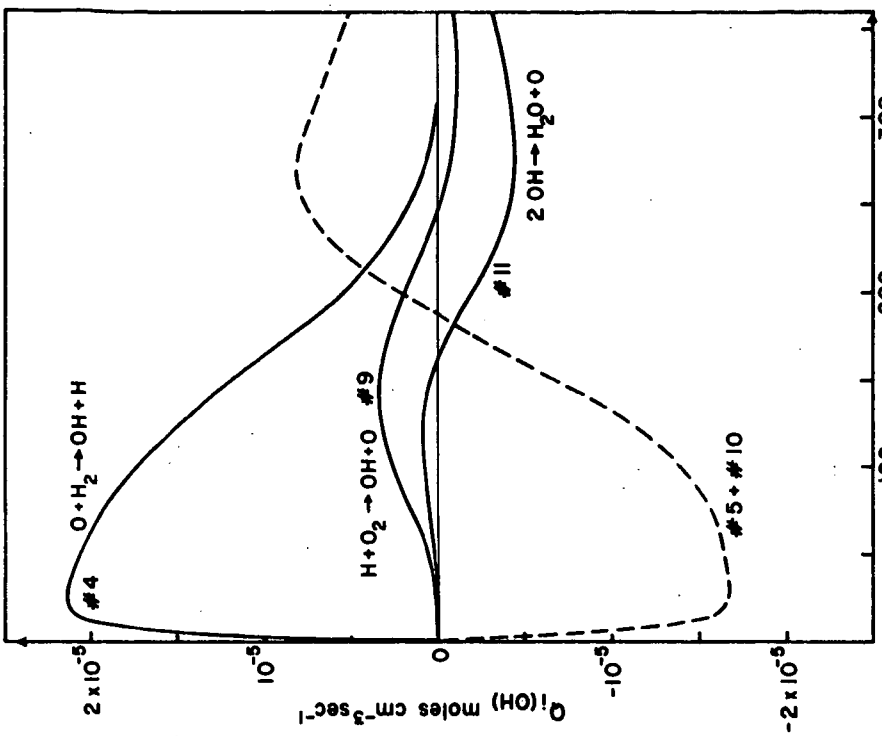

Figure 3a. Second test: OH production rates for N_2O/H_2 = 1:1 (same as 2a).

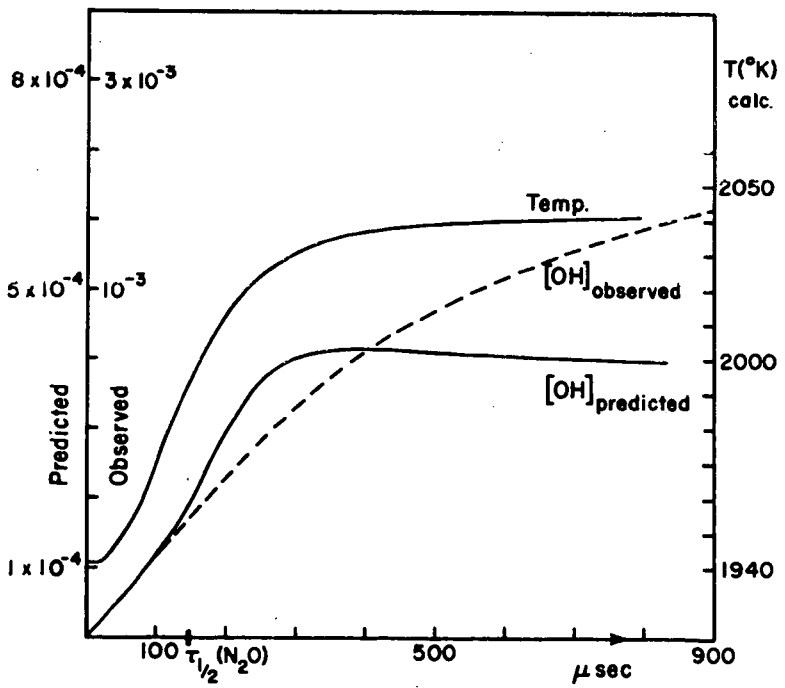

Figure 3b. Net [OH] produced, as a function of time.

SHOCK TUBE-MASS FILTER EXPERIMENTS ON LINEAR TRIATOMIC MOLECULES

R. Linn Belford

Department of Chemistry and Chemical Engineering
Noyes Chemical Laboratory, University of Illinois, Urbana, Illinois

Introduction -- Use of fast mass spectrometry to follow high-temperature gas reactions in a shock tube was first introduced by Bradley and Kistiakowsky(1) and Diesen and Felmlee(2) and has been exploited by several groups, all of whom have used a time-of-flight mass spectrometer. We have developed a combination of shock tube and Paul quadrupole mass filter and are using it to study reactions of linear triatomic molecules akin to CO_2(3-7).

All the mass spectrometric shock sampling techniques have associated with them a number of common problems. These include the uncertainties in temperature caused by our partial ignorance of flow conditions through the sampling orifice into the region of the electron beam and of the rate of gas cooling by thermal transport to the end plate near the sampling leak.

In addition, there are special difficulties, but also special advantages accompanying each particular mass analyzer. The time-of-flight device operates on a cycle in which ionization occurs for only a small fraction of total reaction time (typically about 1/400). This feature limits sensitivity and interferes with noise recognition. However, one gets a full mass spectrum every cycle and can easily survey the species produced in a complex reaction. While a Paul mass filter could be built to operate essentially in the same fashion, it would offer no obvious advantage. It is best suited to the continuous ionization and study of the detailed time behavior of a single mass. Accordingly, mass filter detection is a valuable technique for the study of relatively uncomplicated systems, in which only a few species must be followed. It is also potentially useful for investigating the establishment of flow from the sampling orifice and the approach to steady state conditions in the ion source.

Here I shall outline the principal results of our studies of two related pyrolyses -- NNO and OCS -- and then consider together the existing shock tube data on all molecules of the same family. Of the several stable linear triatomic molecules having the same outer electron structure as that of CO_2, only four -- CO_2, N_2O, CS_2, and OCS -- are common and have been studied under high-temperature shock conditions. Of these, only two -- CO_2 and N_2O -- have been studied extensively, and despite much progress in the past 4 years, there is still disagreement about some details of these decompositions.

Each reactant may be represented $ABC(^1\Sigma)$, where C is a calcogen atom and AB is isoelectronic with carbon monoxide. At low pressure, high temperature, and high dilution in an inert gas (M), the first kinetic step is collisional excitation of the internal modes of ABC followed by rapid dissociation of every sufficiently energized reactant as follows:

$$M + ABC(^1\Sigma) \rightarrow AB(^1\Sigma) + C(^3P) + M. \qquad (1)$$

Under some conditions of temperature and dilution, further steps can occur rapidly. The most important are (2) and (3):

$$C + ABC \rightarrow CA + BC, \qquad (2)$$
$$ABC + C \rightarrow AB + C_2. \qquad (3)$$

With the mass spectral techniques it is easy to follow all of the possible species -- eg., ABC, C, M, CA, BC, AB, C_2 -- and so determine directly the role of steps such as (2) and (3).

Results -- In the nitrous oxide study(3-5) 4% and 2% mixtures of N_2O in Ar were shocked to temperatures between 1500 and 3500°K. All species found were accounted for by Reactions (1)-(3). All O^+ signal could be ascribed to fragmentation. Formation of N_2, NO, and O_2 accompanied destruction of N_2O in the proportion of about 3:2:1:4. This suggests that Reaction (1) is immediately followed by (2) or (3), with equal probability. The chains and other reactions which we have looked into do not explain the observed distribution of species. That Reactions (2) and (3) keep up with (1) over most of the temperature range indicates that of the various reported expressions for k_2, the most reasonable is that of Fenimore and Jones(8) with an Arrhenius frequency factor of 10^{14} cc/mole sec and an activation energy of about 28 kcal. Essentially the same expression would hold for k_3. The general magnitude of these rates has been verified in a number of other shock experiments(9-11). They show an efficient atomic abstraction process with a high activation barrier which implies strong repulsion between triplet-state oxygen atom and N_2O.

Step (1) is of fundamental interest. In order to investigate it, one must know how Reactions (2) and (3) affect the rate. In this case the N_2O starting concentrations were sufficient to insure that the initial rate of N_2O destruction was $2k_1(M)(N_2O)$ at least up to 2500°K. At much higher dilutions, however, Steps (2) and (3) would be sufficiently slow to be negligible at small reaction times, and the initial rate would be $k_1(M)(N_2O)$. If the experimental activation energy for Step (1) remains much higher than for Steps (2) and (3), at very high temperatures the near steady state concentration of O atom will not pertain, and the rate will drop from $2k_1(M)(N_2O)$ to $k_1(M)(N_2O)$. It is not certain whether this situation applies in our experiments; therefore, we give the rate expression established for the points below 2500°K: $k_1 = A\sqrt{T}\,(E/RT)^n \exp(-E/RT)$, with $A \approx 1.2\times10^7$ cc/mole sec $\sqrt{°K}$, E = 60 kcal/mole, $n \approx 5.1$.

In the carbonyl sulfide study(6,7) 4%, 2%, and 0.5% mixtures of OCS in Ar were shocked to temperatures between 2000 and 3200°K. Typical ion current curves are shown in Fig. 1, and results for Step (1) are plotted in Fig. 2. Here the ions OCS^+, CO^+, CS^+, S^+, O^+, SO^+, S_2^+ were seen. O^+ is entirely accounted for by fragmentation, but the others are not, except that at low temperatures CS^+ comes exclusively from fragmentation of OCS. Relative concentrations of S_2 and SO over a temperature range establish that the activation energy for (2) exceeds that for (3) by ca. 19 kcal/mole. In the 0.5% mixtures, the rise of S^+ signal indicates that a steady state in S is not immediate and establishes the initial rate of OCS disappearance as $k_1(M)(OCS)$. From this, $A \sim 1.1\times10^{11}$ cc/mole sec $\sqrt{°K}$, and $n = 1.87$, if E is taken as $D_0° = 71.5$ kcal/mole. From the quantitative behavior of the S_2^+, S^+, and OCS^+ ion currents, we estimate $k_2 \approx 6\times10^{11}$ cc/mole sec at 2600°K. If the steric factor for this reaction is "normal" (0.1 or greater), the activation energy is in the range 20-30 kcal/mole, and there is a barrier to reaction of triplet sulfur atom with OCS that is comparable to the corresponding O + N_2O barrier.

Given the magnitude of k_2 so deduced, one can calculate that at the higher (2% and 4%) percentages of OCS, a near steady-state concentration of S atom would be established almost immediately, and the measured rate would be $2k_1(OCS)(M)$. Although the 2% and 4% measurements were less reliable because of troubles with solid sulfur, which deposited in the sampling orifice, the data indicated a rate about twice that yielded by the 0.5% mixtures, except at the upper end of the temperature range, where the values of k_1 from the 2% mixtures scattered about those from the 0.5% mixtures.

Theory -- The most interesting aspect of the high-temperature study of decomposition of triatomic molecules is the opportunity which it can afford to investigate some consequences of the details of collisional activation. The strong-collision assumption requires that in the steady state all bound quantum states of reactants are populated in Boltzmann fashion, and that the probability of exciting a molecule into an unbound state is proportional to the Boltzmann factor for the final state but independent of initial (bound) state. Thus, to get the reaction rate at low pressures, one need only divide all states into bound and unbound, apply the Boltzmann distribution to all, find the fraction of the Boltzmann population curve which covers unbound states, and multiply by collision rate. Thus, one has an a priori way of predicting reaction rate as a function of temperature (12). The rate should increase somewhat less rapidly with temperature than would be predicted by an Arrhenius extrapolation from low temperature. It is only at very high temperatures that one can expect the difference between the experimental and critical (low-temperature) activation energy to become significant. Thus, accurate data on the temperature dependence of these reaction rates under high-temperature shock conditions are potentially of great fundamental interest.

If the strong-collision assumption is seriously at fault, then reaction may proceed largely by collisional activation of the high-energy bound molecules. This process, in turn, may deplete the populations of the upper bound levels and act to limit the reaction rate. The effect would be expected to increase with temperature and yield a negative contribution to the experimental activation energy.

Accordingly, let us examine pertinent data so far collected on high-temperature activation energies for rupture of molecules of the CO_2 family.

In the case of OCS, the minimum possible critical activation energy is about 71.5 kcal/mole, the over-all dissociation energy D_0°. Our observed activation energy (7) over the range 1950-3150°K is 64.5 kcal/mole. Since at 2550°K the vibrational system of OCS is already excited by 15.5 kcal/mole and as the collision frequency involves an effective activation energy of $(1/2)RT$ = 2.5 kcal/mole, the minimum expected over-all activation energy would be 71.5-13 = 58.5 kcal/mole. On the basis of any strong-collision theory, which states that active molecules are formed in a Boltzmann distribution, about 1.2RT = 6 kcal/mole is stored in vibrations of the average active molecule formed, putting the expected minimum experimental activation energy at 64.5 kcal/mole (=58.5+6), in agreement with that observed. Therefore, according to our current knowledge of the parameters involved in the OCS dissociation, the strong-collision

theory (such as the RRKM treatment) is not in conflict with the experiment. However, we lack independent information about the critical activation energy (which could be higher than the dissociation energy, as is apparently the case in N_2O (5)) or the activated complex (bottleneck) configuration (which tells us how to treat rotations in the strong-collision approach (7,12)). Therefore, predictions based on the strong-collision theory may not be shown to agree with the facts. Indeed, our calculations based on the RRKM theory (7) show that a low (~1%) collisional activation efficiency λ_D is required to fit the observed rates, and this may be considered reasonable grounds for suspecting the strong-collision model, as certainly not 99 of every 100 collisions are elastic. To make λ_D larger, one has to assume a larger critical activation energy, which in turn means that the experimental activation energy shows a negative term not provided by the strong-collision treatment.

In the case of SCS, the critical activation energy is sure to be essentially the dissociation energy, D_o° = 96 kcal/mole for $SCS(^1\Sigma) \rightarrow CS(^1\Sigma) + S(^3P)$; the reaction proceeds through the bent $^3A_2$ state of CS_2, which is stable. The experimental activation energy has been reported(13) as 80.3 kcal/mole over the range 1800 to 3700°K. At 2850°K, 18.3 kcal/mole is stored in the vibrational modes of OCS, and correction for the temperature dependence of collision frequency brings the possible minimum expected activation energy to about 96. + 2.8 - 18.3 = 80.5 kcal/mole. The strong-collision approximation adds about 6.5 kcal to this, bringing the expected strong-collision activation energy to about 87 kcal/mole. It is possible that a rotational correction is required(7,12), which might reduce this by as much as 2 kcal/mole; regardless, there is a discrepancy indicating the effective activation energy to be a bit too small to be explained within the strong-collision framework.

The large number of shock tube studies on N_2O rupture include at least one employing an infrared detection technique(14), two involving ultraviolet absorption measurements(11,14), three employing time-of-flight mass spectrometry, and ours using the quadrupole mass filter. The various investigators report experimental activation energies ranging from 30 to 49 kcal/mole, except for one study(11) which yielded 58 kcal/mole. There appears to be an activation barrier to recombination, giving a critical activation energy in the vicinity of 60 kcal/mole for $N_2O(^1\Sigma) \rightarrow N_2(^1\Sigma) + O(^3P)$. At the mean temperature of most of the experiments (~2250°K), there is roughly 12.5 kcal vibrational excitation; 60-12.5+2.2 ≈ 50 kcal/mole. With active molecules being formed with about 5 kcal average excess energy, in the strong-collision model we might expect an activation energy of about 55 kcal/mole; rotation would decrease it by 1-2 kcal(7). Fig. 3 shows data from various studies fitted to a least-squares Arrhenius line. It would be hard to reconcile the experiments with the strong-collision result. The discrepancy in activation energy is about 4RT. The apparent collisional activation efficiency also is very small.

Several shock studies of OCO decomposition are on record; all have been done by spectroscopic techniques. The experimental activation energies from several of the studies are as follows:

Reference	T	$E_{exp} - \frac{1}{2}RT$	E_a(s.c.)	$\frac{D_o^\circ - E_a(s.c.)}{\langle RT \rangle}$
(15)	2500-3000°K	86 kcal	95	5.5
(16)	2850-4200	95.5	110	2.2
(17)	3000-5000	84.5	99	3.2
(18)	3500-6000	74.5	92	3.7
(19)	6000-11000	62	93	2.1

Here, E_{exp} denotes experimental activation energy ($-d\ell nk/d(1/RT)$) and E_a(s.c.) denotes the critical activation energy which, on a strong-collision model, would be computible with the given E_{exp}. Notice that the highest experimental activation energy obtained is still 30 kcal below the minimum dissociation energy, 126 kcal/mole.

In general, the preponderance of kinetic information so far obtained with shock experiments on low-pressure dissociations of linear triatomic molecules at high temperatures indicates a smaller temperature coefficient of rate than is predicted by the strong-collision theory of vibrational activation. However, more precise experimentation should be done. The effect is evidence of either some fairly widespread systematic error in shock measurements (such as a temperature error) or some serious breakdown of the (strong collision) theory.

Recently, Tardy and Rabinovitch(20) have reported a series of calculations on various stochastic weak-collision models for excitation. They found that the strong-collision rate expression requires a correction factor, β, which proved to be fairly insensitive to the details of the particular model chosen and principally dependent on $\langle\Delta E\rangle/\langle E^+\rangle$, where $\langle\Delta E\rangle$ denotes the average energy transferred per down collision and $\langle E^+\rangle$ denotes the mean energy of the active molecules in the strong-collision model. Ignoring any dependence of $\langle\Delta E\rangle$ on temperature, we find that for β between 0.2 and 0.01, $-d\ell n\beta/d(1/RT) \leq -2\ RT$. There is thus some theoretical justification for blaming an abnormally large high-temperature falloff of experimental activation energy on a weak-collisional energy transfer process.

Conclusion -- Measurements of temperature dependence in the rates of unimolecular reactions of small molecules in the second-order (low pressure) region offer exciting and heretofore unexploited opportunities to investigate certain aspects of the collisional activation process. However, precise data and particularly reliable temperature measurements are necessary. The considerable disagreement among various laboratories in the case of the reactions discussed here is prima facie evidence that accuracy sufficient to the purpose has not been routinely attained by most shock tube groups. Nevertheless, there is a general pattern of anomalously low activation energies at very high temperatures which suggests a weak-collision process with reactive depletion of the upper bound levels.

Acknowledgment -- This work is supported by the National Science Foundation. Professor David Gutman (now of Illinois Institute of Technology) and Dr. Arthur J. Hay (now of E. I. DuPont de Nemours and Co.) were responsible for much of the work, with considerable assistance from Dr. Roy Pancirov and Mr. George Sanzone.

References

(1) J. N. Bradley and G. B. Kistiakowsky, J. Chem. Phys. 35, 256 and 264 (1961).

(2) R. W. Diesen and W. J. Felmlee, J. Chem. Phys. 39, 2115 (1963).

(3) D. Gutman, "High Temperature Gas Kinetic Study of Nitrous Oxide Decomposition Performed with a Shock Tube and Quadrupole Mass Filter," Ph.D. Dissertation, University of Illinois, Urbana, Illinois, May 1965.

(4) D. Gutman, A. J. Hay, R. L. Belford, J. Phys. Chem. 70, 1786 (1966). (Describes the first version of the apparatus and performance tests.)

(5) D. Gutman, R. L. Belford, A. J. Hay, and R. Pancirov, J. Phys. Chem. 70, 1792 (1966). (Describes an N_2O study performed with the apparatus of Ref. 4.)

(6) A. J. Hay, "High-Temperature Gas Kinetic Study of Carbonyl Sulfide Decomposition Performed with a Shock Tube and Quadrupole Mass Filter," Ph.D. Dissertation, University of Illinois, Urbana, Illinois, Feb. 1966.

(7) A. J. Hay and R. L. Belford, J. Chem. Phys, (to appear). (Describes an improved apparatus and its use in an OCS study).

(8) C. P. Fenimore and G. W. Jones, "8th International Symposium on Combustion," Williams and Wilkins Co., Baltimore (1962); J. Phys. Chem. 62, 178 (1958).

(9) E. S. Fishburne and R. Edse, J. Chem. Phys. 44, 515 (1966).

(10) J. E. Dove, Private Communication, and S. C. Barton, Ph.D. Thesis, University of Toronto, Canada, Feb. 1966.

(11) H. A. Olschewski, J. Troe, and H. G. Wagner, Ber. Buns. Ges. 70, 450 (1966).

(12) R. A. Marcus, J. Chem. Phys. 20, 359 (1952) and 43, 2658 (1965). Also G. M. Wieder and R. A. Marcus, ibid. 37, 1835 (1962).

(13) H. A. Olschewski, J. Troe, and H. G. Wagner, Z. fur phy. Chemie, Frankfurt, 45, 329 (1965).

(14) E. S. Fishburne and R. Edse, J. Chem. Phys. 41, 1297 (1964).

(15) T. A. Brabbs, F. E. Belles, and S. A. Zlatarich, J. Chem. Phys. 38, 1939 (1963).

(16) K. W. Michel, H. A. Olschewski, H. Richtering, and H. G. Wagner, Z. fur phy. Chem., Frankfurt, 44, 160 (1965). Also 39, 9 (1964).

(17) E. S. Fishburne, K. R. Bilkawesh, and R. Edse, J. Chem. Phys. 45, 160 (1966).

(18) W. O. Davies, J. Chem. Phys. 41, 1846 (1964).

(19) W. O. Davies, J. Chem. Phys. 43, 2809 (1965).

(20) D. C. Tardy and B. S. Rabinovitch, J. Chem. Phys. 45, 3720 (1966).

Figures

Fig. 1a Sample, experimental oscilloscope traces of ion currents from shocks, OCS 0.5% in Ar, ~2800°K. A:OCS^+. B:CO^+. C:S^+. D:S_2^+. E:CS^+. F:SO^+. The smooth line is a signal from a thin-film resistor in the shock tube end wall. Fine marks appear on the bottom line, 200 μsec. apart.

Fig. 1b Typical adjustment of S^+, CS^+, and CO^+ dynamic in current curves to correct for OCS fragmentation.

Fig. 2 Second-order rate constants (k_1) for the disappearance of OCS, 0.5% in Ar. Open circles correspond to initial pressure of 6 ton; shaded ones, 8 ton. The line is the result of a quantum RRKM calculation for an assumed critical activation energy of 71.5 kcal/mole, and $\lambda_D \approx 0.01$.

Fig. 3 Arrhenius plot of second-order rate constants ($2k_1$) disappearance of N_2O, 1-4% in Ar. +:Our data. Other symbols denote other laboratories. Solid line: $k = 10^{12.4} \exp(-35.4$ kcal/RT mole), from least-squares fit with half-weighting of our data. Dotted line: with equal weighting of all data.

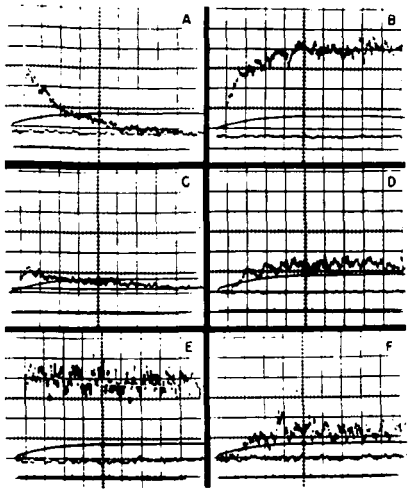

Fig. 1a Sample, experimental oscilloscope traces of ion currents from shocks, OCS 0.5% in Ar, ~2800°K. A:OCS^+. B:CO^+. C:S^+. D:S_2^+. E:CS^+. F:SO^+. The smooth line is a signal from a thin-film resistor in the shock tube end wall. Fine marks appear on the bottom line, 200 μsec. apart.

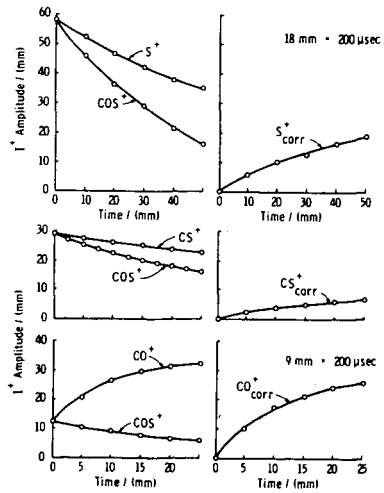

Fig. 1b Typical adjustment of S^+, CS^+, and CO^+ dynamic in current curves to correct for OCS fragmentation.

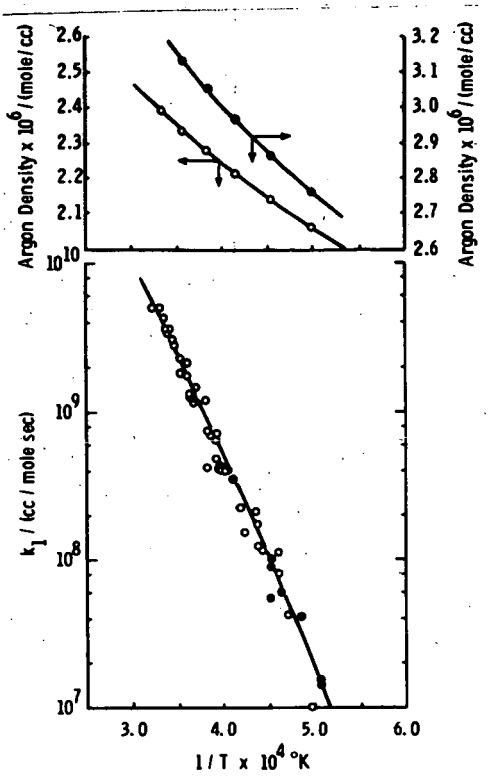

Fig. 2. Second-order rate constants (k_1) for the disappearance of OCS, 0.5% in Ar. Open circles correspond to initial pressure of 6 torr; shaded ones, 8 torr. The line is the result of a quantum RRKM calculations for an assumed critical activation energy of 71.5 kcal/mole, and $\lambda_D \approx 0.01$

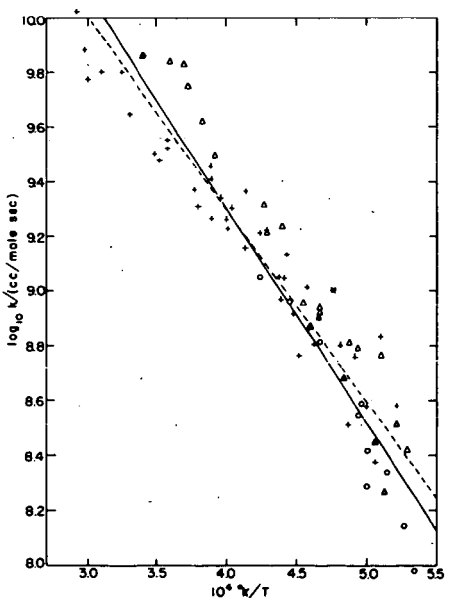

Fig. 3. Arrhenius plot of second-order rate constants for ($2k_1$) disappearance of N_2O, 1-4% in Ar. +:Our data. Other symbols denote other laboratories. Solid line: $k = 10^{12.4}\exp(-35.4 \text{ kcal/RT mole})$, from least-squares fit with half-weighting of our data. Dotted line: with equal weighting of all data.

A SHOCK TUBE STUDY OF THE RADIATIVE COMBINATION OF OXYGEN ATOMS BY INVERSE PREDISSOCIATION

B. F. Myers and E. R. Bartle

Space Science Laboratory, General Dynamics/Convair
San Diego, California, 92112

ABSTRACT

Absolute emission intensity measurements of the radiative combination of oxygen atoms, $O(^3P)$, in the temperature range between 2500°K and 3800°K are presented. The emission intensity was recorded simultaneously in six spectral intervals in the wavelength range between 2300Å and 4511Å. The absolute emission intensity was found to be proportional to the square of the oxygen atom concentration and to be characterized by an activation energy of 28.9±2.2 kcal mole^{-1}. These results are interpretated in terms of an inverse predissociation mechanism in which the oxygen atoms combine along a repulsive potential energy surface with a transition to the $B^3\Sigma_u^-$ state of molecular oxygen and a subsequent radiative transition to the ground electronic state of oxygen. The rate constant for the overall radiative combination of oxygen atoms was found to be 4.3×10^6 exp(- 28900 ± 2200/RT) cm^3 mole^{-1} sec^{-1} for the wavelength range 2300Å to 5000Å.

I. INTRODUCTION

Measurements on the radiative combination of oxygen atoms, $O(^3P)$, in the temperature range between 2500°K and 3800°K are presented. This radiative process was first observed during an investigation[1] on the radiative combination of atomic oxygen and carbon monoxide. In the latter case, it was found that a contribution to the total emission intensity occurred at wavelengths below 4500Å in the presence of oxygen atoms only.

In the present experiments, absolute emission intensity measurements of the radiation resulting from the combination of oxygen atoms were made by shock heating O_3 + Ar gas mixtures to temperatures in the range cited above and to pressures between 0.5 and 2.0 atm. The emission intensity was recorded simultaneously in six spectral intervals in the wavelength range between 2300Å and 4511Å. The emission intensity behind the shock front at the time of essentially complete ozone decomposition was correlated with the oxygen atom concentrations as determined by numerical calculations.

II. EXPERIMENTAL

The experiments were conducted with the 3 inch, internal diameter shock tube facility and the associated optical system and gas handling system previously employed.[1] For the measurement of the emission intensity of the radiative combination of oxygen atoms, the six slits in the image plane of the spectrograph had the center wavelengths and bandpasses given in Table I. The wavelength values listed have an error of less than 3Å. For detection of incident radiation in the spectral interval between 2300Å and 2500Å, two Dumont 7664 photomultipliers with S-13 spectral response and fused silica windows were employed, and in the spectral interval between 3000Å and 4511Å, four RCA type 1P28, photomultipliers with S-5 spectral response, two of which had quartz windows, were employed. The response of the detector system was linearly related to incident radiation[1] and output signal for each spectral channel was not affected by radiation transmitted in the other channels.[1] The output signals were calibrated in terms of the steradiancy of a calibrated tungsten ribbon filament lamp.[1] The entire optical system was

enclosed in a light tight box which could be flushed with Ar to avoid absorption of the emitted radiation by air.

The gas mixtures of O_3 and Ar were prepared from Matheson Co. supplies of Ar (ultra high purity grade) containing less than 12 ppm of contaminants and from Liquid Carbonic O_2 (electrolytic laboratory grade) containing less than 10 ppm of contaminants. The ozone was synthesized from the oxygen in a static ozone generator.[2] The gas mixtures prepared contained from 1% to 18% of O_3. The quantitative analysis of the ozone in the prepared gas mixtures was made by a standard titration procedure.[3] For each experiment the test gas mixture was shock heated within three minutes following addition to the shock tube, and a sample of the mixture was withdrawn from the shock tube for ozone analysis one minute before shock heating the mixture.

The O_3 + Ar mixtures were shock heated to temperatures between 2500°K and 3800°K and pressures between 0.5 and 2.0 atm. At these temperatures and pressures, at least 99% of the ozone had decomposed within 0.1 μsec (particle time) behind the incident shock wave to form atomic and molecular oxygen. The concentrations of oxygen atoms and molecules were determined for each experiment by a numerical calculation based on an assumed decomposition mechanism and corresponding elementary reaction rate constants as discussed below. The numerical calculations were made using the Cornell Aeronautical Laboratory normal shock wave computer program.[4,5] The calculations were performed on an IBM 7090-7094 computer.

III. RESULTS

An oscillogram of the recorded emission intensities is shown in Figure 1. For this experiment, a mixture of 6% O_3 + 94% Ar was shock heated to an initial temperature of 3048°K and a pressure of 1.41 atm; this temperature and pressure correspond to translational, rotational and vibrational equilibrium of the mixture with frozen chemical reactions. Opposite the beginning of each channel trace in Figure 1, the center wavelength and spectral interval are given in Angstrom units. The shock front arrival is indicated by the sudden rise in the upper trace of Figure 1b which shows the response of a heat resistor gauge mounted in the shock tube wall at the cross section of the radiation measurement. The response time of the detector system is ≤ 15 μsec (laboratory time) for all channels except that channel with a center wavelength of 3002Å for which the response time is 20 μsec (laboratory time). To obtain the emission intensity immediately after essentially complete ozone decomposition which occurs within 0.1 μsec (particle time) of shock front arrival at the observation station, the emission-time profiles are extrapolated practically to zero time. Numerical calculations demonstrate that after the ozone decomposes, the concentrations of atomic and molecular oxygen and the temperature change slowly under the present experimental conditions toward an equilibrium state. For that portion of the emission intensity-time profile following the initial rise in signal, the signal was either constant or linearly increasing or decreasing slowly for 50 to 150 μsec (laboratory time), allowing for the noise in the signal; the extrapolation was based on this portion of the trace.

The extrapolated values of the signals near zero time were converted to intensity values for each spectral channel (i) by using the following relation:

$$I_i = \frac{S_i C_i}{[1+R_i]d} \frac{\text{watts}}{\text{str-Å-cm}^2} \qquad (1)$$

where S_i is the extrapolated oscillogram signal in volts, C_i, the calibration factor in watts str^{-1} $Å^{-1}$ cm^{-2} V^{-1}, determined from the measured oscilloscope signal corresponding to the known steradiancy of the standardized, tungsten ribbon filament lamp in each wavelength interval of the spectral channels, d(= 7.70 cm)

the diameter of the shock tube and R_i, the reflectivity at the center wavelength of channel i of the shock tube wall opposite the observation station window which serves as a bounding plane to the optical field. The dependence of the reflectivity on the wavelength which was determined in two independent experiments[6] and the normalization of the intensity with respect to the diameter of the shock tube, d, have been discussed previously.[1]

The values of I_i computed as described above, are shown in Table II; also given are the initial conditions, the shock velocity and the calibration factors for each spectral channel.

Contributions to the observed emission intensity from molecular oxygen, argon or impurities in the test gases were examined by shock heating argon and oxygen-argon mixtures to temperatures up to 3600°K No signal was observed with shock-heated oxygen-argon mixtures until significant decomposition of the molecular oxygen to form oxygen atoms occurred; with shock-heated argon, a signal was observed only in the spectral channel with a center wavelength of 4511Å. This signal was a transient lasting about 50 μsec (laboratory time) and was apparently caused by an impurity in the argon or by residual gases in the shock tube. In applying the extrapolation procedure to the data for this channel, the oscillogram trace for t(laboratory time) < 50 μsec was disregarded. However, when the extrapolation was made using that portion of the trace for which t(laboratory time) ≥ 150 μsec, a lower, but not significantly different value of the signal was obtained. The intensities corresponding to the latter signal values are only considered below in connection with Figure 7. This difference could indicate a contribution to the oscillogram trace by the transient signal for t(laboratory time) > 50 μsec, although this is difficult to establish because of the signal noise.

For each experiment, the oxygen atom concentration immediately behind the shock front was determined by a numerical calculation based on the following reaction mechanism:

$$O_3 + M \rightleftarrows O_2 + O + M \qquad M = O_2,\ O_3,\ Ar \qquad (R1)$$

$$O + O_3 \rightleftarrows O_2 + O_2 \qquad (R2)$$

$$O_2 + M \rightleftarrows 2O + M \qquad M = Ar \qquad (R3)$$

The forward rate constants for these reactions were part of the input data for the computer program[4] while the reverse reaction rate constants were calculated from thermodynamic data and the forward reaction rate constants as part of the computer program. The rate constants for reactions R1 and R2 have been deduced from experiments on the thermal decomposition of ozone at temperatures between 343°K and 383°K in static experiments[7,8] and at temperatures between 689°K and 910°K in shock tube experiments.[9] The relative efficiencies of Ar, O_2 and O_3 in reaction R1 were determined in the low temperature experiments.[7,8] The use of these rate constants at temperatures above 2500°K involves a large extrapolation and recent experiments[10] indicate that the ratio k_1/k_2 is as much as five times smaller than the extrapolated value in the approximate range of temperatures between 1500°K and 2800°K. This conclusion is based on rate constant expressions given in the Arrhenius form.[7,8,9] It will be shown below, however, that this discrepancy is practically resolved for the present experiments by using the rate constant for reaction R1 in the form corresponding to the Hinshelwood-Rice-Ramsperger-Kassel theory of uni-molecular reactions as given by Jones and Davidson[9] and the rate constant for reaction R2 in the collision theory form, i.e., $k = AT^{1/2} e^{-E/RT}$, based on the data of Benson and Axworthy.[7,8] The values of the parameters in these rate constant expressions for reactions R1 and R2 are given in Table III in the group labelled set II; in the group labelled set I, the values of the parameters for the rate constants expressed in the Arrhenius form are given for reactions R1

and R2. The rate constant parameters for the forward direction of R3 are also given in Table III; however, exclusion of the data for R3 from the numerical calculations did not significantly alter the calculated oxygen atom concentration at the time of essentially complete ozone decomposition. To reduce the machine computing time, the calculations were stopped after greater than 99% ozone decomposition and the final oxygen atom concentration was determined by a linear extrapolation based on the concentration of the ozone remaining and on the rate of oxygen atom production per unit ozone concentration in the last machine integration step. Also in making the numerical calculations, the assumption was adopted that the vibrationally excited oxygen, formed in reaction R2,[11] had no effect on the decomposition of ozone. (The chemical relaxation time for ozone decomposition was about 0.1 μsec while the vibrational relaxation time for oxygen in the present experiments was between 0.1 and 1.0 μsec as estimated from the available data.[10,12])

In Table IV, the computed oxygen atom concentrations and the temperatures after ozone decomposition are given. From data in Tables II and IV, it was found that

$$I_i = \Gamma_i (O)^2 \qquad (2)$$

where I_i is the emission intensity in watts str^{-1} $Å^{-1}$ cm^{-3} obtained by extrapolating the emission-time profiles on the oscillograms of shock heated O_3 + Ar mixtures to the time immediately following shock front arrival at the observation station, Γ_i, a constant for each spectral channel and (O), the atomic oxygen concentration in moles cm^{-3}. Three examples of data plotted according to equation 2 are shown in Figure 2. The concentration-normalized, absolute emission intensities, Γ_i are functions of the temperature only and the logarithms of Γ_i are found to be linearly related to the reciprocal of the absolute temperature. This is illustrated in Figures 3 and 4 for the six spectral channels employed (see Table I). The lines drawn through the data points are the least squares fits to the data and the vertical bars indicate the standard deviation at the 90% confidence level. The values of Γ_i plotted in these figures were calculated according to equation 2 with oxygen atom concentrations determined from numerical calculations using the rate constants for R1, R2 and R3 given in set II of Table III. When the oxygen atom concentrations were calculated using the rate constants in the Arrhenius form as given in the literature[7,8,9] and in Table III as set I, the values of Γ_i were found to depend on the initial ozone concentration as shown in Figure 5. In this figure, the lines drawn through the data points are the least squares fits for each initial ozone concentration, $(O_3)_o$. In Figure 5, equation 2 is valid for each set of data corresponding to a particular initial ozone concentration. However, as shown in Figures 3 and 4, the dependence of Γ_i on $(O_3)_o$ can be made insignificant by introducing a reasonable pre-exponential temperature dependence into the rate constant expressions for reactions R1 and R2. For each initial ozone concentration, the data for each spectral channel as shown in Figures 3 and 4 are found not to be significantly different at the 90% confidence level based on the standard deviations determined for the least squares fits to the data at constant $(O_3)_o$ and λ_c.

From the temperature dependence of Γ_i, as shown in Figures 3 and 4, values of the activation energy E_i, in the relation

$$\Gamma_i = A_i \, e^{-E_i/RT} \qquad (3)$$

were determined for each spectral interval employed; the results are shown in Table V. There is no significant dependence at the 90% confidence level of the activation energy on the wavelength. The average of these activation energies and the corresponding standard deviation are 28.6 and 2.2 kcal $mole^{-1}$, respectively.

Rate constants corresponding to the overall radiative combination of oxygen atoms, i.e., for the process

$$O + O \rightarrow O_2 + h\nu \qquad (R4)$$

were calculated at five temperatures and then combined in an Arrhenius expression to obtain the value $k = 4.3 \times 10^6 \exp(-28900 \pm 2200/RT)$ cm^3 mole^{-1} sec^{-1} for the wavelength range 2300Å to 5000Å.

IV. SUMMARY AND DISCUSSION

Absolute intensity measurements were made of the emitted radiation in the wavelength region between 2300Å and 4511Å; this radiation was observed by shock heating mixtures of ozone and argon to temperatures between 2500°K and 3800°K. The presence of oxygen atoms was necessary to observe this radiation and the absolute emission intensity was found to be proportional only to the square of the oxygen atom concentration at a given temperature. Furthermore, the temperature dependence of the absolute emission intensity normalized with respect to the square of the oxygen atom concentration could be characterized by an activation energy of 28.9 ± 2.2 kcal mole^{-1}.

These observations can be rationalized in terms of the potential energy curves for oxygen as shown in Figure 6; the curves presented here were selected from the diagrams of Gilmore.[13] The thermal decomposition of ozone produces ground state oxygen atoms, $O(^3P)$, which may then combine along several potential energy surfaces. Such a process would be proportional to the square of the oxygen atom concentration, at least. The fact that the radiative process observed has an activation energy of 28.9 ± 2.2 kcal mole^{-1} leads to the following suggested mechanism. The ground state oxygen atoms combine along a repulsive potential surface with a subsequent transition to the $B^3\Sigma_u^-$ state of molecular oxygen; the radiative transition from the latter state to the ground state, $X^3\Sigma_g^-$, then occurs. The vibrational levels of the $B^3\Sigma_u^-$ state from which the transitions originate lie at $v' \leq 4$. This conclusion is based on the fact that the energy difference between the $v' = 4$, $J = 0$ level of the $B^3\Sigma_u^-$ state and the ground state of the oxygen atoms is 30.68 kcal mole^{-1} while the upper limit to the experimental activation energy is 31.1 kcal mole^{-1} at the 67% confidence level.

The mechanism described is the reverse of a predissociation mechanism suggested[14] to account for observations made during the photolysis of O_2 at 1849Å. In this case, molecular oxygen is excited to the $B^3\Sigma_u^-$ state and predissociates along a repulsive potential curve to yield two oxygen atoms, $O(^3P)$. Additional photochemical[15] and spectroscopic[16] evidence has been obtained to support this predissociation mechanism.

There are two other mechanisms for the radiative combination of oxygen atoms which are not significant for the shock tube experiments. In one of these, ground electronic state oxygen atoms combine along the potential surfaces leading to the $A^3\Sigma_u^+$, $c^1\Sigma_u^-$ or $C^3\Delta_u$ state of O_2 with subsequent radiative transitions to the states, $X^3\Sigma_g^-$ or to $b^1\Sigma_g^+$. One transition ($A^3\Sigma_u^+ \rightarrow X^3\Sigma_g^-$, in the wavelength range between 2563Å and 4880Å) and also perhaps several of the other possible transitions have been observed[17,18,19] in flow systems containing atomic oxygen at low pressures and near room temperature. However, this mechanism is inconsistent with the present experimental observations since (a) a near zero activation energy is predicted in contrast to the observed activation energy of 28.9 kcal mole^{-1}, and (b) the contribution of the O_2 Herzberg bands to the measured emission intensity is estimated to be less than 3% of the total intensity. The latter conclusion may be demonstrated in two ways. If the value of the room temperature rate constant[18] for the radiative combination of oxygen atoms to give the O_2 Herzberg bands is extrapolated to temperatures greater than 2700°K by assuming a $T^{-1/2}$ dependence, this rate constant becomes at least 30 times smaller than the rate constant derived from the present experimental data. Alternatively, the ratio of the emission intensity, I(Schumann-Runge)/I(Herzberg), may be estimated to be greater than 130 on

the basis of a simplified mechanism as shown in Appendix A. In the second mechanism, the oxygen atoms combine along the potential surface of the $B^3\Sigma_u^-$ state of O_2 after collisional excitation of one of the atoms, $O(^3P) \rightarrow O(^1D)$; the radiative transition $B^3\Sigma_u^- \rightarrow X^3\Sigma_g^-$ subsequently occurs. This mechanism is also inconsistent with the present experimental observations since (a) an activation energy of about 45 kcal mole^{-1} is predicted and this is significantly greater than the observed activation energy, and (b) the spectral intensity distribution resulting from this mechanism is unlikely to result in transitions originating only from $v' \leq 4$ of the $B^3\Sigma_u^-$ state of O_2.

On the assumption that the observed transition is $B^3\Sigma_u^- \rightarrow X^3\Sigma_g^-$, a comparison of the experimental and theoretical relative spectral distribution curves indicates that the observed radiative transitions originate primarily from the $v' = 0$ and 1 levels of the $B^3\Sigma_u^-$ state. The comparison is shown in Figure 7 for temperatures of 2632°K, 3030°K and 3571°K; the experimental data are represented by discrete symbols and the theoretical data are represented, for the sake of clarity, by curves which pass through the data calculated for the experimental spectral intervals which the horizontal bars span. The vertical bars through the symbols represent the standard deviation at the 90% confidence level. In making this graphical comparison, the theoretical relative spectral distribution curves were vertically adjusted so as to coincide with the experimental absolute spectral distribution curve at λ_c = 3002Å. The three curves are calculated for transitions originating from $v' = 0$ and 1, 0, 1 and 2 and 0, 1, 2 and 3 and in this order demonstrate an increasing deviation of the theoretical calculations from the experimental data at wavelengths below 3000Å. (The double points at λ_c = 4511Å are calculated as described above; the error in these data are too large to permit a comparison with the various theoretical relative spectral distribution curves.) However, the comparison is imprecise and is only employed here to introduce the possibility that the observed radiative transitions may originate primarily from the $v' = 0$ and 1 levels of the $B^3\Sigma_u^-$ state. In making the calculations,[21] the assumptions of thermodynamic equilibrium,[20,22,23] of the smeared rotational line model[22,23] and of $\Delta J = 0$ for all vibration-rotation transitions[20,24] were employed. These assumptions are not strictly valid for use in a comparison with the present experimental data. At the least, the inverse predissociation mechanism predicts a truncation of the population distributions in the vibrational and rotational levels near the crossing level (i.e., near an intersection of the potential curves in a certain low approximation, see ref. 25) which would introduce a perturbation in these distributions. In the converse case of a predissociation mechanism, such a perturbation has been observed[26] and corresponds to that predicted[27] in dissociation processes.

Qualitatively, the statement may be made that calculations which include significant contributions by transitions originating in vibrational levels with $v' \geq 2$ will result in a predicted intensity greater than observed at wavelengths less than 3000Å. This is corroborated by noting that, at T = 3030°K, for example, 94% of the observed radiation occurs in the wavelength range between 2640Å and 4400Å; this is expected for transitions solely from $v' = 0$ and 1 to the approximation that the transitions occur only at the classical turning points of the potential curve for the $B^3\Sigma_u^-$ state. Also, for transitions from the various vibrational levels which contribute to the emission intensity observed in a given spectral interval, the strong influence of transitions from $v' \geq 2$ on the intensity is indicated, for example, in the wavelength interval between 2269Å and 2331Å (Channel 1 in Table I) by the relative increase in the Franck-Condon factors; for the levels $v' = 0$, 1, 2, 3 and 4, the relative magnitudes of the Franck-Condon factors are roughly in the ratios[28] $1:10:10^2:10^3:5\times10^3$, respectively.

From the experimental absolute spectral distribution curves and the comparison with theoretical relative spectral distribution curves, the tentative conclusion was

reached that radiative transitions originate primarily from the vibrational levels $v' = 0$ and 1. On the other hand, from the experimental activation energy of 28.9 ± 2.2 kcal mole^{-1}, the conclusion is reached that vibrational levels as high as $v' = 4$ may possibly be occupied by newly formed oxygen molecules in the $B^3\Sigma_u^-$ state. The relation between these conclusions can be qualitatively understood on the basis of two factors. According to the first factor, there is a preferential transition from one to another potential surface into states with large values of J (or N) and small values of $v(< 4)$, i.e., molecules of O_2 are formed with considerable angular momentum.[29] The second factor accounts for the temperature dependence associated with the vibrational deactivation of the newly formed oxygen molecules; inclusion of this factor in the analysis would result in a value of the energy required to reach the crossing point smaller than the experimental activaction energy. These factors will be discussed briefly.

The preferential formation of O_2 in states of large J and small v may be understood in terms of the effective potential curves[30] as shown schematically in Figure 8 rather than in terms of the potential curves for a non-rotating molecule such as those shown in Figure 6. The effective potential curves illustrate that for given v values ($v = 0$ in Figure 8) the potential curves cross at higher energy values for larger values of J when the selection rule $\Delta J = 0$ is taken into consideration.[30] Therefore it is possible to observe an activation energy for molecule formation which is greater than the energy corresponding to the vibrational level occupied ($v = v'$, $J = 0$) as was implied in the conclusions stated above.

The contribution to the temperature dependence of the absolute emission intensity by the vibrational deactivation of newly formed O_2 molecules can be shown with the aid of the following mechanism:

$$O + O \rightleftarrows O_2^*(v' = 1) \qquad \text{(R5)}$$

$$O_2^*(v' = 1) + M \rightleftarrows O_2(v' = 1) + M \qquad \text{(R6)}$$

$$O_2(v' = 1) + M \rightleftarrows O_2(v' = 0) + M \qquad \text{(R7)}$$

$$O_2(v' = 0,1) + M \rightleftarrows O_2 + M \qquad \text{(R8,R9)}$$

$$O_2(v' = 0,1) \rightarrow O_2 + h\nu \qquad \text{(R10,R11)}$$

where $O_2^*(v' = 1)$ is a newly formed molecule in the $v' = 1$ level of the $B^3\Sigma_u^-$ state with the rotational energy corresponding to the crossing level, $O_2(v' = 0 \text{ or } 1)$, a molecule with less rotational energy than $O_2^*(v' = 1)$, and O_2, a molecule in the ground electronic state, $X^3\Sigma_g^-$. For this mechanism, the following expression for the emission intensity can be derived

$$I = \frac{k_5 k_6}{k_{-5} k_{-6}} k_{10}(0)^2 \left\{1 + \frac{k_7}{k_{-7} + k_9 + k_{11} M^{-1}}\right\} \qquad (4)$$

when k_{-5} represents an allowed transition ($k_{-5} \sim 10^{11}$ sec^{-1}),[35] and other rate constants have the values as estimated (see Appendix B). When account is taken of the temperature variation of the bracketed term, the activation energy assigned to k_5 becomes ~ 1.5 kcal mole^{-1} smaller than otherwise in accordance with the estimated values of the rate constants. Thus the energy level of the crossing is found on this basis also to be lower than that corresponding to the experimental activation energy. It may be noted that the variation of the bracketed term of Eq. (4) is primarily a result of the temperature coefficient of the vibrational deactivation process represented by k_7. If, however, the oxygen may be formed in several vibrational levels directly, the effect of vibrational deactivation becomes negligible in the approximations used here. For example, if the following two reactions are added to the above mechanism

$$O + O \rightleftarrows O_2^*(v' = 0) \qquad \text{(R12)}$$

$$O_2^*(v' = 0) + M \rightleftarrows O_2(v' = 0) + M \qquad \text{(R13)}$$

then the emission intensity expression becomes

$$I = \left\{ \frac{k_5 k_6}{k_{-5} k_{-6}} + \frac{k_{12} k_{13}}{k_{-12} k_{-13}} \right\} k_{10}(0)^2 \qquad (5)$$

and the dependence of I on k_7 can be neglected.[31] The reverse of this case occurs in predissociation when a breaking-off in successive vibrational levels is observed.[30] In potential curves of the form of those in Figure 8 but including the several vibrational levels of interest, the energy difference of the breaking-off points is found to be large in predissociation. If the reverse of this process were observed in the inverse predissociation mechanism, considered above, it would imply that the observed activation energy is an average over the energy levels corresponding to the several crossing points.

If the radiative transitions observed in the present experiments originate primarily from vibrational levels $v' = 0$ and 1 of the $B^3\Sigma_u^-$ state, then predissociation ought to be observed at least in the $v' = 2$ level. Several spectroscopic experiments[16,32] have led to the observation of predissociation in the $B^3\Sigma_u^-$ state of oxygen. While interpretation of these experiments does not include predissociation from the $v' = 2$ level, there is not general agreement[33] that predissociation from the $v' = 2$ level is excluded. The spectroscopic studies were conducted in absorption and demonstrated predissociation in levels from $v' = 3$ to $v' = 12$ with maxima at $v' = 4$ and 11 and a minimum at $v' = 9$ in the probability for predissociation. Furthermore, from the investigation[16] of the predissociation at $v' = 3$, 4 and 5, the transition was found to be allowed and therefore[14,16,32] could be represented as $B^3\Sigma_u^- \rightarrow {}^3\Pi_u$. On the basis of calculations, Vanderslice, Mason and Maisch[33] believe the ${}^3\Pi_u$ curve crosses at the bottom of the $B^3\Sigma_u^-$ curve and then rises along the left hand branch of the latter curve; the interpretation of the present experiments is in best agreement with this. In postulating this potential curve shape, these authors reject the explanation[16] that the abnormal widths found in absorption for the rotational lines in the 2-0 and 1-0 bands of the Schumann-Runge bands result from a blending of fine structure and imply that predissociation occurs in the $v' = 0$, 1 and 2 levels. Other potential curve shapes that have been suggested[14,16,32] require a predissociation at $v' \geq 3$; the above experimental results could only be strictly in agreement with this requirement if a systematic error exists in the relative spectral intensity measurements for $\lambda \leq 3000$Å. At the present, no such error has been identified. Furthermore, this disagreement would be reduced where the potential curve shape is such that tunneling is important.[32]

The spectral resolution in the present experiments was too small to permit spectroscopic identification of the radiating species. In the oxygen system of potential curves (Figure 6) there are two allowed transitions, $B^3\Sigma_u^- \rightarrow X^3\Sigma_g^-$[13] and ${}^3\Pi_u \rightarrow X^3\Sigma_g^-$.[32] The latter transition would result in an emission continuum which would shift to lower wavelengths at higher temperatures. Since this is not observed (see Figure 7), the transition $B^3\Sigma_u^- \rightarrow X^3\Sigma_g^-$ was assumed to be that one detected in the present experiments.

APPENDIX A

To estimate the ratio of the emission intensity, I (Schumann-Runge)/I(Herzberg), the following simplified mechanism is assumed to apply to both radiative processes:

$$O + O \rightleftharpoons O_2^* \qquad (A1)$$

$$O_2^* + M \rightleftharpoons O_2^+ + M \qquad (A2)$$

$$O_2^+ + M \rightarrow O_2 + M \qquad (A3)$$

$$O_2^+ \rightarrow O_2 + h\nu \qquad (A4)$$

where O_2^* is a newly formed molecule in either the $B^3\Sigma_u^-$ or the $A^3\Sigma_u^+$, $c^1\Sigma_u^-$ or $C^3\Delta_u$ states, O_2^+, a stabilized molecule in one of these states and O_2, a molecule in the $X^3\Sigma_g^-$ state. If k_2, k_{-2}, and k_3 are assumed to be identical and larger than k_4 M^{-1} for each of the four electronic states, then the ratio of the emission intensities will be

$$\frac{I_{SR}}{I_H} \simeq \left(\frac{k_{4,SR}}{k_{4,H}}\right)\left(\frac{k_{1,SR}}{k_{1,H}}\right)\left(\frac{k_{-1,H}}{k_{-1,SR}}\right) > 130 \qquad (A5)$$

where $k_{4,SR}/k_{4,H} > 10^5$,[18,20]; $(k_{-1,H}/k_{-1,SR}) \sim 10^{13}/10^{11}$,[34,35] assuming k_{-1} to represent an allowed radiationless decomposition[35]; and $(k_{1,SR}/k_{1,H}) \sim 3\ Z_1\ 10^{-2}\ e^{-28900/RT}/7Z_1$, with Z_1, the collision number, 3/7 the ratio of the statistical weights for formation of O_2 in the respective electronic states from which the Schumann-Runge or Herzberg O_2 band transitions originate, and 10^{-2}, the probability of the radiationless transition from the respulsive to the bound state assumed to be equal to the transition probability for the reverse process.[35]

APPENDIX B

Estimates of the rate constants for reactions R6 to R11 were made as follows. For k_6 and k_{-6}, rotational deactivation and activation were assumed to occur at lease once in every four collisions so that at 2500°K and 3500°K, the rate constants were $\geq 1\times10^{14}$ and 1.3×10^{14} cm^3 $mole^{-1}$ sec^{-1}, respectively. The rate constant for vibrational deactivation was estimated using the empirical relation of Millikan and White[12] in the following form

$$\log(p\tau)^* = (\theta^*/\theta)^{4/3} \log p\tau + 8[(\theta^*/\theta)^{4/3} - 1] \qquad (B1)$$

where the starred quantities refer to the excited state, $B^3\Sigma_u^-$ and the unstarred quantities to the ground state, $X^3\Sigma_g^-$; θ is the characteristic oscillator temperature and $p\tau$, the pressure-relaxation time product. The values of τ were estimated from data on T-V process for O_2-O_2[12] and O_2-Ar[12] and from the vibrational relaxation of O_2 by O[10] with the following expression:

$$\tau^{-1} = X_{O_2}\,\tau_{O_2\text{-}O_2}^{-1} + X_O\,\tau_{O_2\text{-}O}^{-1} + X_{Ar}\,\tau_{O_2\text{-}Ar}^{-1} \qquad (B2)$$

where X_i is the mole fraction of i and τ_{x-y}, the relaxation time of x in the presence of y. For the mixtures employed, the average of the estimated values of $k_7 (= \tau^{-1}\ M^{-1})$ were 3×10^{12} and 6×10^{12} cm^3 $mole^{-1}$ sec^{-1} at 2500°K and 3500°K, respectively. The activation rate constant, k_{-7} was estimated from k_7 exp(- 1970 cal $mole^{-1}/RT$). The rate constants for electronic deactivation, k_8 and k_9, were found to be 4.3×10^{12} and 5.1×10^{12}, cm^3 $mole^{-1}$ sec^{-1} at 2500°K and 3500°K, respectively on the assumption that one in one hundred collisions was effective for this process. Finally, the radiative rate constants, k_{10} and k_{11}, were estimated using the relation

$$k = \tau_r^{-1} = 1.013\times10^{-6}\ \Sigma\ q(v', v'')\ \nu^3(v', v'') \qquad (B3)$$

where q is the Franck-Condon factor for the transition $v' \rightarrow v''$ and ν is the wave number, evaluated at the band head in the approximation employed. For both k_{10} and k_{11}, τ_r^{-1} was 2.7×10^7 sec^{-1}; the data of reference 20 were used in this evaluation.

VI. ACKNOWLEDGEMENT

The authors are indebted to E. A. Meckstroth for maintaining the operational standard of the shock tube facility and for help in conducting the experiments and to M. R. Schoonover for his assistance in the computer-code preparation and numerical calculations. We thank Mr. K. G. P. Sulzmann for a critical reading of the manuscript. We gratefully acknowledge support of this work under Contract No. DA-01-021-AMC-12050(Z), ARPA Order 393, Amendment No. 4 through the U. S. Army Missile Command, Redstone, Arsenal, Alabama.

VII. REFERENCES

1. B. F. Myers and E. R. Bartle, J. Chem. Phys., in press.
2. B. F. Myers, E. R. Bartle, P. R. Erickson and E. A. Meckstroth, Anal. Chem. 39, 415 (1967).
3. D. H. Byers and B. E. Saltzman, "Ozone Chemistry and Technology," Advances in Chemistry Series No. 21, American Chemical Society, Washington, D. C., 1959, p. 93.
4. L. J. Garr and P. V. Marrone, "Inviscid, Nonequilibrium Flow Behind Bow and Normal Shock Waves, Part II. The IBM 704 Computer Programs," CAL Report No. QM-1626-A-12(II), May 1963.
5. Received by this laboratory through the courtesy of Dr. W. Wurster, Cornell Aeronautical Laboratory, Inc., Buffalo, New York.
6. We are indebted to Dr. J. T. Neu, Space Science Laboratory, General Dynamics/Convair for conducting these experiments.
7. S. W. Benson and A. E. Axworthy, J. Chem. Phys. 26, 1718 (1957).
8. S. W. Benson and A. E. Axworthy, ibid, 42, 2614 (1965).
9. W. M. Jones and N. Davidson, J. Amer. Chem. Soc. 84, 2868 (1962).
10. J. H. Kiefer and R. W. Lutz, Symp. Combust. 11th, Berkeley, 1966, to be published.
11. W. G. McGrath and R. G. W. Norrish, Proc. Roy. Soc. A242, 265 (1957).
12. R. C. Millikan and D. R. White, J. Chem. Phys. 39, 3209 (1963).
13. F. R. Gilmore, "Potential Energy Curves for N_2, NO, O_2 and Corresponding Ions," Memorandum RM-4034-1-PR, The Rand Corporation, April 1966. Also published in J. Quant. Spectry. Radiative Transfer 5, 369 (1965).
14. P. J. Flory, J. Chem. Phys. 4, 23 (1936).
15. D. H. Volman, ibid, 24, 122 (1956).
16. P. K. Carroll, Astrophysical J. 129, 794 (1959).
17. H. P. Broida and A. G. Gaydon, Proc. Roy. Soc. A222, 181 (1954).
18. R. A. Young and R. L. Sharpless, J. Chem. Phys. 39, 1071 (1963).
19. C. A. Barth and M. Patapoff, Astrophysical J. 136, 1144 (1962).
20. R. A. Allen, Avco-Everett Research Report 236, April, 1966.
21. The method of calculation follows approximately that of reference 20. To obtain the relative spectral distribution curves, the ratios $(\int_{\Delta\lambda_1} \phi\nu^6 d\lambda)/(\int_{\Delta\lambda_3} \phi\nu^6 d\lambda)$ were calculated for transitions originating from the levels $v' = 0$ and 1, 0, 1 and 2 and 0, 1, 2 and 3 which contributed to the emission in the spectral interval $\Delta\lambda_1$; $\Delta\lambda_i$ represents the wavelength interval corresponding to channel i ($i = 1, \cdots, 6$) in Table I; ϕ is the spectral distribution function.
22. J. C. Keck, J C. Camm, B. Kivel and T. Wentink, Jr., Ann. Phys. 7, 1 (1959).
23. R. W. Patch, W. L. Shackelford and S. S. Penner, J. Quant. Spectry. Radiative Transfer 2, 263 (1962).
24. R. A. Allen, J. Quant. Spectry. Radiative Transfer 5, 511 (1965).
25. G. Herzberg, "Spectral of Diatomic Molecules," D. Van Nostrand, 1950, p. 424.
26. B. P. Levitt, Trans. Faraday Soc. 59, 59 (1963).
27. E. E. Nikitin, "Theory of Thermally Induced Gas Phase Reactions," Indiana University Press, 1966.
28. These rations are based on the Franck-Condon factors given in Reference 20.
29. We are indebted to Mr. K. G. P. Sulzmann for bringing this possibility to our attention.
30. G. Herzberg, op. cit., p. 426, 430f.
31. The observed dependence of the absolute emission intensity on $(O)^2$ (see Figure 2, for example) is, within the experimental error, in accordance with the prediction of the mechanisms represented by either Eq. (5) or (6).
32. P. G. Wilkinson and R. S. Mulliken, Astrophysical J. 125, 594 (1947).

33. J. T. Vanderslice, E. A. Mason and W. G. Maisch, J. Chem. Phys. 32, 515 (1960).
34. V. N. Kondrat'ev, "Chemical Kinetics of Gas Reactions," Pergamon Press, 1964, p. 229.
35. G. Herzberg, op. cit., p. 419.

TABLE I: SPECTRAL CHANNEL CENTER WAVELENGTHS AND BANDPASSES

Channel	1	2	3	4	5	6
λ_c, Å	2300	2500	3002	3506	4010	4511
$\Delta\lambda$, Å	62	102	200	206	208	202

TABLE III: FORWARD RATE CONSTANTS, $k^{(a)}$

		Set I			Set II		
	Reaction	A	n	E_a	A	n	E_a
1a	$O_3+O_3 \rightarrow O_2+O+O_3$	1.4×10^{15}	0	23.15	10.91×10^{18}	-1.25	24.35
1b	$O_3+O_2 \rightarrow 2O_2+O$	5.80×10^{14}	0	23.15	5.15×10^{18}	-1.25	24.35
1c	$O_3+Ar \rightarrow O_2+O+Ar$	3.76×10^{14}	0	23.15	3.12×10^{18}	-1.25	24.35
2	$O+O_3 \rightarrow 2O_2$	3.0×10^{13}	0	5.60	1.04×10^{12}	0.50	5.288
3	$O_2+M \rightarrow 2O+M$	1.19×10^{21}	-1.5	118.0	1.19×10^{21}	-1.5	118.0

(a) $k = AT^n e^{-E_a/RT}$; units for A, $cm^3 mole^{-1} sec^{-1}$ or $cm^6 mole^{-2} sec^{-1}$, for E_a, kcal $mole^{-1}$.

TABLE IV: OXYGEN ATOM CONCENTRATIONS AND TEMPERATURES

Run	$(O)\times10^7$ mole cm^{-3}	T, °K	Run	$(O)\times10^7$ mole cm^{-3}	T, °K	Run	$(O)\times10^7$ mole cm^{-3}	T, °K
1014	1.620	2976	1026	0.9073	3130	1041	1.084	3390
1015	1.640	2976	1027	2.218	3097	1042	2.101	3835
1016	2.192	2969	1028	3.360	3164	1043	1.067	3767
1017	2.449	2990	1029	1.500	3259	1044	2.776	3335
1018	0.8171	2939	1030	0.7501	3232	1045	1.422	3728
1019	1.626	2691	1031	2.238	3266	1046	1.365	3530
1020	2.482	2738	1034	1.415	3709	1081	0.3471	3309
1021	0.8370	2718	1035	0.7102	3719	1082	0.5163	3205
1022	1.131	2824	1036	2.119	3698	1083	0.7712	2755
1023	2.186	2841	1039	2.197	3519	1085	0.7963	2494
1024	3.349	2883	1040	1.086	3413	1086	0.6354	2965

TABLE V: THE TEMPERATURE DEPENDENCE OF I_o

λ_c, Å	$A_1\times10^{-6}$, watt str^{-1} $Å^{-1}$ cm^3 $mole^{-2}$	E_1, kcal, $mole^{-1}$
2300	1.14	29.8
2500	7.42	27.4
3002	119.2	27.8
3506	89.1	30.4
4010	47.1	31.1
4511	7.38	25.1

TABLE II: SUMMARY OF EXPERIMENTAL DATA

Initial Conditions and Shock Velocity					$I_\lambda \times 10^9$, watt str^{-1} $Å^{-1}$ cm^{-3}					
Run	T_o, °C	P_o, mm Hg	X_{O_3}	U_s, mm μsec^{-1}	λ_c=2300Å	λ_c=2500Å	λ_c=3002Å	λ_c=3506Å	λ_c=4010Å	λ_c=4511Å
1014	25.6	18.92	0.060	1.822	---	---	---	12.7	5.39	2.49
1015	25.0	19.11	0.060	1.822	0.191	1.83	28.0	12.7	6.36	2.92
1016	24.8	25.54	0.060	1.820	0.313	3.18	48.0	23.0	12.3	4.30
1017	25.0	28.46	0.060	1.827	0.515	4.32	66.4	31.4	14.0	5.51
1018	24.7	9.46	0.060	1.811	0.0441	0.442	6.06	3.32	1.47	---
1019	24.7	20.34	0.060	1.719	0.149	1.285	20.3	8.64	3.85	1.895
1020	24.5	30.62	0.060	1.736	0.307	3.03	46.5	22.4	10.76	0.516
1021	24.4	10.16	0.060	1.731	0.0284	0.321	4.94	2.19	0.960	---
1022	24.7	8.51	0.120	1.799	0.0641	0.735	10.5	5.25	2.88	---
1023	24.7	16.92	0.120	1.797	0.302	2.91	36.8	17.04	10.2	4.56
1024	24.6	25.51	0.120	1.813	0.695	6.80	110.2	47.5	25.0	8.94
1026	24.6	6.17	0.120	1.910	0.066	0.683	9.65	5.03	2.27	1.20
1027	24.5	15.45	0.120	1.900	0.362	4.46	59.5	27.8	13.04	5.85
1028	24.5	23.31	0.120	1.924	1.235	11.05	157.0	69.6	33.5	13.76
1029	24.4	16.60	0.060	1.919	0.277	2.49	36.6	19.4	9.26	3.26
1030	24.7	8.27	0.060	1.910	0.0594	0.564	8.89	4.9	2.06	4.14
1031	24.8	24.80	0.060	1.921	0.632	5.43	86.0	41.5	18.8	7.91
1034	24.6	14.91	0.060	2.060	0.429	3.70	55.9	30.8	13.85	4.81
1035	24.5	7.44	0.060	2.063	0.117	0.905	14.6	7.90	36.8	---
1036	24.5	22.34	0.060	2.057	0.855	8.15	129.0	69.8	33.3	11.2
1039	24.8	14.08	0.120	2.052	0.606	6.43	102.1	51.4	33.7	---
1040	24.5	7.02	0.120	2.018	0.165	1.65	26.1	12.0	5.55	2.06
1041	25.1	7.05	0.120	2.010	0.178	1.64	23.3	12.3	5.49	2.24
1042	25.7	12.93	0.120	2.156	1.01	10.0	161.0	75.0	37.6	---
1043	24.8	6.56	0.120	2.136	0.273	2.34	33.4	18.4	8.51	3.78
1044	24.4	14.40	0.180	2.010	0.944	8.55	128.8	65.9	26.6	---
1045	24.5	6.64	0.180	2.159	0.378	3.47	57.2	29.6	14.1	---
1046	24.9	6.67	0.180	2.088	0.296	2.65	39.5	21.4	9.64	4.30
1081	24.3	17.67	0.0105	1.864	---	---	1.96	1.05	---	---
1082	24.2	26.42	0.0105	1.833	---	---	3.83	2.00	---	---
1083	24.1	40.79	0.0105	1.688	---	---	4.54	2.14	---	---
1085	23.7	45.93	0.0100	1.597	---	---	3.05	1.36	---	---
1086	23.4	34.55	0.0100	1.756	---	---	4.29	2.25	---	---
Calibration factors, $C \times 10^7$, watts $str^{-1} Å^{-1} cm^{-2} v^{-1}$					0.00303	0.0185	0.3485	1.97	6.81	15.82

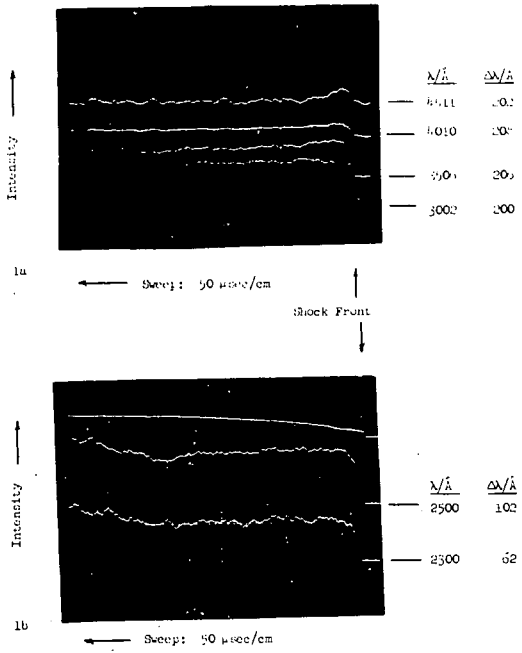

FIGURE 1: INTENSITY TIME OSCILLOGRAM. Oscillogram of the emission behind an incident shock wave traveling through a mixture of 6% O_3 + 94% Ar. Run 1016.

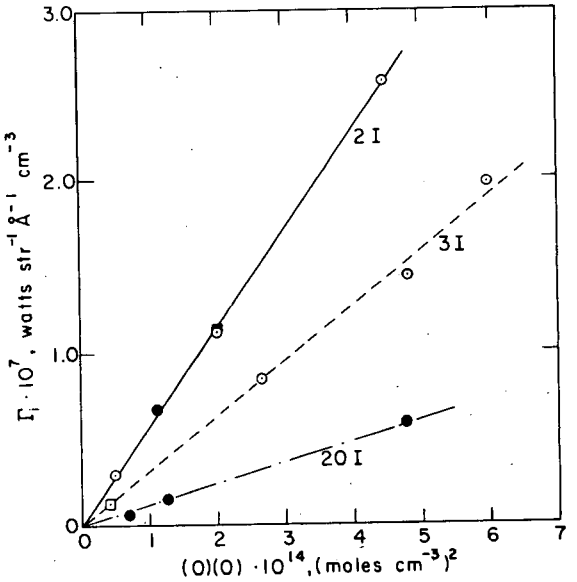

FIGURE 2: ABSOLUTE EMISSION INTENSITY VS. $(O)^2$. For —, λ_c = 3506Å, 3698 ≤ T/°K ≤ 3728; for ---, λ_c = 3002Å, 2965 ≤ T/°K ≤ 2990; for — - —, λ_c = 2500Å, 2718 ≤ T/°K ≤ 2641. For all curves, $(O_3)_o$ is represented by ⊡ for 1%, ⊙ for 6%, ● for 12% and ■ for 18%. Each datum on the figure is selected from the results of a different shock tube experiment.

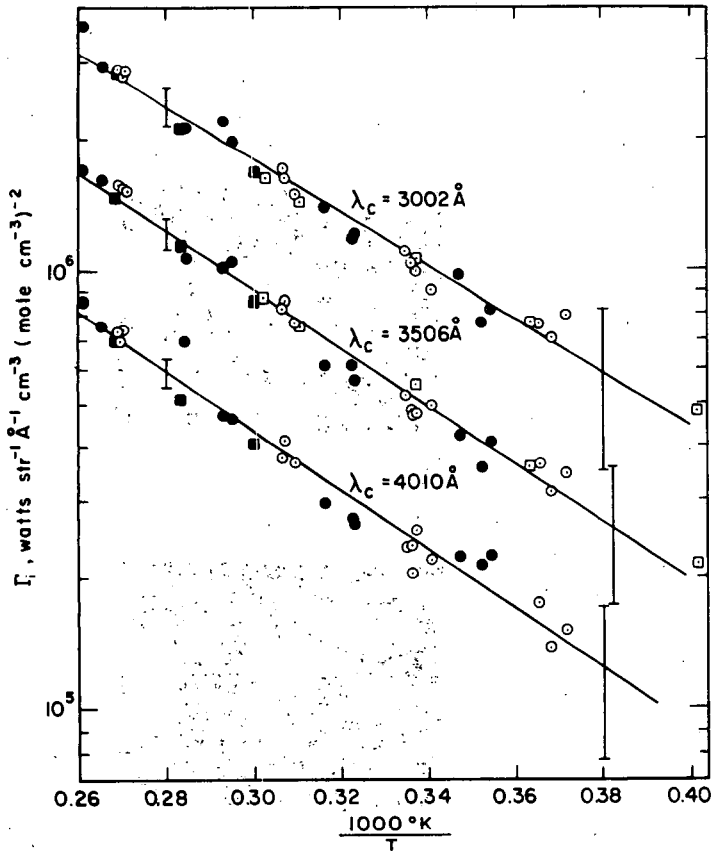

FIGURE 3: LOG Γ_1 VS. 1000°K/T: For $(O_3)_o$ = 1%, the data are represented by ⊡, for $(O_3)_o$ = 6%, by ⊙, for $(O_3)_o$ = 12% by ● and for $(O_3)_o$ = 18% by ■. The solid lines are least squares fits to the data and the vertical bars indicate the standard deviation at the 90% confidence level.

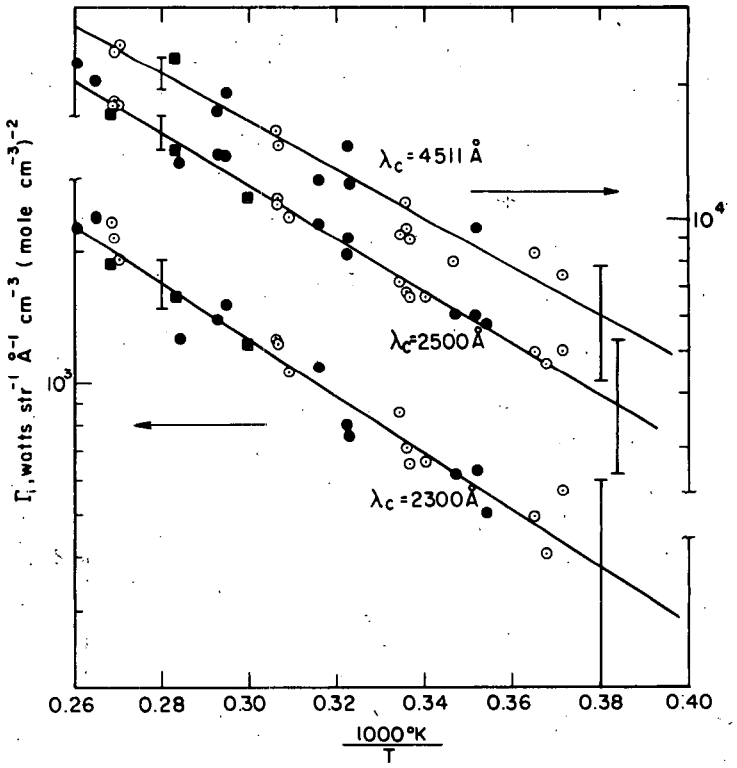

FIGURE 4: LOG Γ_1 VS. 1000°K/T: For $(O_3)_o$ = 1%, the data are represented by ⊡, for $(O_3)_o$ = 6%, by ⊙, for $(O_3)_o$ = 12% by ● and for $(O_3)_o$ = 18% by ■. The solid lines are least squares fits to the data and the vertical bars indicate the standard deviation at the 90% confidence level.

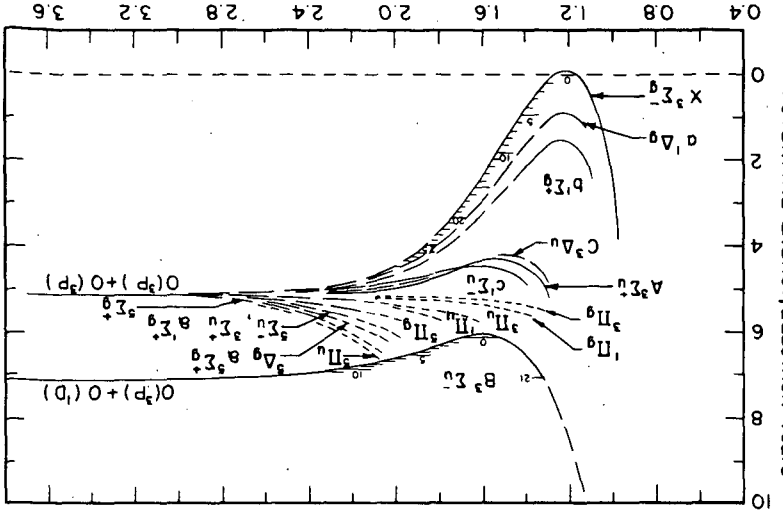

FIGURE 6: POTENTIAL ENERGY CURVES FOR O_2 AFTER GILMORE.[13]

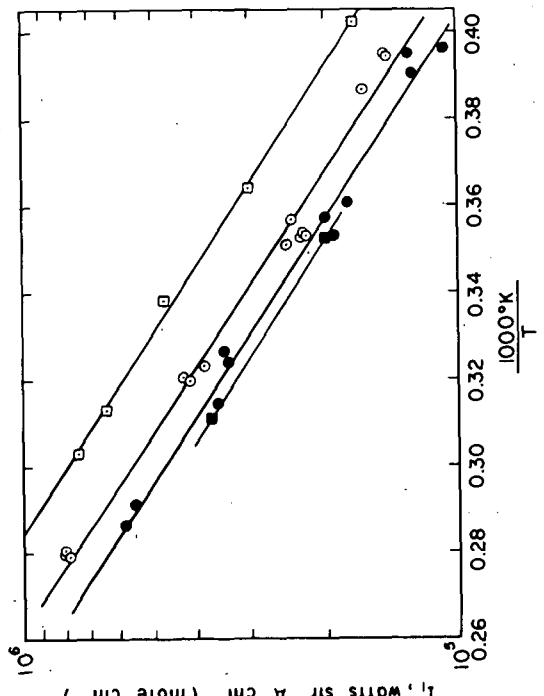

FIGURE 5: LOG Γ_1 VS $1000°K/T$; FOR λ_c = 3500Å; CURVE □ - 1% = $(O_3)_o$; CURVE ⊙ - 6% = $(O_3)_o$; CURVE ● - 12% = $(O_3)_o$; CURVE ■ - 18% = $(O_3)_o$. THE SOLID CURVES ARE LEAST SQUARES FITS TO THE DATA POINTS FOR EACH INITIAL OZONE CONCENTRATION.

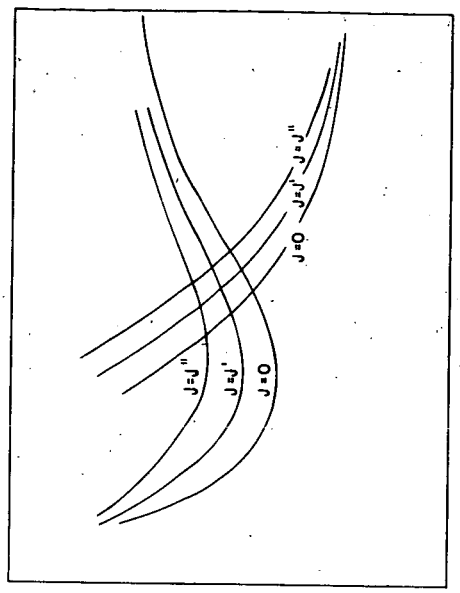

FIGURE 8: EFFECTIVE POTENTIAL CURVES (schematic diagram). The potential energy U is plotted versus the internuclear distance, r for $v' = 0$ and for several rotational levels with $J'' > J' > J$ and spin splitting neglected.

FIGURE 7: ABSOLUTE EMISSION INTENSITY SPECTRAL DISTRIBUTION CURVES. The experimental data points are represented by ○ for 357°K, by ● for 303°K and by △ for 252°K. The vertical bars represent the standard deviation at the 95% confidence level and the horizontal bars represent the spectral interval over which the data are average values. The theoretical relative intensity distribution is represented for each temperature by three curves drawn through the points calculated for the spectral intervals indicated by the horizontal bars. Each set of points has been vertically adjusted so as to coincide with the experimental absolute emission intensity datum at λ_c = 3002Å for each temperature. Contributions to the calculated relative intensity from various vibrational levels of the $B^2\Sigma_u^+$ state have been included as indicated by the legend —— , $v' = 0, 1$; ----, $v' = 0, 1, 2$; — - — - , $v' = 0, 1, 2, 3$. Note that the data sets at the three temperatures have been artificially separated by the factors indicated to improve the clarity of presentation.

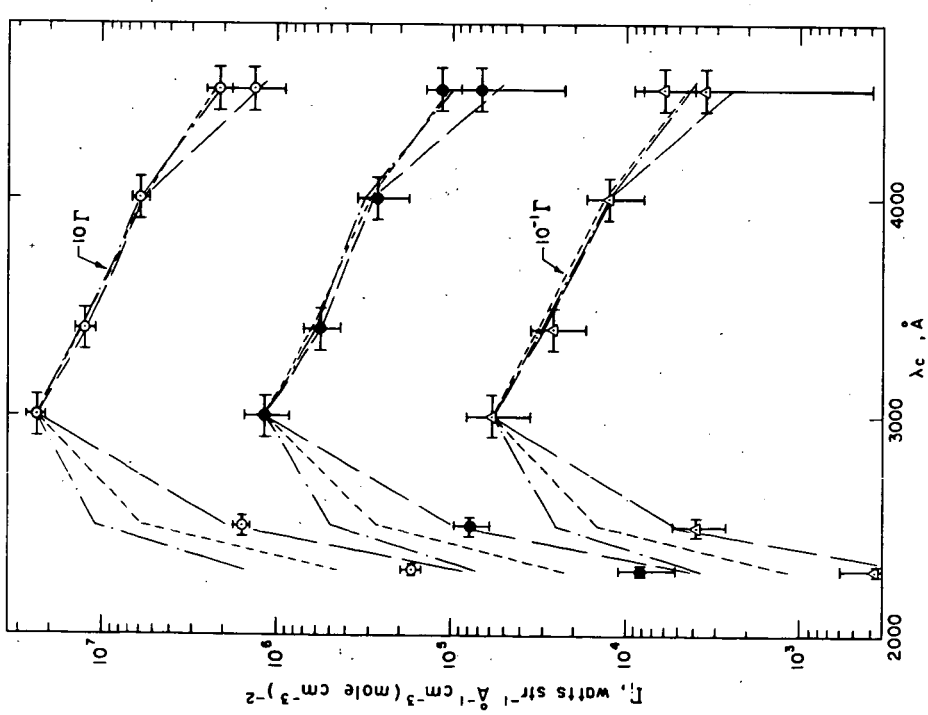

POTENTIAL DESTRUCTIVENESS OF GAS DETONATIONS

J. N. Murphy, N. E. Hanna, D. S. Burgess, and R. W. Van Dolah

Explosives Research Center
Bureau of Mines
U. S. Department of the Interior
Pittsburgh, Pennsylvania 15213

Background

The potential destructiveness of gas detonations was evaluated in terms of the depth of earth that could be heaved when various gas mixtures were detonated in long underground excavations. A number of years ago, a spectacular destruction of 26.8 miles of underground pipeline in Texas was ascribed to the occurrence of a detonation. The pipeline had carried crude oil and was being cleaned by forcing a scraper plug along its length with compressed air. It is not known whether the event was a gas detonation or a heterogeneous detonation of a film on the wall.[1/] The intermittent cratering that occurred seemed curious but now may be explained in terms of the impulse needed to heave the earth cover. No explanation can be offered for the apparent low velocity of propagation indicated by the total elapsed time. An average velocity of only 296 feet per second was reported.

This investigation primarily covered propane-air, acetylene-air and MAPP[2/]-air mixtures. In some cases a partial pressure of oxygen greater than in air was employed. Limits of detonability were obtained from plots of propagation velocity versus fuel concentration in a 7-inch diameter by 12-foot long pipe which was closed at both ends. Impulse, which determines the momentum that can be imparted to a load, was measured from pressure versus time transients in a 24-inch diameter by 163-foot long steel pipe that could be closed at one end. The soil mechanical problems related to earth movement were studied in hand-dug tunnels of 3 foot x 5 foot cross-section and 150 feet length incorporating right angle turns and side entries.

Detonation Velocities and Limits of Detonability

Fuel/air mixtures were admitted to the 7-inch apparatus of figure 1 by the partial pressure method, recirculated via the sideline for 10 minutes, and sampled for gas chromatographic analysis. A solid explosive initiator ranging from 1.1 grams PETN to 100 grams tetryl was detonated and the velocity of the resulting ionization wave was measured between velocity stations with electronic time-interval meters.

A plot of this wave velocity versus fuel concentration is given in figure 2 for MAPP/air mixtures. Velocities in excess of 1400 meters/sec indicate detonation while velocities of about 1000 meters/sec or less are obtained from shocks accompanying deflagration. The difference is clearly shown by the pressure traces of figure 3, wherein trace A indicates deflagration with pressure rising over a period of about 25 milliseconds while in trace B the first pressure pulse is the strongest.

Limits of detonability as defined by this method are somewhat sensitive to the strength of the initiator. Thus, the detonable range for MAPP/air widens appreciably as the initiator is increased from 1 to 10 grams PETN (table 1). Both propane/air and acetylene/air detonate over the full reported range of flammability when initiated with 10 grams PETN.

Pressure-time Transients and Impulses

The major part of the experimental program was carried out using the 24-inch steel tube shown in figure 4. Fuel was metered through calibrated spray nozzles into the 260 cfm output stream of a gasoline-powered blower, which stream was passed through the tube to give three changes of atmosphere. Gas sampling and detonation pressure measurements were accomplished at five stations spaced evenly along the length of the pipe. Initiation was typically effected with 100 grams tetryl, usually at the upstream end of the pipe near the end closure.

Pressure transients at the five stations were compared with predictions derived from standard references[3,4] dealing with one-dimensional gas detonations. Figure 5 shows the predicted transient for stoichiometric acetylene/air at a point 60 feet from an initiation source at the closed end of a 150-foot long pipe. The peak (C-J) pressure was assumed to be twice the constant volume explosion pressure and this proved to be a fairly accurate assumption for measurements within 2 stations (53 feet) of the initiation. For example, with 7.2 percent MAPP in air, the predicted peak was 281 psig while nine measurements averaged 278 $\pm$6 psig. At greater distance from the initiator, peak pressures became progressively more erratic as though the detonation were departing from its one-dimensional character.

The gas expansion behind the C-J plane was calculated by Taylor's equations using an equilibrium gamma which was typically about 1.17. This gave excellent agreement with experimental pressures in the static gas zone, however, the duration of the gas expansion (from D to E in figure 5) was typically underestimated by about 20 percent. Neither this deviation from prediction nor the erratic peak pressures were of any practical consequence to the impulse of the explosion.

The duration of the pressure plateau, EH in figure 5, was about 20 percent overestimated because no account had been taken of the three-dimensional expansion of the wave as it emerged from the open end of the pipe; that is, the interval FG in the figure should actually be shorter than indicated and the rarefaction starts back through the pipe at an earlier time than G. Since the dominant factor in the time interval EH is the velocity of sound in the burned gases, off-stoichiometric mixtures with lower burned gas temperatures had relatively long pressure histories and high impulses. This trend is shown in table 2; note that 4.9 percent MAPP in air is close to stoichiometric while 3.4 percent MAPP is the reported lean limit of flammability.

For the same reason, propane/air and gasoline/air mixtures had impulses comparable to those of acetylene/air and MAPP/air even though their pressure peaks were lower. Thus, the average of impulses at the 5 pressure stations in 6 MAPP/air detonations was 7.7 psi sec, in 6 propane/air detonations 7.4 psi sec and in 3 gasoline/air detonations 7.5 psi sec.

When both ends of the pipe were open, the pressure plateau was nearly eliminated. This is shown by the transients of figure 6 (compare curves C and D with curves A and B). In 7 MAPP/air detonations the average impulse was only 3.2 psi sec and in 5 acetylene/air detonations 3.1 psi sec. Even a partial temporary closure, as exemplified by loose-fitting sandbags in the ends of the pipe, brought the average impulse (for 7.2 percent MAPP/air) back to about 6.3 psi sec.

No particular difference in average impulse could be detected as a result of initiating the detonation at the longitudinal midpoint of the tube or simultaneously at the two ends.

In the dry-walled steel tube, suspended aluminum powder (even though much of it was deposited on the walls) could participate in the post-detonative reactions to give about 50 percent greater impulse. Comparative values are given in table 3. But in dirt tunnels, the powder was collected on the damp walls and played no apparent part in the explosion.

Destructiveness of Gas Detonations to Earthen Structures

In field tests, a surprising fraction, usually 50-100 percent, of the impulse of the explosion was converted into momentum of the overburden. This means that soil mechanical factors such as plasticity and shear strength were unimportant so that the overburden was behaving essentially as a frictionless piston. When the earth velocity was made to exceed 20 ft/sec, as measured at ground level by Fastax photography, the tunnel usually failed. Because of the weakness of end closures, as compared with an end plate on a steel pipe, the largest impulse attained in the field was about 6 psi sec and the greatest depth of burden defeated by a single gas detonation was 8 feet.

REFERENCES

1/ Armistead, George, Jr. Safety in Petroleum Refining and Related Industries, 2nd Edition, Simmonds, N. Y., 1959, p. 43.

2/ MAPP is a commercial mixture of methylacetylene, propadiene and propylene.

3/ Zeldovich, Ya. B., and A. S. Kompaneets, "Theory of Detonation," Academic Press, New York, N. Y., 1960.

4/ Taylor, G. I., "The Dynamics of the Combustion Products behind Plane and Spherical Detonation Fronts in Explosives," Proc. Roy. Soc., v. 200, 1950, p. 285.

TABLE 1. - Limits of Flammability and of Detonability

Mixture	Initiator	Flammable Range	Detonable Range
Propane/air	Spark	2.1 - 9.5%	--
	10 g PETN	--	2.2 - 9.2%
Acetylene/air	Spark	2.5 - 100%	--
	10 g PETN	--	2.0 - 100%
MAPP/air	Spark	3.4 - 10.8%*	--
	1 g PETN	--	4.1 - 7.6%
	10 g PETN	--	2.4 - 13.7%

*Hembree, J. O., et al, Welding Journal, May 1963.

TABLE 2. - Plateau Durations, Plateau Pressures, and Impulses of MAPP/Air Detonations in 24" Diameter by 163' Long Steel Tube with Initiation End Closed

MAPP Concentration (%)	Plateau Duration (milliseconds) at Instrument Stations #1	#2	#3	#4	#5	Averaged Plateau Pressure (psig)	Impulse (psi sec)
3.4	71	54	35	12	2	85	6.8
4.9	58	46	32	15	--	103	8.9
6.1	64	49	35	14	--	98	8.3
8.7	64	52	33	14	--	99	7.8

TABLE 3. - Impulses Obtained in Detonations in the Steel Tunnel with and without Added Aluminum Powder

Gaseous Fuel	Closure of Initiation End	Aluminum (#422)	Impulse (psi sec)*
Acetylene	Open	None	3.0, 3.9
Acetylene	Open	2 lbs on floor	4.5
Acetylene	Closed	None	3.9
Acetylene	Closed	2 lbs on floor	6.5
MAPP	Open	None	3.4
MAPP	Open	2 lbs suspended	5.6
MAPP	Closed	None	4.3
MAPP	Closed	2 lbs on floor	6.6

*As measured at a station close to the open downstream end of the tunnel.

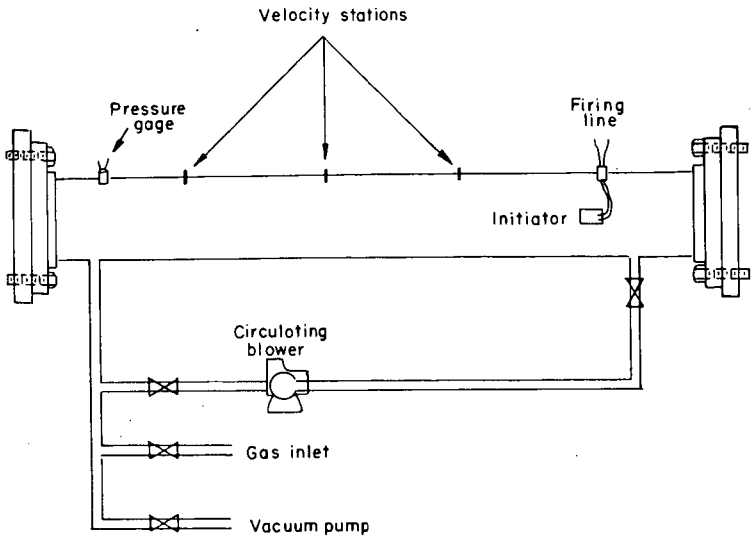

FIGURE 1. - LABORATORY DETONATION TUBE.

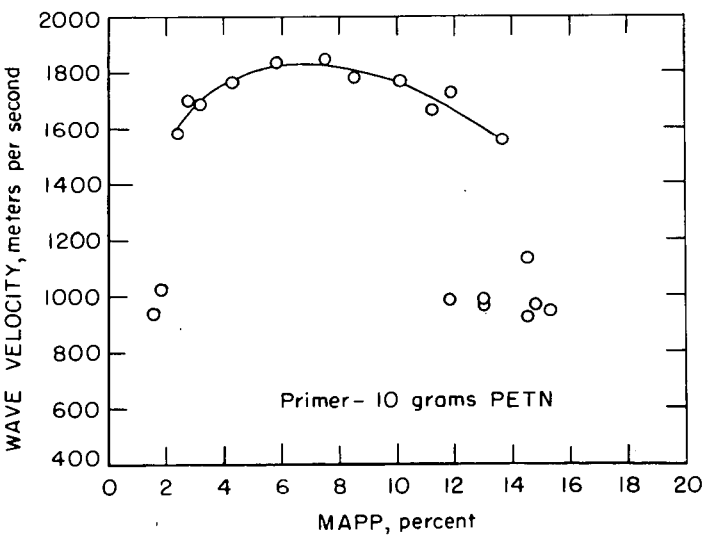

FIGURE 2. - DETONABLE LIMITS OF MAPP/AIR.

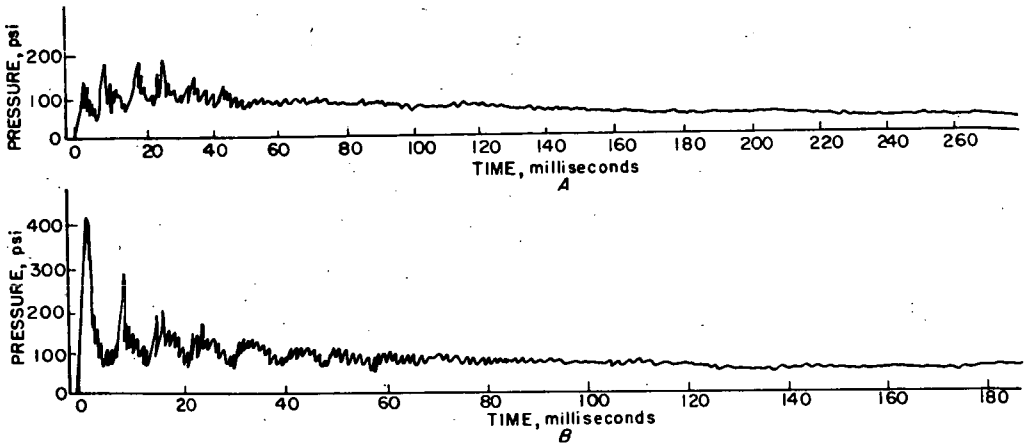

FIGURE 3. - PRESSURE TRANSIENTS IN CLOSED CHAMBER
A. Deflagration
B. Detonation

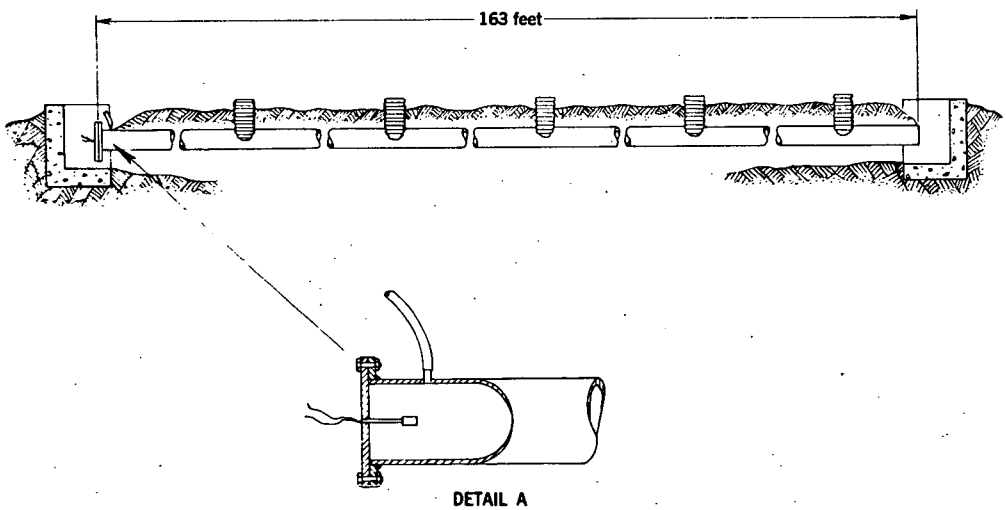

FIGURE 4. - LARGE DETONATION TUBE (2 x 163 FEET).

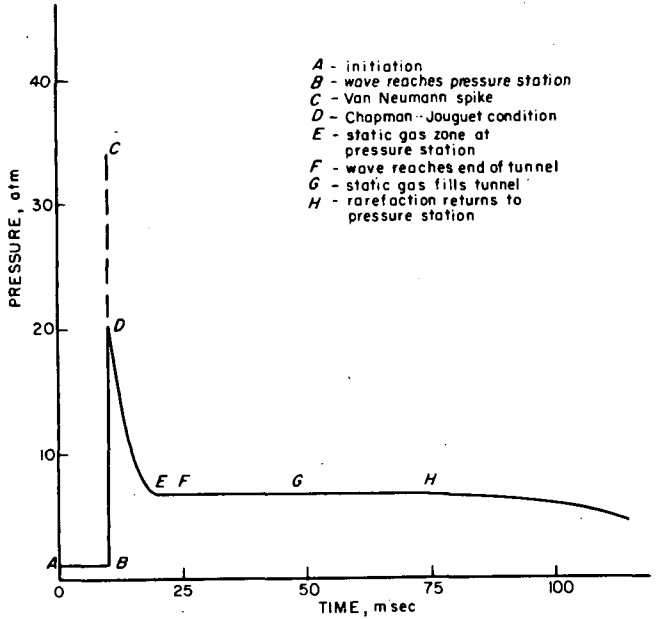

FIGURE 5. - PREDICTED PRESSURE TRANSIENT.

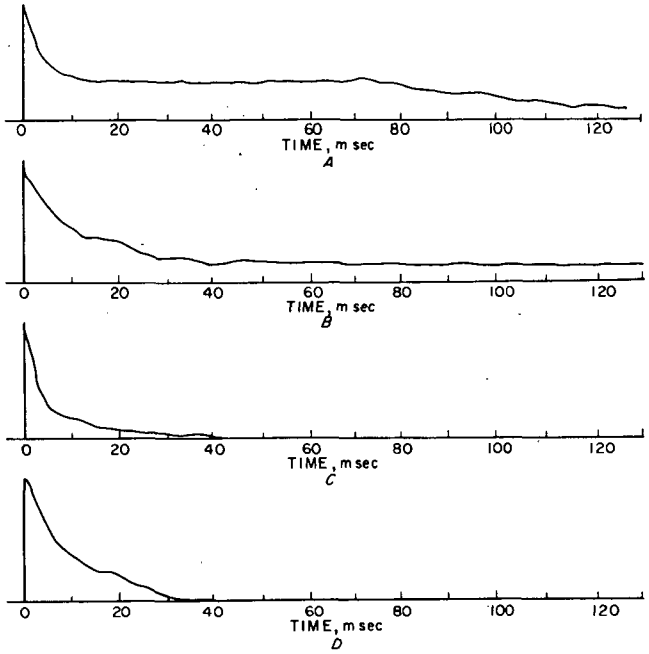

FIGURE 6. - OBSERVED PRESSURE TRANSIENTS
A,B - Initiation end closed; C,D - both ends open
A,C - Transducer near initiation; B,D - transducer downstream

INITIATION OF CONDENSED EXPLOSIVES BY GAS DETONATION

M. L. Weiss, T. J. Schellinger, and E. L. Litchfield

Explosives Research Center
Bureau of Mines
U. S. Department of the Interior
Pittsburgh, Pennsylvania 15213

Introduction

There are two ways in which stimuli may induce detonation in secondary explosives. A strong shock may cause detonation with an induction time of a few microseconds, i.e., time intervals of a few microseconds between application of the stimulus and the appearance of detonation. A weaker shock or a purely thermal stimulus may initiate reactions that begin as a deflagration and accelerate to detonation. The acceleration of the reaction occurs as a consequence of increasing pressure, or self-pressurization, produced by the hot, gaseous decomposition products. Maintenance of pressure for periods of 10's to 100's of microseconds, as may be required to obtain detonation from weak initiation stimuli, is achieved by confinement of the explosive sample.

Although such confinement is usually provided by high-strength metallic containers, for short periods of time it can also be a consequence of inertial effects. If low-strength confinement surrounds the explosive sample the acceleration of the confinement material is directly proportional to the pressure seen by the explosive sample and inversely proportional to the confinement mass per unit area of explosive sample. At early times, the expansion and escape of product gases are limited by the low velocity of expansion of the container and self-pressurization of an explosive sample may be maintained for considerable periods. Inertial confinement, or self-confinement might be provided by a large pile of explosive to a reaction initiated within the interior of the pile.

Examples of the first type of stimulus are initiation by other condensed phase explosives and by projectile impact. Initiation of detonation in condensed explosives has been studied using strong shocks across air gaps[1] or through inert barriers[2,3] and by determining projectile impact initiation parameters.[4,5,6] Threshold initiation shock pressures for condensed explosives range from 1 to 100 kbar. An example of the second type of stimulus is that of thermal ignition transforming to detonation in the confined explosive.[7,8]

This paper describes results obtained with an initiation source producing a stimulus that is continuously variable from less than that required to ignite explosive flours to more than that required to detonate pressed pellets. The initiation source is the detonation wave produced in gaseous mixtures of stoichiometric ethylene-oxygen ($C_2H_4 + 3\ O_2$).

Until recently, gas detonation waves free from incandescent solid debris had to be obtained by run-up in a detonation tube.[9,10,11,12] Such tubes were economically unattractive, inconvenient in use, or restricted in use by the run-up characteristics of the gaseous mixture. In Bureau of Mines' studies, gas detonations have been obtained without run-up in a detonation tube and without explosive detonators.[13]

One possible difference between the shock from a projectile and the gas detonation shock is the difference between a "cold" and a "hot" shock. In the first case, temperature increase in the condensed explosive sample is entirely a consequence of mechanical interactions and conversion of translational energy into heat. In the second case, there is additional thermal energy in the hot ethylene-oxygen combustion

products. Phenomenological analysis and experimental results indicate that the transport from the hot gases is negligible when the explosive is initiated within 1μ sec.

Experimental Procedures

The test container was a 17.8 cm length of 1-inch schedule 80 pipe, reamed to an inside diameter of 2.54 cm. Explosive samples were positioned at one end of the tube and the wires to initiate the gas detonation were positioned near the other end.

The detonable gas mixture was 25 percent ethylene and 75 percent oxygen as determined by partial pressures. Gases were injected into the evacuated chamber through 1/16-inch orifice fittings for mechanical mixing and 20 minutes was allowed for additional diffusional mixing. Gases were from commercial cylinders and were used without further treatment. Initial pressures of the prepared gas mixture were from 3 to 85 atm gage. Initial pressures less than 3 atm were obtained by reducing a 3-atm mixture to the desired pressure.

To initiate the gas, a 0.15 mm (No. 35 B&S) copper wire, 2 cm long, was exploded with the discharge from a 1.5 μf condenser charged to 5.5 kv or more (25 joules energy, or more) using a hydrogen thyratron switch. Control trials in which the wire was exploded with inert gas plus condensed explosive gave no evidence of debris impingement or reaction of the explosive.

Representative particle size analyses of the floured or granulated materials are given in table 1. Particle sizes and distributions under the test conditions may have been slightly different. Gas was injected through orifices to produce turbulent, circulatory gas mixing. This injection must have disturbed the surfaces of the unpressed samples with some increase of "fines" occurring at the top of the sample.

The unpressed flour or granulated samples were prepared by pouring a standard weight of material into the test vessel and tapping lightly to level the sample surface. Standard weights were: 10 gm PETN,* 10 gm RDX,** 13.2 gm tetryl,*** or 14 gm Composition A5.**** Direct determinations of possible densities in the tested charges of floured or granulated explosive have given: for PETN - 0.40 to 0.69 gm/cc; for neat RDX - 0.67 to 0.91 gm/cc; for Composition A5 - 0.93 to 1.02 gm/cc; and for tetryl - 0.93 to 1.14 gm/cc. As initially prepared in the test vessel, densities were near the larger figure in all cases and these are the numbers quoted in the tables. The particle size distributions of table 1 imply adequate porosity to permit pressure equilibration within the floured or granulated sample by gas flow during loading of the detonable gas mixture. Thus, the gas charging pressure would not affect, per se, the density of the charges. As was the case with particle size data, the effect of the gas jet mixing action upon the charge density is not known.

Pellets of Composition A5 and of tetryl were prepared and tested at pellet densities of 1.6 gm/cc and 1.4 gm/cc. Pellets of PETN + 1 percent graphite were tested at densities of 1.6 gm/cc. All pellets were 1 inch long. Comparative tests of PETN and PETN + 1 percent graphite, both in flour form, did not reveal any noticeable difference in sensitivity resulting from the graphite addition.

---

* Pentaerythritol tetranitrate.
** Cyclotrimethylenetrinitramine (hexahydro-1,3,5 trinitro-s-triazine).
*** 2,4,6-trinitrophenylmethylnitramine.
**** RDX + 1% stearic acid coating material.

Measurements were made of the pressure-time history at the initial explosive surface until detonation, location of first appearance of significant reaction, and the propagation velocity on the axis. These data were obtained from resistive pressure transducers[14] and continuous wire probes.[15]

The resistive transducer was a composition resistor of 0.1 watt rating. The variation of resistance with loading pressure has been established in Bureau of Mines investigations.[14] The approximate constancy of the calibration over periods of about 100 μsec after application of the gas detonation shock stimulus has been established in one instance by direct comparison with strain gage measurements. This result provides justification for reading a "pressure at detonation" at the time that detonation is shown by the velocity probe.

The wire probe consisted of a fine, nichrome axial wire helically wound with a nylon filament for insulation from the surrounding, collapsible aluminum tube. Collapse of the aluminum tube altered the probe resistance and gave a direct indication of the physical location of the shorting point. Rates of change of the probe resistance were proportional to the velocities of the pressure front. For trials at charging pressures greater than 14 atm gage, the probe record displayed the time-position loci in both the gaseous and the solid phases.

Results

The explosive flours or granules were observed to react in three different ways depending upon the explosive and the gas charging pressure. At higher gas charging pressures, supersonic reaction was induced with a time delay ≤ 1 microsecond. At lower pressures, significant chemical reaction was evident only after a delay of several microseconds and detonation commenced at some distance below the original surface of the explosive sample. At still lower pressures, granular tetryl or Composition A5 was not initiated to self-sustaining chemical reactions even though a portion of the sample might have been consumed in the test.

Test results are summarized in table 2 where charging pressures are given for the reaction modes of the several samples. PETN flour samples at a density of 0.7 gm/cc required detonable gas mixture charging pressures of 20 atm, gage, to initiate detonation with induction times ≤ 1 μsec. At charging pressures of 0 atm gage the flour was initiated to lower order reaction and transited to detonation after considerable delay (≥ 200 μsec). When pressed to a density of 1.6 gm/cc, PETN required charging pressures of 85 atm gage to produce detonation within 1 μsec of the impact of the detonation wave. At charging pressures less than about 9 atm gage, the 1.6 gm/cc PETN pellet was not initiated to self-sustaining reaction.

The initiation sensitivity for RDX and tetryl also reduced with increasing density as would be expected. In the unpressed, flour or granule form the ordering of the sensitivities, S, is

$$S_{PETN}\ [\rho = 0.7\ gm/cc] > S_{RDX}\ [\rho = 0.9\ gm/cc] > S_{tetryl}\ [\rho = 1.0\ gm/cc];$$

this ordering appears applicable to both the production of detonation with ≤ 1 μsec delay and to the failure to produce a self-sustained reaction. The same ordering of sensitivities appears to apply when pressed pellets of nearly equal density are compared; and is the same ordering as found by drop-weight impact[16] and by projectile impact.[6]

The detonation velocities observed in the present tests were similar to those reported by Hampdon and Stresau[17] with the qualifications noted by Jones and Mitchell.[18] With a gas charging pressure of 2 atm gage, PETN flour was initiated to a velocity of 3.5 mm/μsec after a delay of 4 μsec; 8 μsec later this velocity accelerated to the stable value, 4.8 mm/μsec. When RDX flour was initiated to

detonation with 12 atm gage gas charging pressure, the initial velocity was about 2.6 mm/μsec; after 4 μsec, acceleration to the stable velocity, 5.4 mm/μsec, occurred. With 2 atm gage charging pressure, a subsonic reaction rate of 0.3 mm/μsec in the RDX accelerated to the stable value, 5.4 mm/μsec, after 30 μsec. With 16 atm gage, tetryl flour was initiated at a velocity of 2.8 mm/μsec, and with 6 atm gage, 1.55 mm/μsec was observed. Acceleration to the stable, high rate of 5.3 mm/μsec did not occur. This result is presumed to be a consequence of the dimensions of the explosive sample.[18]

When detonation occurs after induction times of several microseconds, it is to be expected that details of the hot gas-solid explosive-confinement interactions are important in determination of the course of the reaction. It was observed that after the initial pressure pulse impingement, the pressure remained nearly constant for several microseconds and then increased at a high rate. The high rate of pressure increase is seen first as a series of spikes probably due to individual pressure wave interactions followed by an approximately exponential rise to quite high values of pressure. The high values of pressure in the container following the exponential rise are of the same order as detonation wave pressures to be expected in the condensed sample.

Associated with incidence of the approximately exponential rate of increase in pressure, was an increased rate of propagation as shown by the velocity probe. Comparison of records obtained with various initial gas charging pressures showed that the pressure at appearance of the high rate could be correlated with the explosive density and with the explosive type. As an example, with PETN flour and a charging pressure of 0.7 atm gage, the induction time was 24 μsec and the vessel pressure at appearance of detonation was about 2 kbar. With the same type of explosive sample but a charging pressure of 20 atm gage, the induction time was about 1 μsec and the pressure in the vessel at appearance of detonation was again about 2 kbar. This type of observation of a critical pressure for the occurrence of detonation is supported by the results of Price, Wehner, and Roberson.[7]

Table 3 compares pressures for the appearance of detonation as determined in this study, to the shock pressure required to initiate unconfined charges as given by, or derived from, the results of other investigations.[2,4,5,6,19] The reasonable conformity of measured values from such diverse techniques strongly suggests that the tabulated pressures are indeed critical pressures for the occurrence of detonation. The individual values of table 3 and of table 4 are offered as representative data. Additional experience with the sensors and additional experimental data are required before the results are considered to be more than semiquantitative.

Application of Results to a Large Pile of Explosives Under Conflagration Conditions

A. Assumed Stimulus is a Gas Detonation External to the Pile

The stoichiometric mixture of ethylene and oxygen must be charged to pressures of 20, 26, or 26 atmospheres respectively in order that the gas detonation be able to induce detonation in PETN, RDX, or tetryl flours with delay times of about 1 μsec. Buildings, bins, or containers capable of withstanding more than 275 psig are economically and architecturally incompatible with the storage of tons of explosives.

Concern, then, is entirely with pressures of approximately zero psig for such a detonable gas mixture. Table 4 summarizes induction times as functions of detonable mixture charging pressure for PETN and RDX. (According to table 1, tetryl was not initiated to detonation at charging pressures below 3 atm gage.) Induction times of PETN and RDX, at 1 atm charging pressure, are $\geq$200 and 250 μsec respectively. Detonations produced in sufficiently large external volumes of gas could

maintain the gas stimulus at the explosive surface for these, or longer, periods of time[20] but such "gas detonation confinement" would not support the relatively slow buildup of pressure to values in excess of the critical pressure for appearance of detonation (more than 28,000 psi). One test with 1.1 gm/cc, Composition A5 explosive showed transition directly from a level of about 2000 psig in the container without observable pressure run-up in the gas phase close to the explosive surface. However, 2000 psig is beyond the range of sustained pressures available from an unconfined gas detonation.

It is thus improbable that an external, unconfined, gas detonation would cause direct initiation of a large pile of flour explosives of the types tested. If the gas detonation were to produce fragments having velocities of 300 m/sec or more[6] such fragments might produce detonation in the large pile. Existing data on projectile initiation are not sufficiently complete to permit numerical prediction of gas volume versus projectile size and velocity relationships.

B. Assumed Stimulus is Internal to the Large Pile of Explosives

Peak pressure in the reflected gas detonation wave, of these studies, at 0 psig is believed to be less than 0.2 kbar; the Chapmen-Jouguet pressure is even lower, of course. In view of the appreciable difference between these pressures and the critical pressure required for appearance of detonation in the condensed phase, it is probable that the initiation sequence is that of ignition of the explosive particles and then self-pressurization of the test vessel by the decomposition products. The exact mechanism by which deflagration of the explosive particles is initiated, whether by an enthalpy wave, by an internal autoignition of "cook off" gases, or by an external flame, is not of particular importance. The important question is whether or not adequate confinement is provided to permit the pressurization to occur. Two circumstances can be postulated to provide the necessary confinement by an explosive pile--collapse of a cavity formed by erosion, or enfoldment of burning particles by a sliding pile. Because of lack of knowledge about ullage space--induction time relationships and because of the complicated dynamics of the mechanical collapse or enfoldment, it is not presently possible to discuss these circumstances in detail. It may be of academic interest to note that rigid collapse of a 5-meter-high pile of material having a sonic velocity of 2000 m/sec would provide nearly rigid confinement for a time of 200 μsec.

Summary and Conclusions

Gas detonations generated in stoichiometric ethylene-oxygen mixtures have been used to produce detonations in PETN, RDX, and tetryl explosive. The explosive has been tested both as a flour and as pressed pellets. The experimental results suggest the existence of a critical pressure for the appearance of detonation in the condensed explosive. Induction time does not have a strong effect upon the induction pressure--the pressure to which the explosive is subject at the time of appearance of detonation. These induction pressures were sensitive to explosive type, density, and particle size. From these results, it has been deduced that a gas detonation cannot produce detonation of a large pile of these materials without the interposition of some action producing confinement of the ignited explosive grains. The requisite confinement cannot be provided by an unconfined gas detonation.

Induction pressures for the tested flours or granules of PETN, RDX, and tetryl were 2, 3, and 3 kbar respectively. In pressed pellets, pressures for appearance of detonation were: 13 kbar for 1.6 gm/cc PETN; 12 kbar for 1.4 gm/cc Composition A5; 16 kbar for 1.6 gm/cc Composition A5; 16 kbar for 1.4 gm/cc tetryl; and 20 kbar for 1.6 gm/cc tetryl.

References

1. Sultanoff, M., V. M. Boyle, and J. Paszek. Shock Induced Sympathetic Detonation In Solid Explosive Charges. Third Symposium on Detonation, September 1960, Princeton, New Jersey, Office of Naval Research Symposium Report ACR-52, v. 2, pp. 520-533.

2. Seay, G. E., and L. B. Seely, Jr. Initiation of a Low-Density PETN Pressing by a Plane Shock Wave. J. Appl. Phys., v. 32, 1961, pp. 1092-1097.

3. Campbell, A. W., W. C. Davis, J. B. Ramsey, and J. R. Travis. Shock Initiation of Solid Explosives. Phys. of Fluids, No. 4, 1961, pp. 511-521.

4. LeRoux, A. Detonation of Explosives Through the Shock of a Solid Body Launched at High Velocity. Mem. Poudres, v. 33, 1951, pp. 283-321.

5. Eldh, D., P. A. Persson, B. Ohlin, C. H. Johansson, S. Ljungberg, and T. Sjolin. Shooting Test with Plane Impact Surface for Determining the Sensitivity of Explosives. Explosivstoffe, v. 5, May 1963, pp. 97-103.

6. Weiss, M. L., and E. L. Litchfield. Projectile Impact Initiation of Condensed Explosives. Bur. Mines Rept. Investigations 6986, 1967, 17 pp.

7. Price, Donna, J. F. Wehner, and G. E. Roberson. Transition from Slow Burning to Detonation. Further Studies of the Free Volume and the Low Velocity Regime in Cast Pentolite. Naval Ordnance Laboratory Tech. Rept. 63-18, February 1963, 33 pp.

8. Price, Donna, and F. J. Petrone. Detonation Initiated by High Pressure Gas Loading of a Solid Explosive. Naval Ordnance Laboratory Tech. Rept. 63-103, April 1963, 18 pp.

9. Andreev, K. K., and V. P. Maslov. Action of Gas Explosion on Solid Explosives. Comptes Rendus (Doklady) de l'Acad. Sci. (URSS), XXV, v. 195, 1939, pp. 195-197.

10. Gordeev, V. E., A. I. Serbinov, Ya. K. Troshin, G. I. Filatov. Initiation of the Explosive Conversion of Condensed Explosives by Gaseous Detonation. Combustion, Explosion, and Shock Waves, v. 1, No. 2, 1965, pp. 7-13.

11. Makomaski, A. H. Preliminary One-Dimensional Investigation of the Initiation of Low-Density PETN by Hydrogen-Oxygen Detonation Waves. Univ. of Toronto Inst. of Aerospace Studies Tech. Note 83, February 1965, 24 pp.

12. Cook, M. A., and F. A. Olson. Chemical Reactions in Propellant Ignition. AIChE Jour., v. 1, 1955, pp. 391-400.

13. Litchfield, E. L., M. H. Hay, and D. R. Forshey. Direct Electrical Initiation of Freely Expanding Gaseous Detonation Waves. Ninth Symposium (International) on Combustion. Academic Press, Inc., New York, N. Y., 1963, pp. 282-286.

14. Watson, R. Gage for Measuring Shock Pressure. Rev. Sci. Instruments, in press.

15. Gibson, F. C., M. L. Boswer, and C. M. Mason. Method for the Study of Deflagration to Detonation. Rev. Sci. Instruments, v. 30, 1959, pp. 916-919.

16. Copp, J. L., S. F. Napier, T. Nash, W. J. Powell, H. Shelby, A. R. Ubbelohde, and P. Woodhead. The Sensitiveness of Explosives. Phil. Trans. Roy. Soc., v. A-241, 1949, pp. 197-296.

17. Hampdon, L. E., and R. H. Stresau. Small Scale Technique for Measurement of Detonation Velocities. NAVORD Report 2282, December 27, 1951.

18. Jones, E., and D. Mitchell. Spread of Detonation in High Explosives. Nature, v. 161, 1948, pp. 98-99.

19. Coleburn, N. L., and T. P. Liddiard, Jr. Hugoniot Equations of State of Several Unreacted Explosives. Jour. of Chem. Phys., v. 44, March 1966, pp. 1929-1936.

20. Kufer, John H. Air Blast Predictions for Operation Distant Plain. Ballistics Research Laboratory Tech. Note 1612, Aberdeen Proving Ground, Maryland, June 1966.

TABLE 1. - Particle size distributions of explosive flours or granules

Particle size range R, microns	Percent of sample in range			
	PETN	RDX[1/]	RDX[2/]	Tetryl
710 < R	7	2	1	14
350 < R < 710	81	20	85	79
105 < R < 350	7	63	13	6
74 < R < 105	0	2	1	0
R < 74	0	15	0	2

1/Neat RDX.
2/RDX + 1% stearic acid (Composition A5).

TABLE 2. - Threshold charging pressures of stoichiometric ethylene-oxygen mixtures to produce gas detonation initiation of detonation in PETN, RDX, and tetryl

Explosive	Density, gm/cc	Detonation with ≤1 μ sec delay, atm gage	No detonation atm gage
PETN	0.7	20	< 0
PETN[1/]	1.60	85	3/ 9
RDX	.9	26	< 0
RDX2/	1.1	80	8
RDX2/	1.40	84	3/ 15
RDX2/	1.64	> 84	3/ 39
Tetryl	1.0	26	3/ 3
Tetryl	1.39	> 85	3/ 39
Tetryl	1.57	> 85	3/ 67

1/ 1% graphite added.
2/ 1% stearic acid added.
3/ Average from lowest value for detonation and highest value for no detonation.

TABLE 3. - Comparison of minimum shock pressures for initiation of explosive compounds by gas detonation or for initiation with the indicated stimulus

Source	Density, gm/cc	Type of Stimulus	Shock Pressure, kbar
	PETN		
This work	0.7	Gas detonation	1/ 2.1 ± 0.3
LeRoux	0.7	Projectile impact	2/ 2.0
Seay and Seely	1.0	Plane shock wave	2.5
Weiss and Litchfield	1.48	Projectile impact	11.0
Eldh and coworkers	1.53	Projectile impact	2/11.0
This work	1.60	Gas detonation	1/13.3 ± 0.5
	RDX		
Weiss and Litchfield	0.8	Projectile impact	3.0
This work	.9	Gas detonation	1/ 3.1 ± 0.4
LeRoux	1.0	Projectile impact	2/ 3.0
This work	1.1	Gas detonation	3.4 ± 0.5
This work	1.40	Gas detonation	12.
This work	1.64	Gas detonation	1/16. ± 1
Weiss and Litchfield	1.62	Projectile impact	21.0
Eldh and coworkers	1.65	Projectile impact	2/22.0
	Tetryl		
This work	1.0	Gas detonation	3/ 3.
Weiss and Litchfield	1.00	Projectile impact	3.5
LeRoux	1.00	Projectile impact	2/ 3.5
This work	1.39	Gas detonation	3/11.
Weiss and Litchfield	1.57	Projectile impact	19.0
This work	1.57	Gas detonation	13.
Eldh and coworkers	1.65	Projectile impact	2/22.0

1/ Mean and estimated standard deviation per observation.
2/ These values calculated by the authors from projectile velocity data of other investigators.
3/ For low-velocity detonation.

TABLE 4. - Summary of parameters for initiation of flour and pelletized explosive compounds by gas detonation

Explosive	Density gm/cc	Charging pressure, atm gage	Container pressure at detonation, kbar	Induction time, μsec
PETN	0.7	0.0	--	≥200
PETN	.7	0.7	2.2	28
PETN	.7	1.0	--	8
PETN	.7	1.7	--	5
PETN	.7	2.1	--	4
PETN	.7	3.1	1.9	6
PETN	.7	20.0	--	1
PETN	1.60	54.0	13.0	4
PETN	1.60	85.0	13.5	1
RDX	0.9	0.0	--	≥270
RDX	.9	1.0	--	50
RDX	.9	1.4	--	56
RDX	.9	1.7	--	28
RDX	.9	3.1	--	12
RDX	.9	5.9	--	5.7
RDX	.9	20.0	3.3	4
RDX	.9	26.0	2.9	1
RDX1/	1.1	11.2	6.0	70
RDX1/	1.1	11.2	4.0	72
RDX1/	1.1	27.2	3.1	36
RDX1/	1.1	40.4	3.0	16
RDX1/	1.1	58.0	3.4	7
RDX1/	1.1	80.0	--	1
RDX1/	1.40	50.0	--	7
RDX1/	1.40	84.0	12.5	1
RDX1/	1.64	57.0	17.0	14
RDX1/	1.64	82.0	15.0	4

1/ RDX + 1% stearic acid (Composition A5).

EXPLOSIVE BEHAVIOR OF AMMONIUM PERCHLORATE

Donna Price, A. R. Clairmont, Jr., and I. Jaffe

U. S. NAVAL ORDNANCE LABORATORY
White Oak, Silver Spring, Maryland

The inorganic oxidizer, ammonium perchlorate (AP), is widely used as a major propellant ingredient. It is, in addition, a very interesting high explosive because its behavior differs markedly from that of conventional explosives such as TNT. AP is a member of a group of explosives which exhibit more ideal detonation behavior at high than at low porosity.[1] No member of this group has been studied very systematically; only a careful investigation of typical members will enable us to understand these materials at least as well as we understand more conventional explosives. Because AP seems a representative group member, because it is frequently used as a propellant component, and because it has been extensively studied in the related fields of thermal decomposition and combustion, we have started a systematic study of its explosive behavior. The purpose of this paper is to report the results obtained from our recent work.

The detonation of AP has been studied before, chiefly by Andersen and Pesante.[2] But their data had too much scatter, and did not extend sufficiently far into the high charge density region to demonstrate the distinctive explosive behavior defined by the present results. That behavior is typified by a detonability limit curve along which critical density increases with critical diameter, and a finite diameter detonation velocity which is not uniquely defined by loading density, i.e., which exhibits a non-linear curve with a maximum in the detonation velocity.

EXPERIMENTAL

All ammonium perchlorate used was propellant grade; it contained 0.2 to 1% tricalcium phosphate. The three lots of perchlorate had weight-median particle sizes of 10, 25, and 200 μ, respectively. For charge preparation, the material was dried at 50°C for four hours or longer and packed in cellulose acetate envelopes to form 20.32 cm-long cylinders of 1.90 to 7.62 cm diameter. Compacting was by hand, by hydraulic press, or by isostatic press (followed by machining to size), according to the charge density desired and the grain size of the perchlorate. All low density charges were fired almost immediately after preparation to avoid the formation of small cracks and column separation, phenomena which occur with aging.

The best quality charges were, of course, those prepared in the isostatic press from the 10 μ material. As the grain size of the perchlorate increased or as the charge density (ρ_o) decreased, charge quality became poorer. At $\rho_o < 1$ g/cc, the charges were of such poor quality that only a few small diameter charges prepared from the 10 μ material were accepted for firing.

The charges were fired in the experimental setup of Fig. 1 with either tetryl or pentolite boosters. A 70 mm smear camera was used to record the flasher enhanced luminosity of the reaction front. The camera was used at a writing speed of between 1 and 3 mm/μsec to obtain a

smear trace of the disturbance at 45° to the base of the film.

The smear camera photographs were of excellent quality, and detonation velocity was determined from the slope of the trace, i.e., by a least square fit of the linear distance - time data. For the lowest resolution, the maximum error estimated from error in reading these records is 1.5%. In over a dozen replications the maximum deviation was also 1.5%; the mean precision was 0.7%.

RESULTS AND DISCUSSION

Failing Reactions

The first interesting result of this work is that charges of ammonium perchlorate (of any grain size) when subcritical are nevertheless capable of showing fading but vigorous reaction. Such charges of the 10 μ and 25 μ materials, under shock from the booster, produced curved luminous traces persisting to distances as large as 8 - 9 diameters down the charge. As the charge diameter was increased toward its critical value, the curvature of the trace decreased. It was, therefore, almost impossible to determine the exact critical limits for the perchlorate; instead, they were bracketted by two densities at which failure and detonation occurred at a given diameter.

The coarsest material (200 μ) failed to detonate at its pour-density of 1.29 g/cc in a 7.62 cm diameter charge. (Larger charges cannot be used in the available firing facilities.) However, it too showed vigorous reaction persisting for two diameters down the charge.

Detonability Limits

The limit or failure curve for the 10 μ perchlorate in the charge diameter (d) vs ρ_o plane is approximated in Fig. 2. The critical values are d_c, the diameter at and above which detonation propagates, and ρ_c, the density above which detonation cannot occur. The trend of increasing critical density with increasing critical diameter and the consequent definition of ρ_c are both opposite to those for TNT-like explosives.[1] Figure 2 also shows measurements made by two other investigators on fine AP's. The agreement is very good in view of approximating the particle size distribution by the median size and of the difficulty of determining that median.

The limit curve for the 25 μ AP was not as well defined as that for the finer material. The relevant data are:

	ρ_o (g/cc)	
d(cm)	Deton.	Failure
3.81	1.02	1.11
5.08	1.36	1.41
7.62	1.47	1.56

This limit curve will therefore lie above and to the left of that for the finer perchlorate. The limit curve for the 200 μ material is beyond the experimental range of the present work. The trend of particle size effect is the expected one for all explosives, that of increasing d_c

with increasing particle size. The shift in ρ_c is, however, toward lower values for ammonium perchlorate, toward higher for TNT-like explosives.

Detonation Behavior Pattern

The detonation velocity (D) vs ρ_o curves at various diameters of the finest perchlorate are shown in Fig. 3. Typically the D vs ρ_o curve at fixed d shows detonation velocity increasing with increasing density to a maximum value. Beyond this maximum, D decreases as ρ_o increases until it reaches its critical value at the failure limit.

The curve for each diameter has been terminated at the critical density given by the smoothed curve of Fig. 2. The limit line of Fig. 3, which divides the detonation from the failure area, is shown as the dashed line through these terminal points. The curve seems slightly concave upward and gives the critical detonation velocity (D_c) as a function of ρ_o at different diameters, but at fixed particle size.

Fig. 4 shows the analogous pattern, analogously derived, for the 25 μ material. This pattern is very like that of Fig. 3; it is, however, compressed into the smaller diameter range which results from the particle size shift of the limit curve, d vs ρ_o. At any given values of d and ρ_o, the detonation velocity of the finer perchlorate is greater than that of the coarser. This point is further illustrated in Fig. 5 where the particle size effect on the D vs ρ_o curves at d = 5.08 cm is shown. The terminal points of the two curves are on a limit curve (indicated by the dashed line) which gives D_c vs ρ_o at constant diameter but at different particle sizes.

Infinite Diameter Values

Since most of our D vs ρ_o curves are non-linear, our experimental range is one in which diameter effect on D is large. At ρ_o = 1.0 g/cc all data are on the low density side of the maximum D or, in one case, at the maximum. Under these circumstances, the usual D vs d^{-1} curve is linear (Fig. 6) and gives the ideal value D_i of 3.78 mm/μsec at ρ_o = 1.01 g/cc in good agreement with the comparable value of 3.75 determined by Evans et al.[6]

For an analogous selection of data at ρ_o = 1.26 g/cc the solid symbols of Fig. 6 are from the high density side of the maximum D and must be neglected; they would lead to values of D_i which are too high. The remaining data give D_i = 4.79 mm/μsec at ρ_o = 1.25 g/cc in very poor agreement with the Ref. (2) value. However, if the Ref. (2) data are extrapolated as in the present work, the analogous D_i is 4.85 instead of the reported 4.37 mm/μsec.

Even so, it is quite likely that the D_i value obtained in this manner at the higher density (where detonation behavior is less ideal) is too high. Measurements at larger diameters are necessary to decide this. Meanwhile the present values have been used in Figs. 3 and 4 to indicate a portion of the D_i vs ρ_o curve. The data for the 25 μ material also extrapolate to the same curve.

Reaction Zone Lengths, Reaction Times

Of the available diameter effect theories, the curved front theory[7,8]

seems to fit our data best. Ref. (7) gives the detonation reaction zone length by

$$a = d\ (1 - D/D_i) \tag{1}$$

The modified theory[8] gives a zone length

$$z = (s/3.5)\ (1 - D/D_i) \tag{2}$$

where s is the radius of curvature of the reaction front. For the reasonable assumption that s is directly proportional to d, Eqs. (1) and (2) are identical except for a constant factor and will lead to the same relative reaction zone lengths.

The reaction time (τ) is defined and related to the reaction zone length by

$$a = (D - \bar{u})\ \tau \tag{3}$$

where $\bar{u}$ is the average particle velocity between the leading von Neumann shock and the C-J plane of the detonation front. Moreover, according to the grain burning theory[7],

$$\tau = R/\lambda k \tag{4}$$

where R is the average particle radius, λ the molecular diameter, and k the specific reaction rate of a single molecule.

For each ideal value $D_i(\rho_o)$, there is a corresponding detonation temperature $T_i(\rho_o)$. Moreover, these infinite diameter values are independent of the grain size. Hence Eqs. (1) or (2) and (3) can be used to obtain the ratio of the reaction times of the 10 μ and 25 μ perchlorate at T_i. If in addition we assume that this material detonates by a grain burning mechanism, we can incorporate Eq. (4) into the relations to obtain

$$(a_1/a_2) = (z_1/z_2) = (\tau_{1i}/\tau_{2i}) = (R_1/R_2) \tag{5}$$

where the subscripts 1 and 2 denote 10 μ and 25 μ ammonium perchlorate, respectively. Calculation of the ratio of the reaction times by Eq. (5) gives $(\tau_{1i}/\tau_{2i}) = 0.40 \pm 0.04$ over the range of $0.90 \leq \rho_o \leq 1.20$ g/cc. This is in good agreement with the ratio $(R_1/R_2) = 10/25 = 0.40$, a result consistent with the grain burning mechanism for the detonation of this material; such a mechanism is also consistent with its more ideal behavior at greater porosities.

REFERENCES

(1) D. Price, "Contrasting Patterns in the Behavior of High Explosives," Eleventh Symposium (International) on Combustion (1967) pp 19-28, in press.

(2) W. H. Andersen and R. E. Pesante, "Reaction Rate and Characteristics of Ammonium Perchlorate in Detonation," Eighth Symposium (International) on Combustion, Williams and Wilkins Co., Baltimore (1962) pp 705-10.

(3) R. L. Jameson, S. J. Lukasik, and B. J. Pernick, J. Appl. Physics 35, 714-720 (1964).

(4) M. W. Evans, C. M. Ablow, B. O. Reese, and A. B. Amster, "Shock Sensitivity of Low Density Granular Explosives," Proceedings of the International Conference on Sensitivity and Hazards of Explosives, Ministry of Aviation, U. K. (1963).

(5) M. W. Evans, B. O. Reese, L. B. Seely, and E. L. Lee, "Shock Initiation of Low-Density Pressings of Ammonium Perchlorate," Proceedings of the Fourth Symposium on Detonation, October 1965, in press.

(6) M. L. Pandow, K. F. Ockert, and H. M. Shuey, "Studies of the Diameter-Dependence of Detonation Velocity in Solid Composite Propellants I, Proc. of the 4th Symposium on Detonation, October 1965, in press.

(7) H. Eyring, R. E. Powell, G. H. Duffy, and R. B. Parlin, Chem. Revs. 45, 69 (1949).

(8) W. W. Wood and J. G. Kirkwood, J. Chem. Phys. 22, 1920 (1954).

FIG. 1 EXPERIMENTAL ASSEMBLY

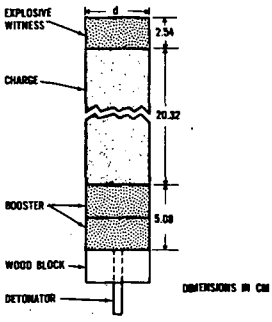

FIG.2 DETONABILITY LIMIT CURVE FOR AP (10μ)

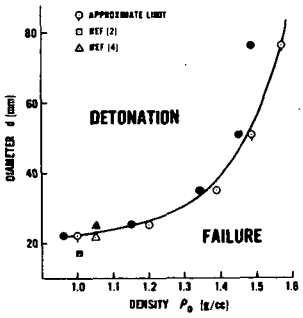

FIG.3 DETONATION BEHAVIOR OF AP (10μ)

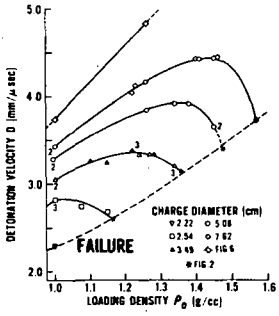

FIG. 4 DETONATION BEHAVIOR OF AP (25μ)

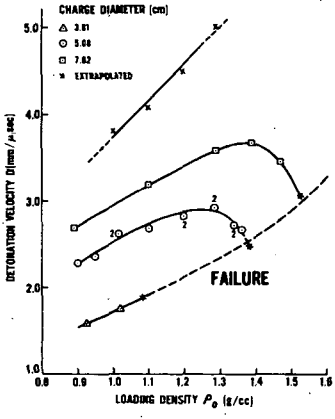

FIG. 5 EFFECT OF PARTICLE SIZE ON DETONATION VELOCITY OF AP (d=5.08 cm)

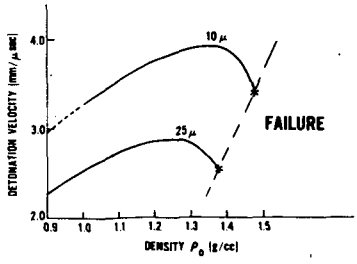

FIG. 6 EXTRAPOLATION TO INFINITE DIAMETER VALUES

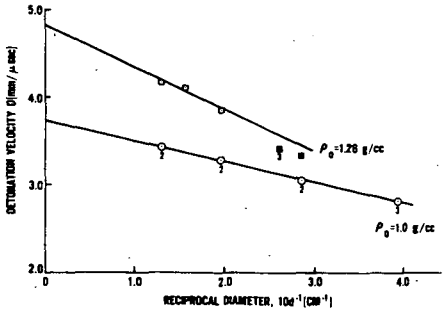

ACCELERATING DETONATIONS IN COMPOSITION B-3 EXPLOSIVE

Robert Sewell, Lawrence Cosner, James Sinclair

U. S. Naval Ordnance Test Station, China Lake, California 93555

INTRODUCTION

The problem of predicting what will happen when a fragment or projectile strikes cased high explosive munitions is complicated not only by the complexity of the projectile-munition geometry but also by the number of different reactions which can and do occur.

Recourse to the literature on the subject exposes one to such terms as no reaction, burning, deflagration, low order, mild low order, large low order, partial detonation, high order and deflagration to detonation transition.

Examining the literature on explosive sensitivity is about as helpful and introduces a series of tests which regularly produce confused ranking of the "sensitivity" of high explosive systems. (The theory or theories of detonation are not a great deal of help either.)

The major problem is actually one of continual attempts to link all the various modes of chemical reaction and all the means of physical excitation into one simple model which would be useful in explosive applications. The probability of success in such a venture is small at best, but an attempt must be made since studies are going to be made with or without adequate models.

In any attempt to tackle this problem the explosive system should first be examined from a chemical as well as a physical viewpoint, the adiabatic auto ignition temperature and its connotations, the shock sensitivity spectrum, experimental results, effects of geometry, and an attempt to create a limited analytic model.

THE EXPLOSIVE

GENERAL COMMENTS

Explosives in general use vary over a wide range of chemical compositions, but do have several similar characteristics.

They consist of chemical compositions which contain both the fuel and the oxidizer in an "unstable" molecular configuration which when broken allows the various atoms to combine into such products as H_2O, CO, CO_2, N_2, etc., with a rapid net production of energy.

The stability of the explosive molecule should and apparently does play an important part in the sensitivity of the explosive.

Analysis of the statistical nature of chemical kinetics shows that some of the molecules are decomposing at any temperature above absolute zero but that the number of molecules decomposing or reacting per second remains "insignificant" up to some critical temperature dependent on the ability of the explosive to dissipate the energy generated by the reacting molecules. Above this temperature the number of molecules involved increases exponentially leading to significant evolution of energy. The dissipative factors involve the heat capacity, the thermal conductivity, the geometry of the explosive, the nature of the confining media, and the temperature of the environment.

(In the presence of air, surface reactions involving the oxygen in the air are, of course, possible.)

In an investigation of the problem of explosive storage and handling, Longwell (ref. 1) measured the adiabatic auto-ignition temperatures of various explosives and developed relations for safe storage times and temperature for various charge geometries.

SHOCK MOLECULAR EFFECTS

When a shock wave strikes a molecule, the molecule absorbs energy and if the energy is high enough, bond rupture occurs. As long as the energy is absorbed into the molecule with no effect from other molecules or their decomposition fragments, the weakest part of the molecule will undergo rupture first. This will be regardless of other factors and certainly is the first effect of the shock wave.

However, once the molecule is disrupted, reactive fragments such as ions and free radicals can collide with the unreacted molecule to cause further bond rupture. Since this latter effect will depend on the spatial features of the molecule, steric factors are important and the bonds disrupted may not necessarily be the weakest in the molecule. In fact they may well be the strongest if the atoms involved are easier to reach by being on the outside of the molecule.

This being the case it is easy to select the bonds that are broken first, i.e., the $N\text{-}NO_2$ and the $C\text{-}NO_2$ (Table I). However, after the initial phase it is probable that the C-H bonds are next ruptured since they occur in both molecules and the hydrogen atoms are on the outside of the molecule.

SHOCK SENSITIVITY SPECTRUM

Energy levels calculated as associated with shock waves in explosives show that for shocks of the order of a few kilobars some chemical reaction is quite probable, but the extent and rate of propagation of the reaction would be strongly dependent on the duration of the pressure pulse as well as its amplitude and thus strongly dependent on the nature of the confinement. Studies by Liddiard et al, (ref. 2) have shown that with proper confinement sustained chemical reaction can be produced in Comp B at pressure amplitudes of the order of 5 to 7 kbars.

This sustained chemical reaction is not to be confused with detonation, which is a chemically supported shock wave, but it can produce burning or deflagration which has often, improperly, been called low order detonation.

Low order detonation--a nonideal detonation--is generally unstable (it is either accelerating or decaying) and is produced when a shock wave with intensity above a given level (dependent on the curvature of the shock front) enters the explosive and either accelerates to full high order detonation or decays to no reaction. The curvature of the wave front during acceleration is strongly dependent on the confinement, the size and shape of the shock producing system, and the physical properties of the explosive.

It has been shown (ref. 3) that for pressures greater than 21 kbars the growth to detonation is dependent upon peak pressure and is relatively independent of impulse. It is interesting to note that the factor of 3 between the values of critical pressures obtained by Liddiard et al. (ref. 4) and Cosner and Burford (ref. 4) correspond to the factor of 3 between the average bond strengths of the $N\text{-}NO_2$ and the C-H bonds.

The initiation of explosive by shock impact is characterized by several zones or thresholds. At very low shock levels no significant chemical reaction occurs, as the shock level is increased surface reactions will be triggered, and as the shock level is increased still further other effects will begin to predominate.

If the input shock level is above 202 kbars (ref. 3), an almost instantaneous jump to stable detonation is observed with a CJ pressure of 272 kbars. Studies have shown that in the region from 21 to 202 kbars the growth of pressure with distance can be represented by

$$\frac{dP}{dx} = k(P - P_c) \quad \text{(ref. 3)} \tag{1}$$

where P_c = 21 kbars and k = 0.132 mm^{-1} with P in kilobars and x in millimeters.

Using an assumption based on Adams' (ref. 5) investigation of nonideal detonation, the pressure is directly proportional to the square of the propagation velocity

$$P = \gamma U^2 \quad \text{(ref. 5)} \tag{2}$$

The constant γ in this expression is found to be 3.38 with P in kilobars and U in millimeters/microseconds.

Integration of eq. (1) yields solutions for pressure as a function of distance and these combined with eq. (2) yield shock velocity as a function of distance and input pressure. A table of parameters of interest associated with these solutions is shown in Table II.

Wedge experiments of the type performed by Boyle, Jameson, and Allison (ref. 6) measure directly the shock velocity as a function of distance. Their determination of the pressure is dependent on the assumption that the explosive will return to its initial density upon release of the pressure. This assumption seems highly unjustified in view of the accelerating reaction which is observed. Their velocity-position data are free of these assumptions and could be used for direct comparison. Unfortunately, "for ease of plotting," Boyle, Jameson, and Allison divided their actual distance by the initiation distance to "normalize" the measurements and failed to publish the actual distances. Working from what they have published, the initiation distance is found to be 15 mm with a variation of about 1 mm. A plot of their data compared to our calculated values is shown in Fig. 1.

If a spherically divergent system is presumed, eq. (1) is modified by substituting r for x and introducing a spherical loss term

$$\frac{dP}{dr} = k(P - P_c) - \frac{P}{r} \tag{3a}$$

or

$$\frac{dP}{dr} = P\left(k - \frac{1}{r}\right) - kP_c \tag{3b}$$

If eq. (3b) is correct and if the constant k is correct a minimum radius of curvature for any stable detonation becomes

$$r = \frac{1}{k} \tag{4}$$

For Comp B-3 this would be $r = \frac{1}{0.133} = 7.52$ mm.

This value is not the limiting radius of a cylinder which would propagate detonation but would be the radius of curvature of the central portion of the detonation wave in the limiting cylinder. Actually since the pressure would not be much above 202 kbar at the limit situation the limiting radius of curvature would be about 8.4 mm. If a hemispherical front is postulated the limiting diameter for full detonation velocity would be 16.8 mm which is equivalent to the d_m^* of ref. 7.

A graph of the pressure required to produce an accelerating detonation as a function of the radius of curvature of the front is shown in Fig. 2. Converging wave fronts (negative radius of curvature) require less pressure than the critical pressure to produce an accelerating front which tends to invert rapidly to a divergent wave front. If during the period of convergence the pressure increases enough over a large enough zone, continued acceleration should occur.

Below and to the left of the positive radius of curvature curve the reaction produced is a decaying detonation. Near the curve, a slight change in radius of curvature through a density change or a void in the explosive could have a large effect on the occurrence of growth to detonation.

REFERENCES

(1) P. A. Longwell, NAVWEPS Report 7646, NOTS TP 2663, China Lake, Calif., Mar 1961.

(2) T. P. Liddiard, Jr. and S. J. Jacobs, NOLTR 64-53, White Oak, Md., 1965.

(3) L. N. Cosner, R. G. S. Sewell, and J. E. Sinclair, NOTS TP 3984, China Lake, Calif., June 1966, pp. 150-64.

(4) M. K. Burford and L. N. Cosner, NOTS TP 3301, China Lake, Calif., Aug 1963, pp. 251-68.

(5) G. K. Adams, "Theory of Initiation to Detonation in Solid and Liquid Explosives," Ninth Symposium (International) on Combustion, Academic Press, New York, N. Y., 1963, pp. 545-53.

(6) V. M. Boyle, R. L. Jameson, and F. E. Allison, BRL Report No. 1250, Aberdeen Proving Grounds, Md., 1964.

(7) M. A. Cook, "The Science of High Explosives," Reinhold Publishing Company, New York, N. Y., 1958.

(8) L. Pauling, "The Nature of the Chemical Bond," 3rd ed., Cornell University Press, Ithaca, N. Y., 1960.

(9) A. D. Little Company, Navy Contract No. W-19-020-ORD 6433, Cambridge, Mass., 1946.

Table I

Average Bond Dissociation Energies

C=C	146 kcal/mole	(ref. 8)
C-H	98.7 kcal/mole	(ref. 8)
C-C	86.6 kcal/mole	(ref. 8)
C-N	72.8 kcal/mole	(ref. 8)
$C-NO_2$	48 kcal/mole	(calcd. from ref. 9)
$N-NO_2$	32 kcal/mole	(calcd. from ref. 9)

Table II

Pressure Distribution and Propagating Velocity for Accelerating Shock

mm x	kbars $\Delta P = (P_o - P_c)e^{kx}$	kbars $P = \Delta P + P_c$	mm/μsec $U = \sqrt{P/\gamma}$	Distance to go to detonation, mm 70 - x
70	181	202	7.78	0
65	93.5	114	5.86	5
60	48.3	69.3	4.56	10
55	25.0	46.0	3.71	15
50	12.9	33.9	3.19	20
45	6.68	27.7	2.88	25
40	3.45	24.5	2.71	30
35	1.78	22.8	2.61	35
30	0.92	21.9	2.56	40
25	0.48	21.5	2.54	45
20	0.25	21.3	2.52	50
15	0.13	21.1	2.52	55
10	0.07	21.1	2.51	60
5	0.03	21.0	2.51	65
0	0.02	21.0	2.51	70

$k = 0.132$ $\gamma = 3.34$

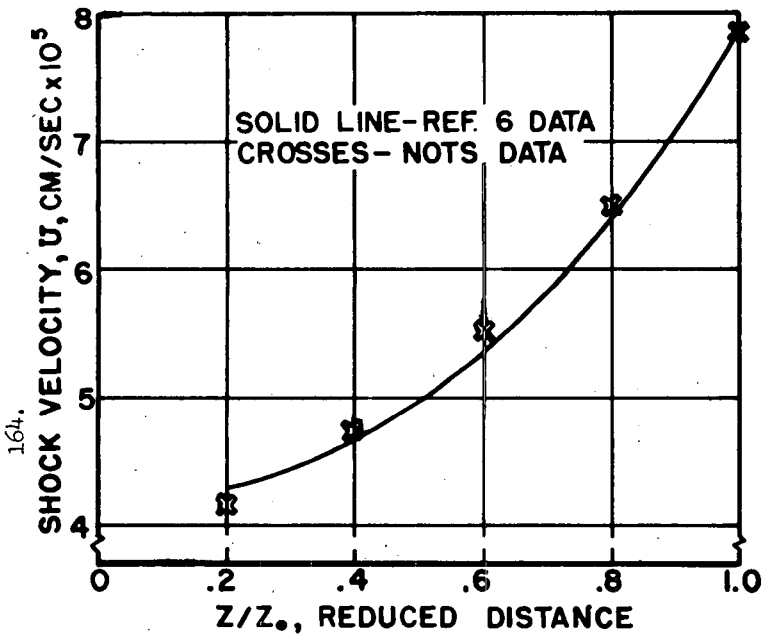

Fig. 1. Shock velocity, U, versus reduced distance Z/Z_0.

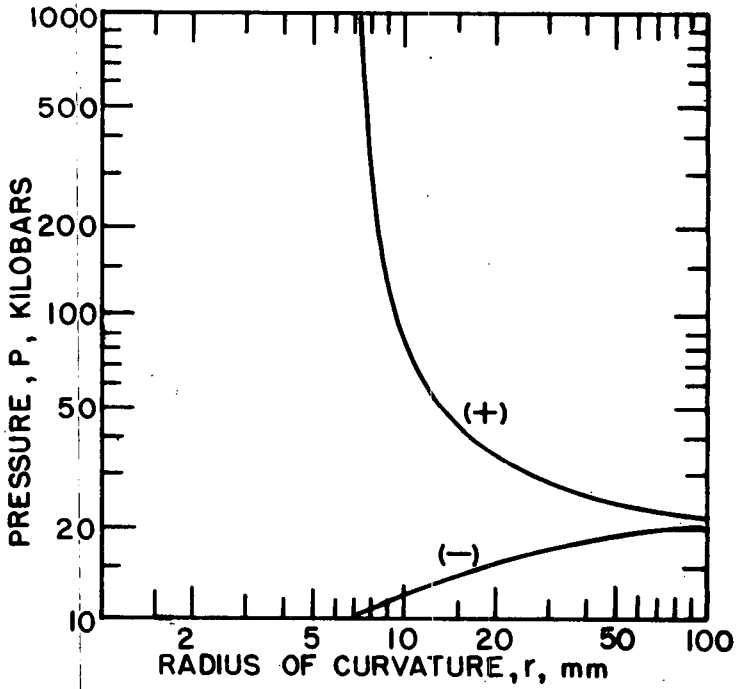

Fig. 2. Shock pressure required to produce an accelerating detonation in Composition B-3 as a function of radius of curvature.

The Heat and Products of Detonation of Cyclotetramethylene tetranitramine (HMX), 2, 4, 6-trinitrotoluene (TNT), Nitromethane (NM), and Bis [2, 2-dinitro-2-fluoro-ethyl] -formal (FEFO)*

Donald L. Ornellas

Lawrence Radiation Laboratory, University of California
Livermore, California

1. INTRODUCTION

Calorimetric measurements combined with product analysis offer a precise method for obtaining fundamental information about the detonation process. This information can then be used to provide normalization and boundary conditions for thermodynamic-hydrodynamic codes that predict explosive performance.

Three pure CHNO explosives and one fluorine containing explosive were investigated. This work is an extension of the work reported[1] for PETN. Jointly, these studies span the range of oxygen balance in explosives that is of greatest interest.

Previous detonation calorimetric work with TNT[2-5] and HMX[6] is not amendable to theoretical interpretation because of the geometries used or the lack of reliable product information. No information concerning the experimental determination of the heat and products of detonation of NM and FEFO has been found in the literature.

2. EXPERIMENTAL

2.1 Apparatus and Operation

The apparatus and its operation have been described; however, some changes have been made.

The thermometric system is a quartz thermometer which has a sensitivity of 1×10^{-4} °C for differential measurements, is easily calibrated, and has direct digital readout.

The heat equivalent of the standard instrument, taken as the average of six calibration runs, was 15, 193 ± 2 cal/°C. The error is the standard deviation of the mean.

Charges are now completely confined by a 1.27-cm thickness of gold. Formerly the ends of the confining cylinder were left open. Since the bottom of the interior of the bomb was most damaged by flying fragments, it was protected by a 0.64-cm-thick, 6.4-cm-diameter stainless steel disc which we replaced after each experiment.

In order to contain NM under vacuum conditions, we sealed the gold cylinder 1.27 cm from each end with a translucent film which is a laminate of 0.025-mm polyethylene and 0.013-mm Mylar. A vacuum-tight seal was obtained by compressing the film between appropriately machined gold surfaces. The weight of film averaged 0.017 g per experiment.

NM was initiated through this film with a 0.75-g PETN booster at a density of 1.71 g/cc. HMX and FEFO were initiated with a 0.3-g booster. No booster was required for the TNT experiments since initiation was effected by means of the detonator alone.

2.2 Explosive Materials

Military specification, grade II HMX was used. Analyses by thin layer

*Work performed under the auspices of the U.S. Atomic Energy Commission.

chromatography showed about 0.5% cyclotrimethylene-trinitramine (RDX) and less than 1% each of an incompletely characterized linear nitramine (compound C) and 1(N) acetal - 3, 5, 7 trinitrocyclotetranitramine (SEX). The melting point was 278-282°C. Charges were machined from billets which had been prepared with a special solvent-pressing technique.

Granular TNT, military specification, grade III was used. Analysis by thin-layer chromatography showed less than 2% impurities. These were identified as 2, 4, 5 TNT, 2, 4 dinitrotoluene and trinitrobenzoic acid. Elemental analyses for carbon, hydrogen, and nitrogen were in agreement with theory for pure TNT within the limits of the analyses. The melting point was 82.0°C. Charges were pressed in increments to a density at which TNT detonates reliably in small diameters.

Commercial grade NM was used. Chromatographic analysis showed a purity of 96.7%. Impurities were nitroethane 0.94%, 2-nitropropane 2.5%, 1-nitropropane 0.03%, and water 0.1% maximum. The empirical formula on which results are based was calculated from the above analyses and adjusted to carbon equals 1.00.

We de-aerated NM to avoid the formation of an air bubble between the booster and liquid when the bomb was evacuated. This was accomplished by subjecting frozen NM to vacuum, sealing the container, and then thawing the NM. This procedure was repeated several times.

FEFO, bis[2, 2-dinitro-2-fluoro-ethyl] -formal was available only in research quantities. It is a liquid with a vapor pressure of about 40 μ at 90°C. The sample was determined to be 94.4% pure by chromatographic analyses. The principle impurity is bis[2, 2-dinitro-2-fluoro-ethyl] -diformal and it contains 0.1% water as received.

Water was removed by vacuum distillation in order to avoid loss of FEFO from the confining cylinder when the calorimeter was evacuated. The expirical formula on which results are based was calculated from elemental analyses and adjusted to carbon equals 5.00.

3. RESULTS and DISCUSSION

3.1 Products from Heavily Confined Charges

Studies[1,2,7] indicate that the products from heavily confined charges represent those found on the Chapman-Jouguet (C-J) isentrope at temperatures in the range of 1500 to 1800°K. Table 1 lists these products and the heats of detonation for HMX, TNT, NM and FEFO.

As one proceeds down the scale of oxygen balance – FEFO, HMX, TNT – the proportion of carbon which appears as solid carbon increases, and which appears as carbon dioxide decreases. Also, the proportion of hydrogen appearing as hydrogen gas increases, and which appears as water decreases. NM, a low-density explosive with a high hydrogen-to-carbon ratio, is the exception to these trends. It has the same oxygen balance as TNT, yet proportionally more carbon appears as carbon monoxide and less as solid carbon than one might expect from the TNT results. In addition, greater amounts of methane are present in the NM products than for any of the other explosives.

It is noteworthy that all of the fluorine in FEFO appears as hydrofluoric acid. Carbon tetrafluoride or other compounds containg the C-F structure were not observed.

The products from heavily confined charges attain equibirium under non-ideal gas conditions since the pressure at 1500 to 1800°K is of the order of 5, 000 to 50,000 atm. In order to calculate the product composition along the C-J isentrope, one must therefore use complex thermodynamic-hydrodynamic calculations. Calculations

were made by using the two best equations of state available, the Becker-Kistiakowsky-Wilson[8] (BKW) equation in the RUBY[9] code, and the LJD[10] equation. The comparisons of observed products with calculated products for the four explosives studied (Tables 2, 3, 4, and 5) are fair. Data of this type will be used to improve equations of state for detonation products.

The ideal experiment to allow isentropic expansion of detonation products is an infinitely long, heavily confined, open-ended charge. For such a configuration end effects would be negligible. However, charge length is limited by the calorimeter dimensions, and end effects are such that some of the detonation products are sufficiently shock heated on colliding with the calorimeter wall to cause re-equilibration. Because of this the ends of the charges were also confined in gold. For oxygen-deficient explosives such as TNT, doing this increases the observed heat of detonation by almost 6%. The change is less for higher oxygen-balanced explosives.

3.2 Products from Unconfined Charges

It has been shown[1] that the temperature at which equilibrium becomes frozen can be found by comparing observed detonation products from unconfined charges with products calculated with ideal gas laws. Work with PETN[1] and the calculations of Jones and Miller[7] indicated a freeze-out temperature of 1500 to 1800°C. Unconfined charges of HMX and TNT were fired and products were compared (Tables 6 and 7) to those calculated. The agreement is good, confirming the earlier work.

The TNT data indicate that solid carbon equilibrates rapidly during the reshocking of products that occurs with unconfined charges. The value for solid carbon, frozen out in the initial isentropic expansion, is 3.65 moles/mole TNT (from Table 1). If it were not equilibrating, the amount found in the products from unconfined charges (1.01 moles/mole TNT, Table 8) should be at least as large as that found in the products from heavily confined charges.

ACKNOWLEDGEMENTS

The author wishes to thank Dr. John W. Kury for his assistance and guidance in the interpretation of results, Dr. Edward L. Lee and Mr. Milton Finger for providing calculations using the BKW equation of state, and Dr. Wildon Fickett (Los Alamos Scientific Laboratory) for providing calculations using the LJD equation of state.

REFERENCES

1. D. L. Ornellas, J. H. Carpenter & S. R. Gunn, Rev. Sci. Instr. 37, 907 (1966).
2. A. Y. Apin, N. F. Velina & Y. A. Lebedev, 2 L. Prik. Mekhan. i. Tkhn. Fiz. 5, 96 (1962).
3. Ministry of Supply, ARE Memo No. 1/51, April 1951.
4. R. Robertson & W. E. Garner, Proc. Roy. Soc. (London) 103A, 539 (1923).
5. ARDE Report (S) 4/56 as quoted by D. Price, Chem. Rev. 59, 801 (1959).
6. H. W. Sexton, ARDE, private communication.
7. H. Jones & A. R. Miller, Proc. Roy. Soc. (London) 194A, 480 (1948).
8. C. L. Mader, Los Alamos Scientific Laboratory, Report LA-2900 (1963).
9. H. B. Levine & R. E. Sharples, Lawrence Radiation Laboratory (Livermore) Report UCRL-6815 (1962).
10. W. Fickett, Los Alamos Scientific Laboratory, Report LA-2712 (1962).

Table 1

The Heat and Products of Detonation of Heavily Confined Charges of Explosives[a,b]

Explosive	HMX	TNT	NM[c]	FEFO[d]
Density (g/cc)	1.89	1.53	1.13	1.60
Charge weight (g)	25	22	15	25
ΔH detonation, 298°K, $H_2O_{(\ell)}$, (cal/g)	1479 ± 5	1093 ± 5	1227 ± 5	1227 ± 5
Products (moles/mole explosive)				
CO_2	1.92	1.25	0.261	3.16
CO	1.06	1.98	0.550	1.88
C(s)[e]	0.97	3.65	0.095	not detected
N_2	3.68	1.32	0.394	1.99
H_2O	3.18	1.60	0.882	2.14
H_2	0.30	0.46	0.294	0.046
HF	0	0	0	1.87[f]
NH_3	0.40	0.16	0.118	0.023
CH_4	0.039	0.099	0.083	0.009
HCN	0.0081	0.020	0.0081	not detected
C_2H_6	0.001	0.004	0.001	not detected

[a]Cylindrical charges, 1.27 cm diameter, confined in 1.27 cm gold.

[b]Corrected for PETN in the initiation system.

[c]NM = $C_{1.00}\ H_{2.96}\ N_{0.96}\ O_{1.92}$ by analysis and adjusted to C = 1.00. Trace amounts of acetylene were observed.

[d]FEFO = $C_{5.00}\ H_{5.74}\ N_{4.09}\ O_{10.06}\ F_{1.87}$ by analysis and adjusted to C = 5.00. Results are corrected for reaction of HF with stainless steel. Charge not confined on the ends.

[e]Determined-by-difference.

[f]From total fluorine contained in FEFO.

Table 2

Comparison of Calculated C-J Isentrope Products with Observed Products from Heavily Confined Charges of HMX

	Moles/mole HMX				
		Calculated			
		BKW C-J Isentrope		LJD C-J Isentrope	
Products	Observed, Heavily Confined	1520°K	1800°K	1490°K	1760°K
N_2	3.68	3.97	3.97	3.98	3.97
H_2O	3.18	3.11	3.67	2.90	3.06
CO_2	1.92	2.39	2.13	2.16	2.01
CO	1.06	0.10	0.071	0.77	0.93
C(s)	0.97	1.13	1.68	0.73	0.81
NH_3	0.40	0.076	0.073	0.047	0.063
H_2	0.30	0.005	0.001	0.36	0.34
CH_4	0.039	0.38	0.11	0.34	0.26
HCN	0.0081	0	0	not allowed	

Table 3

Comparison of Calculated C-J Isentrope Products with Observed Products from Heavily Confined Charges of TNT

	Moles/mole TNT				
		Calculated			
	Observed, Heavily	BKW C-J Isentrope		LJD C-J Isentrope	
Products	Confined	1505°K	1835°K	1500°K	1870°K
C(s)	3.65	3.57	4.50	3.52	3.80
CO	1.98	0.56	0.32	1.60	1.58
H_2O	1.60	1.06	1.87	1.33	1.64
N_2	1.32	1.49	1.48	1.50	1.50
CO_2	1.25	2.19	1.91	1.53	1.39
H_2	0.46	0.043	0.017	0.48	0.40
NH_3	0.16	0.026	0.047	not allowed	
CH_4	0.099	0.68	0.27	0.34	0.23
HCN	0.020	3.6×10^{-6}	1.3×10^{-6}	not allowed	
C_2H_6	0.004	not allowed		not allowed	

Table 4

Comparison of Calculated C-J Isentrope Products with Observed Products from Heavily Confined Charges of NM

	Moles/mole NM				
		Calculated			
	Observed, Heavily	BKW C-J Isentrope		LJD C-J Isentrope	
Products	Confined	1520°K	1835°K	1500°K	1800°K
H_2O	0.88	0.75	0.77	0.81	0.85
CO	0.55	0.18	0.21	0.43	0.48
N_2	0.39	0.47	0.47	0.5	0.5
H_2	0.29	0.049	0.027	0.32	0.29
CO_2	0.26	0.49	0.47	0.38	0.33
NH_3	0.12	0.017	0.027	not included	
C(s)	0.095	0	0	0	0
CH_4	0.083	0.33	0.32	0.19	0.18
HCN	0.0081	0	0	not included	

Table 5

Comparison of Calculated C-J Isentrope Products with Observed Products from Heavily Confined Charges of FEFO

Products	Moles/mole FEFO		
	Observed, Heavily Confined	Calculated BKW C-J Isentrope	
		1520°K	1820°K
CO_2	3.16	3.92	3.82
H_2O	2.14	1.38	1.57
N_2	1.99	2.04	2.03
CO	1.88	0.83	0.85
HF	1.87	1.87	1.85
H_2	0.046	0.045	0.025
NH_3	0.023	0.018	0.026
CH_4	0.0009	0.24	0.16
CF_4	0	0	0.005
C(s)	0	0	0.17

Table 6

Comparison of Calculated Equilibrium Products at Constant Volume with Observed Products from Unconfined Charges of HMX[a]

Products	Moles/mole HMX		
	Observed Unconfined	Calculated for Ideal Gas	
		1500°K	1800°K
N_2	4.01	4.00	4.00
CO	2.65	2.36	2.52
H_2O	2.50	2.36	2.52
H_2	1.53	1.64	1.48
CO_2	1.45	1.65	1.49
HCN	0.0006	0.00002	0.00002
NH_3	not detected	0.0006	0.0002
CH_4	not detected	0.0004	0

[a] 25-g charges at density 1.89 g/cc and 2.54 cm diameter.

Table 7

Comparison of Calculated Equilibrium Products at Constant Volume with Observed Products from Unconfined Charges of TNT[a]

Products	Moles/mole TNT		
	Observed Unconfined[a]	Calculated for Ideal Gas	
		1500°K	1800°K
CO	5.89	5.97	6.00
H_2	2.31	2.10	2.36
N_2	1.36	1.49	1.47
C(s)	1.01	0.81	0.90
H_2O	0.17	0.007	0.003
CO_2	0.063	0.009	0.003
HCN	0.024	0.018	0.056
NH_3	0.022	0.0005	0.0003
CH_4	0.0092	0.192	0.053

[a] 25-g charges at density 1.53 g/cc and 1.27 and 2.54 cm diameter.

QUANTITATIVE INFRARED MULTICOMPONENT ANALYSIS OF MINERALS OCCURRING IN COAL

Patricia A. Estep, John J. Kovach, and Clarence Karr, Jr.

U.S. Department of the Interior, Bureau of Mines,
Morgantown Coal Research Center, Morgantown, West Virginia

INTRODUCTION

The recent development of a new low-temperature ashing technique (12) for obtaining unaltered mineral matter from coal, combined with the extension of the mid-infrared region to 200 cm^{-1}, has shown clearly that infrared spectroscopy is a valuable tool for use in coal mineralogical studies (15). The direct infrared analysis of minerals in coal has been hindered previously by the broad background absorption of the coal itself (11) as shown in Figure 1, curve (b), coupled with the paucity and often nonspecificity of mineral absorption bands in the rock-salt region of 5000 to 650 cm^{-1}. However, when the coal substance, approximately 90% of the sample, is removed at low temperatures in an oxygen plasma (12), there remains unaltered mineral matter with an infrared spectrum exhibiting many diagnostic and analytically useful absorption bands as shown in Figure 1, curve (c). The disappearance of organic absorption bands indicates complete removal of the coal substance. The improved quality of the spectrum obtained on this enriched mineral matter has increased the possibilities for quantitative analysis. In this paper we describe the development of an infrared solid state quantitative analysis for five commonly occurring coal minerals--quartz, calcite, gypsum, pyrite, and kaolinite. The presence of many other minerals in coal in a wide range of concentrations has been shown (6, 9, 16, 28). However, those included in this analysis were selected on the basis of their frequency of occurrence and relative abundance in the coal samples examined in this laboratory. We anticipate that in this continuing broad program using infrared spectroscopy for coal mineralogical studies, qualitative and quantitative analysis can be developed for other minerals.

A large part of the published infrared data for minerals (1, 14, 30) and inorganic compounds (26) is limited to the rock-salt region of 5000 to 650 cm^{-1}. Recently, spectral data in the extended region of 650 to 400 cm^{-1} has been presented for some minerals (31, 37) and down to 240 cm^{-1} for some inorganic compounds (24, 25, 32, 38). However, these collections offer very few high-resolution spectra for naturally occurring minerals to 200 cm^{-1}. The published papers on quantitative infrared analysis of minerals have dealt with a single mineral or the detailed studies of sampling parameters, while very little has appeared on multicomponent mixtures (14, 23).

EXPERIMENTAL

Several specimens of each of the five minerals were obtained from different localities and their infrared spectra checked qualitatively for associated mineral contamination and phase purity by three means: common agreement of the spectra for samples from several sources, literature infrared data, and X-ray powder data. On the basis of this qualitative screening, two sources were

selected for detailed grinding studies in order to establish the infrared absorptivity calibration data. The mineral was placed with an agate ball into an agate vial, approximately one-third full, and ground mechanically in a Spex Mixer Mill. A sample was removed from the vial for infrared analysis at five-minute intervals with a five-minute cooling period. The grinding was continued until measured band absorptivities became constant, at which point a particle size determination was made using a Coulter Counter, Model A (Coulter Electronics). Pellets for the infrared analysis were prepared by weighing one milligram of the pregound mineral and 500 milligrams of cesium iodide powder (Harshaw, 100 to 325 mesh, median particle size 62 μ) on a microbalance and blending by hand for five minutes in a mullite mortar. This mixture was transferred quantitatively to a die and pressed into a pellet according to a triple press method (13). For this the pellet was placed under vacuum, pressed for five minutes at a pressure of 23,000 pounds total load, the pressure relaxed for five minutes, and the procedure repeated twice. The additional pressing steps presumably relieve the strain introduced by the original pressing. The resulting pellet of 0.80 by 13 mm was then scanned immediately on a Perkin-Elmer 621 infrared grating spectrophotometer purged with dry air.

Enriched mineral samples from coal were prepared by low-temperature oxidation at 145° C in an oxygen plasma using Tracerlab's Model LTA-600. Each of the five minerals was exposed to the same ashing conditions as the coal samples. There were no sample alterations, except for the partial dehydration of gypsum to the hemihydrate.

RESULTS AND DISCUSSION

Sampling Parameters

Tuddenham (35) has shown the application of the potassium bromide pellet method to mineral analysis and demonstrated its quantitative potentialities. Most infrared spectroscopists conclude that it is possible to achieve acceptable solid state analysis only with rigorously standardized conditions of sample preparation. The many difficulties encountered in quantitative solid phase spectroscopy have been reviewed by Duyckaerts (10), Kirkland (17), and Baker (5).

Particle Size. Probably the most important single physical factor to be considered in quantitative solid state spectroscopy is that of particle size. This problem has been investigated both theoretically and experimentally by several workers (10, 19, 34, 35). As particle size is reduced there is a reduction of light loss by reflection and scattering and the intensity of an absorption band increases from an apparent absorptivity to its true absorptivity value. Descriptions of this relationship between particle size and absorptivity for the mineral calcite has been given by Lejeune (19) and Duyckaerts (10) and for quartz by Tuddenham (35). Other workers have used the more empirical approach of relating infrared absorptivities to sample grinding time, which is proportional to particle size. The commonly used sedimentation technique for obtaining the required particle size of the sample, while applicable to single component samples, cannot be employed with multicomponent samples (14, 35) since this procedure leads to a differential separation of the individual components. The effects of particle size reduction can vary with different minerals and can vary for absorption bands of different intensities. Kirkland (17) has pointed out that the absorptivities of bands associated with crystallinity

can be more susceptible to particle size variations than those originating from functional group vibrations. These considerations necessitate a careful study of the effects of particle size on absorptivity for each band being considered for quantitative analysis. For this work the expedient method of studying absorptivity as a function of grinding time was chosen. If a strict grinding schedule is followed, particle size need only be determined on those samples ground for lengths of time necessary to produce constant absorptivity values. Thus, knowledge of particle size requirements for constant absorptivities is available with a minimum of effort. A typical example of such a grind study is shown in Figure 2 for the mineral pyrite. The data show that the apparent absorptivity becomes constant after a minimum grinding time and remains constant even with extended grinding and further particle size reduction. The minimum grinding time for a particular mineral can vary with the type of vial used and the amount of sample loaded into the vial. Grind studies on all five minerals reveal that at the minimum grind time, the mean particle size of the sample falls in the range of 4 to 13 microns. This fulfills the theoretical requirement for solid phase spectroscopy, that is, sample particle size should be less than the wavelength of the incident radiation, in order to minimize scattering, reflection, and the Christiansen effect.

While the absorptivities as determined for use in this analysis are constant, they are not necessarily maximum values. Particle size reduction of the cesium iodide matrix can cause band absorptivities to increase markedly. This effect was shown in a grind study in which preground kaolinite was added to samples of cesium iodide, also preground, but for different lengths of time. Each mixture was then hand blended to prepare a pellet according to the chosen procedure. Absorptivities for several kaolinite bands were seen to increase 30 to 50% when prepared with cesium iodide that had been ground for 20 minutes. True absorptivities could not be determined because, at a very fine particle size, cesium iodide pellets crumble. While not recommended for quantitative work, grinding samples for five minutes in a ball mill with cesium iodide is a good technique for improving the qualitative appearance of the spectrum; band resolution improves and background is considerably reduced. The relatively gentle grinding that the cesium iodide receives during the blending stage of pellet preparation reduces its particle size very little as shown by particle size determinations. Since quantitative accuracy is more a function of reproducibility rather than absolute measurement, the relatively simple and highly reproducible method of hand blending was chosen. An additional reason for selecting this method over the technique of mechanical blending in a ball mill is that the cesium iodide mixture packs in the vial and is not quantitatively recoverable.

Sample Alteration. Extensive grinding can cause polymorphic transformations or alteration of mineral composition. For example, Dachille (8) has shown that a few minutes grinding in a Wig-L-Bug with a metal vial and ball can transform calcite to the high-pressure phase of aragonite. He assigns this transformation to a pressure component in the mechanical action of the vibrator. Burns (7) also studied this calcite-aragonite transformation and found that it can occur by grinding at room temperature. Morris (27) found that vibrating for more than one minute in a stainless-steel Wig-L-Bug will cause dehydration of gypsum. Liberti (20) has reported destruction of the crystalline structure of quartz under certain grinding conditions. We have noted changes in the spectrum of kaolinite after it was subjected to severe grinding conditions. However, none of these

alterations were observed by using the chosen procedure, presumably due to the periodic cooling periods during grinding and to the use of an agate grinding ball mill. Since the density of agate is about one-third the density of stainless steel, there is less mechanical stress exerted on the sample in this vial. The absorptivity values of some absorption bands began to decrease with prolonged grinding, although no qualitative spectral changes occurred. Since some form of sample alteration occurred, these bands were not selected for use in the quantitative analysis.

Particle Distribution. If Beer's law is to be followed, all absorbances must show a linear dependence on effective concentration. The concentration is considered effective because the infrared beam does not completely cover the entire pellet in the instrument. The use of sample weight as a concentration factor thus requires a high degree of uniform dispersion, or a homogeneous mixture of sample and matrix. This can be achieved if particle size is small and if blending is thorough. In the instrument used, the infrared beam covers about 50% of the pellet area. As a test of the dispersion achieved with the chosen sample preparation technique, pellets of each of the five minerals were rotated systematically through 360° with scans taken at several settings. For all positions, the band intensities were identical, indicating that dispersion is adequate, and also that there are no polarization or orientation effects.

Choice of Matrix. Several salts were tested for use as a matrix. Cesium iodide appeared to be the best choice on the basis of its superior transparency at long wavelengths. The low background at shorter wavelengths due to scattering was not objectionable since most of the useful absorption bands for minerals are found at longer wavelengths. The triple press method reduced scattering at short wavelengths, often as much as 40% over single pressing. The over-all transmission of a blank cesium iodide pellet was acceptable, as shown in Figure 1, curve (a), and therefore no pellet was used in the reference beam. Although cesium iodide is slightly hygroscopic, there was less difficulty from water adsorption than is generally experienced using the more common potassium bromide matrix. While mechanical grinding of cesium iodide intensified the water absorption bands, hand blending produced no more than 0.02 absorbance units at the 3430 cm^{-1} OH stretching frequency. This behavior of cesium iodide has a decided advantage since coal minerals often have useful OH absorption bands.

The pellet thickness must be controlled in order to prevent interference or fringe patterns. In the longer wavelength region where the requirements for parallel pellet surfaces are relaxed, these fringe patterns can become quite pronounced on thin pellets. In order to eliminate this as a potential source of quantitative error, pellets at least 0.80 mm thick were used.

Other Parameters. There are other sampling problems sometimes encountered in solid state analysis. Among these is interaction of the sample with the matrix, believed to be negligible for the minerals analyzed here. A large refractive index difference between the sample and the dispersion medium can cause a pronounced Christiansen effect, characterized by the asymmetrical shape of an absorption band, and resulting in high light scattering which can introduce errors into quantitative measurements. However, the small particle size used should minimize any error arising from this effect. Departure from Beer's law is possible, but with the base line technique for absorbance measurements and with

controlled particle size, Beer's law was obeyed for concentration ranges of 0.02 to 0.2 wt-pct. One of the limitations in the quantitative analysis of minerals and inorganics is due to their inherently high band absorptivities. With intense absorption, only a very small amount of sample can be included in the pellet, so that the band will still be measurable, thus increasing weighing errors. However, reproducible results could be obtained with a microbalance and a large area of beam coverage of the pellet.

Qualitative Analysis

Since natural mineral specimens, which were used as standards in this analysis, often occur in polymorphic aggregations, it was necessary to determine the qualitative infrared spectral differences for polymorphs of each mineral. In the coal samples thus far investigated no polymorphic mixtures were encountered, although they can be expected. Table 1 lists the spectral data from this laboratory for each of the five minerals and some polymorphic forms.

Quartz. The two quartz samples used as standards, for which bands are presented in Table 1 and absorptivity data in Table 2, are both low-temperature α-quartz. This was established from differences shown in the infrared spectra of samples of polymorphs of crystalline silica in this laboratory, from literature data (21, 33, 39), and from X-ray powder data. The α-quartz form can be distinguished in the 650 to 200 cm^{-1} region from the polymorphic forms of α-tridymite and α- and β-cristobalite. Work remains to confirm the distinction of α-quartz from β-quartz and β-tridymite. The distinction of α-quartz from its crystalline polymorphs and other modifications of silica can be made by the highly unique bands at 256, 363, 388, and 688 cm^{-1}.

Calcite. The natural aggregation of calcite and its dimorph aragonite is common (3). Infrared literature data (2, 3) in the rock-salt region show that hexagonal calcite can be distinguished from orthorhombic aragonite. The data from our laboratory in Table 1 show the marked difference in their spectra and list the additional bands obtained for the region 650 to 200 cm^{-1}. Petrographic distinction between these two polymorphs is often inadequate as shown by the fact that three of our samples labeled aragonite were shown by infrared to be calcite. Adler (3) found that several specimens of aragonite and calcite differed from their museum labels.

Gypsum. For gypsum (monoclinic), it was necessary to show that the crystallographically different anhydrite (orthorhombic), often found in coal, and the hemihydrate (hexagonal, $CaSO_4 \cdot 1/2H_2O$), can be differentiated in the infrared for the preliminary qualitative analysis of the sample. Data from Morris (27) and from our laboratory, in Table 1 show that the hemihydrate has unique bands and can be differentiated from gypsum. These spectral differences were used to show that the low-temperature oxidation technique produced a conversion of gypsum to the hemihydrate. Gypsum was selected for testing in synthetic mixtures since it has been identified and analyzed in coal product samples not subjected to low-temperature ashing. Anhydrite is also readily distinguishable from gypsum. The primary difference is a splitting of the large, broad band of gypsum at 594 cm^{-1} into two sharp bands at 587 and 607 cm^{-1} for anhydrite. The 660 cm^{-1} band of

Table 1. - Infrared Absorption Bands for Minerals

Mineral	Absorption bands, cm^{-1} *
α-Quartz	256 (w), 360 (mw), 388 (mw), 452 (m), 465 (w, sh), 501 (mw), 688 (w), 772 (mw), 790 (m), 1075 (s), 1135 (w), 1160 (w)
α-Tridymite (synthetic)	465 (s), 500 (sh), 782 (m), 1088 (s), 1155 (sh)
α-Cristobalite**	485 (s), 515 (sh), 620 (m), 798 (m), 1104 (s), 1160 (sh), 1204 (w)
Calcite	217 (m), 337 (sh), 307 (s), 707 (m), 842 (vw), 869 (m), 1420 (s), 1600 (w), 1792 (vw)
Aragonite	205 (sh), 245 (s), 288 (sh), 692 (m), 705 (m), 836 (w), 850 (m), 1076 (w, sharp), 1450 (sh), 1464 (s), 1600 (w), 1780 (w)
Gypsum	215 (m), 298 (mw), 412 (w), 445 (w), 594 (m), 660 (m), 998 (vw), 1106 (s), 1132 (s), 1155 (s, sh), 1615 (m), 1680 (mw), 3250 (vw), 3400 (m), 3492 (sh, vw), 3550 (m)
Hemihydrate of $CaSO_4$	235 (m), 250 (sh), 412 (w), 455 (w), 590 (m), 605 (sh, w), 619 (w), 652 (m), 665 (sh, w), 1000 (mw, sharp), 1008 (vw, sh), 1090 (s), 1110 (s), 1128 (s), 1147 (s), 1613 (mw), 3552 (w), 3610 (mw)
Anhydrite	252 (m), 502 (vw), 587 (m), 606 (m), 669 (m), 875 (vw), 998 (vw), 1008 (vw), 1115 (s), 1148 (s)
Pyrite	284 (w), 340 (m), 391 (vw), 406 (s)
Marcasite	285 (w), 321 (m), 350 (m), 396 (s), 407 (s), 422 (vw)
Kaolinite	268 (m), 338 (m), 352 (vw, sh), 405 (vw, sh), 422 (m), 460 (s), 528 (s), 689 (m), 747 (w), 782 (w), 908 (s), 929 (w, sh), 1002 (s), 1026 (s), 1095 (s), 3622 (m), 3652 (w), 3670 (vw), 3698 (m)

* Very weak = vw; weak = w; medium = m; strong = s; shoulder = sh.
** Data from reference (21).

Table 2. - Analytical Absorption Bands and Absorptivities for Minerals

Mineral	Source	Absorption bands, cm^{-1} and absorptivities, 1/mm*
Quartz	Hot Springs, Ark.	360 (448), 388 (525), 452 (1010), 790 (589)
	Rock crystal Ward's Natural Science Establishment, Inc.	
	Berkeley Springs, W. Va. . .	360 (430), 388 (500), 452 (970), 790 (580)
	Oriskany sandstone W. Va. University Geology Department	
Calcite	Germany Valley, W. Va. . .	307 (720), 869 (610), 1420 (2050)
	Crystals W. Va. University Geology Department	
Gypsum . . .	Niagara, N. Y.	594 (245), 660 (251)
	Crystals U. S. National Museum, No. 80022	
	Washington County, Utah . . .	594 (246), 660 (254)
	Crystals Ward's Natural Science Establishment, Inc.	
Pyrite	Park City, Utah	340 (190), 406 (630)
	Ward's Natural Science Establishment, Inc.	
	Gilman, Eagle County, ... Colo.	340 (180), 406 (640)
	Minerals Unlimited	
Kaolinite . .	Macon, Ga., Oneal Pit	338 (353), 422 (505), 460 (986), 528 (1106), 689 (338), 747 (131), 908 (617)
	API Reference Clay Mineral Kaolinite No. 4 Ward's Natural Science Establishment, Inc.	

* Absorptivities in parentheses.

gypsum shifts to 669 cm^{-1} in anhydrite, and the water vibrations appearing at 1615, 1680, 3400, and 3555 cm^{-1} are unique for gypsum. Data in Table 1 also show the differences between the hemihydrate and anhydrite.

Pyrite. Both polymorphs of FeS_2, pyrite and marcasite, have been identified in coal (6, 9, 36). White (37) has presented infrared data to 400 cm^{-1} which is insufficient for differentiation between these two polymorphs. However, the infrared spectra to 200 cm^{-1} obtained on samples in this laboratory show that these two polymorphs are distinguishable in this region. Table 1 shows that, although marcasite exhibits two bands common to pyrite, there are four distinctly different bands which uniquely characterize this polymorph. Further, the band at 340 cm^{-1}, which is unique for pyrite, allows detection of pyrite in marcasite samples. These infrared differences, along with X-ray confirmation, established the phase purity of the pyrite standards selected for calibration and thus also the qualitative identification of pyrite as the observed form occurring in the coal samples studied. It was particularly important to establish by X-ray that no pyrrhotite (FeS) was present in the standard samples since this mineral has no absorption in the entire 5000 to 200 cm^{-1} region. Optical examination is also often unreliable for this mineral class since out of 15 different mineral specimens labeled marcasite, two were pyrrhotite, six were pyrite, and only seven were actually marcasite as shown by infrared analysis.

Kaolinite. Clays other than kaolinite are found in coal. Kaolinite can be identified by infrared in mixtures of clay minerals and even in mixed-layer clay minerals (29). Montmorillonite, illite, and kaolinite predominate in many coals and Angino (4) has discussed the infrared spectral differences among these out to 90 cm^{-1}. The OH region is especially useful in the qualitative identification of kaolinite. Kodama (18) states that the absorption band at 3698 cm^{-1} can distinguish kaolinite from other clay minerals down to a few weight-percent of kaolinite in total amounts of clay minerals. Lyon (22) has shown that the use of ratios for bands appearing in the OH region, along with other spectral differences, enables a unique distinction to be made among the kaolin group minerals of kaolinite, dickite, and halloysite. This literature data, and data obtained in our laboratory from a number of API reference clay minerals, were used to substantiate the identification of kaolinite in the coal low-temperature ash samples and as a guide in the selection of bands for quantitative analysis.

Quantitative Analysis

The apparent absorptivity of a band was calculated from the relationship:

$$a = \frac{A}{b\,c}$$

where a = absorptivity in units of 1/mm;
A = absorbance of the band (baseline technique);
b = pellet thickness, mm;
c = concentration, weight-percent.

The value of absorptivity is specific for a 13 mm diameter pellet.

After completion of grind studies for each mineral, bands were selected for quantitative analysis. These selections were based on both their specificity and the constancy of their absorptivities with prolonged grinding. Table 2 lists the bands selected for analysis. When it is necessary, for the sake of specificity, to use a band which does not remain constant with particle size reduction beyond the minimum grind time, the error introduced must be considered.

Only one source for kaolinite was used for the calibration data because there is extensive mineralogical data for it in the literature. The data in Table 2 are the results of duplicate grind studies that were quite reproducible. Only one source of calcite was used because of the wide variation of absorptivity values from different sources, even though their spectra were qualitatively identical and their particle sizes were the same. Therefore, calcite from the same source was used for synthetic mixtures and for calibration data in order to obtain agreement. Additional work is required to resolve this limitation by examination of these samples by other analytical techniques in order to determine the cause for such a variation.

Several synthetic mixtures, listed in Table 3, were prepared to test the accuracy of the multicomponent analysis. Preground standard mineral samples of the required particle size were used and the same technique for pellet preparation used as described for the mineral standards. The concentration ranges of the pure minerals were selected to represent the concentration ranges commonly encountered in the coal samples examined. No attempt was made to determine the limit of detectability for each mineral since this was different for different sample compositions. Figure 3 shows the infrared spectrum of synthetic mixture No. 7, which approximated the composition of a typical coal low-temperature ash as shown in Figure 1, curve (c), except for the gypsum-hemihydrate conversion. When band overlapping occurred, the required absorbance correction was obtained from the standard spectra of the interfering mineral, using the standard procedures for quantitative analysis. An expedient technique of chart overlay to obtain background and band overlapping corrections was as accurate as the more time consuming procedure of matrix solution. The agreement shown in Table 3, within an average error of 6.2% for all minerals, demonstrates the method to be satisfactory for the multicomponent mixtures investigated. It is difficult, without an independent reliable method of analysis, to determine the accuracy limits of the infrared method when applied to coal ash samples. Greater accuracy is expected with the synthetic mixtures since they were prepared under controlled conditions of particle size and contained no unknown interferences. In our work it was necessary to pregrind coal samples to speed oxidation in the low-temperature asher. This pregrinding was sufficient to achieve the required particle size reduction for an accurate quantitative analysis, as ascertained by particle size measurements on the ash. Optimum particle size was also indicated for at least the mineral kaolinite from a grind study using its bands that appear fairly well resolved in the spectrum of the total coal sample (see Fig. 1). Grind curves similar to those in Figure 2 were obtained with a relatively small increase in absorptivity before becoming constant. It is essential to conduct a grind study on any mineral mixture prior to analysis in order to establish when the required particle size reduction for each component in the mixture has been achieved. The infrared analysis should be made only after absorptivity values have become constant and particle size has been checked.

Table 3. - Analysis of Synthetic Mixtures of Minerals

Synthetic mixture no.	Kaolinite, %		Quartz, %		Gypsum, %		Calcite, %		Pyrite, %	
	Calc.	Found	Calc.	Found	Calc.	Found	Calc.	Found	Calc.	Found
1	71.86	72.70	28.14	27.10						
2	69.60	71.15	30.40	29.13						
3	53.10	43.71	23.17	19.65	23.72	20.10				
4	41.53	41.04	19.29	19.33	39.18	33.50				
5	54.63	55.18	18.51	19.68	26.85	26.98				
6	29.92	29.39	12.50	11.53	47.32	48.10	10.26	10.31		
7	35.72	31.11	24.11	20.77	31.69	30.78	8.48	10.24		
8			12.21	14.22	33.07	31.13	12.20	12.40	42.52	44.92
9			22.90	19.00	31.30	31.20	8.40	7.00	37.40	30.00
10			15.20	12.00	30.50	30.80	10.60	11.30	43.00	35.12
Average error	2.6		1.9		1.7		0.8		5.9	

A limitation of the application of infrared spectroscopy to mineral mixtures in coal is in the analysis of pyrite in the presence of high amounts of kaolinite (15). Both of the analytical bands of pyrite are overlapped considerably by kaolinite bands and amounts of pyrite as high as 20% might be undetected when kaolinite is present to the extent of 30% or greater. For this reason, no attempt was made to analyze synthetic mixtures containing both. Work is continuing to develop a satisfactory analysis for kaolinite-pyrite mixtures when kaolinite content is high.

CONCLUSIONS

This paper describes the development of a quantitative infrared multicomponent analysis for five minerals commonly occurring in coal. It shows that a successful analysis for quartz, calcite, gypsum, pyrite, and kaolinite is possible if sampling conditions are controlled. The infrared region of 650 to 200 cm^{-1} is seen to contain data that contribute to both the preliminary qualitative and the quantitative analysis of these mixtures. The accuracy of the method was evaluated with tests on synthetic mixtures. Average errors were within 6.2% for all five component minerals. Although the method was primarily applied to the analysis of unaltered mineral matter obtained from coal by use of the new technique of low-temperature ashing in an oxygen plasma, the calibration data obtained can be used in the analysis of other materials connected with the mining and utilization of coal. For example, we have determined these minerals directly in coal mine refuse samples, which often have low organic matter content. The development of the analysis revealed that infrared spectroscopy is a valuable tool for differentiating among various polymorphic mineral forms and provides a collection of high resolution standard reference spectra for naturally occurring minerals and their polymorphs to 200 cm^{-1}.

ACKNOWLEDGMENT

Special thanks are due to Edward E. Childers for assistance in obtaining infrared spectra, and to Dr. John J. Renton, Geology Department, West Virginia University, for providing X-ray data on the mineral samples.

REFERENCES

1. Adler, H. H., E. E. Bray, N. P. Stevens, J. M. Hunt, W. D. Keller, E. E. Pickett, and P. F. Kerr, Am. Petrol. Inst., Project 49, Preliminary Rept. No. 8, July 1950, 146 pp.

2. Adler, H. H., and P. F. Kerr, Am. Mineralogist 48, Nos. 1-2, 124 (1963).

3. _____. Am. Mineralogist 47, Nos. 5-6, 700 (1962).

4. Angino, E. E., Nature 204, No. 4958, 569 (1964).

5. Baker, A. W., J. Phys. Chem 61, No. 4, 450 (1957).

6. Brown, H. R., and D. J. Swaine, J. Inst. Fuel 37, No. 285, 422 (1964).

7. Burns, J. H., and M. A. Bredig, J. Chem. Phys. 25, No. 6, 1281 (1956).

8. Dachille, F., and R. Roy, Nature 186, No. 4718, 70 (1960).

9. Durie, R. A., Fuel 40, No. 5, 407 (1961).

10. Duyckaerts, G., Analyst 84, 201 (1959).

11. Friedel, R. A., and J. A. Queiser, Anal. Chem. 28, No. 1, 22 (1956).

12. Gluskoter, H. J., Fuel 44, No. 4, 285 (1965).

13. Harshaw Chemical Co., Pressed Pellet Techniques, Data Sheet 023.

14. Hunt, J. M., and D. S. Turner, Anal. Chem. 25, No. 8, 1169 (1953).

15. Karr, C., Jr., P. A. Estep, and J. J. Kovach, Chem. Ind. (London) 9, 356 (1967).

16. Kemezys, M., and G. H. Taylor, J. Inst. Fuel 37, No. 285, 389 (1964).

17. Kirkland, J. J., Anal. Chem. 27, No. 10, 1537 (1955).

18. Kodama, H., and K. Oinuma, Proc. Nat. Conf. on Clays and Clay Minerals, 11th, Canada, 236 (1962).

19. Lejeune, R., and G. Duyckaerts, Spectrochim. Acta 6, 194 (1954).

20. Liberti, A., and G. Devitofrancesco, Staub. 25, No. 4, 28 (1965).

21. Lippincott, E. R., A. VanValkenburg, C. E. Weir, and E. N. Bunting. J. Res. Natl. Bur. Std. 61, No. 1, 61 (1958).

22. Lyon, R. J. P., and W. M. Tuddenham, Nature 185, No. 4716, 835 (1960).

23. Lyon, R. J. P., W. M. Tuddenham, and C. S. Thompson, Econ. Geol. 54, 1047 (1959).

24. McDevitt, N. T., and W. L. Baun, Tech. Doc. Rept. No. RTD-TDR-63-4172, AF Materials Lab., Wright-Patterson Air Force Base, Ohio, Jan. 1964, 77 pp.

25. Miller, F. A., G. L. Carlson, F. F. Bentley, and W. H. Jones, Spectrochim. Acta 16, Nos. 1-2, 135 (1960).

26. Miller, F. A., and C. H. Wilkins, Anal. Chem. 24, No. 8, 1253 (1952).

27. Morris, R. J., Jr., Anal. Chem. 35, No. 10, 1489 (1963).

28. Nelson, J. B., Brit. Coal Util. Res. Assoc., Monthly Bull. 17, No. 2, 41 (1953).

29. Oinuma, K., and H. Hayashi, Am. Mineralogist 50, 1213 (1965).

30. Omori, K., Sci. Rept. Tohoku Univ., Third Ser. 7, No. 1, 101 (1961).

31. _____. Sci. Rept. Tohoku Univ., Third Ser. 9, No. 1, 65 (1964).

32. Sadtler Research Laboratories, High Resolution Spectra of Inorganics and Related Compounds, Vols. 1 and 2.

33. Saksena, B. D., Proc. Symp. Raman and Infrared Spectry., Nainital, India, 93 (1959).

34. Stewart, J. E., J. Res. Natl. Bur. Std. 54, No. 1, 41 (1955).

35. Tuddenham, W. M., and R. J.P. Lyon, Anal. Chem. 32, No. 12, 1630 (1960).

36. Whelan, P. F., J. Inst. Fuel 27, No. 164, 455 (1954).

37. White, W. B., and R. Roy, Am. Mineralogist 49, Nos. 11-12, 1670 (1964).

38. Yoganarasimhan, S. R., and C. N. R. Rao, Chemist-Analyst 51, 21 (1962).

39. Zarzycki, J., and F. Naudin, Ch. in Advances in Molecular Spectroscopy, Proc. Intern. Meeting on Molecular Spectry., 4th, Bologna and Rome, 1959, ed. by A. Mangini. The Macmillan Co., New York, vol. 3, 1071 (1962).

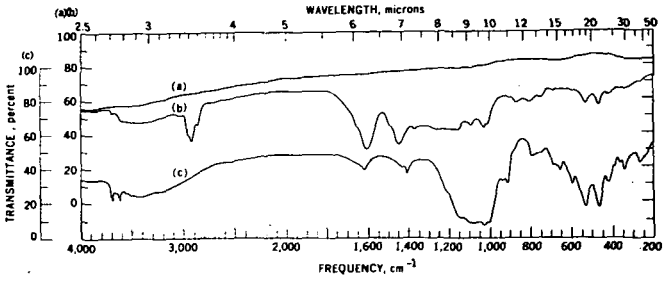

FIGURE 1. - Infrared Spectra of (a) Cesium Iodide, (b) Pittsburgh-seam Coal, and (c) Low-temperature Ash from Pittsburgh-seam Coal.

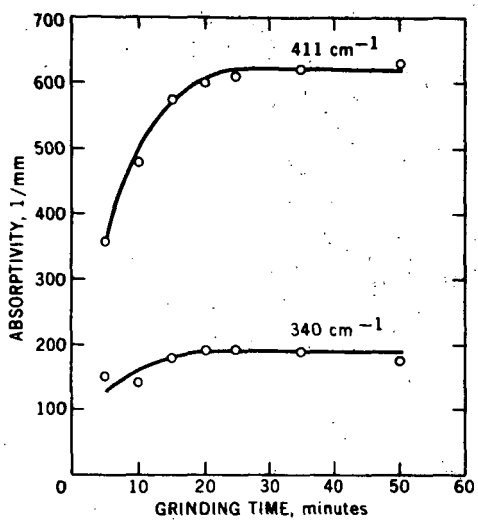

FIGURE 2. - Absorptivity as a Function of Grinding Time for Pyrite, in an Agate Vial.

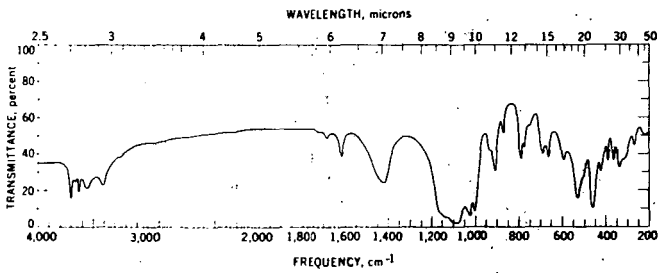

FIGURE 3. - Synthetic Mixture of Kaolinite, Calcite, Gypsum, and Quartz.

Aromatic Ring Proton Determination by Infrared Intensity Measurement in the 1650-2000 Wavenumber Region

Arthur S. Wexler

Dewey and Almy Chemical Division
W. R. Grace & Co.
Cambridge, Massachusetts 02140

The infrared absorption spectra of aromatic compounds in the 1650-2000 cm^{-1} region are well known to be characteristic of ring substitution pattern (5). The observed frequencies in benzene derivatives have been assigned to overtones and combinations of =CH out-of-plane deformations (4). The absorption in this region has been employed for the determination of total aromatics in petroleum distillates (2). Most compounds with =CH out-of-plane deformation vibrations in the 750-1000 cm^{-1} region may also be expected to exhibit absorption bands due to overtones and combination tones in the 1650-2000 cm^{-1} region and such is the case for polynuclear hydrocarbons (3) and olefinics (1). In the course of a survey of the absorption of aromatics at equimolar concentration in carbon tetrachloride, it was observed that the integrated intensity over the entire absorption band complex in the 1650-2000 cm^{-1} region appeared to be a monotonic function of number of aromatic ring protons. This observation prompted a detailed study of the relationship between integrated intensity and aromatic structure which is reported in this paper.

Experimental

All compounds were apparently of sufficient purity so as to be used as is, without purification. Spectra were obtained, where solubility permitted, at 0.5 molar concentration in carbon tetrachloride, in path lengths of 0.5 to 2 mm., with solvent compensation in the reference beam. A few samples were run "neat" in 0.1 or 0.2 mm. cell paths. Compounds of limited solubility were analyzed at a path length of 5 mm. Spectra were obtained in all cases on a Beckman IR-12 infrared spectrophotometer flushed with dry air to remove all but traces of water vapor. Spectra were run in absorbance on a 2x abscissa scale at moderately high resolving power to permit resolution of closely overlapping bands. Areas under the absorption bands were measured with a planimeter. Baselines were usually drawn parallel to the abscissa to intercept the absorption at 2000 cm^{-1}. Integrated intensities were calculated in practical units, cm^{-1} ℓ $mole^{-1}$, log 10 basis.

Results

Spectra in the 1650-2000 cm^{-1} region of aromatic hydrocarbons (0.5 molar, 0.5 mm path), selected to illustrate the characteristic absorption intensities as a function of ring type and substitution, are shown in Figure 1. These spectra are facsimile presentations which also can be used as a guide to determination of ring type or substitution. Obviously the total absorption varies markedly with degree of substitution. Integrated intensities for a group of aromatic hydrocarbons, selected to represent all the twelve possible classes of substituted benzenes, along with values for some dinuclear, trinuclear and condensed ring systems, are listed in Table I by individuals, and in Table II by averages for ring type. The most obvious variable appears to be the ring proton concentration, or number of =CH oscillators per ring. The relationship between integrated intensity and ring proton concentration appears to be monotonic, as shown in Figure 2. A linear relationship between intensity and ring proton concentration was observed for phenyl rings (benzene derivatives and polyphenyls), as shown in Figure 3. The plot for phenyls does not run into the origin, which suggests that some other type of vibration is making a constant contribution per phenyl ring to the total intensity in the combination band region. Polynuclear hydrocarbons fall on a line with a steeper slope, which does

extrapolate to the origin. Substituted naphthalenes and dinuclear heterocyclics appear to fall on a line of intermediate slope, but there are insufficient data on this group at the present to justify a strictly linear plot. Assuming that the absorption in hexasubstituted benzenes is a constant measure of skeletal or other phenyl ring vibrations, a fairly constant intensity of about 100 (cm^{-2} ℓ $mole^{-1}$) per proton in pendent phenyl rings and 75 per proton in interior rings is obtained in the polyphenyls as shown in Table III. In the polyphenyls only the terminal phenyl rings are considered to be pendent while the remaining interior phenyl rings are assumed to contribute only combination tones of =CH oscillators in the 1650-2000 cm^{-1} region.

The effects of some polar and other ring substituents on the aromatic absorption intensity in this region are listed in Table IV. Olefinic double bonds display overtones in this region, as exemplified by the spectrum of styrene with an increased absorption at 1820 cm^{-1} compared with its brominated derivative, shown in Figure 4. The intensity per olefinic =CH oscillator is approximately equal to an aromatic =CH oscillator.

Additional bands are observed in the spectra of monosubstituted benzenes in solution in an inert solvent, as shown in Figure 5, for pure tert. butylbenzene and for a 10-fold dilution in carbon tetrachloride run at equivalent pathlengths times concentration. The two highest frequency bands split into doublets. A suggested assignment for each of these doublets (which were observed in the spectra of nearly all monosubstituted benzenes) as combinations of fundamentals is given for a few cases in Table V. At sufficiently high resolution some splitting can be observed even in undiluted compounds (dotted line of Figure 5).

Discussion

There appears to be little doubt that the integrated absorption intensity of aromatic hydrocarbons in the 1650-2000 cm^{-1} region is a monotonic function of the ring proton concentration, as depicted in Figure 2. This observation is at variance with the apparent constancy per ring, independent of degree of substitution, reported by Bomstein (2) for a number of alkylbenzenes. Bomstein's data, however, does show a significant variation of intensity with substitution. His K values for benzene/mono/di/trialkylbenzenes are in the ratio of 1.6/1.2/1.06/1.0, compared with ratios of integrated intensities in this paper of 1.7/1.35/1.15/1.0. (Differences between the two sets may reflect differences in integration range, background assumptions, types of compounds and instrument performance.) Bomstein stated that naphthalenes have different, presumably higher, K values, reflecting perhaps a higher ring proton concentration. Therefore, the apparent constancy observed by Bomstein for absorption in the 1700-2000 cm^{-1} region independent of degree of substitution holds only because his data were restricted to a relatively narrow range of ring proton concentration, perhaps 1.5 to 2 fold, compared with the 12-fold range explored in this study.

There also appears to be little doubt that the absorption due to phenyl rings is a linear function of ring proton content in both mononuclear hydrocarbons and polyphenyls, as shown in Figure 3. The intersection of this plot above zero on the ordinate can be interpreted as evidence of a background absorption of about 130 cm^{-2} ℓ $mole^{-1}$, associated with ring skeletal vibrations in pendent phenyl rings. The total 1650-2000 cm^{-2} absorption in m-quinquephenyl, for example, consists of a contribution of 260 cm^{-2} ℓ $mole^{-1}$ for the two pendent rings, plus a contribution of approximately 75 cm^{-2} ℓ $mole^{-1}$ for each ring proton, or a total intensity of 1910 cm^{-2} ℓ $mole^{-1}$, compared with an observed value of 2080. A linear plot of the 1650-2000 cm^{-1} absorption intensity against ring proton concentration which extrapolates to zero (Figure 3) was observed for polynuclear hydrocarbons and condensed ring systems, which suggests that all the intensity in this region in constrained ring systems is due to ring protons, with an average

intensity per proton of about 130 cm^{-2} ℓ $mole^{-1}$. For example the integrated absorption intensity of 20-methylcholanthrene in the 1650-2000 cm^{-1} region was found to be 1168 cm^{-2} ℓ $mole^{-1}$ (Table I), equivalent to a value of 8.9 aromatic protons per molecule, compared with a formula value of 9.

Rubrene would present a complex case, since it contains 4 phenyl rings attached to a naphthacene skeleton. If the intensity relations in Table II apply to this compound (not yet measured) the lower and upper limits of numbers of aromatic protons per molecule would be estimated by infrared to be 24 to 30, compared with a formula value of 28. A reasonable expectation is the determination of aromatic protons (provided the molecular weight is known) to within $\pm$ 10% of the formula value of the infrared technique of this paper.

On the basis of integrated intensity measurements, it appears reasonable to include a band near 1620-1640 in para alkylbenzenes with the combination tones. Its inclusion on a frequency basis has already been justified by Whiffen(4).

Sharpening of peaks and splitting of bands were observed for monoalkylbenzenes and other aromatics, as depicted in Figures 1 and 5. The total 1650-2000 cm^{-1} intensity was found to be essentially constant in the range 0.5 molar to 6 molar (approximately 10 times diluted, and undiluted). In the monosubstituted benzenes the two highest frequency bands of the 1650-2000 cm^{-1} set, near 1860 and 1945 cm^{-1}, have been designated as i+h and h+j, summation tones by Whiffen (4). Under sufficiently high resolution partial splitting of one or both of these bands can be observed. More complete splitting was observed in non-interacting solvents such as hexane, carbon tetrachloride and carbon disulfide and the peaks were found to be narrower. The 1865 cm^{-1} peak of monoalkylbenzenes apparently is an i+h summation band but the three remaining peaks at 1880, 1938 and 1955 cm^{-1} appear to be, respectively, i+j, 2h and 2j bands. Little or no splitting was observed in solutions in chloroform and methylene chloride. Presumably the acidic hydrogen in these solvents (and the ring proton of undiluted aromatics) is able to complex with the π electron orbitals of the monosubstituted benzene ring in such a way as to cause the split bands to overlap and merge into broader bands.

It is possible to estimate the aromatic proton content of compounds (benzenoid and heterocyclics) from the infrared absorption intensity in the 1650-2000 cm^{-1} region using average intensities (cm^{-2} ℓ $mole^{-1}$) for each ring proton of 100 for mononuclear, 120 for dinuclear, and 130 for polynuclear hydrocarbons. The number of ring protons is then the total 1650-2000 cm^{-1} intensity divided by the appropriate unit value. As in any spectroscopic measurement, the molecular weight must be known to carry out the analysis. Interference by olefins can be handled by selective bromination or hydrogenation. The intensity of styrene (which contains a conjugated double bond) in this region was found to be equivalent to 7 protons. After bromination (cf. Figure 4) the intensity was observed to be equivalent to 5 protons, demonstrating selective disappearance of an interfering group without disturbing the ring proton contribution.

Literature Cited

(1) Bellamy, L. J., "The Infrared Spectra of Complex Molecules," Wiley, New York, 1958.
(2) Bomstein, J., Anal. Chem. 25 1770 (1953).
(3) Fuson, N. and Josien, M. L., J. Am.Chem. Soc. 78 3049 (1946).
(4) Whiffen, D. H., Spectrochim. Acta 7 253 (1955).
(5) Young, C. W., DuVall, R. B., Wright, N., Anal. Chem. 23 709 (1951).

Table I. Integrated Intensities (cm^{-2} ℓ $mole^{-1}$) of Aromatic Hydrocarbons in the 1650-2000 cm^{-1} Region.

Compound	Proton #	Intensity	Compound	Proton #	Intensity
Hexamethylbenzene	0	140	tert-Butylbenzene	5	525
Hexaethylbenzene	0	120	1-Phenylpentane	5	445
Pentamethylbenzene	1	180	1,1-Dimethylpropylbenzene	5	510
1,2,4,5-Tetramethylbenzene	2	350	n-Hexylbenzene	5	435
1,2,4,5-Tetraisopropylbenzene	2	310	n-Octylbenzene	5	530
2,5-Diisopropyl-p-xylene	2	300	Cyclohexylbenzene	5	455
2-Bromomesitylene	2	260	1-Phenyldodecane	5	450
1,2,3,4-Tetramethylbenzene	2	300	3-Phenyldodecane	5	510
1,2,3,5-Tetramethylbenzene	2	300	Chlorobenzene	5	457
1,2,3-Trimethylbenzene	3	300	Pyridine	5	465
1,2,4-Trimethylbenzene	3	305	2,4,6-Trimethylnaphthalene	5	560
1,2,4-Trichlorobenzene	3	360	Benzene	6	610
2,5-Dibromotoluene	3	355	1,2-Dimethylnaphthalene	6	740
1,3,5-Trimethylbenzene	3	385	1,3-Dimethylnaphthalene	6	648
1,3,5-Triisopropylbenzene	3	385	1,4-Dimethylnaphthalene	6	710
5-tert-Butyl-m-xylene	3	400	1,5-Dimethylnaphthalene	6	830
3-tert-Butyl-5-ethyltoluene	3	365	1,6-Dimethylnaphthalene	6	762
o-Ethyltoluene	4	409	2,3-Dimethylnaphthalene	6	725
o-Diethylbenzene	4	399	2,6-Dimethylnaphthalene	6	687
o-Xylene	4	406	Quinoline	7	760
o-Dichlorobenzene	4	376	iso-Quinoline	7	800
m-Ethyltoluene	4	420	1-Methylnaphthalene	7	815
m-Diethylbenzene	4	401	2-Methylnaphthalene	7	795
m-Xylene	4	412	Naphthalene	8	1030
m-Diisopropylbenzene	4	345	9,10-Dimethylanthracene	8	1130
m-Chlorotoluene	4	406	Retene	8	1000
m-Dichlorobenzene	4	439	20-Methylcholanthrene	9	1168
p-Ethyltoluene	4	425	2-Methylphenanthrene	9	1028
p-Diethylbenzene	4	415	2-Methylanthracene	9	1280
p-Xylene	4	432	9-Methylanthracene	9	1158
p-Cymene	4	452	Phenanthrene	10	1214
p-Diisopropylbenzene	4	478	Anthracene	10	1295
p-tert-Butyltoluene	4	427	Diphenylmethane	10	1100
α-Picoline	4	384	Biphenyl	10	1070
β-Picoline	4	424	Pyrene	10	1330
γ-Picoline	4	428	Chrysene	12	1600
Toluene	5	478	3,4-Benzpyrene	12	1630
Ethylbenzene	5	525	1,2-Benzanthracene	12	1430
n-Propylbenzene	5	440	Perylene	12	1900
iso-Propylbenzene	5	495	Triphenylene	12	1420
n-Butylbenzene	5	415	m-Quaterphenyl	18	1845
iso-Butylbenzene	5	490	o-Quaterphenyl	18	1575
sec-Butylbenzene	5	520	m-Quinquephenyl	22	2080

Table II. Average Intensities by Ring Type of Aromatic Hydrocarbons in the 1650-2000 cm^{-1} region.

Compound Type (and Number)		No. of Ring Protons	Total Intensity	Intensity per Ring Proton	Average
Hexa-alkylbenzene	(2)	0	130	---	
Penta-alkylbenzene	(1)	1	180	180	
Tetra-alkylbenzene	(6)	2	295	147	
Trialkylbenzene	(8)	3	360	119	
Dialkylbenzene	(19)[a]	4	415	104	104 (Mononuclear)
Monoalkylbenzene	(8)	5	485	97	
Dialkylnaphthalene	(7)	6	725	121	
Dinuclear	(4)[a]	7	790	113	118 (Dinuclear)
Polynuclear	(3)	8	1055	132	
Polynuclear	(4)	9	1160	129	
Polynuclear	(3)	10	1290	129	131 (Polynuclear)
Polynuclear	(5)	12	1610	134	
Polyphenyls	(4)	10-22	(Table I)	98	

[a]Including some heterocyclics.

Table III. Intensities of Mononuclear Aromatics and Polyphenyls in the 1650-2000 cm^{-1} Region.

Number of Ring Protons	Total Intensity	Net Intensity[a]	Intensity per Ring Proton
1	180	50	50
2	295	165	83
3	300	230	77
4	415	285	71
5	485	355	71
6	610	480	80
10	1070	810	81
18	1710	1450	81
22	2080	1825	83

[a]Net intensity equals total intensity minus a background or skeletal vibration value of 130 cm^{-2} ℓ $mole^{-1}$ for each pendent aromatic ring.

Table IV. Intensity Effects of Polar and Olefinic Substituents on the Aromatic Absorption in the 1650-2000 cm^{-1} Region.

Substituent	Ring Proton Equivalent
Electron Donating Group	+ 1.5 to 2 protons
Chlorine	Little Change
Nitro	+ 2 protons
Side chains conjugated double bond	+ 1.5 to 2 protons
Isolated olefinic double bond	+ 1.5 to 2 protons

Table V. Frequencies of Absorption Bands of Monosubstituted Benzenes in =CH Out-of-Plane Deformation and Summation Regions.

	Average	Toluene	Chlorobenzene
		Fundamentals[a]	
f	751	728	740
g	837	844	830
i	908	895	902
h	962	966	965
j	982	982	985
		Summation Bands	
o	1742	1731	1731
g+i	1745	1739	1732
o	1797	1797	1788
g+h	1819	1810	1795
o	1865	1853	1861.5
i+h	1870	1861	1867
o	1880	1869	1882
i+j	1890	1877	1887
o	1938	1937	1941.5
2h	1924	1932	1930
o	1955	1955	1962
2j	1964	1964	1970

[a]Fundamentals from Reference 4.

o = Observed frequencies in carbon tetrachloride solution, 0.5 molar.

Captions for Figures

Figure 1. Spectra of aromatic hydrocarbons in 1650-2000 cm^{-1} region at 0.5 molar concentration in carbon tetrachloride, 0.5 mm. path length, compensated with solvent in reference beam.

Figure 2. Integrated intensities (cm^{-2} ℓ $mole^{-1}$) of aromatic hydrocarbons in the 1650-2000 cm^{-1} region as a function of ring proton concentration.

Figure 3. Integrated intensities (cm^{-2} ℓ $mole^{-1}$) of mono and polynuclear aromatic hydrocarbons in 1650-2000 cm^{-1} region as a function of ring proton concentration.
• Polynuclear
x Dinuclear
° Mononuclear and Polyphenyls

Figure 4. Spectra of styrene — and brominated derivative --- in 1650-2000 cm^{-1} region at 10% v/v in carbon tetrachloride, 1 mm. path length.

Figure 5. Spectra of tert. butylbenzene in 1650-2000 cm^{-1} region.
— undiluted, 0.1 mm. path, run at 9 cm^{-1} resolution
··· (offset) undiluted, 0.1 mm. path, run at 1.5 cm^{-1} resolution
--- 10% v/v in carbon tetrachloride, compensated, 1 mm. path, run at 1.5 cm^{-1} resolution.

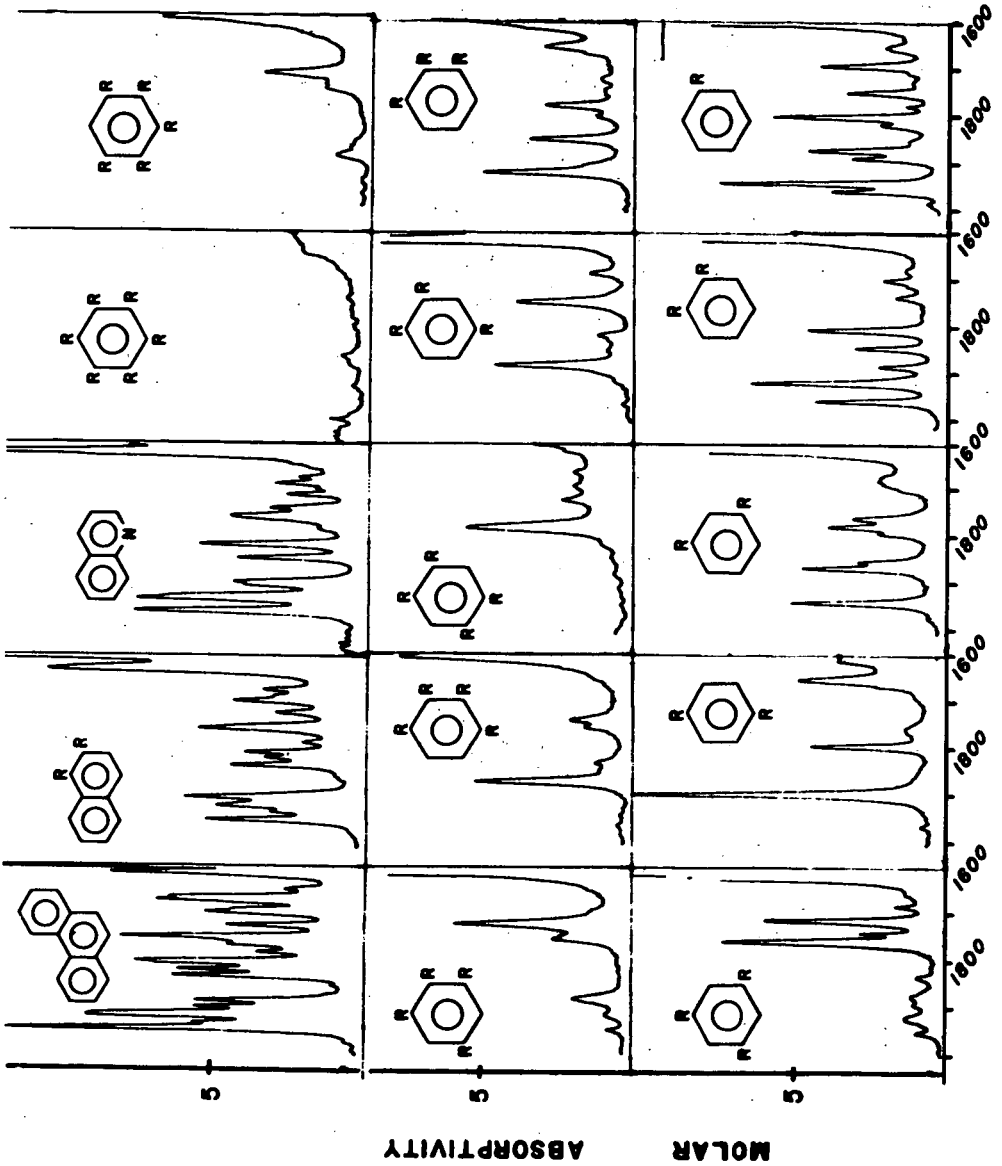
MOLAR ABSORPTIVITY
5
5
5
1600
1600
1600
1600
1600
1600
1600
1600
1600
1600
1600
1600

Figure 1.

FIGURE 3

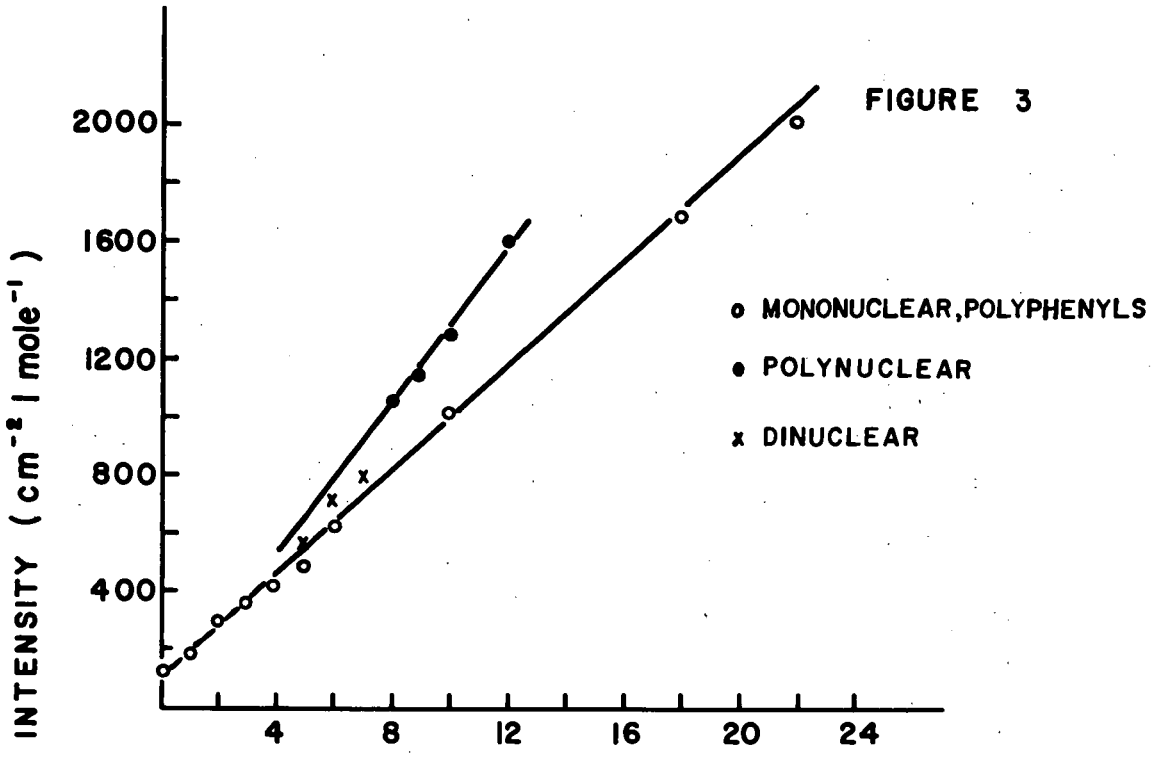

FIGURE 2

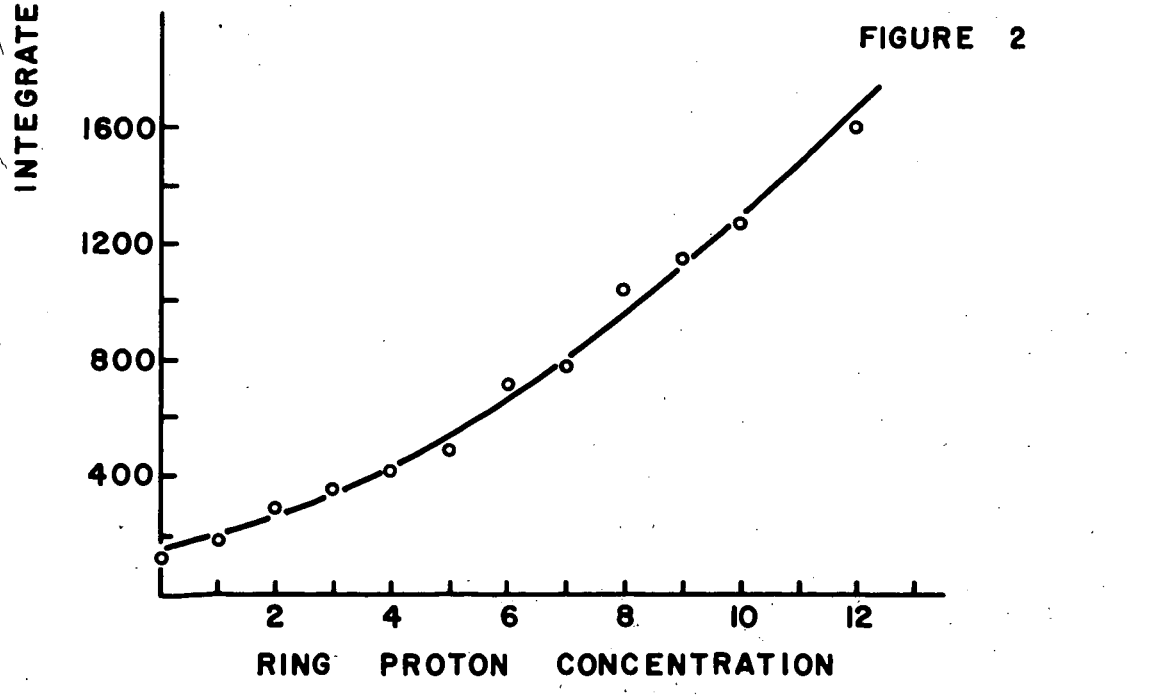

FIGURE 5

FIGURE 4

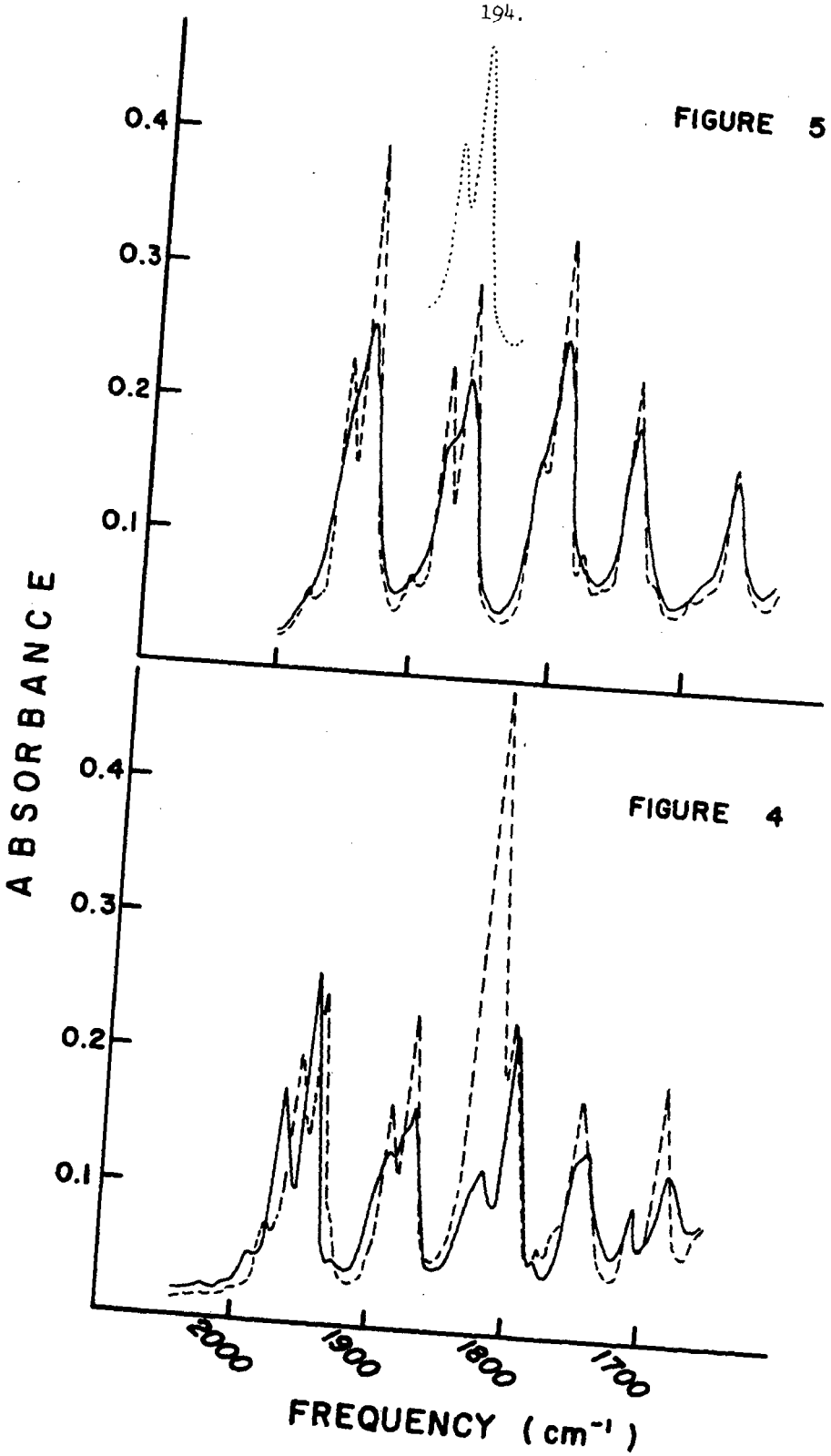

SPECTROSCOPIC STUDIES OF PHYSICO-CHEMICAL EFFECTS OF ULTRA-HIGH PRESSURES

J. W. BRASCH, R. J. JAKOBSEN, and E. JACK KAHLER

BATTELLE MEMORIAL INSTITUTE
Columbus Laboratories
505 King Avenue
Columbus, Ohio 43201

During recent years, a considerable volume of literature has appeared dealing with pressure studies. Inspite of all this work, very little is actually known of the chemical effects, on a molecular level, produced by high pressure. This lack of knowledge stems from the previous necessity of determining changes almost exclusively by postmortem examination of the pressurized material. Obviously, if no permanent phase change or reaction occurred, no pressure effect could be determined.

Battelle has pioneered in the utilization of commercially available equipment for infrared spectroscopic in situ monitoring of changes in liquids under ultra-high pressures. These techniques are now applicable to almost any liquid or solid sample, and potential applications have been shown to bridge virtually every area of physical-chemical endeavor.

It is easily demonstrated, by changes in the infrared spectrum as a sample is pressurized, that moderate pressures of 20 to 50 kilobars can produce significant, but completely reversible, effects on molecular structure. Definitive interpretation of these changes have exciting ramifications in every aspect of chemical knowledge. However, the broad spectrum of pressure studies can be grouped into three phenomenological areas:

1. Phase Behavior. Most liquid solidify under pressure, with polymorphism the rule rather than the exception (even the simple benzene molecule has at least two solid phases and we obtained a "plastic crystal" form of benzene under pressure. High-pressure, high-temperature polymorphic transitions are known for many, if not most, solids, as the eight forms of ice, five forms of amonium nitrate, or seven forms of tripalmitin. In situ measurements will reveal new phases undetectable by conventional postmortem examinations of quenched samples.

   Infrared spectroscopy has played an important role in solid-state studies. While the infrared spectrum is usually characteristic of a particular polymorphic form, it is particularly sensitive to any modification of molecular shape such as rotational isomerism, tautomerism, or conformational differences which may be encountered in high-pressure phases.

2. Intermolecular Forces. Fascinating possibilities for elucidating intermolecular interactions in condensed phases are offered by controlled variation of pressure from ambient to 100 kilobars, and of temperature from ambient to 400 C, on a sample of determinable volume. Questions of particular chemical importance which can now be approached experimentally are:

   (a) At what point do repulsive intermolecular forces exert an appreciable influence on intramolecular forces? For example,

most intramolecular vibrations in condensed phases shift to higher frequencies with increasing pressure. Is this shift simply a dielectric effect related to increasing density with compression, or does it actually represent a decrease in bond length of the particular vibrating entity? While there will be a dielectric effect with compression, evidence from studies of hydrogen-bonded compounds indicates that bond lengths are definitely affected.

(b) When compressions are sufficient to result in decreased intramolecular bond lengths, is the shortened bond more, or less, chemically active? Do polar bonds behave the same as less polar bonds under similar conditions?

(c) Does order or orientation in the liquid approach the order in a corresponding solid as the density of the pressurized liquid approaches the density of that solid? Techniques developed for measuring compressibilities with photomicrographic and infrared spectroscopic data were used to show that some liquid halogenated ethanes compress to the density of the solid before solidification occurs. Also, the pressure behavior of strongly hydrogen bonded liquids indicates a higher degree of order than was previously suspected.

3. Synthesis. Novel syntheses are possible in pressurized systems. For example, we have successfully polymerized a conjugated aromatic substituted acetylenic compound by UV irradiation of a high-pressure solid phase. Reaction was not induced in either the ambient or pressurized liquid phases, nor in a low-temperature solid phase of the material.

These techniques are described and the value of in situ capabilities is demonstrated by completely revisible pressure effects which cannot be detected by post mortem examination. These techniques involve using a diamond anvil high-pressure cell fitted with a metal gasket to contain the liquid. The very small aperture of the diamond cell greatly limits the energy available to the spectrometer and requires unusual instrumental conditions to achieve reliable results. The determination of these operating conditions and their effect on spectral results is discussed. These spectral results clearly show that much more than simple close-packing of moleclues is involved at pressures of 10-100 kilobars. It is a great aid in pressure studies to be able to observe by normal optical microscopy any corresponding changes in the physical state of the sample. This is particularly true for the study of organic liquids, many of which solidify at relatively low pressures. This phenomenon has been used in the easily manipulated diamond cell to grow single crystals, quickly and easily, of many organic compounds. The powerful combination of infrared spectroscopic and optical microscopic monitoring allows some very interesting comparisons of these high-pressure single crystals with normal crystals produced by freezing.

Spectra will be shown of various ranks of coal obtained by high-pressure techniques. These spectra will be discussed both in terms of a routine sampling method for qualitative identification and in terms of new knowledge to be gained concerning the structure of coals.

ATR-PYROLYSIS SPECTRA OF COAL

Stanley E. Polchlopek
William J. Menosky
Louis G. Dalli

Barnes Engineering Company
Instrument Division
30 Commerce Road
Stamford, Connecticut 06902

Infrared spectra of coal have been prepared, historically, as might be expected, by the usual techniques. Each of these has something to recommend it and each has some disadvantage. Both mulls and alkali halide discs have exhibited excessive scattering and have provided good spectra only after long periods of grinding, often under selected solvents.

But even after a sample was prepared and its spectrum recorded, the interpretation was complicated by the presence of a large amount of carbon which contributes nothing. In fact, the presence of a large amount of highly absorbing carbon detracts from the spectrum by imposing attenuation requirements on the reference beam. In addition, the organic components have reacted with alkali halide discs and in some cases spurious water bands have been reported.

The combination of ATR and pyrolysis offers a new approach to the study of coal samples by infrared spectrophotometry. In this study a Barnes PY-2 Pyrolyzer and a Barnes ATR-4 unit were used in conjunction with a Perkin-Elmer 257 Spectrophotometer. The use of this combination of techniques simplifies sample preparation but imposes certain precautions which must be observed in interpretation.

Experimental

Two charges of 250mg each were used to prepare each spectrum. One charge was deposited on each side of an ATR-4 KRS-5 (thallous bromide-iodide crystal). After appropriate experimentation, a time of 90 seconds and 900°C was used for each charge. All of the samples were pyrolyzed in a vacuum of 0.1mm or less. Pyrolysis in a vacuum is necessary in order to eliminate open flame combustion and to minimize possible end group reactions.

Results

Six coals of varying rank were studied. These were obtained from Dr. R. A. Friedel, the symposium chairman. They are described in Table I.

TABLE I

COAL	SOURCE AREA	PERCENTAGE C
Anthracite	Reading, Pennsylvania	92.5%
Bituminous Low volatile	Pocahontas, West Virginia	91.0%
Bituminous Medium volatile	Wyoming County, West Virginia	89.0%
Bituminous High volatile B	Waltonville, Illinois	79.2%
Bituminous High volatile A	Bruceton, Pennsylvania	83.1%
Sub-bituminous	Sweetwater County, Wyoming	73.7%

One of the results of this study which was somewhat surprising is that the same time-temperature conditions could be applied to produce spectra of approximately equivalent appearance for all six of the samples studied.

Fig. 1 shows the ATR spectrum of the pyrolyzate of sub-bituminous coal. The spectrum shows the presence of phenols in large amounts. The -OH band centered at about 3225 cm^{-1}. There are shoulders on both sides of the absorption peak indicating the presence of other species of -OH or perhaps -NH.

In Fig 2, which is the pyrolyzate of high volatile A bituminous, shows clearer separation of bands in the -OH stretch region. The carbonyl region is substantially unchanged and the phenyl frequencies in the 650 to 850 cm^{-1} region have become more complex. The spectrum continues to show the presence of phenols.

The pyrolyzate of high volatile B bituminous shown in Fig. 3 shows that the amount of volatile -OH has decreased in quantity and in complexity. The phenyl frequency region from 650 to 850 cm^{-1} has become somewhat less complicated. The carbonyl region is also changed and shows fewer bands. This indicates that the very volatile components found in very low rank coals are present in decreased amounts.

The spectrum of medium volatile bituminous shown in Fig. 4 shows a pattern in the carbonyl region and in the 1400 to 1500 cm^{-1} region. The -OH stretch region remains about the same. The phenyl frequencies from 650 to 850 cm^{-1} have again become more complex. The appearance of the band at 1420 cm^{-1} may be taken to mean that there has been an increase in the aliphatic substitution of the phenyl systems.

Low volatile bituminous which has almost the same carbon content as the pyrolyzate shown in Fig. 5. The spectrum is not as intense probably because there are not as many volatiles present. The band at 1200 to 1300 cm^{-1} has almost disappeared. The 650 to 850 cm^{-1} region has become quite complex.

The spectrum of the pyrolyzate of anthracite is shown in Fig. 6. This spectrum is not related to the others. It is, in fact, simply a spectrum of tar. The same spectrum has been observed from asphalts used to black top roads and driveways. The only difference is in the size of the charge used to produce the spectrum. A charge of about 25mg of asphalt will produce the spectrum of about the same intensity as a 250mg charge of anthracite.

The spectra in this study show that a combination of ATR and pyrolysis offer a new approach to the study of coal spectra. The major benefit of the technique lies in the fact that it speeds up sample preparation.

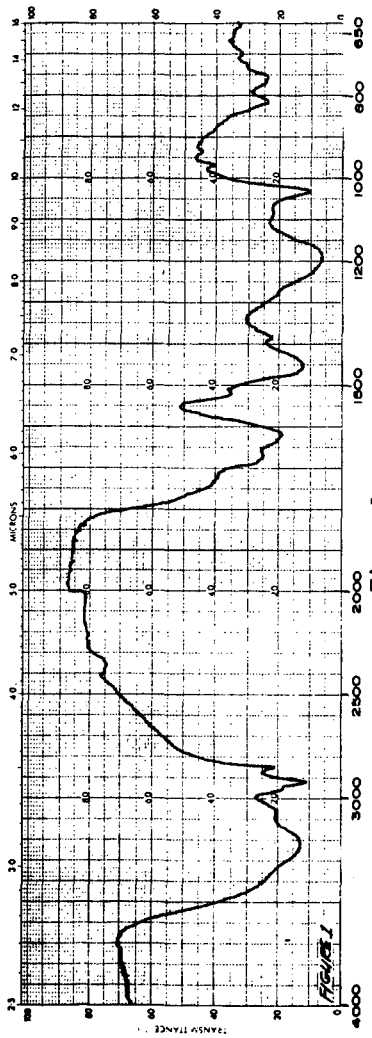

Figure 1.

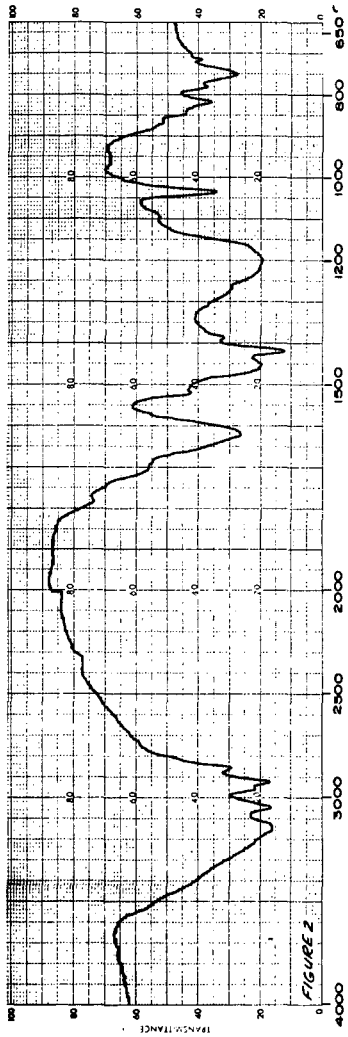

Figure 2.

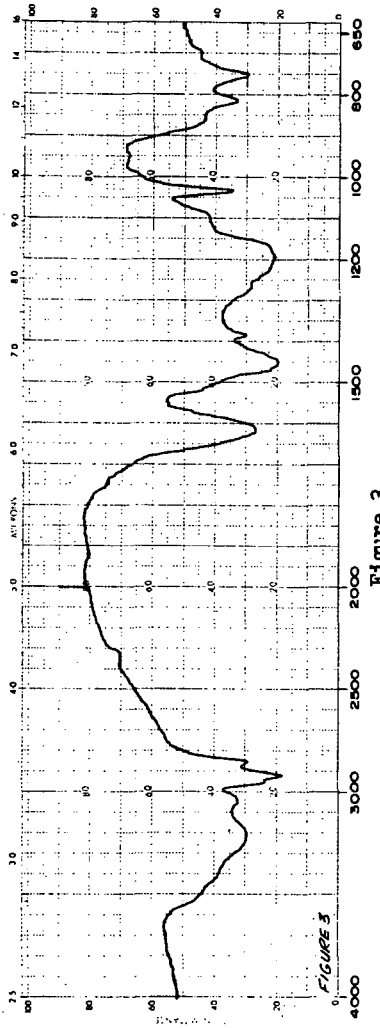

Figure 3.

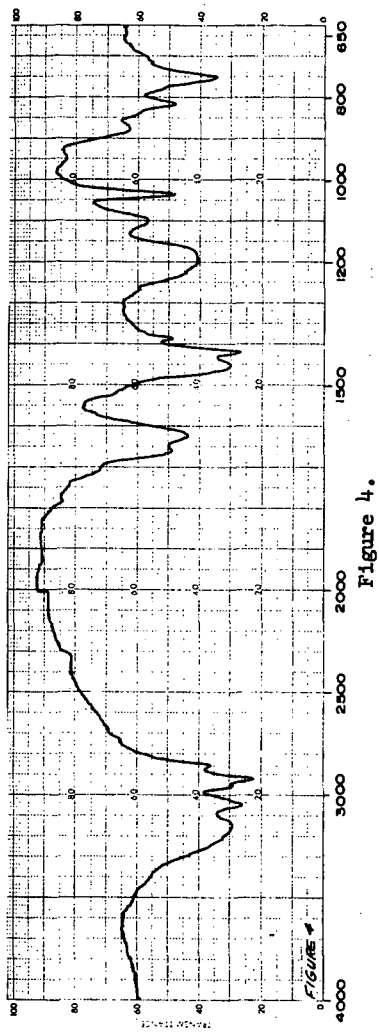

Figure 4.

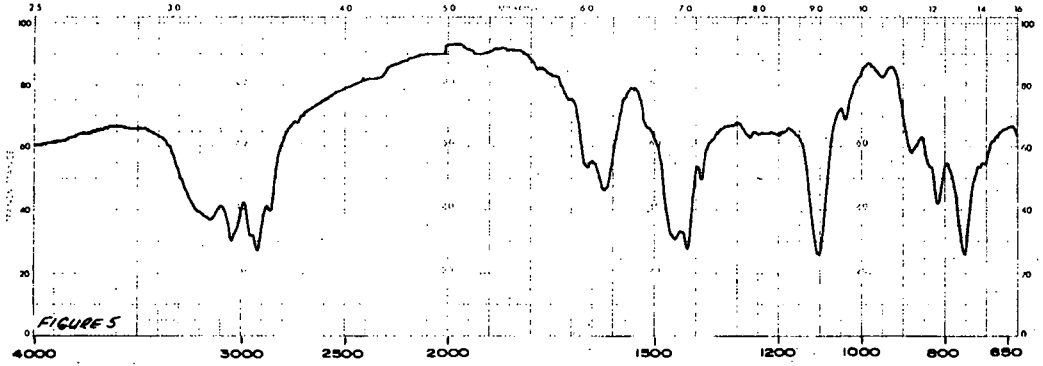

Figure 5.

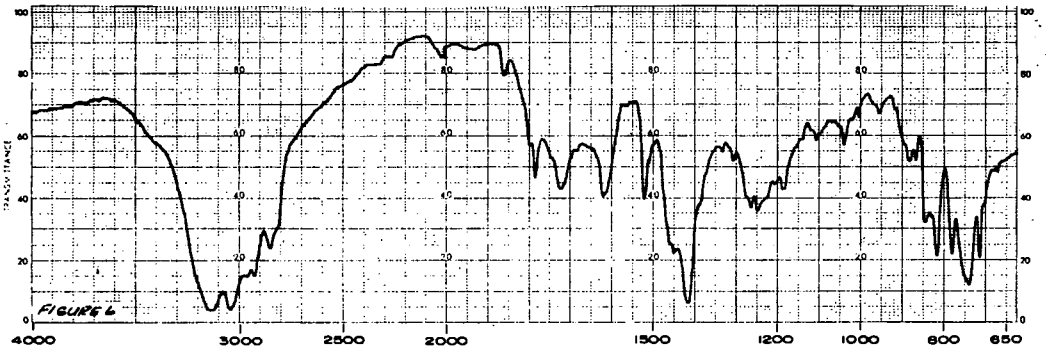

Figure 6.

THE USE OF INFRARED SPECTROSCOPY TO STUDY SURFACE GROUPS AND ADSORBED SPECIES ON CATALYSTS

By Michael R. Basila

Gulf Research & Development Company
Pittsburgh, Pennsylvania 15230

INTRODUCTION In recent years the application of spectroscopic techniques to problems in surface chemistry and catalysis has been growing at an ever-increasing rate. The most popular technique has been infrared followed by nuclear magnetic resonance and electron spin resonance.

Infrared techniques are most useful in surface functional group identification and (through the use of adsorbed molecules as probes) in studying the nature of the active sites for adsorption and reaction. In some cases it has been possible to obtain mechanistic information concerning the nature of intermediates in simple reactions such as the decomposition of formic acid over supported and unsupported metal catalysts (1).

As an illustrative example of the use of infrared techniques in studying the behavior of surface functional groups and the utilization of molecular probes to characterize active surface sites, a review of our studies of the surface of silica-alumina will be given. Here, use was made of nitrogen containing molecules -- pyridine and ammonia -- as probes to characterize the surface acid sites.

SURFACE GROUPS ON SILICA-ALUMINA In Fig. 1 the spectrum of a highly dehydrated silica-alumina (25 wt.% Al_2O_3) is given. The band at 3745 cm^{-1} is due to the OH stretching vibration in surface hydroxyl groups. The bands at 1975, 1866 and 1633 cm^{-1} are overtone and combination lattice vibrations (2). There is also a weak band at 1394 cm^{-1} which is due to an unidentified surface group, possibly a surface impurity. The 3745 cm^{-1} band has been assigned to the OH stretching vibration in hydroxyl groups attached to surface silicon atoms (2). This assignment was made on the basis of similarities in the frequency, band shape and other properties with the surface hydroxyls on silica. It has been confirmed by nuclear magnetic resonance measurements (3). The presence of a single surface hydroxyl group type is rather surprising. A number of workers (4) have observed three to five OH stretching bands due to isolated (non-hydrogen bonded) surface hydroxyl groups on alumina, while only one band at 3750 cm^{-1} is observed on silica (5). The results for silica-alumina suggest that there are no alumina-like areas on the surface or conversely, that the aluminum ions are distributed evenly throughout the lattice. We have looked at other commercial silica-aluminas ($Al_2O_3 \leq 25$ wt.%) and all have only a single surface hydroxyl type (attached to surface silicon atoms). Other workers have made similar observations (6a) however there have been several cases where the presence of alumina-like surface hydroxyl groups have been reported in addition to the silica-like groups (6b).

SURFACE ACID SITES Use has been made of ammonia as a molecular probe to study surface acidity on alumina and silica-alumina catalysts by a number of workers (7). Pyridine on the other hand has only been used in a few studies (8). Pyridine offers the advantage that one can distinguish unequivocably between coordinately bonded (LPY), protonated (BPY), and hydrogen bonded (HPY) adsorbed species (8). The bands that are used in making these distinctions are shown in Table I (8b).

TABLE I

BAND POSITIONS FOR COORDINATELY BONDED, PROTONATED AND HYDROGEN-BONDED PYRIDINE ADSORBED ON SILICA-ALUMINA*

Species	Type	LPY (cm^{-1})	BPY (cm^{-1})	HPY (cm^{-1})
8a	$\nu_{CC(N)}$	1620	1638	1614
8b	$\nu_{CC(N)}$	1577	1620	1593
19a	$\nu_{CC(N)}$	1490	1490	1490
19b	$\nu_{CC(N)}$	1450	1545	1438

*LPY = coordinately bonded pyridine (chemisorbed)

BPY = protonated pyridine (chemisorbed)

HPY = hydrogen bonded pyridine (physically adsorbed)

Chemisorbed NH_3 exhibits two bands that can be used to distinguish between the coordinately bonded and protonated species. The position of these bands are at 1620 (LNH_3) and 1432 cm^{-1} (NH_4^+), respectively (7, 9). However, the (physically adsorbed) hydrogen-bonded species (PNH_3) cannot be distinguished from LNH_3 which introduces some uncertainty in the estimation of Lewis/Bronsted acid site ratios (9).

Figs. 2 and 3 are spectra of pyridine and ammonia adsorbed on silica-alumina. An expression for calculating the ratio of Lewis to Bronsted acid sites on the surface of silica-alumina using the 1490 and 1450 cm^{-1} bands of LPY and BPY has been developed (10).

$$\frac{[LPY]}{[BPY]} = \frac{1.5\ A_{1450}}{A_{1490} - 0.25\ A_{1450}} \quad ; \ A = \text{peak absorbance}$$

The band at 1545 cm^{-1} cannot be used directly in conjunction with the 1450 cm^{-1} band because it has a much smaller absorption coefficient and the ratios are usually considerably greater than 1. The use of the 1490 cm^{-1} band is convenient because for LPY and BPY it has different absorption coefficients with $\epsilon_{BPY}/\epsilon_{LPY} = 6$ (10).

The bands at 1620 and 1432 cm^{-1} of chemisorbed ammonia can be used directly to estimate the Lewis/Bronsted acid site ratio. The relative absorption coefficients are: $\epsilon_{1432}/\epsilon_{1620} = 7$ (9). By these two methods it has been determined that one out of every five (NH_3, (9)) to 7 (PY, (10)) molecules that are chemisorbed are adsorbed as the protonated species for the silica-alumina which was studied comparatively. Other silica-aluminas have different Lewis/Bronsted acid site ratios (10) which is to be expected since the relative amounts of alumina and methods of preparation vary over considerable ranges.

EFFECT OF WATER ON SURFACE ACIDITY More detailed studies of the adsorption of pyridine and ammonia on silica-alumina have exposed some rather interesting behavior. When H_2O is adsorbed on chemisorbed pyridine (8) or ammonia (10) containing samples most of the LPY (LNH_3) is converted to BPY (NH_4^+) (Figs. 2b, c). However, this reaction is reversible and the spectrum returns to the original upon evacuation (Fig. 2d). During this experiment H_2O does not displace pyridine since no pyridine is removed and no band due to HPY is observed. If pyridine is added to chemisorbed H_2O, the same spectrum results but the water is removed by subsequent evacuation (8b). Hence, it appears that the H_2O molecules interact with the chemisorbed LPY and a proton transfer occurs without displacement of LPY.

It is difficult to rationalize the nature of this interaction between water and chemisorbed pyridine or ammonia. It is important to note that pyridine and water in solution do not interact to form pyridinium ion but merely engage in hydrogen bonding interactions (11). The formation of BPY therefore must result from activation of one or both of the components by the surface. The results suggest that the nitrogen containing base stays on the primary acid site and the water participates in a secondary interaction. Presumably adsorption of pyridine to form LPY occurs by an electron transfer interaction from the lone electron pair on the N atom to a trigonal surface aluminum atom leading to a surface complex of the type (I).

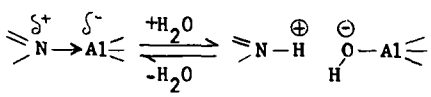

(I) (II)

In the presence of water, the electron transfer from N to surface Al may be essentially complete if a hydrogen atom from the water is transferred to the LPY and the OH radical migrates to the aluminum atom to give a complex of type (II). The same result would occur if a proton was transferred to the pyridine and the hydroxyl ion to the trigonal aluminum atom. In either case the pyridinium ion would then be held on the surface in an ion pair with $(\geq AlOH)^-$. The only difficulty with this model is that the nitrogen base is apparently strongly held during this interaction (8b) since it does not desorb upon evacuation whereas the pyridinium ion should have some surface mobility. The real situation most likely involves an equilibrium between (I) and (II), however, the data suggest that it is strongly displaced to the right since most of the LPY can be converted to BPY. It should be noted that there are no data available to indicate whether the added H_2O molecules are in a 1:1 ratio with the number of LPY molecules. If the ratio were higher, the equilibrium would be pushed toward the right.

SURFACE ACIDITY MODEL These results have led us to postulate (8b) that all of the acidic sites on silica-alumina are of the Lewis or electron acceptor type and that Bronsted type acidity results from a secondary interaction between the molecule chemisorbed on the primary Lewis type site and an adjacent SiOH group. This interaction is pictured as similar to that between water and chemisorbed LPY.

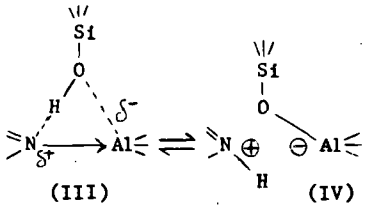

(III) (IV)

This model's chief advantage is that it allows the rationalization of extensive data in the literature which heretofore has been taken as evidence that silica-alumina has predominantly Lewis type sites or conversely predominantly Bronsted sites. It suggests that a proton is available if needed mechanistically such as to form a classical carbonium ion from an olefin, but is not necessarily involved in all acid-catalyzed reactions that proceed over silica-alumina (9).

Spectroscopic evidence supporting this model will now be considered. In Fig. 4 a plot of the concentration of chemisorbed NH_4^+ versus total ammonia adsorbed is given. As would be expected the slope decreases as the total amount of ammonia adsorbed increases. The initial slope is 0.25 which indicates that initially one

out of every five ammonia molecules is chemisorbed as NH_4^+. Fig. 5 is a plot of the concentration of isolated (non-hydrogen bonded) surface hydroxyls versus the total amount of ammonia adsorbed. For analysis the smooth curve is broken into two linear segments. Note that the intersection point coincides with the point (Fig. 4) where the increase in (NH_4^+) as total ammonia adsorbed increases begins to flatten out. The inverse slope of the low coverage linear segment in Fig. 5 is 5.5 ± 0.5 and that of the high coverage linear segment is 0.98 ± 0.09. Hence, at low coverage one out of every five or six chemisorbed ammonia molecules is hydrogen bonded to a surface hydroxyl group. At high coverage every adsorbed ammonia is hydrogen bonded to a surface hydroxyl group, which is typical of the physical adsorption of ammonia on silica gel (no acidic sites). It is evident from these results that the high coverage segment corresponds to physical adsorption and the low coverage segment to chemisorption. The curvature near the transition point is a result of both processes occurring simultaneously.

According to the predictions of the model $[NH_4^+] \leq [OH]_{bonded}$, that is the number of chemisorbed ammonia molecules which are involved in "hydrogen-bonding" interactions with surface hydroxyl groups should be greater than or equal to the concentration of chemisorbed NH_4^+. The results in Figs. 4 and 5 (at low surface coverage) are that one in five ammonia molecules is chemisorbed as NH_4^+ and one in five or six is hydrogen bonded to a surface hydroxyl group, in good agreement with the prediction. Furthermore, it is predicted that hydroxyl groups involved in proton transfer interactions with chemisorbed ammonia molecules should not exhibit an OH stretching band, hence at low surface coverage where chemisorption predominates the intensity of the 3050 cm^{-1} band (due to the hydrogen-bonded OH stretching) should increase at a very much lower rate than at high coverage where physical adsorption predominates. This behavior is evident in Fig. 6 where the peak absorbance of the 3745 cm^{-1} band is plotted versus that of the 3050 cm^{-1} band. This evidence is not conclusive however because the OH groups in a non-proton transfer interaction with chemisorbed molecules may have a different peak frequency and absorption coefficient than those involved in a normal hydrogen-bonding interaction (9).

Additional supporting evidence for the proposed model is shown in Fig. 7. In this experiment the silica-alumina was poisoned by impregnation with potassium acetate followed by calcination. The presence of alkali metals in acidic catalysts is known to poison carbonium ion reactions (13). Fig. 7a shows that the band due to BPY at 1545 cm^{-1} is absent, hence poisoning with potassium ions eliminates Bronsted type acidity. It has been shown (8b) that the strength of the acidic sites is markedly decreased when silica-alumina is poisoned by the addition of potassium. The hydroxyl groups are little effected. When water is adsorbed on the pyridine containing surface the LPY species are converted to BPY (Fig. 7b). Hence the added potassium ions do not prevent the conversion of LPY to BPY by adsorbed water. This result is quite surprising. It eliminates the surface species $(\geq AlOH)^-H^+$ as the source of inherent Bronsted acidity on a fresh silica-alumina surface. If this species were present the K^+ ions would exchange with the H^+ ions and render the sites completely inactive. The fact that water can still convert LPY to BPY suggests that even though the degree of activation of pyridine by the acidic site is decreased (8b) the protonation reaction can still proceed if the proton donor can get close enough.

This behavior can be rationalized in terms of our model as follows and hence is taken as indirect supporting evidence. Since the reactions of the LPY-acid site complex and the adjacent OH are geometrically fixed a decrease in the degree of activation of LPY can prevent the transfer of a proton. However, water molecules are mobile and can come in very close proximity to the complex to effect proton transfer.

SUMMARY The results discussed above demonstrate that infrared spectroscopic techniques can provide details of surface chemistry and the nature of surface functional groups. Spectroscopic techniques do not provide the panacea for all catalytic problembs, however. They sometimes raise more questions than they answer. It can be concluded that they will (and do) constitute an important tool for the catalytic chemist. They are most effective when used in conjunction with other techniques such as gravimetric adsorption measurements (used for example to obtain surface concentrations in Figs. 4 and 5) and isotope exchange techniques.

REFERENCES

1. See review by L. H. Little, "Infrared Spectra of Adsorbed Species," Academic Press, New York, N. Y., 1966, Chapter 5.

2. M. R. Basila, J. Phys. Chem., 66, 2223 (1962).

3. W. K. Hall, H. P. Leftin, F. J. Cheselske, and D. E. O'Reilly, J. Catalysis, 2, 506 (1963).

4. (a) J. P. Peri and R. B. Hannan, J. Phys. Chem., 64, 1526 (1960); (b) J. P. Peri, Ibid, 69, 211 (1965); (c) D. J. C. Yates and P. J. Lucchesi, J. Chem. Phys., 35, 243 (1961); (d) R. H. Lindquist and D. G. Rea, presented at 136th National Meeting, American Chemical Society, Sept., 1959.

5. R. S. McDonald, (a) J. Am. Chem. Soc., 79 850 (1959); (b) J. Phys. Chem., 62, 1168 (1958).

6. (a) J. B. Peri, J. Phys. Chem., 70, 3168 (1966); (b) See reference 1, Chapter 10.

7. See reference 1, Chapter 7.

8. (a) E. P. Parry, J. Catalysis, 2, 371 (1963); (b) M. R. Basila, T. R. Kantner and K. H. Rhee, J. Phys. Chem., 68, 3197 (1964).

9. M. R. Basila and T. R. Kantner, J. Phys. Chem., 71, 467 (1967).

10. M. R. Basila and T. R. Kantner, Ibid, 70, 1681 (1966).

11. A. N. Sidorv, Opt. i Spektroskopiya 8, 51 (1960).

12. A. V. Kiselev, V. I. Lygin and T. I. Titova, Zh. Fiz. Khim., 38, 2730 (1964).

13. (a) D. Stright and J. D. Danforth, J. Phys. Chem., 57, 448 (1953); (b) G. A. Mills, E. R. Boedeker, and A. G. Oblad, J. Am. Chem. Soc., 72, 1554 (1950).

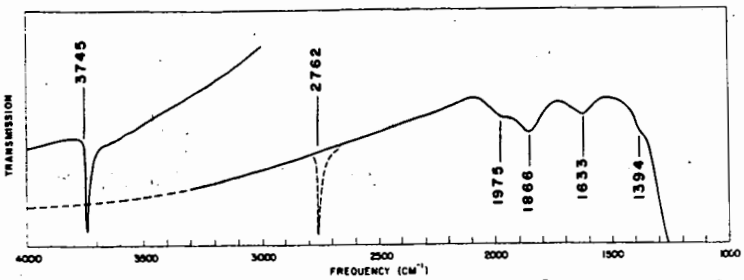

Fig. 1. Silica-alumina dehydrated at 500°C. The dashed lines indicate the spectrum of deuterated silica-alumina.

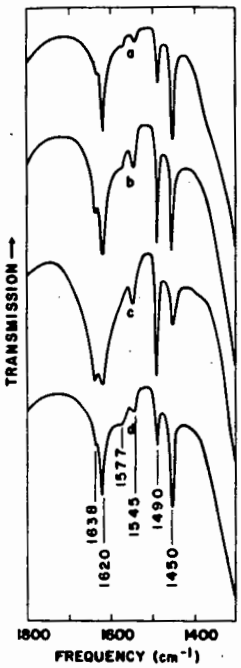

Fig. 2. Dual adsorption of pyridine and H_2O on silica-alumina. (a) SA exposed to pyridine at 17 mm. and 150°C for 1 hr. followed by evacuation at 150°C for 16 hr. (b) Exposure to H_2O at 15 mm. and 150°C for 1 hr. followed by evacuation at 150°C for 1 hr. (c) Exposure to H_2O at 15 mm. and 25°C for 1 hr. followed by evacuation for 1 hr. at 25°C. (d) Evacuation for 16 hr. at 150°C.

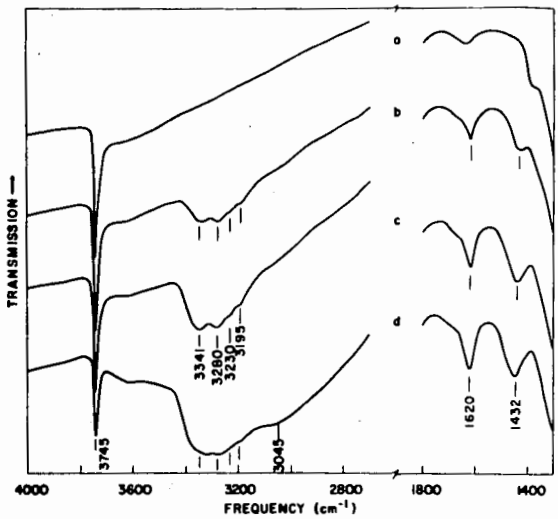

Fig. 3 (a) SA calcined 16 hours in O_2 at 500°C, evacuated 5 hours at 500°C. (b) Exposed to 10 mm NH_3 for 1 hour at 150°C, evacuated 1 hour at 150°C. (c) Subsequently exposed to 10 mm NH_3 for 1 hour at 25°C, evacuated for 1 hour at 25°C. (d) Subsequently exposed to 10 mm NH_3 for 1 hour, no evacuation. Very weak bands due to gaseous NH_3 have been subtracted.

Fig. 4. A comparison of the concentrations of NH_3 and NH_4^+ adsorbed on SA as the total amount of ammonia adsorbed increases. $[NH_3]$ is the sum of $[PNH_3]$ and $[LNH_3]$. The vertical line denotes the point of straight line intersection in Fig. 5.

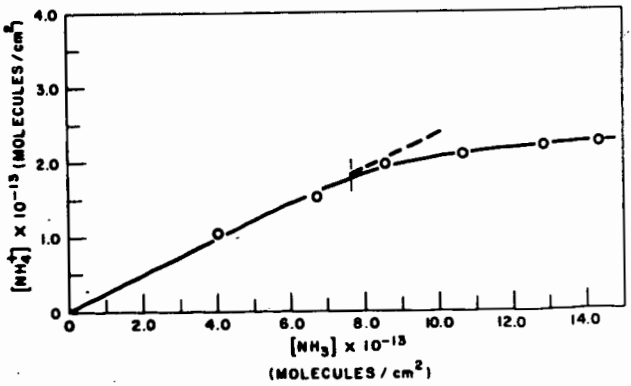

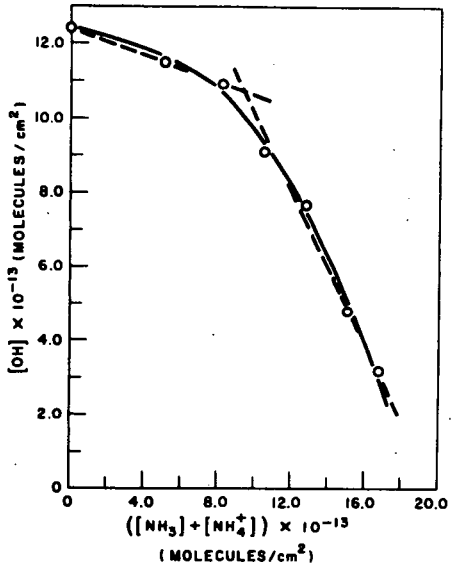

Fig. 5. The concentration of non-hydrogen bonded surface OH groups vs the total amount of ammonia adsorbed on SA. NH_3 is the sum of PNH_3 and LNH_3.

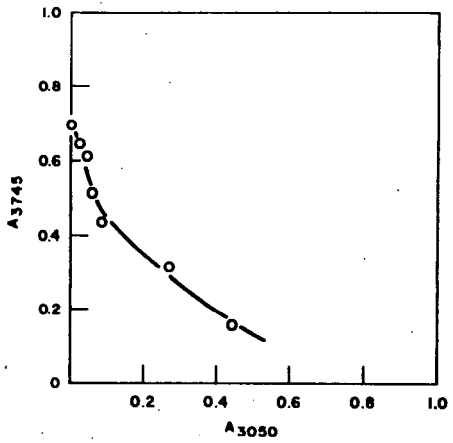

Fig. 6. A comparison of the concentrations of free and hydrogen-bonded surface OH groups as the amount of ammonia adsorbed increases. The values of A are the peak absorbancies of the characteristic bands.

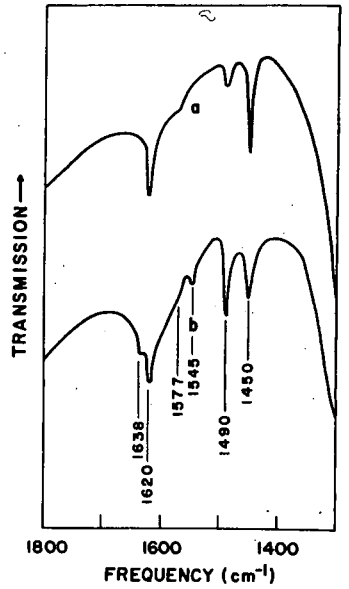

Fig. 7. Dual adsorption of pyridine and H_2O on K-poisoned silica-alumina. (a) KSA exposed to pyridine at 17 mm. and 150°C for 1 hr. followed by evacuation for 16 hr. at 150°C. (b) Exposed to H_2O at 15 mm. and 150°C for 1 hr. followed by evacuation for 1 hr. at 150°C.

SELF-ASSOCIATION OF PHENOL IN NON-POLAR SOLVENTS

Kermit B. Whetsel and J. Harold Lady

Tennessee Eastman Co., Division of Eastman Kodak Co., Kingsport, Tenn. 37660

Although the self-association of phenol has been studied by a variety of methods, our knowledge of the thermodynamics of the process is still incomplete. Thermodynamic constants for the dimerization of phenol in carbon tetrachloride solution have been reported (1, 2), but comparable data for the formation of higher multimers are not available. Furthermore, the effects of solvents on the self-association process have not been reported.

The objective of the present work was to determine thermodynamic constants for the dimer and higher multimers of phenol in carbon tetrachloride and cyclohexane solutions. The intensity of the first overtone O-H stretching band of phenol was measured as a function of concentration and temperature in both solvents and the fit of the data to a variety of self-association models tested. A method was developed for calculating the approximate absorptivity of O-H end groups in linear associated species and for taking this factor into account in the determination of formation constants. The effects of concentration, temperature, and solvent upon the fundamental O-H stretching bands of phenol were investigated briefly.

EXPERIMENTAL

Equipment and Materials. Measurements in the fundamental and first overtone regions were made with Beckman IR-9 and Cary Model 14 spectrophotometers, respectively, equipped with thermostated cell holders. Spectral slit widths were approximately 2.3 cm^{-1} in the fundamental region and 6.4 cm^{-1} in the overtone region. Spectro grade cyclohexane was used as received. Reagent grade carbon tetrachloride was dried over molecular sieve Type 5A. Reagent grade phenol was distilled and stored in a desiccator over Drierite and phosphorous pentoxide. When not being used, all solutions were stored in glass-stoppered flasksin a desiccator.

Calculations. For the self-association equilibria $nC_1 \rightleftharpoons C_n$, the following equations apply:

$$K_n = \frac{C_n}{C^n} \qquad (1)$$

$$A/l = \epsilon_1 C_1 + \epsilon_2 K_2 C_1^2 + \text{---} + \epsilon_n K_n C_1^n = \epsilon_1 C_1 + \sum_{n=2}^{n=n} \epsilon_n K_n C_1^n \qquad (2)$$

$$C_A^s = C_1 + 2K_2 C_1^2 + 3K_3 C_1^3 + \text{---} + nK_n C_1^n = C_1 + \sum_{n=2}^{n=n} nK_n C_1^n \qquad (3)$$

where A is absorbance, l is path length, C_1 is monomer concentration, C_A^s is stoichiometric concentration, ϵ_1 is monomer absorptivity, and ϵ_n is the absorptivity of polymeric species. For the special case of $\epsilon_n = 0$, equations 2 and 3 reduce to

$$A/l = \epsilon_1 C_1 \tag{4}$$

and

$$C_A^\circ = A/l\epsilon_1 + \sum_{n=2}^{n=n} nK_n \, (A/l\epsilon_1)^n \tag{5}$$

The number of unknown parameters in Equation 5 can be reduced by imposing the restriction that the stepwise formation constants for all multimers above dimer are equal. This type of association is described by the expressions:

$$C_1 + C_{n-1} \rightleftharpoons^{K} C_n \qquad K = \frac{(C_n)}{(C_1)\ (C_{n-1})} \tag{6}$$

where $\underline{K}$ is independent of $\underline{n}$ when $\underline{n} > 2$. Under these conditions K_n is equal to $K_2 K^{n-2}$, and the only unknowns in Equation 5 are K_2, K, and ϵ_1.

The values of ϵ_1 required for the solution of Equation 5 were determined by extrapolating plots of apparent absorptivity versus C_A° to infinite dilution. The formation constants were calculated using a computer and a standard least squares method for polynomials. The program used to solve the general form of Equation 5 allowed formation constants to be calculated for single multimers or any combination of multimers from dimer through octamer. The program used to solve the restricted form allowed the contribution of up to 20 species to be taken into account.

Equation 5 is not directly applicable when $\epsilon_n \neq 0$, but it can be used to determine formation constants by an iteration procedure as follows: Initial estimates of K_n are obtained by assuming than $\epsilon_n = 0$ and using Equation 5 in the normal manner. A small increment of end group absorptivity ($\Delta\ \epsilon_n = 0.05$ to 0.10) is assumed and a set of corrected A/l values generated by using the equation

$$(A/l)_{C(1)} = (A/l)_{obs} - \Delta\ \epsilon_n \sum_{n=2}^{n=n} K_n \, (1/\epsilon_1)^n \ \ (A/l)_{obs}^n \tag{7}$$

This set of values is substituted into Equation 5 to obtain second estimates of K_n. The second estimates of K_n and the first set of corrected A/l values are substituted into the right side of Equation 7 to obtain a second set of corrected A/l values. Successive estimates of K_n and corrections of A/l are made until the standard error of fitting Equation 5 passes through a minimum. The values of K_n giving the minimum error are taken as the best estimates of these quantities. The approximate end group absorptivity is equal to $\underline{N}(\Delta\ \epsilon_n)$, where $\underline{N}$ is the number of iterations required to obtain the minimum error. The best estimate of the end group absorptivity is calculated from the equation

$$(A/l)_{obs} = (A/l)_{C(N)} \ + \epsilon_n \sum_{n=2}^{n=n} K_n \, (1/\epsilon_1)^n \ (A/l)_{C(N)} \tag{8}$$

where $(A/l)_{C(N)}$ is the set of corrected A/l values which gives the minimum error in fitting Equation 5.

The iteration procedure was used only with the model involving dimerization and stepwise association constants, where $K_n = K_2K^{n-2}$. The results obtained when the method was tested with synthetic data are shown in Table I. While the method does not converge to the theoretical values, it yields values for the formation constants and ϵ_n that are within 5 and 20%, respectively, of the true values.

RESULTS

Spectral Data. Solutions of phenol above a few hundredths molar show three O-H bands in the fundamental region. The free O-H band is near 3612 cm^{-1} and the two bonded O-H bands are near 3500 and 3350 cm^{-1}. The band near 3500 cm^{-1} is normally assigned to a cyclic dimer species and the one near 3350 cm^{-1} to linear associated species. The relative intensity of the band near 3350 cm^{-1} increases with increasing concentration and decreasing temperature.

The principal feature of the first overtone spectrum is a free O-H band near 7050 cm^{-1} whose apparent absorptivity decreases as self-association occurs. Bonded O-H groups are evidenced only by a broad, weak band extending from about 7050 to 6000 cm^{-1}. The absorptivity of the monomer is approximately 50% greater in cyclohexane than in carbon tetrachloride. Self-association occurs more readily in the hydrocarbon solvent, however, and at concentrations above 0.1 or 0.2M the order of apparent absorptivities is reversed.

Model Fitting. In the initial attempts to find the best model, only the data for phenol concentrations less than 0.1M were used. Several different models gave satisfactory fits over this limited concentration range. But when the formation constants derived from these tests were applied to data for higher phenol concentrations, the agreement between calculated and observed absorbances deteriorated rapidly.

A variety of models were tested using data for phenol concentrations up to 0.65M in cyclohexane and 1.0M in carbon tetrachloride. The standard errors for the different models are shown in Table II. Several of the models which gave good fits over a limited range of concentration gave negative values for one or more constants when tested over the more extended range. The model involving a dimerization constant and equal stepwise association constants for higher multimers gave the best fit in both solvents.

In Figure 1 the fits of several different models are shown graphically. The good fit of the dimer-stepwise model and the poor fit of most of the other models are evident. These curves indicated that certain combinations of simpler models might give good fits, and subsequent calculations showed that a trimer-hexamer model did, indeed, provide a good fit. This model does not appear to be as plausible physically as the dimer-stepwise model, and it was not studied further.

Application of the end group correction to the data for the carbon tetrachloride system is illustrated by the curves in Figure 2. With the data taken at 2.5°, the minima in the standard error curves correspond to an end group absorptivity of approximately 0.3 l./mole-cm. The average value of ϵ_n determined at temperatures between 2.5 and 46° was 0.4 l./mole-cm., which is equivalent to $0.11\epsilon_1$.

When the end group correction was applied to the data for the cyclohexane system, the standard error of fit decreased at four temperatures but did not at three others. The maximum value for ϵ_n was $0.08\epsilon_1$ and the average was only $0.03\epsilon_1$. In view of these results, we do not feel that application of the correction to the data for the cyclohexane system is valid.

Thermodynamic Results. Plots of formation constants vs 1/T for dimerization and stepwise association are shown in Figure 3. The thermodynamic constants derived from the plots are summarized in Table III. The lines in Figure 3 for the carbon tetrachloride system represent data to which the end group correction was applied. In Table III the thermodynamic constants calculated for both the original and the corrected data are shown for comparison.

DISCUSSION

Coggeshall and Saier (3) found that a dimerization-stepwise association model adequately describes the effects of self-association on the fundamental O-H band of phenol in carbon tetrachloride solution. Our results obtained in the first overtone region confirm the validity of the model and show, in addition, that it is applicable to self-association in cyclohexane solution.

Our values of 0.94 and 3.25 l./mole for K_2 and K in carbon tetrachloride at 25° can be compared with values of 1.39 and 2.94 l./mole found by Coggeshall and Saier at ambient instrument temperature and with values of 0.70 and 0.83 l./mole reported by West and coworkers (1, 2) for K_2 at 25°. Our heat of dimerization of -5.03 kcal./mole is in excellent agreement with the value of -5.1 kcal./mole reported by Maguire and West (1). A more recent value of -3.6 reported by Powell and West (2) seems abnormally low. No direct comparison can be made for the heat of formation of higher multimers, but our value of -4.32 kcal./mole agrees well with an overall heat of association of -4.35 kcal./mole reported by Mecke (4). Mecke worked with relatively high concentrations of phenol, and his value is heavily weighted toward the stepwise heat of formation.

Both the dimerization constants and the stepwise formation constants are approximately twice as large in cyclohexane solution as in carbon tetrachloride solution. The heats of formation in the hydrocarbon solvent, however, are only 10 to 20% higher than those in the chlorinated solvent. Similar results have been obtained recently for a variety of hydrogen bonded complexes of phenol in these two solvents (5).

The average value of 0.4 l./mole-cm. found for the end group absorptivity in carbon tetrachloride solution is approximately 0.1 as large as the absorptivity of the free O-H group. This result indicates either that the O-H end groups interfere only slightly at the frequency where the monomer band occurs or that the concentration of end groups is much lower than one would expect on the basis of a linear association model. A low concentration of end groups could result from the formation of cyclic multimers or three dimensional aggregates. Most workers in this field have assumed that end group absorption is negligible but have recognized that the assumption might introduce major errors in the calculated formation constants. The present results show that the assumption is reasonably valid, at least in the first overtone region. Data recently presented by Bellamy and Pace (6) indicate that the end group absorptivity may be as large as $0.3\epsilon_1$ in the fundamental region.

The question of whether alcohols and phenols form linear or cyclic dimers, or both, has been discussed widely. Considerable evidence favoring the predominance of cyclic dimers has been presented, but recent work by Bellamy and Pace (6), Ibbitson and Moore (7), and Malecki (8) emphasizes the importance of linear dimers. Our thermodynamic results indicate that a significant fraction of the phenol dimer is in the linear form.

The apparent dimerization constant and heat of formation of the dimer are related to the individual values for the linear and cyclic forms as follows (9):

$$K_A = K_L + K_C \tag{10}$$

$$\Delta H_A = \frac{K_L(\Delta H_L) + K_C(\Delta H_C)}{K_A} \tag{11}$$

where the subscripts A, L, and C represent apparent, linear, and cyclic. If we assume that the heat of formation of the linear dimer is equal to the stepwise heat of formation of higher multimers, we can calculate values of ΔH_C, ΔS_C, and ΔS_L for various assumed ratios of K_L and K_C (Table IV). Making the reasonable assumption that ΔS_C is larger than ΔS_L but somewhat less than twice as large, we conclude that the ratio of K_L to K_C is at least 0.5 and possibly greater than unity.

LITERATURE CITED

1. M. M. Maguire and R. West, Spectrochim. Acta, 17, 369 (1961).
2. D. L. Powell and R. West, Spectrochim. Acta, 20, 983 (1964).
3. N. D. Coggeshall and E.L. Saier, J. Am. Chem. Soc., 73, 5414 (1951).
4. R. Mecke, Discussions Faraday Soc., 9, 161 (1950).
5. J. H. Lady and K. B. Whetsel, Unpublished results.
6. L. J. Bellamy and R. J. Pace, Spectrochim. Acta, 22, 525 (1966).
7. D. A. Ibbitson and L. F. Moore, J. Chem. Soc. (B), 1967, 76.
8. J. Malecki, J. Chem. Phys., 43, 1351 (1965).
9. L. E. Orgel and R. S. Mulliken, J. Am. Chem. Soc., 79, 4839 (1957).

TABLE I

TEST OF METHOD FOR END GROUP CORRECTION (SYNTHETIC DATA)

	Theoretical	Calculated	
		Uncorrected	Corrected
ϵ_n	$1.53(0.3\epsilon_1)$	0	$1.22(0.24\epsilon_1)$
K_2	2.96	3.17	2.92
K	9.97	7.05	9.45
Standard Error	0	0.0069	0.0001

TABLE II

TEST OF MODELS FOR SELF-ASSOCIATION OF PHENOL

Model	Standard Error	
	Cyclohexane[a]	CCl_4[b]
Dimer	0.058	0.061
Trimer	.035	.032
Tetramer	.019	.010
Pentamer	.009	.013
Hexamer	.009	.029
Dimer-Trimer	----[c]	----[c]
Dimer-Tetramer	----[c]	----[c]
Dimer → Tetramer	----[c]	----[c]
Dimer → Pentamer	----[c]	----[c]
Dimer → Octamer	----[c]	----[c]
Dimer-Stepwise	.004	.005

[a] Phenol concentrations up to 0.65M at 22.2°.

[b] Phenol concentrations up to 1.0M at 20.7°.

[c] Negative values for one or more constants.

TABLE III

THERMODYNAMIC CONSTANTS FOR SELF-ASSOCIATION OF PHENOL

Thermodynamic Constant	Dimer Formation	Higher Multimer Formation
	Cyclohexane Solution	
$K_{25}°$, l./mole	2.10	6.68
ΔF, kcal./mole	- 0.44	- 1.13
ΔH, kcal./mole	- 5.63±0.21	- 5.22±0.13
ΔS, cal./mole-degree	-17.4	-13.7
	CCl_4 Solution (With End Group Correction)	
$K_{25}°$, l./mole	0.94	3.25
ΔF, kcal./mole	0.04	- 0.70
ΔH, kcal./mole	- 5.03±0.27	- 4.32±0.28
ΔS, cal./mole-degree	-17.0	-12.2
	CCl_4 Solution (Without End Group Correction)	
$K_{25}°$, l./mole	1.09	2.74
ΔF, kcal./mole	- 0.05	- 0.60
ΔH, kcal./mole	- 6.08±0.21	- 4.07±0.06
ΔS, cal./mole-degree	-20.2	-11.7

TABLE IV

THERMODYNAMIC CALCULATIONS FOR PHENOL DIMERIZATION

Assumed	CCl_4[a]			Cyclohexane[b]		
K_L/K_C	$-\Delta H_C$	$-\Delta S_C$	$-\Delta S_L$	$-\Delta S_C$	$-\Delta S_C$	$-\Delta S_L$
0	5.03	17.0	∞	5.63	17.4	∞
0.1	5.10	17.4	19.3	5.73	17.9	20.9
0.5	5.40	19.0	17.0	5.85	18.9	17.9
1.0	5.74	20.8	16.0	6.05	20.2	17.4
2.0	6.44	24.0	15.4	6.48	22.4	16.9

[a] ΔH_L = -4.32 kcal./mole

[b] ΔH_L = -5.22 kcal./mole

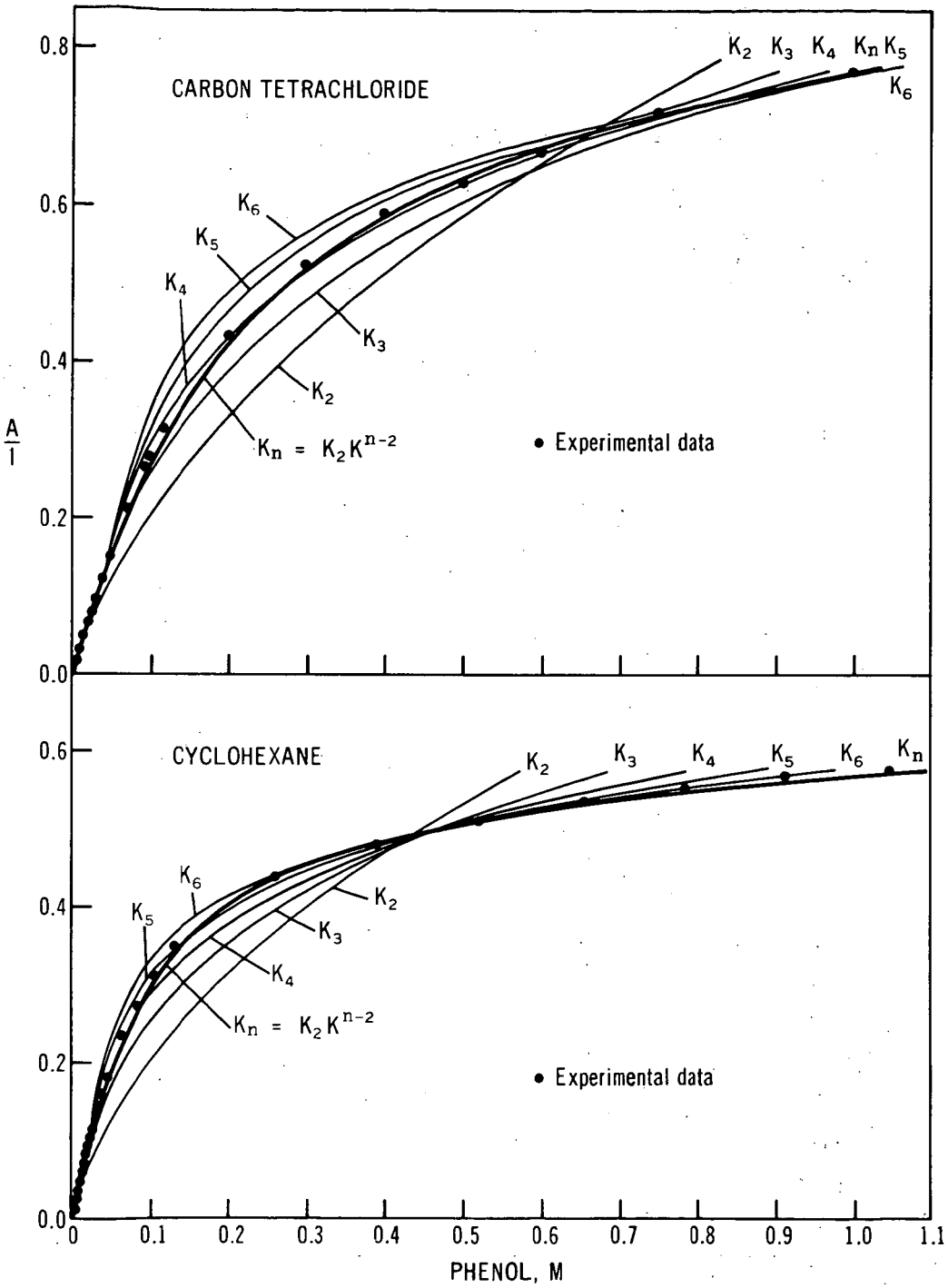

Figure 1. Fit of Experimental Data to Various Self-Association Models

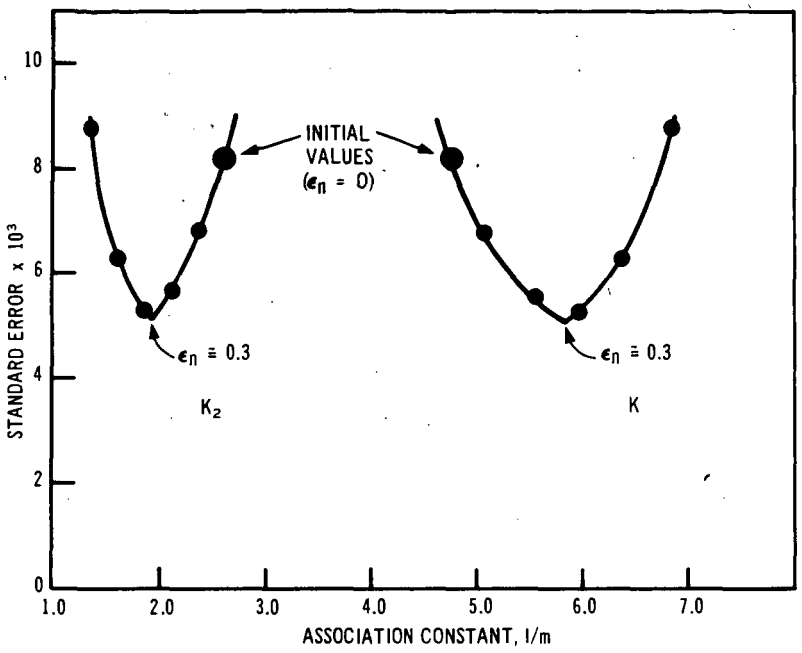

Figure 2. Correction for End Group Absorptivity (CCl_4 Solutions at 2.5°)

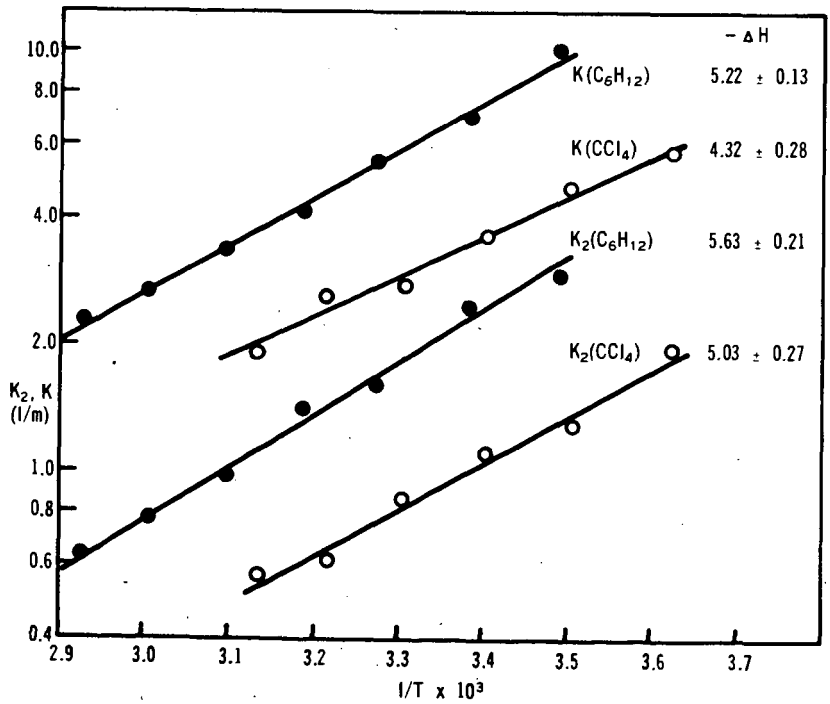

Figure 3. Enthalpies for Dimerization and Stepwise Association.

Infrared Interferometry - Emission Spectra in the Sodium Chloride Region

L. R. Cousins and K. H. Rhee

Gulf Research & Development Company
Pittsburgh, Pa.

Introduction

Spawned primarily by the space industry,(1) infrared interferometry is a relatively new technique to the practicing spectroscopist. Interferometry differs from spectrophotometry in two major areas. First, in interferometry the radiation is not dispersed into monochromatic frequencies but rather the radiation is modulated by means of a vibrating mirror. The modulation process results in an interferogram that in itself does not give very much information. However if the interferogram is fed into a wave analyzer, spectral information can be extracted. Another difference between spectrophotometry and interferometry is in the physical form of the entrance aperture. In a spectrophotometer the energy enters through narrow slits, just a few tenths of a millimeter wide. In an interferometer the energy enters through a window over an inch in diameter. Consequently, the amount of energy available to the detector of an interferometer is orders of magnitude greater than that available to the detector of a spectrophotometer.

These differences give rise to the main advantage of an interferometer, sensitivity. A secondary advantage is scanning speed. A complete interferogram can be recorded in a little over a tenth of a second although more typical scanning speeds are in the order of second.

These characteristics make the interferometer first choice for anyone interested in infrared emission.(2) Some of the possibilities of infrared emission spectroscopy are that samples can be scanned "in situ" with no need of disturbing the sample. This ability could save considerable sample handling in a process-control type of analysis or make analysis of hazardous materials more feasible. Infrared emission spectroscopy is completely non-destructive to the sample and could be used in the analysis of such things as valuable oil paintings. Interferometry can also be used to analyze samples too big for conventional spectrophotometers; for example, our atmosphere in air pollution studies. And it can be used to analyze samples too small; for example, pesticide residue on plant growth.

Experimental

The heart of the interferometer is the optical head. The head is fairly small, about 3 x 6 x 7 inches and is readily portable. The head is connected to the control panel by a ten-foot cable. The aperture is 1-1/4 inches in diameter and has a field of view of eighteen degrees. No special optics are required to get the sample's radiation to enter the optical head; you simply point the aperture at the sample. Unwanted radiation from material in the field of view can be masked out with aluminum foil. The foil being very reflective has essentially zero emissivity.

The head is also readily adapted to a mirror-type telescope making it possible to analyze samples at a remote distance. Smoke has been reportedly analyzed from stacks up to one-half mile away.(3)

Figure 1 is a diagram of the optical head. The interferometer is of the Michelson type. Radiation incident on the window passes into the optical head and strikes the beam divider. Here the radiation is split into two beams; one beam traveling to a stationary mirror and returning and the other beam traveling to a vibrating mirror and returning. Upon reaching the beam divider, the two beams unite and are reflected to the detector, a thermister bolometer. Some energy is lost exiting out through the entrance aperture.

The position of the vibrating mirror when both beams have the same path length is called the zero position. Consider for the moment that the incoming radiation is monochromatic. At the mirror's zero position, all waves will arrive at the detector in-phase giving a maximum signal. As the mirror moves infinitesimally in either direction from its zero position the relative path lengths of the two beams will change and all the waves will not arrive at the detector in-phase. Destructive cancellation will result and the detector's output will be diminished. When the mirror has moved 1/4 wavelength away from the zero position the total path difference will be 1/2 wavelength, and complete cancellation of the beam will result giving a minimum output from the detector. As the mirror continues to move away, the signal will start to increase until at mirror position 1/2 wavelength away from zero position, the retardation will be one full wavelength and all waves will be in-phase again. The detector output at this point will be a maximum equal to the first maximum. As the mirror continues to travel maxima are reached every even quarter wavelength from the zero position and minima are reached every odd quarter wavelength. The continuous output then is a sine wave. The frequency of this sine wave is related to the monochromatic input radiation by the equation:

$$f = L/T \times 1/\lambda$$

Where L is the length of the mirror's repetitive travel in microns and T is the time in seconds. Lambda is in microns. For most of our work L is 500 microns and T is one second. Thus, 2 micron radiation would give rise to a 250 cycles/sec audio sine wave. A wavelength of 16 microns would result in a 31 cycles/sec sine wave. Hence, all the frequencies in the interferogram of radiation between 2 to 16 microns can be found in the audio range below 250 cycles/sec. The length of the mirror's path also determines the resolution of the interferometer. The longer the path length the better the resolution. Our normal resolution is 20 cm^{-1}, the reciprocal of the path length.

Figure 2 shows the sawtooth nature of the mirror's travel and the resulting interferograms. Note that the return time for the mirror is very short and that the mirror's travel is very linear. The interferograms shown are not of monochromatic light.

To visualize what happens when polychromatic radiation enters the interferometer is a little more difficult. At the mirror's zero position, all the frequencies will still be in-phase and a maximum output of the detector will be obtained. However, as the mirror moves away from the zero position destructive cancellation occurs diminishing the output but not in the regular fashion of a sine wave. The result is a very sharp peak at the mirror's zero position with highly damped side bands.

One of the major drawbacks to interferometry is that it is impossible to recognize a spectrum from the interferogram; the interferogram must be filtered to obtain the spectrum. The filtering may be done in several ways. The interferogram can be fed repetitively into a variable filter or wave analyzer. The wave analyzer is set for the first audio frequency and a signal is recorded that is proportional to the amount of that frequency present in the interferogram. The wave analyzer is automatically advanced to the next audio frequency and its signal recorded. As this process is continued the spectrum is recorded.

Alternatively the interferogram may be mathematically filtered by means of the Fourier transformation. The equation for this transformation is:

$$G_{(\nu)} = \int_{0}^{\infty} I_{(x)} \cos 2\nu\pi x \, dx$$

where $G_{(\nu)}$ is the intensity of the spectrum

$I_{(x)}$ is the intensity of the interferogram

ν is the frequency in wave numbers

x is the path difference in cm

A rather novel way of filtering the interferogram is to transfer the data to a photographic film and place it in a laser beam. Lenses can then be used to optically perform the Fourier transformation and the image recorded on another piece of film.

Results

Figures 3a and 3b show a comparison between an absorption spectrum as recorded by a spectrophotometer and an emission spectrum derived from an interferogram. The spectra are very similar but not identical. The differences are primarily in resolution and relative intensities.

The effect of temperature on the emission spectrum of beta-hydroxyethyl acetate is shown in Figure 4. The spectrum is of course more intense at the higher temperature but otherwise they are very similar. The carbonyl band near 1700 cm^{-1} is relatively more intense in the hotter spectrum and this is consistent with the Boltzmann distribution giving the higher energy levels a greater population in the hotter sample. To obtain these spectra, the acetate was poured onto a piece of aluminum foil and then allowed to drain. The thin film that remained on the foil was sufficient to give the observed results. The foil was heated by conduction.

One of the major problems of infrared emission spectroscopy is shown in Figure 5. The subject is the emission spectrum of "Saran". The bottom spectrum is of one single layer of "Saran" and shows good band structure. However, with four layers of "Saran" all of the band structure between 800 and 1500 cm^{-1} completely disappeared and we have recorded essentially the spectrum of a black body. This phenomenon is attributed to self-absorption.

Interferograms of samples which have a temperature within a few degrees of the detector's temperature are very noisy because of the low signal level. In these cases, it is necessary to time average or co-add several hundred interferograms to obtain a satisfactory spectrum.[2]

Conclusion

An infrared interferometer covering the region 2-16 microns is seen as a potential tool for the practical spectroscopist. It does not have the universal applicability of the more conventional infrared techniques but its unique characteristics of high sensitivity, rapid scanning, and portability will certainly be used to solve specific problems that would be otherwise difficult if not impossible to solve.

---

(1) L. C. Block and A. S. Zachor, Appl. Optics 3, 209 (1964).

(2) M. J. D. Low and I. Coleman, Spectrochimica Acta 22, 369 (1966).

(3) Chemical and Engineering News 45, No. 7, 54 (1967).

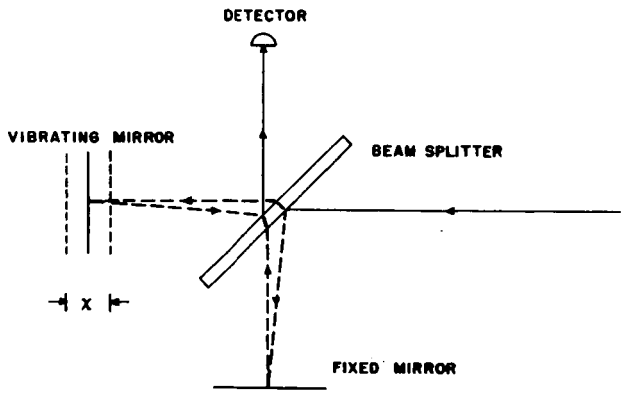

Figure 1. OPTICAL HEAD

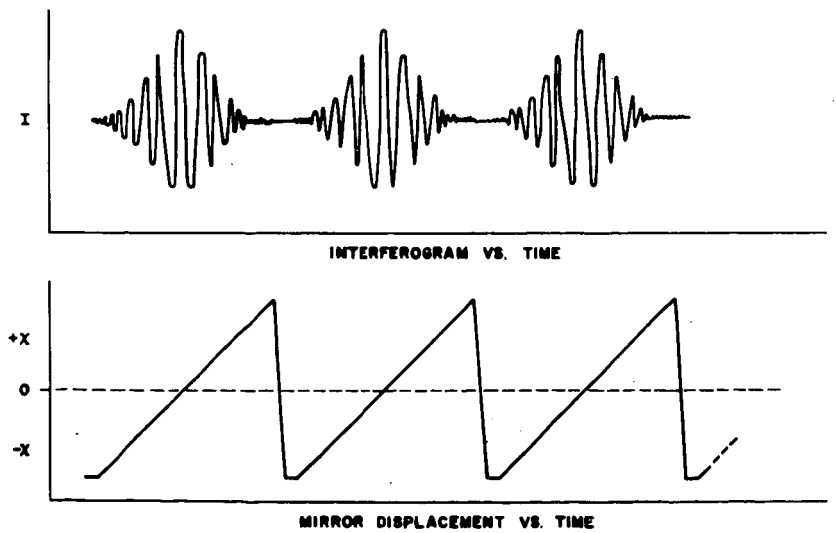

Figure 2. MIRROR TRAVEL AND RESULTING INTERFEROGRAM

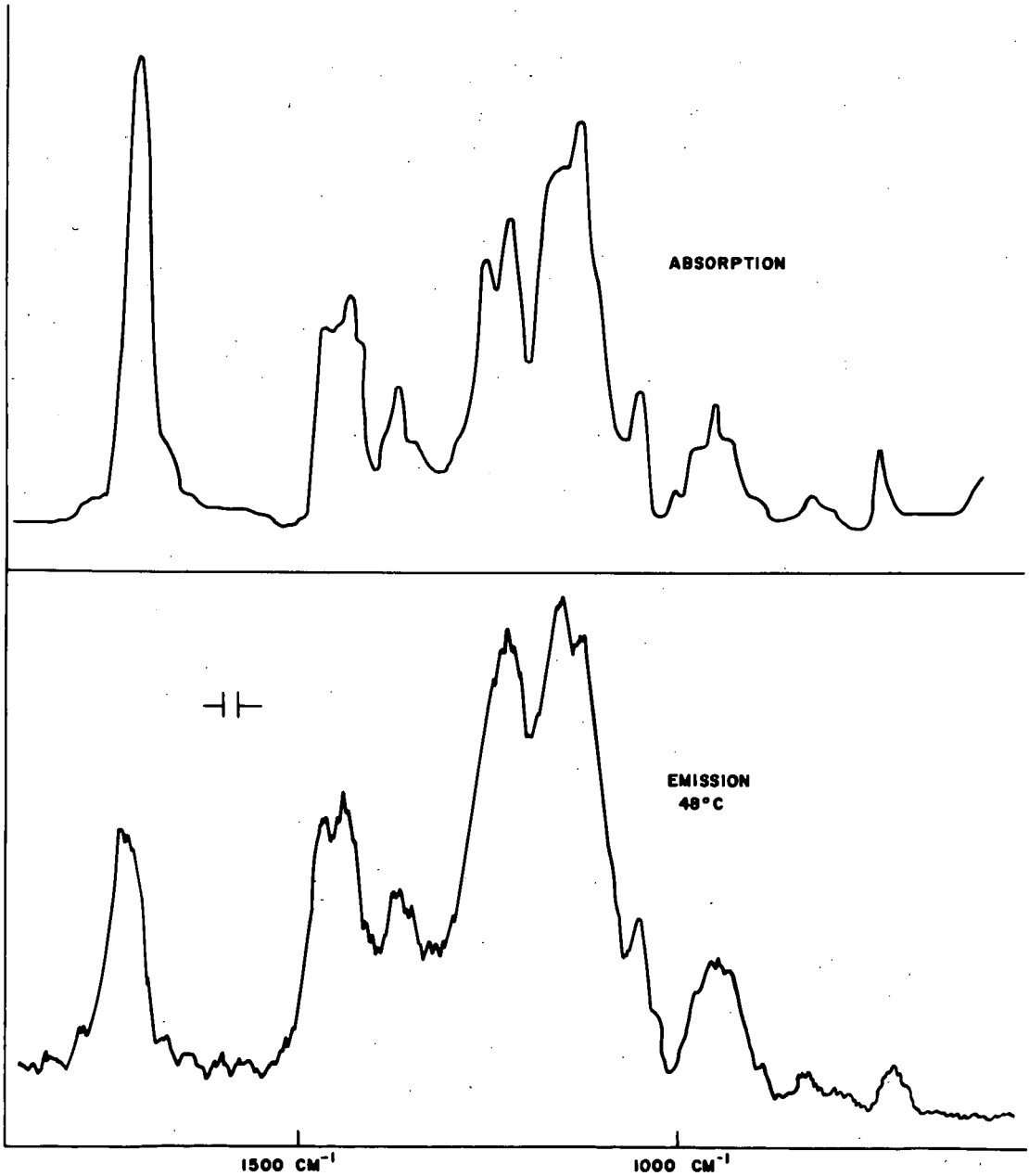

Figure 3a. and 3b. INFRARED SPECTRA OF "KRYLON"

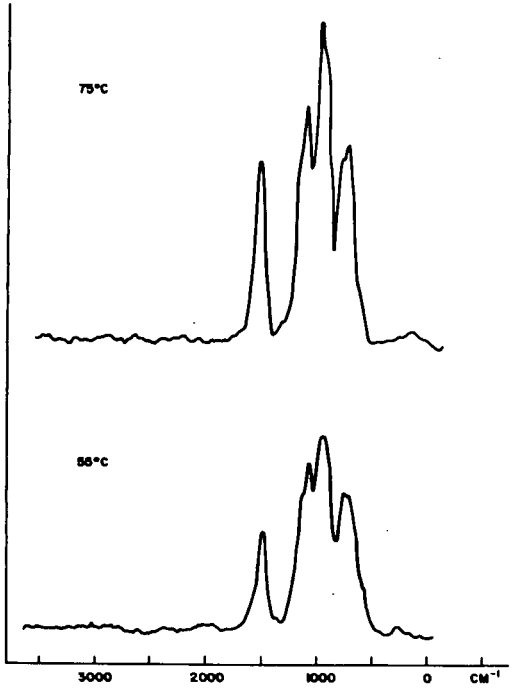

Figure 4. EMISSION SPECTRA OF β-HYDROXYETHYL ACETATE

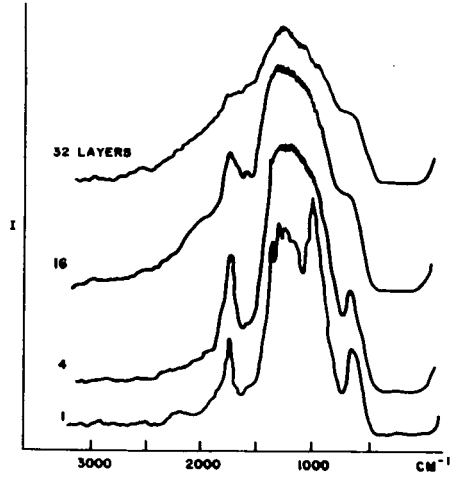

Figure 5. EMISSION SPECTRA OF "SARAN"

INFRARED CHEMICAL ANALYSIS: A NEW APPROACH

Mark M. Rochkind

Bell Telephone Laboratories, Incorporated
Murray Hill, New Jersey 07971

Utilizing an unusual low temperature sampling technique, a new approach to infrared chemical analysis which exhibits micromole sensitivities has been developed. The principal attribute of this new approach is that it offers a very general method for gas mixture analysis; a method which requires no previous knowledge of mixture composition and which entails no preanalytical separation of classes of components. Mixtures containing alkanes, alkenes, aldehydes, ketones, ethers, inorganics and aromatics may be at least qualitatively analyzed by a single step spectrophotometric procedure. Because this new approach to infrared analysis offers a very general method for determining the components of gas mixtures, it should find application in the fuel industry as a tool for kinetic and mechanistic studies of chemical combustion and as an aid in the study of combustion intermediates. This area of research is taking on increasing immediacy as we become more sensitive to the ecological menace posed by air pollution.

Sample preparation consists of diluting the gas mixture to be analyzed with a large excess (usually at least 100 fold) of nitrogen followed by condensation of the diluted gas mixture in pulsed fashion onto an infrared transmitting window previously cooled to 20°K. Using semiautomated procedures, sample preparation and deposition may be completed in less than one minute. A standard double beam spectrophotometer is used for recording the spectral data although enhanced analytical sensitivity may be obtained with modified instruments. The time required for recording a suitable spectrum varies with the problem in hand. Exhaustive analysis of an unknown mixture would, of course, require more time than would a search for some specified set of mixture components.

In the May issue of Analytical Chemistry, this technique of low temperature infrared matrix dispersion analysis is described and application of the technique to the analysis of a series of thirteen simple hydrocarbons is reported (Rochkind, M. M. (1967)). Since that writing, an additional fifty gases and volatile liquids have been examined (see, Table I), and we are now in a position to make concrete remarks regarding the analytical potential of this technique as it is applied to a broad range of chemical compounds. This will be done at the Symposium. In addition to discussing actual performance of this technique as an analytical tool, the equipment requirements will be outlined and some attention will be paid to the adaptation of automated methods with regard to sample preparation and sample deposition.

Table I. Gases and Volatile Liquids for which Standard Spectra Have Been Recorded

ALKENES

Allene
Butadiene
1-Butene
cis-Butene
trans-Butene
2,3-Dimethyl-2-Butene
Ethylene
3-Ethyl-1-Pentene
3-Ethyl-2-Pentene
Isobutylene
3-Methyl-1-Butene
2-Methyl-2-Butene
2-Methyl-1-Pentene
4-Methyl-1-Pentene
trans-4-Methyl-2-Pentene
1-Octene
1-Pentene
Propylene
2,4,4-Trimethyl-1-Pentene

ALKYNES

Acetylene
Ethyl Acetylene
Methyl Acetylene

ALDEHYDES

Acetaldehyde
Propionaldehyde

ETHERS

n-Butyl Ethyl Ether
tert-Butyl Ethyl Ether
Dimethyl Ether
Ethyl Ether
n-Propyl Ether
Vinyl Ethyl Ether

AROMATICS

Benzene

ALKANES

Butane
Cyclopropane
2,4-Dimethylpentane
Dimethyl Propane
Ethane
Heptane
Hexane
Isobutane
Isopentane
Methane
Octane
Pentane
Propane
2,2,5-Trimethylhexane
2,4,4-Trimethylpentane

KETONES

Diethyl Ketone
Dimethyl Ketone
Dipropyl Ketone
Ethyl Butyl Ketone
Ethyl Propyl Ketone
Methyl Butyl Ketone
Methyl Ethyl Ketone
Methyl Isobutyl Ketone
Methyl Pentyl Ketone
Methyl Propyl Ketone

INORGANICS

Ammonia
Carbon Monoxide
Carbonyl Sulfide
Hydrogen Sulfide
Sulfur Dioxide
Water

Different levels of sophistication may be pursued in connection with analysis of the raw spectral data. These range from hand analysis, using specially prepared tables, to strictly computer controlled analyses where the raw spectral data are digitized, transmitted over telephone lines to some centrally located computer facility and analyzed within the computer. An intermediate level of sophistication, one manifestly practical, involves transmitting via teletype a list of frequencies and approximate relative intensities to a central computer at some remote location within which analysis of the relevant data is performed. While the latter approach obviates digitization of the raw spectra, it poses the requirement that competent personnel must be present at the site of the experiment to reduce the spectral graphs to a list of meaningful frequencies and relative intensities. This level of sophistication, though less efficient on an absolute scale than a strictly computer controlled analysis, is very much easier to effect and suggests some exciting possibilities which utilize the time sharing capabilities of new generation computers. The paper to be presented will discuss this data handling problem in detail from the points of view of communications, equipment requirements, cost analysis and effectiveness. Computer controlled microfilm facilities for storing spectral data - where intelligible data need to be retained in an available state - will be discussed as well.

As pointed out in the May issue of Environmental Science and Technology, this method of infrared chemical analysis is strikingly computer oriented (Rochkind, M. M. (1967)). This is so because the sampling technique results in narrow bands (2-6 cm^{-1} bandwidths) which occur at well distributed frequencies, reproducibly from sample to distinct sample. It thus is possible to completely characterize a chemical species by a short list of frequencies (and, perhaps, relative intensities), each accurate to 1-2 cm^{-1}. This greatly simplifies the data handling and the data storing problems.

It appears as though solids may also be susceptible to the kind of matrix dispersion analysis described above for gases. A proposal for preparing samples from solid material which employs pulsed lasers and molecular beams will be considered and some possible attendant problems will be discussed. Relatively nonvolatile liquids (i.e., those having vapor pressures of less than 1 torr at room temperatures) present yet more difficult problems, but even these may be surmounted if need be.

In summary, it appears as though low temperature matrix dispersion - a technique whereby gaseous materials are sufficiently dispersed (not isolated) that in the solid state they exist in a quasi-homogeneous environment within which molecular interactions are minimized - provides a practical technique for

sample preparation and permits a new approach to infrared chemical analysis. Work is currently underway to define precisely the quantitative capabilities of the method. Progress in this area will be briefly reported.

References Cited

1. Rochkind, M. M., Anal. Chem. 39, 567 (1967).

2. Rochkind, M. M., Environ. Sci. Technol. 1, 434 (1967).

Acknowledgement

The author is indebted to Robert V. Albarino who prepared gas mixtures for analysis and who recorded many of the spectral measurements.

THE ANALYSIS OF COAL WITH THE LASER-MASS SPECTROMETER

by

F. J. Vastola, A. J. Pirone, P. H. Given, and R. R. Dutcher
College of Earth and Mineral Sciences
Pennsylvania State University, University Park, Pa.

INTRODUCTION

The laser-mass spectrometer has been used to pyrolyse petrographic constituents of coal and record the mass spectrum of the pyrolysis products thus produced. The laser-mass spectrometer has been described in detail elsewhere (1,2). Essentially it consists of a small pulsed ruby laser (max. output energy 0.1 joule) whose output can be focused on the surface of a coal target located in the ionization chamber of a time-of-flight mass spectrometer. A modified microscope optical system is used to focus the laser; irradiated targets can be as small as 10 microns in diameter. Since the target to be irradiated can be viewed through the same microscope system, selected areas of the coal sample can be pyrolysed. With the 10 micron diameter limit of the irradiation zone different petrographic constituents of a coal sample can be pyrolysed in-situ and their mass spectra recorded. These spectra can be used to study the chemical composition and structure of coal or even more simply can be used as "fingerprints" to differentiate between the various heterogeneous constituents of coal.

LASER HEATING

The energy from the laser that irradiates the coal sample is not great (~0.01 cal.). However, since the energy is delivered in a short pulse and the high coherency of the laser light enables it to be focused on a small area, flux densities of 10^6 cal./sec./cm.^{2} can be established at the coal surface. These high flux densities result in extremely rapid heating rates.

It is difficult to assign a temperature to a laser pyrolysis. If one assumes that only the material vaporized was heated estimated temperatures would be about 50,000°C. This value would be decreased considerably if the heat of decomposition of the coal was taken into account. Another factor even more difficult to evaluate is the shielding of the coal surface from the laser radiation by the plume of decomposition products. The presence of high molecular weight products in the mass spectrum would seem to indicate that the bulk of the pyrolysed coal did not reach temperature much above 1000°C. The high flux output of the laser establishes large temperature gradients in the heated solid but the short pulse length restricts pyrolysis to that material in the immediate vicinity of the irradiated zone. This is demonstrated by the fact that a second laser heating of a target produces a mass spectrum characteristic of a char rather than the original material, however if the laser is fired at an area 100 microns removed from a pyrolysed crater the resulting spectrum is the same as an unheated coal.

OBTAINING THE SPECTRA

The pulse length of the laser depends upon the pumping energy, under the conditions used in this investigation a typical pulse length would be about 300 microseconds. Most of the pyrolysis of the coal sample will take place during the actual laser burst. However, pyrolysis products are still being evolved several milliseconds after the laser burst due to the finite cooling time of the coal. The TOF mass spectrometer is capable

of making mass analysis of the species in the ionization chamber at 50 to 100 microsecond intervals enabling several spectra to be recorded during the pyrolysis.

The intensity of the masses recorded decreases exponentially with time. The rate of decay is not the same for all masses. In general the higher masses have the longer time constant. The distribution of decay rates cannot be accounted for by the effect of mass on pumping speed of the mass spectrometer vacuum system. A more likely explanation of the variation in decay rates of the different species is that the pyrolysis product distribution changes as the temperature of the coal decreases. For this investigation a single spectrum was recorded representing the composition one millisecond after the start of the laser burst.

THE SPECTRA

Figure 1 shows spectra obtained under similar conditions of the vitrain component of coals of several ranks. The ionization potential for all the spectra was 25 volts. The spectrum above mass 100 is magnified for ease of presentation for both the semi-anthracite and the sub-bituminous coals. With just a cursory glance one can see how easily vitrinites can be separated by the "fingerprint" technique. The general appearance of the mass spectra give some indication of the structure of the material. In the high mass region of the sub-bituminous vitrinite spectrum there are many mass peaks of about equal intensity. This tends to indicate a complex mixture of hydroaromatics and alkyl substituted aromatics. The HVA bituminous vitrinite has a much more differentiated spectrum in this region indicating more organization of structure. The semi-anthracite has a very simple mass spectrum as would be expected for a low hydrogen content, highly condensed ring system.

Figure 2 shows some comparison spectra. The high degree of similarity is seen between two HVA bituminous vitrinites from different sources. This can be contrasted to the dissimilarity between the spectrum of vitrain in sample number 1 and that of the non-vitrinitic material within 100 microns of the vitrain band edge. Although the latter two spectra have many of the same masses, differentiation can be easily accomplished by comparing selected peak ratios.

Major mass peaks can be found in the HVA spectra for the alkyl substituted benzenes and naphthalenes but the mass distributions of the spectra can not be accounted for by a mixture of stable molecules. The spectra indicate the presence of thermally produced free radicals in the pyrolysis products.

The laser-mass spectrometer is capable of differentiating between microscopic heterogeneities in coal. In order to understand the structural basis of this differentiation the behaviour of known materials under these pyrolysis conditions will have to be studied.

ACKNOWLEDGEMENT

This work was supported by a grant from the National Science Foundation.

LITERATURE CITED

1. Vastola, F. J., Pirone, A. J., Div. of Fuel Chem. preprint 151st National Meeting ACS, p. C-53, 1966.

2. Vastola, F. J., Pirone, A. J., Knox, B. E., Proceedings of the Fourteenth Annual Conference on Mass Spectrometry and Allied Topics, ASTM Committee E-14, p. 78, 1966.

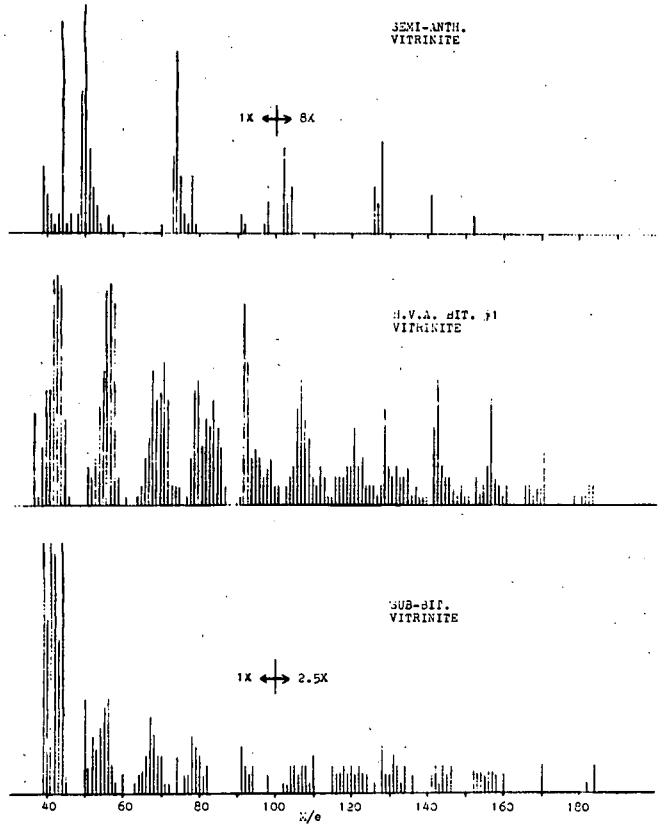

Figure 1: Mass spectra of vitrinites from selected coals.

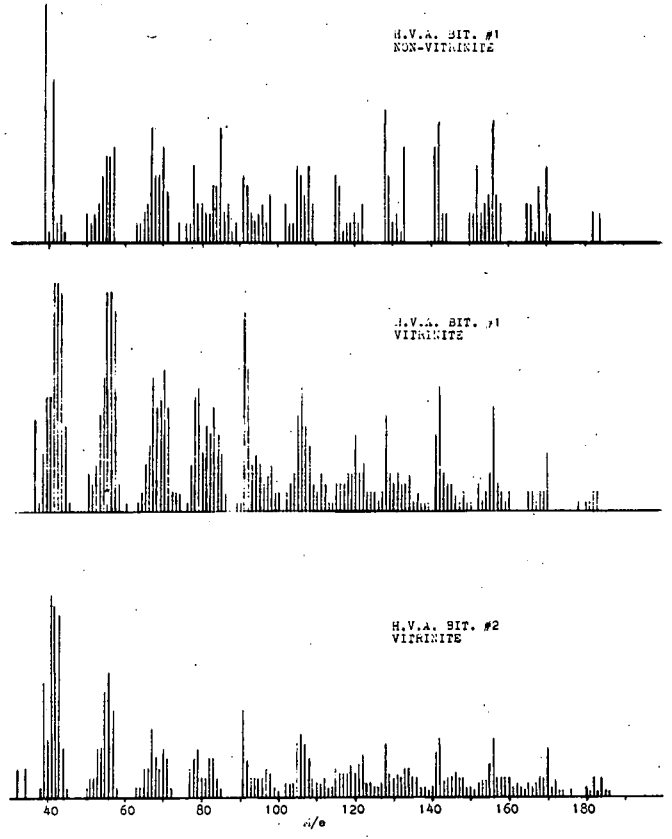

Figure 2: Mass spectra of selected components from h.v.a. bit. coals.

APPLICATIONS OF HIGH RESOLUTION MASS SPECTROMETRY IN COAL RESEARCH

A. G. Sharkey, Jr., J. L. Shultz, T. Kessler,
and R. A. Friedel

U.S. Department of the Interior, Bureau of Mines
Pittsburgh Coal Research Center, Pittsburgh, Pa.

INTRODUCTION

The Pittsburgh Coal Research Center of the Federal Bureau of Mines is attempting to determine which specific organic structures are most influential in enhancing desirable properties in commercially important fractions of coal tars such as road tar and electrode binder pitch. The current emphasis is on a survey of the types of hydrocarbon structures in coal-tar pitch detectable by high-resolution mass spectrometry. This information will provide the basis for an investigation of weathered road tar and other altered fractions of coal tar.

E. J. Greenhow and G. Sugowdz summarized the literature on pitch chemistry to 1961 by stating that less than 100 organic compounds in pitch have been isolated and identified[1]. In these investigations quantitative data were obtained for only a few of the structures identified.

In a previous investigation at our laboratory, mass spectrometric analyses were obtained for three fractions of pitch from the high-temperature carbonization of coal[2]. Semiquantitative data were reported for 34 structural types as well as carbon number distribution data for alkyl derivatives. Approximately 70 percent of the 80° to 85° C softening point pitch was investigated. An average molecular weight of approximately 250 and a value of 4.5 for the mean structural unit (number of aromatic rings per cluster) were derived from the mass spectrometric data. An aromaticity value of 0.94 (aromatic carbon/total carbon) calculated from these data is in excellent agreement with measurements by nuclear magnetic resonance.

Changes in the characteristics of road tar during weathering and in the carbonization properties of various coals following storage possibly involve alteration of certain organic constituents by reactions with oxygen, nitrogen, and sulfur. In our previous investigations of pitch by mass spectrometry only the hydrocarbon portion could be studied in detail as structures containing the heteroatoms nitrogen, oxygen, and sulfur have, in many instances, the same nominal molecular weights as hydrocarbons. Procedures commonly used to study the chemical constitution of coal-tar pitches, such as solvent fractionation, result in a separation according to molecular size but not chemical type as is required to detect changes in heteroatom concentrations.

High-resolution mass spectrometry offers a new approach to studies of species containing heteroatoms. Separation of the components is not necessary if the instrument has sufficient resolution and sensitivity. The addition of a heteroatom results in a slight change in the precise molecular weight of the species producing distinctive peaks for the various combinations of atoms.

In this preliminary study of the high-resolution mass spectrum of coal-tar pitch the investigation consisted of:

(1) Obtaining spectra by fractionating the pitch directly in the mass spectrometer ion source to effectively concentrate species in particular molecular weight ranges.

(2) Making precise mass determinations and deriving empirical formulas for components in the 150 to 320 mass range. This mass range includes components comprising approximately 70 percent by weight of the pitch.

(3) Showing that many of the high molecular weight species detected for the first time could arise from the condensation of radicals.

EXPERIMENTAL PROCEDURE

A Consolidated Electrodynamics Corp. Model 21-110B double focusing mass spectrometer was used for this study of a Koppers 80° to 85° C softening point pitch. A direct insertion probe was used to introduce the pitch into the region of ionization for the fractionation experiment. The mass spectrum and the weight of the sample vaporized were determined at the following probe temperatures: 100°, 175°, 250°, 290°, and 325° C.

A conventional umbrella-type glass introduction system was used for the precise mass study.[3]

Mass measurements on standards were accurate to $\pm$ .003 amu. The peak matching technique with perfluorokerosene as a standard was used for all mass assignments. For most of the high-resolution determinations, the instrument was operated with a resolving power of approximately 1 part in 8 to 10 thousand and with an inlet and source temperature of 300° C. The resolution was high enough to permit accurate mass assignments to approximately mass 300 and represented a compromise between sensitivity and desired resolving power. The resolving power required at mass 300 for complete separation of several of the mass doublets of interest is shown in table 1; however, complete separation is not generally required for precise mass assignments. In many instances 50 percent of the theoretical resolving power is adequate.

RESULTS AND DISCUSSION OF RESULTS

A. Mass Spectra of Pitch Fractionated in Mass Spectrometer.

Data obtained for the fractional distillation of the 80°-85° C softening point pitch in the mass spectrometer ion source are shown in table 2. Fractionation of the sample by increasing the temperature of the direct introduction probe was effective in concentrating species in a limited molecular weight range. Precise mass determinations, made as a second part of this investigation, substantiated structural assignments to about molecular weight 350.

At a probe temperature of 100° C 25.5 percent of the pitch sample was vaporized. Masses 178 and 202 are the most intense peaks in this spectrum, indicating anthracene and/or phenanthrene and 4-ring peri-condensed structures such as pyrene distill preferentially at these temperature-pressure conditions. Species with molecular weights as high as 420 were detected. When the probe temperature was increased to 175° C an additional 22.4 percent of the pitch vaporized. The molecular weight of the species showing maximum intensity increased to 252, corresponding to a 5-ring, peri-condensed aromatic structure(s); the molecular weight range of the spectrum increased to mass 526. At 250° C an additional 20.1 percent of the pitch distilled. The mass with maximum intensity was

Table 1.- Major mass doublets in mass spectrum of coal-tar pitch

Doublet	ΔM (amu)	Resolution required to separate doublet at mass 300
C_2H_8-S	.0906	3,300
CH_4-O	.0364	8,200
CH_2-N	.0126	24,000
$C^{12}H$-C^{13}	.0045	67,000

Table 2.- Fractional distillation of Koppers 80°-85° C softening point pitch in mass spectrometer ion source

Probe temperature, °C	Distillate, weight percent		Mass spectrum	
	Cumulative	Fractional	Mass with Max. intensity	Maximum mol. wt.
100	25.5	25.5	178-202	420
175	47.9	22.4	252	526+[a]
250	68.0	20.1	228	550+[a]
290	68.0[b]	-	326	620+[a]
325	68.0	-	326	570+[a]

a. Accurate mass numbers could not be assigned to trace peaks appearing at higher molecular weights.
b. No change in weight of residue detectable at probe temperatures > 250° C.

Table 3.- Mass assignments for several perfluorokerosene (PFK) and polynuclear hydrocarbon peaks

Experimental	Calculated (amu)	ΔM	P.P.M.	
204.9888	204.9896	.0008	4	(P.F.K.)
218.9856	218.9852	.0004	2	do
230.9856	230.9847	.0009	4	do
242.9856	242.9855	.0001	0.4	do
254.9856	254.9854	.0002	0.8	do
268.9824	268.9810	.0014	5	do
280.9824	280.9811	.0013	5	do
202.0776	202.0783	.0007	4	4-ring, peri-condensed
228.0937	228.0939	.0002	1	4-ring, cata-condensed

228, corresponding to a 4-ring, cata-condensed aromatic hydrocarbon, and the molecular weight range of the spectrum increased to mass 550. At higher probe temperatures, 290° and 325° C, the spectra indicated that the average molecular weight and ring size of the components continued to increase. The mass with maximum intensity occurred at 326 at temperatures of 290° and 325° C. The spectra indicated components with molecular weights higher than 620. There was no weight change detectable at probe temperatures greater than 250° C. Thus, the spectra obtained at 290° and 325° C represent only a very small portion of the pitch. The total amount of pitch vaporized was 68 weight percent of the charge. This value agrees well with the 70 percent vaporization obtained in our previous studies of the same pitch.[2] The mass spectra obtained at probe temperatures greater than 100° C contained trace peaks whose masses could not be assigned; these ions indicated molecular weights up to about 800.

The increased molecular weight range of the material vaporized at higher probe temperatures is illustrated in figures 1 and 2. These figures, based on low-ionizing voltage mass spectra, were plotted at the University of Pittsburgh Computer Center using a program obtained through the courtesy of the Graduate School of Public Health at the University. The trace ions up to approximately mass 800, which could not be effectively reproduced in these figures, correspond in molecular weight to structures containing at least 12 aromatic rings.

B. Precise Mass Assignments.

Table 3 lists precise mass values obtained by the peak matching technique for several peaks in the perfluorokerosene marker spectrum and for the molecular ions of 4-ring peri- and cata-condensed aromatic hydrocarbons. These data show that mass assignments can be made to within a few parts per million by this technique.

Empirical formulas were derived from the measured masses in the 150 to 319 range of the 80°-85° C coal-tar pitch. Species having from 12 to 28 carbon atoms were observed. A total of 273 peaks were indicated, many resulting from doublets and triplets at nominal masses. In addition to the hydrocarbon species, the precise masses indicated the presence of at least 10 structural types containing oxygen, 9 containing sulfur, and 10 containing nitrogen. Measured and calculated masses showed agreement in general from a few tenths to 3 millimass units. Nineteen of these masses represent structural types not previously reported for coal tar.[4]

The nominal molecular weight and atomic species for each of the components detected is shown in figures 3 and 4. The ability of the instrument to resolve complex mixtures is illustrated at mass 212 where empirical formulas were obtained for structures containing carbon-hydrogen, carbon-hydrogen-oxygen, and carbon-hydrogen-sulfur, all having the same nominal molecular weight.

Table 4 gives the formulas for 13 new high molecular weight species detected in the high-resolution mass spectrum of pitch. The formulas were derived from the observed precise masses. The particular structural type(s) cannot be identified as many isomeric variants are possible for each formula. Also shown are formulas and structures of several compounds containing (C,H), (C,H,O), (C,H,N), and (C,H,S) previously identified in coal tar.[4] The last two columns of table 4 illustrate how the high molecular weight species, with molecular formulas determined in this investigation, can arise from condensation reactions.[5] The addition of C_4H_4 or C_6H_5 radicals to radicals from previously identified structures will produce the molecular formulas shown.

Table 4.- Formation of high molecular weight components by condensation of radicals

Previously identified[a]		High molecular weight components detected this investigation					
			Precise mass (amu)			Possible origin of component	
Compound	m/e (amu)	Formula	Observed	Theoretical	Δ	Radical from original structure	Addition required[b]
Benzo[kl]xanthene	218.0732	$C_{20}H_{12}O$	268.0894	268.0888	.0006	$C_{16}H_8O$	C_4H_4
		$C_{24}H_{14}O$	318.1052	318.1045	.0007	$C_{16}H_6O$	$2(C_4H_4)$
Naphtho[2,1,8,7-klmn]xanthene	242.0732	$C_{22}H_{12}O$	292.0880	292.0888	.0008	$C_{18}H_8O$	C_4H_4
Benzo[b]naphtho-[2,1-d]thiophene	234.0503	$C_{20}H_{12}S$	284.0657	284.0660	.0003	$C_{16}H_8S$	C_4H_4
Dibenzo[b,def]-chrysene	302.1095	$C_{28}H_{16}$	352.1161	352.1252	.0091	$C_{24}H_{12}$	C_4H_4
5H-Benzo[b]-carbazole	217.0891	$C_{20}H_{13}N$	267.1079	267.1048	.0031	$C_{16}H_9N$	C_4H_4
		$C_{24}H_{15}N$	317.1250	317.1204	.0046	$C_{16}H_7N$	$2(C_4H_4)$
4H-Benzo[def]-carbazole	191.0735	$C_{22}H_{13}N$	291.1077	291.1048	.0029	$C_{14}H_5N$	$2(C_4H_4)$
Acridine	179.0735	$C_{21}H_{13}N$	279.1086	279.1048	.0038	$C_{13}H_5N$	$2(C_4H_4)$
Phenanthrene	178.0783	$C_{20}H_{14}$	254.1056	254.1095	.0039	$C_{14}H_9$	C_6H_5
Chrysene	228.0939	$C_{24}H_{16}$	304.1205	304.1252	.0047	$C_{18}H_{11}$	C_6H_5
Benzo[ghi]perylene	276.0939	$C_{26}H_{14}$	326.1116	326.1095	.0021	$C_{22}H_{10}$	C_4H_4
Coronene	300.0939	$C_{28}H_{14}$	350.1122	350.1095	.0027	$C_{24}H_{10}$	C_4H_4

a/ Listed in "Properties of Compounds in Coal-Carbonization Products," ref. 4.
b/ M/e of added radical: C_4H_4 - 52; C_6H_5 - 77.

CONCLUSIONS

Approximately three times the number of components reported in previous investigations of coal-tar pitch by other techniques were detected in this study. While the identification of particular structural types is not possible, the precise masses indicate the atomic species present. This study shows that high-resolution mass spectrometry provides a means of detecting changes in either the concentration or composition of organic compounds in fractions of coal tar following exposure to various atmospheres. Such information should lead to a better understanding of the properties of road tars and other commercially important fractions of coal tar.

References

1. Greenhow, E. J., and Sugowdz, G. Coal Research in C.S.I.R.O., Australia, No. 15, Nov. 1961, pp. 10-19.

2. Shultz, J. L., Friedel, R. A., and Sharkey, A. G. Jr. Fuel, 44, No. 1, Jan. 1965, pp. 55-61.

3. Lumpkin, H. E., and Taylor, G. R. A Solids Inlet System for a Mass Spectrometer. Anal. Chem., 33, 1961, pp. 476-477.

4. Anderson, H. C., and Wu, W. R. K. Bureau of Mines Bull. No. 606, 1963, 834 pp.

5. Sharkey, A. G., Jr., Shultz, J. L., and Friedel, R. A. Carbon, 4, 1966, pp. 365-374.

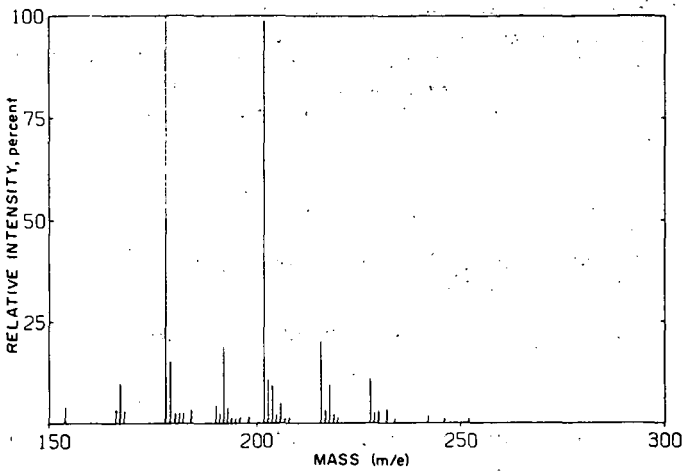

Figure 1.—Mass spectrum of 80°-85°C softening point pitch fractionated at 100°C in spectrometer.

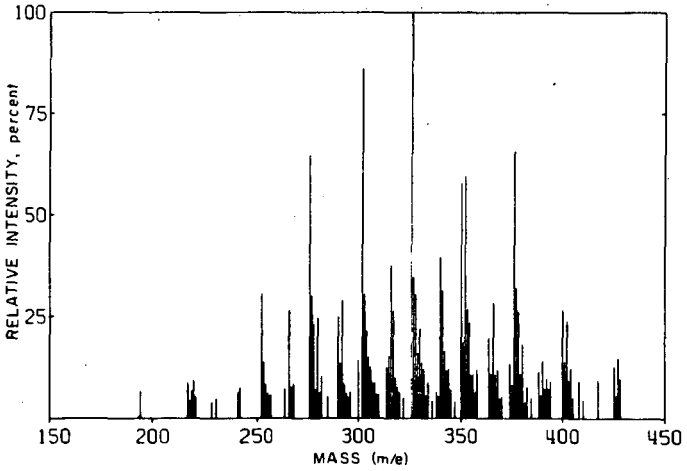

Figure 2.—Mass spectrum of 80°-85°C softening point pitch fractionated at 325°C in spectrometer.

L-9546-A

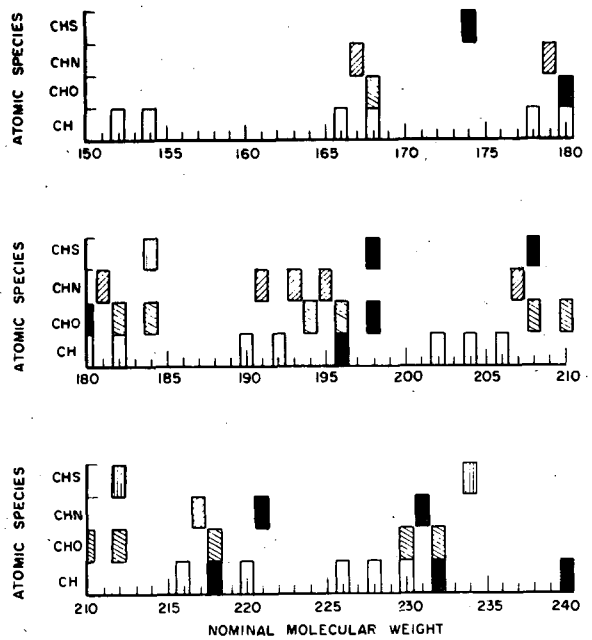

Molecular weight of and atomic species in components observed in 80°–85°C pitch by high-resolution mass spectrometry. Mass range 150–240

Figure 3. L-9942

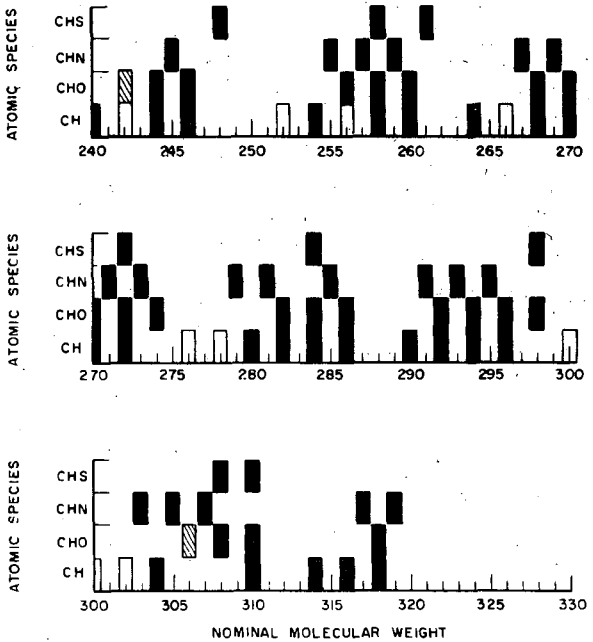

Molecular weight of and atomic species in components observed in 80°–85°C pitch by high-resolution mass spectrometry. Mass range 240-319.

Figure 4. L-9943

FIELD IONIZATION MASS SPECTROMETRY - STRUCTURE CORRELATIONS FOR HYDROCARBONS

Graham G. Wanless

Esso Research and Engineering Co.
Analytical Research Division
P. O. Box 121
Linden, New Jersey

ABSTRACT

Field ionization is a preferred way of looking at molecules and mixtures thereof. Ionization is accomplished by electron abstraction in an electrostatic field of very steep gradient, of the order of 10^8 volts/cm. In contrast to spectra from electron impact, these spectra possess much greater parent ion abundances and relatively fewer fragment ions. This result facilitates analysis of unknown mixtures greatly.

Because the spectra are simpler, greater use can be made of the metastable ions for structural interpretation. An unexpected result is the fact that there is a close correlation between kind and abundance of field ionization primary metastable ions and compound structure. A more complete study of branched hydrocarbons (showing these structure correlations) will be presented than that published recently (Anal. Chem. 39, No. 1, 2-13, Jan. 1967).

The present state of development will be described. Principal problems are (a) to increase signal strength, (b) to develop improved field ion anode devices, and (c) to improve repeatability of successive spectra. How the signal averaging computer can convert the present-quality spectra to precision field-ion mass spectra will be demonstrated with examples.

NUCLEAR MAGNETIC RESONANCE STUDIES OF HYDROGEN BONDING

Norman C. Li

Duquesne University, Pittsburgh, Pennsylvania

Hydrogen bonding is a very significant type of interaction, and is of widespread occurrence. According to Pimentel and McClellan[1], a hydrogen bond exists between a functional group A-H and an atom or a group of atoms D in the same or a different molecule when there is evidence of bond formation, and when the bond linking A-H and D involves the hydrogen atom already bonded to A. Infrared method, based mainly on intensity measurements of the band assigned to the monomeric species, has been used extensively in the determination of equilibrium constants of hydrogen-bonded systems. It offers the advantages that different hydrogen-bonded complexes can be distinguished, and that relatively low concentrations can be used. For very weak complexes however, the infrared method has not proved to be a sufficiently sensitive probe of the quantitative aspects of hydrogen bonding. High resolution nuclear magnetic resonance (nmr) scores easily in providing a sensitive measure of interaction, because it permits the measurements of frequencies which can be done very accurately, rather than intensities which are more subject to uncertainty. This paper describes several ways in which nmr is used to obtain equilibrium constants and thermodynamic functions of various hydrogen-bonded systems. In addition, an application of hydrogen-bonding data to the determination of the preferred form of a beta-diketone is given.

It is well known that the formation of hydrogen bonds usually shifts the nmr signals to lower field, except in certain cases involving aromatic molecules or electron donors in which unusual magnetic anisotropic effects are present [2,3]. Virtually all hydrogen bonds are broken and re-formed at a sufficiently fast rate, so that separate resonances for both hydrogen-bonded and nonhydrogen-bonded states in the same medium are not observed. Consequently, the observed frequency ν will correspond to the average of the characteristic frequencies of the complexed and uncomplexed protons (ν_c, ν_f), weighted according to the equilibrium fraction in each form (X_c, X_f):

$$\nu = X_f\nu_f + X_c\nu_c \qquad (1)$$

For an equilibrium between a monomeric hydrogen donor, A-H, and an electron-donor, D, to form a 1:1 complex C, the following equation may be derived[4] when the concentration of the electron-donor is much greater than that of C:

$$\frac{1}{\nu - \nu_f} = \frac{1}{K(\nu_c-\nu_f)}\,\frac{1}{\underline{d}} + \frac{1}{\nu_c-\nu_f} \qquad (2)$$

In eq. 2, ν is the measured nmr frequency of the hydrogen-bonding proton at a concentration $\underline{d}$ of D, ν_f is the frequency of monomeric A-H proton signal at $\underline{d} = 0$, and K is the association constant

$$K = \frac{(C)}{(A\text{-}H)d} \qquad (3)$$

It is interesting to note that this equation is of the same form as one used for treatment of ultraviolet spectral data on 1:1 complexes,

$$\frac{1}{E-E_f} = \frac{1}{K(E_c-E_f)}\frac{1}{d} + \frac{1}{E_c-E_f} \qquad (4)$$

where the E's are molar extinction coefficients[5]. For the treatment of infrared spectral data for 1:1 complexes, the following equation can be derived

$$\frac{1}{E_f-E} = \frac{1}{K\,E_f}\frac{1}{d} + \frac{1}{E_f} \qquad (5)$$

if intensity measurements are made on the band assigned to the monomeric and uncomplexed species and if complexed species do not absorb radiation at the same frequency, so that $E_c = 0$.

Benzenethiol complexes. Mathur,et al.[4], report nmr studies of hydrogen bonding of benzenethiol with N,N-dimethylformamide (DMF), tributyl phosphate (TBP), pyridine, N-methylpyrazole, and benzene to serve as models of bonding of -SH to the carbonyl oxygen, phosphoryl oxygen, organic nitrogen bases, and an aromatic π electron system, respectively. Table I lists the results obtained.

Table I
Thermodynamic data for benzenethiol bonding to electron-donors

Electron donor	$\nu_c-\nu_f$ (ppm)	K_{26}^{o} l./mole	$-\Delta H$ kcal./mole
Pyridine	1.2	0.22	2.4
N-methylpyrazole	1.5	.14	2.1
TBP	1.8	.43	2.0
DMF	2.2	.24	1.8
Benzene	-2.5	.039	0.5

The extent of hydrogen-bonding in these systems, as measured by the equilibrium constants and enthalpy changes, is much smaller than that for the same electron donors interacting with phenol. For example, the values of K for phenol-pyridine and phenol-DMF are 77 and 64 l./mole, respectively [6,7]. These suffice to show the weakness of -SH hydrogen bonding relative to -OH. It is only because of the fairly large association shift, $\nu_c-\nu_f$, and the precision of nmr frequency measurements, that the thermodynamic functions of -SH bonding systems can be obtained. In benzene the ring current effect dominates the sign and magnitude of $(\nu_c-\nu_f)$. As shown in Table I, benzene behaves as π-electron donor and hence capable of forming weak hydrogen bond with benzenethiol.

2-Propanol complexes. When 2-propanol is used as the hydrogen donor, eq. 2 has to be modified since self-association of the alcohol occurs, and this may affect the equilibrium involving its complex formation with D. Takahashi and Li[8] have derived the following modified equation

$$\frac{1}{\nu-\nu'} = \frac{1}{K(\nu_c-\nu')}\frac{1}{dx} + \frac{1}{\nu_c-\nu'} \qquad (6)$$

in which x is the fraction of 2-propanol in the form of monomer at a concentration of alcohol which is not hydrogen-bonded to D (assuming the alcohol to be a mixture of monomeric and polymeric species), and v' is the weighted average OH frequency of the 2-propanol which is not hydrogen-bonded to D. Table II lists the results obtained with N-methylacetamide and N,N-dimethylacetamide as electron donors.

Table II: Thermodynamic data for 2-propanol bonding to acetamides

Temp., °C	K, l./mole	ν_c, ppm
	(A) N-methylacetamide	
36	3.61	5.00
24	5.02	5.17
14	6.01	5.23
0	8.94	5.35
	(B) N,N-dimethylacetamide	
40	2.23	4.20
29	2.56	4.30
21	2.88	4.33

Muller and Reiter[9] suggest that the nmr frequency of the complexed species depends quite strongly on the degree of excitation of the hydrogen-bond-stretching vibrational mode. They reason that because this is an unusually low-frequency motion, several excited states are significantly populated even at temperatures as low as 200°K, and their calculations show a temperature dependence of ν_c. The data of Table II on the values of ν_c at different temperatures do indicate that ν_c increases slightly with decrease in temperature. This is not in agreement with the assumption of several authors[4,10-12] that the hydrogen bond shifts do not vary with temperature.

Amine complexes. Takahashi and Li[13] report nmr studies of hydrogen bonding between the amino protons of t-butylamine and aniline, and several electron donors, in chloroform medium. CCl_4 cannot be used because of its reaction with amine. When $CHCl_3$ is used as the solvent, eq. 2 has to be modified since the proton in $CHCl_3$ also acts as a hydrogen donor to the electron donor. The modified equation is

$$\frac{1}{\nu-\nu_f} = \frac{1}{K(\nu_c-\nu_f)} \cdot \frac{1+K_s(S)}{d} + \frac{1}{\nu_c-\nu_f} \qquad (7)$$

where K and K_s are equilibrium constants of the reactions

$$\text{Amine} + D = \text{amine}\ldots D \qquad K$$
$$Cl_3CH + D = Cl_3CH\ldots D \qquad K_s$$

and (S), d are the total concentrations of $CHCl_3$ and D, respectively. The experiments were carried out so that (S) is much greater than d and d much greater than the total concentration of the amine. From eq. 7, a plot of $1/(\nu-\nu_f)$ vs. $(1+K_s(S))/d$ therefore should yield a straight line, from which K can be determined. The value of K_s is determined in separate experiments by measuring

the nmr frequency of the chloroform proton signal in CCl_4 solutions containing 0.05M $CHCl_3$ and various amounts of the electron donor.

The hydrogen-bonding of N-methylacetamide (NMA) to the amines may be represented by the equation

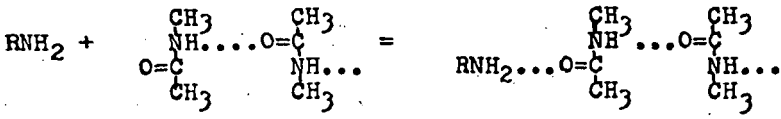

(8)

The values of $\nu_c - \nu_f$ for NMA bonding to the amines are independent of temperature between -19 and 36°. This means that in this system, the hydrogen-bond shift is temperature independent and that the self-association of NMA does not interfere with its bonding with the amines. The relative hydrogen-donor strength of $-NH_2$, -OH, and -SH may be obtained by noting that the association constant for aniline bonding to NMA (K = 58 at 36°) is smaller than for phenol bonding to NMA (K = 105 at 30°) and larger than for benzenethiol bonding to NMA (K = 0.13 at 37°).

Water complexes. Takahashi and Li[14] and Ting, et al.[15], report nmr studies of water as hydrogen donor to tetrahydrofuran, acetone, N,N-dimethylacetamide, N,N-dimethylformamide and dimethyl sulfoxide. In their experiments water is the hydrogen donor at low concentrations (mole fraction in the range of X_w = 0.003 to 0.02), in the presence of an electron donor (mole fraction in the range X_d = 0.5 to 0.99), and cyclohexane as an inert solvent. Since water is not soluble in the inert solvent, the presence of an appreciable excess concentration of D is necessary. In the region of low water content, linear plots of the nmr frequency of the water protons vs. the mole fraction of water, at a given value of X_d, are obtained. The extrapolation of the water proton frequency to zero water concentration is easily made, and in the limit of $X_w = 0$, only two species are considered: the 1:1 complex, $OH_2 \cdots D$, and the 1:2 complex, $OH_2 \cdot D_2$. The two species are considered to be in equilibrium according to the relation

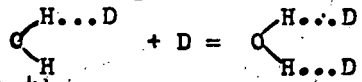

(9)

The characteristic nmr frequencies of the 1:1 and 1:2 complexes are designated ν_{11} and ν_{12}, respectively, and the following equation is derived

$$\frac{1}{\nu_o - \nu_{11}} = \frac{1}{K(\nu_{12} - \nu_{11})} \cdot \frac{1}{X_d} + \frac{1}{\nu_{12} - \nu_{11}} \qquad (10)$$

In eq. 10, ν_o is the extrapolated frequency of the water protons at zero water concentration and K is equilibrium constant of eq. 9. The authors assume that $(\nu_{12} - \nu_{11})$ is approximately independent of temperature and draw plots of $1/(\nu_o - \nu_{11})$ vs. $1/X_d$. The correct ν_{11} is taken to be the value which makes the

plots at different temperatures come to a common intercept. From the plots and eq. 10, the values of K and v_{12} are obtained.

Equilibrium constants and enthalpy changes for water bonding to N,N-dimethylformamide (DMF) are larger than the corresponding values for water-N,N-dimethylacetamide (DMA). This order is surprising, since DMF is a weaker electron-donor than DMA towards phenol. It may be that the CH proton in DMF functions as a weak hydrogen donor to the oxygen of water, the protons of which are bonded to other DMF molecules. This would result in a greater hydrogen-donor strength of water toward DMF than toward DMA.

It is of interest to note that Muller and Simon[16] determine proton chemical shifts for dilute solutions of water in mixtures of dioxane and carbon tetrachloride. When the mole fraction of water is below 1.5×10^{-3}, self-association of water is negligible, and the authors treat the data assuming that there are three solute species, free water, a 1:1 water-dioxane complex, and a 1:2 complex. The characteristic frequencies of the complexes appear to be independent of temperature in the range 11-70°, in accordance with the assumption made by Takahashi and Li[14] and Ting, et al.[15]

β-Diketone complexes. Pukanic, et al.[17], report nmr studies of hydrogen bonding between β-diketones- thenoyltrifluoroacetone, hexafluoroacetylacetone, and trifluoroacetylacetone- and several neutral organophosphorus compounds- tributyl phosphate, diethyl ethyl phosphonate, and tri-n-octyl phosphine oxide. Of the three diketones studied, hexafluoroacetylacetone gives the most stable complex with a given phosphorus compound and this is as expected, since it has two electron-withdrawing CF_3 groups in the same molecule. Its greater hydrogen-donor strength is in line with its greater acid strength (pK_a of hexafluoroacetylacetone, thenoyltrifluoroacetone and trifluoroacetylacetone = 4.35, 5.70 and 6.40, respectively). With a given diketone, the equilibrium constant of hydrogen bond formation with the phosphorus compounds increases in the order tributyl phosphate, diethyl ethyl phosphonate, and tri-n-phosphine oxide and is in line with the relative basicity of the phosphorus compounds.

Pukanic, et al.[17], give an example of the application of hydrogen bonding data to the determination of the preferred enol form of thenoyltrifluoroacetone (HTTA). In CCl_4 as solvent, two possible enol structures (I and II) can be postulated

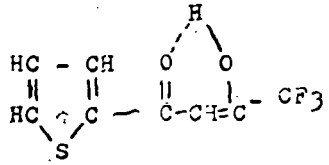

I

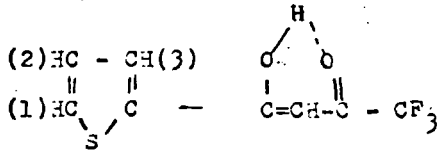

II

Intermolecular hydrogen bonding between HTTA molecules is negligible because HTTA remains monomeric and the nmr frequencies remain constant over wide range of HTTA concentrations in CCl_4 at constant temperature and in the absence of a second solute. In the presence of tributyl phosphate up to 1M, the fluorine-19 nmr resonance remains the same as in the absence of it. Under the same conditions, with hexafluoroacetylacetone in place of HTTA, the fluorine-19 signal moves upfield by 0.25 ppm. The data show that the preferred enol form of HTTA is II, rather than I, because tributyl phosphate would bond with HTTA through the enolic -COH. If the preferred enol form of HTTA were I, then the presence of tributyl phosphate should have affected the fluorine frequency, as it does with hexafluoroacetylacetone. Since no effect was observed with HTTA, the conclusion is that the preferred enol form is II, where the fluorine atoms are farther away from the hydrogen-bonding site.

Current studies. Dr. S. Nishimura and Mr. C.H.Ke in our Laboratory are carrying out nmr studies with water and chloroform bonding to organophosphorus compounds and several amines. At the Symposium in September I hope to include a discussion of their important results.

References

1 G.C.Pimentel and A.L.McClellan, "The Hydrogen Bond", W.H.Freeman and Co., San Francisco, Calif., 1960.
2 J.A.Pople, W.G.Schneider, and H.J.Bernstein, "High Resolution Nuclear Magnetic Resonance", McGraw-Hill Book Co., New York, 1959.
3 D.P.Eyman and R.S.Drago, J.Am.Chem.Soc., 88, 1617 (1966).
4 R. Mathur, E.D.Becker, R.B.Bradley, and N.C.Li, J.Phys.Chem., 67, 2190 (1963).
5 H.Baba and S.Suzuki, J.Chem.Phys., 35, 1118 (1961).
6 A.K.Chandra and S. Banerjee, J.Phys.Chem., 66, 952 (1962).
7 M.D.Joesten and R.S.Drago, J.Am.Chem.Soc., 84, 2696 (1962).
8 F.Takahashi and N.C.Li, J.Phys.Chem., 68, 2136 (1964).
9 N.Muller and R.C.Reiter, J.Chem. Phys., 42, 3265 (1965).
10 E.D.Becker, Spectrochim. Acta, 17, 436 (1961).
11 C.M.Huggins, G.C.Pimentel and J.N.Shoolery, J.Chem.Phys., 23, 1244 (1955).
12 J.C.Davis, Jr., K.S.Pitzer, and C.N.R.Rao, J.Phys.Chem., 64, 1744 (1960).
13 F. Takahashi and N.C.Li, J.Phys.Chem., 69, 2950 (1965).
14 F.Takahashi and N.C.Li, J.Am.Chem.Soc., 88, 1117 (1966).
15 S.F.Ting, S.M.Wang and N.C.Li, Can.J.Chem., 45, 425 (1967).
16 N.Muller and P.Simon, J.Phys.Chem., 71, 568 (1967).
17 G. Pukanic, N.C.Li, W.S.Brey, Jr., and G.B.Savitsky, J.Phys. Chem., 70, 2899 (1966).

THE POTENTIAL OF C^{13} NMR IN COAL RESEARCH

H. L. Retcofsky and R. A. Friedel

U.S. Department of the Interior, Bureau of Mines
Pittsburgh Coal Research Center, Pittsburgh, Pa.

SUMMARY

Current carbon-13 nuclear magnetic resonance (C^{13} NMR) studies of coal, coal derivatives, and related materials are presented and discussed. Broadline and pulsed NMR techniques have been applied to a few solid materials isotopically enriched in carbon-13, while high-resolution NMR studies of a wide variety of pure compounds and several coal derivatives have been carried out. The former techniques are used to derive spectral second moments and nuclear magnetic relaxation times. High-resolution C^{13} NMR is potentially a powerful tool for the direct quantitative determination of the aromaticity (f_a) of soluble products from coal. Values of f_a for light oils from coal and lignite and for a carbon disulfide extract of coal have been estimated from their C^{13} NMR spectra.

INTRODUCTION

Since the first published report of successful NMR measurements of the hydrogen distribution in a coal derivative[1] and the first determination of a high-resolution spectrum of a coal extract[2], proton magnetic resonance spectrometry has been used by many authors[3] to aid in the elucidation of the structure of coal. Brown and Ladner[4] developed a method for applying the hydrogen distribution data to the analysis of carbon structure, with particular emphasis on estimating three important structural parameters: f_a, the aromaticity; σ, the degree of aromatic substitution; and H_{aru}/C_{ar}, an indication of the size of the condensed aromatic ring system. C^{13} NMR offers a method by which f_a can be measured directly and realistic limiting values can be placed on the latter two parameters.

Broadline NMR, first observed for the protons in coal by Newman, Pratt, and Richards[5], is a means of determining second moments and may for very simple molecules give information on hydrogen-hydrogen distances. Values of various parameters for the mean structural units in coals have been estimated from experimentally determined second moments.[3] C^{13} NMR has been detected in natural abundance for only a few solid substances; the principal investigators being Lauterbur[6] and Davis and Kurland[7]. Observation of the C^{13} resonance in graphite has been reported by Abragam[8] using the method of Overhauser dynamic polarization. An attempt to find the C^{13} resonance in synthetic diamond proved unsuccessful[9]. Solid state C^{13} NMR studies of C^{13} enriched materials may give information on carbon-carbon or carbon-hydrogen bond distances[10].

No measurements of relaxation times for nuclei in coal have been reported in the literature to date and C^{13} nuclear relaxation times have been reported for only two substances containing naturally occurring carbon-13[11]. Preliminary measurements of proton relaxation times in a bituminous coal and C^{13} relaxation times in a few isotopically enriched materials were carried out under Bureau supervision during the course of this investigation.

EXPERIMENTAL

The high-resolution C^{13} NMR spectra obtained during the course of this investigation were of two types. Rapid passage dispersion mode C^{13} spectra were obtained using a Varian Associates V-4300C high-resolution NMR spectrometer operating at 15.085 MHz. These spectra exhibit asymmetric peaks, do not have a continuous baseline, and peak shapes and intensities are dependent upon the direction of magnetic field sweep. Thus, spectra are presented in pairs with the spectrum obtained while sweeping the applied magnetic field from low to high values being at the top of each figure. Quantitative estimates of f_a were determined by the method of Friedel and Retcofsky[12]. Time-averaged absorption mode C^{13} spectra were kindly provided by E. G. Cummins of Perkin-Elmer, Ltd., and were obtained using an R-10 spectrometer. Values of f_a were determined directly from electronic integration of the spectra.

Broadline C^{13} NMR spectra were also obtained on the Varian instrument mentioned above. The modulation and detection systems used for the broadline studies were components of a Varian V-4500 electron paramagnetic resonance spectrometer.

C^{13} magnetic relaxation times were measured from oscillographic recordings of free induction decay curves (for T_2) and of the NMR signal amplitude following 180°-90° pulse sequences (for T_1). This work was generously performed for us by NMR Specialties, Inc., using their PS-60-A pulsed spectrometer system.

RESULTS AND DISCUSSION

High-Resolution Studies

Rapid passage dispersion mode spectra of neutral oils from coal and lignite are shown in figures 1 and 2 respectively. The signal-to-noise ratio, although not high and certainly an important limiting factor in accurate determinations of f_a, is remarkably good considering the low natural abundance of C^{13}, and the complexity of the coal derivatives. The higher aromaticity of the oil from high-temperature cracking of the coal carbonization product is readily apparent from the spectra. Aromaticities for three neutral oils were estimated using the calibration procedures reported previously. The results are given in the table below and compared with f_a's estimated from proton NMR data by the Brown and Ladner[4] method. Spectra of a CS_2 extract of coal (representing 3% to 5% of the whole coal) are shown in figure 3. The signal-to-noise ratio here is considerably worse due to the presence of a large amount of the CS_2 solvent. The f_a value determined from C^{13} NMR is 0.6.

Aromaticities of Neutral Oils

Source	C/H	f_a	
		H^1	C^{13}
800° C cracking of a high-temperature coal carbonization product	1.05	0.83	0.78
700° C cracking of a low-temperature coal carbonization product	0.86	0.68	0.70
Distillation of a lignite carbonization product	0.64	0.38	0.39

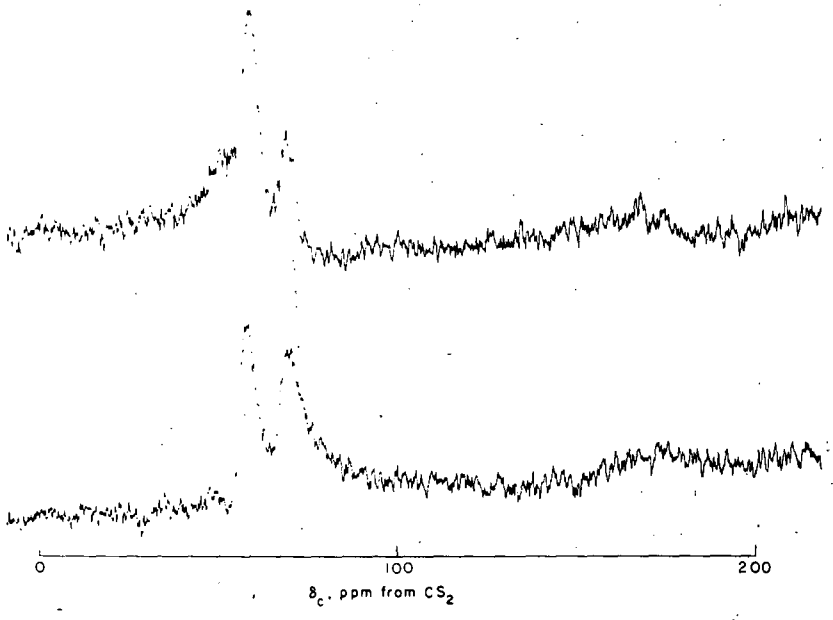

Figure 1. C^{13} magnetic resonance spectra of neutral oil from 800°C cracking of condensed tar from High Splint Coal.

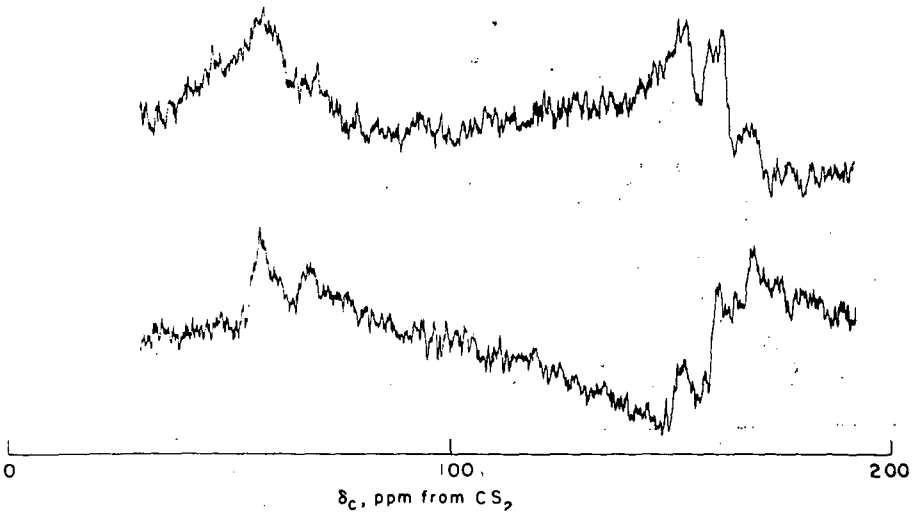

Figure 2. C^{13} magnetic resonance spectra of neutral oil from distillation of Sandow Lignite Tar.

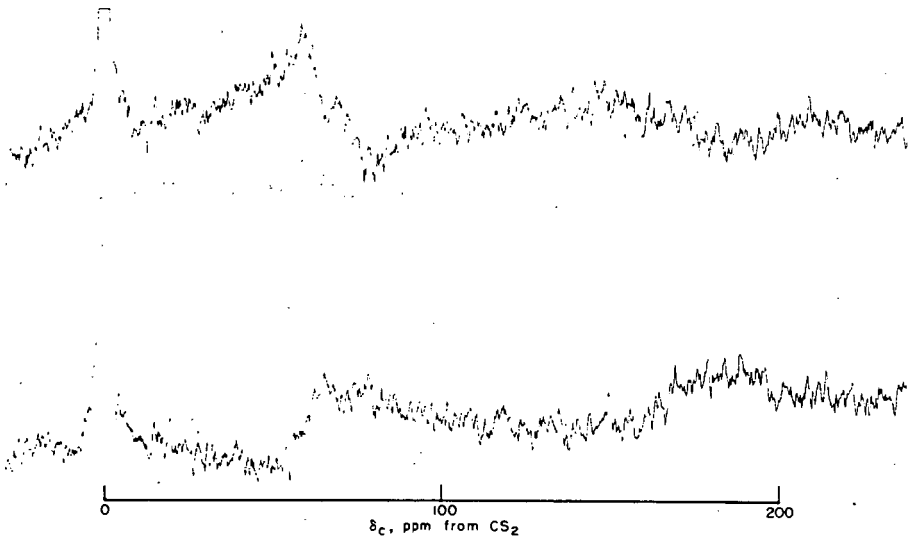

Figure 3. C^{13} magnetic resonance spectra of carbon disulfide extract of Pittsburgh Seam Vitrain.

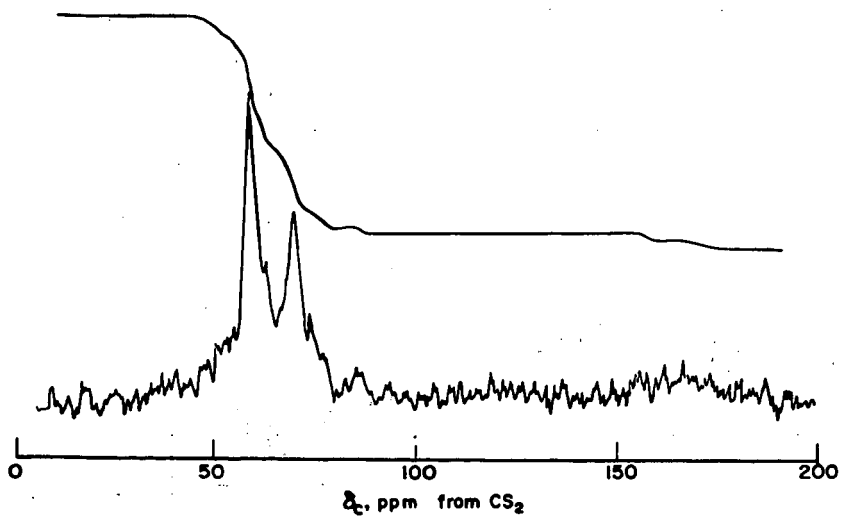

Figure 4. Absorption mode C^{13} magnetic resonance spectrum of coal tar.

The disadvantages in trying to obtain quantitative values of f_a from rapid passage dispersion mode C^{13} spectra are obvious from figures 1 and 2 and have been indicated in the foregoing discussion. Nevertheless it must be remembered that this is the first direct method for determining this heretofore very elusive structural parameter. With the advent of the time-averaging computer and its successful application in NMR experiments, the time is now here that highly precise and reasonably accurate f_a values can be obtained from absorption mode C^{13} NMR spectra. That is, spectra can be obtained under conditions similar to those used in proton NMR. Such a spectrum obtained from nearly 1,000 scans of the C^{13} spectral region is shown in figure 4 for the CS_2-soluble material of coal tar. The f_a value can be gotten directly from the integral reproduced along with the spectrum. The potential of this technique in coal structure research is an exciting one and will be pursued in our laboratory.

Broadline NMR

The C^{13} NMR spectrum of an isotopically enriched amorphous carbon produced by the 1000° C reduction of $C^{13}O_2$ is shown in figure 5. The spectrum shown is handdrawn using 6 actual spectra as guides. Isotopic enrichment is around 55 percent. The peak to peak linewidth is 5.2 gauss and the second moment was measured to be 6.0 guass^2. The spectral linewidth of the carbon can be compared to that found for barium carbonate (around 1.0 gauss) in which dipole-dipole interactions are essentially negligible and the width is determined primarily by the chemical shift anisotropy[6] of the carbonate anion.

Pulsed NMR

The C^{13} enriched carbon was also examined by pulsed NMR techniques. Room temperature measurements of the spin-lattice relaxation time (T_1) and the spin-spin relaxation time (T_2) yielded the values 360 milliseconds and 80 microseconds respectively. The free precession decay curve is shown in figure 6. One important conclusion that can be made from these measurements is that the transmitter power level used for obtaining the broadline NMR spectrum was low enough to avoid saturation. Thus true line shapes are observed. T_1 and T_2 were found to be 27 seconds and 13 seconds respectively for the carbonyl carbon in 55% C^{13} enriched liquid acetic acid. In contrast the proton relaxation times in an 84% carbon coal are 50 microseconds (T_1) and 9 microseconds (T_2).

CONCLUSIONS

The carbon-13 NMR results described here illustrate the first application of the technique to coal derivatives. The potential of the techniques described is nearly unlimited and possibly much more information than that described here will be obtained. For example, C^{13} has been shown to be a very useful tool for the characterization of carbonyl groups. Such groups are thought to be present in coal. The most recent experimental techniques involve the use of time averaging computers, instruments which are at this time beginning to appear on the work bench of many industrial, government, and academic research laboratories. The main disadvantage to C^{13} NMR spectroscopy is the long times involved in the accumulation of spectral data. Thus, although it may not become as widely applied as NMR of other nuclei such as H^1 and F^{19}, the information obtained from C^{13} NMR may be much, much more important.

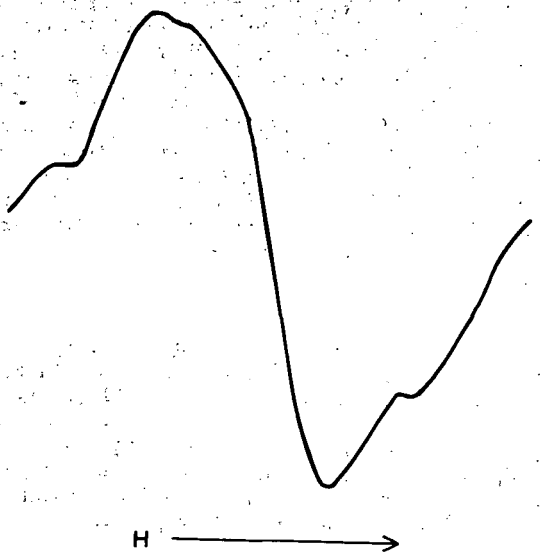

Figure 5. C^{13} magnetic resonance spectrum of amorphous carbon. (55% enriched in carbon-13)

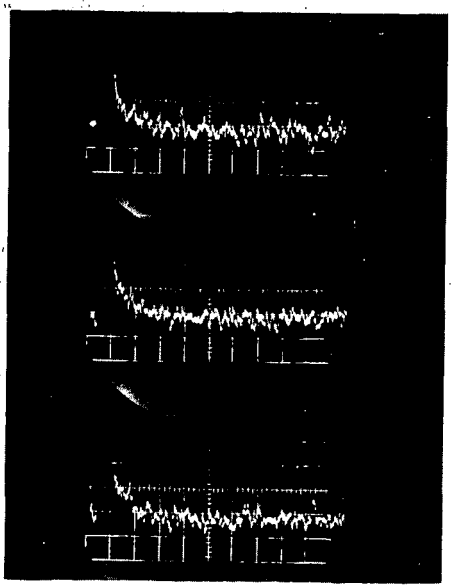

Figure 6. Free induction decay curves for amorphous carbon.

References

1. Friedel, R. A. Absorption Spectra and Magnetic Resonance Spectra of Asphaltene. J. Chem. Phys., v. 31, No. 1, pp. 280-281, July 1959.

2. Friedel, R. A., and H. Retcofsky. Spectral Studies of Coal. Paper presented at Fifth Carbon Conference, Pennsylvania State University, University Park, Pa., June 19-23, 1961.

3. For a review and leading references see:
Tschamler, H. and E. DeRuiter, Physical Properties of Coals, Chap. 2 in "Chemistry of Coal Utilization," Supl. vol. ed. H. H. Lowry, John Wiley And Sons, New York, 1963, pp. 35-118.

4. Brown, J. K., and W. R. Ladner. A Study of the Hydrogen Distribution in Coal-like Materials by High-Resolution Nuclear Magnetic Resonance Spectroscopy. II. A Comparison with Infra-red Measurement and the Conversion to Carbon Structure. Fuel, v. 39, pp. 87-96, 1960.

5 Newman, P. C., L. Pratt, and R. E. Richards. Proton Magnetic Resonance Spectra of Coals. Nature, v. 175, p. 645, 1955.

6. Lauterbur, P. C. Anisotropy of the C^{13} Chemical Shift in Calcite. Phys. Rev. Letters, v. 1, No. 9, pp. 343-344, 1958.

7. Davis, D. G., and R. J. Kurland. Carbon-13 NMR of Paramagnetic Iron-Group Cyanides. J. Chem. Phys., v. 46, pp. 388-390, 1967.

8. Abragam, A., A. Landesman, and J. Winter. Effet Overhauser dans les Charbons et graphite. Comptes Rendus, v. 247, 1852-1853, 1958.

9. Lauterbur, P. C. Private communication.

10. Slichter, C. P., Principles of Magnetic Resonance with Examples from Solid State Physics. Harper and Row, New York, p. 61, 1963.

11. McConnell, H. M., and C. H. Holm. Anisotropic Chemical Shielding and Nuclear Magnetic Relaxation in Liquids. J. Chem. Phys., v. 25, p. 1289, 1956.

12. Friedel, R. A., and H. L. Retcofsky. Quantitative Application of C^{13} Nuclear Magnetic Resonance: C^{13} NMR Signals in Coal Derivatives and Petroleum. Chem. and Ind. 1966, pp. 455-456.

Spin Echo Nuclear Magnetic Resonance Studies of Fast Chemical Reactions

T. Alger, H. S. Gutowsky and R. L. Vold

University of Illinois, Urbana, Illinois

Since the original work of Gutowsky, McCall and Slichter[1] in 1953 high resolution nuclear magnetic resonance has developed into a useful tool for studying fast chemical reactions in liquids. These reactions occur in systems at dynamic equilibrium and involve rapid, reversible transfer of nuclear spins between magnetically non-equivalent environments. For example, intermolecular hydroxyl proton transfer in ethanol,[2] ring inversion in cyclohexane,[3] and hindered internal rotation in N,N-dimethylacetamide[4] have all been studied by high resolution NMR methods. Useful reviews of such studies have been made by Lowenstein and Connor[5] and by Johnson.[6]

If the rate at which spins transfer between non-equivalent magnetic environments or "sites" is less than the difference between the resonant frequencies of the sites, separate resonance lines are observed in the spectrum. For faster exchange rates, the spins experience an average resonant frequency, and the resolved lines are collapsed; one or more lines are observed at the average resonant frequencies. By analysis of the details of the lineshape at various temperatures, it is possible to obtain the temperature dependence of the exchange rate constant.

High resolution NMR has been used for many years to measure exchange rates; it is the purpose of this paper to discuss the recently developed spin echo method, which depends on measuring the spin-spin or transverse relaxation rate. The transverse relaxation rate is measured most conveniently by the Carr Purcell method (see Fig. 1). The weak, continuous, oscillating magnetic field of high resolution NMR is replaced by a much stronger oscillating field which is turned on only in short bursts or pulses with duration of a few microseconds. The first pulse, applied at time zero, instantaneously tips the nuclear magnetization into a plane perpendicular to the constant magnetic field (xy plane). The magnetization, as viewed in a coordinate system rotating at the average larmor frequency, dephases because the constant field is not perfectly homogeneous and spins in different parts of the sample precess at different rates. The rest of the pulses, applied at times τ, 3τ, 5τ, etc., flip the magnetization by 180°, and cause the magnetization to refocus and form spin echoes at times 2τ, 4τ, 6τ etc. The decay of the envelope of echo maxima is independent of magnetic field inhomogeneity, and its time constant defines the transverse relaxation time.

It is reasonable that transfers of spins between different sites should affect the relaxation rate as well as the high resolution lineshape. Spins in magnetically non-equivalent sites precess at different rates around the constant magnetic field, and since individual spin transfers occur at random times, their macroscopic effect is to cause an additional dephasing of the magnetization; a faster relaxation rate. The amount of dephasing which occurs depends on the exchange rate (average time which a spin spends precessing in one site or the other), on the chemical shift between the sites (difference in precessional frequency), and on the spacing of the 180° refocussing pulses. The latter parameter affects the amount of dephasing because it determines the length of time in which the spins can dephase before being refocussed.

The dependence of observed relaxation rate upon rf pulse spacing forms the basis of the spin echo method of determining exchange rates. For exchange rates which are less than the chemical shift, the observed relaxation rate attains a limiting value at long pulse spacings which depends on the rate constant for exchange but not the chemical shift. At short pulse spacings, the observed

relaxation rate approaches another limit which is independent of the chemical exchange rate. At intermediate pulse spacings, the relaxation rate is somewhere between these limiting values. By analysis of the dependence of relaxation rate upon pulse spacing, it is possible to obtain values for the rate constant, chemical shift, and relaxation rate in absence of exchange.

Figure 2 shows some relaxation curves, or graphs of relaxation rate versus inverse pulse spacing, obtained by Allerhand and Gutowsky[7] for N,N-dimethyltrichloroacetamide. In this molecule the rate process is hindered rotation around the C-N bond, which exchanges the non-equivalent methyl groups. At low temperatures the relaxation rate depends strongly upon pulse spacing, but at higher temperatures the relaxation rate appears to become independent of pulse spacing. This behavior is due to the fact that at higher temperatures the exchange rate is larger, and it is not possible in practice to reduce the pulse spacing sufficiently to prevent dephasing.

For simple systems such as N,N-dimethyltrichloroacetamide the spin echo method appears to be superior to high resolution NMR methods of measuring exchange rates. A larger temperature range is experimentally accessible since exchange contributions comparable to the true "natural linewidth" (without inhomogeneity broadening) can be measured. In addition, analysis of the relaxation curves usually yields values for the chemical shift at each temperature as well as the rate constant. This is important because an undetected and uncorrected temperature dependence of the chemical shift can result in large errors, particularly in the entropy of activation.[8]

These advantages of the spin echo method make its extension to more complicated systems a potentially useful theory. To date, it is possible in principle to calculate spin echo amplitudes for an arbitrarily complicated spin system, including homo- and heteronuclear spin coupling as well as chemical exchange processes.[9] In practice even large computers require two or three minutes to calculate relaxation curves for systems with about twelve lines in their spectra; this appears to be the current practical limit of complexity.

Ethanes which have been substituted with four or five chlorine or bromine atoms provide a quite stringent test of the spin echo method. There are relatively high barriers to internal rotation about the C-C bond in these molecules,[10] and for unsymmetrically substituted molecules there are three different rotational isomers, each of which may involve spin coupling. The effect of homonuclear spin coupling is to introduce strong modulation of the echo train, and it is then not feasible to define a transverse relaxation rate (see Fig. 3). Heteronuclear spin coupling is usually not observable in Carr Purcell spin echo experiments unless the coupled nuclei are involved in an exchange process. Even in this case the heteronuclear spin coupling does not produce modulations, it contributes to the effective chemical shifts of the exchanging nuclei[9] (see Fig. 4).

In 1,1-difluoro-1,2-dibromodichloroethane, there are two possible exchange processes: between the rotamer with bromine atoms in a trans conformation and either of the d,ℓ pair of "gauche" rotamers, and between the two gauche rotamers. Homonuclear spin coupling between fluorines in the gauche rotamers is observable because the two fluorines are non-equivalent in this case. The low temperature spin echo trains therefore show characteristic modulation patterns[11] (see Fig. 3). In agreement with theory, the details of the modulation depend on the rf pulse spacing.

At temperatures above about -60°C the modulation disappears and the echo trains become exponential. This is because the chemical exchange is sufficiently rapid to "average out" effects of coupling. A high resolution NMR spectrum at this temperature would show a single, broad featureless line. The apparent relaxation rate depends upon rf pulse spacing up to about -20°C, and the dependence can be

analysed to yield values of the free energy barrier for gauche-trans internal rotation (11.0 kcal/mole) and for gauche-gauche internal rotation (12.0 kcal/mole).

For 1-fluoro-1,1,2,2-tetrachloroethane, only one exchange process is observable by magnetic resonance: the interchange of the rotamer with hydrogen and fluorine in a trans conformation with either of the magnetically equivalent "gauche rotamers". It is easy to show that for spin echo experiments, the observed echo trains should be a sum of two contributions, each corresponding to a two site exchange process.[12] The two processes occur at the same rate but with different effective chemical shifts, given by the true proton chemical shift between gauche and trans rotamers, plus or minus one half the difference of the heteronuclear coupling constants for each rotamer. At the field strengths used (corresponding to proton resonance at 26.8 and 17.7 MHz) the chemical shift is small, and the two effective chemical shifts are equal, and independent of field strength (see Fig. 4). In this compound the free energy barrier for interconversion of the gauche and trans rotamers was found to be about 8.7 kcal/mole. It is less than the barriers found in CF_2BrCCl_2Br because in the former compound the activated complex involves eclipse of smaller atoms than in the latter.

References

[1]H. S. Gutowsky, D. W. McCall, and C. P. Slichter, J. Chem. Phys. 21, 279 (1953).

[2]J. T. Arnold, Phys. Rev. 102, 136 (1956).

[3]F. A. L. Anet, M. Ahmad, and L. D. Hall, Proc. Chem. Soc. (London) p. 145 (1964).

[4]M. T. Rogers and J. C. Woodbrey, J. Phys. Chem. 66, 540 (1962).

[5]A. Lowenstein and T. M. Connor, Ber. Bunsenges. Physik. Chem. 67, 280 (1963).

[6]C. S. Johnson, Jr., Advances in Magnetic Resonance 1, 33 (1965).

[7]A. Allerhand and H. S. Gutowsky, J. Chem. Phys. 41, 2115 (1964).

[8]A. Allerhand, H. S. Gutowsky, J. Jonas and R. Meinzer, J. Am. Chem. Soc. 88, 3185 (1966).

[9]H. S. Gutowsky, R. L. Vold and E. J. Wells, J. Chem. Phys. 43, 4107 (1965).

[10]R. A. Newmark and C. H. Sederholm, J. Chem. Phys. 43, 602 (1965).

[11]R. L. Vold and H. S. Gutowsky, J. Chem. Phys. (submitted)

[12]T. Alger, H. S. Gutowsky and R. L. Vold, (to be published).

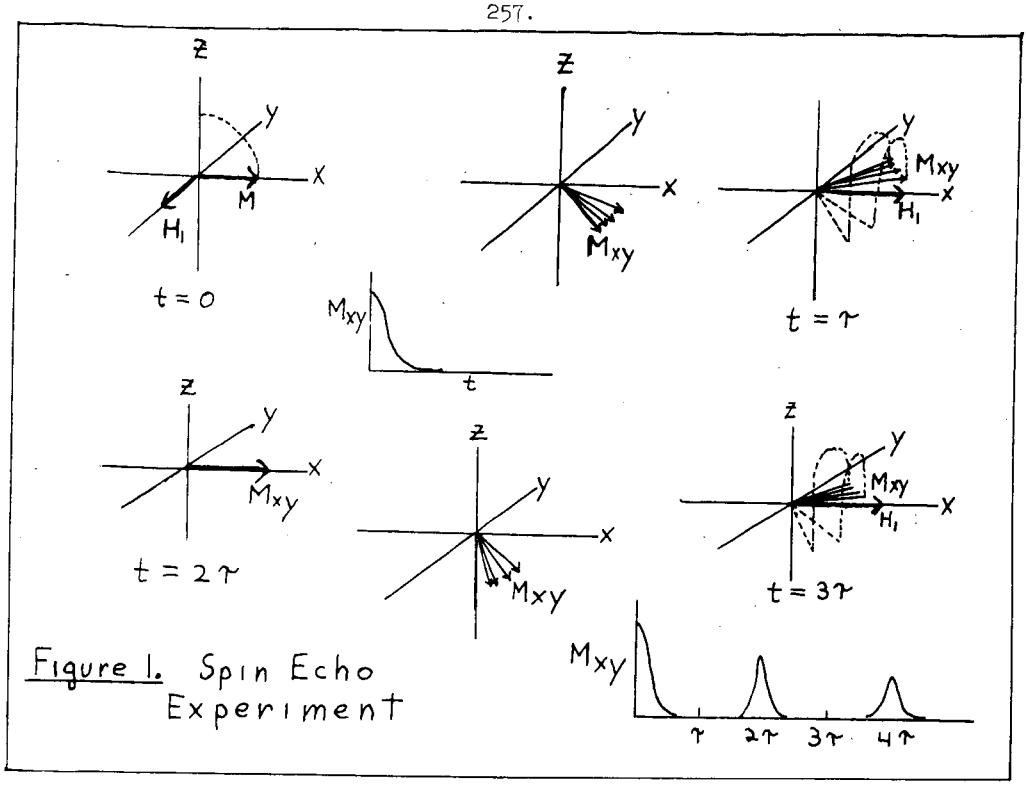

Figure 1. Spin Echo Experiment

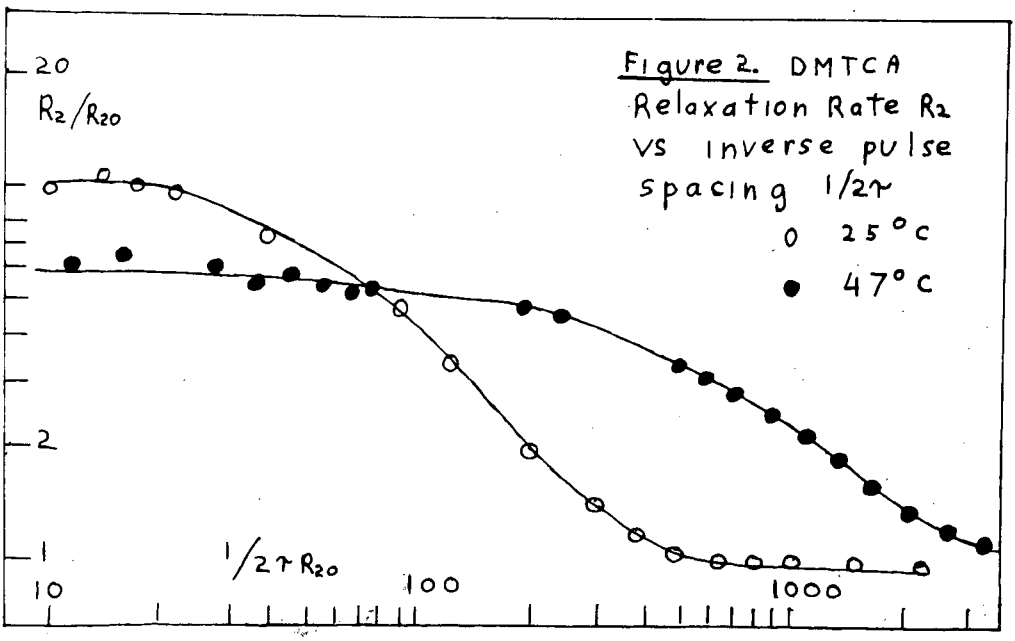

Figure 2. DMTC A Relaxation Rate R_2 vs inverse pulse spacing $1/2\tau$

○ 25°C

● 47°C

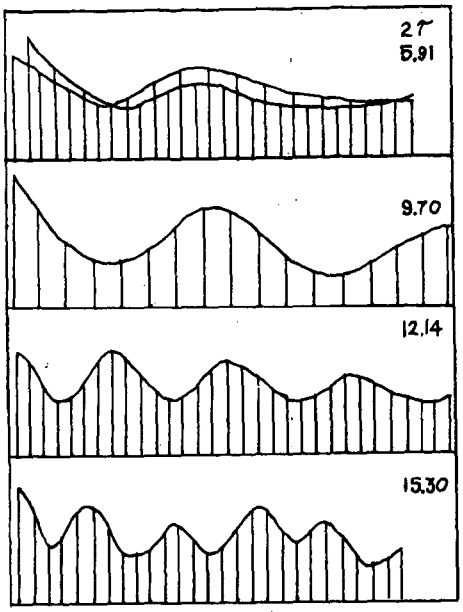

Figure 3. Fluorine spin echoes from CF_2BrCCl_2Br at -100°C and 25.27 MHz. The vertical lines represent echo amplitudes plotted on an arbitrary scale, and for each echo train the spacing between the lines is the rf pulse spacing, given in milliseconds above each echo train. The solid curves define characteristic modulation patterns for each pulse spacing.

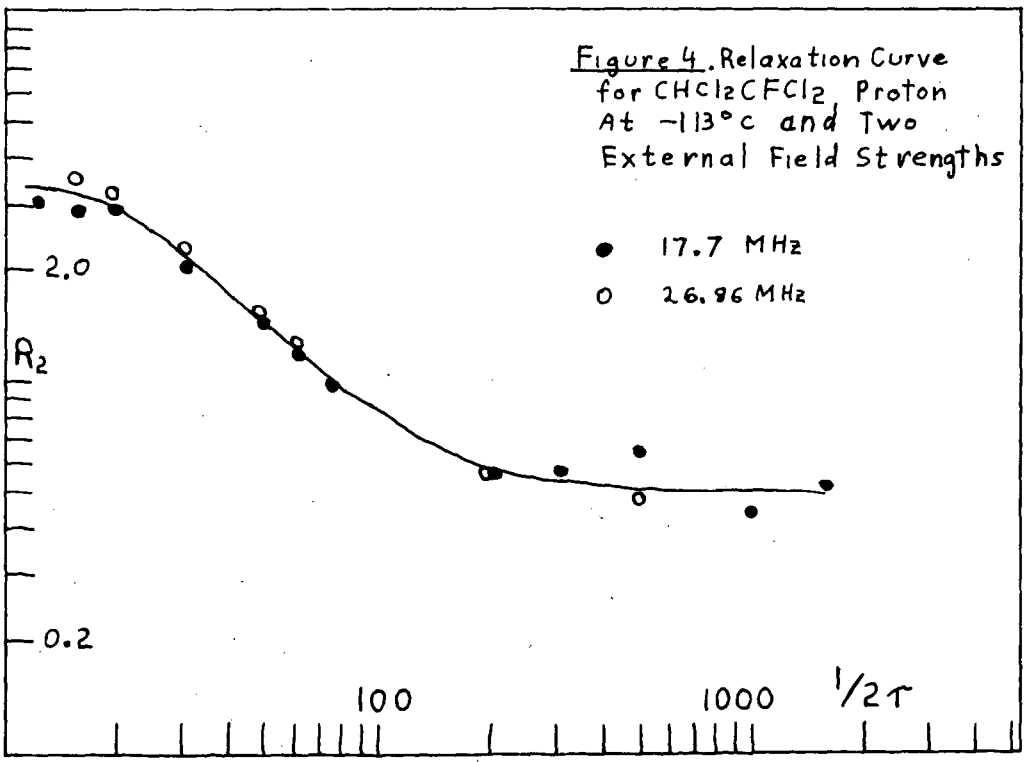

SOME SPECTRAL OBSERVATIONS ON TWO COKING LIGNITES

R.M. Elofson and K.F. Schulz
Research Council of Alberta
Edmonton, Alberta

INTRODUCTION

Berkowitz[1] and Berkowitz and Schein[2] first drew attention to the abnormal properties of a hard black lignite from the Sharigh region of Pakistan. These properties included a low heat of wetting of about 5 Cal./g. in methanol, a low inherent moisture content of 1.7%, and caking properties corresponding to a free swelling index of 5 to 5 1/2. Since these properties occurred in a coal with a carbon content of about 75% (daf) they were considered atypical and were attributed in part to unusual tectonic conditions occurring in the early stages of the formation of the coal. These were postulated to be of such a nature as to produce the low pore volume characteristic of the British medium volatile bituminous coals. Subsequently Kreulen[3] examined another lignite from Rasa in Istria (Yugoslavia), and noted a high swelling index of 9, a low inherent moisture content, and a high sulfur content of 11.0%, again with a low carbon content of 74.8%. Kreulen drew attention to the fact that if the carbon and sulfur contents are added together the result, about 86%, is equal to the carbon content of "normal" high swelling coals.

Both of these coals, together with a number of Alberta coals, have been examined in our laboratories by means of infrared spectroscopy and electron spin resonance techniques. In the case of the lignites another property of coking coals, the formation of chloroform-soluble material upon shock heating to about 400°C[4], has also been examined. Analyses of these coals on a dry-ash-free basis are presented in Table I.

RESULTS

Infrared spectra were prepared using the potassium-bromide pellet technique and the absorption patterns for the various coals are presented in Figure 1 for the long wavelength region. These spectra show that both the Rasa and the Sharigh lignites have the three characteristic bands[5,6] near 740, 810, and 870 $cm.^{-1}$ normally associated with coals with carbon contents of greater than 85%. Moreover, the pattern is stronger for the strongly swelling Rasa coal, FSI 9, than for the Sharigh coal, FSI 5.0 - 5.5.

These three bands have been associated with out-of-plane deformation vibrations of one, two, and four adjacent aromatic CH groups respectively[7]. The absence of these absorptions in normal lignites and subbituminous coals is an indication that in these materials the aromatic lamellae are heavily substituted and crosslinked. As a result, heating does not produce plasticity and related swelling. In bituminous coals the aromatic systems are less substituted and crosslinked as indicated by the presence of the three infrared absorption bands. Heating therefore results in the development of the plasticity behavior of coking coals. In the coking lignites the presence of these bands indicates that despite their low carbon content, the aromatic lamellae are sufficiently free of crosslinking to produce a product that is thermoplastic. In other words, the various ring systems can decompose in such a manner as to produce lamellae that, upon heating, can move about relative to each other. It should be noted that these bands are strong in anthracites as well but because of the growth of the lamellae[8] the attractive forces between lamellae are too strong

to allow movement so that there is no thermoplasticity.

Closely related to the aromatic substitution pattern of bituminous coals as an indication of mobile lamellae is the development of considerable chloroform-soluble material upan shock heating these coals to the vicinity of 400°C. Again, the lack of crosslinking in the bituminous coal and the resultant need to break fewer bonds to produce thermoplastic polymers is indicated. Application of this test to the Sharigh and Rasa lignites produced the results shown in Figure 2. For comparison results are also shown for a subbituminous coal (Drumheller) and for a normal coking coal (Michel). It is readily seen that the coking lignites resemble the normal coking coal and not the subbituminous coal of comparable carbon content to the lignites. The peak in the plot of chloroform extractibles for the Rasa coal is much broader and occurs at a lower temperature than those of the other coals. It is apparent that the low molecular weight thermally produced material, which presumably acts as a plasticizing agent, produced in these lignites is similar to that from normal bituminous coal. This confirms the lack of crosslinking in these lignites in agreement with the infrared results.

The e.s.r. signals of the two lignites in question and of a number of Alberta coals were measured using a Varian Model 4500 electron paramagnetic resonance spectrometer fitted with 100 KC modulation. About 10 mg. of dry coal was placed in a glass tube and evacuated to 10^{-4} mm. for 1 hour. Measurement of the e.s.r. signals produced the results shown in Table II. The number of spins observed in the coking lignites is in the lower range observed for coals of comparable carbon contents[9] and much below that observed for normal coking coals. Accurate measurements of the g-values obtained by using a dual sample cavity showed that the three higher rank coals (Luscar, Michel, and Canmore) had g-values close to 2.0031 and the three lower rank coals (Wabamun, Drumheller, and Lethbridge) had g-values of 2.0036 to 2.0037. The coking lignites again resembled the low rank coals in having high g-values. The signals for the Pakistan lignite and two of the bituminous coals are distinctive in having dual peaks, Figure 3. The weak narrow signal is reversibly suppressed by the presence of oxygen. The g-values of the narrow signals in all cases was close to 2.0030 regardless of the position of the main signal. Since signals sensitive to oxygen are characteristic of material heated to temperatures in excess of 500°C these results suggest that charred material from local heating or very severe tectonic conditions might have been the source of the narrow signals.

DISCUSSION

The infrared spectra and shock heating experiments show quite definitely that the chemical structures of the coking lignites are responsible for the swelling properties of the two coals. Basically this is because the degree of crosslinking of the aromatic lamellae as indicated by the infrared absorption bonds is quite low. Lack of polar functional groups accounts in part for the low moisture content and the so-called "liquid" structure and resulting low porosity accounts for the low heat of wetting.

The problem remains of deciding whether the lignites have these properties because of unusual starting material – both coals are high in sulfur – or because of unusual tectonic conditions or both.

The e.s.r. results which include low numbers of spins and high g-values are similar to the results for the low rank coals and in contrast to the results for the high rank coals. However, shifts in g-value of this magnitude result chiefly from atomic spin orbit coupling of atoms such as oxygen[10]. Thus the g-values of the coking lignites may be high simply because the free radicals

are associated with moieties containing sulfur which cause an even larger g shift than oxygen atoms[11]. The narrow signal present in the Sharigh lignite may be indicative of severe tectonic conditions to which we know the Luscar and Michel coals were subjected.

The lack of substitution of the aromatic lamellae indicated by the infrared results suggests that breaking of weak sulfide bridges is not responsible for thermoplasticity. This is in agreement with the findings of Iyengar et.al.[12] who found no sulfide linkages in Sharigh lignite by oxidation studies. This indicates that sulfur seems to be to quite a large extent in the heterocyclic aromatic donor or quinonoid acceptor structures the interaction of which is responsible for the free radical signals[12]. This suggestion is in agreement with the finding of Kavcic of 70% of the S in Rasa coal occurring in ring structures[14].

The low number of spins in the coking lignites compared with normal bituminous coals may be a result of the sulfur content. That is sulfur may be a poorer donor compared to carbon or a weaker acceptor compared to oxygen and charge transfer complexes are as a result weaker. This point is supported by the light color of the Rasa coal.

On balance the infrared and e.s.r. evidence suggests that these lignites were subjected to fairly severe tectonic conditions. Because of the unusual constitution of the starting material, a low carbon content resulted but with the aromatic structures resembling a normal bituminous coal as revealed by the infrared evidence.

REFERENCES

1. N. Berkowitz, Fuel 29, 138 (1950).
2. N. Berkowitz and H.G. Schein, Fuel 31, 19 (1952).
3. D.J.W. Kreulen, Fuel 31, 462 (1952).
4. I.G.C. Dryden and K.S. Pankhurst, Fuel 34, 363 (1955).
5. R.R. Gordon, W.N. Adams and G.I. Jenkins, Nature 170, 317 (1952).
6. J.K. Brown and P.B. Hirsch, Nature 175, 229 (1955).
7. H.L. McMurray and V. Thornton, Anal. Chem. 24, 318 (1952).
8. P.B. Hirsch, Proc. Roy. Soc. (London), A-226, 143 (1954).
9. J. Smidt and D.W. van Krevelen, Fuel 38, 355 (1959).
10. M.S. Blois, H.W. Brown and J.E. Maling, in Free Radicals in Biological Systems by M.S. Blois et.al. Academic Press, New York, 1961, pp. 117.
11. K.F. Schulz and R.M. Elofson, presented at 49th Conference, Can. Institute of Chem., Saskatoon, June 1966.
12. M.S. Iyengar, S. Guha and M.L. Bera, Fuel 39, 235 (1960).

13. R.M. Elofson and K.F. Schulz, Amer. Chem. Soc., Div. Fuel Chem., Preprints 11 (2) 513 (1967).

14. R. Kavcic Bull. Sci. Conseil Acad. RPF, Yugoslav. 2 12 (1954) C.A. 49 5809 (1955).

TABLE I

Analyses of Coals

Coal	% - d.a.f.			
	C	H	N	S
Rasa	75.0	5.71	1.7	11.22
Sharigh	75.80	6.08	1.7	4.15
Wabamun	75.9	4.7	-	0.1
Drumheller	75.9	5.1	2.0	0.6
Lethbridge	79.7	5.6	2.5	0.9
Michel	89.1	5.2	1.4	0.4
Luscar	90.6	5.0	1.3	0.2
Canmore	91.5	4.4	1.9	0.6

TABLE II

E.S.R. Spectra of Coals

Coal	g-value (in vacuo)	spins/g. (in vacuo)	width (oersted)
Rasa	2.00395	3.8×10^{18}	6.9
Sharigh	2.00381 Broad	4.3×10^{18}	7.9
	2.00288 Narrow	4×10^{16}	1.0
Wabamun	2.00372	1.1×10^{19}	7.1
Drumheller	2.00360	7.5×10^{18}	6.3
Lethbridge	2.00370	1.8×10^{19}	7.5
Michel	2.00304 Broad	1.5×10^{19}	6.5
	2.00285 Narrow	2.2×10^{17}	0.8
Luscar	2.00310 Broad	1.1×10^{19}	4.7
	2.00310 Narrow	2.4×10^{17}	0.5
Canmore	2.00317	1.6×10^{19}	4.7

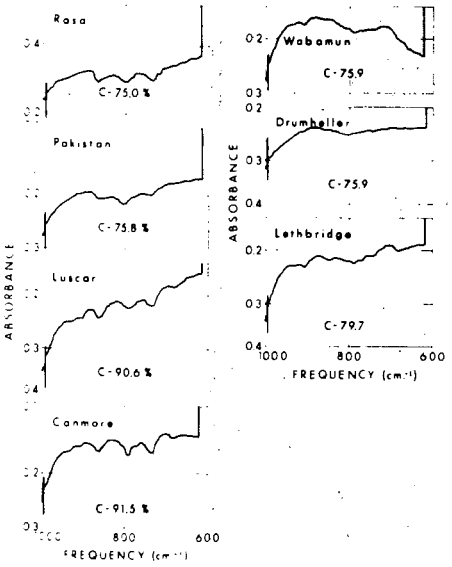

Fig.1. Infrared spectra of coals in the region of 1000 - 600 cm.$^{-1}$ (0.2% in KBr).

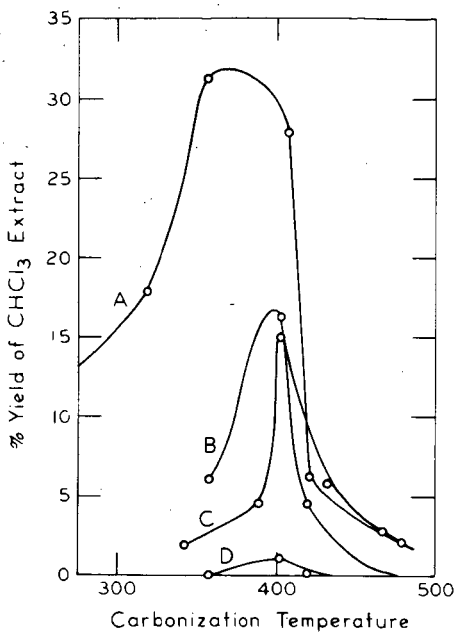

Fig.2. Yield of chloroform - soluble material as a function of temperature of shock heating of coal.
(A) Rasa; (B) Sharigh; (C) Michel, B.C.; (D) Drumheller, Alberta.

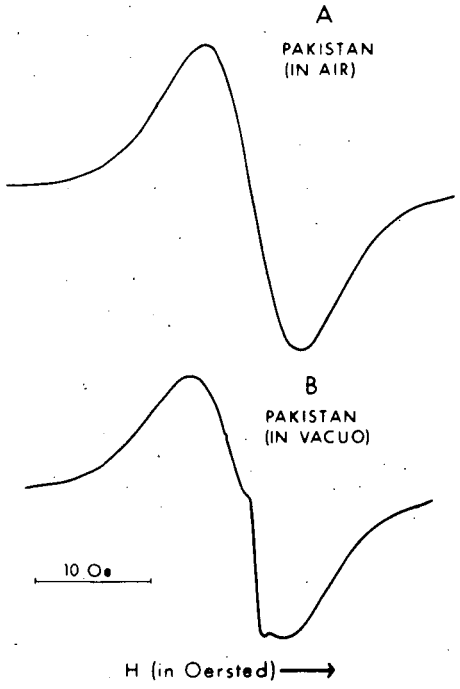

Fig.3. Electron spin resonance spectra of Sharigh lignite.
(A) spectrum from the sample in air;
(B) spectrum from the sample in vacuo.

ELECTRON SPIN RESONANCE OF PETROLEUM ASPHALTICS

By

Teh Fu Yen, Edmund C. Tynan and George B. Vaughan
Mellon Institute, Pittsburgh, Pa. 15213

and

Laurence J. Boucher
Chemistry Department, Carnegie Institute of Technology

Introduction

A considerable body of information about the Electron Spin Resonance (ESR) properties of petroleum asphaltenes has developed during the past few years. Among the basic parameters obtained by ESR measurements are N_g, the number of unpaired spins per gram of material; $|A|$, the electron-nuclear spin coupling constant; and g, the effective Landé g-factor for the unpaired electron spins. A review of what is already known, and the addition of new data may both clarify the present state of understanding of asphaltene ESR and stimulate further research in this area. The ESR studies briefly considered here may be divided into two parts: (1) measurements of the free radical absorption, and (2) measurements of the ESR absorptions due to naturally occurring vanadium and synthetic vanadium chelates.

Nature of Free Radical

The asphaltic fraction of petroleum has been found to yield a single ESR resonance near a g-value of 2.00[1,2,3]. For most asphaltics the line shape is between Lorentzian and Gaussian. The inhomogeneous broadening characteristics indicate that, in addition to dipolar interactions, the magnetic electron interacts with hydrogen or other nuclei to produce multiplet line structures. The apparent absence of fine structures in the radical absorption appears to be the result of a superposition of many such multiplets. The g-values of most asphaltics fall in the narrow range of 2.0027-2.0036. The differences between measured g-values and the g-value of a free electron (g_e), $|g - g_e|$, are shown in Fig. 1 for six native asphaltenes and a variety of other types of free radicals. It may be deduced that the unpaired spins in asphaltene do not appear to belong to the semiquinone or the radical ion families. However, they are close to neutral radicals, in contrast to the radicals in coals and L-forms of carbons which are semiquinones[1].

Intensity measurements are usually troublesome, but when properly done with suitable modulation amplitude and correct power levels (not causing saturation), the spin concentration, N_g, can be used as a basis for differentiating or classifying different asphaltic samples. Figure 2 displays the N_g data for 11 native asphaltenes from different sources: 2 native gilsonite asphaltenes, 3 refinery asphaltenes, 5 heat-treated asphaltenes[4], 3 carbenes, 4 cokes and one lithium-reduced asphaltene. Aromaticity, f_a, as obtained from x-ray analysis[5] for these materials is apparently linearly related to log N_g. These data indicate that the free radical sites of these materials are associated with the aromatic moities of the asphaltic skeleton. Present findings confirm the previous observation[1] that different families of carbonaceous substances, e.g., asphaltenes, resins[6], coals, and carbons, show a characteristic slope and intercept when their f_a values are plotted against log N_g.

No effects on N_g were observed due to the action of light, oxygen or solvents; however, these factors do affect the spin-lattice relaxation time[7]. The free radical species of asphaltics are stable, in contrast to coal hydrogenation asphaltene[8]. Further, it was found[1] that the color intensity of asphaltics, i.e., the integrated intensity obtained by absorption spectrometry over the 600-800 mμ region also increases with the ESR intensity (Fig. 3). These data indicate that the free radical is stabilized by the resonance of the delocalized π-system in the asphaltic structure.

Vanadium Unpaired Spin

Most asphaltics contain vanadium in concentrations ranging from 6000 to less than 1 ppm. Common valence states of vanadium are +2, +3, +4, and +5. The +5 state is diamagnetic. The +3 state, although paramagnetic, is usually not observable by ESR due to internal electric field effects. Both the +2 and the +4 states can, however, be detected at room temperature. In contrast to oxovanadium (IV), V^{+2} is unstable and easily oxidized. The +4 state requires a non-cubic field for ESR observability, and this is fulfilled by the oxovanadium (IV) VO^{+2} type complexes[9]. The vanadium 51 nucleus (~100% abundance) has a nuclear spin 7/2, and so a magnetic electron coupled to it can exhibit an absorption spectrum of either 8 symmetric lines (isotropic case), or 8 unsymmetric lines (anisotropic case: 8 parallel and 8 perpendicular features in the first derivative of the spectrum).

For native asphaltenes in general a 16-feature anisotropic spectrum has been observed for this d^1 system in either solid form or in solution in non-polar organic solvents (Fig. 4). Assignment of the absorption lines is in general agreement with the assignment for the axial symmetry case as described previously by O'Reilly[10]. The line positions have been carefully examined in a second derivative format[11], and with multi-amplitude recordings (Fig. 5). The line positions of the vanadium resonance for nine different asphaltenes have recently been measured and are shown in Fig. 6. When compared with a sample of vanadyl etioporphyrin I, whose line positions are also

shown in Fig. 6, a number of additional lines are observed for the asphaltenes. Whether the additional lines represent other paramagnetic species or other structural environments for the vanadium in the asphaltene samples is still unknown. However, such a difference is useful in qualitatively differentiating asphaltenes from different sources.

Another empirical criterion for differentiating among asphaltenes is obtained by measuring the spacings of the $g_{//}$ features: $2_{//} - 1_{//}$ and $8_{//} - 7_{//}$. Tentatively, two parameters can be derived (Table I); one is the $A_{//}$ value which is the average spacing of the parallel features, and the other is the difference of the spacings, Δ, representing a second-order effect arising because of the dependence of the spectrum on the strength of the external magnetic field. The real meaning of the latter quantity has not yet been fully explored, but it is thought to represent deviations from axial symmetry. It appears that all asphaltenes studied here have axial symmetry except for the samples from Bachaquero (CY), Baxterville (GS), and Wafra A-1. Since both the $A_{//}$ and Δ values of Bachaquero (CY) asphaltene differ from those of Wafra A-1 asphaltene, it might be expected that there would be a structural difference between the two asphaltenes. Analysis of the anisotropic spectrum of the asphltenes to yield complete values of $g_{\perp}$, $g_{//}$ and $A_{\perp}$, $A_{//}$ is hindered by overlapping line structures and the difficulty of converting the spectrum into an isotropic one.

Conversion of an anisotropic spectrum ("bound") of the vanadium in asphaltene into an isotropic spectrum ("free") can be effected by dissolving the asphaltenes in a polar solvent such as benzyl n-butyl ether, tetrahydrofuran or diphenylmethane and heating at an elevated temperature[12]. Such a conversion is reversible. From the relative intensities of the isotropic and anisotropic spectra taken at different temperatures, the disassociation energy can be obtained. For a given asphaltene, identical energy values have been observed regardless of the solvent system. The energy values of three asphaltenes are given in Table II. These results suggest that the observed "bound" vanadium is associated with the asphaltene molecule, probably with the aromatic portion. The fact that this "associated" or "bound" type of vanadium becomes disassociated is further supported by dilution studies in a given solvent system. In dilute solutions (~0.4 Wt. %) a nearly isotropic "free" type of spectrum was observed. In solvents with differing basicities the vanadium-containing asphaltene usually shows some indications, though small, of the isotropic vanadium ESR absorptions even at room temperature. The relative effectiveness of solvents for producing the "free" vanadium species may be ranked as follows: diphenylmethane < benzyl n-butylether < 1-ethylnaphthalene < benzene < nitrobenzene < pyridine < tetrahydrofuran.

Nitrogen Superhyperfine Splittings (s.h.f.)

The literature indicates no nitrogen s.h.f. for the oxovanadium (IV) in a quadridentate nitrogen ligand except for the case of vanadyl tetraphenylporphin in chloroform or carbon disulfide "glass" reported by Lee[13]. We have been able to observe nitrogen s.h.f. for vanadyl

phthalocyanine doped at a concentration of 2000 ppm into either a condensation polymer of anthracene or of phenanthrene, or a gilsonite asphaltene (natural vanadium content < 1 ppm). Figure 7 shows the 9-line pattern of nitrogen s.h.f. structures superimposed on the vanadium No. $4_\perp$ line for vanadyl phthalocyanine doped into a polymer made from anthracene and formaldehyde. For four equivalent nitrogen nuclei the relative intensities of the nine lines are expected to be 1, 4, 10, 16, 19, 16, 10, 4, 1. The intensity distribution patterns of the nitrogen lines for vanadyl phthalocyanine either in anthracene polymer or in the gilsonite asphaltene drop off rapidly for the outer nitrogen lines, but in general retain the bell shape. However, when 2000 ppm vanadium in the form of vanadyl etioporphyrin I was doped into gilsonite asphaltene or an aromatic medium such as perylene, there were no nitrogen s.h.f. structures observed. On the other hand, there is indication that there may be nitrogen splittings in the petroporphyrins (vanadium) of native asphaltene. The repeated scan of the No. $2_\perp$ region in a second derivative format for Bachaquero (VX) asphaltene is given in Fig. 8. In addition to the line shown, fine structure suggestive of nitrogen lines appears in the overlapping region of the Nos. $4_\perp$ and $4_{//}$ features. Typical poorly resolved nitrogen lines superimposed on a vanadium line are illustrated in Fig. 9. The coupling constant observed for both the vanadyl phthalocyanine and petroporphyrin (vanadium) is $A_\perp^N = 2.6$ G. This value agrees with the nitrogen splitting observed for the vanadyl tetraphenylporphin in chloroform or carbon disulfide, $A_{//}^N \simeq 2.9$ G., $A_\perp^N \simeq 2.8$ G.[13]. Roberts, Koski and Caughey[14] attribute the appearance of the nitrogen s.h.f. to a configuration interaction rather than to covalent bonding. At present it seems that the added aromaticity in the macrocycle does possibly bring out the nitrogen s.h.f. It may be that the π-electron system provides excitation for configuration interaction. The slight nitrogen s.h.f. found in asphaltene may indicate that there are minor constituents of the macrocycles in the form of benz-substituted porphins. Such structures have been demonstrated by mass spectrometry to be present in asphaltenes, e.g., the proposed β,β-benzoporphin[15].

Models for Non-porphyrin Vanadium

"Non-porphyrin" is used here to indicate any quadridentate macrocycle which does not belong to the alkyl- or cycloalkano-porphins (Etio and DPEP series), e.g., the rhodoporphyrin[15,16], mixed quaterenes, etc. Two classes of non-porphyrin vanadium were synthesized and characterized by ESR. The first class is vanadyl complexes of the meso-aromatic ring-substituted porphins. This series consists of vanadyl complexes of tetraphenylporphyrin (TPP), tetra-1-naphthylporphin (T1NP), and tetra-4-biphenylporphin (T4BP). The anisotropic scans of the vanadyl derivative of T1NP and T4BP are similar to that of vanadyl TPP. Each of these compounds is a 4 nitrogen ligand system.

The second class is the vanadyl complexes of β-ketoimines, i.e., quadridentate having 2 nitrogen and 2 oxygen donor atoms. This series consists of vanadyl complexes of bisacetylacetone-ethylenediimine (Acen), bisacetylacetonepropylenediimine (Acpn), bisbenzoylacetone-ethylenediimine (Bzen) and bisbenzoylacetonepropylenediimine (Bzpn). The g-values and vanadium nuclear coupling constants for some of the non-porphyrin vanadium model compounds are tabulated in Table III. One of the qualitative features of the vanadium spectra of β-ketoimines is that the Nos. $4_{\perp}$ and $4_{//}$ lines are resolved in contrast to the case of etioporphyrin I.

A plot of A_o vs. g_o (the isotropic coupling constant and g-value respectively) for a variety of vanadyl square-planar complexes, both porphyrin and non-porphyrin, is useful to characterize the particular types of ligands (Fig. 10). Samples at the upper left are those containing ligands which delocalize the unpaired vanadium spins, and these are characterized by low A_o value and a g_o value approaching that of the free electron, $g_e = 2.0023$. Samples at the lower right corner usually have ligands of an electronegative nature, and these are characterized by high A_o values and low g_o values. The average values from the resulting three groups of vanadyl complexes are shown from left to right as: 4 nitrogen type (porphins), 2 nitrogen, 2 oxygen type (β-ketoimines), and the 4 oxygen type (acetylacetonates). It can be predicted that the 3 nitrogen, 1 oxygen type and the 1 nitrogen, 3 oxygen type ligands will also fall into the nearly straight line relationship. The data for asphaltenes (Bachaquero, VX; Boscan, VY) included in the plot were obtained from a polar solution at elevated temperatures. The relative location of these two points falls in the region typical of the 4 nitrogen donor system. It is hoped that by using this plot non-porphyrin types of vanadium chelates contained in asphaltenes may be readily identified.

ACKNOWLEDGMENT

This work was sponsored by Gulf Research & Development Company as part of the research program of the Multiple Fellowship on Petroleum.

REFERENCES

(1) T. F. Yen, J. G. Erdman, and A. J. Saraceno, Anal. Chem., 34, 694 (1962).

(2) T. F. Yen, J. G. Erdman, and A. J. Saraceno, Bitumen, Terre, Asphalte, Peche, 15, 141 (1964).

(3) J. Q. Adams, K. H. Altgelt, R. L. LeTourneau, and L. P. Lindeman, ACS, Div. Petroleum Chem., Preprints, 11 (2) B140 (1966).

(4) J. G. Erdman, and J. P. Dickie, ACS, Div. Petroleum Chem., Preprints, 9 (2) B69 (1964).

(5) T. F. Yen, and J. G. Erdman, in "Encyclopedia of X-Rays and Gamma Rays" (G. L. Clark, Ed.), Reinhold Publishing Company, New York, 1963, pp. 65-68.

(6) R. A. Gardner, H. F. Hardman, A. L. Jones, and R. B. Williams, J. Chem. Eng. Data, 4, 155 (1959). In this reference, the term "petrolene" is used rather than resin. These petroleum fractions were thermal diffusion cuts, prepared by Gardner and coworkers from the pentane soluble fraction of an 85 to 100 penetration asphalt derived from a blend of Illinois and Oklahoma crudes by oxidation of a 200 penetration vacuum distillation residuum.

(7) A. J. Saraceno and N. D. Coggeshall, J. Chem. Phys., 34, 260 (1961).

(8) R. A. Friedel, J. Chem. Phys., 31, 280 (1959).

(9) A. J. Saraceno, D. T. Fanale, and N. D. Coggeshall, Anal. Chem., 33, 500 (1961).

(10) D. E. O'Reilly, J. Chem. Phys., 29, 1188 (1958).

(11) C. L. Wolfe, E. C. Tynan, and T. F. Yen, Pittsburgh Conference on Analytical Chemistry and Applied Spectroscopy, Paper No. 54, March, 1967.

(12) E. C. Tynan, and T. F. Yen, ACS, Div. Petroleum Chem., Preprints, 12 (2) A89 (1967).

(13) S. K. Lee, M. S. Thesis, UCLA (1964); cf. D. Kivelson and S. K. Lee, J. Chem. Phys., 41, 1896 (1964).

(14) E. M. Roberts, W. S. Koski, and W. S. Caughey, J. Chem. Phys., 34, 591 (1961).

(15) E. W. Baker, T. F. Yen, J. P. Dickie, R. E. Rhodes, and L. F. Clark, J. Am. Chem. Soc., 87, July 5 issue (1967).

(16) M. F. Millson, D. S. Montgomery, and S. R. Brown, Geochim. Cosmochim. Acta, 30, 207 (1966).

(17) L. J. Boucher, E. C. Tynan, and T. F. Yen, to be published.

TABLE I

Empirical Parameters from Anisotropic Spectra

Petroporphyrin Sample	$A_{//}$ (G)	Δ' (G)
Boscan (SR)*, Venezuela	176	4.6
Boscan (VY)*, Venezuela	172	4.0
Baxterville, Mississippi	171	-2.6
Taparito, Venezuela	172	3.6
Bachaquero (CY)**, Venezuela	170	0
Wafra A-1, Neutral Zone	179	12
Wafra 17, Neutral Zone	174	3.1
Bachaquero (VX)**, Venezuela	173	2.1
Mara, Venezuela	172	4.6
VO Etio I (castor oil)	175	11
VO Etio I (in gilsonite)	171	6.7
VO Etio I (toluene)	175	9.3
VO Acac (in gilsonite)	168	0.5
VO Acen (THF)	183	14
VO Bzpn (THF)	179	8.8
VO Bzpn (toluene)	181	8.3

* Boscan (SR) collected in 1959; Boscan (VY) collected in 1962 upper and lower Boscan sand.

** Bachaquero (CY), Maracaibo; Bachaquero (VX), Well Largo.

TABLE II

Activation Energy of Association for Vanadium in Asphaltenes

Asphaltene	V Content (ppm)	Dissociation Energy (kcal)
Bachaquero (VX)	2700	14.3
Boscan (VY)	4700	10.0
Gilsonite (CB) doped*	2700	10.4

* with vanadyl etioporphyrin I.

TABLE III

Vanadium Nuclear Hyperfine Splittings and g-Values for Non-porphyrin Model Compounds

Vanadyl Complex*	A_o**	g_o	$A_{//}$**	$A_{\perp}$**	$g_{//}$	$g_{\perp}$
Acen	101.7	1.974	182.5	61.3	1.957	1.982
Acpn	102.5	1.974	183.8	60.4	1.945	1.999
Bzen	102.4	1.975	183.3	62.0	1.952	1.986
Bzpn	103.4	1.975	182.5	63.9	1.953	1.986

* in THF.

** in Gauss.

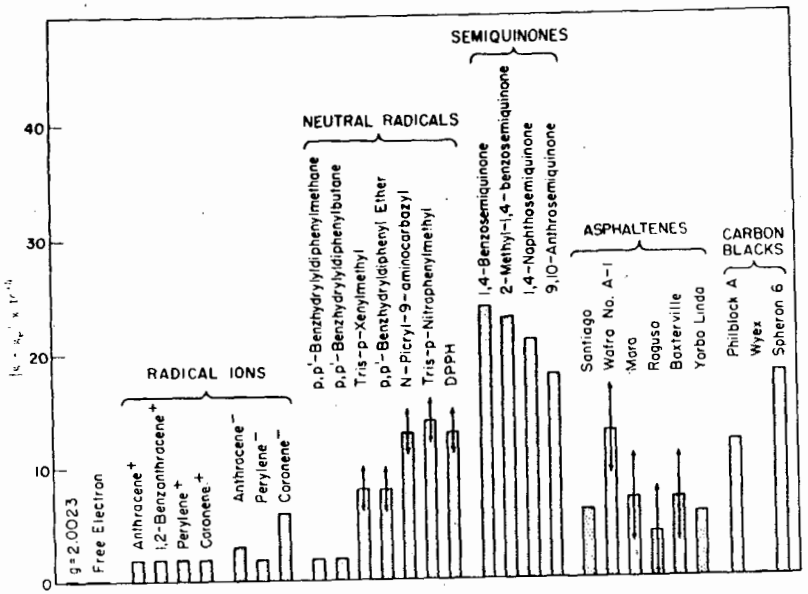

FIGURE 1: Lande g-Values of Petroleum Asphaltenes and Other Radical-Containing Substances.

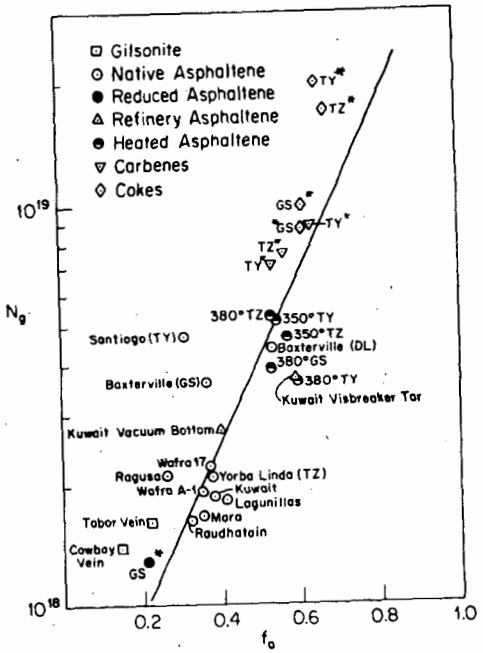

FIGURE 2: Dependence of Spin Concentration on Aromaticity.

(- A fraction from the corresponding asphaltene.)

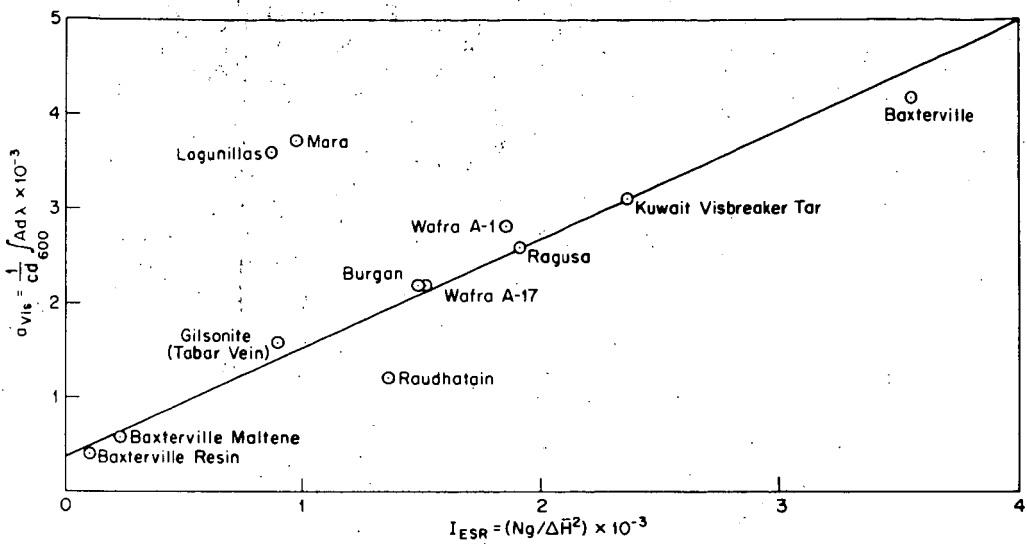

FIGURE 3: Integrated Visible Spectral Absorptivity vs. ESR Free Radical Absorption Intensity.

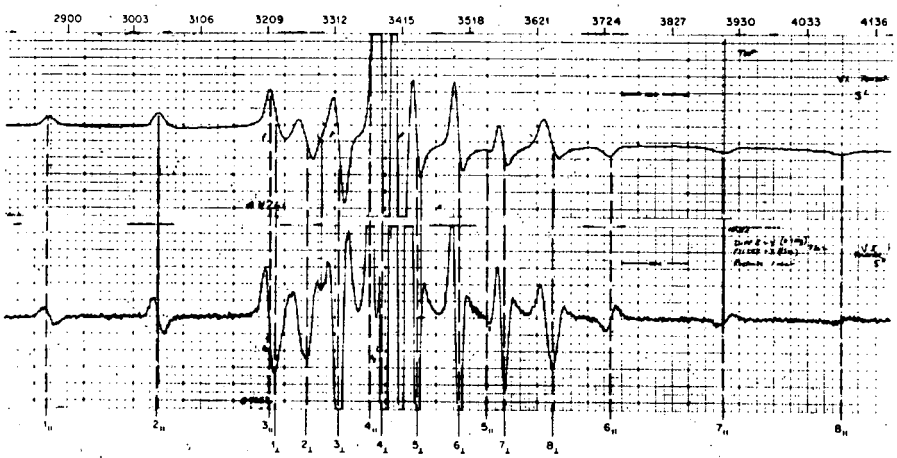

FIGURE 4: Vanadium Anisotropic Spectra of a Bachaquero (VX) Asphaltene (Upper, First Derivative Format; Lower, Second Derivative Format).

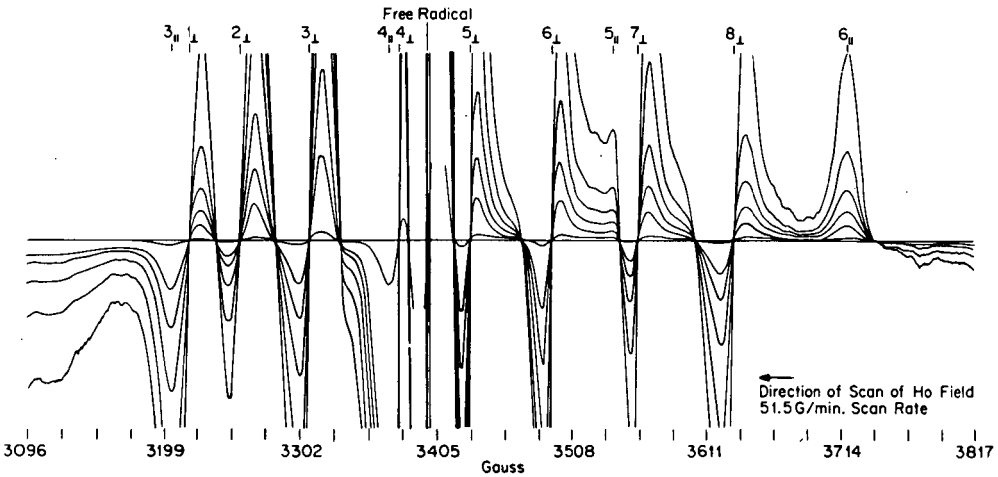

FIGURE 5: Central Portion of an Anisotropic Vanadium Spectrum from a Multi-amplitude Recording

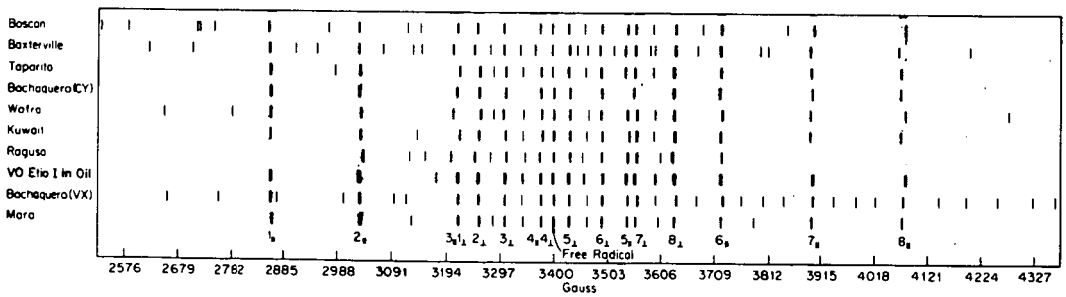

FIGURE 6: Field Positions of ESR Spectra of Native Asphaltenes

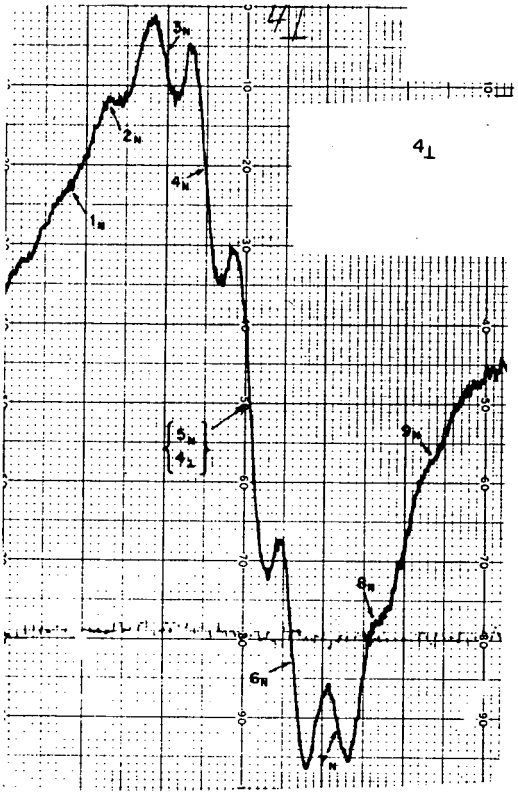

FIGURE 7: Nitrogen s.h.f. Structures of Vanadyl Phthalocyanine-Doped Anthracene Polymer

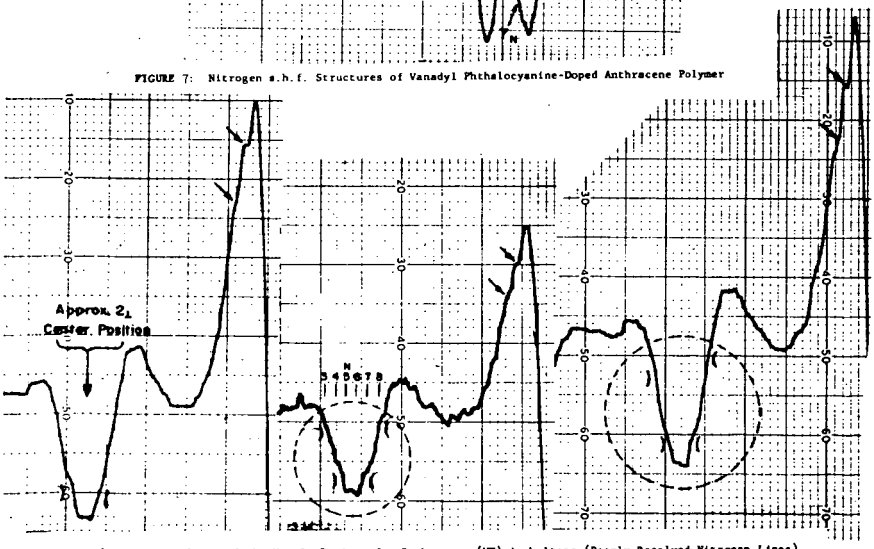

FIGURE 8: Repeated Scans of the No. $2_\perp$ Region of a Bachaquero (VX) Asphaltene (Poorly Resolved Nitrogen Lines).

FIGURE 3: Nitrogen s.h.f. Lines Superimposed on Vanadium Lines (Typical Case).

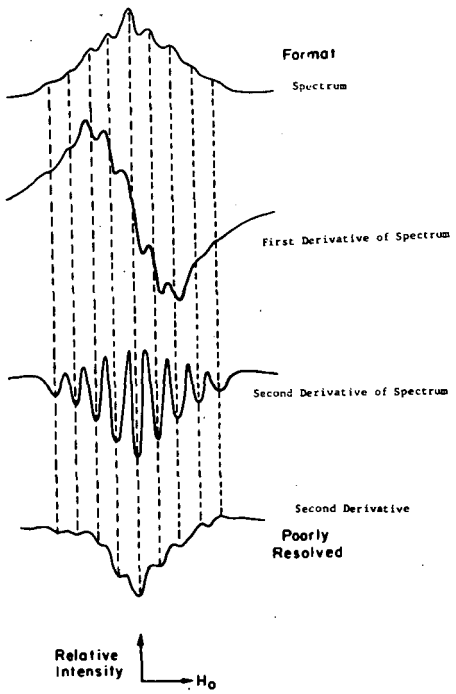

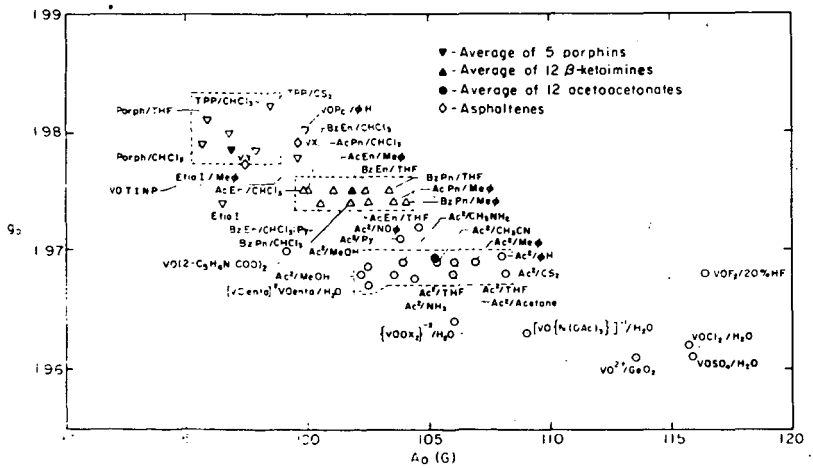

FIGURE 4 : Relationship Between g_o and A_o for a Series of Vanadyl Ligands

Application of Luminescence Spectroscopy to the Analysis of Fuels

Harold F. Smith

Perkin-Elmer Corporation, Norwalk, Connecticut

Luminescence spectroscopy is based on the absorption and re-emission of light by a molecule, ion or atom. It is of great analytical utility because the emitted light is characteristic of the electronic structure of the emitting species. The phenomenon of luminescence is not a newly discovered one. The first monograph on luminescence was written by Liceti[1] in 1640. In 1845 Herschel[2] reported on the luminescence characteristics of quinine sulfate. Stokes[3] in 1852 observed that in all cases the light emitted from a molecule was at longer wavelengths than that which it absorbed. His observation was termed the "Stokes shift" and has since become well understood. In 1895 Weidman and Schmidt[4] and in 1907 Stark and Mayer[5] reported the first systematic study on luminescence of aromatic molecules.

Lommel[6] in 1877 first reported on the quantum efficiencies of certain molecules, and in 1907 Nichols and Merritt[7] discussed their observations of the interesting "mirror image" relationship between absorption and emission spectra. From the preceding observation it is apparent that the luminescence properties of molecules have been known for a long time. The successful exploitation of luminescence had to wait, however, until other areas of technology were sufficiently advanced to permit the observation and measurement in a controlled and quantitative manner.

That fluorescence and phosphorescence techniques are being accepted rapidly in all areas of analytical chemistry is emphasized by referring to the 1964 and 1966 Analytical Chemistry Annual Reviews[8,9] covering the four-year period from December 1961 to December 1965, in which 1,049 references to a large variety of analytical applications of fluorescence and phosphorescence are contained.

Before proceeding into the discussion of specific applications of fluorescence and phosphorescence, the relationship of these phenomenon to each other and the absorption process should be shown (Fig. 1).

In both fluorescence and phosphorescence spectroscopy one may determine two different kinds of spectra (Fig. 2). The difference between these two spectra is that the emission spectrum is obtained by spectrally recording the light emitted from a sample while being excited by some selected wavelength of light. An excitation spectrum on the other hand is obtained by measuring the intensity of emitted radiation from a sample at a specific wavelength as the excitation light is varied continuously.

For example, Figure 3, the absorption spectrum of a 1 ppm anthracene solution, and Figure 4, the excitation and emission spectra of the same sample, show great structural similarity. The emission bands are all at longer wavelength than the absorption band, but the excitation bands fall at exactly the same wavelength as the absorption bands. A significant point is that the excitation spectrum of a molecule gives the same information as its absorption spectrum.

troscopy in fuels analysis is the method for qualitatively and quantitatively determining anthracene and napthalene at low concentrations in a benzene-type matrix. The three aromatic types represent the majority of aromatic molecules in fuels.

Experimental

All standard samples were prepared using reagent grade anthracene and naphthalene after recrystallization from a saturated hydrocarbon. The matrix was made from a 50/50 volume/volume mixture of toluene and o-xylene, spectroquality from Matheson, Coleman and Bell.

The spectra were run on a Hitachi-Perkin-Elmer MPF-2A Fluorescence Spectrophotometer. High quality, low-fluorescence, silica sample cells were used for obtaining the data.

Discussion of Results

A sample containing 10 ppm naphthalene and 10 ppm anthracene in the matrix was prepared and the qualitative emission spectra of the sample determined at several excitation wavelengths. Figure 5 shows the emission spectra obtained from the sample excited at 270mμ and at 280mμ. The principal emission, Spectrum A, is observed in the region between 360 and 440mμ, with a low intensity emission band in the 300 to 340mμ range. The emission between 380 and 440mμ arises from the anthracene whereas that in the 300 to 340mμ region arises from the naphthalene. Spectrum B in this figure was taken from the sample without removing it from the instrument. The only change was the excitation wavelength from 270 to 280mμ. Some rather dramatic changes in the spectrum are evident. The overall intensity of both band systems has been increased greatly and the ratio of the naphthalene to anthracene emission has completely reversed. It is apparent from this spectrum that one could easily determine the concentration of each of these components independently of the other in this aromatic matrix. One cannot do such an analysis by absorption spectroscopy.

The spectrum shown in Figure 6 was from the sample excited at 290mμ. In this case the naphthalene intensity continued to increase sharply, whereas the anthracene decreased. The spectra shown in Figure 7 show the anthracene intensity increasing and the naphthalene intensity fading. The Spectrum A was produced by exciting the sample at 300mμ whereas Spectrum B was produced by the 310mμ excitation.

The series of spectra shown in Figure 8 were run while exciting with 320, 330 and 340mμ excitation respectively and in these spectra all evidence of naphthalene presence was lost. The significance of the behaviour noted in Figures 6, 7 and 8 is that one can take a mixture of aromatic hydrocarbons and produce different spectra dependent on the wavelength of excitation. By choosing the appropriate excitation wavelengths, one can emphasize the presence of one component relative to the others and in many cases completely eliminate the appearance of any component other than the one of specific interest.

Our next point of concern was ability to selectively excite the three aromatic types, benzene, naphthalene and anthracene, individually. For this experiment the sample containing 10 ppm naphthalene and 10 ppm anthracene in the o-xylene-toluene matrix was diluted 1:100 with isooctane giving concentrations of 0.1 ppm naphthalene, 0.1 ppm anthracene and 1% o-xylene-toluene. The series of three spectra shown in Figures 9, 10 and 11 were obtained by exciting this solution with 280, 290 and 350mμ radiation respectively. Figure 9 shows the emission

spectrum of the benzene-type aromatics. Figure 10 is that of naphthalene and Figure 11 is that of anthracene. One not only can qualitatively identify these three aromatic types, but can determine their approximate concentration by simply altering the excitation wavelength and measuring the emission from each aromatic type independently of the others.

While the data shown in the preceding discussion indicate the qualitative applicability of luminescence spectroscopy to the basic types of aromatic molecules found in petroleum and coal based fuels, it does not provide an insight into the usefulness of the technique for quantitative analysis. Hercules[10] has shown that luminescence intensity and concentration are related as follows:

$$S(f)_\lambda = f(\Theta)\, g(\lambda)\, I_o\, \phi_f\, abc\left[1 - \frac{abc}{2!} + \frac{abc^2}{3!} - \cdots \frac{abc^n}{(n+1)!}\right]$$

Where abc are the molar absorptivity, cell path and concentration respectively; $f(\Theta)$ is the solid angle of interception of radiation by the detector; $g_{(\lambda)}$ is the quantum conversion factor for the detector which is a function of wavelength; I_o is the intensity of the exciting radiation and ϕ_f is the quantum efficiency of the molecule. There are two concentration regions where this arrangement may be greatly simplified. The one of greatest interest to the analytical chemist is the one in which the concentration of fluorescent materials is small. In such case abc 0.05. This allows us to write Equation 1 as

$$(S_f)_\lambda = f(\Theta)\, g(\lambda)\, I_o\, \phi_f\, abc$$

From this equation it may be seen that the relationship between fluorescence intensity and concentration will be linear through a point of maximum concentration, $C_{max} = \frac{0.05}{(a)_\lambda b}$, where $(a)_\lambda$ is the molar absorptivity of the compound at the wavelength of excitation. It should be emphasized that this concentration is not the maximum at which useful data may be obtained. Beyond this level the curve relating fluorescence intensity to concentration is not linear. A calibration curve relating concentration to fluorescence intensity can be used to extend the range of useful analysis over at least another order of magnitude.

The other extreme condition where equation one may be simplified is that of very high concentration of absorbing and emitting molecules such that the absorption of incident radiation is almost complete. In that case, equation one may be reduced to

$$(S_f)_\lambda = f(\Theta)\, g(\lambda)\, \phi_f$$

showing that the detector signal is independent of fluorescer concentration. This condition is important in determining quantum efficiencies for quantum counters and scintillation counters. Analysis under these conditions is most effectively done by using front surface illumination and viewing of the sample. With this geometry, penetration effects and self-absorption problems are minimized. This geometry is generally required when the fluorescence or phosphorescence spectrum of a solid, opaque or highly turbid sample is analysed. Using the front surface viewing geometry even raw crude oil samples may be excited and their luminescence observed.

As indicated by the terms in Equation (1) there is an intermediate concentration range for each absorber and fluorescer at which the intensity concentration relationship will become nonlinear. One generally observes that the fluorescence intensity approaches a limiting value as the concentration is increased. The principal precaution,

therefore, in using luminescence techniques for quantitative analysis is to realize that there is a range above which the concentration intensity curve will become nonlinear, and if it is required to work in the nonlinear region, a sufficient number of standard points be taken to accurately describe the intensity concentration curve.

Curves showing the intensity concentration relationship for naphthalene and anthracene in Figures 12 and 13. The naphthalene standards were prepared in o-xylene-toluene matrix. Each contained 10 ppm anthracene. The anthracene standards were prepared in the same matrix and each contained 10 ppm of naphthalene. The curves are practically linear in the lower concentration range, but begin to deviate from linearity at the higher end of the range.

In order for a measurement technique to be useful for quantitative analysis, stability of the measurement system must be such that good repeatability is possible. Unfortunately, the feeling exists that fluorescence measurement is imprecise. Admittedly, this has been and is true in many cases but it was an equipment rather than a technique limitation. Figure 14 shows an example of excellent repeatability. Here three spectra of a 10 ppb anthracene sample are superimposed and only would be hard pressed to show better repeatability by any other analytical technique.

Summary

Luminescence spectroscopy has broad application in the analysis of fuels and related products. All aromatic types are subject to analysis by fluorescence or phosphorescence. It is possible by using the incremental excitation technique to obtain spectra of each aromatic type completely independent of the others present and, therefore, more effectively analyzed for components of mixtures.

Luminescence spectroscopy has broad application in the analysis of fuels and related products. All aromatic types are subject to analysis by fluorescence or phosphorescence. It is possible by using the incremental excitation technique to obtain spectra of each aromatic type completely independent of the others present and, therefore, more effectively analyzed for components of mixtures.

Bibliography

1. I. B. Berlman, "Handbook of Fluorescence Spectra of Aromatic Molecules" p. 2, Academic Press, New York, 1965.
2. J. Herschel, Phil. Trans. Roy. Soc. (London) 135, 143 (1845).
3. G. G. Stokes, Phil. Trans. Roy. Soc. (London) 142, 463 (1852).
4. E. Wiedeman and G. C. Schmidt, Ann. Physik., 56, 18 (1895).
5. J. Stark and R. Meyer, Physik. Z. 8,250 (1907).
6. E. Lommel, Pogg. Ann. 160, 75 (1877).
7. E. L. Nichols and E. Merrit, Phys. Rev. 31, 376 (1910).
8. C. E. White, Analytical Chemistry Annual Reviews, Part One, 116R, 1964.
9. C. E. White, Analytical Chemistry Annual Reviews, 155R, 1966.
10. D. M. Hercules, Analytical Chemistry, 38, 29A, 1966.

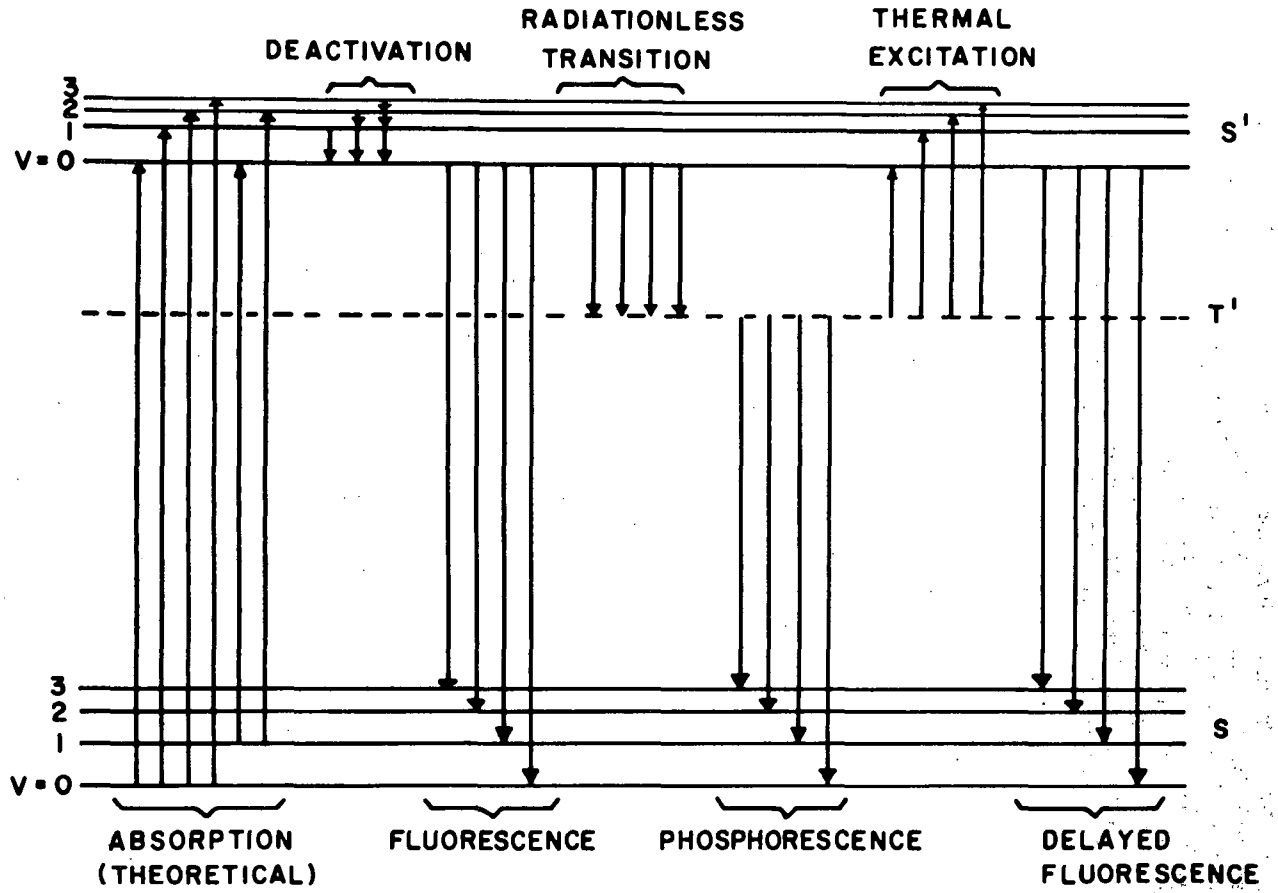
DEACTIVATION
RADIATIONLESS TRANSITION
THERMAL EXCITATION
3
2
1
V=0
S'
T'
3
2
1
V=0
S
ABSORPTION (THEORETICAL)
FLUORESCENCE
PHOSPHORESCENCE
DELAYED FLUORESCENCE

FIGURE 1

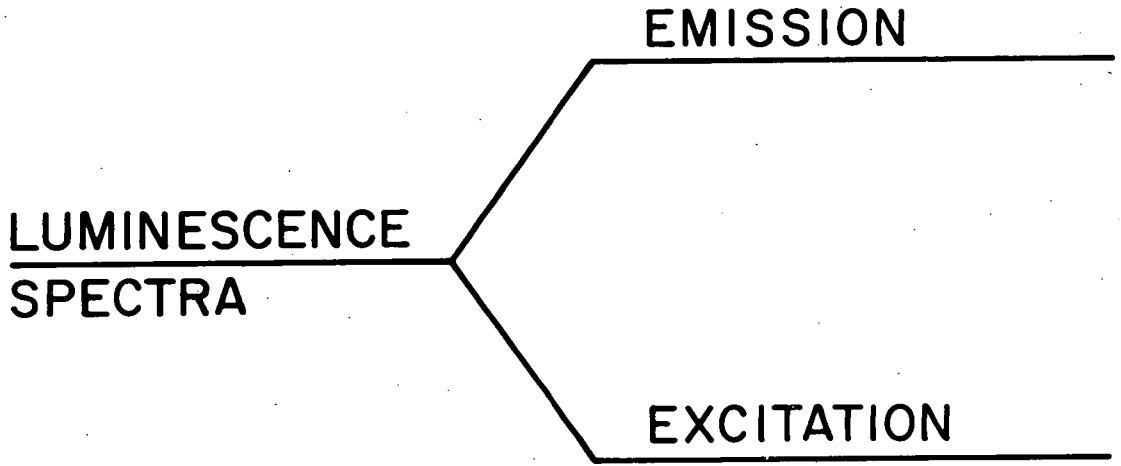

FIGURE 2

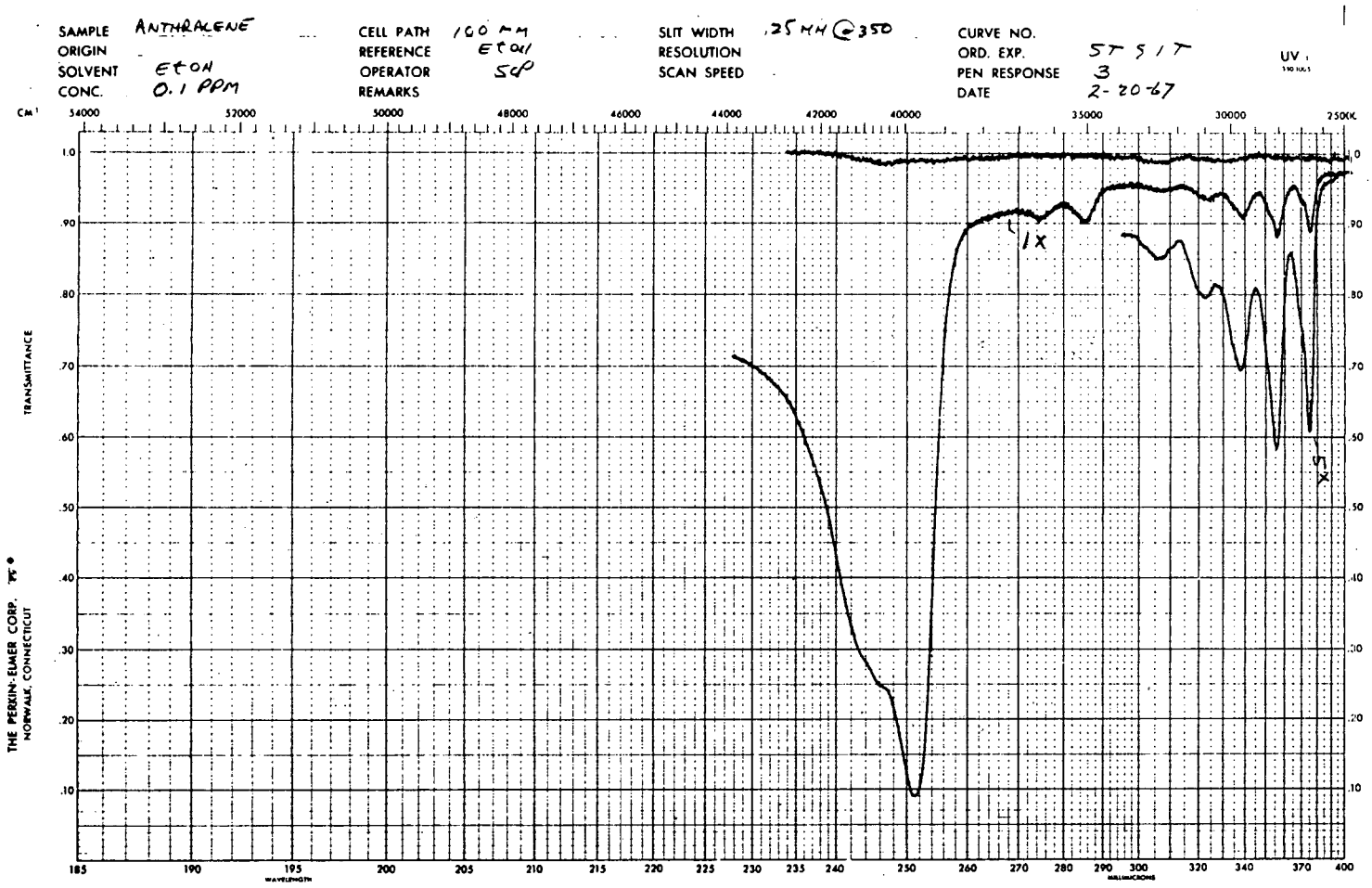
SAMPLE ANTHRACENE
ORIGIN
SOLVENT EtOH
CONC. 0.1 PPM
CELL PATH 100 MM
REFERENCE EtOH
OPERATOR SP
REMARKS
SLIT WIDTH .25 MM @ 350
RESOLUTION
SCAN SPEED
CURVE NO.
ORD. EXP. 5T 5 / T
PEN RESPONSE 3
DATE 2-20-67
UV
CM⁻¹
54000 52000 50000 48000 46000 44000 42000 40000 35000 30000 25000
TRANSMITTANCE
1.0 .90 .80 .70 .60 .50 .40 .30 .20 .10
1X
5X
THE PERKIN-ELMER CORP. NORWALK, CONNECTICUT
185 190 195 200 205 210 215 220 225 230 235 240 250 260 270 280 290 300 320 340 370 400
WAVELENGTH
MILLIMICRONS

FIGURE 3

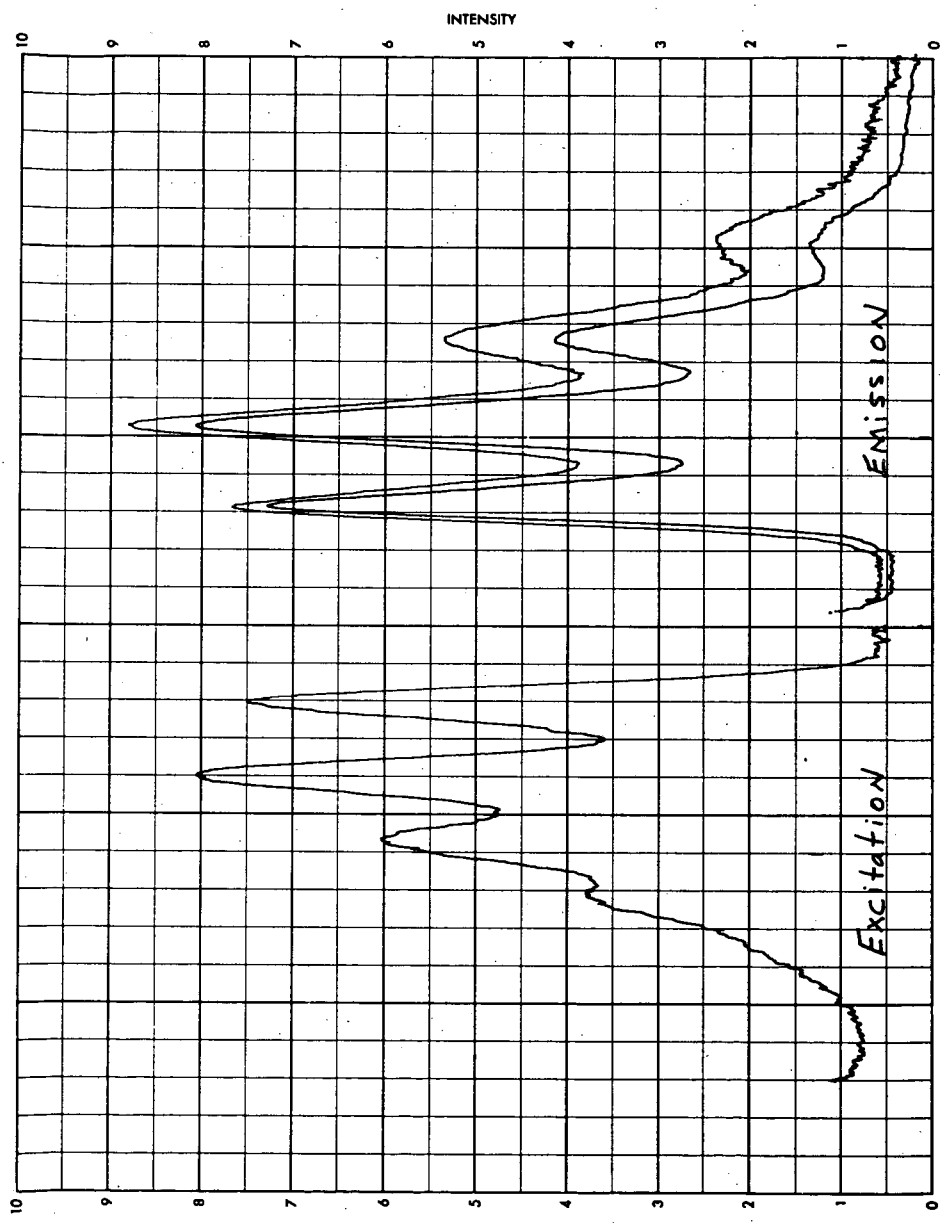

FIGURE 4

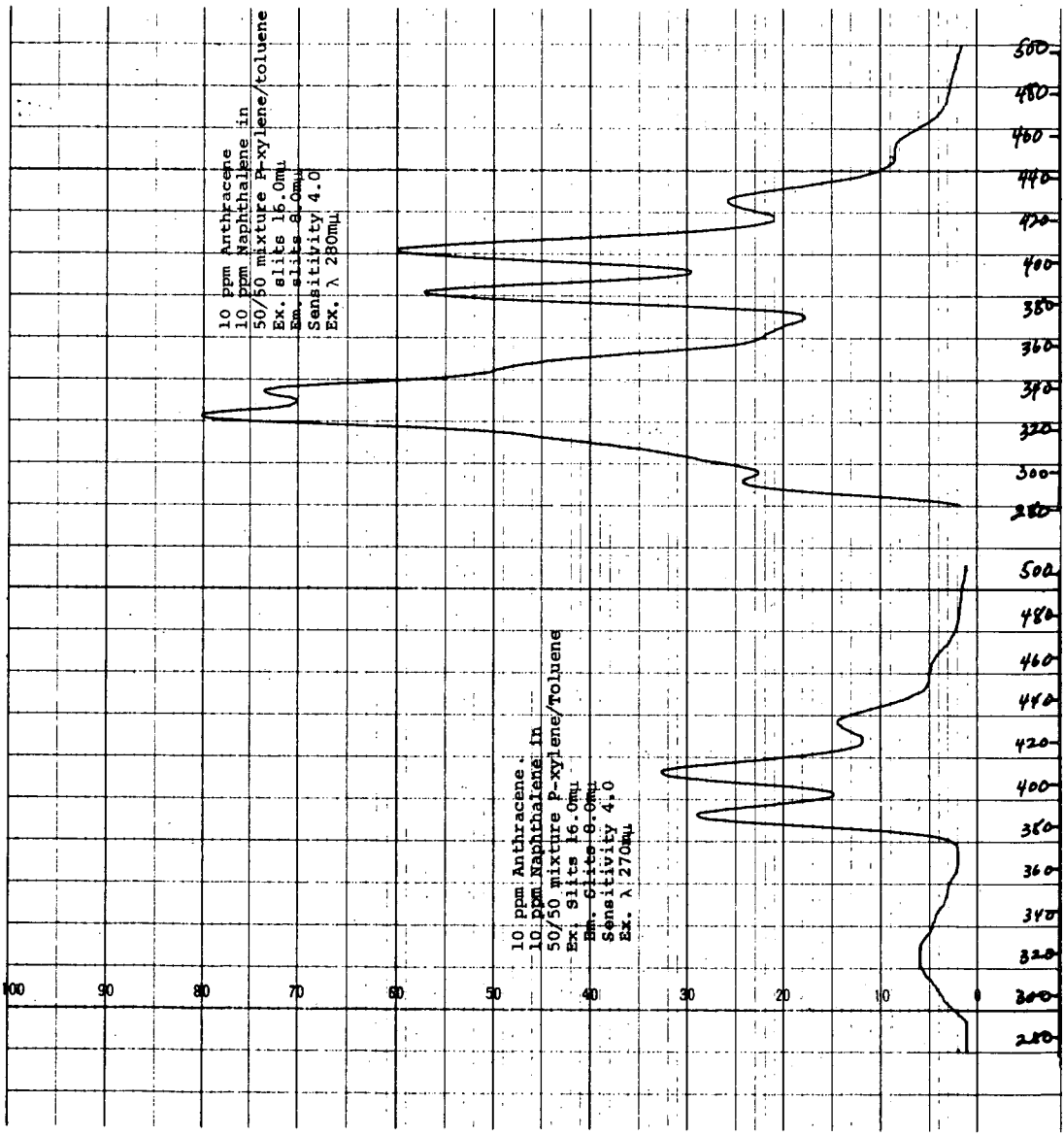
10 ppm Anthracene
10 ppm Naphthalene in
50/50 mixture P-xylene/toluene
Ex. slits 16.0mμ
Em. slits 8.0mμ
Sensitivity 4.0
Ex. λ 280mμ
10 ppm Anthracene
10 ppm Naphthalene in
50/50 mixture P-xylene/Toluene
Ex. slits 16.0mμ
Em. slits 8.0mμ
Sensitivity 4.0
Ex. λ 270mμ
100
90
80
70
60
50
40
30
20
10
0
500
480
460
440
420
400
380
360
340
320
300
280

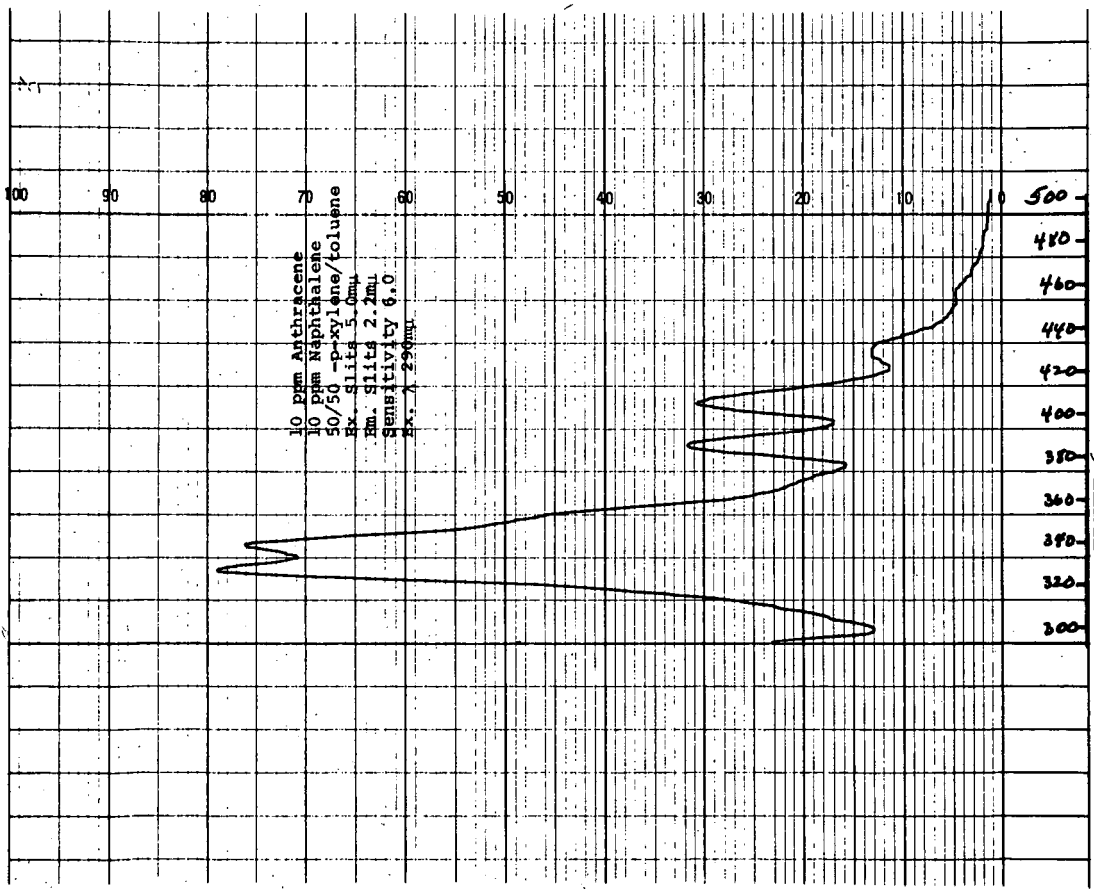
10 ppm Anthracene
10 ppm Naphthalene
50/50 -p-xylene/toluene
Ex. Slits 5.0mμ
Em. Slits 2.2mμ
Sensitivity 6.0
Ex. λ 290mμ
100
90
80
70
60
50
40
30
20
10
0
500
480
460
440
420
400
380
360
340
320
300

FIGURE 6

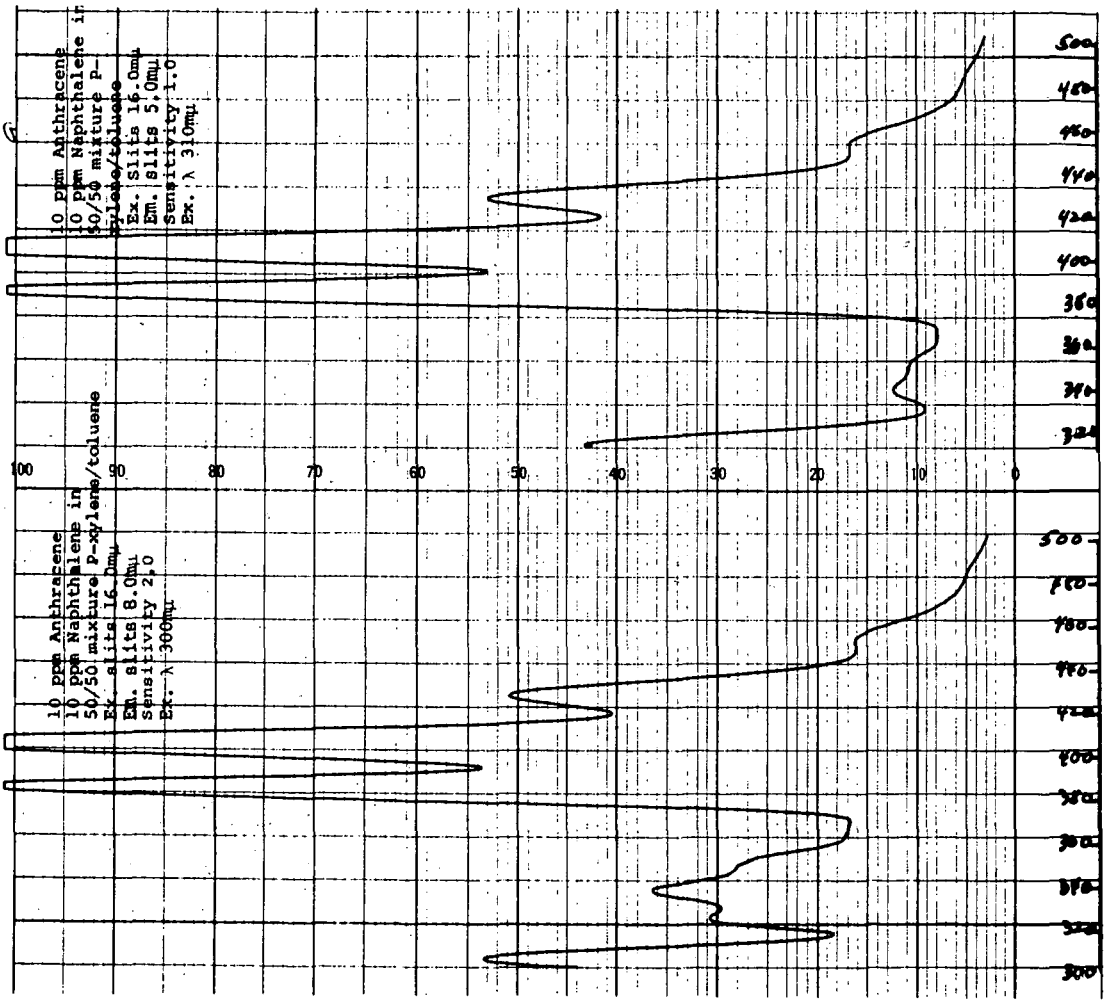
10 ppm Anthracene
10 ppm Naphthalene in
50/50 mixture P-xylene/toluene
Ex. slits 16.0mμ
Em. slits 8.0mμ
Sensitivity 2.0
Ex. λ 300mμ
10 ppm Anthracene
10 ppm Naphthalene in
50/50 mixture P-
xylene/toluene
Ex. slits 16.0mμ
Em. slits 5.0mμ
Sensitivity 1.0
Ex. λ 310mμ
100
90
80
70
60
50
40
30
20
10
0
500
480
460
440
420
400
380
360
340
320
500
480
460
440
420
400
380
360
340
320
300

FIGURE 7

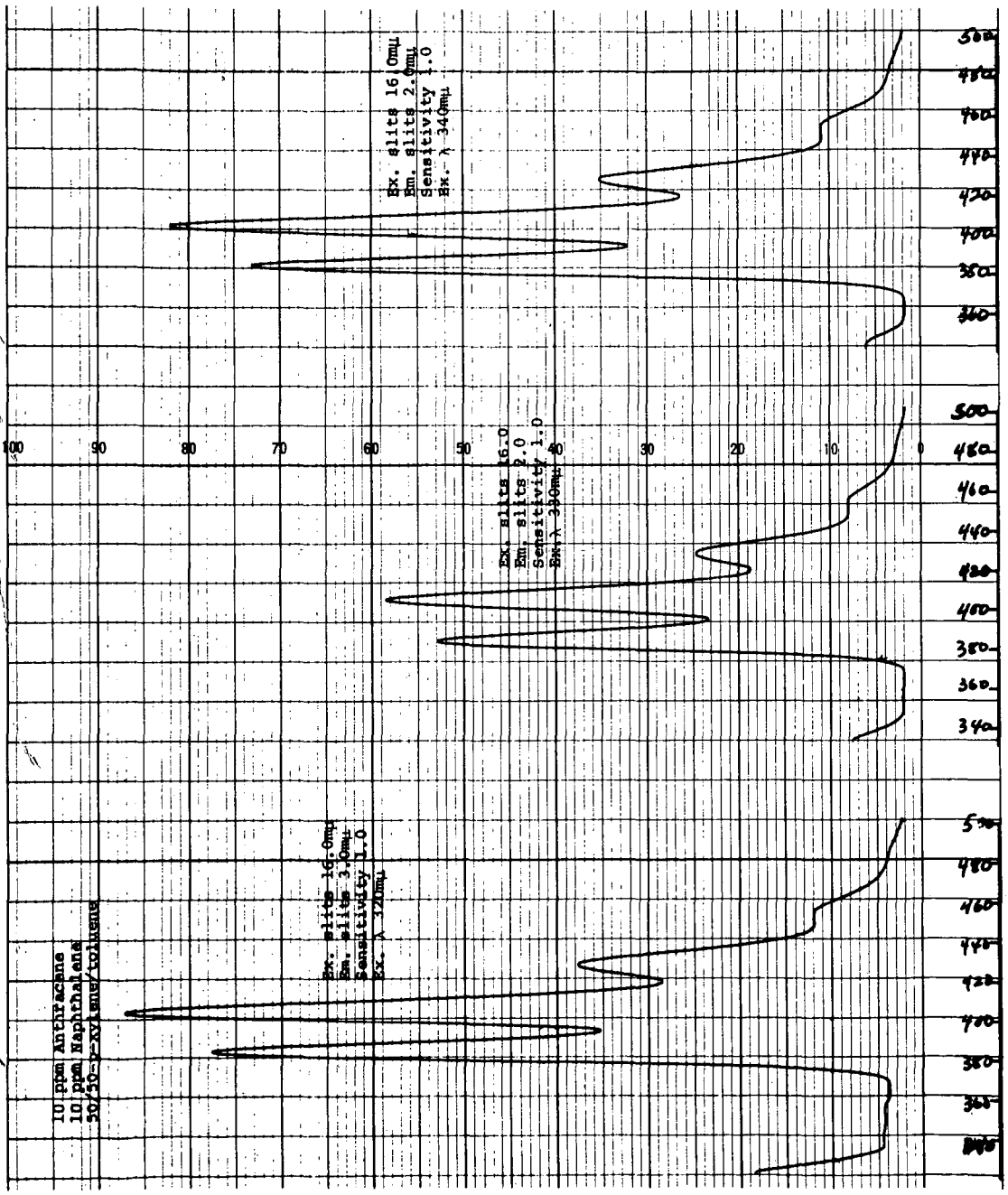
10 ppm Anthracene
10 ppm Naphthalene
50/50-p-xylene/toluene
Ex. slits 16.0mμ
Em. slits 3.0mμ
Sensitivity 1.0
Ex. λ 320mμ
Ex. slits 16.0
Em. slits 2.0
Sensitivity 1.0
Ex. λ 390mμ
Ex. slits 16.0mμ
Em. slits 2.0mμ
Sensitivity 1.0
Ex. λ 340mμ
100
90
80
70
60
50
40
30
20
10
0

FIGURE 8

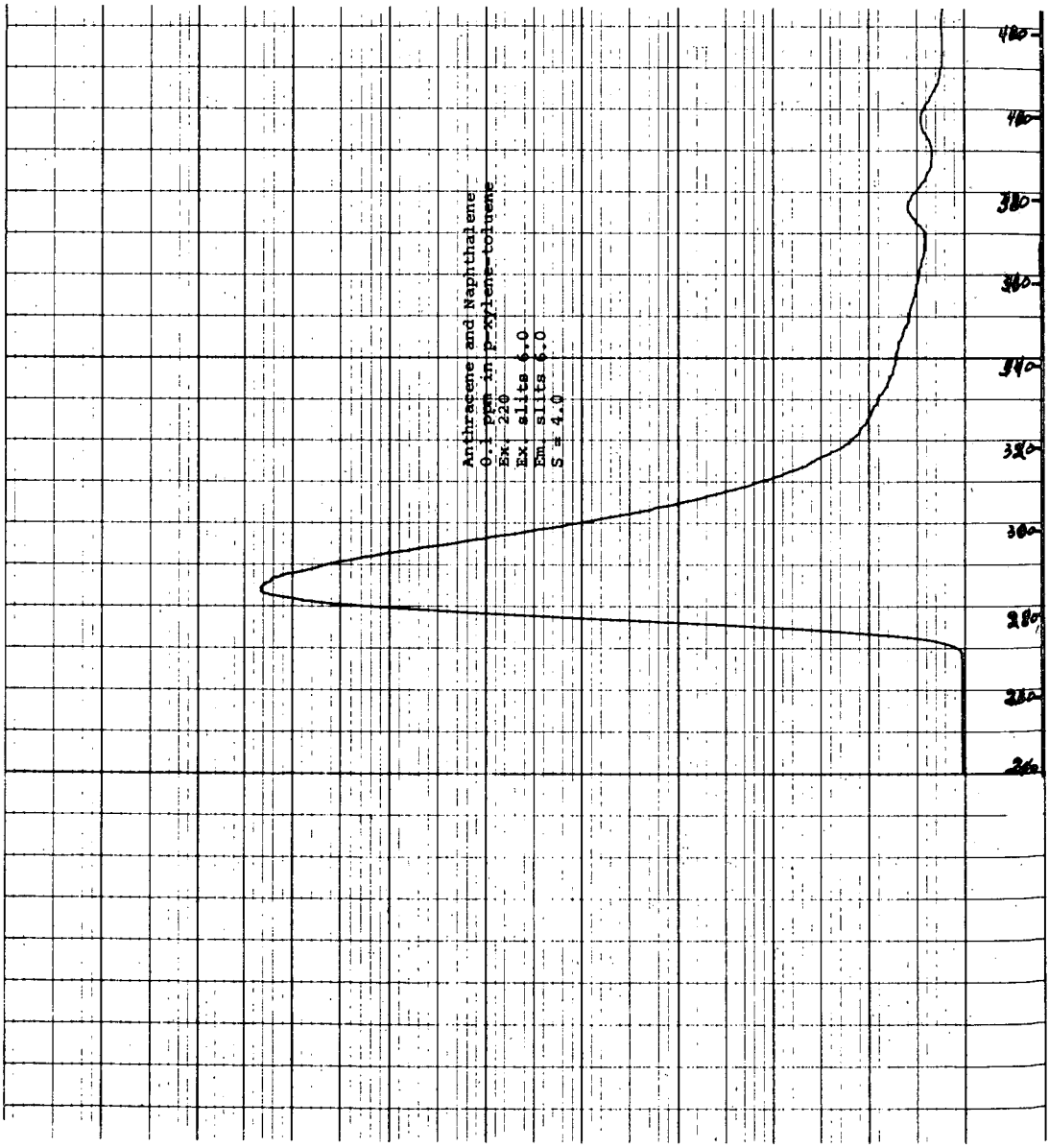
Anthracene and Naphthalene
0.1 ppm in p-xylene-toluene
Ex. 220
Ex. slits 6.0
Em. slits 6.0
S = 4.0
420
400
380
360
340
320
300
280
260

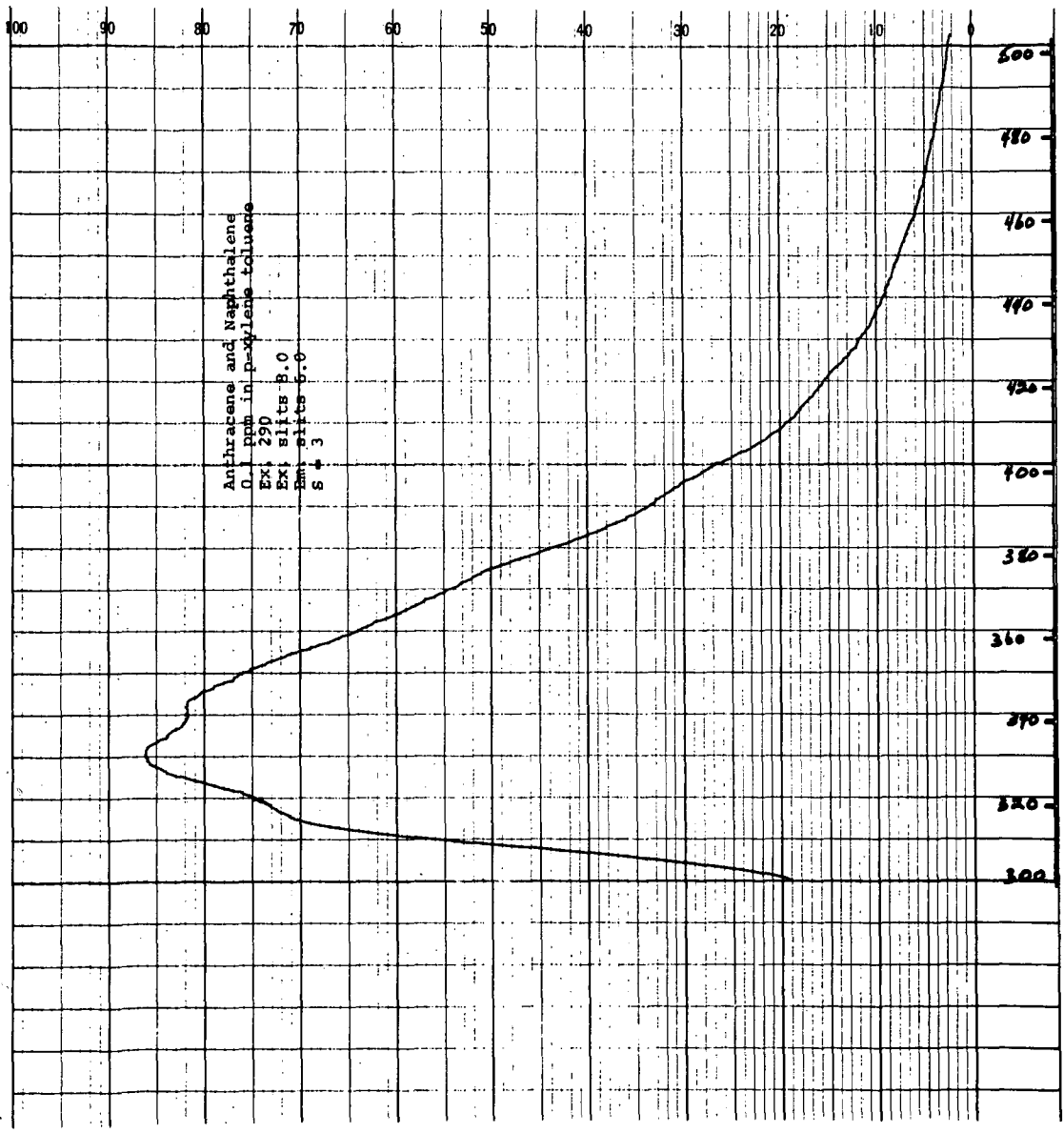
Anthracene and Naphthalene
0.1 ppm in p-xylene toluene
Ex; 290
Ex; slits 8.0
Em; slits 6.0
s + 3
100
90
80
70
60
50
40
30
20
10
0
500
480
460
440
420
400
380
360
340
320
300

FIGURE 10

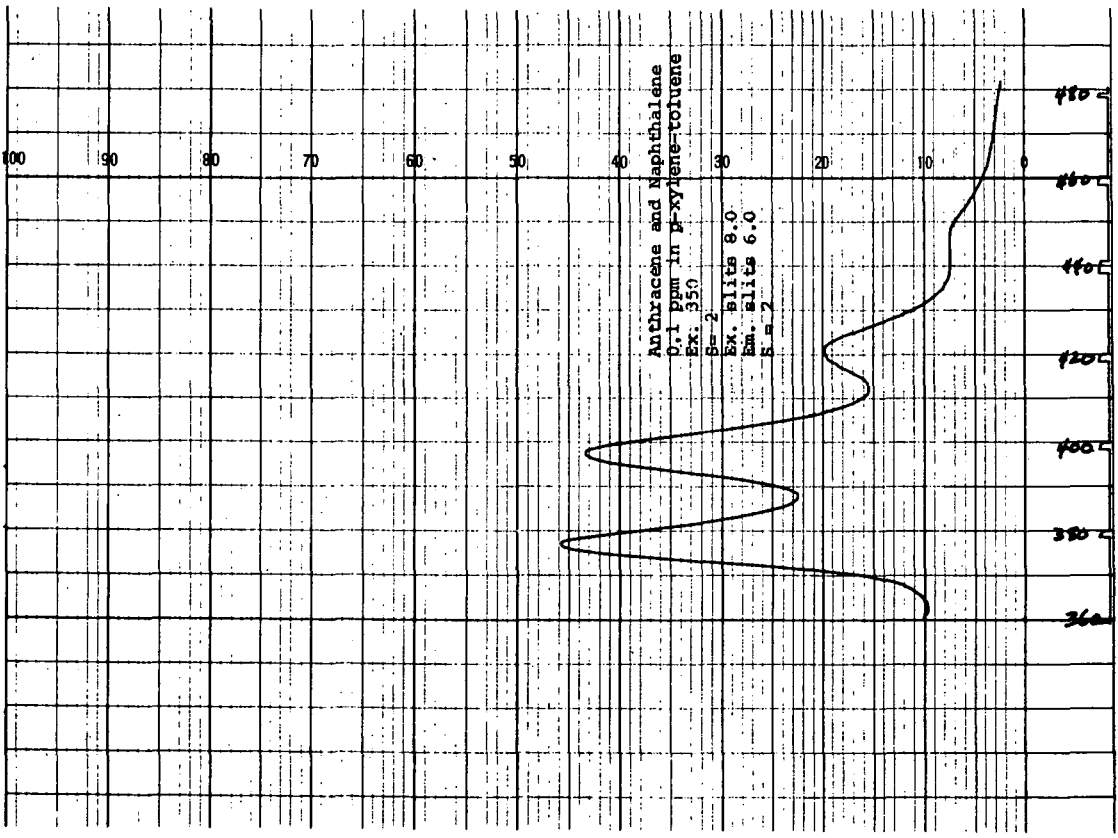
Anthracene and Naphthalene
0.1 ppm in p-xylene-toluene
Ex. 350
Em. 2
Ex. slits 8.0
Em. slits 6.0
S = 2
100
90
80
70
60
50
40
30
20
10
0
450
440
430
420
410
400
390
380

FIGURE 11

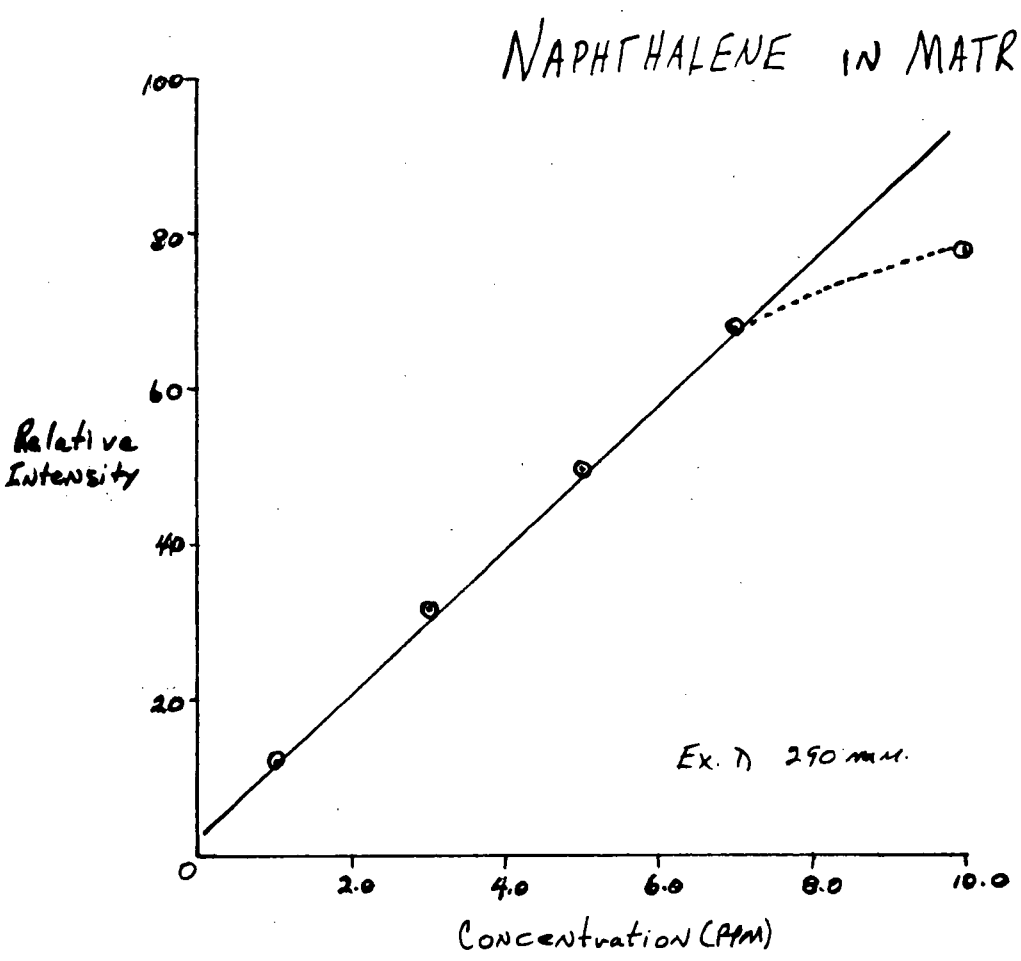
NAPHTHALENE IN MATRIX
100
80
60
40
20
0
Relative Intensity
Ex. λ 290 mμ.
2.0
4.0
6.0
8.0
10.0
CONCENTRATION (PPM)

FIGURE 12

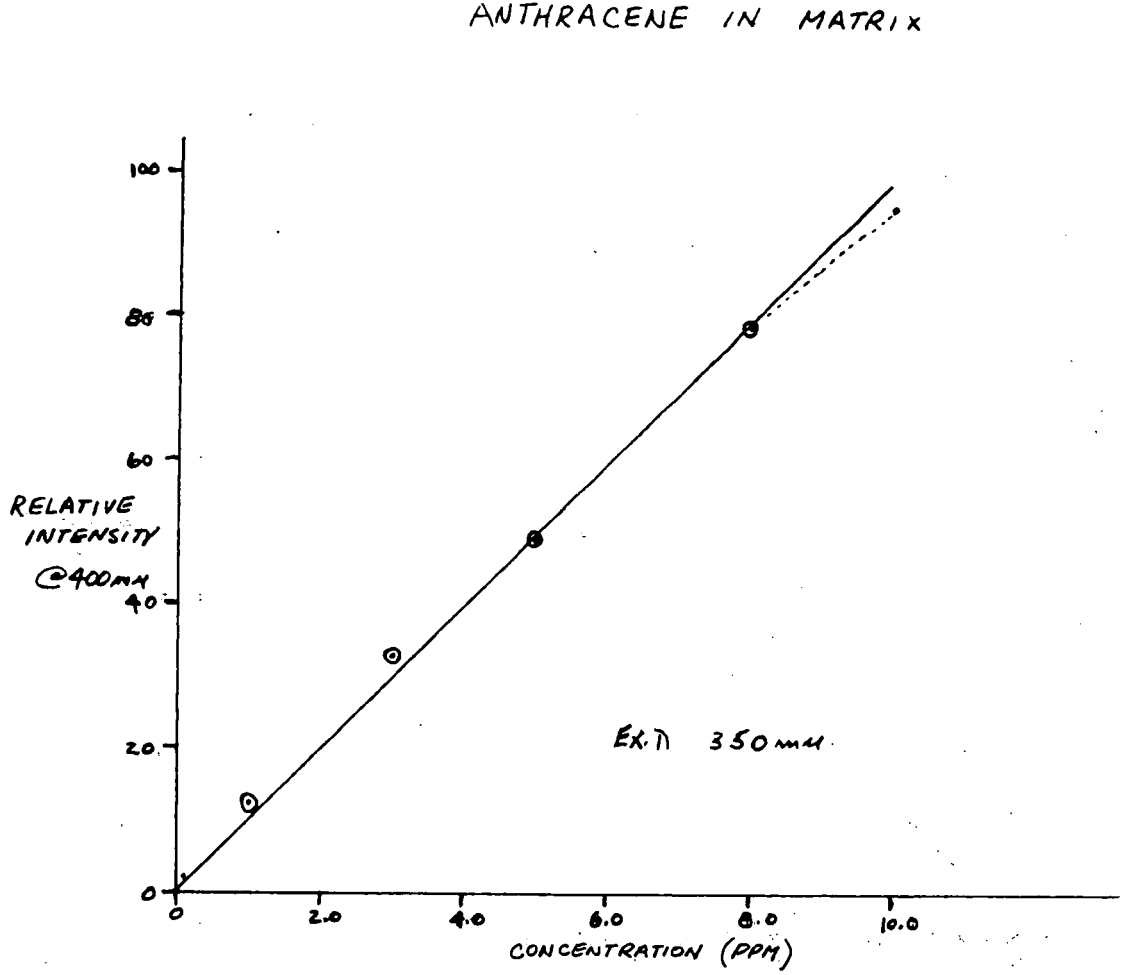
ANTHRACENE IN MATRIX
100
80
60
40
20
0
RELATIVE INTENSITY @400mμ
Ex. λ 350mμ
0
2.0
4.0
6.0
8.0
10.0
CONCENTRATION (PPM)

FIGURE 13

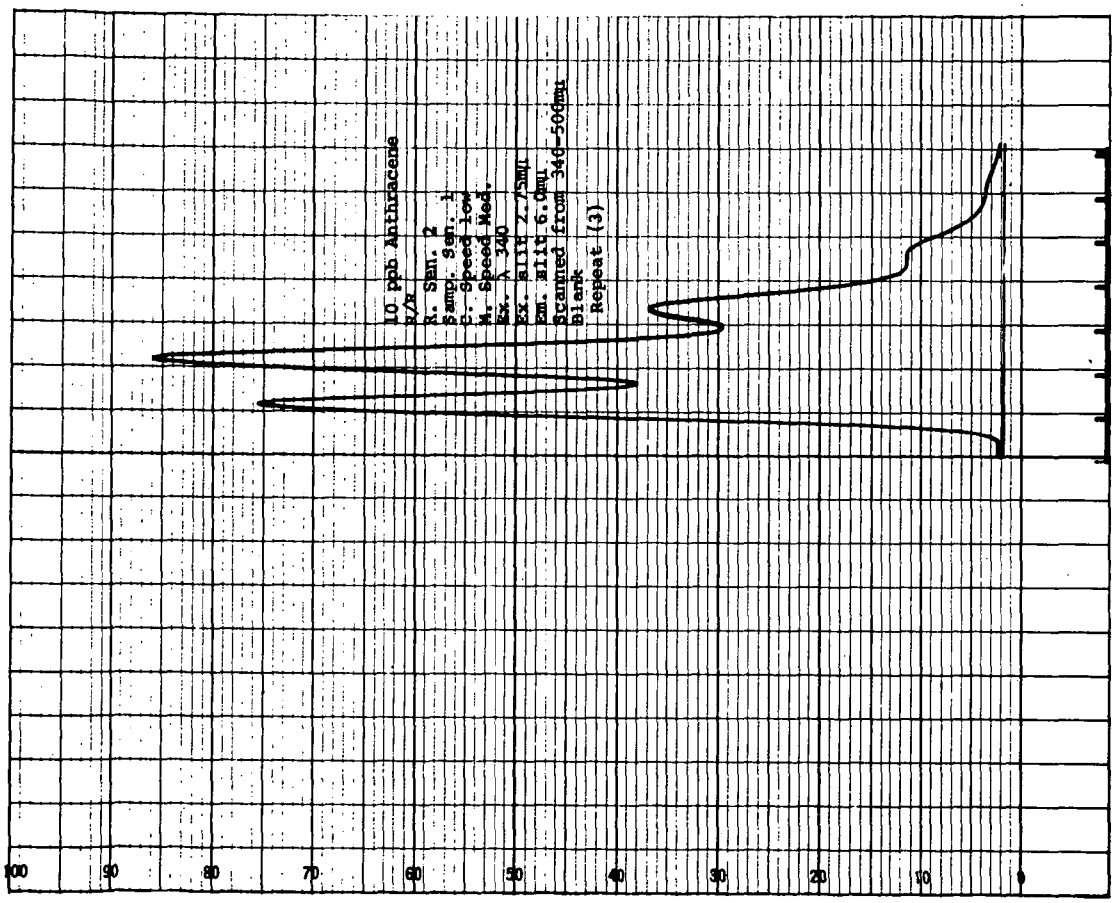
10 ppb Anthracene
R/R
R. Sen. 2
Samp. Sen. 1
C. Speed Low
M. Speed Med.
Ex. λ 340
Ex. slit 2.75mμ
Em. slit 6.0mμ
Scanned from 340-500mμ
Blank
Repeat (3)
100
90
80
70
60
50
40
30
20
10
0

DOUBLE RESONANCE MODULATED MICROWAVE SPECTROSCOPY

G. W. Flynn*, O. Stiefvater, and R. Volpicelli

Research Systems Inc., 236 Grove St., Lexington, Mass.

I. Introduction

A large number of molecular systems which have measurable vapor pressures at dry ice or room temperature can be studied by microwave spectroscopy. In general it is necessary that these molecules possess a permanent dipole moment (usually greater than 0.1 Debye) and have rotational states with energy level spacings which correspond to frequencies in the microwave spectral range (8-40 GHz, or 0.29 - 1.33 cm^{-1}). Most molecules have been studied in the microwave range with a "standard" Hughes and Wilson Stark-modulated spectrometer.[1] In this sytem the molecule is placed in a waveguide cell at a pressure of 10-100 μ of Hg. Microwave radiation is passed through the cell and absorbed by the molecular system at frequencies corresponding to the energy level separations of certain pairs of rotational states. It is important to realize that this resonance absorption for levels i, j with $E_i - E_j = h\nu_{ij}$ (where E_i, E_j are the energies of states i,j and h is Planck's constant) involves only two levels (we neglect here possible overlap between two or more transitions and degeneracies). In order to enhance the sensitivity for detection of the absorbed microwave radiation, a large electric field (0-2000V/cm) is applied to the gas in the cell. The interaction of the molecular dipole moment with this field causes a shift in the rotational energy level spacings and a consequent shift in the microwave absorption frequencies. The large electric field is modulated in square wave fashion, usually at 100KHz, and hence the absorption of radiation is also modulated at the same frequency and can be detected with a phase sensitive detector.

The standard Stark spectrometer can be characterized as a single resonance device because it involves the resonant absorption for only a single line (one pair of rotational energy levels). It is also possible to simultaneously irradiate a gaseous system with two microwave radiation fields with frequencies corresponding to two different rotational resonances of the molecule. Such experiments have been pursued by several authors[2-4] in Stark modulated spectrometers where the basic detection scheme still involves the molecular Stark effect. However, when two microwave fields are applied to a gaseous sample, it is possible to eliminate the standard high voltage Stark modulated cell by modulating one of the microwave fields instead.[5,6] This last spectroscopic scheme has been characterized as double resonance modulated microwave spectroscopy and constitutes the main concern of this abstract.

II. Theoretical Considerations

The theoretical treatment used here assumes that the resonance lines are pressure broadened. The average lifetime of a rotational state is taken as the mean time between collisions. Only three rotational energy levels, 1, 2, 3 with energies $E_1<E_2<E_3$ are considered. The transitions 1→2 and 2→3 are assumed to be allowed with dipole moment matrix elements μ_{12} and μ_{23} and resonance frequencies $\omega_o' = 2\pi\nu_{12}$, $\omega_o = 2\pi\nu_{23}$. Two radiation fields are allowed to impinge upon the gaseous sample, a strong field $E' = E_o'\cos\omega' t$ and a weak field $E = E_o \cos\omega t$ with ω' near ω_o' and ω near ω_o but $|\omega'-\omega| > |$GHz. (See figure 1a) τ is defined to be the average collision lifetime for the states 1, 2, 3 and n_1, n_2, n_3 are the number of molecules per cm^3 in states 1, 2, 3 for the gas at thermal equilibrium. It is useful to define the parameters $x = (\mu_{23}E_o)/(2\hbar)$ and $y = (\mu_{12}E_o')/(2\hbar)$.

All double resonance experiments of interest in this work are such that the transitions induced by the fields E and E' occur between pairs of rotational levels which have one common energy level (i.e. level 2 for 1 → 2, 2 → 3). The power in the radiation field E' is taken to be sufficient to "saturate the transition 1 → 2. This is equivalent to saying $|y|^2\tau^2 >> |$. The power in E however is assumed to be so low that the 2 → 3 transition is not "saturated" ($|x|^2\tau^2 << |$). Physically, saturation corresponds to a situation where the rate of transitions induced by a radiation field between two levels is such that the population difference between the levels involved in the transition is no longer described by the thermal equilibrium value.

The main features of microwave modulated double resonance spectroscopy are: (1) the strong (high power) field E' is used to modulate the gaseous molecular sample by interacting with the energy levels 1 and 2; (2) the modulation produced by E' causes small but readily detectable changes in the absorption of radiation from the weak field E by transitions between the levels 2 and 3; (3) the signal detected consists essentially of the power absorbed from the weak field E; (4) the strong field E' is blocked from the crystal receiver and is never detected.

Javan[7] in a classic paper has given a mathematical description of a three level system interacting with two radiation fields. The theory is directly applicable to microwave double resonance but the mathematical details are too complex to present here. Therefore only a very qualitative and intuitive description will be given in what follows.

For weak radiation fields it is generally true that only single quantum transitions can take place in a molecular system due to absorption of radiation. Thus a molecule can absorb a photon from field E and go from state 2 to state 3. In the presence of a very large field such as E' at the 1 → 2 molecular resonance frequency and a weaker field E at the 2 → 3 molecular resonance frequency, it is possible for a molecule in state 1 to simultaneously absorb a photon from both E' and E and make a transition to state 3 directly via a double quantum transition. Such transitions are allowed due to the strong quantum mechanical mixing of states 1 and 2 by E'. In a double resonance experiment the power absorbed from E consists of two terms: (1) power absorbed by molecules making the usual single quantum transition 2 → 3; (2) power absorbed by molecules making a two quantum jump from 1 → 3.

In a microwave modulated double resonance spectrometer the field E' is square wave modulated between the values $E' = E'_0 \cos\omega' t$ $\omega'_1 = \omega'_0$ and $|\omega'_2 - \omega'_0| = 20$ MHz. In such a situation, for power levels in the E' field of the order of one watt or less, $E' = E'_0 \cos \omega'_2 t$ generally has only a small effect on the molecular system because ω'_2 is so far from ω'_0. Thus it is possible to take $E' = 0$ for half the square wave cycle without introducing much error.[8] If phase sensitive detection locked to the modulation frequency of E' is used to detect the power absorbed from E, the power absorbed from E during the $E' = 0$ half of the modulation cycle will be essentially identical to an ordinary single resonance absorption. The power absorbed during the $E' = E'_0 \cos \omega'_0 t$ half cycle will have the double resonance shape predicted by Javan's theory.

III. Pressure Dependence and Intensity of Double Resonance Signal

In the case where E' is only an 0.1 watt field at the J=0-1 resonance frequency the lineshape for the OCS J=1-2 transition will have the appearance shown in figure 1b. As the pressure increases the signal "height" S will decrease and the "line width" will increase in a somewhat complex manner.[9]

Using a computer to simulate line shapes in OCS, the "line intensity" S for the J=1→2 transition with an 0.1 Watt pump field at the J=0-1 resonance frequency has been determined as a function of pressure. These calculations correspond to the line shape shown in figure 1b. A table of S versus pressure and τ is given in Table 1 below for this case.

Table 1

S (arbitrary units)	P (μ of Hg)	τ^* (sec x 10^{+6})
3.15	2	12.40
3.19	10	2.48
3.03	20	1.24
1.05	100	0.248
0.27	200	0.124

*$\Delta\nu$ = 12 MHz/mm, full width at half height, see ref. 10.

At low pressure, for E' a 1 Watt pump field, it is possible to compare the theoretical intensity S_1 (Figure 1c) with that which can be obtained from a single resonance Stark modulated spectrometer. When the S_1 and S_2 lines are well resolved, S_1 is very similar to a single resonance absorption and it might be expected that the intensity is the same as that for the equivalent Stark modulated line. This is not true normally and the theoretical intensity is expected to be less in general for the double resonance spectrometer. The problem which arises here has to do with the effect of the pumping radiation on various molecular M states (M is the projection of the total angular momentum J on a space fixed axis). This effect becomes small as higher J values are studied and is treated in detail elsewhere.[9] There are also some practical technical problems to be considered in comparing Stark and double resonance spectrometers. Because of the absence of a Stark plate in the double resonance system, the double resonance wave guide cell can easily be made about five times as long as the corresponding Stark cell thus enhancing the signal intensity by a substantial amount. Finally, there are some subtle intensity effects in a double resonance spectrometer which arise from the rate of relaxation of the rotational states and may lead to some enhancement in signal intensity over the Stark case. These effects should be negligible in most cases.[9]

IV. Experimental Results

Several molecules have been investigated in the present experiments using a double resonance modulated spectrometer similar to that of reference 6. Only the results for propionaldehyde are considered here. For this molecule the $2_{11} \rightarrow 3_{12}$ ($\omega_o/2\pi$ = 33,347 MHz) transition was observed while the $2_{02} \rightarrow 2_{11}$ ($\omega'_o/2\pi$ = 13474.9 MHz) transition was pumped. The line shape corresponded to that shown in Figure 1b. Figure 2 is a plot of the signal height S (see Figure 1b) as a function of pressure for pure propionaldehyde.

It can be seen that the signal height begins to fall off drastically for pressures in excess of about 25μ of Hg. This behavior is qualitatively similar to that predicted using computer simulated line shapes for the molecule OCS (see Table 1).

The reason for the initial rise in the signal height in the pressure range 0-20 μ of Hg is readily understood by the following considerations. For pressures below about 10 μ of Hg the linewidth of the signal is not determined by collision processes and hence the theoretical discussion presented earlier does not apply to this region. Before pressure broadening sets in, the linewidth will generally be a constant (determined by the modulation frequency, temperature, and cell dimensions) and the line intensity will increase directly as the density of the sample. This is similar to the situation observed in a Stark spectrometer except that for the Stark case the maximum signal height is independent of pressure in the pressure broadened range. For the double resonance case the line intensity drops in the pressure broadened range because of incomplete modulation.

For gas samples which are mixtures of several components (all or only one of which have a microwave spectrum) curves similar to that shown in Figure 2 are observed for a given component. The peak of the signal generally occurs at a different pressure than that for the pure sample due to the difference in collision cross sections for the various constituents of the sample. It is worth noting that the double resonance technique serves as an unambiguous identification method for a molecule in the presence of many other molecules. This is because the observation of a double resonance signal for a given microwave pump and observation frequency requires that the sample have a resonance at each of these respective frequencies and that these resonances must have a common energy level. That such a series of circumstances might arise for more than one molecule is highly unlikely.

V. Conclusions

1. At moderate or low pressures (about 20μ of Hg) it is expected that a microwave modulated double resonance spectrometer will have a better signal to noise ratio than a Stark modulated spectrometer provided the double resonance waveguide cell is at least several times longer than the Stark cell.

2. At high pressures, due to incomplete modulation, the double resonance technique is less advantageous than the Stark technique.

3. The double resonance technique is extremely useful for identification of molecules in a mixed sample due to the highly selective nature of the double resonance phenomenon.

REFERENCES

* Department of Chemistry, Columbia University, New York, N.Y.

1. K.B. McAfee, R.H. Hughes, and E.B. Wilson, Jr. Rev. Sci. Inst. 20 821 (1949)
2. A. Battaglia, A. Gozzini, and E. Polacco, Nuova Cimento 14, 1076 (1959)
3. T. Yajima and K. Shimoda, J. Phys. Soc. Japan 15 1668 (1960)
4. A.P. Cox, G.W. Flynn, and E.B.Wilson, Jr. J.C.P. 42 3094 (1965)
5. A. Battaglia, A. Gozzini, and E. Polacco, Arch. des Sciences, Switzerland 13, F A S C 171 (1960)
6. R.C. Woods III, A. Ronn, and E.B. Wilson, Jr., "A Double Resonance Microwave Spectrometer" (to be published)
7. A. Javan, Phys. Rev. 107 1579 (1957)
8. Sometimes, however, the small effects introduced by the off resonant field ω_2 can be readily detected even when $|\omega_2' - \omega_0'| \sim 500$ MHz (O. Stiefvater, unpublished results).
9. G. W. Flynn (to be published)
10. Molecular Microwave Spectra Tables, NBS Circular 518.

Figure 1.

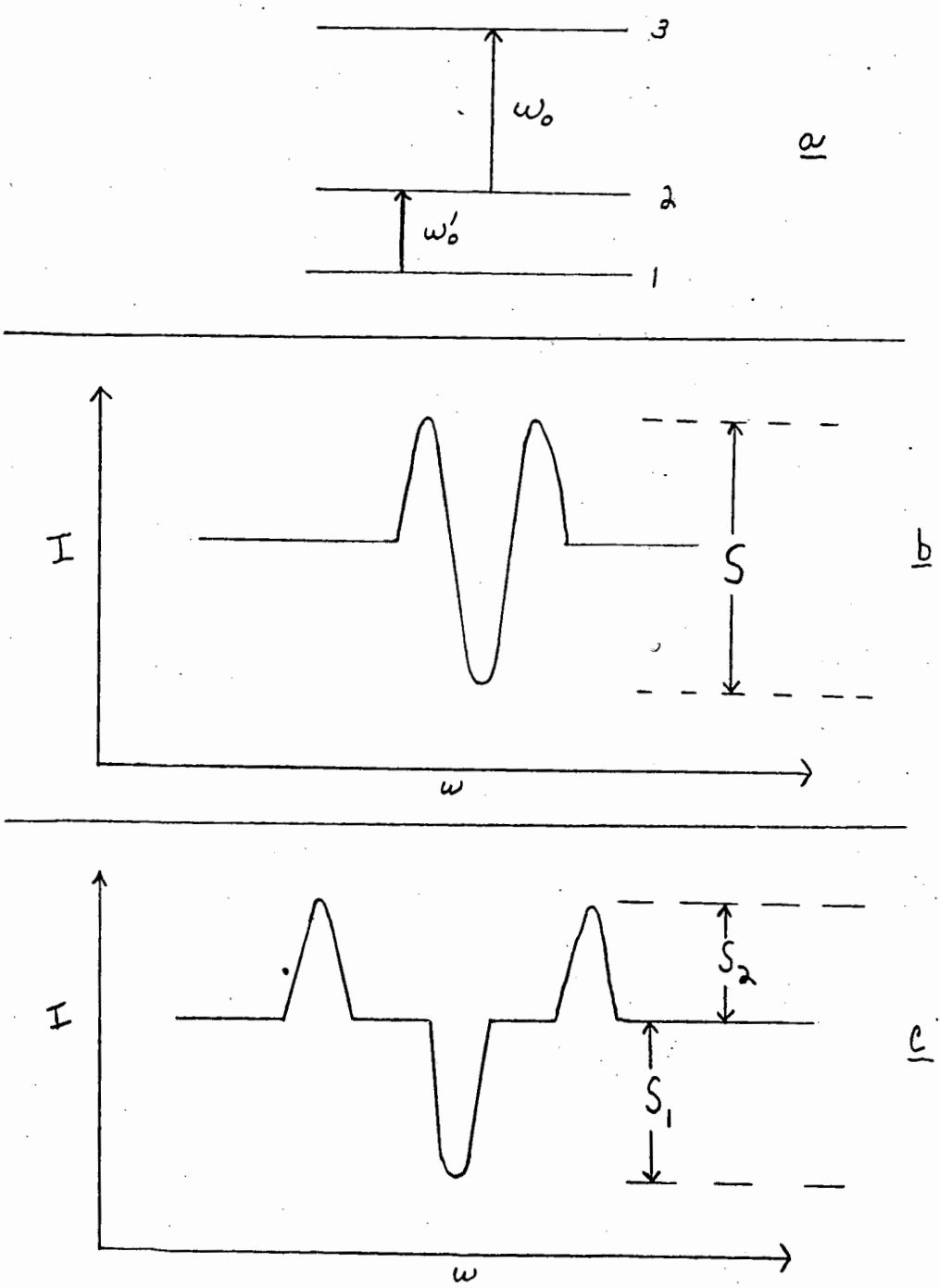

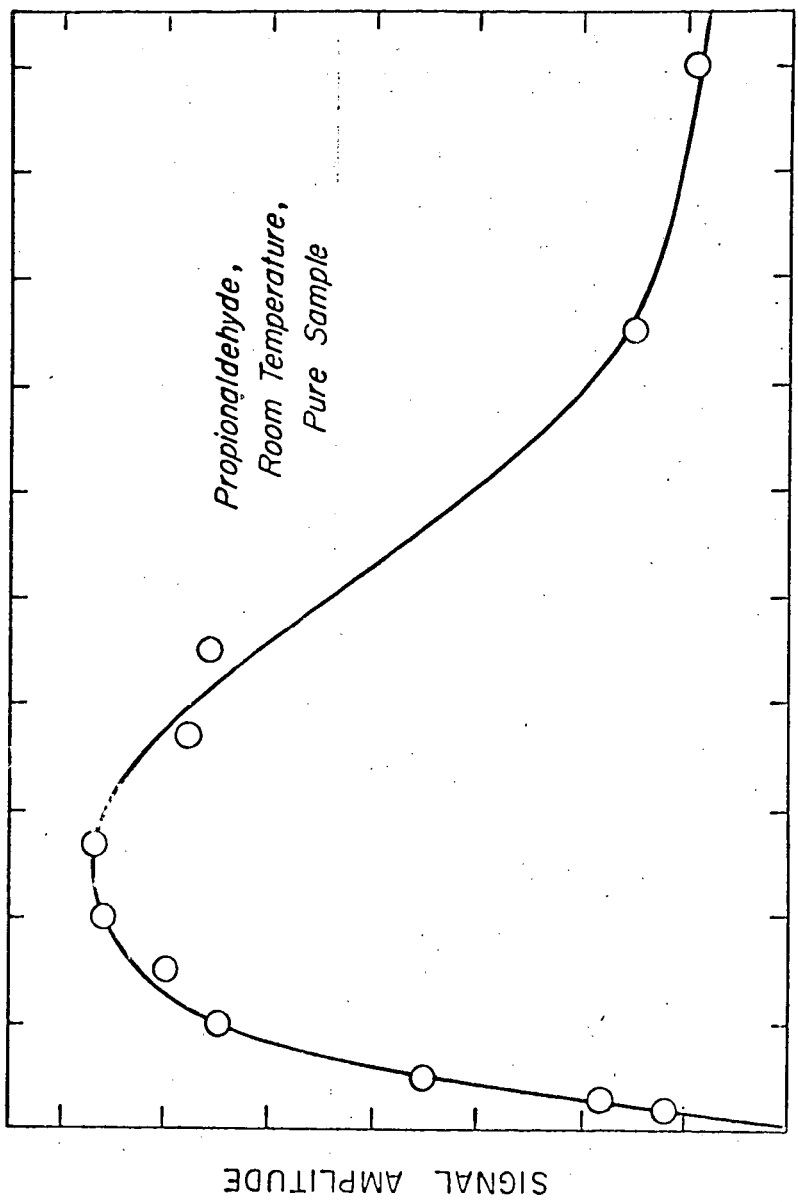
Propionaldehyde,
Room Temperature,
Pure Sample
SIGNAL AMPLITUDE
PRESSURE IN μ
0
10
20
30
40
50
60
70
80
90
100

Figure 2.

INVESTIGATIONS IN NQR SPECTROSCOPY

William L. Truett

Wilks Scientific Corporation, So. Norwalk, Conn.

NQR Spectroscopy refers to that branch of spectroscopy in which energy is absorbed by various atomic nuclei in the region from ∿ 1-1000 Mc/s. A full and excellent discussion of all the theoretical and experimental aspects of the subject has been given by Semin[1]. Among the more important nuclei which show the effect are Cl^{37}, Cl^{35}, Br^{81}, Br^{79}, I^{127}, Sb^{121}, Sb^{123}, Al^{27}, N^{14}, Ga^{69}, Ga^{71}, and V^{51}; in all 131 isotopes can absorb RF energy.

The precise position of the absorption depends upon the electron density about the nucleus and the number of allowed absorption bands upon the nuclear spin. In general with nuclei of spin 3/2, one line will be observed from each chemically distiguishable nucleus. Thus with Cl^{35}, spin 3/2, Table I summarizes the number of bands to be expected in the indicated structures.

TABLE I

STRUCTURE	ABSORPTION BANDS
	1
	1
	2
	3

Until recently nqr spectra could be obtained only with considerable difficulty due to the wide range of frequencies over which any particular isotope might absorb (50-100 Mc/s) and the slowness of search due to the frequent necessity of adjusting the oscillators used. The instrument developed by Peterson and Bridenbaugh[2] has made a dramatic difference in the ease of search over wide ranges by an essentially automatic and unattended spectrometer.

In addition to the components customarily present in an oscillator of the superregenerative sort, the Peterson instrument contains an electro-mechanical servo loop which serves to stabilize the oscillator over wide ranges by feeding back a voltage to the grid of the oscillator tube, customarily a 12AU7, which results in a stabilized output at constant noise. Thus, searches are readily conducted over ranges of 20-40 Mc/s which contain the vast majority of organo chloro compound absorption bands, or 200-300 Mc/s which contain the vast majority of organo bromo compounds; the time required for such searches is 2 to 4 hours.

Some additional refinements to the Peterson spectrometer have been noted by Graybeal[3], but full detials on relative performance have not been published.

Previous examination of the quantitative aspects of nqr spectroscopy has largely been limited to determination of the effect of impurities on the peak intensities of absorption bands[4] with minor references to the utility of peak intensities to determine the relative numbers of chemically different nuclei present in a molecule[5,6]. Relatively minor references will be noted in papers concerned with nqr spectroscopy with regard to sample size. It is apparent from papers containing absorption data on large numbers of compounds[1,7] that while chemical shifts comparable in principle to those observed in nmr spectra are present, splittings due to the effects of neighboring atoms are not present.

Unfortunately, a type of splitting is encountered which has to do with the fact that spectra can be determined only upon crystalline solids and is designated crystal splitting. It is due to the fact that chemically equivalent nuclei in a crystalline lattice may be physically non equivalent by virtue of relative lattice positions. Normally, it can be recognized by the extent of the splitting ~0.2 Mc/s, and the equal intensities of the two bands[8]. In certain cases it simplifies the interpretation of a spectrum for it has been found that virtually all trichloromethyl groups show a trio of bands of equal intensity separated by about 0.1-0.2 Mc/s.

Examination of mixtures of p-dichlorobenzene and p-dibromobenzene along the lines noted by Dean[9] give very similar results using the Wilks Scientific Corporation NQR-1A NQR Spectrometer. Additional examples of p-dichlorobenzene and γ-hexachlorocyclohexane indicates that the peak height is an excellent way to determine the concentration of impurities present in a crystal of a chloro compound in the range from 0.01 to 1.0%, and that calibration curves of the sort generally useful in quantitative infrared measurements can easily be constructed.

With regard to the amount of sample required it has been found that employing the NQR-1A it is possible to determine usable spectra of p-dichlorobenzene on samples of 25-50 mg., although routinely 500mg will suffice for any unknown. It has been found that in general a much smaller sample, 100mg, routinely suffices for any bromo compounds where the absorption frequencies are much higher, while compounds that absorb at frequencies near 5 Mc/s will require 1000mg routinely for detection.

Careful examination of a number of spectra of diverse types of organic chloro compounds makes it apparent that nqr spectra can be used to determine the relative numbers of the different types of chloro atoms present. It has been found that peak height alone is sufficient to this end and that integration of the area is unnecessary. Thus, with 2,4-dichlorophynoxy acetic acid we find two bands of matched intensity, Spectrum 1. A molecule of γ-hexachlorocyclohexane is known to contain 3 axial and 3 equitorial chloro atoms, and due to their spatial arrangement there are effectively 4 types of chloro atoms present. The spectrum shows 4 lines of a 1:2:2:1 peak height relationship which fits the known structure[10].

Unfortunately, instruments of the Peterson type cannot be used routinely for the measurement of the spectra of nitrogen compounds due to saturation phenomena precisely encountered in other types of resonance measurements. The use of other types of oscillators such as the Robinson or P-K-W oscillator[11,12] can furnish data on many types of nitrogen compounds.

At the present time there are relatively few examples in the literature of the use of nqr to determine the structure of an organic molecule; Kozima has

used this technique to differentiate between the chlorination products of cyclohexane, 2,2-dichlorocyclohexane and 2,6-dichlorocyclohexaneone[13].

Application of the nqr technique to γ-hexachlorocyclohexane has been noted above. A similar study of β-1,2,3,4,5,6-hexachlorocyclohexane revealed that only a single strong band is observed near 37.0 Mc/s. This agrees with the known structure in which the chloro atoms are all trans and all possess the equitorial configuration. It is of interest to note that the only easily attained isomer of 1,2,3,4,5,6-hexabromocyclohexane has a very complex spectrum and is clearly not related to the β-chloro isomer above.

γ-1,2,3,4-tetrachloro - 1,2,3,4-tetrahydronapthalene has been the subject of a recent nmr investigation[14] and has the configuration noted symbolically below:

An nqr spectrum of this compound shows two bands of equal intensity at 35 and 36.5 Mc/s and is in agreement with the nmr assignment.

The nqr spectrum of 2,4-dichlorobenzotrichloride, Formula I, might be expected to show three bands representing the three types of chloro atoms

present in a 1:1:3 intensity, with probable splitting of the band due to the trichloromethyl group into a triplet. The actual spectrum (Spectrum 2) shows the expected 3 bands, however, the band at 39.0 Mc/s which is due to CCl_3 is split into a distinct doublet at a 2:1 intensity. A reasonable interpretation of this effect is that the ortho chloro group is interferring sterically with the free rotation of the trichloromethyl group. As a result of this the two chloro atoms of the trichloromethyl group nearer the ortho chloro group are different from the one which is farther.

If collection of data of the sort in references 1 to 7 are studied, it is possible to develop correlation charts of the Colthrup type which have proved so popular in infrared spectroscopy. In such a chart it will be noted that in the case of organic chloro compounds that a range of 30-55 Mc/s embraces virtually all classes of chloro compounds. Acid chlorides show bands near 30 Mc/s while N-chloro compounds lie at the other end of the range near 55 Mc/s. Aromatic and aliphatic chloro compounds absorb near 34-35 Mc/s for the simple types while the more highly substituted types absorb at higher frequencies, for example; the trichloromethyl group near 39Mc/s. Spectra of compounds containing as many as 5 chemically different chloro atoms have shown five distinct bands.

REFERENCES

1. Semin, G.K., and Fedin, E.I., "Use of Nuclear Quadrupole Resonance in Chemical Crystallography." Available through Consultants Bureau, New York (1964) 227 West 17 Street, New York, New York. Unlisted chapters in the Mossbauer Effect and Its Applications in Chemistry, V. I. Gol'danskii.

2. Peterson, G.E., and Bridenbaugh, P.M., The Review of Scientific Instruments, 35, 698 (1964).

3. Graybeal, J.D., and Croston, R.P., The Review of Scientific Instruments, 38, 122 (1967).

4. Duchesne, J., and Monfils, A., Compt. Rend., 238, 1801 (1954).

5. Holmes, R.R., Carter, R.P., and Peterson, G.E., "Molecular Structures of PCl_4F, PCl_3F_2 and PCl_2F_3: Pure Chlorine Nuclear Quadrupole Resonance and Low Temperature F^{19} NMR Spectra," The Journal of Chemical Physics, 3, 1748 (1964).

6. Lorenzo, J.V.D., and Schneider, R.F., Inorganic Chemistry, 6, 766 (1967).

7. Hooper, H.O., and Bray, P.J., The Journal of Chemical Physics, 33, 334 (1960).

8. Dewar, M.J.S., and Lucken, E., Journal of Chemical Society, 426 (1958)

9. Dean, D., The Journal of Chemical Physics, 23, 1734 (1955).

10. Brame, E.G., Analytical Chemistry (In press).

11. Schempp, E., and Bray, P.J., The Journal of Chemical Physics, 46, 1186 (1967)

12. O'Konski, C.T., "Nuclear Quadrupole Resonance Spectroscopy," Determination of Organic Structures as Physical Matters, 2, Ch. 11, Academic Press, New York (1962).

13. Kozima, K., and Saito, S., "Nuclear Quadrupole Resonance of di-Chlorocyclo-nexanone, " The Journal of Chemical Physics, 31, 560 (1961).

14. De la Mare, P.B.D., et al, Journal of Chemical Society 3, 827 (1966).

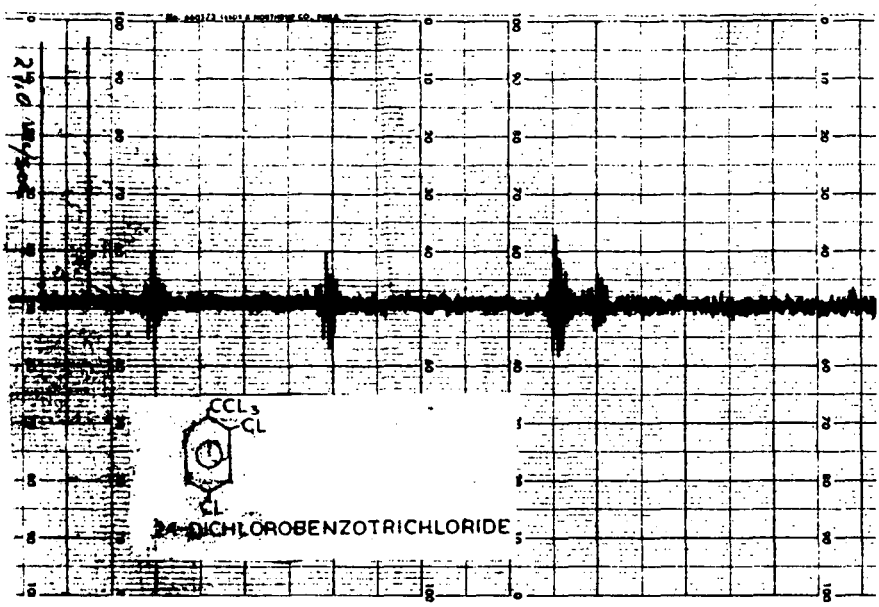

SPECTRUM 1

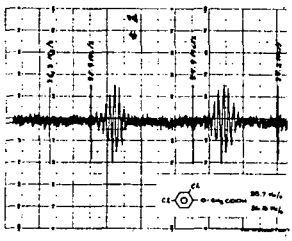

SPECTRUM 2

MÖSSBAUER SPECTROSCOPY: PRINCIPLE AND PRACTICE

Carl W. Seidel

Nuclear Science & Engineering Corporation
Pittsburgh, Pennsylvania 15236

ABSTRACT

Mössbauer Spectroscopy has started to come into its own as an analytical tool. In order to understand what has been accomplished and the potential applications of the Mössbauer Effect, one must understand nuclear resonance absorption and how it is effected by the environment of the absorbing nucleus. The perturbation of the nuclear energy levels of Mössbauer nuclides and the resultant characteristics of Mössbauer spectra are reviewed. This includes the isomer shift and its dependence on the electron density about the nucleus, quadrupole splitting and magnetic hyperfine splitting as well as the temperature dependence of these properties. Correlations of the above properties with the ionic state, electronegativity of a bonding component or with theoretical electron density calculations can be accomplished. The Debye-Waller factor for both the source and absorber material places certain restrictions on the ability to observe the Mössbauer Effect with all possible Mössbauer nuclides. Two typical Mössbauer spectrometer systems are described. One utilizes a constant velocity mode of operation for obtaining data, at one velocity at a time. The other utilizes a constant acceleration mode of operation which scans the chosen velocity range repetitively, storing the counting data in a multichannel analyzer. The basic detection system is the same for both systems but the readout devices may differ. Application of Mössbauer Spectroscopy in the study of surface effects such as adsorption and the study of the bonding of some organo metallic compounds will be discussed.

Another technique has been added in the field of spectroscopy. This new method of analysis depends upon the observance of nuclear resonance absorption which in turn depends upon the recoil free emission and recoil free absorption of gamma rays, or the Mössbauer effect. The term Mössbauer Spectroscopy has been applied to this new and very useful instrumental method which complements the more established techniques of NMR, ESR and x-ray diffraction.

The theory behind the Mössbauer effect has been fully described by Mössbauer (23), Frauenfelder (24) and Wertheim (3) and will not be described in detail here. Certain nuclides (Mössbauer nuclides) exhibit a nuclear decay scheme where the transition from the first excited nuclear level (and sometimes second excited nuclear levels) to the ground state may occur with the recoilless emission of a gamma ray. This gamma ray is uniquely capable of raising a similar nucleus in the same type environment from the ground state to the first (or second) excited nuclear level by recoilless absorption (resonant absorption). Most of the elements that have one or more of these Mössbauer nuclides are shown on the accompanying chart (Fig. 1). The resonant absorption process depends on the fact that the emitting (source) and absorbing (sample) species are bound in a crystal lattice.

Resonance absorption may be destroyed by employing the Doppler effect. If we move either source or absorber relative to the other we may alter the conditions

necessary for resonance absorption. Essentially what happens is that by moving either the source or absorber toward the other (a positive Doppler velocity) we increase the energy of the gamma ray as seen by the absorbing species. By moving one away from the other (a negative Doppler velocity) we decrease the energy of the gamma ray as seen by the absorbing species. A complete Mössbauer spectrum would therefore be the plot of the rate of transmission of the gamma ray through the absorbing sample as a function of this Doppler velocity. The resonant condition results in a noticeable decrease in transmission (resonant peak). The parameters of such a spectrum include M (or ε), the percent decrease in transmission (magnitude of the peak) at the resonant velocity and Γ, the width of the resonant peak at half maximum as shown in Fig. 2.

Resonance absorption occurs at zero velocity only if both the emitting and absorbing species are in the same physical environment. If this is not true then the resonance absorption may occur at a non-zero velocity. This displacement of the resonance from zero velocity is called the chemical or isomer (I.S.=δ) (Fig. 3). The isomer shift value is a linear function of the s electron density and for Fe-57 decreases with increasing s electron density (1). The d electron density affects the isomer shift mostly by shielding the s electron from the nucleus. Adding d electrons to the atom of interest decreases the electronic charge density at the nucleus, an effect just the opposite of that resulting from the addition of s electrons. The contribution to the shift from the p electrons is very small (3).

Since the electron density at the nucleus is a function of the oxidation state of the absorbing atom and of the electronegativity of its nearest neighbors we have a means of qualitatively identifying compounds, determining oxidation states and structural information concerning the absorbing material. For example, in Fig. 4 we can see how different tin (IV) halides give very noticeably different isomer shifts. The SnF_4 gives a quadrupole splitting because of the inhomogeneous field of surrounding F atoms (it is believed to have a polymer like structure).

Quadrupole splitting (QS=Δ= distance between the two resonance peaks) is due to the interaction of the inhomogeneous electric field at the nucleus (due to the environment) with the electric quadrupole moment of the excited nucleus. The result is a doublet or two resonant peaks. This occurs because the first nuclear excited level splits into two sublevels and two transitions (of slightly different energy) may occur (Fig. 5). Quadrupole splitting may be related quantitatively to the oxidation state and the nature of the chemical bonding of the absorbing atom (1). It also may be used as a method of determining the symmetry of crystals and crystal distortion incurred by substitution in the compound as shown in Fig. 6. The isomer shift of a quadrupole split spectrum is taken as the displacement of centroid from zero velocity. In Fig. 6 the isomer shift of the nitroprusside is different than that of the ferrocyanide due to the fact that the s electron density about the iron atom has changed when one of the ligands changed.

Another interaction, that of the nuclear magnetic moments and the external or intermolecular magnetic fields results in magnetic hyperfine splitting (MHS) of the spectra (a nuclear Zeeman effect). (Fig. 7) In the case of iron we may obtain a spectrum with six resonances. Identification of magnetically ordered structures and determination of Curie and Neel temperatures for many materials may be accomplished by studying their MHS spectra (3). The MHS of rare earth intermetallic compounds has been used to determine the magnetic properties and structure of these materials (25).

Double six line spectra may be obtained when the iron present in the absorber may be in either of two different environments (having different nearest neighbors) or two different crystal structures (tetrahedral and octohedral) where the internal magnetic field is different at each site. A composite of a six line and a one or two line spectrum may occur when two forms (magnetic and nonmagnetic) of a material such as Fe_2O_3 are present in the absorber.

The isomer shift for split spectra is recorded by taking the centroid of the spectrum and measuring its displacement from zero velocity.

Mössbauer spectra may not always be as uncomplicated as one of the three basic forms described. But combinations and perturbations of the basic forms can usually be separated into component factions (basic forms) with little difficulty, (especially with computer curve fitting programs) providing a wealth of information about the absorber sample. Generally it may be said that the area under the resonance peak is proportional to the amount of the element under investigation in a particular type of sample (22). Mössbauer Spectroscopy can provide quantitative information as well as qualitative information about the sample.

Examples of some of the information obtained using Mössbauer spectroscopy may be shown with a few typical spectra. We have seen the different isomer shifts of the tin (IV) halide compounds. In most iron compounds a quadrupole splitting is typical, as shown in Fig. 8 (a wide splitting for ferrous and a narrow splitting for ferric compounds).

Many different iron compounds have their isomer shifts and quadrupole splittings listed in a table compiled by Fluck et al. The accompanying diagram (Fig. 10) shows certain band locations on the velocity axis where isomer shift and quadrupole split values may be found. The influence of temperature on these values is generally linear from -120°C to +80°C (1). The influence of pressure varies according to the crystal structure (22).

Temperature dependence of the electric quadrupole splitting and isomer shift values can provide much information on chemical structure and bonding (26). For example, the sixth electron in excess of the half filled shell in ferrous compounds (d^6) causes a sharp temperature dependence on the quadrupole splitting. At the lower temperature the lowest molecular orbital is most populated and therefore we find the highest quadrupole splitting. As the temperature rises all molecular orbitals are populated equally and ΔE approaches zero. The d^5 configuration for iron has a much smaller temperature dependency. Brady, Duncan and Mok have reported the temperature dependence on a number of high and low spin iron compounds (27).

Pressure dependence of Mössbauer spectra may be much smaller than temperature dependence unless the material can be significantly compressed to alter the bond lengths or the environment of the absorbing nucleus. If all the bonds were symetric and changed equally with pressure the electron density would change resulting in an isomer shift. Quadrupole splittings may change with pressure if asymmetry is present in the absorber. Mössbauer Spectroscopy may thus detect small asymmetries which are not measurable by x-ray diffraction (28).

Other studies of isomer shifts have been made on iron compounds (13), iron organic compounds (14), tin compounds (2, 15, 16), and iodine compounds (17).

Studies on the bonding of clatherates (Kr) and rare gas compounds (3) have been made using Mössbauer Spectroscopy. Structural data on many compounds such as iron carbonyls, ferrates, dipyridyl iron complexes and SnF_4 (polymer-like structure) (1, 2) have also been studied using this new non-destructive method of analysis.

Wertheim and co-workers have correlated the isomer shift values of Fe-57 as a function of 3d and 4s electron charge density (13). Their diagram is shown in Fig. 9 and it provides a useful aide in determining electron charge density for compounds of interest.

Since most of the original work in the field of Mössbauer Spectroscopy has been with iron, many potential applications of this technique in the non-destructive testing of metals and alloys have already been discussed (5, 6). Mössbauer Spectroscopy may be used in quality control or for the study of alloy structure and its relation to the magnetic hyperfine fields of the alloy. Corrosion and certain surface defects on metals or gas absorption on metal surfaces (e.g. catalysts) may also be studied using this technique. Mineral assay methods are being developed since certain minority ingredient can usually be detected in a host matrix (2).

Many of the above studies require thick samples which prohibit transmission type experiments. Therefore a scattering technique is used. This requires that both the source and detector be on the same side of the absorber (shielded from one another). The re-emitted radiation (from the decaying resonantly excited absorber nucleus) is detected and instead of a decrease in counting rate at resonance we observe an increase in detection of the Mössbauer gamma ray, resulting in a Mössbauer spectrum just the inverse obtained in a transmission experiment.

Investigation of iron compounds has extended the use of Mössbauer Spectroscopy to the field of biology. Gonzer, Grant and Kregzde (10) have studied hemoglobin and some of their results are shown on Fig. 11. The different spectra result from different ligands bound to the central iron atom. A more extensive study of hemoglobin has recently been published by Lang, et al. Other work has been done with heme and hemin compounds (12) ferrodoxin (11) and iron porphyrins (8).

Iodine is another element that has recently allowed Mössbauer Spectroscopy to be used in the biological field.

Cryogenic techniques (to provide a stiff matrix) have been developed that allow the experimenter to study species stable or more easily available in solution. Some of these techniques and the general application of Mössbauer Spectroscopy in Biology were the subject of discussion at a 1965 symposium (9).

The study of other Mössbauer elements is discussed extensively in recent publications (18, 19, 22). A new index of all publications concerning Mössbauer investigations has recently been published (20). This Mössbauer Effect Data Index has the compilation of all the data obtained and lists the parameters by nuclide.

Although many applications have been found using Mössbauer Spectroscopy, the field is just blossoming. Most of the results must be interpreted on an empirical basis. Spectra must be compiled and instruments compared to a standard reference point in order that the values obtained by different investigators be correctly interpreted.

It is interesting to note that the National Bureau of Standards in the United States now offers a standard reference crystal of sodium nitroprusside which gives a sharply defined quadrupole split spectra. The distance between the peaks (in mm/sec.) provides an accurate calibration of the investigators velocity scale. Dr. J. J. Spijkerman of the NBS Laboratory has authored a recent review article on Mössbauer Spectroscopy which provides a compilation of publications for 1965, categorized by element with comments on the nature of each study, as well as an excellent list of references(22). Another excellent review was recently published by Greenwood in England (26).

It is obvious from the expanding number of publications that the Mössbauer Effect is becoming a more effective analytical technique. The fact that Mössbauer Spectroscopy has been accepted as a member of the spectroscopy family is also obvious from the availability of commercial Mössbauer Effect Spectrometers.

Commercial and homemade Mössbauer Spectrometers may be divided into two basic types, mechanical (usually constant velocity) and electro-mechanial (usually constant acceleration). The mechanical systems are many and include precision lathes, cam devices, pulley arrangements and piston type drives. All of these devices are limited to the relatively low velocities (usually less than 2 cm/sec.) but may be used to study most iron and tin systems. A precision lathe type of Mössbauer Spectrometer that is commercially available (Fig. 12) moves either the source or absorber at a given velocity (between 0.05 and 15 mm/sec.). This instrument employs a synchronous motor, and a ball-disc integrator transmission system to vary the velocity. An o-ring coupling moves the precision machined steel lead screw which in turn moves the source or absorber stage. When operating a constant velocity system, taking data for one velocity at a time, one must be very careful that the detection electronics do not drift or the resultant spectrum will be worthless.

An electromechanical transducer is the type of instrument used for a constant acceleration type of Mössbauer Spectrometer. A voltage signal (triangular, sawtooth or sinesoidal) is transformed into a velocity in the transducer. Thus the transducer may sweep through a spectrum of velocities (from the maximum in one direction through zero to a maximum in the other directions) during each cycle. A feedback system corrects for any deviation from the reference voltage signal.

When operating at constant velocity the data is accumulated in one or two scalers. A multichannel analyzer operating in the multiscaler mode is required when operating at constant acceleration. Each channel will represent a scaler for a given velocity. Therefore the motion of the transducer must be synthronized to the MCA while it is advancing through its channels. Synchronization is most frequently established by slaving the Mössbauer spectrometer to the MCA by deriving the reference velocity signal from the address register of the MCA.

The National Bureau of Standards system uses the analog signal from the address register to drive the transducer, with a maximum velocity of 20 cm/sec. (commercial units are available up to 60 cm/sec.) (Figs. 13A, B). A constant velocity mode of operation is also included in the NBS system.

The usual detection system used with a Mössbauer Spectrometer would include a detector, a high voltage supply pre-amplifier, a linear amplifier, single channel analyzer scaler and timer. A multichannel analyzer capable of operating in the multiscaler mode should be included if operating in the constant acceleration

mode. This mode of operation is favored because it averages any small electronic drift problems in the detection system. The type of detector chosen depends upon the gamma ray of interest. Gas filled proportional counters are generally used below 40 Kev.

Velocity spectra may be obtained directly from the MCA by using an x-y recorder. Digital data is obtained with a typewriter or paper readout system. This is necessary if you wish to perform a computer analysis of the data.

Cryogenic accessories to cool both source and absorber during Mössbauer experiments are sometimes necessary. Cooling is required in order to measure the Mössbauer effect in systems containing certain nuclides (ones with low Debye temperatures). Many commercially available dewars are designed to contain different cryogenic liquids including helium. Another system available provides cooling by the Joule-Thomson expansion of hydrogen gas. Control of gas pressure allows temperature variation from 16°K to 70°K to better than ± 0.5°K. In any cryogenic system one must be extremely careful that the unit does not introduce any vibration to the source or absorber or resonance absorption may be destroyed.

Mössbauer sources for many nuclides are also available commercially and may vary in composition. Some may be electroplated (Co-57 on copper, palladium or platinum) or just potted in plastic (Sn-119m as $BaSnO_3$). Absorbers are easily made by mounting the sample (foil or powder) between two sheets of 5 mil mylar with the help of double backed tape. Cryogenic mounts are usually metallic for better heat conduction properties.

Studies into the bonding of organo metallic compounds (especially organo-tin compounds) have been fairly numerous. Interpretation of isomer shift values and a compilation of different data has been summarized in two papers by Herber et al (29, 30). Fig. 14 shows how the Mössbauer parameters for a number of tin compounds may be grouped. Various organo-tin compounds fall in the crosshatched areas.

A recent investigation into the bonding of iron in coal using Mössbauer Spectroscopy was done by Lefelhocz and Kohman of Carnegie-Mellon University and Friedel of the Bureau of Mines in Pittsburgh (31). Various coal samples were run to study the organically bound iron in the coal. Their preliminary work confirms that the iron sulfide in coal consists mainly of pyrite and indicates that non-pyrite iron is in a high spin iron (II) state having octohedral coordination.

The Mössbauer spectra obtained by Lefelhocz et al. could not be compared directly to any other reported spectra. Some spectra with similar δ and Δ values has led them to believe that the iron may be bound to heterocyclic nitrogen aromatic groups in the coal macerals or possibly in a clay-like silicate mineral or gel.

Another area of usefulness for Mössbauer Spectroscopy is the investigation of catalysts and their functions. Very little has been published on this type of work. NSEC has recently been working with a number of companies in this area. Initial results have shown different Mössbauer patterns for new and used catalysts of iron oxides as well as complex iron compounds. Both magnetic and non-magnetic forms may sometimes be present in different ratios for the new and used catalysts. Hopefully future work will include investigation of these catalysts in working systems to see what influence adsorption (and perhaps reaction) may have on the Mössbauer Spectrum.

Some work has been done on adsorption studies using the Mössbauer effect. Flinn and co-workers studied iron on the surface of Al_2O_3 (32). An anisotropy of thermal vibration relative to the surface was observed. This resulted in unequal peaks in the quadrupole split spectrum. The large quadrupole split also indicated that the iron was present in a highly assymetric electrical field. The amplitude of vibration was greatest along the axis of the electric field gradient (normal to the surface) compared to that parallel to the surface.

Other adsorption studies have been made by Burton, Goodwin and Frauenfelder at the University of Illinois (33) and by Shpinel and co-workers in Russia (34) and others (35, 36, 37). Comparisons were made between atoms in the bulk of the matrix, in the surface of the matrix and on the surface of the matrix. Variations of the resultant spectra with temperature for each type sample were used to explain the surface dynamics of an atom. It is hoped that Mössbauer Spectroscopy will prove more useful in the study of the surface dynamics, chemical states and magnetic properties of adsorbed particles (including very thin films).

This explanation of Mössbauer Spectroscopy, description of equipment available and the examples of the applications that have been given are all too brief. Much new information concerning the elements we are able to study has been obtained using this very sensitive analytical technique. Some of this information can be obtained by no other method. Other information compliments what has been obtained using NMR, ESR and x-ray diffraction and other analytical techniques. Therefore, we can look forward to increased references to data obtained from Mössbauer spectra and further refinement of Mössbauer Spectroscopy.

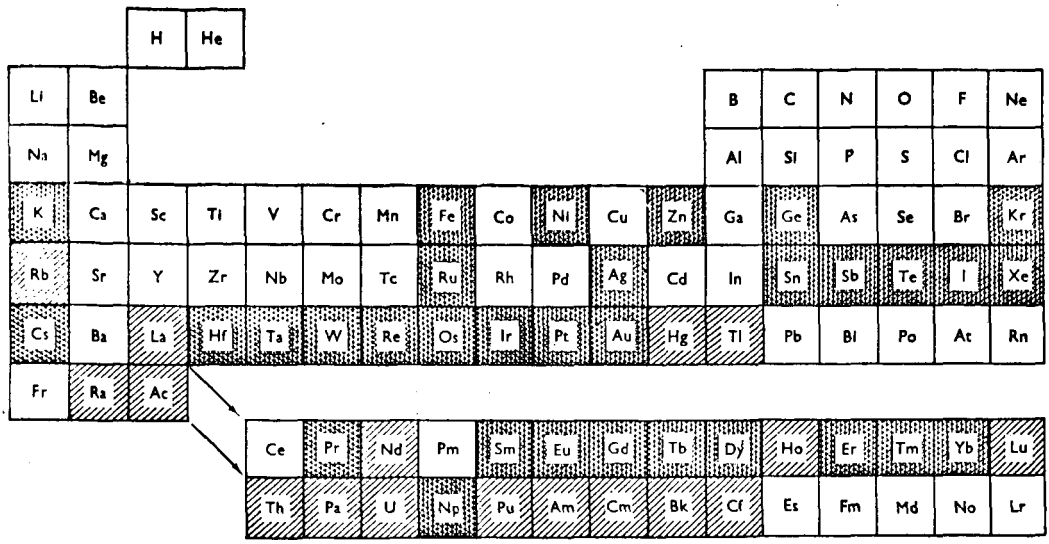

FIG. 1. Occurrence of the Mössbauer Effect (26)

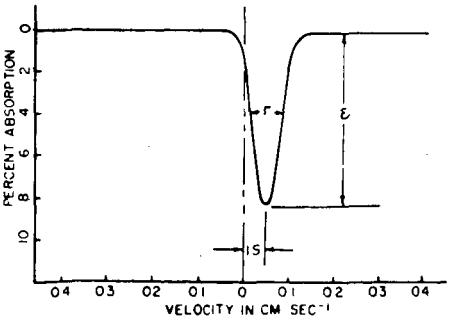

Fig. 2. Typical Mössbauer spectrum. (4)

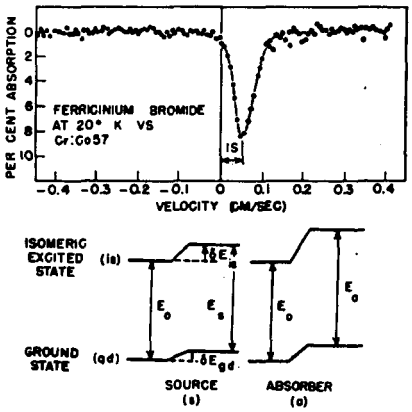

$$\delta = \frac{4\pi}{5} Ze R^2 \frac{\Delta R}{R} \left(|\psi_a|^2 - |\psi_s|^2 \right)$$

Fig. 3. Isomer shift. The effect of the electric monopole interaction is to shift nuclear levels without separating the magnetic sublevels. The shifts are very small as compared to the total energy of the gamma ray, 10^{-12} E_γ. (7)

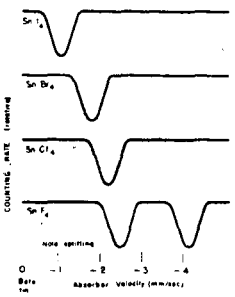

Fig. 4. Mössbauer spectra can contain more than one line, if energy levels are split by interaction that depends on nuclear orientation. In this case SnF_4 spectrum is doublet because Sn^{119} electric moment interacts with inhomogeneous field of surrounding F atoms.(2)

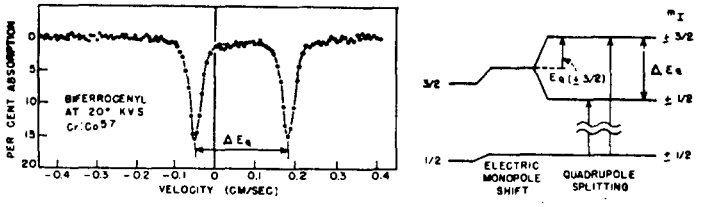

$$\Delta E_q = \frac{eqQ}{2}$$

Fig. 5. Quadrupole splitting. The interaction of the nuclear quadrupole moment, Q, with the gradient of the electric field, eq, is illustrated for nuclear ground-state spin $I_{gd} = 1/2$ and for isomeric-state spin $I_{is} = 3/2$; the diagrams are applicable to Fe^{57}, Sn^{119}, and Tm^{169}, among other isotopes. For the ground state, or any state with $I = 1/2$, Q is inherently zero. An example of a pure quadrupole Mössbauer absorption spectrum is shown. (7)

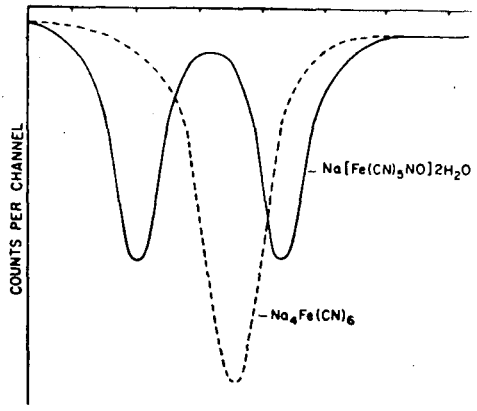

Fig. 6. Mössbauer spectra of an octahedrally symmetric complex $[Na_4FeCCN)_6]$ and of a distorted octahedral complex $[Na_2[Fe(CN)_5NO]\cdot 2H_2O]$, showing the effect of a non-vanishing electric field gradient at the Mössbauer lattice point. (4)

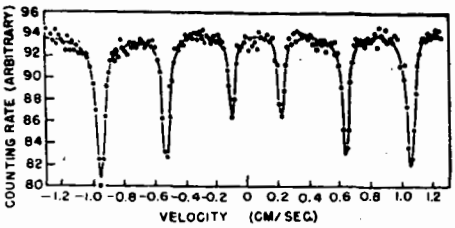

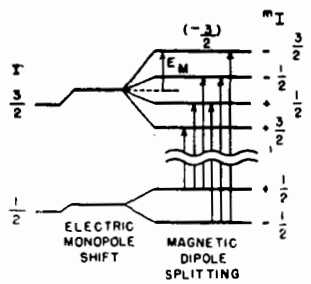

$$\Delta E_M = \frac{\mu H}{I}$$

Fig. 7. Magnetic hyperfine splitting for $I_{gd} = 1/2$, $I_{is} = 3/2$. As a result of the selection rule, $\Delta m = 0, \pm 1$, only six of the possible eight lines are observed. The graph shows the Fe^{57} hyperfine splitting of FeF_3, which corresponds to a field of 620,000 oersteds. (7)

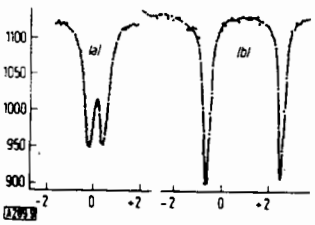

Fig. 8. Mössbauer spectra (a) of $FePO_4 \cdot 4\,H_2O$ and (b) of $FeSO_4 \cdot 7\,H_2O$ (1)
Ordinate: transmission [arbitrary units]
Abscissa: velocity of the source relative to the absorber [mm/sec]

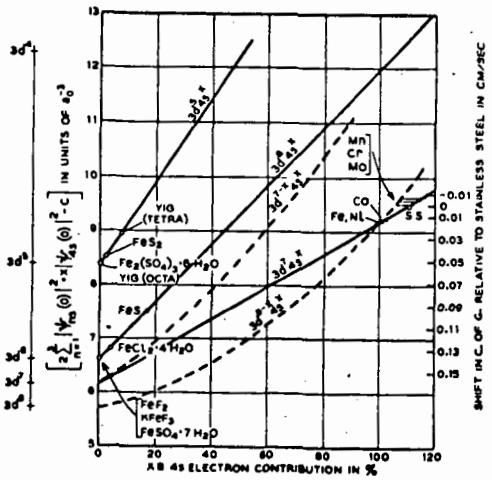

Fig. 9. A possible interpretation of the Fe^{57} Mössbauer isomer shifts in various solids. The total s-electron density is plotted as a function of the percentage of $4s$ character for various d-electron configurations. The reasons for placing the experimental data on given theoretical curves are discussed in the text. The constant $C = 11\,873\ a_0^{-3}$. (13)

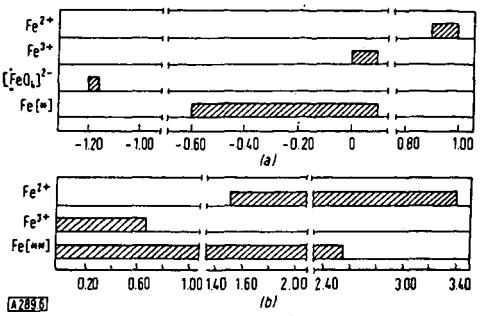

Fig. 10. (a) Values for the isomeric shifts and (b) values for the quadrupole splittings of Mössbauer lines in ferrous and ferric compounds. (1)
Radiation source: ^{57}Co in platinum at 25 °C.
Abscissa: Velocity of the source relative to the absorber [mm/sec].
Fe [*] = iron in complexes and metals.
Fe [**] = iron in complexes.

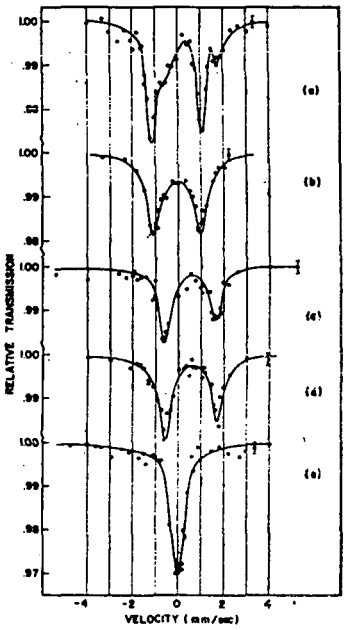

Fig. 11. Mössbauer absorption spectra with a source of Co^{III} diffused into Pt and kept at room temperature and absorbers of (*a*) rat red cells at 4°K and isotopically enriched with Fe^{III}, (*b*) crystalline rat oxyhemoglobin at 77°K, (*c*) human CO_2-hemoglobin (in a CO_2 atmosphere) at 77°K, (*d*) human hemoglobin (in a N_2 atmosphere) at 77°K, and (*e*) human CO-hemoglobin (in a CO atmosphere) at 77°K. We have used the standard notation that source approaching absorber is positive velocity. (10)

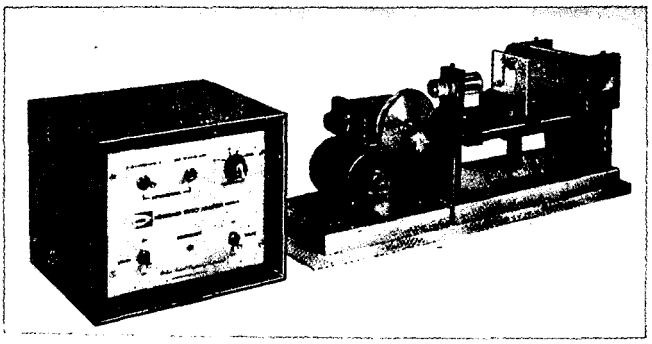

Fig. 12. A Constant Velocity Mössbauer Effect Analyzer

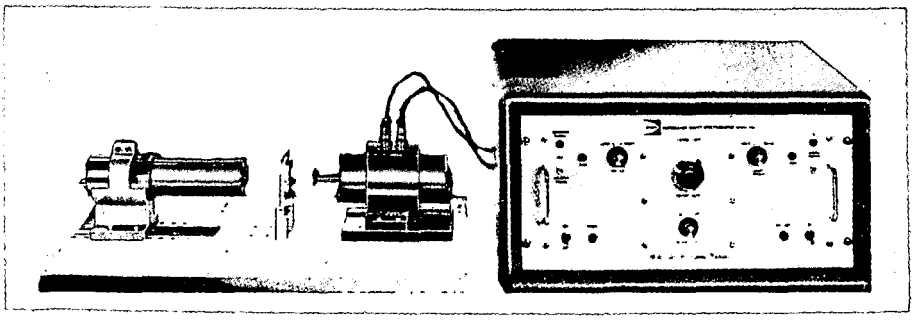

Fig. 13. A Constant Acceleration Mössbauer Effect Spectrometer

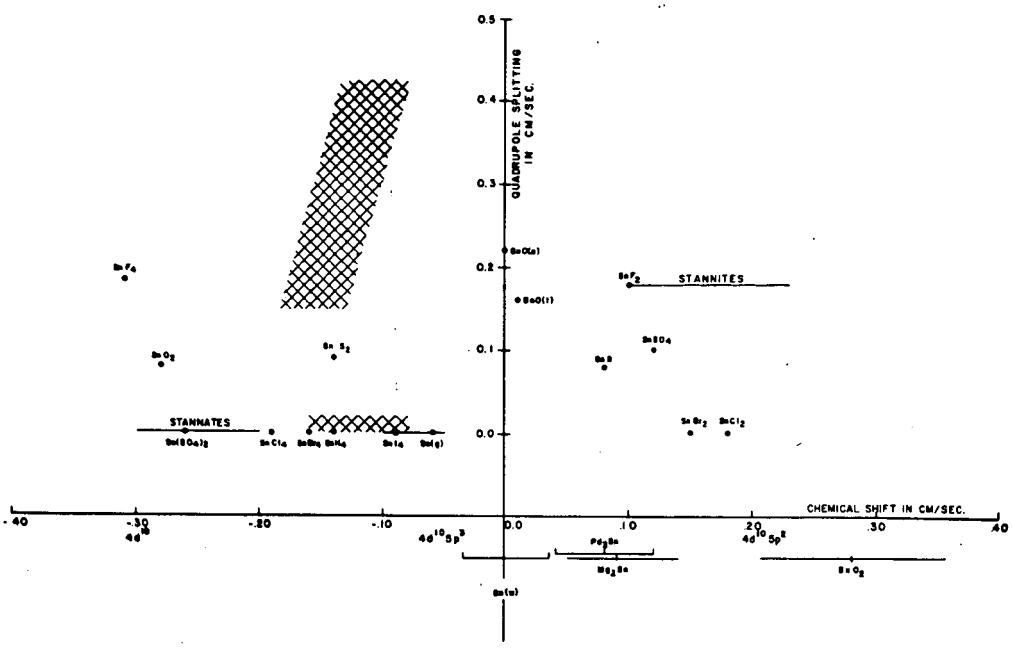

Fig. 14. Correlation diagram of the quadrupole splitting and chemical shift values for Tin Compounds at 78°K (38)

References

1. Fluck, E., Kerler, W., Neuwirth, W., Angew. Chem. 75, 461 (1963).
2. Goldanskii, V.I., Intern. Science & Tech., December (1963).
3. Wertheim, G.K., "Mössbauer Effect, Principles and Applications", Academic Press, New York, 1964.
4. Herber, R.H., J. Chem. Ed. 42, 180 (1965).
5. Johnson, C.E., Ridout, M.S., Cranshaw, T.E., Madsen, P.E., Phys. Rev. Letters 6, 450 (1961).
6. Wertheim, G.K., Phys. Rev. Letters, 12, 24 (1964).
7. Wertheim, G.K., Science 144, 253 (1964).
8. Maling, J.E., Neissbluth, M., "Mössbauer Resonance Studies in Iron Porphyrins and Heme-proteins", in Electronic Aspects of Biochemistry, B. Pullman, Ed., Academic Press (1964).
9. Kettering Foundation Symposium, March 1965, A. San Pietro, Ed., Antioch Press (1965).
10. Gonser, U., Grant, R.W., Kregzde, J., Science 143 (1964).
11. Pillinger, W.L., Stone, J.A., AEC Report DP878 (1964).
12. Bearden, A.J., Moss, T.H., Caughey, W.S., Beaudreau, C.A., Proc, Nat. Acad. Sci. 53, 1246 (1965).
13. Walker, L.R., Wertheim, G.K., Jaccarino, V., Phys. Rev. Letters 6, 98 (1961).
14. Herber, R.H., King, R.B., Wertheim, G.K., Inorg. Chem. 3, 101 (1963).
15. Bryukhanov, V.A. et al, Soviet Phys. JETP (English Translation), 16, 321 (1963); see also ibid 16, 310 (1963); 16, 879 (1963).
16. Cordey-Hayes, M., J. Inorg. and Nuclear Chem. 26, 915 (1964).
17. DeWaard, H., DePasquali, G., Hafemeister, D., Phys. Letters 5, 217 (1963); Rev. Mod. Phys. 36, 358C (1964).
18. Fluck, E., "The Mössbauer Effect and Its Application in Chemistry" in Advances in Inorganic Chemistry and Radiochemistry - Vol. 6, Emeleus, H.J. Sharpe, A.G., eds., Academic Press, New York (1964).
19. Proceedings of the 3rd International Conference on the Mössbauer Effect, Rev. Mod. Physics 36, #1 Part II (Jan. 1964).
20. Muir, A.H. et al, "Mössbauer Effect Data Index", 1958-1965 Interscience - John Wiley and Sons, New York City (1967).
21. Lang, G., Marshall, W., Proc. Phys. Soc. 87, 3 (1966).
22. DeVoe, J.R., Spijkerman, J.J., Anal. Chem. - Annual Reviews 38, 382R (1966).
23. Mossbauer, R.L., Ann. Rev. Nuclear Sci. 12, 123 (1962).
24. Frauenfelder, H., "The Mössbauer Effect", W. A. Benjamin Inc., New York (1962).
25. Nowik, I., Bell Telephone Laboratories, Murray Hill, New Jersey (to be published).
26. Greenwood, N.N., Chemistry in Britain 3, No. 2 56-72 (1967).
27. Brady, P.R., Duncan, J.F., Mok, K.F., Proc. Royal Soc. (London) 287A, 343-62, (1965).
28. Christ, B.W., Spijkerman, J.J., Giles, P.M., Ruegg, F.C., Trans. Met. Soc. of AIME (Tech. Letter to be published).
29. Herber, R.H., Stoeckler, H.A., Reichle, W.T., J. Chem. Phys. 42, 2447 (1965).
30. Herber, R.H., Nuclear Sci. Abstr. 19 No. 8 13518 (1965).
31. Lefelhocz, J.F., Friedel, R.A., Kohman, T.P., (Submitted to Geochimica et Cosmochimica Alta April 1967).
32. Minn, P.A., Ruby, S.L., Kehl, W.L., Science 143, 1434 (1964).

33. Burton, J.W., Frauenfelder, H., Goodwin, R.P., Nuclear Sci. Abstracts No. 20 40078 (1965).
34. Karasev, A.N., Polak, L.S., Shlikhter, E.B., Shpinel, V.S., Kinetika i Kataliz 6 710 (1965).
35. Kundig, W. et al, Phys. Rev. 142 327 (1966).
36. Suzdalen, I.P. et al, J.E.T.P. 22, 979 (1966).
37. Hobson, M.C., Nature 214 79 (1967).
38. Spijkerman, J.J., Symposium on "The Mössbauer Effect and Its Application in Chemistry" to be published in the Advances in Chemistry Series (1967) by A.C.S.

GASIFICATION OF CAKING COAL IN A FREE-FALL, FLUID-BED REACTOR

A. J. Forney, R. F. Kenny, and J. H. Field

Pittsburgh Coal Research Center, U. S. Bureau of Mines,
4800 Forbes Avenue, Pittsburgh, Pennsylvania 15213

INTRODUCTION

The Bureau of Mines is investigating the gasification of caking coals in a fluid-bed reactor as part of the Bureau's overall program of converting coal to liquid or gaseous fuels. The caking coals, common to the East and Midwest, cannot be gasified without being pretreated, usually with steam and oxygen. The method of gasification discussed in this report is free-fall pretreatment combined with fluid-bed gasification.

The primary objectives of the project are: 1) To check our earlier method of pretreating caking coals before gasification;[2, 3] 2) to determine the minimum amount of oxygen needed for pretreatment; 3) to maximize the methane content in the product gas. A secondary aim, which developed from the above tests, is to study a method of substituting air for oxygen.

EXPERIMENTAL PROCEDURE

The pretreatment is achieved by dropping Pittsburgh-seam coal (70 percent through 200 mesh) through a free-fall reactor 6 inches in diameter and 10 feet high (later reduced to 7 feet). This pretreater is located above a fluid-bed reactor 3 inches in diameter and 3 feet high (later increased to 6 feet). The oxygen and steam for the gasification enter the bottom of the reactor, figures 1 and 2. The gases from the gasifier flow up through the free-fall section to pretreat and carbonize the coal as it falls. They are enriched with an oxygen-steam feed entering the side of the free-fall section to further pretreat the coal because the gases rising from the gasifier did not pretreat sufficiently to prevent agglomeration.

Pressures from 2.5 to 20 atmospheres, temperatures of 835° to 955° C, and oxygen-coal ratios from 0 to 5.9 were used.

RESULTS AND DISCUSSION

Pressure Effects

The pressure was gradually increased from 2-1/2 to 20 atmospheres as shown in table 1 and figure 3. The methane content gradually increased to 14 volume percent of the product gas. This means that more methane can be produced in this gasification than would be produced in subsequent methanation to produce high-Btu gas. For example, in experiment N-12 the 50 percent H_2+CO would yield less methane during methanation than the 14 percent methane already produced in gasification. As the pressure was increased from 2-1/2 to 20 atmospheres,

figure 3, the percentage of methane in the product gas increased from 8 to 12, while the hydrogen and carbon monoxide percentages decreased. Also the carbon dioxide increased while the hydrogen and carbon monoxide decreased at the same rate, verifying Schuster's[8] claim that the methane-making reaction in gasification is $2H_2 + 2CO \rightarrow CH_4 + CO_2$. These curves, figure 3, based on average values from several experiments are similar to those of O'Dell.[4]

Table 1.- Effect of Pressure on Methane Yield

Test No.[1]	F-19	F-33	F-46	N-10	N-12	N-13	N-17
Pressure, atm	2.5	5	10	15	20	20	20
Coal[2]	D-2	D-4	D-4	D-4	D-4	D-4	D-4
Coal feed, lb/hr	0.43	0.70	1.53	1.60	1.60	1.63	3.40
Input, SCFH:							
Gasifier, steam	18	25	50	60	60	60	100
Gasifier, oxygen	1	1.5	4	4	4	4	16
Pretreater, steam	10	10	20	30	30	20	20
Pretreater, oxygen	1	1.5	3	4	4	4	4
Nitrogen	4	4	8	6	6	5	5
Temperature, °C:							
Pretreater	375	409	390	375	400	400	400
Gasifier, avg	893	891	893	880	882	876	883
Gasifier, max	900	900	900	900	900	900	900
O_2/coal, SCF/lb	4.6	4.3	4.6	5.0	5.0	4.9	5.9
Steam/coal, SCF/lb	42	36	33	37	37	37	29
Carbon conversion, pct	67	68	60	66	65	73	68
Steam conversion, pct	12	10	15	17	14	23	--
Product gas,[3] SCF/lb	19	19	16	17	15	18	16
Methane, SCF/lb	2.1	1.8	2.5	2.7	3.3	3.7	3.4
Product gas, pct:							
H_2	44	41	39	39	34	36	35
CH_4	8	7	11	11	14	14	14
CO	21	25	22	20	16	18	18
CO_2	27	27	28	30	36	32	33
Tar, pct of coal feed	10	6	3	3	4	3	5

1/ F series with 3-foot reactor; N series with 6-foot reactor.
2/ D-2: H 5.1, C 72.9, N 1.4, O 8.2, S 1.3, Ash 11.1 percent.
D-4: H 5.1, C 76.5, N 1.5, O 8.1, S 1.0, Ash 8.0, VM 34.8 percent; FSI = 7-1/2.
3/ $H_2+CO+CH_4$.

Tar Plus Oil

As the pressure increased the tar yield decreased from 10 to about 5 percent. The tars were analyzed by chromatography to find the effect of pressure on the composition of the tar. Results were inconclusive; no correlation could be made.

The coal feed rate was increased from 1.54 pounds per hour (33 lb/hr ft^2) to 6.1 pounds per hour (133 lb/hr ft^2) at 20 atmospheres pressure (table 2). The carbon conversion was lower at the higher coal rate. The methane yield was almost steady at 3 SCF/lb, although its percentage in the product gas increased from 12 to 15 percent.

Table 2.- Effect of Increased Coal Feed on Product Distribution at 20 Atmospheres Pressure

Test No.	N-11	N-15	N-17	N-19	N-21	N-24	N-22	Lurgi[1]
Coal[2]	D-4	D-4	D-4	D-5	D-5	D-5	D-5	
Feed, lb/hr	1.54	2.25	3.40	5.40	5.82	6.1	5.2	
Coal feed, lb/hr ft^2	33	49	74	120	127	133	113	
Coal feed, lb/hr ft^3	6	8	12	20	21	22	18	
Input, SCFH:								
Gasifier, steam	60	65	100	150	180	180	198	
Gasifier, oxygen	4	6	16	24	22	18	6	
Pretreater, steam	30	15	20	24	36	36	36	
Pretreater, oxygen	4	3	4	6	6	6	6	
Nitrogen	6	6	5	5	5	5	5	
Temperature, °C:								
Pretreater	375	400	400	400	400	400	400	
Gasifier, avg	889	885	883	907	864	890	889	
Gasifier, max	900	898	900	959	890	910	900	
O_2/coal, SCF/lb	5.2	4.0	5.9	5.6	4.8	4.0	2.3	4
Steam/coal, SCF/lb	39	29	29	28	31	30	38	19
Carbon conversion, pct	73	68	68	75	59	55	52	90[3]
Steam conversion, pct	14	28	21	29	12	12	15	
Product gas,[4] SCF/lb	19	19	16	16	13	12	15	19
Methane, SCF/lb	3.2	3.3	3.4	3.2	3.0	2.7	3.2	2.6
Product gas, pct:								
H_2	38	39	35	33	33	34	40	40
CH_4	12	13	14	13	15	15	17	10
CO	21	23	18	19	16	18	18	25
CO_2	29	25	33	35	36	33	25	25
Tar, pct of feed	4	4	5	9	4	3	3	

1/ Westfield plant coal: Moist. = 15.6, ash = 14.6, VM = 28.7, FC = 41.1 pct.
2/ D-4: H 5.1, C 76.5, N 1.4, O 8.1, S 1.0, Ash 8.0, VM 34.8 pct; FSI = 7-1/2.
D-5: H 5.0, C 74.9, N 1.5, O 7.6, S 1.1, Ash 9.9, VM 34.7 pct; FSI = 8-1/2.
3/ Estimated.
4/ H_2+CO+CH_4.

The results of N-23 (table 3) and N-19 (table 2) may be compared with those of the Westfield[7] Lurgi. Our methane percentage is higher, and our methane yield slightly higher. We used more oxygen and more steam and had a lower carbon conversion; however, the Lurgi could not be operated with the caking coal used in our tests.

Effect of Low Oxygen Feed

In test N-22 the oxygen feed to the gasifier was reduced from the 4 to 5 cubic feet per pound used in the other tests to 1 cubic foot per pound. Comparing test N-22 with N-19 shows that the carbon conversion decreased, the methane yield remained the same, but the percentage of methane in the product gas increased from 13 to 17 percent (table 2). This increase is desirable, but a commercial gasifier would have to be heated externally to operate with such a low oxygen feed.

Table 3.- Effect of Temperature on Product Distribution at 20 Atmospheres Pressure

Test No.	N-26	N-25	N-24	N-27	N-23	N-28	N-30
Coal[1]	D-6	D-6	D-5	D-6	D-6	D-6	D-6
Coal feed, lb/hr ft^2	123	136	133	140	133	140	136
Feed, lb/hr	5.65	6.25	6.1	6.5	6.0	6.4	6.3
Input, SCFH:							
Gasifier, steam	180	180	180	180	180	180	120
Gasifier, oxygen	18	18	18	18	24	18	18
Pretreater, steam	36	36	36	36	36	36	36
Pretreater, oxygen	6	6	6	6	6	6	6
Nitrogen	5	5	5	5	5	5	5
Temperature, °C:							
Pretreater	400	400	400	400	400	400	400
Gasifier, avg	835	860	890	880	900	901	912
Gasifier, max	857	880	910	910	955	934	963
Oxygen/coal, SCF/lb	4.3	3.8	4.0	3.7	5.0	3.8	3.8
Steam/coal, SCF/lb	32	29	30	28	30	28	19
Carbon conversion, pct	51	58	55	59	81	65	56
Steam conversion, pct	4	--	12	--	24	--	--
Product gas,[2] SCF/lb	11	14	12	14	19	16	13
Methane, SCF/lb	2.5	2.9	2.7	3.5	3.6	3.2	2.9
Product gas, pct:							
H_2	31	36	34	34	36	36	33
CH_4	15	14	15	17	13	14	16
CO	20	17	18	17	20	20	18
CO_2	34	33	33	32	31	30	33
Tar, pct of feed	7	8	3	4	3	5	4

1/ D-5: H 5.0, C 74,9, N 1.5, O 7.6, S 1.1, Ash 9.9, VM 34.7 pct: FSI = 8-1/2.
D-6: H 5.1, C 74.4, N 1.5, O 8.2, S 1.1, Ash 9.7, VM 36.1 pct; FSI = 8.
2/ H_2+CO+CH_4.

Effect of Temperature

For two reasons the temperature was not varied widely in these tests. The safe limit for the reactor at 20 atmospheres is 950° C and carbon conversion decreased markedly below 850° C. The yield of product gas increased from about 11 SCF of H_2+CO+CH_4 per pound of coal at 860° C to 19 at 950° C (table 3). The methane percentage decreased but not drastically. However, the yield of methane per pound coal feed did increase from 2.5 to 3.6 SCF per pound. In test N-30 the steam rate was reduced from 30 SCF per pound of coal to 19; the temperature increased in the gasifier but the carbon conversion dropped. Some sintering of the ash occurred at the base of the reactor, indicating that the flow of steam was too low. The optimum temperature seems to be about 900°-950° C. Further tests may be necessary to determine the maximum temperature because the methane yield may decrease so much at higher temperatures that the advantage of our method of operation may be lost.

Oxygen Needed for Pretreatment

Changing the port of entry for the pretreating steam and oxygen from the middle of the free-fall section, as shown in figure 1, to the top of the free-fall section reduced the amount of oxygen necessary for pretreatment. When the pretreating gases were fed at the top they entered through a tube surrounding the coal feed inlet port. Thus the coal was entrained by the treating gases for about 2 feet before it fell 5 feet into the fluid bed. In tables 1 and 2 the results of both systems represented by tests N-12 and N-24 are compared. The amount of oxygen needed for pretreatment was decreased from 2.5 SCF per pound (N-12) to less than 1 SCF per pound (N-24). When the pretreating steam and oxygen were fed at the middle of the free-fall section, some oxygen was used in gasification because of the high temperature in this zone. When they were fed at the top of the reactor, oxygen was used only for pretreatment.

Studies in Glass Equipment of a System Using Air Instead of Oxygen

Oxygen accounts for about 10 to 14 cents per MCF of the cost of making high-Btu gas. Many different systems have been tried both in England and America in the hope of substituting air for oxygen.[1,5,6] Our approach is to feed air and steam through separate entry ports to a single fluid bed so the products of combustion can be separated from the products of steam gasification. Two designs to achieve this are shown in figures 4 and 5, and glass models based on these designs have been made. The model similar to figure 4 is constructed with a straight baffle in a 6-inch-diameter glass tube; with an L/D ratio of 2 (12-inch height/6-inch diameter), the mixing of the air and inert gas streams is only 5 to 10 percent if the baffle extends 1 to 2 inches into the bed. When the baffle is raised above the bed, the mixing is 30 to 40 percent. When the ratio is 3, the mixing is about 25 percent. The second model similar to figure 5 was constructed with a 4-inch-diameter tube inserted into a 6-inch-diameter tube. The areas of the annulus and the inner tube are about the same. This model shows more mixing of the gases than the first--21 percent when the center tube is embedded 2 inches into a 6-inch layer of coal.

After a satisfactory model has been designed for gas flow, we will use a 6-inch-diameter steel reactor to study the mixing of the solids to determine if uniform temperatures in the bed can be obtained.

CONCLUSIONS

Caking coals can be gasified in a combined free-fall, fluid-bed gasifier. The methane in the product gas is about 14 to 15 percent, which means more methane is being produced in the gasification than would be produced in the subsequent methanation. The oxygen needed for pretreatment is about 1 cubic foot per pound coal feed.

A conceptual process being investigated substitutes air for oxygen during gasification.

BIBLIOGRAPHY

1. Curran, G. P., C. H. Rice, and E. Gorin. Carbon Dioxide Acceptor Gasification Process. Division of Fuel Chemistry, A.C.S., Philadelphia, Pa., April 5-10, 1964.

2. Forney, A. J., R. F. Kenny, S. J. Gasior, and J. H. Field. Fluid-Bed Gasification of Pretreated Pittsburgh-Seam Coal. Division of Fuel Chemistry, A.C.S., New York, N. Y., Sept. 1966.

3. Forney, A. J., R. F. Kenny, S. J. Gasior, and J. H. Field. Decaking of Coals in a Fluid Bed. BuMines Rept. of Inv. 6797, 1966, 22 pp.

4. O'Dell, W. W. Gasification of Solid Fuels in Germany by the Lurgi, Winkler and Leuna Slagging Type Gas Producer Processes. BuMines Inf. Circ. 7415, 1946, 46 pp.

5. Pieroni, L. J., G. T. Skaperdas, and W. H. Heffner. Development of the Kellogg Coal Gasification Process. A.I.Ch.E. Symposium on Processing of Coal and its Byproducts, Philadelphia, Pa., Dec. 5-9, 1965.

6. Raynor, J. W. R. Gasification by the Moving Burden Technique. Gasification and Liquefaction of Coal Symposium, A.I.M.E., New York, N. Y., Feb. 20-21, 1952.

7. Ricketts, T. S. The Operation of the Westfield Lurgi Plant and the High Pressure Grid System. The Institution of Gas Engineers 100th Annual General Meeting, May 1963, London, England.

8. Schuster, Fritz. The Chemical Reaction of Methane Formation in Oxygen Pressure Gasification. Das Gas und Wasserfach 104 (49), 1963, pp. 1418-1419.

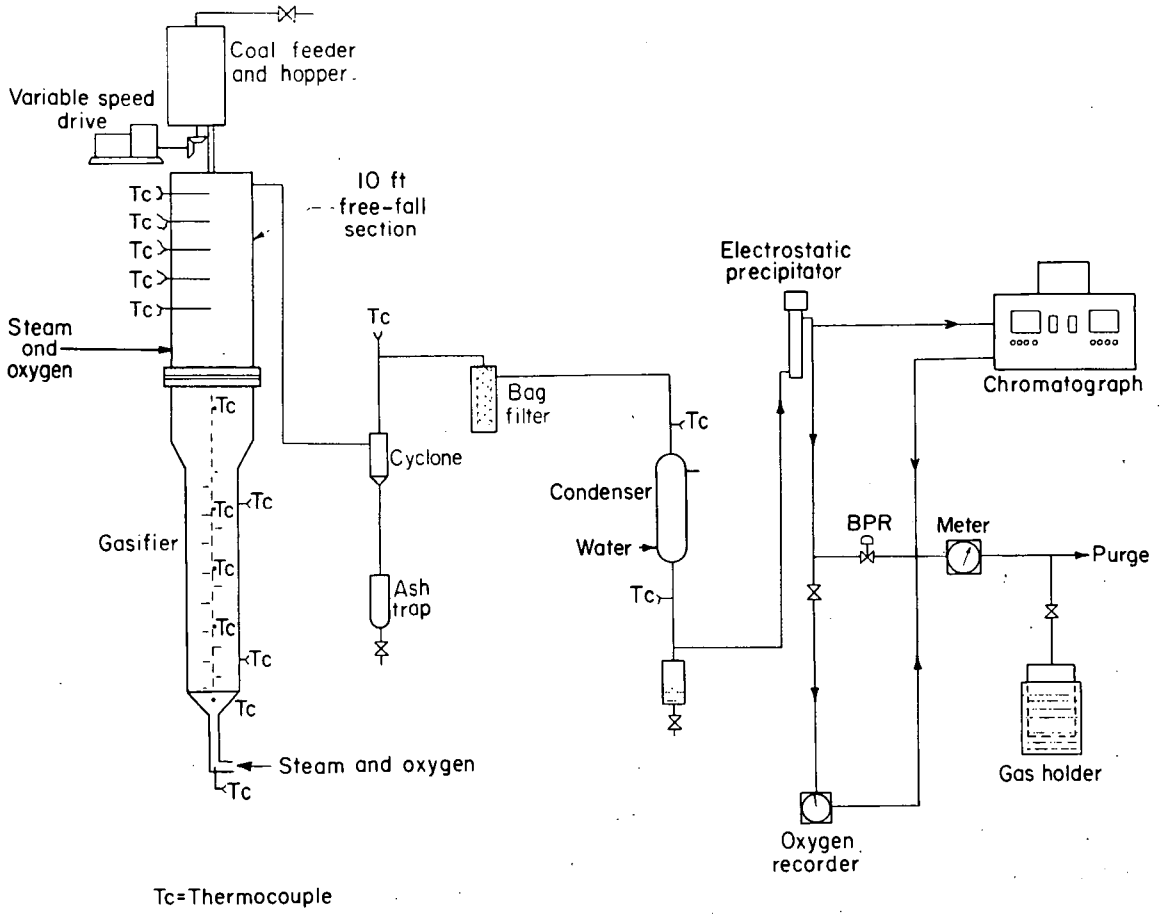

Figure 1. Flowsheet of Gasification Equipment.

9-1-65 L-9024

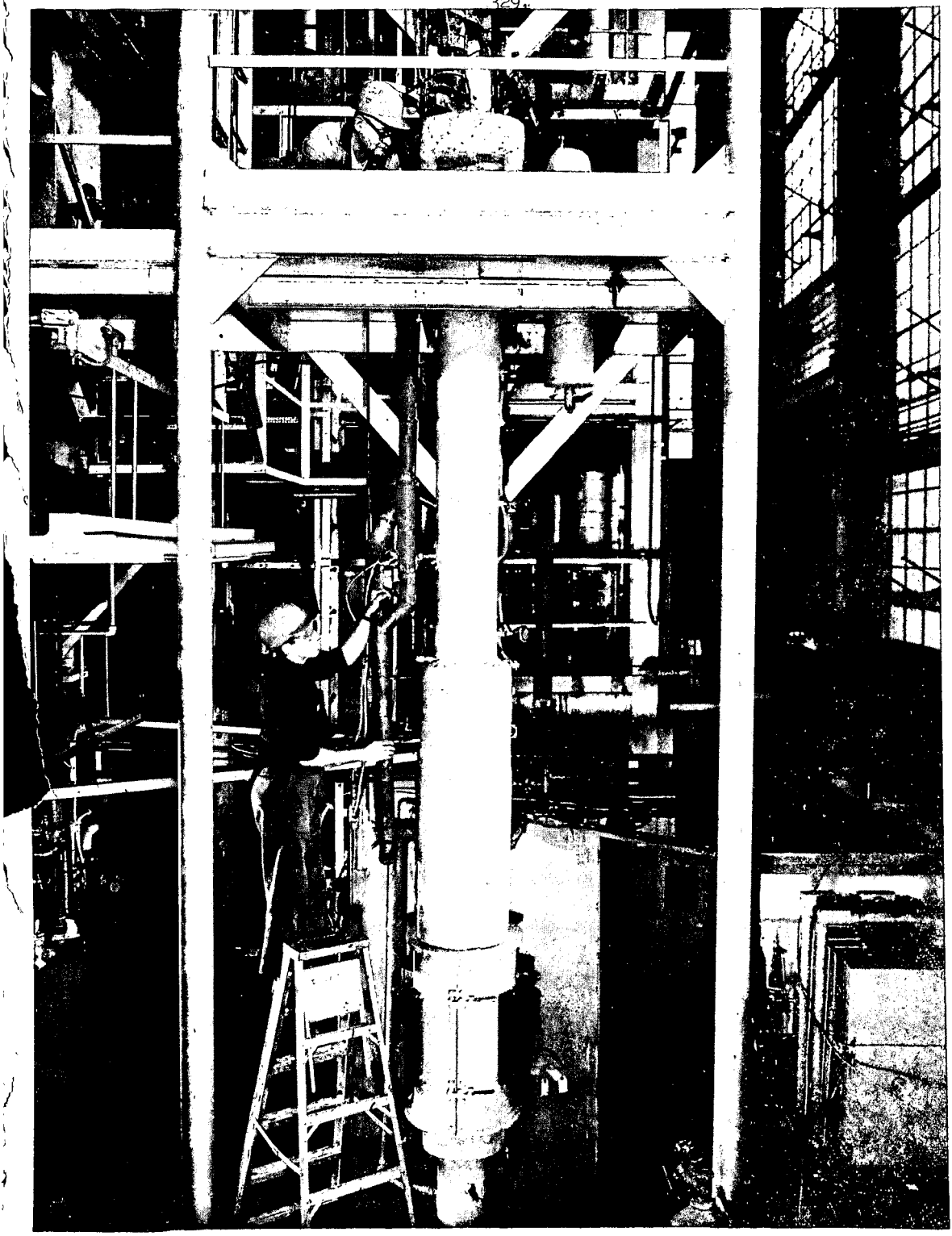

Figure 2. Gasification Equipment.

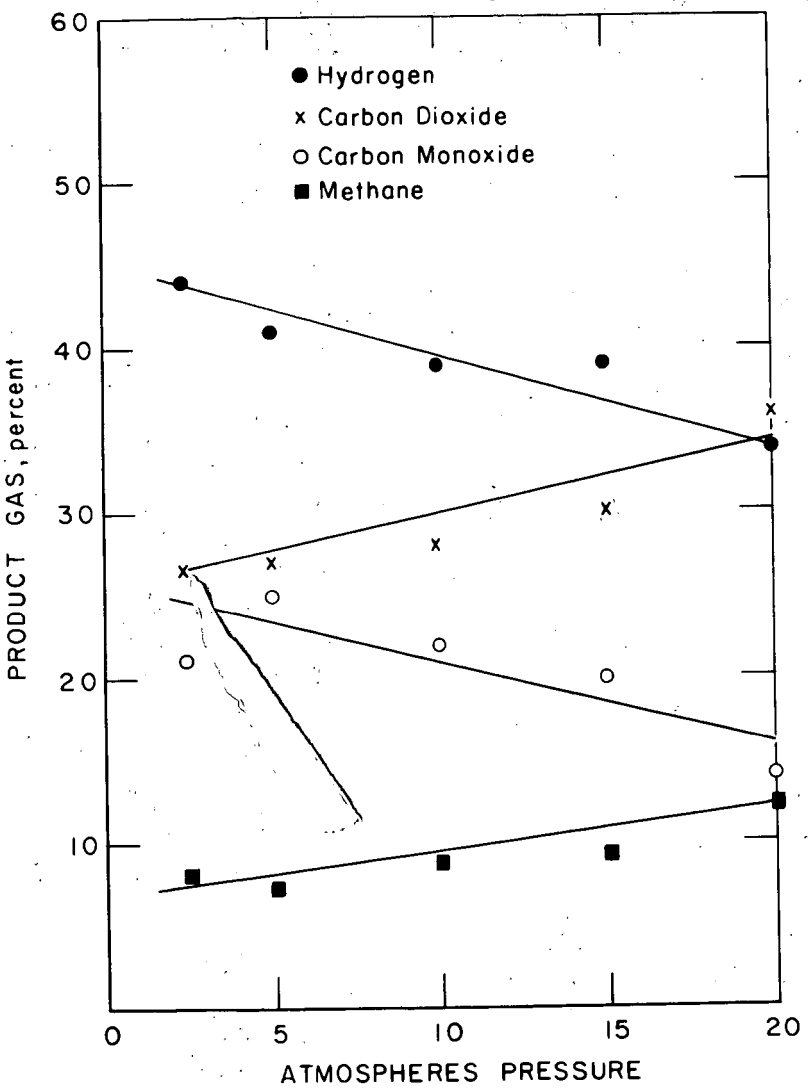

Figure 3.- Effect of pressure on the product gas.

4-13-67 L-9907

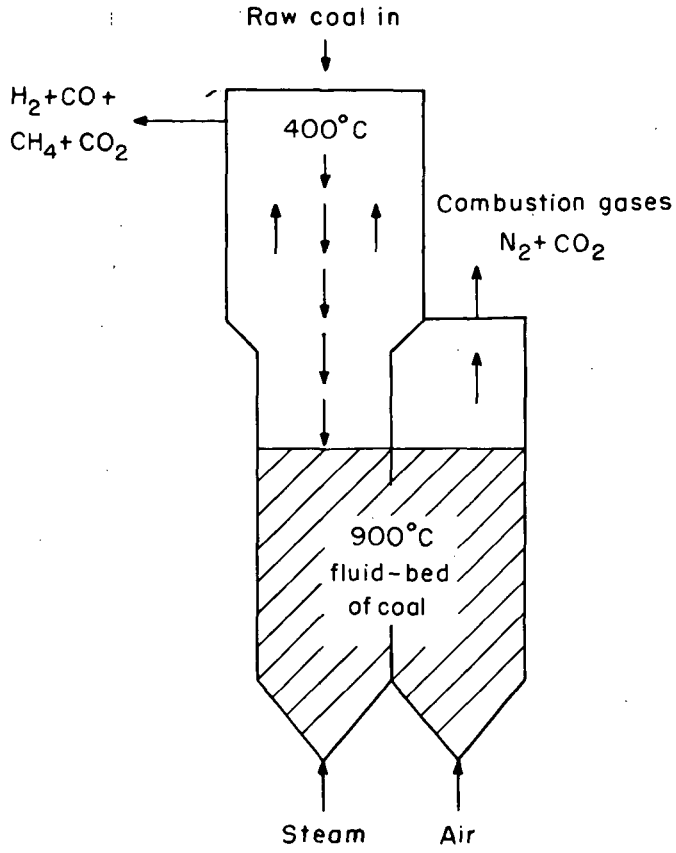

Figure 4 - Steam-coal, air-coal reaction in single fluid-bed gasifier

L-9749

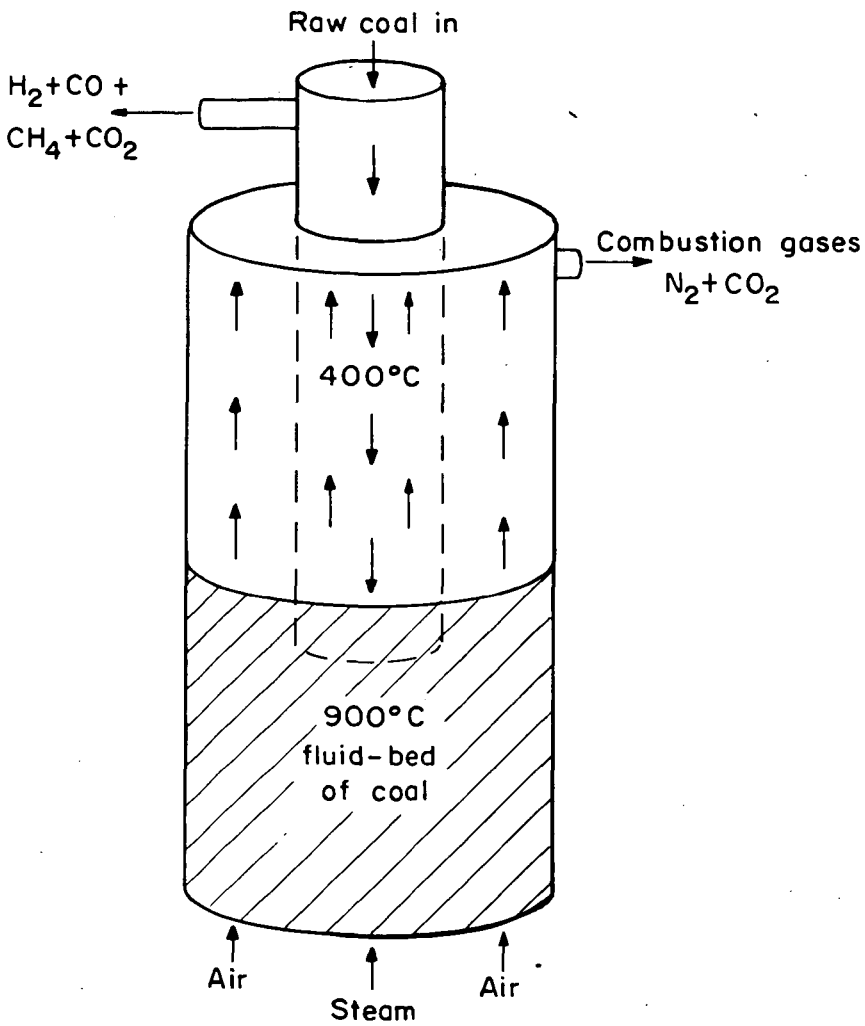

Figure 5. — Steam-coal, air-coal reaction in single fluid-bed gasifer.

4-5-67 L-9889

COMPUTER STUDY OF STAGE 2 REACTIONS IN THE BCR TWO-STAGE SUPER-PRESSURE COAL GASIFICATION PROCESS

E. E. Donath and R. A. Glenn

Bituminous Coal Research, Inc., Monroeville, Pennsylvania

INTRODUCTION

In the BCR two-stage gasification process, recycle char is used in Stage 1 to produce hot synthesis gas by reaction with oxygen and steam. The hot products from Stage 1 heat the fresh coal and steam entering Stage 2 and react with them to produce methane and additional synthesis gas.(1,2)* A schematic flow diagram of the process is given as Figure 1.

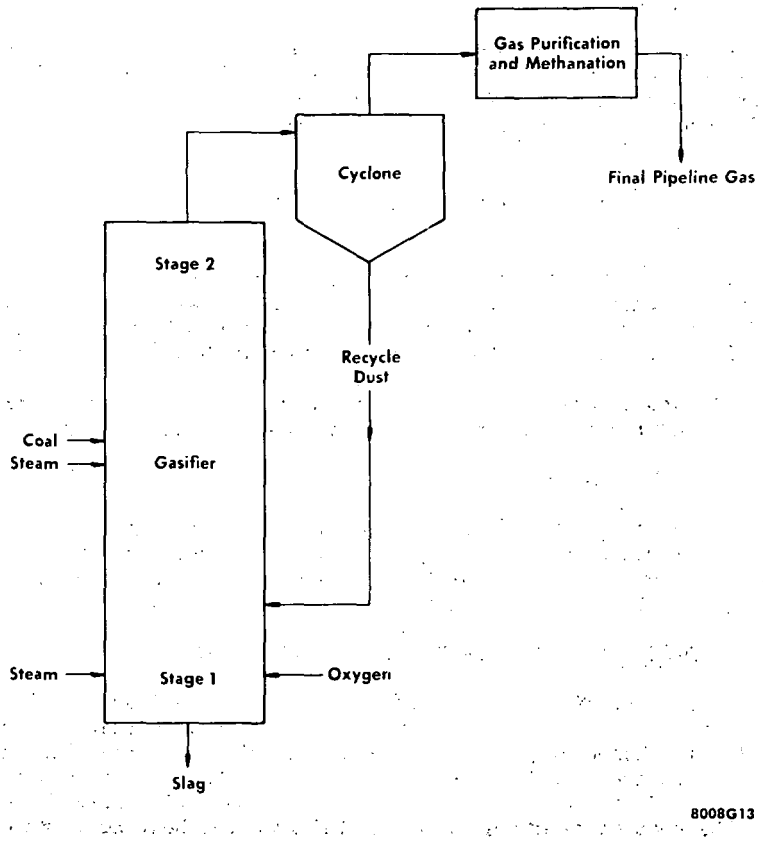

Figure 1. Simplified Flow Diagram for Two-stage Super-pressure Gasifier

* Numbers in parenthesis refer to list of References at end of paper.

For the past two years, laboratory research has been under way to establish the optimum conditions for operation of Stage 2 of this conceptual process. Results of some of these experimental studies have already been reported.(3,4) This paper reports the results of a computer study of the thermochemistry of the two-stage process with emphasis on the effects of variations in the operating conditions. These data were needed: (a) to guide the experimental studies; and, (b) to indicate the corresponding effects of these variables on the final cost of pipeline gas as derived in the initial economic evaluation of the process.(1,2)

According to the initial economic evaluation of the overall process (1), the yield of methane produced directly from coal is of major importance for the economics of the process. In a study of the thermochemistry involved, consideration must be given to this reaction and means must be available for determining the extent it occurs.

At the time the study was begun, kinetic data for the rate of methane formation were not available; however, it was known that methane formation at the temperatures visualized for Stage 2 is a very rapid reaction (5), and that observed methane yields correspond to the thermodynamic equilibrium of the reaction

$$C + 2H_2 = CH_4 \qquad (1)$$

if an activity that varies from 1 to 3.4 is assumed for the carbon.(6)

Therefore, it was arbitrarily assumed for the present study that methane yields computed on this basis would be apt to respond to changes in Stage 2 temperature and pressure, and thus, they would be more realistic than selection of fixed methane yields. In addition, it was assumed that the rest of the carbon would be converted to $CO + H_2$ by reaction with steam and oxygen.

For the well known water-gas shift reaction, it was assumed that the reaction came to equilibrium at reaction temperature according to the equation:

$$CO + H_2O = CO + H_2 \qquad (2)$$

For the evaluation of the effects of the various operating parameters, such as oxygen/coal ratio, steam/coal ratio, operating pressure, preheat temperatures, etc., one further assumption is necessary--namely, thermal equilibrium in each stage of the gasifier is achieved.

BASIS AND PROCEDURE FOR COMPUTER PROGRAM

In making the computer calculations, values for the various operating conditions prevailing in Stage 1 and Stage 2 are first designated, together with an arbitrarily chosen Stage 1 product gas composition. Then, the heat of reaction is calculated for the reaction of recycle char with oxygen and steam in Stage 1 to form the Stage 1 product gas of the arbitrarily chosen composition. The heat of reaction is calculated from the heating value of the recycle char and of the Stage 1 product gas, and then used to calculate the Stage 1 gas exit temperature.

Assuming that the water-gas shift equilibrium is established at this temperature of Stage 1, a new gas composition is calculated next and then used to correct the gas temperature. This process is repeated until a Stage 1 exit gas temperature is found that has a calculated accuracy of $\pm$ 5 C.

The Stage 1 product gas is then used in Stage 2 where coal and steam are added and reacted to form CH_4 in a concentration corresponding to the equilibrium of Equation 1 at a designated carbon activity and at an estimated temperature. The carbon in the coal which is not used in making methane is reacted with steam to form CO and H_2. Oxygen, nitrogen, and sulfur in the coal form H_2O, N_2, and H_2S; and the remaining hydrogen in the coal is liberated as gaseous hydrogen.

For this combination of gas from Stage 1 and Stage 2, again the temperature of the resultant gas mixture is calculated and the composition adjusted to reflect establishment of the shift reaction equilibrium. With the new composition, the equilibria for methane formation and the shift reaction are combined and the calculations reiterated until a Stage 2 temperature is obtained which is within $\pm$ 5 C of the actual temperature.

Computer Input

The nature of the input data required for the various individual computer calculations is shown in Table 1. The values for the different operating parameters were varied from one calculation to the next in accordance with the particular effect being evaluated.

TABLE 1. EXAMPLE OF COMPUTER INPUT DATA

Item	Stage 1	Stage 2	Total
Coal, daf, lb	--	100.0	100.0
Coal Preheat, C	--	204	--
Carbon Reacted,%	67	33	100.0
Carbon Activity, Equation 1	--	1.0	--
Oxygen, lb	71.0	--	71.0
Oxygen Preheat, C	327	--	--
Steam, lb	36.0	104.9	140.9
Steam Preheat, C	538	538	--
Pressure, atm	72.4	72.4	--
Heat Loss, Btu/lb Coal	250	--	250

Available data (7) for the heats of combustion, enthalpies, and thermodynamic equilibria were used in the computer program.

Computer Output

The type of information given in the printout for each computer run is shown in Table 2.

In addition to the results given in the computer output, some parameters indicative of the cost of the final gas, such as "total methane after methanation," "oxygen consumption lb/MM Btu in the final gas," or "the CO_2 production" have been manually calculated.

TABLE 2. EXAMPLE OF COMPUTER OUTPUT DATA

Item	Stage 1, Moles	Stage 2, Moles	Stage 2, Mole Fraction
Gas Composition			
CO	3.900	3.473	0.3138
H_2S	0.000	0.084	0.0076
CH_4	0.000	1.165	0.1052
H_2	1.036	3.900	0.3524
N_2	0.000	0.057	0.0052
CO_2	0.787	2.390	0.2159
Total	5.723	11.069	1.0001
H_2O	--	3.902	--
(CO + H_2)	--	7.373	--
Temperatures, C	1715	935	--
Oxygen/Steam Ratio	1.972	--	--
Oxygen/Coal Ratio	--	0.710	--
Preformed Methane,%	--	38.722	--
C as Methane,%	--	16.575	--

COALS USED

Three coals varying in rank from high volatile A bituminous to lignite were used in the study to obtain an indication of the effect of coal composition. The analyses used for these coals are given in Table 3.

TABLE 3. COAL ANALYSES USED FOR COMPUTER STUDY

	Seam		
	Pittsburgh	Illinois No. 6	Lignite
H_2O, lb per 100 lb daf Coal	1.3	1.3	1.3
Ash, lb per 100 lb daf Coal	7.7	9.1	15.5
Ultimate Analyses, Percent daf			
C	84.4	81.3	74.3
H	5.7	5.4	4.8
N	1.6	1.5	0.9
O	5.6	9.6	18.5
S	2.7	2.6	1.5
Net H per 100 C	5.3	4.6	3.0
Gross Heating Value, Btu/lb	15,270	14,480	12,270

RESULTS AND DISCUSSION

The data from the thirteen runs using Pittsburgh seam coal in normal operation of the gasifier are summarized in Tables 4 and 5. These were Runs 27 through 37, 42, and 43. The data from the four runs with char withdrawal are summarized in Table 6; these were Runs 48, 49, 50, and 53, using Pittsburgh seam coal. Runs 38 and 39 using Illinois No. 6 seam coal, and Runs 51 and 52 using North Dakota lignite are summarized in Table 7.

The computer data were used to calculate parameters that can be used directly in comparing the costs of gases obtained with different computer input data or different operating conditions. These parameters are referred to one million Btu in the final gas after methanation, and are based on costs derived from the initial economic evaluation (1) as follows:

Coal:	15¢/MM Btu
Oxygen:	\$5/ton = 0.25¢/lb
CO_2 Removal:	\$1/ton = 0.05¢/lb
Steam:	30¢/1000 lb

Oxygen/Coal Ratio and Temperature

For Pittsburgh seam coal, the influence of a change in the oxygen/coal ratio is shown in Figure 2, the oxygen/coal ratio is plotted versus Stage 2 temperature, oxygen consumption, CO_2 production, carbon as methane, and gasification efficiency. As expected, with increases in the oxygen/coal ratio, the Stage 2 temperature increases and all parameters connected with gasification cost indicate increased costs.

The data shown in Figure 2 are replotted in Figure 3 to show the effects of changes in Stage 2 temperature on these same parameters. Over the range studied, a Stage 2 temperature increase of 12 C causes a corresponding decrease in methane formation equal to about 1 percent of the carbon in the coal.

Carbon Activity

On the basis that experimental results may indicate a higher conversion to methane at a given temperature than indicated by Figures 2 and 3, adjustments were made in the computer calculations to reflect a higher activity for the carbon in Stage 2.

The results of computer runs using carbon activity 3.4 and 2, respectively, are compared in Table 8. The data show the influence of changes in methane yield from 14 to 24.6 percent on a carbon basis on the cost of the pipeline gas. A 1 percent unit increase in the conversion of the carbon in the coal into methane decreases the cost of raw materials and utilities for the pipeline gas by about 0.6¢/MM Btu.

In the initial evaluation of the processes (1), conversions of carbon into CH_4 in Stage 2 of 15, 20, and 24 percent were assumed; a 1 percent increase in the carbon conversion to methane decreased the pipeline gas cost by about 0.8¢/MM Btu.

Total Operating Pressure

In this study, the thermodynamic equilibrium is used to obtain the methane yield; therefore, the operating pressure exerts a major influence on the

TABLE 4. SUMMARY OF RESULTS OF COMPUTER RUNS 27-33

	Run Number 8014 BKC-						
	27	28	29	30	31	32	33
INPUT DATA							
Type of Coal	Pgh.	Pgh.	Pgh.	Pgh.	Pgh.	Pgh.	Pgh.
System Pressure, atm	72.4	72.4	72.4	72.4	72.4	72.4	102.4
Input Temperature, °C							
Coal	204	204	204	204	204	204	204
Steam	538	538	538	538	538	538	538
Oxygen	327	327	327	327	327	327	327
Stage 2							
Coal Feed Rate, lb daf	100.0	100.0	100.0	100.0	100.0	100.0	100.0
Steam Feed Rate, lb	95.4	24.0	95.4	95.4	95.4	95.4	95.4
Carbon Activity	1.0	1.0	1.0	1.0	1.0	1.0	1.0
Carbon Reacted, %	33.3	33.3	33.3	33.3	29.9	24.7	33.3
Stage 1							
Steam Feed Rate, lb	36.0	36.0	36.0	36.0	36.0	36.0	36.0
Oxygen Feed Rate, lb	71.0	71.0	71.0	71.0	74.5	80.0	71.0
Heat Loss, Btu/lb Coal	250	250	500	0	250	250	250
CALCULATIONS							
Stage 2							
Temperature (Exit) °C	935	945	905	955	955	985	955
Temperature (Exit) °F	1715	1733	1661	1751	1751	1805	1751
Gas Composition, Moles							
CO	3.473	4.990	3.180	3.662	3.616	3.796	3.374
H_2S	0.084	0.084	0.084	0.084	0.084	0.084	0.084
CH_4	1.165	0.958	1.303	1.077	1.046	0.882	1.254
H_2	3.900	3.209	3.639	4.064	4.013	4.147	3.643
N_2	0.057	0.057	0.057	0.057	0.057	0.057	0.057
CO_2	2.390	1.079	2.544	2.289	2.365	2.349	2.399
H_2O	3.902	1.043	3.886	3.915	4.027	4.222	3.981
Stage 1							
Temperature, °C	1715	1715	1575	1865	1735	1765	1715
Temperature, °F	3119	3119	2867	3389	3155	3209	3119
Gas, Moles							
CO	3.900	3.900	3.861	3.937	4.142	4.499	3.900
H_2	1.036	1.036	1.075	0.999	1.054	1.083	1.036
CO_2	0.787	0.787	0.826	0.749	0.784	0.792	0.787
H_2O	0.962	0.962	0.923	1.000	0.945	0.915	0.962
Stage 2							
Total Gas, Dry Moles	11.068	10.377	10.807	11.232	11.181	11.315	10.811
Total (CO + H_2) Moles	7.373	8.198	6.819	7.725	7.629	7.943	7.017
Preformed CH_4, %	38.7	31.9	43.3	35.8	35.4	30.7	41.7
Carbon as Methane, %	16.6	13.6	18.5	15.3	14.9	12.5	17.8
Total							
Thermal Efficiency	0.836	0.864	0.825	0.842	0.828	0.813	0.830
Steam Decomposition, %	47	69	47	47	45	42	45
Moles, Total Methane after Methanation	3.01	3.01	3.01	3.01	2.95	2.86	3.01
% Btu in Coal, Total Methane after Methanation	75.5	75.5	75.5	75.5	74.0	71.7	75.5
Oxygen Consumption, lb/MM Btu in CH_4	61.8	61.8	61.8	61.8	65.9	72.7	61.8
CO_2 Production, Mole per Mole CH_4	4.02	4.02	4.02	4.02	4.08	4.17	4.02
CO_2 Production, lb/MM Btu in Gas	154	154	154	154	159	167	154

TABLE 5. SUMMARY OF RESULTS OF COMPUTER RUNS 34-37, 42, AND 43

	Run Number 8014 BKC-					
	34	35	36	37	42	43
INPUT DATA						
Type of Coal	Pgh.	Pgh.	Pgh.	Pgh.	Pgh.	Pgh.
System Pressure, atm	51.0	72.4	72.4	72.4	72.4	72.4
Input Temperature, °C						
Coal	204	204	204	204	204	204
Steam	538	538	538	538	538	538
Oxygen	327	327	327	327	327	327
Stage 2						
Coal Feed Rate, lb daf	100.0	100.0	100.0	100.0	100.0	100.0
Steam Feed Rate, lb	95.4	104.9	95.4	95.4	95.4	60.0
Carbon Activity	1.0	1.0	3.4	2.0	1.0	1.0
Carbon Reacted, %	33.3	33.3	39.8	39.8	39.8	33.3
Stage 1						
Steam Feed Rate, lb	36.0	36.0	36.0	36.0	36.0	36.0
Oxygen Feed Rate, lb	71.0	71.0	63.9	63.9	63.9	71.0
Heat Loss, Btu/lb Coal	250	250	250	250	250	250
CALCULATIONS						
Stage 2						
Temperature (Exit) °C	905	925	965	935	885	945
Temperature (Exit) °F	1661	1697	1769	1715	1625	1733
Gas Composition, Moles						
CO	3.476	3.256	2.792	2.961	3.045	4.137
H_2S	0.084	0.084	0.084	0.084	0.084	0.084
CH_4	1.121	1.220	1.729	1.595	1.475	1.065
H_2	4.070	3.895	2.768	3.134	3.529	3.636
N_2	0.057	0.057	0.057	0.057	0.057	0.057
CO_2	2.430	2.551	2.506	2.471	2.306	1.825
H_2O	3.819	4.326	3.906	3.807	3.652	2.401
Stage 1						
Temperature, °C	1715	1715	1665	1665	1665	1715
Temperature, °F	3119	3119	3029	3029	3029	3119
Gas, Moles						
CO	3.900	3.900	3.458	3.458	3.458	3.900
H_2	1.036	1.036	1.009	1.009	1.009	1.036
CO_2	0.787	0.787	0.773	0.773	0.773	0.787
H_2O	0.962	0.962	0.990	0.990	0.990	0.962
Stage 2						
Total Gas, Dry Moles	11.238	11.063	9.936	10.302	10.697	10.804
Total (CO + H_2) Moles	7.546	7.152	5.560	6.095	6.575	7.772
Preformed CH_4, %	37.3	40.6	55.4	51.1	47.3	35.4
Carbon as Methane, %	16.0	17.4	24.6	22.7	21.0	15.2
Total						
Thermal Efficiency	0.838	0.830	0.832	0.840	0.847	0.848
Steam Decomposition, %	49	45	46	48	50	55
Moles, Total Methane after Methanation	3.01	3.01	3.12	3.12	3.12	3.01
% Btu in Coal, Total Methane after Methanation	75.5	75.5	78.3	78.3	78.3	75.5
Oxygen Consumption, lb/MM Btu in CH_4	61.8	61.8	53.5	53.5	53.5	61.8
CO_2 Production, Mole per Mole CH_4	4.02	4.02	3.91	3.91	3.91	4.02
CO_2 Production, lb/MM Btu in Gas	154	154	144	144	144	154

TABLE 6. SUMMARY OF RESULTS OF COMPUTER RUNS 48, 49, 50, AND 53

	Run Number 8014 BKC-			
	48	49	50	53
INPUT DATA				
Type of Coal	Pgh.	Pgh.	Pgh.	Pgh.
System Pressure, atm	72.4	72.4	72.4	72.4
Input Temperatures, °C				
Coal	204	204	204	204
Steam	538	538	538	538
Oxygen	327	327	327	327
Stage 2				
Coal Feed Rate, lb daf	100.0	100.0	100.0	100.0
Steam Feed Rate, lb	71.0	2.0	2.0	2.0
Carbon Activity	1.0	1.0	3.4	7.0
Stage 1				
Steam Feed Rate, lb	24.0	24.0	24.0	24.0
Oxygen Feed Rate, lb	65.0	28.0	20.0	20.0
Heat Loss, Btu/lb Coal	250	250	250	250
CALCULATIONS				
Stage 2				
Temperature (exit) °C	1035	945	915	945
Temperature (exit) °F	1895	1733	1679	1733
Gas Composition, Moles				
CO	3.178	0.954	0.526	0.452
H_2S	0.084	0.084	0.084	0.084
CH_4	0.583	0.548	0.933	0.001
H_2	3.567	1.668	0.971	0.774
N_2	0.057	0.057	0.057	0.057
CO_2	1.601	0.572	0.572	0.579
H_2O	3.378	1.518	1.445	1.506
Stage 1				
Temperature, °C	2355	995	725	725
Temperature, °F	4271	1823	1337	1337
Gas, Moles				
CO	1.737	1.551	1.129	1.129
H_2	0.244	0.845	0.981	0.981
CO_2	1.285	0.522	0.551	0.551
H_2O	1.088	0.488	0.351	0.351
Stage 2				
Total Gas, Dry Moles	9.070	3.882	3.143	2.946
Total (CO + H_2) Moles	6.745	2.621	1.497	1.225
Preformed CH_4, %	25.7	45.5	71.4	76.6
Carbon as Methane, %	8.3	7.8	13.3	14.2
Char Produced, lbs C	20.0	60.0	60.0	60.0
TOTAL				
Thermal Efficiency	0.651	0.325	0.331	0.327
Steam Decomposition, %	36.1	-5.1	0.0	-4.0
Total Methane after Methanation				
Moles	2.27	1.202	1.306	1.306
% Btu in Coal	57.5	30.5	32.9	32.9
% Btu in (Coal minus Char)	70.2	69.2	75.0	75.0
Btu in Char as % of Btu in Coal	18.6	55.7	55.7	55.7
Btu in Gas and Char as % of Btu in Coal	76.1	86.2	88.6	88.6
Oxygen Consumption, lb MM Btu in CH_4	75.5	60.5	40.0	40.0
CO_2 Production, Mole/Mole CH_4	1.36	0.73	0.56	0.56
CO_2 Production, lb MM/MM Btu in Gas	156	83	64	64

TABLE 7. SUMMARY OF RESULTS OF COMPUTER RUNS 38, 39, 51, AND 52

	Run Number 8014 BKC-			
	38	39	51	52
INPUT DATA				
Type of Coal	Illinois	Illinois	Lignite	Lignite
System Pressure, atm	72.4	72.4	72.4	72.4
Input Temperatures, °C				
Coal	204	204	204	204
Steam	538	538	538	538
Oxygen	327	327	327	327
Stage 2				
Coal Feed Rate, lb daf	100.0	100.0	100.0	100.0
Steam Feed Rate, lb	95.4	95.4	55.0	95.4
Carbon Activity	1.0	1.0	1.0	1.0
Carbon Reacted,%	30.6	41.4	22.6	22.6
Stage 1				
Steam Feed Rate, lb	36.0	36.0	36.0	36.0
Oxygen Feed Rate, lb	71.0	60.0	65.0	65.0
Heat Loss, Btu/lb Coal	250	250	250	250
CALCULATIONS				
Stage 2				
Temperature (exit) °C	955	885	915	895
Temperature (exit) °F	1751	1625	1679	1643
Gas Composition, Moles				
CO	3.388	2.855	3.055	2.357
H_2S	0.081	0.081	0.047	0.047
CH_4	0.975	1.391	0.910	1.038
H_2	3.837	3.395	2.853	3.039
N_2	0.054	0.054	0.032	0.032
CO_2	2.405	2.522	2.220	2.790
H_2O	4.180	3.791	2.839	4.640
Stage 1				
Temperature, °C	1705	1635	1405	1405
Temperature, °F	3101	2975	2561	2561
Gas, Moles				
CO	3.906	3.196	4.184	4.184
H_2	1.052	0.987	1.330	1.330
CO_2	0.792	0.771	0.604	0.604
H_2O	0.947	1.011	0.669	0.669
Stage 2				
Total Gas, Dry Moles	10.741	10.299	9.118	9.304
Total (CO + H_2) Moles	7.225	6.251	5.908	5.397
Preformed CH_4, %	35.1	47.1	38.1	43.5
Carbon as Methane, %	14.4	20.5	14.7	16.8
Total				
Thermal Efficiency	0.822	0.845	0.833	0.815
Steam Decomposition, %	43	48	44.0	36.6
Total Methane after Methanation, Moles	2.78	2.95	2.39	2.39
Total Methane after Methanation, % Btu in Coal	73.7	78.1	74.7	74.7
Oxygen Consumption, lb/MM Btu in CH_4	66.5	53.2	71.0	71.0
CO_2 Production, Mole per Mole CH_4	3.99	3.82	1.59	1.59
CO_2 Production, lb/MM Btu in Gas	165	148	183	183

TABLE 8. EFFECTS OF CHANGES IN CARBON ACTIVITY IN STAGE 2
(Basis: Pressure, 72.4 atm; Heat Loss, 250 Btu/lb Coal)

	Stage 2 Temperature, 935 C				Stage 2 Temperature, 965 C			
	Carbon Activity		Difference		Carbon Activity		Difference	
	2.0	1.0	Units	¢/MM Btu in Gas	3.4	1.0	Units	¢/MM Btu in Gas
Oxygen, lb/100 lb Coal	63.9	71.0	--	--	63.9	75.9	--	--
Carbon as CH_4, %	22.7	16.6	--	--	24.6	14.0	--	--
Gasification Efficiency, %	78.3	75.5	--	--	78.3	73.2	--	--
Oxygen, lb/MM Btu in Gas	53.5	61.8	8.3	2.07	53.5	68.1	14.6	3.65
CO_2, lb/MM Btu in Gas	144.0	154.0	10.0	0.50	144.0	163.0	19.0	0.95
Steam, lb/MM Btu in Gas	110.0	114.5	4.5	0.13	110.0	118.0	8.0	0.24
Coal, MM Btu/MM Btu in Gas	1.277	1.325	0.048	0.72	1.277	1.367	0.09	1.35
TOTAL				3.42				6.19

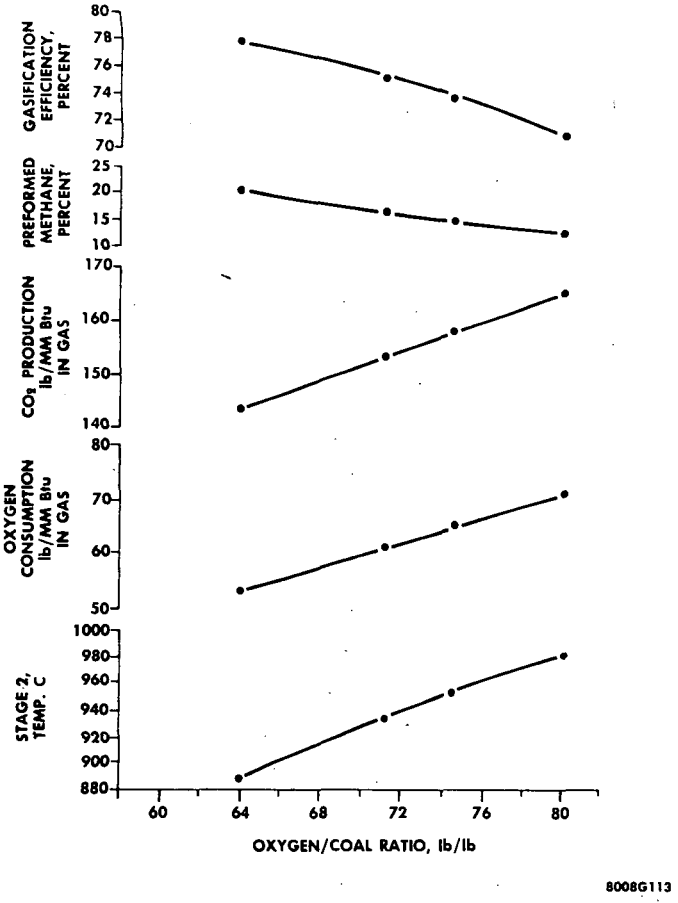

Figure 2. Computer Program Results: Effects of Changes in Oxygen (Basis: Pressure, 72.4 atm, Heat Loss: 250 Btu/lb Coal)

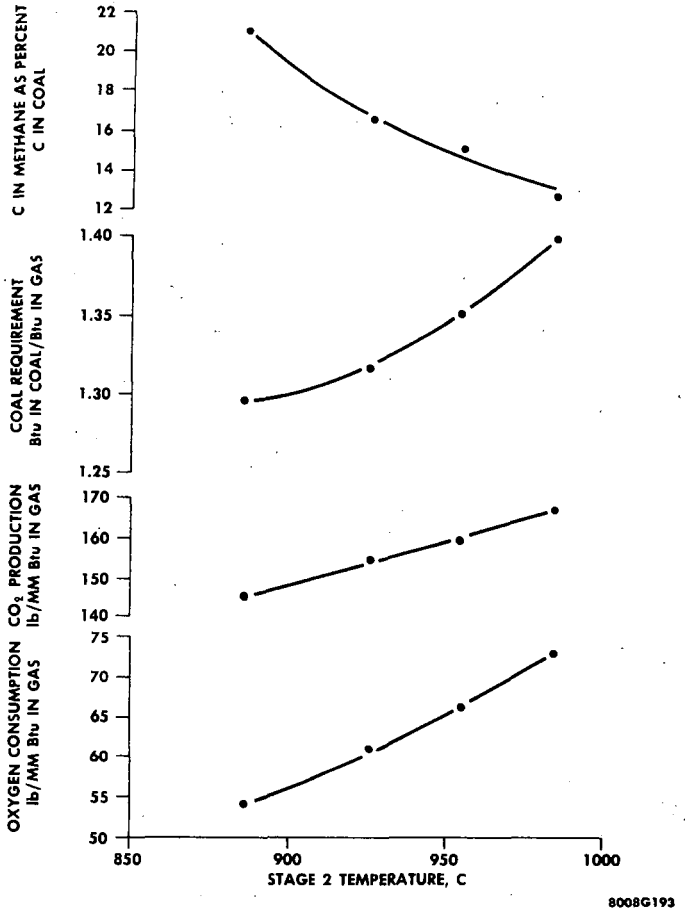

Figure 3. Effects of Changes in Stage 2 Temperature (Basis: Pressure, 72.4 atm, Heat Loss: 250 Btu/lb Coal)

yield. By comparing the results from Run 33 and Run 34 with those from a run at the standard operating pressure, it is noted that a change in pressure, either from 72.5 to 51 atm, or from 72.5 to 102 atm, produces a change in raw material and utility costs equivalent to about 2¢/MM Btu pipeline gas; operation at the higher pressure gives the cheaper gas in each case. By comparison, the same change in gas cost of 2¢/MM Btu would be produced by a change of about $10 million in the investment costs for a 250 MM scfd plant. Further economic evaluations and experimental results will be needed to find the optimum pressure for the lowest cost of gas and/or capital investment.

Heat Loss and Preheat Temperature

Another factor influencing the gas yield is the heat loss in the gasifier. As reference value, a heat loss of 250 Btu/lb of coal, or 1.6 percent of the heating value of Pittsburgh seam coal, has been assumed. This is an arbitrarily chosen figure that is based on extrapolation of available data to pressure operation. Computer Runs 29 and 30 for heat losses of 500 and 0 Btu/lb of coal, respectively, were compared with results for 250 Btu heat loss at the same Stage 2 temperature. An increase in heat loss of 250 Btu/lb coal increases the gas cost by about 2¢/MM Btu pipeline gas. Again, experimental studies will be needed to determine whether the actual methane yield is influenced to the extent indicated here. Only experiments in a large pilot plant will establish reliable data for the heat loss in a commercial unit.

A study of different preheat temperatures of reactants did not appear necessary. Differences in the enthalpies of the various materials due to changes in preheat temperature, have the same influence as changes in heat loss.

Steam/Coal Ratio

Several computer runs were made using various steam/coal ratios:

In Computer Runs 28 and 35, data for 24.0 and 104.9 pound steam per 100 pound coal in Stage 2 were obtained for comparison to the "standard" quantity of 95.4 pound; no changes were made in the amount of steam entering Stage 1, 36.0 pound steam per pound coal being used in all instances.

In Computer Run 28 with 60 pound total steam per 100 pound coal, the Stage 2 temperature was 20 C above that in Run 35, being 945 C, as compared to 925 C.

Unless reaction kinetics demand a high steam/coal ratio, a ratio below 130 lb/100 lb coal should be selected for purely heat balance reasons. A further study of the utilization of the gasification steam in the shift reactor is indicated. Such a reactor would be part of an integrated pipeline gas plant.

Withdrawal of Recycle Char

On the premise that it may become desirable to withdraw recycle char for use as boiler fuel rather than fresh coal, Computer Runs 48, 49, 50, and 53 were made to indicate results which might be expected with such an operation. The partial gasification shows lower costs for pipeline gas in all cases: the lowest difference is 2.4 cents, the highest 13.3 cents per MM Btu based on raw material and utility costs only, assuming a char credit at the Btu price of the coal and only a minor char handling expense.

Additional experimental data are needed to better define the methane yield and operating temperature for char withdrawal in comparison to these same parameters for complete gasification.

Changes in Coal Feed Stock

To obtain data on the effect of coal rank on the cost of pipeline gas, several computer runs were made with coals differing in rank from Pittsburgh seam coal, namely, Runs 38 and 39 with Illinois No. 6 coal and Runs 51 and 52 with lignite. For Pittsburgh seam coal and Illinois No. 6 coal at the same price per MM Btu in the dried coal and the same Stage 2 temperature, the pipeline gas cost is similar. On the same basis, the greater thermal ballast in the lignite, mainly its high oxygen content, leads to a higher cost of gas made from lignite. However, if one assumes a 60 C lower Stage 2 temperature for lignite, the gas cost becomes the same.

Again, further experimentation will lead to a better definition of the best operating temperature for the various coals and a better comparison of cost will be possible.

Comparison of Experimental and Computer Results

Experimental Stage 2 gasification data for lignite (3) are compared with computer results in Table 9. The experimental results show a somewhat higher methane yield in spite of higher Stage 2 temperatures. This discrepancy is not surprising since the methane yield is determined by reaction kinetics and factors such as partial pressures of reactants and the ratios of Stage 1 gas, steam, and coal, rather than by the thermodynamic equilibria.

The higher experimental yield of ($CO + CO_2$) will lead to a smaller amount of char available for Stage 1 than used in the computer run. This will, at the same oxygen/coal ratio, lead to a higher Stage 1 temperature. To attain the higher temperature in Stage 2 indicated by the experiments, a higher oxygen/lignite ratio than the 0.65 lb/lb assumed in computer Run 51 will be needed. In the feed streams entering Stage 2 in the experimental runs, the partial pressure of ($CO + H_2$) is lower; and that of CO_2 is higher than in the computer run. This is in accord with a higher oxygen/lignite ratio as required to attain the higher temperature used in the experimental runs. It may be noted that the Stage 1 gas/lignite ratios and the steam/lignite ratios in the two experimental runs bracket these same parameters in the computer runs.

The computer data reported in this study have been useful in providing guidance for the selection of experimental parameters such as feed stream composition and reactant ratios for the externally-heated experimental 5 lb/hr flow reactor being used for the study of Stage 2 reactions. They will be equally useful in the operation of the internally-heated 100 lb/hr process and equipment development unit now being erected.

The computer program used in this study may also be useful as a basis in preparing an improved program in which the methane content of the Stage 2 gas is determined by kinetic data. It is expected that further operation of the 5 lb/hr unit, and later the 100 lb/hr unit, will supply such data.

TABLE 9. EXPERIMENTAL AND COMPUTER DATA FOR LIGNITE GASIFICATION IN STAGE 2

	Experimental Data		Computer Data
	Run 36	Run 38	Run 51
Temperature °C, Stage 1	--	--	1405
Stage 2	970	965	915
Pressure, atm	70	81.5	72.4
Lignite, g C/min	5.9	18.8	--
Stage 1 Gas, Nl/g C in Lignite	4.9	1.56	1.84
Steam, g/g C in Lignite	2.1	0.9	1.22
Partial Pressure of Gases Entering Stage 2, atm			
CO	25.5	26.5	30.8
H_2	8.4	8.7	9.8
CO_2	7.5	7.9	4.4
H_2O	24.5	34.0	27.4
Ar	4.1	4.4	--
Yields in Stage 2 alone as Percent of Lignite:			
C in CH_4	16.9	15.4	14.7
C in (CO + CO_2)	22.0	18.1	7.9
C Gasified in Stage 2	38.9	33.5	22.6
Btu in CH_4	33.8	29.5	28.2
Btu in (CO + H_2)	4.5	10.2	3.8

ACKNOWLEDGMENT

This paper reports results from a program of research being conducted by Bituminous Coal Research, Inc., with support from the Office of Coal Research, U.S. Department of the Interior, under Contract No. 14-01-0001-324. The authors wish to thank the Office of Coal Research for permission to publish this paper.

The authors also wish to express their thanks to Mr. E. J. Vidt and the Blaw-Knox Company for preparing the computer program and making the computations.

REFERENCES

1. "Gas Generator Research and Development - Survey and Evaluation," (Bituminous Coal Research, Inc., Report L-156), Two Volumes, 650 pp, Washington, D.C.: U.S. Government Printing Office, 1965.

2. Donath, E. E. and Glenn, R. A., "Pipeline gas from coal by two-stage entrained gasification," Proc. AGA Production Conference, 1965, 65-P-147 to 65-P-151 (1965).

3. Glenn, R. A., Donath, E. E., and Grace, R. J., "Gasification of coal under conditions simulating stage 2 of the BCR two-stage super-pressure gasifier," Am. Chem. Soc., Div. Fuel Chem. Preprints 10 (4), 97-122 (1966).

4. Glenn, R. A. and Grace, R. J., "Laboratory-scale flow reactor for studying gasification of coal under conditions simulating stage 2 of the BCR two-stage super-pressure gasifier," Presented at North-Central Regional AIChE Symp. on Current Trends in Pilot Plants, Pittsburgh, Pa., 1967.

5. Peters, W., "Schnellentgasung von Steinkohlen," Thesis, Aachen, 1963; Peters, W. and Bertling, H., "Kinetics of the rapid degasification of coals," Fuel 44, 317-31 (1965).

6. Squires, A. M., "Steam-oxygen gasification of fine sizes of coal in a fluidised bed at elevated pressure," Trans. Inst. Chem. Engrs. (London) 39 (1), 3-22 (1961).

7. Wagman, D. D., et al, "Heats, free energies, and equilibrium constants of some reactions involving O_2, H_2, H_2O, C, CO, CO_2, and CH_4," U.S. Dept. Commerce, Natl. Bur. Std., Res. Rept. 1634 (1945).

CATALYTIC DEHYDROGENATION OF COAL
III. HYDROGEN EVOLUTION AS A FUNCTION OF RANK*

R. Raymond, L. Reggel, and I. Wender

Pittsburgh Coal Research Center, U. S. Bureau of Mines,
4800 Forbes Avenue, Pittsburgh, Pa. 15213

Dehydrogenation of coal using a one percent palladium on calcium carbonate catalyst in the presence of phenanthridine as solvent gives almost pure hydrogen gas as the product. The rank of coal affects the yield of hydrogen from the corresponding vitrain; for coals ranging from high volatile C bituminous to anthracite, the hydrogen evolution decreases gradually with increasing rank of coal; lignites and subbituminous coals give less hydrogen than do low rank bituminous coals. For bituminous coals, the hydrogen evolution (atoms of hydrogen evolved per 100 carbon atoms in the coal) is a linear function of the atomic H/C ratio and also of the atomic O/C ratio. Lignites and subbituminous coals fall outside of the lines defining the bituminous coals. Some ideas on the process of coalification are presented: it is suggested that lignites and subbituminous coals contain some cyclic carbon structures which are neither aromatic nor hydroaromatic; that low rank bituminous coals contain large amounts of hydroaromatic structures; and that higher rank bituminous coals contain increasing amounts of aromatic structures.

INTRODUCTION

The vast literature on chemical reactions of coal[1,2] contains (until quite recently) very few references to any work on dehydrogenation. This may be due in part to the paucity of systematic studies on the dehydrogenation of organic compounds under conditions which might be expected to cause relatively little disruption of the coal structure; i.e., dehydrogenation in the liquid phase† at temperatures below 400°C. The dehydrogenation reagents usually used for pure compounds are metallic catalysts[3], sulfur[3], selenium[3], and quinones[3,4]. The dehydrogenation of coal by sulfur[5] has received considerable attention; the hydrogen removed from the coal is evolved as hydrogen sulfide. Selenium has not, to our knowledge, been used with coal; because of the higher temperature required and the poor yields usually obtained, selenium seldom offers any advantage over sulfur[3]; in a selenium dehydrogenation, the hydrogen removed is evolved as hydrogen selenide. Benzoquinone with coal has been investigated[6]; the reaction is a hydrogen transfer[4], giving hydroquinone, and the results are difficult to interpret[7]. Iodine as a dehydrogenation agent has also been studied with coal[8]; the hydrogen removed from the coal is evolved as hydrogen iodide. Again, the results are not easy to evaluate; the temperature of reaction is high; and there is very little work on organic compounds which can serve as a basis for comparison[9,10]. Bromine, one of the oldest dehydrogenation reagents[3], has been of little value[1].

The first use of a metallic catalyst for the dehydrogenation of coal was reported by the present authors[11]; the reaction was conducted in the presence of a solvent (vehicle), and almost pure hydrogen gas was evolved. The reversibility of the reduction and dehydrogenation of coal has also been investigated[12]. In this paper we wish to summarize the development of the method, the experimental

---

*For the preceding papers in this series, see references 11 and 12.
† For an excellent and up to date review see ref. 3.

procedure, and, most important, the effect of the rank of the coal upon the amount of hydrogen formed. The purpose of these studies is twofold: first, to obtain information which may give some insight into the structure of coal; second, to obtain large amounts of hydrogen from coal. It is hoped that development of cheaper solvents and catalysts might enable hydrogen to be produced economically; the coal residue could then be burned for fuel.

EXPERIMENTAL

Preliminary experiments in which coal, catalyst, and vehicle were refluxed showed that the hydrogen evolution was influenced by reflux rate, heating rate, bath temperature, and depth of immersion of the reaction flask into the bath. Accordingly, the previous apparatus used a stirrer and a heating mantle[11,12]. A Hershberg tantalum wire stirrer with a glass bearing lubricated with silicone grease was used; later, a magnetic stirrer was found to be more convenient, to give superior results, and to obviate crust problems (see below). When the Hershberg stirrer was used, the reactants (0.500 g of dried, -200 mesh coal, 0.550 g of catalyst, and 7.50 g of the vehicle) were weighed into a 50 ml two-neck flask. The charge was mixed thoroughly with a spatula. The flask was then fitted with the stirrer and with an adapter which included both a dip-tube to serve as a thermocouple well and a side arm which was attached to a 250 ml gas buret. Provision was made for admission of helium to the system and for sampling the evolved gas after the reaction. The apparatus was thoroughly flushed with helium and pressure-tested for leaks. Flushing consisted essentially of admitting helium to the system, expelling the gas, adding fresh helium, and repeating this procedure three to five times. As a check upon the efficacy of flushing, the last expelled flush can be sampled; it should contain at least 99 percent helium (all gases were analyzed by mass spectrometry). The charge was then vigorously refluxed (heating mantle) with stirring for 5.0 h, preceded by a carefully standardized 0.5-h period of heating up to temperature. The reduced 1 percent palladium on calcium carbonate catalyst was prepared by Engelhard Industries, Inc., Newark, N. J. The same batch of catalyst was used in all of the runs described here, with the exceptions noted below. (See Discussion.) The catalyst was dried at 60°C and 1 mm; coals were dried to constant weight at 100° and 1 mm.

This experimental procedure was effective, but it was not convenient, and the stirrer sometimes jammed in the bearing, requiring repetition of a run. Also, some catalysts were found to convert the coal to a hard, brittle, insoluble crust after only a short heating period; this gave low and erratic values for hydrogen. (Crust formation could sometimes be avoided by very slow and prolonged heating to reflux.) It was found that magnetic stirring circumvented these problems and was also much more convenient. A 35 ml one-neck flask heated by an electric mantle was used. A pyrex-enclosed alnico stirring bar, 7/8 in. long, was placed in the flask. An alnico horseshoe magnet (ca. 50 pound pull) was located below the mantle and rotated by an ordinary stirring motor. The rest of the apparatus was as described above. With this modification, stirring was much more vigorous and crust formation usually did not take place. If in any run a solid crust began to form on the surface of the boiling liquid or on the walls of the flask, stirring was stopped and a small alnico magnet was brought near a point on the side of the flask; this pulled the stirring bar away from the large magnet, and the bar was moved around to break the crust. The small magnet was then removed, and stirring resumed with the large magnet. A few repetitions of this broke up any crust.

For most coals, the bulk of the gas was evolved during the first two hours of reflux, but gas evolution was still continuing at a slow rate (ca. 4 or 5 ml in 30 min) after 5 h. At the end of the reaction period, the gas volume was measured and the gas then thoroughly mixed and sampled. A typical analysis (helium-free basis) for the gas from an hvab coal is 96.4 percent H_2, 0.5 percent N_2, 0.4 percent CH_4, 0.1 percent ethylene, 0.6 percent CO, 0.1 percent ethane, 1.5 percent CO_2, and small amounts (0.1 percent) of other alkanes and alkenes. Lower rank coals gave larger amounts of CO, CO_2, and CH_4. Only the molecular hydrogen itself was considered to be hydrogen evolved; hydrogen in hydrocarbons was disregarded. In the calculations, it was assumed that the gas was saturated with water vapor. In all instances, blank runs (vehicle and catalyst, no coal) were made and corrections applied. The blanks were found to be a function of both the vehicle and the catalyst; two different batches of the same catalyst would give slightly different blanks. Coal-vehicle blanks (without catalyst) were found to be negligible and were disregarded. As would be expected, inadequate flushing of the apparatus led to low hydrogen values. It was also found that slight air oxidation of vitrains resulted in low hydrogen values; it is desirable to use a sample within a period of two weeks of grinding.

We thank D. E. Wolfson for obtaining many of the coal samples used. We are very grateful to B. C. Parks, Pittsburgh Mining Research Center, Bureau of Mines, who prepared the hand picked vitrain samples.

DISCUSSION

In the preliminary development of the method, some experiments were done on the dehydrogenation of 1,2,3,4,5,6,7,8-octahydrophenanthrene, using a 5 percent rhodium on alumina catalyst and refluxing o-terphenyl (bp 332°C) as a vehicle. No stirring was used. With a bath temperature of 300°-350°C for 1 h, about 98-99 percent of the theoretical amount of hydrogen gas was obtained, but the hydrogen evolution was never quite 100 percent. No formation of triphenylene (by cyclodehydrogenation of o-terphenyl) could be detected. In one experiment octahydrophenanthrene was dehydrogenated in the presence of about 5 percent by weight of dibenzothiophene (no vehicle); the hydrogen evolution was high (in addition, some hydrogen probably was used to cleave carbon-sulfur bonds) and the yield of phenanthrene was over 95 percent. It is thus apparent that the sulfur in coal should not poison the dehydrogenation catalyst. This is in accord with several reports on the dehydrogenation of partially reduced heterocyclic sulfur[10], oxygen[13], and nitrogen[14-17] compounds, in good yield, with little cleavage of the carbon-hetero atom bond; for example, 1,2,3,4-tetrahydrodibenzothiophene is converted to dibenzothiophene by palladium on carbon in 80 to 94 percent yield[10].

Experiments were then done on dehydrogenation of vitrain from Bruceton coal (hvab, Pittsburgh Bed, Bruceton, Allegheny County, Pa.) with various catalysts. Vitrain refluxed (without stirring) 2 h with o-terphenyl and 30 percent palladium on calcium carbonate gave off about 7.3 percent of the hydrogen in the vitrain as hydrogen gas; a pyridine-soluble extract of Bruceton vitrain under the same conditions gave 9.0 percent of its hydrogen; the pyridine soluble extract with phenanthridine as vehicle and 30 percent palladium on calcium carbonate gave 13.7 percent hydrogen in 2 h reflux and 30 percent hydrogen in 7 h. Bruceton vitrain with 30 percent palladium on carbon heated at 377° to 402°C (no vehicle) gave 0.2 percent hydrogen. Bruceton vitrain refluxed with o-terphenyl and various palladium, ruthenium, and rhodium catalysts gave 3 to 7 percent hydrogen. Bruceton vitrain refluxed 2 h with o-terphenyl and a molybdenum sulfide or tungsten sulfide catalyst gave both hydrogen (about 2 percent) and hydrogen sulfide; these results did not seem promising and no further work was done with sulfide catalysts.

All of the experiments discussed above were done with a refluxing system but no stirrer. Attention then turned to the development of an apparatus which could be stirred. Our previously published work[11,12] was done using the Hershberg stirrer. The remainder of the work discussed in this paper used the magnetic stirrer (see Experimental), and is concerned with the effect of the rank of the coal upon the hydrogen evolved from the corresponding vitrain. It should be pointed out that comparison of the present results with previous data showed that, for most vitrains, magnetic stirring gave significantly greater yields of hydrogen than did the Hershberg stirrer. It seems probable that even with those vitrains and catalysts which have little tendency to form crusts with the Hershberg stirrer, an insolubilization reaction (polymerization, cross-linking, etc.) takes place during dehydrogenation which results in the coal being made too insoluble in the vehicle to react further, after partial but not complete dehydrogenation. With the more efficient magnetic stirring, dehydrogenation goes at a more rapid rate and is completed before insolubilization can have much effect on the final hydrogen evolution. Some data substantiating this is given in table 4, which shows that for two representative vitrains (Harmattan and Pocahontas No. 3), which give more hydrogen with magnetic than with Hershberg stirring, the magnetically stirred run evolves gas at a faster rate. However, for Bruceton vitrain (the only vitrain giving essentially the same hydrogen value for both stirring methods) the rates of gas evolution are almost the same for both runs.

Table 1 gives the identity and source of 36 coals used in this work. Of these, cannel coal was taken with the thought that its high hydrogen content might lead to a large hydrogen evolution, a hope which did not materialize. Cannel coal was used as the whole coal. The two semianthracites were also whole coals; microscopic examination showed that the Western Middle Field contained over 90 percent vitrain; the Bernice Field was less than 25 percent vitrain. The other 33 coals were used in the form of hand-picked vitrains. Tables 2 and 3 give the ultimate analyses of the samples and the results of dehydrogenation. The results are expressed in three ways: percent of the total hydrogen in the coal which is evolved as hydrogen gas; atoms of hydrogen evolved per 100 carbon atoms in the starting material; and milliliters of hydrogen evolved per gram of starting material.* The last figure (ml/g) can be converted to cubic feet per ton by multiplying by 32.0. This would obviously be of interest in indicating in a very rough way the possible economic value of the process. The largest value obtained is for the vitrain from a Utah hvcb coal (Liberty mine) which gives 9380 cubic feet of H_2 gas per ton on a dry basis, or 9890 cubic feet per ton on a dry ash-free basis. The second figure (H/100 C atoms) is related to the hydroaromatic† structures in the starting coal (neglecting side reactions for the present); any completely reduced structure such as cyclohexane, decalin, or perhydrocoronene would give a value of 100 H/100 C. The first figure (percent H_2 evolved) is also related to the amount of hydroaromatic structure in the coal, but not in a simple and direct manner; it is, however, a convenient figure in that it expresses a yield of product.

---

*The first two of these are independent of ash content; the third is not, and is on an maf basis.

† The term hydroaromatic is used in the sense defined by Fieser and Fieser[18]. Hydro derivatives of aromatic compounds are called hydroaromatic. Alicyclic substances containing six-membered rings but having substituents that block conversion to the aromatic state unless they are eliminated (such as 1,1-dimethylcyclohexane or 9-methyldecalin) are not classified as hydroaromatic.

Table 1. Identity and source of samples used in dehydrogenation

Lignite, Beulah-Zap Bed, Zap Mine, North American Coal Co., Zap, Mercer County, North Dakota
Lignite, Kincade Mine, Burke County, North Dakota
Lignite, Beulah-Zap Bed, North Unit, Beulah Mine, Knife River Coal Mining Co., Beulah, Mercer County, North Dakota
Subbituminous, Roland-Smith Bed, Wyodak Strip Mine, Wyodak Coal and Manufacturing Co., Gilette, Campbell County, Wyoming
Subbituminous, Dietz Bed, Big Horn Mine, Sheridan County, Wyoming
Subbituminous, Laramie Seam, Washington Mine, Clayton Coal Co., Erie, Weld County, Colorado
Subbituminous, Pioneer Canon No. 1 Mine, W. D. Corley Co., Florence, Fremont County, Colorado
Subbituminous, Rock Springs No. 7, 7-1/2, 9, and 15 Coal Beds, Superior, Sweetwater County, Wyoming
High-volatile B bituminous, Illinois No. 6, Green Diamond Mine, Mid-Continent Coal Corp., Marissa, St. Clair County, Illinois
High-volatile B bituminous, Illinois No. 6 Seam, Mecco Mine, Atkinson, Henry County, Illinois
High-volatile C bituminous, No. 11 Coal Bed, Rainbow No. 7 Mine, Gunn-Quealy Coal Co., Quealy, Sweetwater County, Wyoming
High-volatile C bituminous, Illinois No. 7 Bed, Harmatten Mine, Vermillion County, Illinois
High-volatile C bituminous (possibly high-volatile B bituminous), Liberty Bed, Liberty Mine, Liberty Fuel Co., Helper, Carbon County, Utah
High-volatile B bituminous, Illinois No. 6 Bed, Orient No. 3 Mine, Freaman Coal Mining Corp., Waltonville, Jefferson County, Illinois
High-volatile B bituminous, Kentucky No. 9, Pleasant View Mines 9-11, Western Kentucky Coal Co., Madisonville, Hopkins County, Kentucky
High-volatile B bituminous, Kentucky No. 9, DeKoven Mine, Sturgis, Union County, Kentucky
High-volatile A bituminous, Pittsburgh Bed, Bruceton, Allegheny County, Pennsylvania
High-volatile A bituminous, Pond Creek Coal, Majestic Mine, Pike County, Kentucky
High-volatile A bituminous, Powellton Bed, Elk Creek No. 1 Mine, Logan County, West Virginia
High-volatile A bituminous, Eagle Bed, Kopperston Mine, Kopperston, Wyoming County, West Virginia
Medium-volatile bituminous, Sewell Bed, Lochgelley Mine, New River Coal Co., Lochgelley, Mt. Hope, Fayette County, West Virginia
Medium-volatile bituminous (possibly high-volatile A bituminous), Lower Freeport Bed, Coal Valley No. 7 Mine, Indiana County, Pennsylvania
Low-volatile bituminous, Lower Kittanning Bed, Melcroft Mine, Eastern Associated Coal Corp., Fayette County, Pennsylvania
Medium-volatile bituminous, Lower Banner, Buccaneer Mine, Patterson, Buchanan County, Virginia
Medium-volatile bituminous, Sewell Bed, Marianna Mine, Wyoming County, West Virginia
Low-volatile bituminous, Beckley Bed, Maben Mine, Raleigh County, West Virginia
Medium-volatile bituminous, Sewell Seam, Crab Orchard Mine, Winding Gulf Coals, Inc., Raleigh County, West Virginia
Low-volatile bituminous, Lower Hartshorne Bed, Garland Coal and Mining Co., Prospect opening, Arkoma Coal Basin, Le Flore County, Oklahoma

(Continued)

Low-volatile bituminous, Upper Kittanning Bed, Stineman No. 10 Mine, Johnstown, Cambria County, Pennsylvania
Low-volatile bituminous, Pocahontas No. 4 Bed, McAlpine Mine, Winding Gulf Coals, Inc., McAlpine, Raleigh County, West Virginia
Low-volatile bituminous, Lower Kittanning Bed, Toth Mine, Hooversville, Cambria County, Pennsylvania
Low-volatile bituminous, Pocahontas No. 3 Bed, Buckeye No. 3 Mine, Page Coal and Coke Co., Stephenson, Wyoming County, West Virginia
Semianthracite, Bernice Field, Buckwheat No. 1 Mine, E and B Coal Co., Mildred, Sullivan County, Pennsylvania
Semianthracite, Western Middle Field, Buckwheat No. 5 Mine, Trevorton Anthracite Co., Trevorton, Northumberland County, Pennsylvania
Anthracite, Dorrance Mine, Lehigh Valley Coal Co., Luzerne County, Pennsylvania
Cannel coal, Mine 27, Island Creek Coal Co., Logan County, West Virginia

Table 4. Evolution of gas from vitrains during the dehydrogenation process

Run No.	Vitrain	Stirring	Gross gas evolved, ml[a]				
			1 h	1.5 h	2 h	2.5 h	5.5 h
8R-61	Harmatten	Hershberg	62	84	100	111	155
8R-184	Harmatten	Magnetic	66	104	122	134	172
8R-109	Bruceton	Hershberg	51	77	92	104	147
8R-172	Bruceton	Magnetic	60	85	95	111	148
7R-167	Pocahontas No. 3	Hershberg	26	33	38	41	60
8R-182	Pocahontas No. 3	Magnetic	37	48	55	61	83

[a] Approximate value for total gas evolved by the sample at the end of the indicated time, corrected to room conditions (ca. 25°C and 740 mm Hg pressure). The time given is from the beginning of the run; since the reaction mixture takes about one-half hour to reach operating temperature, the actual reaction time is about 0.5 h less than the time given. No correction for gas composition has been made.

Table 2. Analyses (moisture-free basis) of vitrains used for dehydrogenation

Run No.	Vitrain	C	H	N	S	Ash	O (by difference)	C, maf
9R-32	Beulah-Zap (Zap Mine)	64.18	5.28	0.85	0.58	5.35	23.76	67.81
8R-190	Kincade	64.96	4.59	.61	.55	4.73	24.56	68.19
9R-40	Beulah-Zap (Beulah Mine)	66.45	5.40	.31	1.40	3.60	22.84	68.93
9R-42	Roland-Smith (Wyodak)	62.76	5.35	1.01	1.14	10.58	19.16	70.19
9R-3	Dietz (Big Horn)	68.55	4.90	.99	.57	3.23	21.76	70.84
9R-134	Laramie (Washington)	68.11	5.30	1.57	.45	4.80	19.77	71.54
9R-132	Pioneer Canon No. 1	68.75	5.07	.90	1.25	5.23	18.80	72.54
8R-156	Rock Springs	73.21	5.17	1.38	.80	.66	18.78	73.70
8R-161	Illinois No. 6 (Green Diamond)	74.30	5.56	1.13	2.52	1.79	14.70	75.65
8R-162	Illinois No. 6 (Mecco)	74.71	5.39	1.03	2.05	1.77	15.05	76.06
9R-34	No. 11 (Rainbow No. 7)	75.54	5.63	1.92	.84	1.28	14.79	76.52
8R-184	Illinois No. 7 (Harmatten)	75.79	5.29	1.31	1.76	1.03	14.82	76.58
9R-41	Liberty	73.72	5.85	1.65	.72	5.06	13.00	77.65
8R-186	Illinois No. 6 (Orient No. 3)	77.64	5.16	1.87	1.14	1.89	12.30	79.14
8R-159	Kentucky No. 9 (Pleasant View)	78.12	5.89	1.58	1.97	1.54	10.90	79.34
8R-158	Kentucky No. 9 (DeKoven)	78.59	5.81	1.30	2.04	2.61	9.65	80.69
8R-143	Pittsburgh (Bruceton)	81.72	5.50	1.27	1.30	1.65	8.56	83.09
8R-172	Pittsburgh (Bruceton)	81.72	5.50	1.27	1.30	1.65	8.56	83.09
8R-147	Pittsburgh (Bruceton)	81.72	5.50	1.27	1.30	1.65	8.56	83.09
8R-149	Pittsburgh (Bruceton)	81.72	5.50	1.27	1.30	1.65	8.56	83.09
8R-160	Pond Creek (Majestic)	82.41	5.48	1.34	.81	1.59	8.37	83.74
8R-187	Powellton (Elk Creek No. 1)	84.46	5.28	1.53	.96	.69	7.08	85.05
8R-157	Eagle (Kopperston)	84.44	5.52	1.45	.97	2.03	5.59	86.19
8R-165	Sewell (Lochgelley)	85.74	5.20	1.44	.79	.79	6.04	86.42
8R-176	Lower Freeport (Coal Valley No. 7)	85.17	5.13	1.42	1.15	2.42	4.71	87.28
8R-175	Lower Kittanning (Melcroft)	85.34	5.00	1.51	1.46	2.32	4.37	87.37
8R-167	Lower Banner (Buccaneer)	85.37	5.23	1.29	.71	3.42	3.98	88.39

(Continued)

Run No.	Vitrain	C	H	N	S	Ash	O (by difference)	C, maf
8R-164	Sewell (Marianna)	88.15	5.00	1.43	.77	.88	3.77	88.93
8R-174	Beckley (Maben)	87.79	4.70	1.60	1.12	1.29	3.50	88.94
8R-166	Sewell (Crab Orchard)	87.79	4.99	1.36	.59	1.68	3.59	89.29
9R-133	Lower Hartshorne	86.06	4.80	1.70	.73	3.87	2.84	89.52
8R-185	Upper Kittanning (Stineman No. 10)	87.64	4.84	1.44	.87	2.70	2.51	90.07
8R-181	Pocahontas No. 4 (McAlpine)	89.23	4.59	1.49	.81	1.15	2.73	90.27
8R-183	Lower Kittanning (Toth)	88.35	4.82	1.32	.74	2.34	2.43	90.47
8R-182	Pocahontas No. 3 (Buckeye No. 3)	89.57	4.67	1.25	.81	1.53	2.17	90.96
9R-119	Semianthracite (Bernice)[a]	79.22	3.43	1.01	.65	11.97	3.72	89.99
9R-118	Semianthracite (Western Middle)[b]	77.55	3.42	1.25	.85	14.36	2.57	90.55
8R-189	Dorrance anthracite	91.06	2.49	.96	.83	1.79	2.87	92.72
8R-188	Cannel coal[c]	79.93	6.44	1.69	1.05	4.55	6.34	83.74

[a] Whole coal, ca. 25 per cent vitrain (see text).

[b] Whole coal, over 90 per cent vitrain (see text).

[c] Whole coal.

Table 3. Results of dehydrogenation with phenanthridine as vehicle and 1 per cent palladium on calcium carbonate catalyst[a]

Run No.	Vitrain	C, maf	Per cent H_2 evolved[b]	H/100 C evolved[c]	H evolved, ml/g[d]	H/C atomic	O/C atomic
9R-32	Beulah-Zap (Zap Mine)	67.81	26.6	26.1	165	0.981	0.278
8R-190	Kincade	68.19	26.1	21.9	140	.842	.284
9R-40	Beulah-Zap (Beulah Mine)	68.93	39.2	38.0	244	.969	.258
9R-42	Roland-Smith (Wyodak)	70.19	26.7	27.2	178	1.016	.229
9R-3	Dietz (Big Horn)	70.84	33.9	28.9	191	.852	.238
9R-134	Laramie (Washington)	71.54	24.5	22.8	152	.928	.218
9R-132	Pioneer Canon No. 1	72.54	30.6	26.9	182	.879	.205
8R-156	Rock Springs	73.70	31.2	26.3	181	.842	.193
8R-161	Illinois No. 6 (Green Diamond)	75.65	39.0	34.8	246	.892	.149
8R-162	Illinois No. 6 (Mecco)	76.06	38.9	33.4	238	.860	.151
9R-34	No. 11 (Rainbow No. 7)	76.52	43.6	38.7	277	.888	.147
8R-184	Illinois No. 7 (Harmatten)	76.58	44.0	36.6	262	.832	.147
9R-41	Liberty	77.65	45.1	42.6	310	.946	.132
8R-186	Illinois No. 6 (Orient No. 3)	79.14	37.1	29.4	217	.792	.119
8R-159	Kentucky No. 9 (Pleasant View)	79.34	39.1	35.1	260	.899	.105
8R-158	Kentucky No. 9 (DeKoven)	80.69	35.4	31.2	235	.881	.0922
8R-143	Pittsburgh (Bruceton)	83.09	37.4	30.0	232	.802	.0786
8R-172	Pittsburgh (Bruceton)	83.09	37.1	29.8	231	.802	.0786
8R-147	Pittsburgh (Bruceton)	83.09	35.7	28.7	222	.802	.0786
8R-149	Pittsburgh (Bruceton)	83.09	37.0	29.7	230	.802	.0786
8R-160	Pond Creek (Majestic)	83.74	33.5	26.6	207	.793	.0762
8R-187	Powellton (Elk Creek No. 1)	85.05	35.3	26.3	209	.745	.0629
8R-157	Eagle (Kopperston)	86.19	29.0	22.6	182	.779	.0497
8R-165	Sewell (Lochgelley)	86.42	27.4	19.8	160	.723	.0529
8R-176	Lower Freeport (Coal Valley No. 7)	87.28	26.3	18.9	154	.718	.0415
8R-175	Lower Kittanning (Melcroft)	87.37	28.3	19.7	160	.698	.0384

Continued

Run No.	Vitrain	C, maf	Per cent H_2 evolved[b]	H/100 C evolved[c]	H evolved, ml/g[d]	H/C atomic	O/C atomic
8R-167	Lower Banner (Buccaneer)	88.39	24.0	17.5	144	.730	.0350
8R-164	Sewell (Marianna)	88.93	22.3	15.1	126	.676	.0321
8R-174	Beckley (Maben)	88.94	21.6	13.8	115	.638	.0299
8R-166	Sewell (Crab Orchard)	89.29	19.6	13.3	110	.678	.0307
9R-133	Lower Hartshorne	89.52	20.5	13.6	114	.665	.0248
8R-185	Upper Kittanning (Stineman No. 10)	90.07	21.3	14.0	118	.658	.0215
8R-181	Pocahontas No. 4 (McAlpine)	90.27	19.1	11.6	99	.613	.0230
8R-183	Lower Kittanning (Toth)	90.47	21.2	13.8	116	.650	.0206
8R-182	Pocahontas No. 3 (Buckeye No. 3)	90.96	22.5	14.0	119	.621	.0182
9R-119	Semianthracite (Bernice)	89.99	1.0	.5	5	.516	.0353
9R-118	Semianthracite (Western Middle)	90.55	2.4	1.2	11	.526	.0249
8R-189	Dorrance anthracite	92.72	0.0	0.0	0	.326	.0237
8R-188	Cannel coal	83.74	30.2	29.0	227	.960	.0595

[a] All runs used catalyst lot C-2842 except for 8R-147, 149 which used lot 7902. All runs used magnetic stirring. Samples were —200 mesh.

[b] Per cent of hydrogen in starting material which is evolved as H_2 gas.

[c] Atoms of hydrogen evolved as H_2 gas per 100 C atoms in starting material.

[d] Milliliters of hydrogen gas evolved per gram of m.a.f. starting material.

In Table 2, the four runs on Pittsburgh (Bruceton) vitrain gave some idea of the reproducibility which can be expected. The first two runs are with one batch of catalyst, the second pair is with another batch of catalyst. (All of the other runs listed were made with the same catalyst used for the first pair on Bruceton vitrain.)

Figure 1 shows the hydrogen evolution as a function of carbon content (maf) of the starting vitrain. In discussing this, it should be noted that the system used for classification of coals according to rank[19,20] is not based upon the chemical structure of the coal. Instead, rank classification is based partly upon fixed carbon (which is not directly related to the carbon content determined by a standard combustion analysis), partly upon volatile matter (which again does not correspond to any usual chemical determination), partly upon Btu content (which of course is related, but in no specific way, to chemical composition), and partly upon agglomeration properties. In Figure 1, for 24 vitrains, all obtained from coals ranging in rank from high volatile C bituminous to low-volatile bituminous, the data scatter about a reasonably smooth curve, in which the hydrogen evolution decreases gradually as the carbon content increases from 75.7 percent maf to 91.0 percent maf. Three other points, for semianthracite and anthracite, suggest that the hydrogen evolution decreases rapidly for ranks above low-volatile bituminous, reaching zero for an anthracite. This is reasonable; it is generally agreed that the coalification process involves an increase in the aromatic nature of the coal, and it is not surprising that, by the time anthracite is reached, there are no hydroaromatic structures remaining in the coal.*

The low rank vitrains do not seem to fall on the same curve defined by the vitrains from bituminous coals. Two of the three lignite vitrains and all five of the subbituminous vitrains fall well below the band established by the bituminous vitrains. This difference can be brought out more clearly by plotting the hydrogen evolved (H/100 C) against the atomic H/C ratio, or even better, against the atomic O/C ratio, of the vitrain. These two graphs are shown in Figures 2 and 3. In Figure 2, it can be seen that a plot of H/100 C against H/C ratio gives a fairly good straight line for the 24 bituminous vitrains. The solid line shown is a least squares straight line for these 24 points. The equation of the line is given by: $H/100\ C = 93.11\ (H/C) - 46.68$. For the straight line, the standard error of estimate is 2.54; the multiple correlation coefficient is 0.966. The dashed lines on either side of the solid line are at distances of twice the standard error of estimate; this means that 95 percent of the points should lie within the two dashed lines. Put in other words, if a point lies outside the area between the two lines formed by the twice standard error, there is only a probability of 1/20 that this point belongs with the set of data used to draw the least squares line. It can be seen that one subbituminous falls within the area; one lignite and one subbituminous fall barely outside; and the other three subbituminous and two lignites fall outside of the area.

---

*Cannel coal is included on the graph for the sake of completeness; it is an atypical whole coal and will not be discussed.

Figure 3 is a similar plot of H/100 C against the O/C ratio. For the 24 bituminous vitrains, the equation of the least squares straight line is: H/100 C = 190.5 (O/C) + 10.51. For this straight line, the standard error of estimate is 3.20; the multiple correlation coefficient is 0.946. Since the oxygen analysis is by difference, it is subject to a larger error than are the other analyses. The O/C ratio is therefore less accurate than the H/C ratio, and the increased standard error and decreased multiple correlation coefficient for the O/C curve (as compared with the H/C curve) is to be expected.

In Figure 3, it is seen that all of the lignite and subbituminous points fall well outside the area of twice the standard error. For any one lignite point, the probability of it belonging with the bituminous straight line is 1/20; therefore, it might be said that the probability of all three lignite vitrains belonging to the bituminous set is 1/8000, or 0.000125. There is an even lower probability that all five subbituminous vitrains belong with the bituminous set. It is significant that all eight points fall on the same side of the least squares straight line.

Another approach to the data has been to find the least squares straight line for the combined 32 points (24 bituminous, 5 subbituminous, and 3 lignites). The equation for this line (which is not shown in any figure) is: H/100 C = 59.1 (O/C) + 18.1. For this line, the standard error of estimate has increased to 7.25; the multiple correlation coefficient has decreased to 0.581. The standard error has thus more than doubled, and the multiple correlation coefficient has decreased greatly. This again indicates that the subbituminous and lignite vitrains are not part of the bituminous group.

From the above discussion we may draw the following conclusion: that there is a fundamental chemical difference between bituminous coals on the one hand, and subbituminous coals and lignites on the other hand. This difference manifests itself in the amount of hydrogen gas produced by catalytic dehydrogenation in the presence of a solvent. This, in turn, must be related to the general structure of the coal and in particular to its hydroaromaticity. Thus, although a high volatile C bituminous coal and a subbituminous A coal are distinguished from each other solely on the basis of calorific limits and agglomerating properties[19,20], there must nevertheless be a real difference in their chemical structure.

One may wonder why this demarcation is more obvious in the O/C plot (Figure 3) than it is in the H/C plot (Figure 2). One possible explanation is that for the entire bituminous group of coals, the hydrogen varies only slightly, being in the range of 4.5 to 6.0 percent; the carbon, however, varies from 68 to 90 percent. On the other hand, the oxygen and carbon values both vary considerably, and they vary in opposite directions; so that the O/C plot is probably a more sensitive indication of the structural change.

We come now to a consideration of the reasons for the sharp difference between the bituminous coals and lower rank coals, as shown by dehydrogenation. It is generally assumed that one of the major reactions of the coalification process is aromatization[21]. A decreasing yield of hydrogen obtained from coals of increasing rank can be simply explained on the basis of the higher rank coals being more aromatic. The low yield of hydrogen from low rank coals remains to be explained, however. At first thought, one is inclined to assume that a process of continual aromatization must by its very nature also be a process of dehydroaromatization; that is, aromatization should cause loss of

hydroaromatic structures. This is not true, however, because aromatization may take place by changes in structures which are not themselves hydroaromatic. A schematic representation (Figure 4) illustrates a possible series of reactions for this process. The (R) portion is intended to represent the bulk of a coal molecule, with attention focused on the ring system attached to it. In structure (I), there is no hydroaromatic system (as per the definition given above) and no normal dehydrogenation can take place; the angular methyl group slows aromatization[3], since it must either migrate or be eliminated before dehydrogenation can take place. If the natural coalification process involves an aromatization* we may presume that the methyl group either migrates from the angular 9-position, which permits easy dehydrogenation to (II) and then further dehydrogenation to (IV); or alternatively the methyl group is eliminated from (I) as methane, which permits dehydrogenation to (III) and then further dehydrogenation to (V). We may consider (I) as corresponding to lignites and subbituminous coals; high hydrogen but no hydroaromatic structures. We may consider (II) and (III) as corresponding to bituminous coals; in the process of coalification (I → II + III) there has been simultaneous formation of aromatic structures and of dehydrogenatable hydroaromatic structures. Thus we have a model for a process in which a non-hydroaromatic structure (I) is partly aromatized to give aromatic structures which also contain hydroaromatic rings. In a continuation of the coalification process, (II) and (III) are aromatized to (IV) and (V), which are completely aromatic (anthracite) and hence cannot give any hydrogen gas upon treatment with a dehydrogenation catalyst. This greatly simplified series of reactions, I → II → IV and I → III → V, offers a model for the seemingly peculiar situation in coal, where very low rank coals yield less hydrogen than do some higher rank, more aromatic coals.

It must be emphasized that the mechanism in Figure 4 is very schematic, is capable of many variations, and that several of these variations might proceed simultaneously. For example, the blocking group in the 9-substituted decalin structure (I) need not be methyl; it could be other groups, e.g., carboxyl. The blocked low rank structure (I) could be a 1,1-disubstituted cyclohexane type, which would undergo a similar series of transformations, or it could be a bridged six membered ring of the bicycloheptane type.

While this theory is not without its attractiveness, it may be asked whether coal can reasonably be expected to contain blocked structures of the type of (I). Coal is usually considered to arise by changes in the lignin and perhaps in the cellulose of the plant material which is its precursor[21]. Neither lignin nor cellulose contains polycyclic structures of the type of (I). Lignin contains benzene rings with reactive side chains. It is quite possible to visualize formation of condensed ring systems from cellulose, from lignin, or from an interaction of the two. Further, many plants contain appreciable amounts of other materials† more closely related in structure to (I). These include tricyclic diterpenes (abietic acid types), pentacyclic triterpenes (amyrin types), and tetracyclic sterols (stigmasterol and lanosterol types), which contain 1,1-dimethyl groups and angular methyl groups; and bicyclic terpenes

---

*For the purpose of this discussion we neglect the detailed mechanism of the coalification process and do not consider the loss of oxygen (perhaps as water) which takes place during coalification.

† The structures of some of these compounds are shown in Figure 5.

(pinene and camphane types) which contain bridged rings and 1,1-dimethyl groups. Also to be considered are some of the complex polycyclic alkaloids containing heterocyclic nitrogen, which occur in large amounts in some plants. It is possible that compounds of these types play a more important part in the coalification process than has heretofore been realized.

It remains to consider three possible sources of error in the hydrogen values obtained, all of which we believe are minor. These are interaction of the coal with the vehicle; cross-linking of coal structures during dehydrogenation, with formation of hydrogen*; and effect of phenolic groupings in the coal. It is known that the vehicle reacts with the coal, and it has so far proven impossible to remove all of the phenanthridine from a dehydrogenated coal[12]. Obviously, the reaction: Coal-H + Vehicle-H → Coal~Vehicle + H_2 would lead to a high value for hydrogen liberated. However, vehicle-vitrain blanks have been shown to be negligible and vehicle-catalyst blanks have been deducted, although this does not preclude interaction between coal and vehicle in the presence of catalyst. In addition, a reaction of the type: Coal-H + Vehicle-H → H-Coal~~~Vehicle-H would also account for the impossibility of removing vehicle from dehydrogenated coal and yet would not lead to hydrogen formation. Further experiments may throw some light on this process. We do know that one vehicle (1-azapyrene) liberates large amounts of hydrogen when heated only with a catalyst and that at least one other vehicle (2-azafluoranthene) gives very high values for hydrogen evolution from coal[11] which are almost certainly incorrect. Nevertheless, there is no real reason to believe that the phenanthridine contributes significantly to the evolved hydrogen, although this possibility must be kept in mind. Second, there is the question of "cross-linking," a somewhat vague term implying chemical reaction between two coal platelets. Here again, there are two possible reactions analagous to the two given above:

$$\text{Coal-H} + \text{Coal-H} \rightarrow \text{Coal}\sim\text{Coal} + H_2$$

$$\text{Coal-H} + \text{Coal-H} \rightarrow \text{H-Coal}\sim\sim\sim\text{Coal-H}$$

The first of these would lead to extra evolution of hydrogen, the second would not. The insolubilization of the coal which takes place during dehydrogenation could be used as an argument in favor of cross-linking; however, one might reasonably expect the dehydrogenated coal to be less soluble than the starting material in any case. Third, we have found that certain phenolic compounds yield hydrogen, probably by reactions of the type

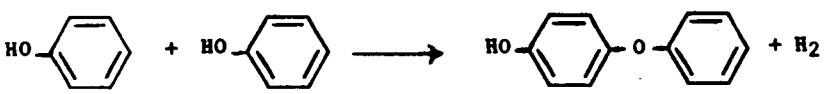

This reaction can be eliminated by the use of the silyl ethers in place of the free phenols. However, there is some evidence (based on the dehydrogenation of silyl ethers of phenols) that the phenolic groups in coal give little or no hydrogen, and that this side reaction is of slight consequence in coal dehydrogenation.

---

*Infrared spectra did not yield any useful information. The presence of vehicle; the small number of protons; and the difficulty of grinding; all contribute to loss of spectral information. A similar situation was found by Friedel and Breger[22] for a cross-polymerized coal formed by neutron irradiation.

REFERENCES

1 Lowry, H. H., editor, Chemistry of Coal Utilization (2 volumes). Wiley: New York, 1945

2 Lowry, H. H., editor, Chemistry of Coal Utilization, Supplementary Volume. Wiley: New York, 1963

3 Valenta, Z., in Technique of Organic Chemistry, volume XI, edited K. W. Bentley, pp. 581-642. Interscience: New York, 1963

4 Jackman, L. M., in Advances in Organic Chemistry, volume II, edited R. A. Raphael, E. C. Taylor, and H. Wynberg, pp. 329-366. Interscience: New York, 1960

5 Mazumdar, B. K., Chakrabartty, S. K., De, N. G., Ganguly, S., and Lahiri, A. Fuel, Lond. 1962, 41, 121

6 Peover, M. E. J. Chem. Soc., Lond. 1960, 5020

7 Mazumdar, B. K., Bhattacharyya, A. C., Ganguly, S., and Lahiri, A. Fuel, Lond. 1962, 41, 105; Peover, M. E., Fuel, Lond. 1962, 41, 110

8 Mazumdar, B. K., Choudhury, S. S., and Lahiri, A. Fuel, Lond. 1960, 39, 179

9 Shishido, K. and Nozaki, H. J. Soc. Chem. Ind. Japan 1944, 47, 819. Eberhardt, M. K. Tetrahedron 1965, 21, 1383. Eberhardt, M. K. Tetrahedron 1965, 21, 1391. Raley, J. H., Mullineaux, R. D. and Bittner, C. W. J. Am. Chem. Soc. 1963, 85, 3174. Mullineaux, R. D. and Raley, J. H. J. Am. Chem. Soc. 1963, 85, 3178. Slaugh, L. H., Mullineaux, R. D. and Raley, J. H. J. Am. Chem. Soc. 1963, 85, 3180. King, R. W. Hydrocarbon Processing 1966, 45, 189

10 Rabindran, K. and Tilak, B. D. Proc. Indian Acad. Sci. 1953, 37A, 557

11 Raymond, R., Wender, I. and Reggel, L. Science 1962, 137, 681

12 Reggel, L., Wender, I., and Raymond, R. Fuel, Lond. 1964, 43, 229

13 Baxter, R. A., Ramage, G. R. and Timson, J. A. J. Chem. Soc. (Suppl. Issue No. 1) 1949, S30

14 Albert, A., Brown, D. J. and Duewell, H. J. Chem. Soc. 1948, 1284

15 Horning, E. C., Horning, M. G. and Walker, G. N. J. Am. Chem. Soc. 1948, 70, 3935

16 Grob, C. A. and Hofer, B. Helv. Chim. Acta. 1952, 35, 2095

17 Horrobin, S. and Young, R. J. British Patent 745,400, 1956; Chem. Abstr. 1956, 50, 16875e

18 Fieser, L. F. and Fieser, M. Advanced Organic Chemistry p. 645. Reinhold: New York, 1961

19 Ode, W. H. and Frederick, W. H. United States Department of the Interior, Bureau of Mines, 'The International Systems of Hard-Coal Classification and Their Application to American Coals.' Rept. of Inv. 5435, pp. 3-12, U. S. Government Printing Office, 1958

20 1965 Book of ASTM Standards, Part 19. Gaseous Fuels; Coal and Coke. Page 74. American Society for Testing and Materials: Philadelphia, Pa.

21 Van Krevelen, D. W. Coal, pp. 101-109, 445-452. Elsevier: Amsterdam, 1961

22 Friedel, R. A. and Breger, I. A. Science 1959, 130, 1762-1763

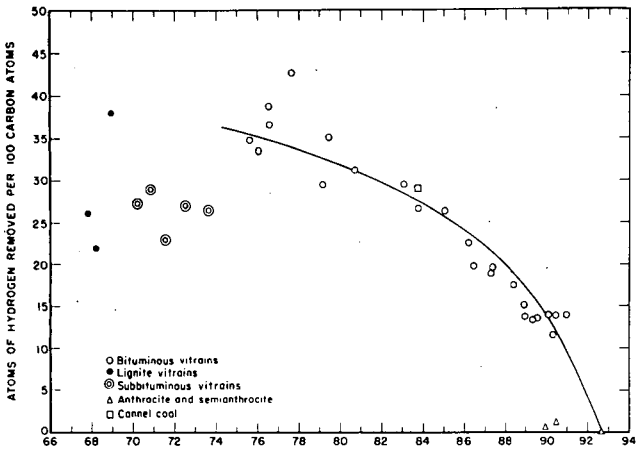

Figure 1.– Dehydrogenation of vitrains and cannel coal with 1 percent palladium on calcium carbonate catalyst, phenanthridine vehicle

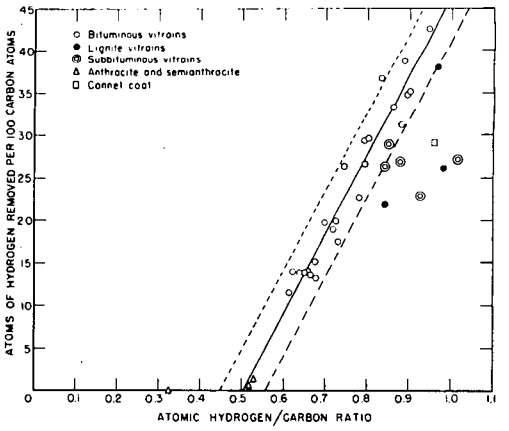

Figure 2.- Dehydrogenation of vitrains with one percent palladium on calcium carbonate catalyst, phenanthridine vehicle, plotted as a function of the atomic H/C ratio. The solid line is the least squares straight line for the 24 bituminous vitrains. The dashed lines are drawn at a distance of twice the standard error of estimate.

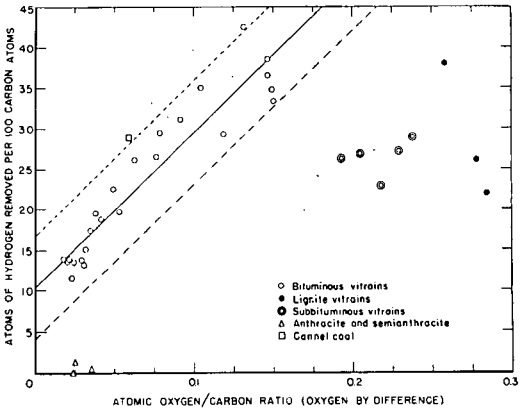

Figure 3.- Dehydrogenation of vitrains with one percent palladium on calcium carbonate catalyst, phenanthridine vehicle, plotted as a function of the atomic O/C ratio (oxygen analysis by difference). The solid line is the least squares straight line for the 24 bituminous vitrains. The dashed lines are drawn at a distance of twice the standard error of estimate.

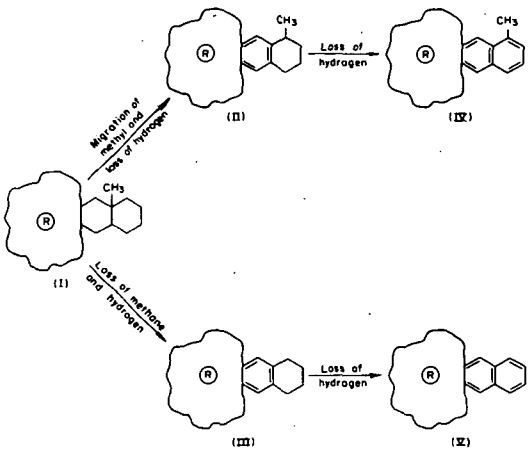

Figure 4.–Schematic representation of the coalification process.

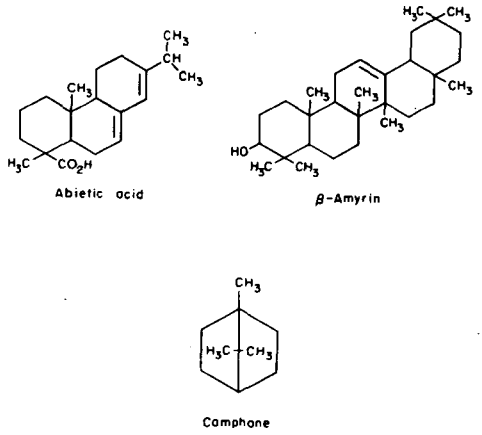

Figure 5–Structures of compounds found in plants which may be coal precursors (see text)

A RAPID, SIMPLE METHOD FOR THE DETERMINATION OF THE THERMAL CONDUCTIVITY OF SOLIDS

Neal D. Smith
Fay Fun
Robert M. Visokey

UNITED STATES STEEL CORPORATION
Research Center
Monroeville, Pennsylvania

The rational design of equipment such as shaft coolers, heaters, and rotary kilns for the heating and cooling of solids requires that the thermal properties of the solids be known. Thermal conductivity is one of these properties that to measure necessitates elaborate equipment and time-consuming techniques.

A rapid, simple method has been developed for determining the thermal conductivity of solids. The solids can be either porous or nonporous and of either high or low conductivity. If high-conductivity materials are tested, then both the thermal conductivity and heat capacity can be simultaneously measured by the method.

The procedure involves preparing a cylindrical briquette of the test solid that has a thermocouple located in the center. This briquette is heated to a constant temperature after which it is suspended in an open-end glass tube and cooled by a known flow of nitrogen or any other nonreactive gas. The thermal conductivity is then computed from a digital computer comparison of the cooling curves for the test solid versus a reference solid of known thermal properties and similar size that has undergone the same heating and cooling cycle. The method was validated by using the known thermal properties of lead, aluminum, and silver and computing the theoretical cooling curves. The theoretical curves were in close agreement with the experimentally measured cooling curves for these materials.

Theory

The mathematical basis for determining thermal conductivity by the described method is discussed in a paper by Newman[1] and is summarized as follows. Consider a cylindrical briquette as shown in Figure 1. The differential equation for unsteady state heat transfer by conduction in the x-direction is (see nomenclature for definition of the variables):

$$\frac{\partial t}{\partial \theta} = \alpha\left(\frac{\partial^2 t}{\partial x^2}\right) \qquad (1)$$

For a briquette of thickness 2a, the central plane being at $x = 0$ and assuming:

1) uniform temperature at the start of cooling of the initially hot briquette

then $t = t_o$ when $\theta = 0$ (2)

2) the final temperature of the briquette will be the temperature of the surroundings:

therefore $t = t_s$ when $\theta = \infty$ (3)

3) there is no heat flow across the central plane because of symmetry:

consequently $-k \left(\frac{\partial t}{\partial x}\right) = 0$ at $x = 0$ (4)

The heat balance on the briquette surface is made by equating heat transferred to the surface by conduction with heat transferred from the surface by convection. In differential form, the heat balance is:

$$-k \left(\frac{\partial t}{\partial x}\right) = h\ (t - t_s) \text{ at } x = \pm a \quad (5)$$

Newman[1] showed that the solution to Equations (1) through (5) expressed in terms of a dimensionless temperature ratio Y_x is:

$$Y_x = \frac{t - t_s}{t_o - t_s} = \sum_{n=1}^{\infty} A_{ne}^{-(\beta_n^2 X_a)} \cos\left(\beta_n \frac{x}{a}\right) \quad (6)$$

where $A_n = \dfrac{m_a}{(1+\beta_n^2\ m_a^2 + m_a)\ \cos\beta_n}$ and

β_n are defined as the first, second, third, etc., roots of the transcendental equation:

$$\beta_n \tan \beta_n - 1/m_a = 0 \quad (7)$$

The surface to solid thermal resistance ratio, m_a, is defined as:

$$m_a = k/ha \quad (8)$$

and X_a is defined as: $X_a = \alpha\theta/a^2$ (9)

where the thermal diffusivity is: $\alpha = k/\rho\ C_p$ (10)

Similarly, considering radial heat transfer, the radial briquette heat balance is

$$\frac{\partial t}{\partial \theta} = \alpha\left[\frac{\partial^2 t}{\partial r^2} + \frac{1}{r}\frac{\partial t}{\partial r}\right] \quad (11)$$

The initial condition equation is:

$$t = t_o \text{ when } \theta = 0 \quad (12)$$

The final temperature equation is:

$$t = t_s \text{ when } \theta = \infty \quad (13)$$

The boundary condition equations are:

$$-k \left(\frac{\partial t}{\partial r}\right) = 0 \text{ at } r = 0 \quad (14)$$

and $$-k\left(\frac{\partial t}{\partial r}\right) = h\,(t-t_s) \text{ at } r = R \tag{15}$$

Solving Equations (11) through (15) gives:

$$\frac{t-t_s}{t_o-t_s} = 2\sum_{n=1}^{\infty} A_n\, e^{-(\beta_n^2\ X_r)}\ J_o(\beta_n \frac{r}{R}) = Y_r \tag{16}$$

where

$$A_n = \frac{m_r}{(1+\beta_n^2 m_r^2)\ [\ J_o(\beta_n)]} \tag{17}$$

and β_n are the first, second, third, etc., roots of the equation:

$$\beta_n J_1\ (\beta_n) - 1/m_r J_o(\beta_n) = 0 \tag{18}$$

The surface to solid thermal resistance ratio, m_r is

$$m_r = k/hR \tag{19}$$

and $$X_r = \alpha\theta/R^2 \tag{20}$$

The complete differential equation for the case shown in Fig. 1 is:

$$\frac{\partial t}{\partial \theta} = \alpha\left(\frac{\partial^2 t}{\partial r^2} + \frac{1}{r}\frac{\partial t}{\partial r} + \frac{\partial^2 t}{\partial x^2}\right) \tag{21}$$

and the solution to Equation (21) is:

$$Y = \frac{t-t_s}{t_o-t_s} = Y_r \cdot Y_x \tag{22}$$

If the center temperature defined at $r = 0$, $x = 0$ is t_c, then Equation (22) becomes:

$$Y_c = \frac{t_c-t_s}{t_o-t_s} = Y_r \cdot Y_x \tag{23}$$

where Y_r and Y_x are evaluated at $r = 0$ and $x = 0$.

The preceding mathematical analysis shows that the rate of cooling, or change in center temperature for a cylindrical briquette is a function of time (θ), density (ρ), thermal conductivity (k), the surface heat transfer coefficient (h), specific heat (C_p) and the briquette dimensions as expressed by Equation (23).

The experimental technique can now be described in terms of the previous discussion. If the change in center temperature with time is measured experimentally for a material of known thermal and physical properties (standard briquette), the surface heat transfer coefficient can be calculated from Equation (23), since it is the only unknown.

The surface heat transfer coefficient (h) is a function of the flow rate of the cooling gas and the geometry and size of the briquette. It is independent of all other physical, thermal, or chemical properties of the briquette. Therefore, any other briquette having similar dimensions and cooled at the same flow rate will have the same value for (h).

Once (h) has been determined using the standard briquette, the thermal conductivity of any test material can be determined from Equation (23) since all other variables are known.

A computer program has been written which through an iterative process determines the best value of (h) which makes the calculated values for the dimensionless temperature ratio equal to the experimental values obtained when the standard briquette is cooled.

With (h) determined, another computor program is run for the test specimen. Thermal conductivity is now the unknown variable and through another iterative scheme, the best value for (k) that makes the calculated and experimental values for the temperature ratios equal is found.

The input data for both programs consist of density, specific heat, time, briquette dimensions, and several experimental values for the temperature ratio. The output from the first program (standard) is the best value for (h). Using this value for (h), the second program used to determine the k value for any test material. If a highly conductive material is tested, then it is possible to determine its heat capacity since the solid thermal resistance will be small compared to the surface thermal resistance. A transient heat balance can be written for the test solid cooling in a stream of coolant gas.

$$V\rho C_p \frac{dt}{d\theta} = hA\ (t - t_s) \tag{24}$$

In the above equation, $t = t_c$ since the thermal gradient in the solid is neglected. Integrating Equation (24) and using the dimensionless temperature ratio, Y_c gives:

$$Y_c = \exp -(hA/\rho C_p V)\,\theta \tag{25}$$

Thus, if the internal solid thermal resistance is negligible, a plot of the experimental Y_c versus θ data on semilog paper should be linear as shown by Equation (25). The heat capacity, C_p, can be calculated from the slope of the line for Y_c versus θ since (h) is the same as for the standard briquette and the density, ρ, and total surface area, A, for the test material are also known.

Materials and Experimental Work

A primary advantage of the transient technique for determining thermal conductivities is the ease and swiftness with which the experiment can be conducted.

In so far as sample preparation is concerned, any solid that can be briquetted, cast, or fabricated around a centrally located rigid.

thermocouple (x = 0; r = 0) may be tested. Finished test sample cylinders should be approximately one inch in diameter, and one-half inch in height; however, other dimensions can be used.

Experimental Apparatus

The experimental apparatus (see Figure 2) consists simply of a 3-inch diameter glass tube approximately 3 feet in length. One end of the tube is completely stoppered except for a one-half inch circular opening through which the coolant gas flows. The other end of the tube is open to the atmosphere. A small electric furnace is used to heat the briquette, and an automatic single point temperature recorder connected to the embedded thermocouple is used to measure the center temperature of the briquette.

Experimental Procedure

The experimental procedure is the same for both the standard and test briquettes. Either the standard (aluminum was chosen since its thermal properties are well established), or the test briquette is connected to the temperature recorder by way of the thermocouple leads. The briquette is heated until the center temperature has reached a constant, predetermined value. The briquette is then quickly removed from the furnace and suspended in the cooling tube with the cooling gas flowing at a constant rate. The briquette is usually cooled to the temperature of the cooling gas within 20 minutes.

Data Processing

For the standard briquette, the experimental dimensionless temperature ratio versus time data points for the standard briquette along with the known thermal properties are used to calculate the surface coefficient, h, in the following manner. A digital computer program is written to compute Y_C from Equations (6) through (23). By iteration and assuming various values of (h), the computed values of Y_C can be made to converge on each of selected experimental Y_C versus θ data points. Thus, for a selected data point, the best experimental (h) is that which when used in Equations (8) and (19) results in equal values for the computed and experimental Y_C values.

For low conductivity test materials, the same method is used to determine the best experimental value of k by using the h determined for the standard and the other properties of the test material. If the test material is a good conductor as discussed in the theory section, then experience has shown that h should be computed from the experimental cooling curve and then this value is used to compute k by the same method as for low conductivity test materials.

Discussion and Results

Three briquettes of aluminum, lead and silver were made to test the validity of the experimental technique since their thermal properties were available from the literature as shown in Table I.

Sintered, dense hematite (Fe_2O_3) and a briquette of porous carbon made from a partially devolatized coal were used as test materials. For these materials, all properties except the thermal conductivities shown in Table I were previously measured. Cooling curves for each briquette were measured for a nitrogen flow rate of 0.9 scfm. Surface heat transfer coefficients for lead, silver and aluminum were calculated by the method discussed in the data processing section. For these materials, the literature conductivity values were used to calculate the surface coefficient. Table I shows that the calculated or experimental h values for each metal are nearly identical. This result is consistent with the theoretical basis of the experiment and may be considered as establishing the validity of the method. Also as additional evidence, aluminum was chosen as the standard and k values for lead and silver were calculated using the h value for aluminum. Table I shows that the calculated or experimental k values were within 0.5 percent of the literature values. The conductivities for hematite and porous carbon were calculated using aluminum as the standard. Figure 3 shows the experimental data points with the solid lines calculated from the theory. Note that the line for the carbon is curved whereas those for the metals and hematite are linear. As discussed previously, a linear cooling curve is obtained if the surface to solid thermal resistance ratios are relatively large. Note that for the metals, lead which has the lowest conductivity and thermal diffusivity cooled the fastest. This result is explained by examination of eqn. (25) which shows that for similar gas flows and briquette dimensions, the rate of cooling for different materials is determined by the heat content, ρC_p. It can be seen in Table I that the heat content for lead is the lowest of all metals tested.

Summary

A rapid, simple method for determining thermal conductivity for a solid has been developed. The solid can be either porous or nonporous and of either high or low conductivity. If high conductivity materials are tested, then both conductivity and heat capacity can be simultaneously measured from one cooling experiment. The method was validated by using the known thermal properties of lead, aluminum, and silver and the experimental cooling curves in a comparison with the computed results.

References

1. Newman, A. B., Industrial and Engineering Chemistry, Vol. 28, 1936, pp. 545-548.

Nomenclature

a = Half height of briquette; ft

A = Area; ft^2

A_n = Coefficient in infinite series solution for temperature distribution in briquette

C_p = Specific heat; BTU/lb °F

h = Surface heat transfer coefficient; BTU/hr ft^2 °F

k = Thermal conductivity; BTU/hr ft^2 °F/ft

m_a = Axial surface resistance; dimensionless

m_r = Radial surface resistance; dimensionless

R = Maximum radius of briquette; ft

r = Radius of briquette; ft

t = Temperature; °F

t_c = Temperature at center of briquette; °F

t_o = Initial temperature of briquette; °F

t_s = Temperature of cooling gas; °F

x = Distance of direction; ft

$X_a = \frac{\alpha\theta}{a^2}$ Dimensionless time parameter for axial component

$X_r = \frac{\alpha\theta}{R^2}$ Dimensionless time parameter for radial component

Y_x = Symbol for temperature ratio, axial component; dimensionless

Y_r = Symbol for temperature ratio, radial component; dimensionless

α = $(k/\rho C_p)$ Thermal diffusivity; ft^2/hr

θ = Time; minutes or hours

ρ = Density; lb/ft^3

Table I

THERMAL AND PHYSICAL PROPERTIES FOR THE BRIQUETTES

	Aluminum	Silver	Lead	Hematite	Porous Carbon
a	.01842	.02059	.01842	.01842	.01958
R	.04208	.04210	.04117	.04208	.04121
ρ	168.50	655.20	707.43	306.00	75.0
C_p	.2273	.0578	.0306	.2090	.2360
ρC_p	38.30	39.31	21.65	63.95	17.70
h (experimental)	5.58	5.70	5.60	5.58	5.58
k (experimental)	Not Measured	240.3	18.99	12.10	.0307
k (literature)	121.7	240.0	19.00	none	none
α (experimental)	3.178*	6.113	.8770	.1892	.00173

*Average of literature sources

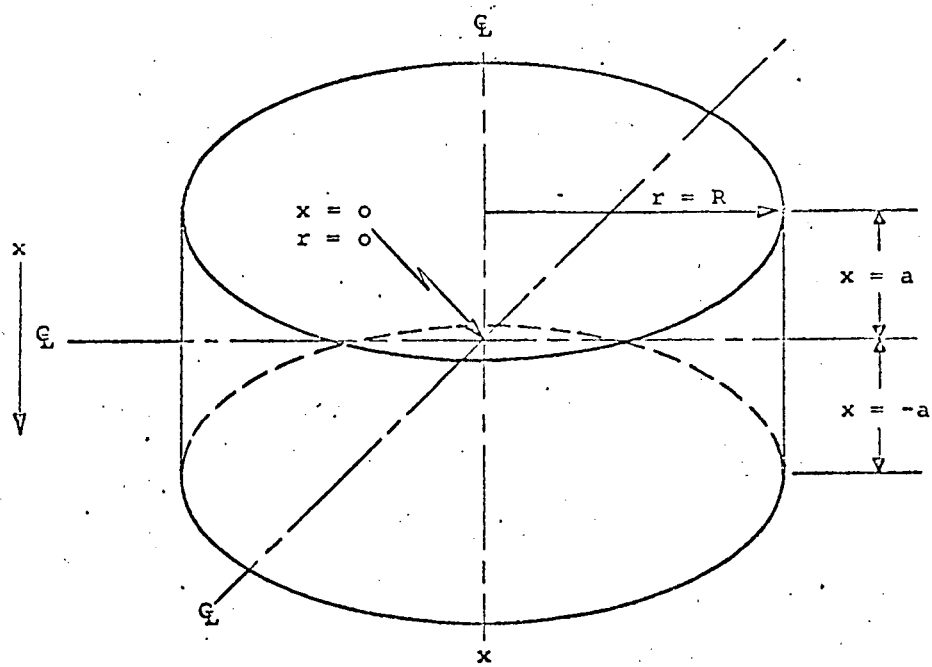

STANDARD CYLINDRICAL BRIQUETTE

Figure 1

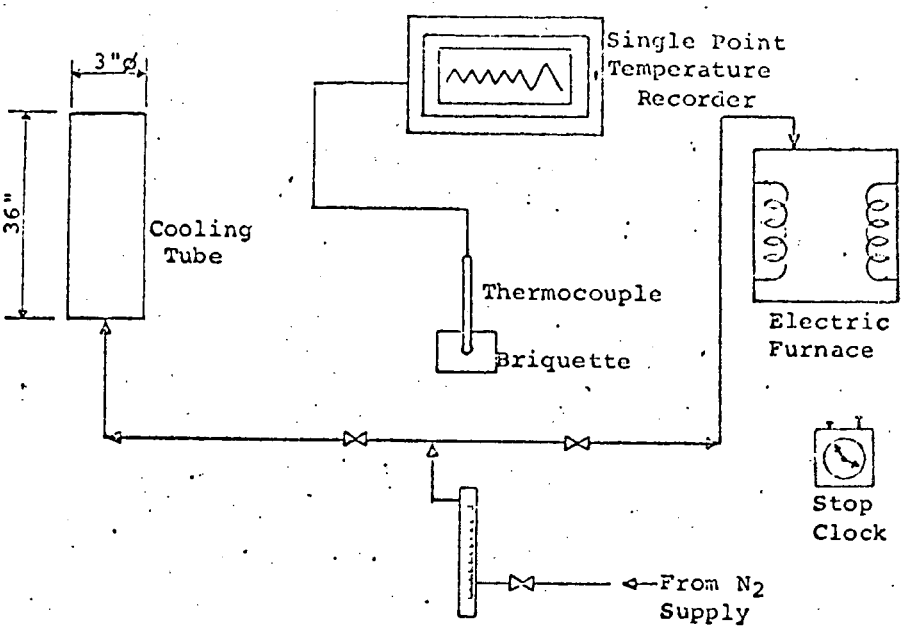

EXPERIMENTAL APPARATUS

Figure 2

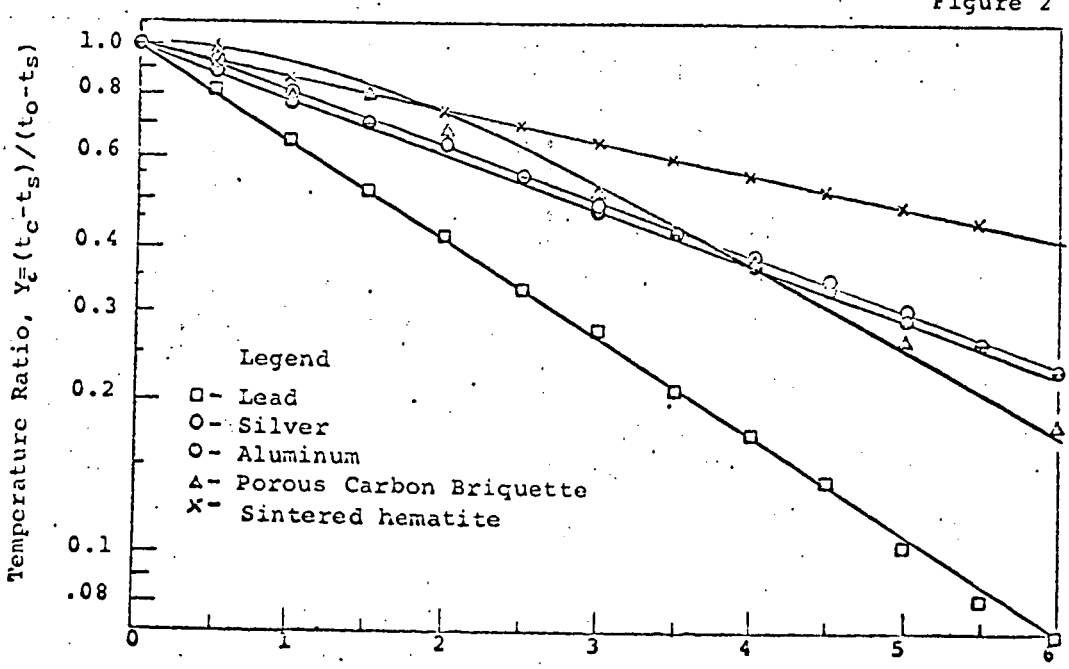

Theoretical Cooling Curves and Experimental Points for five Materials

Figure 3